School of Chemistry
Yr Ysgol Cemeg

Computational Nano-Materials And Catalysis: Modelling of Structural and Magnetic Properties of Bare and Ligand-Protected Cobalt Nanoparticles

Barbara Farkaš

Supervisor: Prof Nora H de Leeuw

A thesis submitted to Cardiff University
In partial fulfillment of the requirements for the Degree of
Doctor of Philosophy (PhD)

Cardiff University, School of Chemistry
July, 2021

This work is part of the research programme of the *Nanomaterials and catalysis*, which was financially supported by the Engineering and Physical Sciences Research Council (EPSRC) and through a Research Scholarship from the School of Chemistry, Cardiff University.

This work was performed using the computational facilities of the Advanced Research Computing @Cardiff_(ARCCA) Division, Cardiff University and ARCHER, the UK's national high-performance computing service, which is funded by the Office of Science and Technology through EPSRC's High End Computing Programme.

For, You see, so many out-of-the-way things
had happened lately that very few things
indeed were really impossible.
- Lewis Carroll

Table of Contents

List of Figures

List of Tables

The work described in this thesis and other related works have been published in the following scientific publications:

1. **Farkaš B.**, de Leeuw N.H., AuCo nanoparticles: magnetisation, ordering, and morphology trends predicted by DFT, (2021) *to be submitted*

2. **Farkaš B.**, de Leeuw N.H., A Perspective on Modelling Metallic Magnetic Nanoparticles in Biomedicine: From Mono-Metals to Ligand-Protection and Nano-Alloys *Materials*, (2021) **14** 3611

3. **Farkaš B.**, de Leeuw N.H., Effect of Coverage on the Magnetic Properties of -COOH, -SH, and -NH_2 Ligand-Protected Cobalt Nanoparticles *Nanoscale*, (2021) **13** 11844-11855

4. **Farkaš B.**, Terranova U., de Leeuw N.H., The Mechanism Underlying the Functionalisation of Cobalt Nanoparticles by Carboxylic Acids: a First-Principles Computational Study, *Journal of Materials Chemistry B*, (2021) **9** 4915-4928

5. **Farkaš B.**, Perry C.B., Jones, G., de Leeuw N.H., Adsorbate-Induced Segregation of Cobalt from PtCo Nanoparticles: Modeling Au Doping and Core AuCo Alloying for the Improvement of Fuel Cell Cathode Catalysts *Journal of Physical Chemistry C*, (2020) **124** 18321-18334

6. **Farkaš B.**, Terranova U., De Leeuw N.H., Binding modes of Carboxylic Acids on Cobalt Nanoparticles *Physical Chemistry Chemical Physics*, (2020) **22** 985

7. **Farkaš B.**, De Leeuw N.H., Towards a morphology of cobalt nanoparticles: size and strain effects *Nanotechnology*, (2020) **31** 195711

8. **Farkaš B.**, Santos-Carballal D., Cadi-Essadek A., de Leeuw N.H., A DFT+U Study of the Oxidation of Cobalt Nanoparticles: Implications for Biomedical Applications *Materialia*, (2019) **7** 100381

I also co-authored scientific publications listed below:

1. **Farkaš B.**, Živković A., Uahango V., de Leeuw N.H., Dzade N.Y., Stabilisation of ZnP_2 Nanoparticles through 4-Amino-Thiophenol Functionalisation, (2021) *submitted*

2. **Farkaš B.**, Živković A., Uahango V., de Leeuw N.H., Dzade N.Y., Insights from DFT Calculations into the Effects of the Adsorption and Dissociation of Water on the Surface Properties of ZnP_2 Nanocrystals, *Physical Chemistry Chemical Physics*, (2021) *under review*

3. Živković A., **Farkaš B.**, Uahango V., de Leeuw N.H., Dzade N.Y., First-Principles DFT Insights into the Structural, Elastic, and Optoelectronic Properties of α and β-ZnP_2: Implications for Photovoltaic Applications *Journal of Physics: Condensed Matter*, (2019) **31** 265501

Acronyms

AIMD	Ab Initio Molecular Dynamics
BOMD	Born Oppenheimer Molecular Dynamics
CA	Contrast Agent
CPMD	Car-Parrinello Molecular Dynamics
CV	Collective Variable
DFPT	Density Functional Perturbation Theory
DFT	Desnity Functional Theory
DOS	Density of State
GGA	Generalised Gradient Approximation
GTH	Goedecker, Teter, and Hutter (basis set)
HF	Hartree-Fock (method)
IR	Infrared (spectroscopy)
KS	Kohn-Sham (equations)
LB	Localised Basis Set
LDA	Local Density Approximation
LSDA	Local Spin-Polarised Density Approximation
MAE	Magnetic Anisotropy Energy
MC	Monte Carlo
MCA	Magneto-Crystalline Anisotropy
MD	Molecular Dynamics
mNPH	Magnetic Nanoparticle Hyperthermia
MRI	Magnetic Resonance Imaging
NEB	Nudged Elastic Bands
NMR	Nuclear Magnetic Resonance
NPs	Nanoparticles
PAW	Projector-Augmented Wave Method
PBE	Perdew, Burke, Ernzerhof (functional)
PW	Plane Waves (basis set)
SAR	Specific Absorption Rate
SCF	Self-Consistent Field
SHP	Specific Heating Power
SOC	Spin-Orbit Coupling
TS	Transition State
USPP	Ultrasoft Pseudopotentials
VASP	Vienna Ab Initio Simulation Package
WHO	Wolrd Health Organisation

Acknowledgments

One of the secrets of life is that all that is really worth doing,
is what we do for others.
- Lewis Carroll

First and foremost, I would like to express my sincere gratitude to my supervisor Prof Nora H. de Leeuw for her continuous support, incentives, and guidance in all the time of my PhD studies. For all the opportunities she brought my way and all the challenges she put in front of me as they have shaped my passion to explore the boundaries and changed my perspective on overcoming them.

My sincere thanks also goes to the rest of my research team and cherished new and not-so-new connections, which count many talented individuals each contributing in their own unique ways to where I currently stand in the research community. I would like to thank research groups of the University of Namibia and Johnson Matthey Research Centre in Pretoria for a chance to share my enthusiasm and knowledge, gain invaluable experience, and contribute to the internationally excellent science.

I am incredibly grateful to have had this PhD journey filled with people who went above and beyond to never stop believing in me, providing inspiration, motivation, and, above all, encouragement. To my parents and my sister for their unconditional love and patience in the time I have been away from them during this stage of my life. To new friends and old friends, to Stjepan, Daniel, Ieva, Jonas, and Simona, for there is no better feeling in the world than the feeling of belonging. To all of you, thank you for your endless support, selflessness, and understanding which have made the impossible things possible. Thank you for sharing the good times and bearing with me in not-so-good times. Thank you for helping me grow as a person. Thank you for being the sun in my sky, the wind in my back, and the sense in my nonsense. Thank you for making me see magic in ordinary things.

A big thank you also goes to my examiners Dr Ricardo Grau-Crespo and Dr David Willock for their efforts in evaluating this work, and for the fruitful discussion which has most certainly deepened my understanding in this field and improved the scientific messages conveyed.

And to all of you reading this thesis, thank you for appreciating my efforts to make a small contribution to the scientific world, and may it sparkle inspiration for something exceptionally magical.

This thesis is dedicated to those
who can find magic every day in what they already have.

Abstract

Up to now, cancer treatments have been based on the combination of chemotherapy and radiation, which are on a day-to-day basis experiencing a rise of serious risks as many tumour types are developing specific refractory mechanisms. For cancer patients, these so-called 'side effects' can seem to take over daily life or seriously contribute to the deterioration of their medical condition. Recently, hyperthermia directed specifically to cancer cells through the use of relaxation mechanisms of magnetic nanoparticles resulted in the localised heat generation and showed a promising shift in reducing the share of healthy areas exposed to the treatment sources. Although magnetic nanoparticle hyperthermia has imposed many challenges and requirements and is still a highly experimental cancer treatment, new research shows that the therapy is, in fact, clinically effective. Given the overall goal of generating the heat locally within the tumour, the primary objective of the therapy is in the nanoparticle design - maximising the power deposition. Nanoparticles that are most easily adjusted *in vivo* and have the best biocompatibility (magnetic oxides), however, are not necessarily the ones that provide the greatest heating effects. The effectiveness of the therapy, as well as its possible adverse effects, depend on a number of physiochemical characteristics of the nanoparticles, such as chemical composition, size, shape, as well as on their magnetic behaviour.

With the highest magnetisation of transition metals and most metal oxides, cobalt is offering a promising power dissipation within the size limitations of the cancer diagnostic and treatments therapies. The aim of this thesis is to investigate theoretically, by means of density functional theory and *ab initio* molecular dynamics and metadynamics, some of the current challenges in employing cobalt nanoparticles as biomedical agents. In particular, the focus will be on the physical and magnetic properties that are related to the imaging and heating efficiency, by unfolding the connection between the size, structure, reactivity, and magnetic behaviour as the most important relationship towards making reliable predictions on the dependence of desired properties on nanoparticle morphology. Coating and alloying effects will also be contemplated as changes in the magnetic behaviour can be induced by an active interplay between the surfactants and nanoparticle or between different metallic phases. This constitutes a necessary gateway before attempting a rational, engineered tuning of the magnetisation of cobalt nanoparticles for real-life applications. The idea is to build a sound model for further theoretical simulations on magnetic nanoparticles, and to provide experimentalists with useful guidelines for the design of magnetic nanocomposites with improved hyperthermia efficiencies.

INTRODUCTION

You know what the issue is with this world?
Everyone wants some magical solution to their problem
and everyone refuses to believe in magic.
- Lewis Carroll

Cancer remains one of the most devastating diseases of our time, with worldwide cancer cases predicted to increase by 50 % in the next two decades (World Health Organisation, WHO [1]), making new and improved treatments amongst highest priorities of biomedical research. Although detection and therapies are presently much easier and more effective than they were in the past, most of the used methods still have limited efficiency and wreak havoc in healthy tissues.[2] In order to destroy only targeted cancer cells whilst leaving the surroundings intact, more intelligent approaches need to be developed beyond drug injections and chemotherapy. Nanomaterials are offering a promising solution, due to their exceptional properties, tunable size, and simple modification strategies, providing controllable means for targeting and interacting with specific cells.[3] Magnetic nanoparticles (mNPs) have been especially interesting in this field - with dimensions proportional to the size of entities controlling body processes, and through the easy manipulation of optic, mechanic, magnetic, and electronic properties, they can be readily utilised in biomedicine and adjusted to create perfect weapons against malignant disease.[4] Novel methods for locating, tracking, and treating cancer which are exploiting the advantageous properties of mNPs are contrast agent-promoted magnetic resonance imaging (MRI) and magnetic nanoparticle hyperthermia therapy (mNPH). The latter is probably the best example of the efficacy of mNPs, where the obsolete *outside-in* treatments were transformed to *inside-out* therapies as the source of heating was moved into the targeted cells, minimising the temperature gradient in surrounding tissues.[5]

Although mNPH has been approved in Europe to target brain tumours [6], it is still not widely utilised. In the hospitals around the world, this treatment is still awaiting an approval. The lack of widespread adaptation can be attributed to demanding requirements, which lead to the gaps in development of optimal mNPs as hyperthermia agents. Finding the perfect match between mNP type, size, and desired properties is still the biggest challenge for this new area of research. In recent years, many experiments have been conducted to validate the performance of different mNPs. The most thoroughly studied are iron oxide NPs due to the favourable biocompatibility, but their relatively low

saturation magnetisation requires use of large particles, high concentrations, and strong external fields, usually harmful for humans, to achieve sufficient heating effects.[7] Great efforts have been put into optimising the heating efficiency of magnetite and maghemite NPs - alternations in shape such as nanocubes [8, 9], core-shell nanostructures [10, 11], and multicore NPs [12] were all reported to result in the unprecedented magnetic heat generation, with heat dissipation per unit mass five to ten times higher than for previously developed NP structures. Unfortunately, with all these modifications, performance of iron oxides seems to have reached its limit. Utilisation of materials with better magnetic properties is therefore envisioned, since it would allow for a significant improvement in the efficacy of hyperthermic treatments.

High saturation magnetisation of transition metal mNPs means greater power at lower concentrations. The utmost drawback is reactivity of metals, especially towards oxidising compounds, which can easily lead to compositional and structural changes and, ultimately, to an inversion of initial magnetic properties. This behaviour is a complex problem when employing metallic NPs in biomedicine, hence, it is not surprising an alternative path was considered prior to their implementation. Many recent studies have revealed a promising shift by doping iron oxides with transition metals such as cobalt, resulting in mNPs of smaller diameters with improved magnetic properties: up to a fourteen-fold increase in MRI contrast and a fourfold enhancement in mNPH effects.[13, 14] Overall efficiency is, despite major advancement, still insufficient, and, although pure metallic mNPs have not been the first choice because of high reactivity, their performance by far exceeds any metallic oxide (doped or undoped) and should be employed. Therefore, new modification processes, which will provide protection against oxidation and retain the magnetic properties of metallic mNPs, are becoming crucial in the progress of their implementation for biomedical applications.

Experimentally obtained heating rates for different materials [15] accentuated iron and cobalt NPs as promising candidates for the novel cancer therapy. Despite higher heating rates of Fe NPs over the cobalt counterparts, their peak is observed at diameters of ∼12-13 nm, which surpasses Co NPs maximum for about 5 nm. Once coupled with modification agents, such larger particles would quickly get endocytosed by macrophages and removed from the organism. Co NPs therefore offer a wider range of functionalisation strategies, which can be conducted to a greater extent and coupled with additional features like drug delivery with reduced risk of immune system recognition. To date, Co NPs have mainly been investigated for applications in magnetic storage [16] and catalysis [17], whereas relatively less effort has been expanded towards their implementation in biomedicine, owing to the possible toxicity of elemental cobalt.[18] Nonetheless, reactivity and toxicity problems share a common solution - prevention of direct exposure of NP surface to the environment. In other words, protection through functionalisation can make it possible to utilise the promising properties Co NPs are offering in respect with the further improvement of cancer treatments. For the optimal performance of mNPs in biomedical applications, it is hence important they show biocompatibility and non-toxicity, colloidal stability, opportune surface modification, appropriate particle size, and,

above all, adequate magnetic properties. The dependence of magnetic properties on the structural parameters of mNPs, namely their size and shape, is very well-known, with paramount examples in the literature.[19, 20, 21, 22, 23, 24, 25] However, determination of this correlation is by no means easy neither exempt from complications. Even with the advanced control in the experimental preparation of mNPs and their subsequent characterisation, an ever present distribution of particle sizes ultimately prevents the assignment of specific magnetic features to a particular size or morphology. Furthermore, capping agents increase the complexity of the system, adding even more uncertainty in the origin of specific magnetic behaviour. These impediments in the determination of a specific connection between the mNP morphology, coating, and magnetisation are a substantial limitation in the development of property-tuning strategies, which are an ultimate tool in engineering of mNPs for specific application. It is in this sense that the computational modelling becomes a powerful complementary technique to experiments, by unfolding the connection between the properties of mNPs and their structural factors.

The main goal of this dissertation is the development of a sound structural model for simulating the dependence of magnetic properties of bare and ligand-protected Co mNPs on various intra- and interstructural factors, and interpretation of their expected behaviour in real-life experiments. This work should serve as a guidance for any future theoretical and experimental work correlated to the interest of improving the diagnostics and hyperthemia therapies based on the magnetisation phenomena at nanoscale.

The outline is as follows: Chapter 1 provides theoretical background on magnetic nanoparticles and biomedical applications considered, while Chapter 2 gives an overview of models and methods used. To study a complex system, one needs to start from a simpler system and add increasing layers of complexity until the actual system has been reached. And justify methodological choices somewhere in between. That is why in Chapter 3, Co NPs and their morphologies have been investigated from smallest clusters to particles of a few nm in diameter, how do they behave in the framework of the chosen level of theory: what are the known problems, are there solutions suggested, and are those solutions actually needed? Since biomedical applications require NPs to be inherently surrounded by oxidising compounds, modelling of arising adsorption and reaction processes, and their influence on the magnetisation are presented in Chapter 4; experimentally observed surface structures have been captured and those so far unexplored have been predicted. Aim of Chapter 5 is in defining atomic details behind the interaction of biomedically relevant ligands and Co NPs. Following two chapters, Chapter 6 and Chapter 7, are extended studies on biocompatible functionalisation, focused on the mechanism of coating formation and ligand-induced changes in magnetic properties. Chapter 8 serves as an overall conclusion and contains suggestions for further progress in this topic.

... but, I nearly forgot. You must close Your eyes,
otherwise You won't see anything.

CHAPTER 1

AGNETIC NANOPARTICLES

In another moment down went Alice after it, never once considering how in the world she was to get out again.
- Chapter 1, Down the Rabbit-Hole

1.1 Where smaller is more powerful

It is believed that the impact of nanotechnology will soon exceed the impact that the electronic revolution has had on our lives. Nanotechnology is a novel branch spread through the fields of engineering, chemistry, physics, and biology, which encompasses understanding of the fundamental principles of nanometre-scale objects. It changed for better theretofore common way of thinking by introducing the ability to see and control individual atoms and molecules.

Nanoparticles are microscale entities with size range approximately from 1 to 100 nm. If one dimension does not fall into that range, they are classified as nanowires, nanofibers, or nanotubes. If only one of the three dimensions is in the nanoscale range, they are called nanoplates or nanodiscs. Nanopowders are agglomerates of either nanoparticles or nanoclusters, while nanometre-sized crystals are often referred to as nanocrystals. All are considered to be the connection between bulk materials and atomic structures, and can provide explanation for differences in micro- and macroscopic properties of materials, giving a deeper insight into many unresolved phenomena.

Consequently, all materials synthesised either by a natural flow, incident or a manufacturing process, which are made of at least 50 % of particles in the number size distribution with one or more external dimensions in the size range 1 - 100 nm, in an unbounded state or as an aggregate, agglomerate or composite, are referred to as nanomaterials. In recent years, the role of nanomaterials has drastically changed; from barely known and new features they became crucial participants in a wide range of disciplines. Development of novel applications is driven by the fact that, at nanoscale, properties are altered as the percentage of atoms at the surface becomes significant. Nanoparticles, in particular, are offering immense potential across all of the life aspects: car bumpers are made lighter, clothing is more stain repellent, sunscreen is more radiation resistant, synthetic bones are stronger, electronic components are more flexible, and balls for various sports are made more durable.

NPs can be classified as organic or inorganic. Inorganic NPs can be branched into metallic (Au, Ag, bi-/multi-metallic), semiconducting (metal oxide NPs, C-based NPs, quantum dots), and metal salt NPs. Organic NPs include micelles, dendrimers, liposomes, hybrid, and compact polymeric NPs. Additionally, further classifications can include anything from size-based distribution (e.g. ultrasmall iron oxide NPs, USPION [26, 27]), or the atomic ordering (core-shell, $L1_0$ ordered, and disordered bimetallic NPs [28, 29]), to the property-specific distinction (e.g., magnetic Fe_3O_4, Co, FePt NPs). NPs often possess size-dependent property changes, as they are small enough to confine their electrons and produce quantum effects. These include quantum confinement in semiconductor NPs [30, 31], surface plasmon resonance in some metallic NPs [32, 33], and superparamagnetism in magnetic NPs [34, 35], and each of them has shown attractive performances across different fields.

1.2 Magnetic nanoparticles

Among different types, magnetic nanoparticles, mNPs, are of a special interest because of their commendable magnetic properties which can be classified as intrinsic or extrinsic. Former are more important since they are derived from the interactions on an atomic length scale and highly depend on chemical composition and grain size, shape, and crystal microstructure. Additionally, they are much more influenced by surface effects and therefore give a rise to specific manifestations, such as superparamagnetism, that can only be found at the nanoscale level. These properties include magnetic saturation, magnetic anisotropy, and Curie temperature.

mNPs can be synthesized from any material characterised by some degree of magnetism, but the most commonly used are ferromagnetic metals or ores. Only in rare instances NPs and material bulk phases showcase inverse magnetic behaviour, as in the case of gold NPs.[36] Ferromagnetic materials possess permanent magnetic moment in the absence of an external field as a result of uncancelled electron spins present in the electronic structure. If the diameter of the particle is larger than the critical value, D_C, coupling interactions cause mutual spin alignment of adjacent atoms over large volume regions called magnetic domains. Domains are separated by domain walls, in which the direction of magnetisation of dipoles rotates smoothly from direction of one domain towards the direction of the other. Once the diameter falls under the critical value (typically between 3 and 50 nm), particles can no longer accommodate a wall and each of them becomes a single domain. Additionally, since each domain is a separate particle, there can be no interactions or ordering of domains within a sample and particles do not retain any net magnetisation once the external field has been removed. This phenomenon is known as superparamagnetism. Superparamagnetic substances are, as the name says, much alike paramagnets contradictory to the fact that this property arises from the ferromagnetic materials. Their normal ferromagnetic movements combined with very short relaxation times enable them to randomly flip direction under the influence of temperature or to rapidly follow directional changes in the applied field. Temperature above which the

thermal energy will be sufficient to suppress ferromagnetic behaviour is called the blocking temperature, T_B. Below T_B, ferromagnetism is relatively stable, while for $T > T_B$ spins are free as in a paramagnetic system and particles behave superparamagnetically. Blocking temperatures of most mNPs are below 100 K.[37, 38, 39] Their behaviour is therefore paramagnetic, as for most temperatures they are only magnetised in the presence of the external field, but their magnetisation values are in the range of ferromagnetic substances. Moreover, strength of the external field needed for reaching saturation point of superparamagnetic NPs is comparable to that of ferromagnetic NPs.

This highest magnetisation that mNPs can obtain, when exposed to a sufficiently large magnetic field, is called saturation magnetisation, M_S. It is the maximum value of the permeability curve, where permeability, μ, is the measure of magnetisation that a material obtains in response to an applied magnetic field (total magnetisation of material per volume). It is often correlated with the ratio of magnetisation and intensity of applied magnetic field (M/H), which is known as magnetic susceptibility, χ, and describes whether a material is attracted into or repelled out of the magnetic field. The magnitude of saturation is a function of temperature and, once reached, no further increase in magnetisation can occur even by increasing the strength of the applied field. Unique temperature limit at which ferromagnetic mNPs can maintain permanent magnetisation is called Curie temperature, T_c. The equivalent property of antiferromagnetic materials is called Nèel temperature, T_n. Notably, when the NP size is reduced from multi-domain to a single domain, the magnitude of M_S decreases due to the increment of the spin disorder effect at the surface; thus, the M_S value is directly proportional to the size of mNPs.

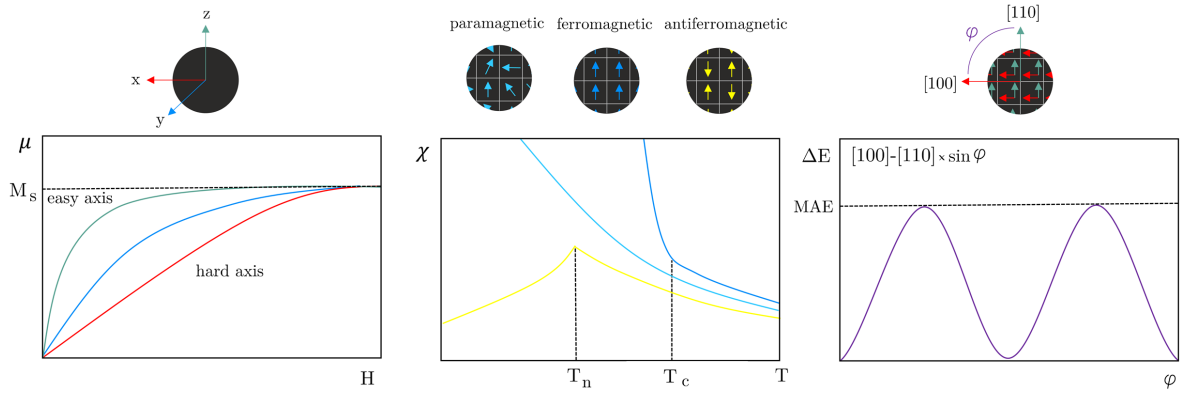

Figure 1.1: Intrinsic characteristics of magnetic nanoparticles: permeability as a function of the strength of applied magnetic field with saturation point (**left**); susceptibility as a function of temperature with Curie and Nèel temperatures (**middle**); difference in the energy for [100] and [110]× sin(φ) directions of magnetisation (**right**).

In almost all cases, magnetic materials contain some type of anisotropy that affects their magnetic behaviour. The most common types of anisotropy are: (a) magnetocrystalline anisotropy (MCA); (b) surface anisotropy; (c) shape anisotropy; (d) exchange anisotropy; and (e) induced anisotropy (by stress, for example). In mNPs, MCA and shape

anisotropy are the most important. MCA is the tendency of the magnetisation to align along specific spatial direction rather than randomly fluctuate over time. It arises from the interaction of the spin magnetic moment with the crystal lattice and energetically favours alignment of magnetic moments along the so-called easy axis, where the value of MCA presents an energy required to divert the magnetic moment from easy to hard direction in a single crystal. Factors affecting the MCA are type of the material, temperature, and impurities, whereas it does not depend on the shape and size of the mNP. Morphology effects are included in the shape anisotropy. Stress anisotropy implies that magnetisation might change with stress, for example, when the conditions require shear stress adaptation. Due to the large ratio of surface to bulk atoms, the surface anisotropy of mNPs can also be very significant as it captures coating-effects on the spin-canting of surface atoms. Different types of anisotropy are often expressed simply as magnetic anisotropy energy (MAE), which determines the stability of the magnetisation by describing the dependence of the internal energy on the direction of spontaneous magnetisation. It has a strong effect on the values of extrinsic properties. Intrinsic properties are schematically represented in Figure 1.1.

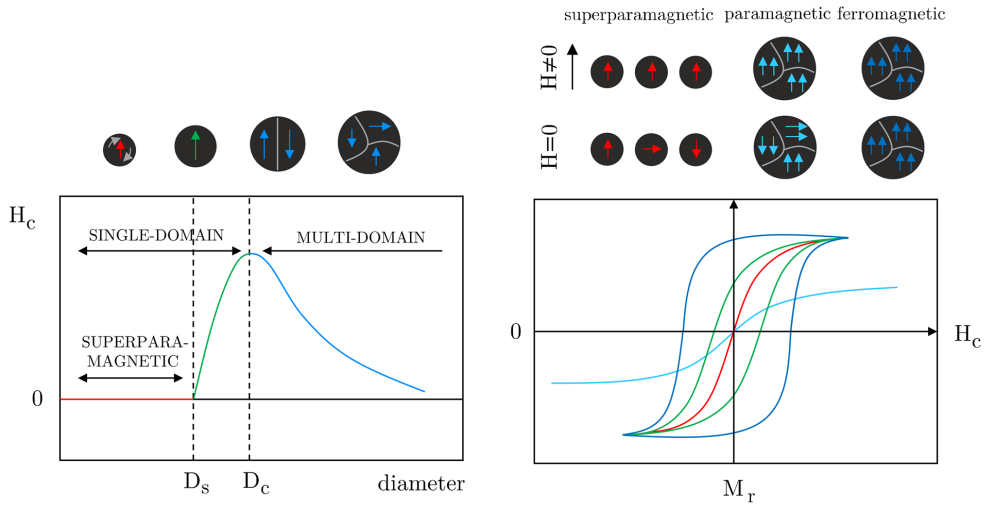

Figure 1.2: Extrinsic characteristics of magnetic nanoparticles: magnetic coercivity as a function of NP diameter (**left**), and hysteresis loops (**right**).

Extrinsic properties are not as essential as intrinsic; they are derived from long-range interactions and include magnetic coercivity and remnant magnetisation, which are dependent on the microstructural factors, such as orientation of intermetallic phases.

Magnetic coercivity, H_C, can be described as a resistance of a magnetic material to changes in magnetisation, and it is equivalent to the magnitude of external magnetic field needed to demagnetise material that has previously been magnetically saturated. Ferromagnetic material that reached saturation point cannot return to zero magnetisation in the same direction once the applied field has been removed, but requires magnetic field

applied in the opposite direction. This process leads to the creation of a loop known as hysteresis. Such hysteresis loops indicate correlation between the magnetic field and the induced flux density (B/H curves). Superparamagnetic NPs each have only one domain and no hysteresis loops are obtained when applied field is reversed. Remnant magnetisation, M_r, is magnetisation remaining after the magnetic field has been removed. Once the saturation has been reached and the external field is not furtherly applied, ferromagnetic NPs will resist toward a sudden change and produce an auxiliary magnetic field to remain magnetised. Contrary, superparamagnetic NPs will behave as paramagnets with instant need for demagnetisation and negligible M_r. This property allows for ferromagnetic NPs to gain the magnetic memory. Extrinsic characteristics of mNPs are shown in Figure 1.2.

1.3 Applications

Indeed, the specific structure and characteristics of mNPs have changed the aspects of energy production, material manufacture, ecology approaches, and clinical treatments, giving them a whole new dimension.

In electronics and energetics, one of the most researched future applications of mNPs is their incorporation in lithium batteries. They are considered to be promising candidates for anode material which would exhibit superior electrochemical performances such as longer lifetime and reduced recharging time. [40, 41] Reason for this is the surface of the nanoconstructed electrodes, which is much larger than that of the conventional electrodes and allows higher charge-discharge rates and shorter path length for electronic/ion transport. Another application is their assembly for magnetic media. Magnetic recording is rapidly reaching its limits and, while the pursuit of higher areal densities continues, interest in mNPs is growing.[42] mNP anisotropy could be a key contribution to the areal density improvements with one possibility being a novel approach called Heat-Assisted Magnetic Recording (HARM). [43] One more highly investigated research field is the photoelectrolysis of water. mNPs were introduced in the photoelectrochemical water splitting (PWS) due to the global demand for hydrogen with dwindling fossil energy sources.[44] They are important catalysts in Fischer-Tropsch synthesis as well, because of the improved reaction kinetics compared to the traditional catalysts owing it to the large share of surface atoms and magnetic nature which allows for facile recovery and recycling.[45]

In environmental sciences, mNPs have been attracting particular attention in water remediation because of their convenient magnetic field-assisted separation.[46, 47] They have also shown extraordinary performance in pollutant removal and were found to be cost-effective, simple to use, and environmentally sound compared to other adsorbents employed for the mitigation of toxicity of heavy metals.[48, 49] In addition, re-usage of mNPs after the desorption of contaminants and regain of removal capacity were also presented.[50] These results were obtained due to the advantages mNPs are offering for contaminant elimination: large removal capacity, fast kinetics, high reactivity, high surface-to-volume ratio for significant adsorption power, and simple removal with an external magnetic field.

Implementation of mNPs in biomedical applications is a new, highly interdisciplinary field. Essential advantages of mNPs for medical tasks are their nanoscale dimensions, magnetic properties, and capability of carrying active biomolecules. They are small enough to pass through the narrowest blood vessels and to penetrate through cell membranes, making it possible to access any part of the living system and easily reach desired destinations.[51] Control of the position of mNPs by the external magnetic field is important for preconcentration, separation, capture of analytes, and detection, with major benefits being reduction of drug wastage, lower frequency of drug administration, and avoidance of unwanted side-effects.[52, 53, 54] mNPs are also physiologically very well tolerated.[55] Moreover, by virtue of their size, they are able to overcome the influence of the gravitational field, magnetic field gradient, and the potential magnetic agglomeration.[56] On the other hand, as the size decreases, the reactivity magnifies, and they might be attracted to each other as a result of London-type van der Waals attractive forces. In order to minimise interactions of particles with system environment, to ensure stability, and to prevent agglomeration, surface coating may be required to provide steric repulsion.[57] Nevertheless, mNPs make excellent candidates for biomedical applications as most of the biological processes occur at the nanometre scale. Their unique combination of properties and modification strategies is just at the beginning of being fully realised in a range of medical diagnostic and therapeutic applications, as described in the following sections.

1.3.1 Magnetic resonance imaging

Magnetic resonance imaging (MRI) is a non-invasive, powerful, and sensitive tomographic visualisation technique widely used in biomedicine for obtaining high resolution scans of body cross-sections. MRI image originates from the measurement of nuclear magnetic resonance (NRM) signals which are collected as responses of tissue-abundant water protons to the applied magnetic field. In rare cases, signals are detected from other nuclei, such as C^{13}, P^{31}, or Na^{25}. A strong static magnetic field is first applied to align the magnetic moments of proton nuclei, which are then deflected in the transversal plane upon the application of a short radiofrequency pulse. Magnetic moments spontaneously return to the original longitudinal direction of the magnetic field, and the time necessary for the complete realignment is called relaxation time. One can distinguish between the T1 relaxation time corresponding to the longitudinal recovery, and T2 relaxation time of the transversal decay. Both are sources of tissue contrasts in MRI scans, which depend on the net magnetic effect of a large number of nuclei within a specific voxel of tissue. Contrasting black and white areas of the MRI image correspond to the disproportionate T1 and T2 proton relaxation times of various biological tissues as a consequence of differences in their compositions and proton density resulting in distanced signal intensities. However, the limited virtue of these differences can sometimes cause low sensitivity of the technique, resulting in inadequate contrasts for certain clinical objectives. Because the relaxation process involves an interaction between protons and their immediate molecular environment, it is possible to administer MRI contrast agents, CA, that will alter the magnetic characteristics within specific tissues or anatomical regions and improve the

image contrast. Those are individual molecules or particles with unpaired electrons (paramagnetic metal-ligand complexes or magnetic particles) which produce inhomogeneities in the magnetic field causing a rapid de-phasing of nearby protons and change in their relaxation rate. CA can be divided into those that shorten the longitudinal recovery time resulting in a brighter image - positive or T1 agents, and those which shorten the transversal decay time - negative or T2 agents. Principle of MRI and use of CA is shown in Figure 1.3. Contrast agents are used in 40-50 % of all MRI examinations.

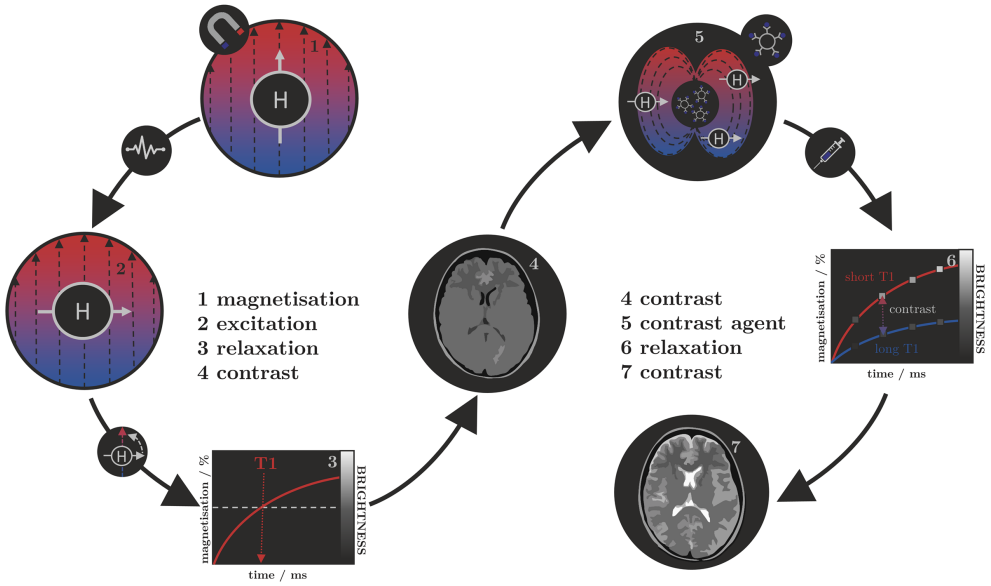

Figure 1.3: Schematic representation of the principle behind the MRI contrast agents.

The first paramagnetic complex approved for use in cancer patients to detect brain tumours was gadolinium(III) diethylenetetraamine pentaacetic acid (GdDTPA) back in 1987. With the rising concerns over the safety of Gd-complexes, which have been found to remain in the body after multiple MRI scans, the WHO issued a series of restrictions on their use as contrast agents in 2009. This stimulated intense interest in creating responsive superparamagnetic T2 agents which show higher biocompatibility and safety. Currently, the majority of T2 CA are iron oxide-based superparamagnetic NPs (SPIONs) coated with dextran, silicates or other polymers with variable T2 relaxivities. This flexibility makes them attractive for detecting specific biological tissues, but their relatively large sizes can impede cell penetration and delivery, while lower values of their magnetic moment require increased clinical uptake to compensate for the poor contrast obtained when compared to gadolinium-based agents. This led to a discontinuation of a number of prominent iron oxide CA in recent years [58, 59, 60], and only ultra-small particles (USPIONs) remain in clinical use up to date. Superparamagnetic FePt NPs have been reported to have significantly better T2 relaxivities than SPIONs and USPIONs [61], while Fe NPs offer an order of magnitude greater susceptibility at room temperature.[62, 63] As a result, these are currently agents of significant interest and the topic of much investigation, together

with cobalt NPs, whose very high saturation magnetisation (bulk Co M_S is 1422 emu cm^{-3} compared to 395 emu cm^{-3} for iron oxide at room temperature) offers a larger effect on proton relaxation, promising improved MRI contrast and allowing smaller particle cores to be used without compromising sensitivity.[64, 65]

1.3.2 Hyperthermia

Hyperthermia, in terms of medical treatments, is defined as a moderate increase in temperature (up to 40-45 °C) sufficient to cause death of tumorous cells whose vulnerability originates from the poor blood flow and insufficient oxygenation in the affected region which prevents efficient heat conduction and convection.[66, 67, 68] The final outcome can be a result of two different processes: increase in temperature will cause either thermal ablation of tissues (direct decay of cells by interruption of natural enzymatic processes responsible for viability, with temperatures above 47 °C) or thermal sensitisation of cells (the increased response to other treatment modalities, with temperatures between 41 and 45 °C). The main reason why the first approach is favourable, although the thermal sensitisation was confirmed to successfully destroy tumorous tissue, is the fact that 50 % of tumours regress temporarily after the treatment with less invasive heating. Higher temperatures also result in tissue necrosis, coagulation or carbonisation after a few minutes while moderate temperatures require longer treatments (in the order of hours) to obtain desired sensitivity. Hyperthermia can additionally intensify cytotoxic effects of anti-cancer drugs and/or radiation, if applied simultaneously, which has already been demonstrated to improve control of therapies and patient survival rates.[69]

First hyperthermia treatments used water baths; today, conventional therapies proceeded to non-contact external devices for transfer of thermal energy either by irradiation with light or by electromagnetic waves (microwave, radiofrequency, ultrasound or laser sources). However, the realisation of its full clinical potential was limited due to the inability of heat sources to target tumorous cells efficiently and locally. As the effectiveness reduces steeply with the distance from the source, targeted regions are not receiving enough thermal energy, while maximal temperature gradient is obtained on the body's surface. Moreover, a large share of energy was dissipated, causing serious damage in the healthy tissues situated near the main path of the radiation beam. Additional problem can be dissipation of heat by blood if close-by tissues are well-vascularised. Altogether, conventional hyperthermia showed no discrimination between targeted and surrounding environment. Growing usage of magnetic nanosystems initiated creative solution, where the external source could now be circumvented by the intravenous administration of mNPs, followed by the use of an alternating magnetic field which resulted in localised transformation of electromagnetic energy into heat by means of mNP relaxation mechanisms. By changing the primary source of heat from radiation to magnetic particles, direction of heat release is reversed since particles are placed inside the tissue and radiation source is situated externally. For this reason, conventional therapies are referred to as *outside-in* hyperthermia, and treatments using magnetic particles as *inside-out* hyperthermia. This nanoparticle-targeted approach is known as magnetic nanoparticle hyper-

thermia (mNPH), and it allows local heating of tumorous cells with minimal impact on the surrounding tissues. The principle of mNPH is presented schematically in Figure 1.4.

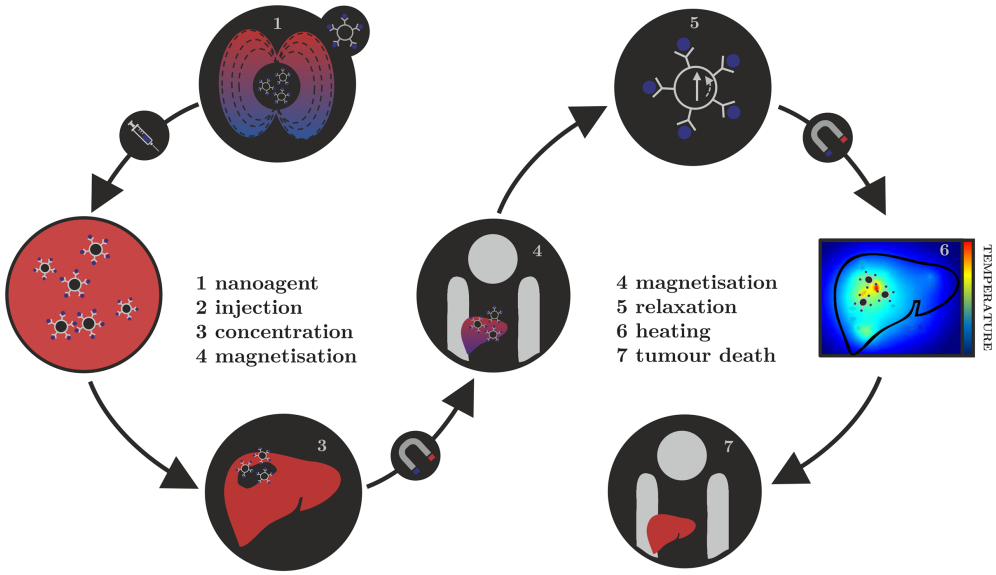

Figure 1.4: Schematic representation of magnetic nanoparticle hyperthermia therapy.

The so far implemented magnetic nanoagents are mostly magnetite and maghemite NPs.[70, 71, 72, 73] However, despite the promising results of preclinical trials, there are many ongoing challenges in making mNPH a universal cancer treatment. These include the establishment of optimal limits of the strength and frequency of the applied magnetic field, their correlation with the duration of the treatment, and determination of sufficient mNP concentration.[74, 75, 76, 75] As the magnetic gradient decreases with the distance from the source of the applied magnetic field, restrictions of the human-safe magnetic field strengths impose challenges for obtaining necessary gradients to control the residence time of mNPs in the desired area. Additionally, the estimates of the magnetic field strengths and gradients based on the hydrodynamic conditions of vascular vessels showed the highest effectiveness of magnetic targeting in the regions of slower blood flow which are usually near the surface.[77, 78, 79] Research on the internal magnets implanted in the vicinity of the targeted tissue using minimally invasive surgery is ongoing, and several studies have succeeded in simulating the interaction between an implant and a magnetic agent.[80, 81] In terms of the amount of mNPs that can be incorporated by a single living cell, admissible intake is of the order of a few pictograms.[6, 82] This makes high magnetic moment of the nanoparticular agents as the strictest requirement, because a relatively small number of particles (between 10^3 and 10^4) has to be capable of increasing the intracellular temperature by several degrees, where metallic NPs have an important advantage over the relatively weak magnetic moments of iron oxides. There are several excellent reviews on principles and requirements of mNPH.[83, 84, 85, 86]

1.3.3 Targeted drug delivery

One of the most rapidly developing areas of modern pharmacology is targeted drug delivery, with the aim to reduce the drug intake per dose and prevent exposure of healthy tissue to chemically active analytes. In 1906, Paul Erlich introduced the term *magic bullet*, describing the drug capable of locating the causative agent of the disease and provide the adequate treatment without further distribution to unaffected areas.[87] Several decades later, first drug delivery systems were developed, containing active medical substances attached to a surface of an organic carrier or encapsulated within the carrier which possesses specific cell affinity contained within molecular vectors and would disintegrate and release the capsulated drug upon the contact with diseased cells.[88, 89, 90] Disadvantages of the organic and carbon-based nanocarriers and capsules were soon revealed, ranging from limited chemical and mechanical stability of organic NPs, over the questionable toxicity of carbon nanotubes, to the general susceptibility to microbiological attack, lack of control over the carrier movement and the rate of drug release, and, finally, high cost.[91, 92, 93, 94] Hence, the search for an optimal carrier shifted direction towards utilising the magnetically induced movement of magnetic nanosystems. Their main advantages are simple visualisation (based on the principles of MRI), easy guidance and retention in the desired area by externally applied magnetic field, and controllable drug detachment triggered by heat released in the variable magnetic field (based on the principles of magnetic hyperthermia). In addition, it is possible to engineer mNPs to either avoid or interact with the immune system in specific ways.[95, 96]

In common with the previous two applications, most attention has been devoted to iron oxide NPs.[97, 98] However, limitations of magnetic drug delivery promote materials of higher magnetic moments.[99] This is due to the decrease in the magnetic gradients connected to the distance from the source as well as to the fluid hydrodynamics correlating with the depth of the affected tissue - same as with the mNPH. So far, combination of relatively strong magnetic fields with SPION drug carriers showed to reach an effective depth of 10-15 cm in the body.[34] Other restrictions relate to the acceptable size of the NPs; first, they have to be below the critical size for optimal magnetic properties which is a prerequisite to avoid magnetic memory and agglomeration once the magnetic field is removed, and second, they have to be small enough such that after the attachment of drug molecules on their surface they can still effectively pass through narrow barriers.[100, 101] The small size implies a reduced magnetic response, and hence requires materials of high magnetisation, such as metallic mNPs, over metallic oxides. Recently, 5-25 nm diameter AuCo NPs with a core-shell structure and tailorable morphology were synthesised for the purpose of obtaining high magnetisation drug carriers.[102] The major advantage of implementation of cobalt within the mNP core is that saturation magnetisation of Co NPs (120-137 emu g^{-1} [64, 103]) is nearly twice that of iron oxide NPs (68-88 emu g^{-1} [104, 105]).

1.4 Desired properties for biomedical applications

Specifics of the application of interest govern the desired properties of materials used, as it was briefly described for the diagnostics and therapy methods in previous paragraphs. When it comes to biomedicine, safety of the treatment towards a patient is a priority, and hence superparamagnetic mNPs are preferred because they are magnetised only under the influence of an external magnetic field and quickly demagnetise otherwise, which makes them safer for human body. This implies that no coercive forces or remanence exist, preventing magnetic interactions between particles and their aggregation, which could lead to adverse problems derived from the formation of clots in the blood circulation system. Saturation magnetisation is also a substantial factor for two reasons: (i) mNPs with high M_S have more prominent response to the external magnetic field; (ii) high M_S makes the movements of mNPs more controllable and guarantees efficient response to the magnetic field implying reduced time of residence and lower dosages of mNPs. M_S is dependent on the mNP magnetic moment, size, and distribution, and it is thus important to take them into consideration. An increase in size yields higher M_S, however, above the critical diameter, mNPs become ferromagnetic and show undesired behaviour due to the formation of agglomerates and magnetic memory. Also, very small diameter sizes are highly desired for reaching regions of limited access; in order to cross the blood-brain barrier, d ~12 nm magnetic core size or less is required. Therefore, a suitable balance should be found between the size distribution and magnetic properties. Since mNP-based therapies work by directing the mNPs to a target site using an external magnetic field, magnetic anisotropy is also a very important factor.

Alongside these general requirements which are applicable to all biomedical applications, to enhance the performance of mNPs within MRI diagnostics and hyperthermia therapy it is essential to gain an insight into the inherent mechanisms behind their magnetic processes and assess the properties of mNPs and external magnetic field parameters for optimal treatment results.

1.4.1 Prospective MRI properties

The mechanism of relaxation enhancement directed by MRI contrast agents arises from the dynamic interactions of water molecules with the magnetic centres. Established classical models have significantly contributed to the correlation between the CA properties and performance, paving a way to the smarter design of new materials. These models are based on the interpretation of proton-electron interactions between water protons and contrast agents, which is the most important mechanism behind the T1 and T2 contrasts within the CA assisted MRI.[106, 107, 108]

For CA consisting of magnetic centre-ligand complexes, interacting water protons are classified into inner-sphere, second-sphere, and outer-sphere protons, each having distinct interaction mechanisms. The inner-sphere mechanism involves direct magnetic centre-water coordination, whereas the second-sphere mechanism describes interaction between the magnetic centre and water protons situated within the second coordination sphere

through hydrogen bonds. The outer-sphere includes the magnetic centre influence on the translational diffusion and rotational motion of the remaining bulk water protons.[109, 110] However, for CA consisting of magnetic particles, the direct coordination of water is atypical and the largest share of the nuclear magnetic relaxation of water protons in solutions (or suspensions) of magnetic particles arises from pure magnetic interactions at the molecular level. In essence, this amounts to the reformulation of the outer-sphere mechanisms from a single metal atom complex centre to the solution of mNPs.

Superparamagnetic mNPs with large magnetic susceptibility produce local magnetic field under the influence of an external magnetic field. As a result, the local magnetic field causes perturbation in the motion and relaxation of nearby water protons. Hence, the relaxation is induced by the fluctuating dipolar interaction between the nuclear magnetic moment of the water proton and the global magnetic moment of mNP, just like in the case of classical outer sphere theory. The reformed outer-sphere theory now describes the change in the relaxation of solvent protons as the water molecules diffuse into the neighbourhood of a solute particle and start interacting with its magnetic dipolar moment. This type of local perturbation shortens the T2 relaxation time, also known as spin-spin relaxation, of water protons during water diffusion. The mNP CA catalytically relax water protons at the particle/solvent interface emanating in T2-weighted MRI images. The extent to which the mNP CA affects the relaxation rate of tissue water can be quantitatively characterised by its transversal relaxivity, r_{CA}, and the final relaxation rate of the tissue, r_2, is given by:

$$r_2 = \frac{1}{T_2} = \frac{1}{T_2^{\mathrm{o}}} + r_{\mathrm{CA}}[\mathrm{CA}]. \tag{1.1}$$

mNP relaxivity is thus defined as a proportionality constant between the induced increase in the relaxation rate of the tissue and the concentration of the CA. By definition, low doses of high-relaxivity CA provide an equivalent contrast magnification as higher concentrations of CA with inferior r_{CA}. Every tissue has an inherent relaxation rate, $1/T_2^{\mathrm{o}}$, and in order to generate an observable contrast, the relaxivity of CA should be at least at 10 % of the inherent rate.

Outer-sphere theory for T2 relaxivity has developed an expression for the dependence of relaxivity performance of superparamagnetic mNPs on their intrinsic properties - saturation magnetisation and the effective radius:

$$r_2 = \kappa_\gamma V_{\mathrm{eff}} M_{\mathrm{S}}^2 \frac{r^2}{D(1 + l/r)} \tag{1.2}$$

where κ_γ is the constant derived from the gyromagnetic ratio of solvent protons, V_{eff} is the effective volume fraction ($V/[\mathrm{CA}]$), M_{S} is the saturation magnetisation, r is the radius of magnetic core, l is the thickness of impermeable mNP coating, and D is the diffusion coefficient of water molecules. Simplistically saying, increased M_{S} value is reflected in the increased response of mNP CA to be magnetised by the external field, resulting in the higher r_2 relaxivity. Similarly, improved relaxivities can be achieved with a larger

magnetic core radius. As the proton relaxation occurs mainly at the interface of the mNP and surrounding aqueous environment, nanoparticle coatings also influence the rate of T2 relaxation through the coating thickness.

T2 relaxation processes occur through three mechanisms. First mechanism, known as Curie spin relaxation, arises from the dipolar interactions between water protons and a large magnetic moment of unpaired mNP electrons. It depends on the strength of applied magnetic field and it is a function of the mNP size and water diffusion time, $r^2/4D$. This mechanism is prominent for small-sized mNP CA at strong fields, while it decreases rapidly for larger mNPs where T2 relaxation is mostly dominated by the remaining two mechanisms: dipole-dipole coupling between metal ions and hydrogen nuclei, and scalar or contact relaxation processes. Hence, a primary factor affecting r_2 is the mNP generated inhomogeneity, which depends largely on total magnetisation. In general, more efficient inhomogeneity originates from materials with high saturation magnetisation, which can also influence a greater volume of surrounding water. However, the effective magnetisation of mNPs is often several times lower than that of the bulk counterpart, caused primarily by an increased magnetic anisotropy. Due to the presence of a magnetically 'dead' or tilted layers of atoms on the mNP surface, the surface atomic spins are largely canted, thereby enhancing the MAE and reducing overall magnetisation. Additionally, MAE is also affected by the mNP morphology and surface interactions. For particles of the same volume, a reduced shape and surface anisotropy lead to the spin state similarity between the surface and the core, increasing the magnetisation. Moreover, changes in the magnetic moments of surface atoms can be enforced through surface functionalisation.

Diffusion dynamics of water molecules in the magnetic field gradients is another important factor for effective r_2 rates. It is characterised by the number of water molecules diffused into the close proximity of the CA interface and their residency time within that region. mNPs with large magnetic moments have stronger tendency to form dipole interactions with water protons, to generate a larger area of influence, and to provide a greater possibility of relaxing the diffused water molecules. Certain coatings can also be beneficial in this matter, while others may hinder water diffusion or prolong water residency within ligand pockets, reducing the image contrast. Coatings forming a hydrophilic mNP surface favour diffusion and retention of water molecules in the mNP outer-sphere. Finally, fine-tuning of the thickness, charge (ligands rich in π-electrons create small magnetic fields increasing inhomogeneity), and porosity of the coating allows for the optimised water accessibility and residency.

Hence, the dynamic interactions behind the relaxation mechanisms depend predominantly on the magnetic properties of mNP CA, which, in turn, are attributed to a large extent to the mNP structural features. Relaxivity of superparamagnetic mNPs can be enhanced not only via their magnetic properties, but also through the coating optimisation. The last parameter directly included in the equation, without specifically considering its effect on the magnetic properties, is the diameter of the magnetic core. From the relationship, r_2 value can be increased by increasing the core size; however, biomedical

applications are limited by the superparamagnetic size limit. Within this critical diameter, theoretical studies have identified three mNP size regimes depending on the r_2 rate trends: the motional average regime (MAR), the static dephasing regime (SDR), and the echo-limiting regime (ELR).[111] With the growing mNP size in the MAR regime, relaxivity increases, reaching a plateau in the SDR regime. With any further size increment, mNPs fall in the ELR regime where r_2 steeply decreases. Accordingly, the highest r_2 is achieved for mNPs within the SDR, but so far employed nanoparticulate CA have been within the MAR regime to limit the mNP aggregation through magnetic interactions.[112, 113]

1.4.2 Prospective hyperthermia properties

The heating efficiency of the magnetic nanoparticle hyperthermia depends on the power dissipated in a mNP due to the application of an alternating magnetic field and it is often quantified through the specific absorption rate (SAR). SAR is the rate at which the power is absorbed by a volume of dielectric material, such as biological tissue, exposed to electromagnetic radiation (or other source of energy). It is often mentioned interchangeably with the specific heating power (SHP), which is defined as the thermal power per unit mass dissipated by the magnetic material and accurately describes material's heating efficiency. The interconversion of magnetic field energy into heat by mNPs can arise through three mechanisms: eddy currents, hysteresis, and relaxation processes. Eddy currents are loops of localised electric current induced by the varying magnetic field. Their existence depends on how resistant the material is towards current heating, and they are usually present in bulk crystals. Prevailing heating mechanism in multi-domain mNPs is hysteresis loss, while single-domain superparamagnetic mNPs have high electrical resistivity, and, thus, such power loss is negligible compared to the one originating from relaxation mechanisms. Relaxation mechanisms have two modes: following the removal of the external magnetic field, magnetic moments relax either through the motion of the internal spin (Néel relaxation) or by the rotation of the mNP around its own axis (Brownian relaxation). Either relaxation of magnetic moment back to the initial position releases thermal energy and induces local heating due to the friction. If the mNP undergoes Néel relaxation, heat is dissipated by the rearrangement of atomic dipole moments where internal friction causes phase lagging between the applied field and magnetic moments. If the mNP relaxes through a Brownian relaxation mechanism, the power loss arises from the shear stress in the surrounding medium. Additional power loss can occur due to the physical relaxation of the liquid.

Quantification of specific heating power of mNPs is derived as:

$$\mathrm{SHP} = \frac{1}{2}\omega\mu_0\chi_0 H^2 \frac{\omega\tau}{1+\omega^2\tau^2} \tag{1.3}$$

where ω is the angular frequency of the external magnetic field and equals $\omega = 2\pi f$, μ_0 is the magnetic permeability constant of free space, χ_0 is the magnetic susceptibility, and H is the magnitude of the external magnetic field. The fractional term leads to the maximal power at $\omega\tau = 1$; in this case, matching ω is called the critical frequency. Estimated goal

for the material development is the SHP in order of 1000 W g^{-1}, based on the amount of mNPs that can be incorporated by a single living cell.[114] The most critical factor is hence the relaxation time of mNPs, τ, resulting from prevailing heating mechanisms.

Relaxation time can be defined as the time needed for magnetic moments of mNPs to vanish once the external magnetic field has been shut off. For Néel relaxation, time constant of the external magnetic field is short enough so that magnetic moment alternates from parallel to antiparallel orientation and back without the change in the physical orientation of the particle. As excitation occurs against the anisotropy energy barrier, process strongly depends on mNP volume and anisotropic properties, and is not influenced by the conditions of the surrounding environment. The relaxation time for Néel relaxation, τ_{N}, can be described by:

$$\tau_{\mathrm{N}} = \frac{\tau_0}{2}\sqrt{\pi\frac{kT}{KV}}\; e^{KV/kT} \tag{1.4}$$

where τ_0 is the characteristic relaxation time and equals $\tau_0 = 1/f_0$, f_0 =10^9-10^{13} s^{-1}, k is the Boltzmann constant, T is the temperature, K is the anisotropy constant, and V is the mNP volume. KV is somehow equivalent to an activation energy that has to be exceeded by the thermal energy, kT, to overcome the inherent magnetic anisotropy energy barrier. In contrast, Brownian relaxation prevails when magnetic anisotropy is sufficient to overcome inertial resistance in which case external magnetic field causes rotation of a whole particle with magnetic moment remaining fixed relative to the crystal axis. The Brownian relaxation time is highly dependent on the hydrodynamic properties of both mNPs and surrounding medium, such as viscosity of the fluid and hydrodynamic volume of mNPs which includes any surfactant layer added for colloidal stability. Equation that describes Brownian relaxation time, τ_{B}, is:

$$\tau_{\mathrm{B}} = \frac{3\eta V_{\mathrm{H}}}{kT} \tag{1.5}$$

where η is the viscosity of the medium, and V_{H} is the hydrodynamic volume of mNPs. When these two processes are parallelly involved, effective relaxation time which describes energy transfer rate takes both into consideration, and final expression is:

$$\frac{1}{\tau} = \frac{1}{\tau_{\mathrm{N}}} + \frac{1}{\tau_{\mathrm{B}}}. \tag{1.6}$$

Overall, the shorter of two dominates the effective relaxation time - Néel for small particles in viscous solutions and Brownian for particles with large hydrodynamic volume in an environment of lower viscosity. Exact division between mechanisms depends mainly on the mNP anisotropy constant. In mNPH, mNPs are embedded in the tumorous tissue and internalised by cancer cells either by adhesion to the cell walls or in the form of a restraint of movement provided by cell plasma. Because of this immobilisation, Brownian mechanism is damped and Néel relaxation occurs almost exclusively.[115]

mNPs can be re-magnetised only after their relaxation is completed; therefore, frequency of the external field has to match the relaxation times in order to obtain efficient

heating rates. SHP is maximised under the condition $\omega\tau = 1$ and since typical Brownian relaxation times in systems where this mechanism dominates over Néel relaxation are around 10^{-5} s, effective frequencies would need to be 10^5 rad s^{-1} (15 kHz), which is much lower than any frequency reported in hyperthermia studies (100-300 kHz range) that therefore favours relaxation times of 10^{-6} s or below.[86, 116] This confirms Néel relaxation as a predominant heating mechanism in mNPH and accentuates requirement of magnetic anisotropy energies that significantly exceed the thermal energy ($KV \gg kT$); if anisotropy constant is not satisfactory, no noteworthy heating is expected. Therefore, SHP shows connection to the size of mNPs, their magnetic properties and anisotropy energies, as well as to the characteristics of the applied magnetic field.

From the equation for τ_N, MAE is an important factor in enhancing Néel relaxation time. However, within the limitation of $\omega\tau = 1$ for maximising SHP, an enhancement of relaxation time may not always yield higher SHP values, and the frequency of external magnetic field must be chosen accordingly. Only through that correlation can efforts to increase the MAE of mNPs lead to a higher heating efficiency and, ultimately, by satisfying the $\omega\tau = 1$ condition, allow for the use of lower magnetic field frequencies.[117]

mNPH involves excitation of mNPs suspended in a fluid medium using the external magnetic field, meaning that parameters of magnetic field itself should also be optimised for desired results. Changes in frequencies and amplitudes are proportionally influencing the heating power of mNPs, where SHP increases rapidly with the increase in the magnetic field strength. Enough heating power must be generated for destruction of cancerous tissue, while in the same time frequency and strength of applied magnetic field have to be safe for human body. These requirements are putting strict limitations on the frequencies ranging from 0.05 to 1.2 MHz and the magnetic fields strengths from 0 to 15 kA m^{-1}. Higher values would lead to serious problems such as aggregation of mNPs causing embolisms while lower frequencies would stimulate skeletal, cardiac, and peripheral muscles and trigger arrhythmias. Amplitudes are usually in the range of 5-30 kA m^{-1}. External magnetic fields with $H_0 \times f$ less than 4.85×10^8 A m^{-1} s^{-1} have been approved as safe.[118]

Different combinations of superparamagnetic materials and biocompatible ligands have been investigated, however, reached efficiencies are far from ideal and further efforts are directed to find the best nanocomposite. The most important advance in the last ten years has been the commencement of the first-ever clinical studies of therapeutic mNPH induced by mNP heating.[74] The study successfully demonstrated that magnetite NPs can be safely applied for the treatment of brain tumours and that hyperthermic temperatures are achieved. Magnetite and maghemite NPs exhibit (up to this point) medium heating efficiency with little or no control of temperature changes when compared to other magnetic materials, but their biocompatibility, non-toxicity, and ability to escape the reticuloendothelial system makes them preferred candidate NPs for mNPH. However, low SHP values [84] (less than 100 W g^{-1} for 400 kHz frequency and 10 kA m^{-1} external magnetic field strength) seriously hamper successful usage of iron oxides, promoting the implementation of mNPs with higher specific magnetisation. Many efforts have been

made in order to improve properties of magnetite NPs. One route of optimisation was by changing the morphology of the NPs, where the heating efficiency of 200 W g^{-1} measured for the cubic and deformed-cubic FeO/Fe_3O_4 NPs owing to their large anisotropy overpowers the spherical NP equivalents with efficiency of 135 W g^{-1} known to have higher saturation magnetisation.[119, 120] Another valuable strategy was to increase the magnetic anisotropy by total or partial substitution of Fe^{2+} ions by Co^{2+} ions. Cobalt ferrites showed comparatively high thermal and oxidative stability with large saturation magnetisation, suitable magnetic anisotropy energies, and consistently large heating effects with SHP values reaching 720 W g^{-1}, which are significantly higher than the rates reported for the iron oxide NPs (22-200 W g^{-1} [121, 122, 123]). The current focus of research is on cobalt mNPs to further improve the mNPH heating efficiency.

1.4.3 Prospective drug delivery properties

Magnetic targeting of drug delivery carriers is based on the external field induced attraction of mNPs. For the mNP drug carrier to be efficiently trapped in the magnetic field at the targeted site, the magnetic field gradient has to exert a sufficient translational force on the particle-drug complex. This magnetic force, F_{mag}, can be expressed as:

$$F_{\mathrm{mag}} = (\chi_2 - \chi_1) V \frac{1}{\mu_0} B(\nabla B) \tag{1.7}$$

where $\chi_{1,2}$ are magnetic susceptibilities of the medium and the mNP, V is the volume of mNPs, μ_0 is the magnetic constant, B is the strength of the magnetic field, and ∇B is the field gradient. Susceptibility of the biological medium is usually very small compared to that of mNPs and can be disregarded. From the expression, the effective capture of the mNPs depends on the magnetic properties and volume of the particles, as well as on the parameters of the applied magnetic field. As the magnetisation of the mNP decreases, the ability of magnetic field to capture and lead them also decreases. Correspondingly, insufficient field strengths and gradients have limited penetration depth and generate weak translational force. Estimations from experimental studies and extended theoretical investigation of the hydrodynamic conditions of mNP drug carrier targeting indicated the minimal field strength of 200-700 mT at the target site with gradients along the z-axis of approximately 8-100 T m^{-1} depending on the flow rate.[77, 78]

1.5 Design of mNPs for biomedical applications

mNPs should also remain stable over long periods of time, which is the biggest obstacle in the biomedical applications due to the chemically and physically challenging environment. Superparamagnetic NPs are often unstable and tend to degrade into the constituent elements or react with present species. This is especially true in the case of metallic NPs which can easily lose their magnetic properties through oxidation. As a result, biomedically functional mNPs are made of three different, yet connected parts: magnetic core, protective coating, and functional surface. It should be kept in mind that overall properties of mNP nanofluids are not only result of the characteristics of the mNPs

as individual building blocks, but also depend of the interactions between mNPs as well. Challenge in this area is to put all these components together in a small, nanometre-scale space.

Core materials At the centre of the carrier is the superparamagnetic core which allows for the magnetic manipulation of the particle in the presence of the external magnetic field. A variety of magnetic materials can be employed, depending on the application specific properties. However, many of these materials, such as cobalt and chromium, are highly toxic and unlikely to be used as biomedical agents *in vivo* without a non-toxic, protective coating with high mechanical strength. Iron oxide-based materials such as magnetite and maghemite, on the contrary, are relatively safe and are currently in use for multiple applications.

Coating materials Because of their high surface-to-volume ratio, mNPs are more reactive than their respective bulk phases and, as a result, they need to be passivated. Different coatings are possible, not only to reduce the corrosion, but also to prevent the potential toxicity and agglomeration. Biocompatibility is of a high importance in biomedicine and that is why the nature of the coating and the ease of further functionalisation have to be considered to suit specific application.

Linkers Biomolecules may not bind to the mNPs before their surface has been modified. Even if they do, the interaction could be weak, and the final result would be an instant release with little or no control during the delivery. It is therefore necessary to enhance the biomolecule binding and gain control over the system by implementing organic linkers which alter the mNP surface to make it suitable for interaction with biomolecules in changeable conditions. Common organic linkers are amines, thiols, carboxylic acids, and aldehydes. Among these, the most popular are the ones creating electrostatic interactions which can easily be manipulated (by the addition of ions or altering the pH). In other cases, catalytic or redox reactions may be involved for the release process. Organic linkers can be built up on top of each other through organic reactions if necessary.

Successful application of mNPs in the biomedicine is strictly connected to their surface modification, functionalisation, and biocompatibility. Schematic representation of the nanoparticle design is shown in Figure 1.5.

1.5.1 Organic coatings

One of the most developed metal mNP modification approaches is use of organosulfur compounds. There are a few reasons behind it: organosulfur groups strongly coordinate to various metals, such as Ag, Cu, Pt, Hg, Fe, or Au.[124, 125, 126, 127, 128] Moreover, sulphur possesses a huge affinity for metal surfaces leading to spontaneous adsorption. There are two different interaction possibilities, first being adsorption of the intact R-SH molecule on the surface; second is chemisorption in the form of thiols or disulphides, which eventually generate SR groups, followed by the concomitant cleavage of the S-H bond. Intact disulphides are not adsorbed as such, but are split in two thiolate moieties

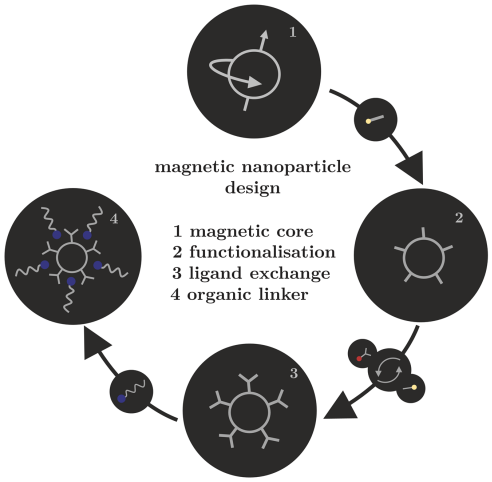

Figure 1.5: Schematic representation of the process of nanoparticle design.

upon chemisorption. Once the organosulfur shell has been completed, it can be modified through the thiol-thiol exchange process. This can be a formidable task due to the strength of the sulfur-metal bond and the conditions with which modifier may not be compatible. For the complete exchange, a considerable excess of incoming ligand is required, but deliberate partial exchange may also be useful. Nevertheless, resulting layers will invariably be composed of both previous and the incoming ligands in a certain ratio, which is the main reason for the preferential use of the weakly bonded ligand, which is afterwards completely displaced by thiols.

Another method is adsorption of amines. The main difference between the amine and thiol coatings is the stability of the created nanocomposite due to the better dispersion provided through amine functional group. Formed bond is much weaker than that of thiols. Nonetheless, methods can be complementary such as in the case of the peptides, where amino acids are linked to mNPs through both thiol and amine functional groups. It has been shown that acetylation of the amine molecules can significantly improve the cytocompatibility and hemocompatibility of mNPs.[129]

Another group of organic compounds that can be used for surface modification are carboxylic acids. Carboxylic acids are excellent capping agents since they bind strongly to the metallic surface through the carboxyl group.[130, 131, 132, 133, 134] Oleic acid, which has a C18 tail with a cis-double-bond in the middle, is the most common because it can form a kink necessary for effective stabilisation. Stearic acid, as a C18 counterpart without the double-bond in its tail, fails as a stabiliser of mNPs. Another advantage of oleic acid is the formation of dense protective monolayer, thereby producing NPs in the highly uniform size range. Moreover, it was found that oleic acid coatings result in no appreciable changes in the overall magnetic behaviour of magnetite or other ferrite materials.[135]

The modification of metallic mNPs by phosphines is easy to achieve and consequently

very interesting. The biggest drawback compared to the previous organic compounds is the weakness of formed interactions which results in poor mNP stability. Consequently, exchange with other ligands is carried on effectively through a complete replacement of phosphine molecules. Thus, higher stability of mNPs can be achieved by exchange of phosphine with, for example, thiols. However, lack of stability can be overcome by using polyphosphine ligands. It was demonstrated that the multiphosphine ligands are firmly coordinated at the surface of Pd NPs.[136]

1.5.2 Inorganic coatings

Silane is often used to modify and endow the functionalised end groups directly to the surface of mNPs for post-connecting with metal ions, polymers, biomolecules or other biological entities. Significantly, this modification maintains saturation magnetisation values of magnetic core. The most common agents of this type are 3-aminopropyltriethoxysilane (APTES), p-aminophenyltrimethoxysilane (APTS) and mercaptopropyltrimethoxysilane (MPTES) with post-anchoring of the -NH_2 and -SH function groups.[137, 138]

Carbon coatings gained considerable interest due to good chemical and thermal stability and high intrinsic electrical conductivity of C-protected mNPs. They also provide good oxidation and corrosion barrier and are considered as one of the best solutions for the encapsulation of the mNPs not only for advantageous physiochemical characteristics, but because carbon is cheap, light, and biocompatible.[139, 140] In addition, it can be easily thinned/removed from the surface by hydrogen or oxygen gas if desired.

Silica coatings can screen the magnetic dipolar attraction between mNPs and enhance their dispersion. Silica also increases the stability and provides protection in an acidic environment, unique magnetic responsivity, low cytotoxicity, and easy chemical modification through the variation of shell thickness.[141] The main challenge in practice is homogeneous modification of each particle - every mNP should be coated with a close-to-uniform silica layer with no core-free silica particles remaining in the mixture. The major reason causing uneven heating in mNPH and drug distribution can be attributed to the disproportionate silica shell thickness.

A very simple approach for mNPs modification is controlled oxidation of the metal core, a technique long known for the passivation of air sensitive supported catalysts.[142] Special care has to be taken when it comes to the final properties because, upon modification, mNPs exhibit characteristics of both metal oxides and metallic cores which can, in some cases, lead to the substantial loss of magnetic properties. Another oxide-based approach is coating composed of metal oxides with different nature in respect to the magnetic core, where titanium and aluminium oxides have shown the most promising results.[143] Surfaces of these oxides are readily modified with phosphorylated molecules, which can be very useful for biological applications.

Non-metallic protective layer can potentially reduce magnetic properties of the mNPs, which is the main reason inert metal coatings can be more favourable. Noble metallic NPs

are offering a palette of fascinating characteristics, amongst which the most interesting for the biomedical applications are surface plasmon resonance (SPR) and surface-enhanced Raman scatting (SERS). Combining noble metal coatings with magnetic cores hence promotes powerful combination of two unique physicochemical features: optic activity and superparamagnetism. In general, core-shell, core-satellite, and dumbbell nanostructures exhibit biomedically beneifical binary/polynary properties, and their surfaces can be modified through functionalisation for improved stability and compatibility. Gold coating addresses almost all restrictions of using mNPs in biomedicine; it provides conductivity, optic properties (both the SPR and SERS along with photoacoustic detection and suitability for dark field spectroscopy), biocompatibility, bioaffinity through functionalisation by amine/thiol terminal groups, and chemical stability through inertness towards aggregation and oxidation. Another positive aspect of gold-coated mNPs is the fact that their optic and magnetic properties can be easily tuned and tailored for a variety of applications by simply altering the size, shape, coating thickness, or through surface modification. Magnetic properties of the magnetic core remain unaffected upon the gold passivation and, furthermore, many different synthesis pathways have already been established for these promising entities.[144, 145, 146, 147, 148, 149]

1.5.3 Polymer coatings

Polymer modification is better than the passivation by small molecules in a way that it provides not only a variety of functional groups and higher colloid stability, but it also determines biological fate in the manner of bio-distribution. Polymers as ligands are designed to respond to both intrinsic (pH, redox, enzymes) and external stimuli (temperature, light, magnetic field), which makes them great candidates for improvement of interaction between mNPs and body environment. By changes in structure, composition, sequence, and ratio of monomers in polymer coatings, morphology and size of mNPs can be influenced as well. They may carry bio-specific groups to bind selectively to cells and/or toxins, to enable their selective removal, and to protect biological tissues against toxicity.[150, 151, 152]

CHAPTER 2

WHY DO SIMULATIONS OF MATERIALS?

Alice: "This is impossible."
The Mad Hatter: "Only if you believe it is."
- Chapter 2, The Pool of Tears

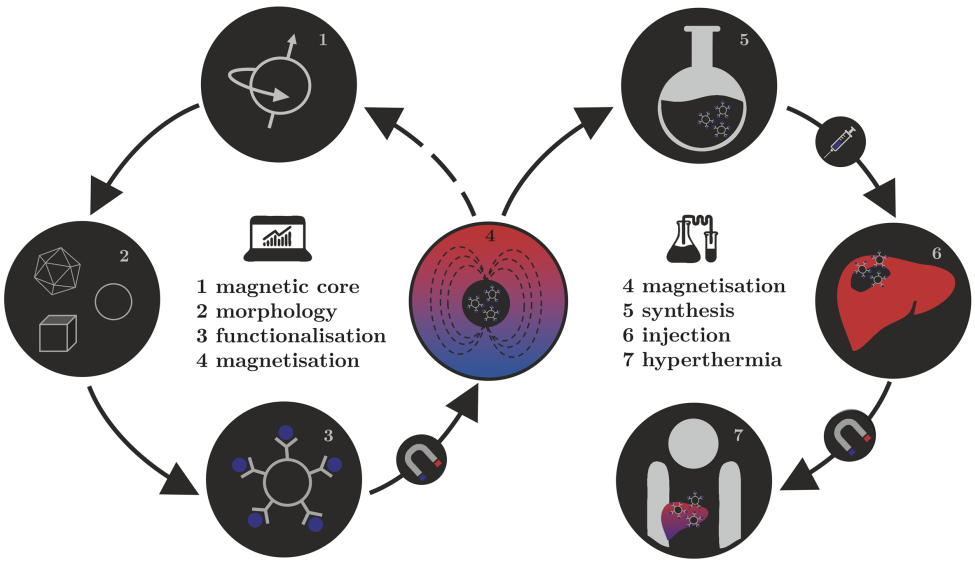

Figure 2.1: Schematic representation of the synergy between computational simulations and experiments on an example of magnetic nanoparticle hyperthermia.

Comprehension of various phenomena observed in materials, prediction of their behaviour under varying conditions, and design of cost-effective alternatives with improved properties are some of the primary objectives in materials research. With the modernisation of experimental methods, understanding of physical and chemical activities of materials has also improved, but envisioning of their responses to the changes in the surroundings and development of new materials have often relied upon empirical models. Recent ascent of interest in microscopic observables, interatomic interactions, and nanomaterials, all of which require description at the quantum level, as well as need for comprehension of the dynamics of complex systems and their evolution over time, combined with tremendous improvements in computational resources, triggered growth of the role theoretical

simulations have in materials science. Correspondingly, the field has evolved from initial objective of reproducing experimental results, to the idea of offering deeper insights and creating predictions. So far, computational modelling has made it possible to detect materials properties starting just from atomic numbers and to simulate their behaviour under desired conditions. Indeed, this synergy between theory and experiment, schematically shown in Figure 2.1, has vastly accelerated progress in many scientific areas, and day-to-day evolution of computational techniques, including Hartree-Fock approach, density functional theory, molecular dynamics, and qm/mm methods, is constantly opening doors to the unknown.

2.1 Basic procedures of computational materials science

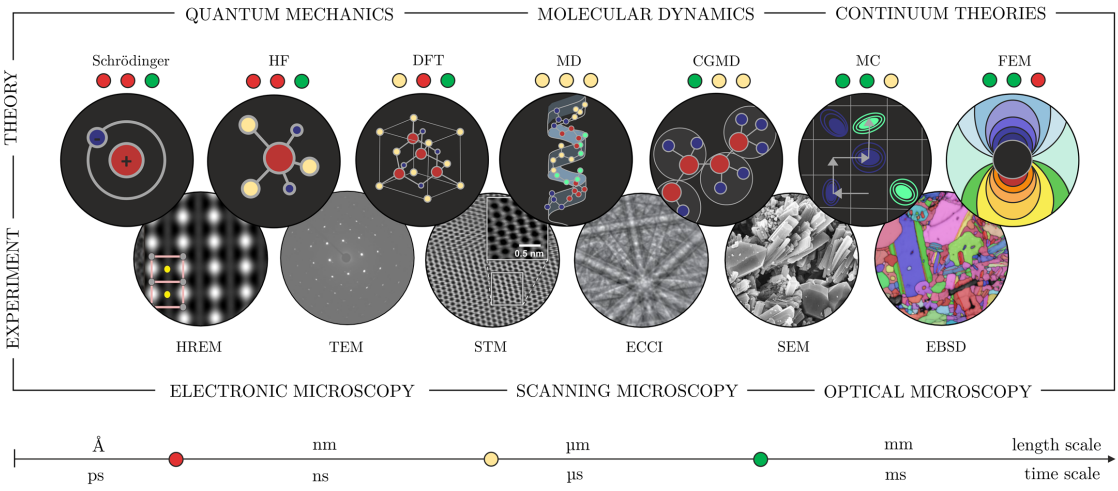

Figure 2.2: Overview of theoretical and experimental methods in respect of the ascending length and time scales. The performance of computational approaches regarding the reachable system sizes, simulation times, and result accuracy is represented within the three circles in the following order: length-time-accuracy. Colours represent favourable (green), medium (yellow), and limited (red) ranges, which are shown in more detail as length and time scales in the bottom.

Basic procedures of computational material science revolve around the definition of subatomic and atomic particle interactions, and they consist of six principal steps: (i) designate the property of interest, (ii) create a model that will represent the particle system accordingly, (iii) select the relevant rules (classical/quantum mechanics, desired accuracy), (iv) select property calculation method, (v) run simulation, analyse the results, and refine under better-defined conditions, (vi) produce data, compare it with experimental and/or theoretical results, predict new phenomena. By performing simulations, realistic events are recreated in a simplified, well-controlled manner and must therefore be critically approached. Development of various methods through the years has made classifications according to their performance and limitations in terms of the system size and simulation

time. Figure 2.2 shows typical theoretical and experimental methods within their length- and time-scale abilities. As the time and size increase, the discipline changes from physics over chemistry, to materials science, and engineering.

To gain an insight in the physics behind the structure of magnetic nanoparticles, chemistry involved in their reactivity, and finally their behaviour as materials in biomedicine, methods employed in this thesis span over both quantum mechanics and molecular dynamics scales, which are presented in more detail in the following subchapters.

2.2 DFT

Nuclei and electrons are building blocks of all atoms, molecules, and materials. The very governing force of these subatomic particles is, in fact, the electromagnetic force - what happens in any of the materials comes ultimately from this basic interaction. If an accurate description of the electromagnetic interactions can be reached, then all experimentally relevant properties and phenomena can be determined accordingly. The law behind the portrayal of subatomic interactions is known as quantum mechanics, and the whole of behaviour of crucial particles, i.e. electrons, can be summed up in the most important formulation of the last century - Schrödinger equation. Shortly after the Schrödinger equation was defined, Dirac famously observed that the general theory of quantum mechanics is now almost complete by stating:

"The underlying physical laws necessary for the mathematical theory of a large part of physics and the whole of chemistry are thus completely known, and the difficulty is only that the exact application of these laws leads to equations much too complicated to be soluble." - Dirac, 1929

The quantum mechanical wavefunction obtained as a solution of the *too complicated* Schrödinger equation contains, in principle, all desired information about the given system. Unfortunately, the exact solution can be identified only for hydrogen atom containing one electron and a few additional simplest cases, while scientifically relevant materials contain a substantial quantity of atoms, each of them having well-defined number of electrons. While the analytical solutions to the Schrödinger equation of such systems may be hardly reachable, numerical approaches for obtaining approximate solutions of the electronic structure have become invaluable in materials science. In this context, calculations from first principles, which allow the prediction of materials' behaviour based solely on the quantum mechanical foundations without requiring higher order parameters (such as fundamental properties), represent a promising tool for deeper insight in faintly investigated characteristics of widely known or completely new matter, and are known as *ab-initio* methods. In principle, the only information these methods require are the atomic numbers of the constituent atoms. With those at hand, all the subatomic interactions and arising electromagnetic properties, that are unattainable in other schemes such as molecular dynamic calculations, can be modelled. To obtain electron wavefunctions for materials of interest, a whole machinery of methods was developed starting with the

Hartree-Fock approximation and leading to a vast variety of modern quantum chemical models. However, all these wavefunction-based methods have one severe limitation; the effort involved in computing and storing the wavefunction increases exponentially with the number of electrons, and they are thus still limited to rather small systems.

These computational efforts received a critical boost in 1964/1965, when Hohenberg, Kohn, and Sham reformulated the Schrödinger equation, which initially involved all the $3N$ spatial coordinates of N interacting electrons, into density functional theory (DFT), by proposing the electron density as a physical quantity that defines the system uniquely without growing in complexity as a function of the number of electrons, but is rather a function of only three spatial coordinates. The resulting Kohn-Sham (KS) equations reconstructed the intractable complexity of the detailed many-body interactions into a computationally manageable single-particle effective potential via exchange-correlation functional. While the 'divine functional' that would make this reformulation exact is still being pursued, approximate functionals have proven satisfactory in describing many materials and their properties. DFT methods have therefore become a backbone of materials science and DFT calculations are today a common component of many materials research efforts.

2.2.1 Schrödinger equation

The foundation of the theory of electronic structure is the time-independent, non-relativistic Schrödinger equation:

$$\hat{H}\Psi = \varepsilon\Psi \tag{2.1}$$

where $\hat{H}$ is the Hamiltonian operator, Ψ is the wavefunction, and ε is the energy of the state Ψ. $\hat{H}$ operator accounts for the kinetic and potential energy of all particles that build up the system; it contains five terms:

$$\hat{H} = \hat{T}_\mathrm{e} + \hat{T}_\mathrm{n} + \hat{V}_\mathrm{ee} + \hat{V}_\mathrm{ext} + \hat{V}_\mathrm{nn} \tag{2.2}$$

$$\begin{aligned}\hat{H} = &-\frac{\hbar}{2m_\mathrm{e}}\sum_{i=1}^{N}\nabla_i^2 - \frac{\hbar}{2}\sum_{A=1}^{M}\frac{1}{M_A}\nabla_A^2 + \frac{1}{2}\sum_{i=1}^{N}\sum_{j>i}^{N}\frac{e^2}{4\pi\varepsilon_0}\frac{1}{r_{i,j}} \\ &-\sum_{i=1}^{N}\sum_{A=1}^{M}\frac{e^2}{4\pi\varepsilon_0}\frac{Z_A}{r_{i,A}} + \frac{1}{2}\sum_{A=1}^{M}\sum_{B>A}^{M}\frac{e^2}{4\pi\varepsilon_0}\frac{Z_A Z_B}{r_{A,B}}\end{aligned} \tag{2.3}$$

with the first two corresponding to the kinetic energies of electrons and nuclei, respectively, and the following three to the potential energies from electron-electron, electron-nucleus, and nucleus-nucleus interactions, in that order. Electrons are denoted by lower case subscripts and nuclei by upper case subscripts, so that m_e, e, and r_i are the mass, charge, and positions of the electrons, and M_A, Z_A, and r_A are the mass, charge, and positions

of the nuclei. The term 'external' in the $\hat{V}_{\text{ext}}$ refers to the fact that, from the electron's viewpoint, the Coulomb attraction by the nuclei is external and, thus, system dependent. The system-independent internal potential (the electronic kinetic energy plus the repulsive electron-electron potential) has a universal character, meaning it can be applied to any system.

Solutions of the Schrödinger equation are the eigenvalues of the Hamiltonian, ε, and therefore correspond to the allowed energy levels; the lowest energy level represents the ground-state energy and the most stable form of the system. However, for real systems, the situation complicates way beyond the scope of computational abilities to solve the corresponding Schrödinger equation - a well-defined collection of atoms such as a molecule or a crystal, due to the number of electrons and nuclei involved, represents a many-body problem. Many-body problem generally refers to the determination of properties of microscopic systems containing a significant amount of mutually interacting particles, with microscopic addressing the need of quantum mechanics laws, and significant number of particles addressing systems with three or more particles. This is the point where, without approximations, the equation has no practical use.

In order to simplify calculations, several strategies have been proposed. First, forget about gravity, relativity, and time - an electron's mass is so small and its speed much slower than the speed of light. Also, if only the ground-state energy of electrons is of interest, then the potential energy of the system can be considered constant in time. This is why the time-independent, non-relativistic version of the Schrödinger equation is a good place to start. Second, forget about nuclei. Nuclei are by far more massive than electrons and, thus, electrons instantaneously respond to any movement of the nucleus and always occupy the ground-state of the momentary nuclear configuration. This means that the positions of nuclei are considered to be frozen and become not variables but parameters from electron's perspective. Kinetic energy of the nuclei can therefore be completely left out, which is known as the Born-Oppenheimer approximation. Additionally, the nucleus-nucleus Coulomb interaction can also be excluded, because it is constant for a fixed ionic configuration, and hence results only in a simple shift of the Born-Oppenheimer energy. After these approximations, the system is much simpler - Hamiltonian and the corresponding wavefunction depend only on the electron positions, $\vec{r}_i$:

$$\left[-\frac{\hbar}{2m_{\text{e}}}\sum_{i=1}^{N}\nabla_i^2+\frac{1}{2}\sum_{i=1}^{N}\sum_{j>i}^{N}\frac{e^2}{4\pi\varepsilon_0}\frac{1}{r_{i,j}}-\sum_{i=1}^{N}\sum_{A=1}^{M}\frac{e^2}{4\pi\varepsilon_0}\frac{Z_A}{r_{i,A}}\right]\Psi(\vec{r}_i)=\varepsilon\Psi(\vec{r}_i) \tag{2.4}$$

This is the starting point for computational material science, and the ground-state properties of any system can be determined by setting up the Hamiltonian, inserting it in the Schrödinger equation, and obtaining the observables. The equation works surprisingly simple, assuming the $\hat{H}$ and Ψ are known: the energy operator $\hat{H}$ operates on the wavefunction Ψ, giving the product of the energy and the wavefunction, $E\Psi$. Ψ remains as Ψ, and energy, E, comes out as a constant known as an eigenvalue, which is physically observable quantity and is what is wanted from the equation. The whole process is like a

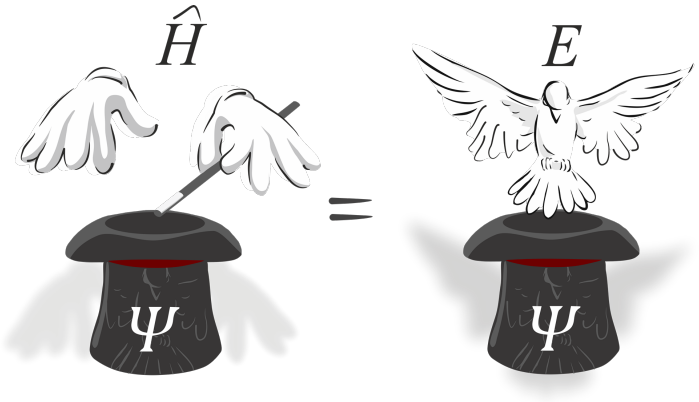

Figure 2.3: Magician - Schrödinger equation analogy.

magician (≡ operator) taking a dove (≡E) out of a supposedly empty hat (≡Ψ) - the dove is clearly somewhere out of the sight, and the magician simply moves it into the hat in a tricky way before revealing it, Figure 2.3. There is no change to the hat by the magic act. Similarly, all necessary information about E is contained in Ψ, and it shows up only after the operation of $\hat{H}$. The equation with this unique property is specifically called the eigenvalue problem.

2.2.2 Early first-principles calculations

Even after excluding nuclei as variables, dealing with N electrons, where each electron interacts with all the others, is still too complex to solve even numerically, and this is the case for any many-body system. The conclusion is obvious: one has to resort to further levels of approximation without sacrificing the parameter-free nature of the first-principles methods. To simplify the problem, each electron can be assumed to be an independent entity and its interaction with the rest expressed in an average manner, such that it does not recognise each electron as a single particle, but all of them as a mean-field. Hence, an N-electron system becomes a set of non-interacting individual electrons that move in an average electron density, and Ψ can be approximated as a product of individual electron wavefunctions, $\Psi(\vec{r}_i) = \Psi_1(\vec{r}_i)\Psi_2(\vec{r}_i)...\Psi_N(\vec{r}_i)$. This expression is known as the Hartree product, named after Douglas Hartree, 1928, who also proposed the self-consistent field (SCF) method for reaching its solution.[153, 154] The Hamiltonian of so approximated system contains three terms:

$$\left[-\frac{\hbar}{2m_\mathrm{e}}\sum_{i=1}^{N}\nabla_i^2 + \hat{V}_\mathrm{ext}(\vec{r}) + \hat{V}_\mathrm{H}(\vec{r})\right]\Psi(\vec{r}_i) = \varepsilon\Psi(\vec{r}_i) \tag{2.5}$$

where $\hat{V}_\mathrm{H}$ is the Hartree potential representing the classical Coulomb repulsive interaction between each electron and the mean-field. However, the Hartree method gave only crude estimates of energy because such oversimplifications, in addition to disregarding the exchange and correlation energies coming from the N-electron nature of the actual

system, violate two basic principles of quantum mechanics - the antisymmetry principle and, thus, Pauli's exclusion principle.

Hartree and Fock enhanced the method in 1930 by approximating the N-electron wavefunction as a linear combination of non-interacting one-electron wavefunctions in the form of a Slater determinant which guarantees the antisymmetry and fulfils Pauli's principle. Proofs of this are out of the scope of the thesis and can be found elsewhere.[155, 156, 157, 158] The electron-electron potential energy now contains two terms: the Hartree energy and the exchange energy coming from the antisymmetric nature of the wavefunction in the Slater determinant form. The latter is responsible for correction of the overestimated Hartree energy and makes the Hartree-Fock (HF) model more accurate. Nevertheless, the electron-electron correlation energy is still unaccounted for.

By introducing the Slater determinant wavefunction and the mean-field approximation, the HF method was able to ease the calculations while maintaining the parameter-free nature. Still, the overall number of electrons in materials imposed high computational costs. If a single molecule of CO_2 is considered, the full wavefunction is already 66-dimensional (3 dimensions for each of the 22 electrons), while HF scheme requires 22 one-electron wavefunctions. If, on the other hand, a simple nanocluster of 100 Pd atoms is of interest, the full wavefunction requires more than 23,000 dimensions, and even the HF simplification does not suffice in a reasonable reduction of computational efforts. Therefore, its practical applications remain limited to small systems with up to several tens of atoms. The breakthrough finally happened when Hohenberg and Kohn, 1964, presented two theorems concerning electron density and energy functionals, and after Kohn and Sham, 1965, came up with the scheme of density functional theory.

2.2.3 Variational principle

In quantum mechanics, a system under given conditions can have only one ground-state energy (if there are no degenerate states). This implies that, if the system's energy is minimised with respect to the wavefunction, the final energy obtained will be the ground-state energy, which is a formulation of the variational principle.

Since electrons are mutually interacting, expressing the wavefunction as a single Slater determinant is subject to a systematic improvement to the exact function. Due to the non-linearities introduced by the HF method, it adopts the iterative self-consistent procedure for the solution of the wave equation. This is performed in five steps: (i) choose a proper set of wavefunctions, $\{\Psi_i\}$; (ii) calculate electron density; (iii) calculate the three energy terms of Hamiltonian for N electrons; (iv) insert them into the wave equations and solve to get a set of $\{E_i\}$ and a new set of $\{\Psi_i\}$; (v) repeat the process until self-consistency is reached and input $\{\Psi_i\}$ and output $\{\Psi_i\}$ become the same in a predetermined range of error. The obtained $\{E_i\}$ will be the ground-state energies of each electron, and their sum is the ground-state energy of the system. Through the variational process, the initial approximated wavefunctions in the Slater determinant converge towards the true

ground-state wavefunctions. This approach is a very fundamental principle applied in all first-principles methods.[159]

2.2.4 Modern DFT

Although obtaining solutions of the Schrödinger equation can be viewed as the fundamental problem of quantum mechanics, it is worth noting that the wavefunction cannot be directly observed. The quantity that is of any physical interest, and can (in principle) be measured, is the probability that the N electrons are at a particular set of coordinates, $\vec{r}_1 ... \vec{r}_N$, which corresponds to $|\Psi(\vec{r}_1 ... \vec{r}_N)|^2$. A closely related quantity is the electron density at a particular position in space, $\rho(\vec{r})$. This function of only three spatial coordinates contains a great amount of information and it is physically observable, unlike the full wavefunction solution which is a function of $3N$ coordinates. Hence, for a nanocluster of 100 Pd atoms, the electron density theorem reduces the wavefunction search from more than 23,000 dimensions to a problem with only three dimensions. A quantum mechanical system is now an electron-density-dependent problem; there are no individual electrons but only their three-dimensional density, and computational efforts are thus drastically reduced to the level of practical use for molecules, crystals, solids, and materials with hundreds of atoms.

Anticipation of the potential role electron density could have in electronic calculations was built up for a long while until the formal verification of Hohenberg and Kohn who formulated two theorems, providing a sound foundation for the designation of electron density as the key factor in DFT.

Theorem 1: The external potential, $\hat{V}_{\text{ext}}(\vec{r})$, is (to within a constant) a unique functional of $\rho(\vec{r})$; since $\hat{V}_{\text{ext}}(\vec{r})$ fixes $\hat{H}$, the full many-particle ground-state is also a unique functional of $\rho(\vec{r})$.

From the theorem, it stands that at the ground-state, the electron density alone can define the external potential and vice versa. Since the internal energy is system- and $\hat{V}_{\text{ext}}(\vec{r})$-independent, its dependence on the electron density can be expressed as a universal functional $F[\rho(\vec{r})]$ although its explicit formula, which is same for all systems, remains unknown:

$$E[\rho(\vec{r})] = F[\rho(\vec{r})] + \int \hat{V}_{\text{ext}}(\vec{r})\rho(\vec{r})d\vec{r}. \tag{2.6}$$

Finally, Hamiltonians of various systems differ only by their external potential, which depends on the type of nuclei; therefore, electron density defines external potential, Hamiltonian, wavefunction, and all ground-state properties of the system:

$$\rho(\vec{r}) \rightarrow |\Psi[\rho(\vec{r})]\rangle, \qquad \rho(\vec{r}) \rightarrow \hat{V}_{\text{ext}}(\vec{r}). \tag{2.7}$$

In summary, different external potentials will always generate different electron densities and, if the interests are confined only within the ground-state properties of the system,

the sole knowledge of the electron density at a given external potential is sufficient to deduce the total energy or any other property. This is the base of all conventional DFT calculations.

Theorem 2: A universal functional for the energy $E[\rho(\vec{r})]$ in terms of electron density $\rho(\vec{r})$ can be defined valid for any external potential $\hat{V}_{\text{ext}}(\vec{r})$, and for any particular $\hat{V}_{\text{ext}}(\vec{r})$ the ground-state energy of the system is the global minimum value of this functional, and the density $\rho(\vec{r})$ that minimises the functional is the exact ground-state density:

$$E_0 = \min_{\Psi} \langle \Psi | \hat{T} + \hat{V}_{\text{ee}} + \hat{V}_{\text{ext}} | \Psi \rangle = \min_{\rho(\vec{r})} E[\rho(\vec{r})]. \tag{2.8}$$

The second Hohenberg-Kohn theorem defines an important property of the functional: the electron density that minimizes the energy of the overall functional is the true electron density corresponding to the full solution of the Schrödinger equation. If the true functional form were known, then the $\rho(\vec{r})$ could be varied until the energy from the functional is minimised, giving a prescription for finding the relevant electron density. This proved that the ground-state of a system could be reached by variational principle. As the exact functional is not known, the variational principle is used in practice with approximate functional forms. Mathematical proofs of these theorems are outside the scope of this thesis and interested readers are referred to review papers and relevant textbooks.[160, 161, 162, 163]

Although the Hohenberg-Kohn theorems rigorously proved a functional of the electron density exists that can be used to solve the Schrödinger equation, they said nothing about what this functional actually is. Up to date, significant efforts are focused towards development and improvement of such functionals, with intention of reaching as realistic description of electron behaviour as possible.

Earlier attempts to adopt electron density without the use of wavefunctions in the first-principles calculations were not very successful. In the present context, these approaches are only of historical interest and they are refrained from an in-depth description. The earliest method was developed by Thomas and Fermi in 1927, before the relation between the system energy and electron density was confirmed.[164, 165] In their quantum statistical model, a simple expression for the kinetic energy based on the $\rho(\vec{r})$ of a uniform electron gas was combined with purely classical expressions for the nucleus-electron and electron-electron potentials to obtain the total energy of the system. Properties arising from such description were only of limited use because of the very coarse approximation of the true kinetic energy and complete omittance of the exchange and correlation effects. However, the energy was given completely in the terms of $\rho(\vec{r})$ and no recourse to the wavefunction has been taken. Later adaptations by Bloch, 1929, and Dirac, 1930, to name a few, introduced modifications by including density-dependent expressions of quantum mechanical exchange effects.[166, 167] However, none of these extensions was particularly successful mainly due to the poorly expressed electron kinetic energy.

Given the two Hohenberg-Kohn theorems, Kohn and Sham proposed a reformulation of the energy functional in 1965. At the centre of their idea was exactly the realisation that most of the problems with previous methods are connected with the expression for the kinetic energy based on the uniform electron gas model. Since the HF orbital-based approaches performed much better in this respect, Kohn and Sham (KS) introduced the concept of a non-interacting reference system built from a set of orbitals (one-electron functions) such that the major part of the kinetic energy can be computed to a good accuracy. The remainder is merged with the non-classical contributions of the electron-electron repulsion, which are also unknown. Within this method, as much information as possible is computed exactly, leaving only a small part of the total energy to be determined by an approximate functional. As the electrons in the KS system are non-interacting, the KS wavefunction is a single Slater determinant constructed from a set of orbitals, ψ_i, known as KS orbitals, that are the lowest energy solutions to the KS equations:

$$\left[-\frac{\hbar}{2m_\mathrm{e}}\nabla^2 + \hat{V}_\mathrm{eff}(\vec{r})\right]\psi(\vec{r}_i) = \varepsilon_i\psi(\vec{r}_i) \tag{2.9}$$

where $\hat{V}_\mathrm{eff}$ is the effective potential in which the non-interacting particles move, and ε_i is the orbital energy of the corresponding one-electron orbital. The connection of the artificial non-interacting system and the real system is established by choosing an effective potential in the one-electron Hamiltonian operator such that the resulting density exactly equals the ground-state density of the real system of interacting electrons:

$$\rho(\vec{r}) = \sum_{i=1}^{N}|\psi_i(\vec{r})|^2 = \rho_0(\vec{r}). \tag{2.10}$$

By mapping the interacting N-electron system on the N non-interacting one-electrons under the given external energy, the expression for the overall Hamiltonian is:

$$\hat{H}[\rho(\vec{r})] = \hat{T}_\mathrm{s}[\rho(\vec{r})] + \hat{V}_\mathrm{H}[\rho(\vec{r})] + \hat{V}_\mathrm{xc}[\rho(\vec{r})] + \hat{V}_\mathrm{ext}[\rho(\vec{r})] \tag{2.11}$$

where $\hat{T}_\mathrm{s}$ represents kinetic energy functional for a fictitious system of non-interacting electrons with the same electron density as the interacting system ($\rho_0(\vec{r})$), $\hat{V}_\mathrm{H}$ is the Hartree energy arising classically from the mutual Coulomb repulsion of all electrons, and $\hat{V}_\mathrm{xc}$ is the correction term called exchange-correlation functional, which accounts for all the many-body effects. Of course, the non-interacting kinetic energy is not equal to the true kinetic energy of the interacting system even if the systems share the same density, and Kohn and Sham accounted for that by including the difference in the expression for $\hat{V}_\mathrm{xc}$:

$$\hat{V}_\mathrm{xc}[\rho(\vec{r})] = (\hat{T}[\rho(\vec{r})] - \hat{T}_\mathrm{s}[\rho(\vec{r})]) + (\hat{V}_\mathrm{ee}[\rho(\vec{r})] - \hat{V}_\mathrm{H}[\rho(\vec{r})]). \tag{2.12}$$

By definition, $\hat{V}_\mathrm{xc}$ equals to

$$\hat{V}_\mathrm{xc}(\vec{r}) = \frac{\delta E_\mathrm{xc}(\vec{r})}{\delta\rho(\vec{r})} \tag{2.13}$$

but its exact form remains unknown. Nevertheless, approximate and practical forms are widely available and can sufficiently reduce time and cost of calculations. Finally, to uniquely determine the orbitals in the non-interacting reference system such that they really provide a Slater determinant which is characterised by the density of the real system, orbital dependence of each energy term needs to be indicated (development is omitted from this thesis and can be found in [168, 169, 170]). Resulting formulation identifies the sum of $\hat{V}_{\mathrm{H}}$, $\hat{V}_{\mathrm{xc}}$, and $\hat{V}_{\mathrm{ext}}$ to be exactly equal to $\hat{V}_{\mathrm{eff}}$ from the non-interacting reference system. Thus, once these contributions are known, $\hat{V}_{\mathrm{eff}}$ is available and can be inserted into the one-particle equations, which in turn determine the orbitals and hence the ground-state density and energy. It should be noted that $\hat{V}_{\mathrm{eff}}$ already depends on the density through the Coulomb term. Therefore, just like the HF equations, the KS one-electron equations also have to be solved iteratively. From an initially guessed electron density, the eigenfunctions ψ_i are obtained as solutions of the KS equations, and $\hat{V}_{\mathrm{H}}(\vec{r})$ and $\hat{V}_{\mathrm{ext}}(\vec{r})$ are computed using this initial guess. Mixing the electron density from so obtained potentials with the preceding one, a better estimate of the density is obtained for further iterations. This procedure is repeated until a converged electron density is reached within the self-consistency cycle. Finally, the self-consistent electron density is used to compute the ground-state energy as:

$$E[\rho(\vec{r})] = \sum_{i=1}^{N} \varepsilon_i - \frac{1}{2} \int d\vec{r} \hat{V}_{\mathrm{H}}(\vec{r}) \rho(\vec{r}) - \int d\vec{r} \hat{V}_{\mathrm{ext}}(\vec{r}) \rho(\vec{r}) + E_{\mathrm{xc}} \rho(\vec{r}). \tag{2.14}$$

All non-trivial many-body quantum-mechanical effects (the non-classical effects of self-interaction correction, exchange and correlation), together with a portion belonging to the kinetic energy of interacting system, have been separated in the unknown exchange-correlation functional, $\hat{V}_{\mathrm{xc}}$. It is this functional which needs to be approximated and determines the accuracy of any DFT calculation.

2.2.5 Exchange-Correlation Functionals

Owing to the KS one-electron model, a practical method for solving the electronic ground-state problem of systems comprising of what is considered to be a sensible number of atoms in terms of materials science was finally given. However, solving the KS equations requires knowledge of the correct form of the exchange-correlation functional. Through the many-body quantum-mechanical effects, this functional is the connection between the true and one-electron systems, and it is currently not known in a closed and analytic form. Many approximate functionals were reported so far with various accuracies and computational costs.

The first attempt at obtaining a faithful representation of the exchange-correlation functional was the local density approximation (LDA).[171] LDA assumes that the exchange-correlation energy density is the same at every position in space as it would be for the homogeneous electron gas:

$$E_{\mathrm{xc}}^{\mathrm{LDA}}[\rho(\vec{r})] = \int d\vec{r}\rho(\vec{r})\varepsilon_{\mathrm{xc}}^{\mathrm{hom}}[\rho(\vec{r})] = \int d\vec{r}\rho(\vec{r})\{\varepsilon_{\mathrm{x}}^{\mathrm{hom}}[\rho(\vec{r})] + \varepsilon_{\mathrm{c}}^{\mathrm{hom}}[\rho(\vec{r})]\} \tag{2.15}$$

where $\varepsilon_{\mathrm{xc}}$ is the exchange-correlation energy density per electron. The exchange part, ε_{x}, which represents the exchange energy of an electron in a uniform electron gas of a particular density, is given in an analytical form:

$$\varepsilon_{\mathrm{x}}^{\mathrm{hom}}[\rho(\vec{r})] = -\frac{e^2}{4\pi\varepsilon_0}\frac{3}{4}\left(\frac{3\rho(\vec{r})}{\pi}\right)^{1/3}. \tag{2.16}$$

For the correlation part, ε_{c}, no such explicit expression is known, but it is rather obtained through highly accurate numerical simulations of the homogeneous electron gas. The LDA exchange-correlation potential is thus a fully local function depending only on the density at position $\vec{r}$. LDA has been extended to handle spin-polarised systems as the local spin-polarised density approximation (LSDA), where $\varepsilon_{\mathrm{xc}}$ and, thus, $E_{\mathrm{xc}}^{\mathrm{LSDA}}$, are functionals of two spin densities, $\rho(\uparrow)$ and $\rho(\downarrow)$.[172]

However, real systems are evidently not homogeneous and have varying density landscape. In order to account for this non-homogeneity, the local approximation was extended in terms of the gradient of the electron density, $\nabla\rho(\vec{r})$:

$$E_{\mathrm{xc}}^{\mathrm{GGA}}[\rho(\vec{r})] = \int d\vec{r}\rho(\vec{r})\varepsilon_{\mathrm{xc}}^{\mathrm{GGA}}[\rho(\vec{r}), \nabla\rho(\vec{r})]. \tag{2.17}$$

Most such functionals are constructed in the form of a correction term which is added to the LDA:

$$E_{\mathrm{xc}}^{\mathrm{GGA}}[\rho(\vec{r})] = \int d\vec{r}\rho(\vec{r})\varepsilon_{\mathrm{xc}}^{\mathrm{LDA}}F(s) = E_{\mathrm{xc}}^{\mathrm{LDA}}[\rho(\vec{r})] - \int d\vec{r}\rho^{(4/3)}\vec{r}F(s). \tag{2.18}$$

The argument of the function F is a local inhomogeneity parameter that depends on both the electron density and its gradient ($s = |\nabla\rho(\vec{r})|/\rho^{(4/3)}(\vec{r})$), and assumes large values not only for large gradients, but also in regions of small densities, such as the exponential tails far from the nuclei. Depending on the form of F, one can obtain different functional approximations, known as generalised gradient approximations (GGA), such as the parameter free PBE and PW91, and the empirical BLYP.[173, 174, 175]

If a ~10-fold increase in computational cost is affordable, advanced functionals beyond common GGA are available. They incorporate additional variables (such as higher-order density gradient) or, since the exchange contributions are significantly larger than the corresponding correlation effects, a certain amount (~25 %) of the exact non-local HF exchange energy. The latter are known as hybrid functionals. The HF methods do not account for the correlation energy, which causes spatially closer electrons, smaller bond lengths, larger binding energies, wider band gaps, and thus higher total energies. In DFT, on the other hand, systematic errors occur in the opposite way. Thus, it is expected that

the best compromise between computational costs and reduced errors can be achieved by introducing an HF exchange energy into the GGA approximated functional, typically in the form of:

$$E_{\mathrm{xc}}^{\mathrm{hybrid}} = CE_{\mathrm{x}}^{\mathrm{HF}} + (1-C)E_{\mathrm{x}}^{\mathrm{GGA}} + E_{\mathrm{c}}^{\mathrm{GGA}}. \tag{2.19}$$

The most commonly used hybrid functionals are B3LYP, PBE0, and HSE06.

2.2.6 DFT-X methods for improved treatment of electron correlation

GGA corrects most of the problems arising from the oversimplifications introduced by LDA, however, many features of the actual exchange and correlation effects are still missing. While the exchange energy of a collection of electrons can, in principle, be evaluated exactly and progress in such direction was realised by introducing hybrid functionals, the same cannot be achieved for the electron correlation. Additionally, due to the approximated nature of both effects, unphysical self-interaction is not completely removed from the final expression. As a result, physical properties that are governed primarily by electron correlation are challenging for approximate functionals. Two important examples are weak long-range interactions between atoms and the electronic structure of strongly correlated materials. Over the years, so-called DFT add-ons have been developed to treat such cases in appreciable fashion.

2.2.6.1 Dispersion interactions and DFT-D

Relationship between the electron correlation and long-range forces between atoms arises from the electron oscillations that lead to the deformations of the electron density and, consequently, to a transient dipole moment. The existence of such dipole moments creates a net dispersion interaction which, for two spherically symmetric atoms at a large distance R_{ij}, yields $-1/R_{ij}^6$ asymptotic behaviour. The simplest concept to account for these interactions within DFT is to add a dispersion-like contribution between each pair of atoms to the total DFT energy, and it is known as the DFT-D method:

$$E_{\text{DFT-D}} = E_{\mathrm{DFT}} - S\sum_{i\neq j}\frac{C_{ij}}{R_{ij}^6} f_{\mathrm{damp}}(R_{ij}) \tag{2.20}$$

where C_{ij} is a dispersion coefficient which can be calculated from the tabulated properties of individual atoms, and f_{damp} is a damping function to minimise contributions from interactions within typical bonding distances. S is a scaling factor applied uniformly to all pairs of atoms and it is estimated empirically. In this case, the correction only depends on the nuclei positions. A step further was achieved with DFT-D2 by adding a simple pair-wise force-field. The more sophisticated DFT-D3 uses environment-dependent dispersion coefficients and, unlike DFT-D and DFT-D2 which are based on all atom pairs, it also considers triplets of atoms to account for three-body effects. These formulations made DFT-D3 less empirical, i.e. the most important parameters are computed from first

principles, consistent within all chemically relevant elements of the periodic system, and, overall, more accurate than previous versions.

Because the dispersion correction is an add-on term, it does not directly alter the wavefunction or any physical or chemical property. However, it effects the structure by contributing to the forces acting on the atoms, which bears an impact on all properties.

2.2.6.2 Strongly correlated electron systems and DFT+U

When a system has strongly localised d- or f-orbitals, an extra repulsive interaction takes place between two electrons in those sites. In these cases, an electron is transferred from the delocalised to the localised state, and becomes more prone to the unphysical self-interaction. In other words, the motion of strongly localised electrons becomes 'correlated', and their wavefunction acquires a marked many-body character - the full account of the multi-determinant nature of the wavefunction and many-body terms of the electronic interactions. Thus, the HF method, which describes the electronic ground-state with a variationally optimised single determinant and discards any correlation, cannot appropriately capture the physics of strongly correlated materials. In DFT, on the other hand, the electron-electron interaction is a functional of the electron density, which is represented through effective single particle KS equations, and problems of strongly correlated systems can be traced to the overly-delocalised valence electrons, imprecise description of the exchange interaction, and consequent incomplete cancellation of the self-interaction.

One of the approaches formulated to account for strong correlation is the Hubbard model, where the electron-electron repulsion of electrons in a highly correlated site is quantified by the on-site Hubbard parameter U. The Hubbard Hamiltonian is the simplest many-body Hamiltonian to explicitly include electron correlation, and it contains two terms: a kinetic term allowing for the tunnelling of electrons between the sites, and a potential term consisting of an on-site interaction:

$$\hat{H}_{\mathrm{Hub}} = -t \sum_{i,\sigma} (c^{\dagger}_{i,\sigma} c_{i+1,\sigma} + c^{\dagger}_{i+1,\sigma} c_{i,\sigma}) + U \sum_{i} \hat{n}_{i\downarrow} \hat{n}_{i\uparrow} \tag{2.21}$$

where $\hat{n} = c^{\dagger}_{i,\sigma} c_{i,\sigma}$ is the spin-density operator for spin σ on the i-th site, and $c^{\dagger}_{i,\sigma}$ and $c_{i,\sigma}$ are fermion creation and annihilation operators. The first term describes the destruction of a fermion of spin σ on site i and its creation on site $i+1$ (or vice-versa) with the hopping allowed only between two sites which are adjacent. In virtue of the strong localisation, the Coulomb repulsion is only accounted for between electrons on the same atom through a second term which is proportional to the product of the occupation numbers of atomic states on the same site, whose strength is U (the 'Hubbard U').[176] This term is zero if the site is empty or has a single electron, and it assumes the value of U if the site is doubly occupied, necessarily by electrons of the opposite spin.

The LDA+U method (where +U correction can be applied to any generic DFT functional, not necessarily LDA) has an improved accuracy in describing the ground-state of

correlated systems through the implementation of the Hubbard Hamiltonian to describe strongly correlated electronic states, while the rest of the valence electrons are treated at the standard level of approximation. Within LDA+U, the total energy functional is given as the sum of DFT total energy functional and a correction term which depends on the orbital occupation numbers of a given shell of orbitals n_{s}:

$$E_{\mathrm{LDA+U}}[\rho(\vec{r})] = E_{\mathrm{LDA}}[\rho(\vec{r})] + E_U[n_{\mathrm{s}}] - E_{\mathrm{dc}} \tag{2.22}$$

where E_U is modelled by the Hubbard Hamiltonian, and E_{dc} is a double-counting term that represents the contribution to the DFT energy from correlated electrons as a mean-field approximation to the E_U to account for the additive nature of the $+U$ correction. The E_U term is derived according to the HF treatment of the electron-electron interaction of electrons within the designated shell. This formalism involves several approximations: (i) energy correction is meant only for a specified shell, (ii) the electron-electron repulsion operator is replaced by an operator representing screened electron-electron repulsion between electrons in a given shell, (iii) in the atomic limit of localisation, the orbitals that belong to the given shell do not mix among themselves. By invoking these approximations, the screened Coulomb and exchange integrals are combined with the orbital occupation dependency, resulting in implicit self-interaction, where a self-Coulomb energy term is cancelled exactly by a self-exchange term. Therefore, one can interpret the Hubbard correction as replacing the mean-field density-density interaction with an expression similar to HF for highly localised orbitals with double occupancy. The Hubbard correction is only applied to the localised states, and it is therefore a functional of occupation numbers that are often defined as projections of occupied KS orbitals on the states of a localised basis set.

Physically, the orbital energy of a fully occupied orbital in a designated shell is subject to a down shift proportional to the strength of U, whereas the empty orbitals are shifted up in energy by a factor proportional to U. As a result, if the treated orbitals form the frontier orbitals of the system, DFT+U is able to introduce a band gap opening proportional to the on-site strength U. As the effect of DFT+U is to shift d- or f-bands up and down in energy, one can easily imagine that, as the value of U is increased, at some point, one band is shifted over another. In other words, one could change the energetic ordering of different bands or alter the hybridisation between the states when varying the values of U parameter. As a consequence, improvement of the electronic structure will only take place within a certain range of U values. Hence, the strength of the correction to approximate DFT functionals is controlled by the effective on-site electronic interaction represented by the Hubbard U whose value is not known *a-priori*. In order to obtain quantitatively predictive results, it is crucial to have a method to compute the Hubbard U in a reliable way. The value of U is usually tuned in a semi-empirical way, through seeking agreement with available experimental data and using the so-determined value to make predictions on other aspects of the system's behaviour.

2.2.7 Periodicity and Bloch's theorem, basis sets and plane waves

DFT replaces the many-electron Schrödinger equation with a system of single-particle KS equations within approximation for the exchange-correlation functional. However, the correlated nature of the electrons is not the only obstacle in materials science; when it comes to a condensed matter system, where arrangements of atoms are repeated periodically in space, the number of electrons effectively reaches infinity. Therefore, in the computational treatment of materials, reduction of the system size is crucial, and it relies heavily on this periodicity of solids.

A specified set of atoms which, when repeated in every direction, creates the full three-dimensional crystal structure, together with the vectors that define the volume of the cell where those atoms are positioned, collectively describes a unit cell. By imposing periodic boundary conditions on a unit cell, it is duplicated periodically through the space in all directions effectively representing a bulk solid. This significantly reduces the number of atoms, and thus electrons, that are being simulated, and the problem becomes solving the KS equations only within a single unit cell, which is now viewed as a set of mathematical points in space (called lattice) that satisfy translational symmetry. To capture the behaviour of electrons more easily, it is convenient to introduce a concept of reciprocal space, where the reciprocal lattice represents the Fourier transform of the real lattice. So-transformed unit cell is known as Brillouin zone. The lattice points in the reciprocal space, called the k-points, therefore represent normals of the corresponding set of planes in the real space, and wavefunction becomes simply a grid with the lattice points defining the allowed wave vectors. Thus, the electrons of the crystals can be treated mathematically as waves in reciprocal space.

By exploiting the advantages of periodicity, which applies to atoms as well as to physical quantities (such as electron density), the number of electrons is considerably lowered. However, due to the complex number involved in the phase factor, wavefunction is not periodic. To obviate this problem, Bloch utilised the observation that the wavefunction differs from the plane waves of free electrons only by a periodic modulation, and that real electrons in an atom can be considered as perturbed free electrons. By mapping the plane waves onto the structurally repeating pattern of a solid, wavefunctions were made quasi-periodic in expression known as Bloch's theorem:

$$\psi_j(\vec{r}) = u_j(\vec{r})e^{ik(\vec{r})} \tag{2.23}$$

where ψ_j is the Bloch's wave, u_j is a periodic function with the same periodicity as the crystal, and k is the crystal wave vector. Since u_j is a periodic function, it may be expanded in terms of a Fourier series, $u_j(\vec{r})\sum_G c_{j,G}e^{iG\vec{r}}$, where G are reciprocal lattice vectors and $c_{(j,G)}$ are plane wave expansion coefficients. The electron wavefunctions may therefore be written as linear combinations of plane waves:

$$\psi_{j,k}(\vec{r}) = \sum_G c_{j,k+G}e^{i(k+G)\vec{r}}. \tag{2.24}$$

This theorem proved that it is possible to solve the Schrödinger equation for each value of k independently. Since any point in the reciprocal space can represent a k-point, there is an infinite number of discrete k-vectors well qualified to represent a wavefunction. Fortunately, the wavefunction varies smoothly over the space so that it can be simply sampled over a finite number of k-points that each represent a small region. It turns out that many parts of mathematical problems posed by DFT are much more convenient to solve in terms of k than they are to solve in terms of r. The net effect of Bloch's theorem has therefore been to change the problem of an infinite number of electrons to considering only a number of electrons in the unit cell at a finite number of k-points chosen so as to appropriately sample the Brillouin zone. In principle, the set of plane waves should also be infinite; in practice, the series can be truncated to require reasonable computational efforts. The coefficients for the plane waves have a kinetic energy defined through $\hbar^2|k + G^2/2m|$. Since plane waves with the low kinetic energy are typically contributing more than those of high kinetic energy, a kinetic energy cut-off can be introduced to achieve a finite basis set.

Exploiting the lattice periodicity by using Bloch's theorem has led to the re-expression of one-electron wavefunctions in terms of a Fourier expansion using plane waves as a basis set. Although plane waves are certainly not the only possible basis set that can be used (others include e.g. atomic wavefunctions, Gaussian- or Slater-type orbitals), they have the advantage of being mathematically simple, and the set is in principle complete, that is, it completely spans the Hilbert space without being biased towards any particular region. This is specifically important when there is no *a-priori* knowledge of the form of the electronic wavefunctions. Additionally, plane waves are already solutions for a free electron and thus satisfy the Bloch condition. On the negative side, using plane waves as a basis set results in regions deprived of electron density having equal quality of coverage as regions where electron density is substantially high.

2.2.8 Pseudopotentials

Plane waves have one serious drawback - slow convergence. A typical solid state system contains two basic categories of electrons: (i) core electrons which are chemically inert, described by localised wavefunctions, and tightly bound to the nuclei on very deep energy levels; and (ii) valence electrons responsible for the formation of atomic bonds, almost delocalised (electron gas in metals), and having most impact on the material's properties. The slow convergence is caused by the necessity to reproduce the nodal character of the valence orbitals, which, in turn, is a consequence of the valence orbitals being orthogonal to the fast oscillating tightly bound core orbitals. Hence, the heart of the problem is traced back to the cores. The most convenient way of reducing the computational burden of the core electrons is the use of pseudopotentials. Conceptually, a pseudopotential replaces the electron density of a chosen set of core electrons with a smoothed density chosen to match various physical and mathematical properties of the true ion core. The properties of the core electrons are then fixed in this approximate fashion in all subsequent calculations. With this frozen-core approximation, the valence electrons

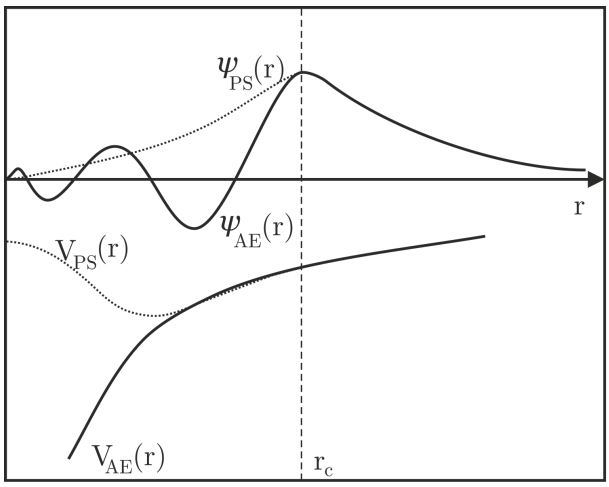

Figure 2.4: Schematic representation of a pseudopotential for a single electron, $V_{PS}(r)$, compared to the potential the same electron experiences in the field of all other electrons, $V_{AE}(r)$. Pseudo-wavefunction, $\psi_{PS}(r)$, contains no nodes inside the core region $r < r_c$ and becomes the exact one-electron wavefunction in the field of all other electrons, $\psi_{AE}(r)$, for $r > r_c$.

become the lowest-lying states with no core electron orthogonality requirements. Thus, the wavefunctions and the potentials with ions of the valence electrons can be softened through the so-called pseudisation process where r_{cut} is determined, so that the core part ($r < r_{cut}$) of the wave function is node-less and smooth, while for $r > r_{cut}$ the pseudo and all-electron wavefunctions coincide with each other and have the same eigenstates, Figure 2.4. Implementation of pseudopotentials therefore reduces both, the number of electrons and the number of plane waves needed for a complete expansion. Three common types of pseudopotentials are norm-conserving, ultrasoft (USPPs), and projector-augmented wave (PAW) pseudopotentials.

Combination of plane wave basis set and pseudopotentials is powerful enough to deal with thousands of electrons, which allows targeting of a wide range of materials science problems with first-principles calculations.

2.2.9 Determination of electronic properties

2.2.9.1 Bader analysis

The properties of materials are often described in terms of an interatomic charge transfer and the presence of ionic charges or electric multipoles on specific atoms. Since atomic charges are not observables and are not as such defined by quantum mechanical theory, they have to be extracted from calculated charge densities. Many different schemes have been proposed to partition the charge amongst fragments of the system from the continuous charge density output of the quantum mechanical calculations, some based on electronic orbitals (e.g., Mulliken population analysis) which are more suitable for localised basis sets, and others based on the charge density (e.g., Bader analysis).

Common algorithms based entirely on electron density as proposed by Bader rely on dividing the system space into regions by building the gradient vector field of the electron density. Sets of trajectories which trace out the density gradient $\nabla\rho$ terminate where the density is at maximum (each nucleus), and the system is partitioned into basins (atoms), where an atom is defined as a region bounded by surfaces with zero-flux in $\nabla\rho$. By integrating the electronic density within the Bader regions, the total charge on each atom can be estimated. Since this analysis is based solely on the mapped charge density, it is rather insensitive to the basis set used. However, these algorithms are known to have convergence problems for large systems and require significant computational efforts due to their complexity. Fast and robust algorithm for Bader decomposition of charge density by Henkelman puts no effort in trying to find critical points of electron density nor performing integration, and it only searches for the local maximum in ρ on the 3D charge density grid.[177]

The input for the Bader decomposition by Henkelman is the electron density specified on a regular grid of points in space, with the spacing between the grid points fine enough so that a linear interpolation between the points suffices in defining the bonding region between atoms. In order to find out which grid points belong to which Bader region, a path of steepest ascent in ρ is defined for each grid point (requiring only 26 subtraction and multiplication operations per grid point); the set of points whose paths end in the same maximum of ρ belong to the same Bader region. The total electronic charge within each region is then approximated by the sum over the corresponding grid points. This grid-based analysis is highly efficient: since the steepest ascent paths get terminated when a previously assigned point has been reached, there is a fixed amount of calculation required per grid point and the computational effort is therefore independent on the number of atoms in the system and scales linearly with the number of grid points.

Henkelman's implementation for performing Bader analysis [177] was employed for calculating the atomic charges based on the charge densities obtained by VASP, where the core and valence charge densities have been calculated on a fine grid and summed prior to the analysis to accurately reproduce the correct total core charge. The local magnetic moments were also extracted by this method using the spin-up and spin-down charge polarisation.

2.2.9.2 Work function analysis

The work function is, alongside atomic charges and local magnetic moments, another fundamental physical property of the solid which is related to its electronic structure. It is defined as the potential that an electron at the Fermi level must overcome to reach the level of zero kinetic energy in the vacuum immediately outside the solid. Hence, the work function is not a characteristic of bulk materials, but rather of their surfaces, and investigations into clean surfaces of metals testify to the substantial dependence of the work function on the atomic structure of a surface, where the work functions of different crystal planes may differ by as much as 20-25 %.[178, 179] It can be regarded as the difference in energy between an electron at rest in the vacuum and the most loosely

bound electrons in the solid (top of the valence band). Thus, certain physical phenomena where electrons are removed from the solid are highly sensitive to the value of the work function. The work function is also a very useful parameter in chemisorption systems where large changes in the charge density are induced, and the work function is thereby strongly dependent on the position and coverage of the adsorbate atoms. Dipole moments generated by the interatomic charge transfer between surface atoms and adsorbates often give a jump in the electrostatic potential between the material and the vacuum.[180, 181]

Work functions within this thesis were calculated as a difference between the potential in the vacuum of the simulation cell and the calculated Fermi level energy. The potential in the vacuum was determined by obtaining the planar average of the electrostatic potential within the z-direction by employing the Vaspkit postprocessing tool for VASP.[182] Convergence of the vacuum-level potential versus vacuum thickness has been carefully examined. Fermi level energy was taken as the energy of the highest occupied state.

2.3 MD

Once the atomic nature of matter became firmly established, quantum mechanics took charge of the microscopic world and DFT calculations provided reliable means for determination and prediction of electronic structure of smaller chemical systems. However, systems of biochemical and biophysical interest typically involve macromolecules with substantial number of atoms in their condensed phase environment. The inherent dynamical nature of such systems and the mobility of their environments demand that large number of conformations be subjected to energy calculations. Thus, an energy function is required that allows for 10^6 or more energy calculations on systems containing on the order of 10^6 atoms. Fortunately, a great deal of the behaviour of matter in its various states can still be understood in classical (meaning non-quantum) terms, and so it is that the classical N-body problem is also central to understanding matter, not only at macroscopic, but also at the microscopic level. These requirements of bio-systems are therefore fulfilled within computational studies using the empirical energy functions, whose mathematical equations include relatively simple terms, to describe the physical interactions that dictate the structure and dynamic properties of biological molecules. By the use of atomistic models, atoms become the smallest particles in the system rather than the electrons and nuclei used in quantum mechanics. These two simplifications allow for the required number of energy calculations on biomolecules to be attained within satisfactory accuracy. In standard treatment of such propagations, the classical equations of motion governing the microscopic evolution of a many-body entity represented by nuclei are solved numerically, subject to the boundary conditions. Therefore, the method is, in principle, classical, and nuclei are treated as classical point-like particles. It is the task of the numerical solution of this problem, which allows for investigation of the statistical and dynamical properties of a real poly-atomic system at the molecular level, that molecular simulation methods address.

In dynamical system theory, all possible states of a system are represented by a space called phase-space, with each state corresponding to a single unique point the system could visit during its trajectory travel over time. The phase-space trajectory serves as the common thread that binds diverse tools into molecular simulations. It is computed using classical mechanics and its features can be described in terms of classical non-linear dynamics. A molecular-scale simulation therefore consists of three principal steps: (1) construction of a representative system model, (2) calculation of its phase-space trajectory, and (3) analysis of the trajectory to obtain desired properties. The way in which molecular positions are computed in step (2) is used to discriminate among different methods. In molecular dynamics (MD), the positions are obtained by numerically solving differential equations of motion and, hence, the positions are connected in time - they reveal dynamics of individual molecules as in a motion picture. In other simulation methods, the molecular positions are not temporally related. For instance, in Monte Carlo (MC) simulations, the positions are generated stochastically such that a molecular configuration depends only on the previous configuration. There is also a possibility of combining the stochastic features of MC and deterministic features of MD for computing positions by using hybrid schemes. MC methods exhibit a powerful ability to analyse thermodynamic equilibrium but are unsuitable for investigating dynamic phenomena. MD methods are useful for thermodynamic equilibrium, but are more advantageous for investigating the dynamic properties of a system in a nonequilibrium situation, because it is usually the dynamics between initial and final states that carries the reasoning of certain events. To obtain system properties, analysis of the trajectory is performed by appealing to kinetic theory, statistical mechanics, and sampling theory. Taken together, these tools form the basis of molecular simulation making it a convenient method for studying the behaviour of large atomic ensembles, provided that the dynamics of interest is not of a duration that makes the simulation time impractical. Since work provided within the scope of this thesis includes only MD simulations, MC and hybrid methods will not be revisited.

2.3.1 Newtonian and Hamiltonian Dynamics

The foundation of modern MD is the so-called Hamiltonian mechanics. Hamiltonian mechanics is, in principle, equivalent to the Newton's equations of motion, with the only difference being that the equations of motion can be derived easily in non-Cartesian coordinates. In the Newtonian interpretation of dynamics, the translation motion of a spherical molecule i is governed by a force $\vec{F}_i$, where the motion and the applied force are explicitly related through Newton's second law:

$$\vec{F}_i = m\frac{d^2\vec{r}_i}{dt^2} \tag{2.25}$$

where m is the mass of the molecule and $\vec{r}_i$ now represents a position vector of an atom. For N spherical molecules, Newton's second law represents $3N$ second-order, ordinary differential equations of motion. If no external force acts on the molecule i, this reduces to Newton's first law: a molecule initially at rest will remain at rest and a molecule moving with a specified velocity will continue to move with that velocity until a force acts on it.

Although molecular forces and positions change in time, the functional form of Newton's second law is time independent. Consequently, there has to be a function of positions and velocities that is also constant in time - Hamiltonian, $H(\vec{r}^N,\vec{p}^N) = \text{const}$. For an isolated system, one of conserved quantities that can be identified as H is the total energy E, as the sum of kinetic and potential energies:

$$H(\vec{r}^N,\vec{p}^N) = \frac{1}{2m}\sum_i \vec{p}_i^2 + \mathcal{U}(\vec{r}^N) \tag{2.26}$$

where $\mathcal{U}$ results from intermolecular interactions. Obtained equations of motion from such time-independent Hamiltonian have the form of:

$$\frac{dH}{dt} = \sum_i \frac{\partial H}{\partial \vec{p}_i}\frac{d\vec{p}_i}{dt} + \sum_i \frac{\partial H}{\partial \vec{r}_i}\frac{d\vec{r}_i}{dt} = \frac{1}{m}\sum_i \vec{p}_i\frac{d\vec{p}_i}{dt} + \sum_i \frac{\partial \mathcal{U}}{\partial \vec{r}_i}\frac{d\vec{r}_i}{dt} = 0 \tag{2.27}$$

which can be satisfied only if:

$$\frac{\partial H}{\partial \vec{r}_i} = -\frac{d\vec{p}_i}{dt} \quad \text{and} \quad \frac{\partial H}{\partial \vec{p}_i} = \frac{\vec{p}_i}{m} = \frac{d\vec{r}_i}{dt}. \tag{2.28}$$

These equations are known as Hamilton's equations of motion and, for a system of N spherical molecules, they represent $6N$ first-order differential equations equivalent to Newton's $3N$ second-order equations. Comparison yields:

$$\frac{\partial H}{\partial \vec{r}_i} = -m\frac{d^2\vec{r}_i}{dt^2} \quad \text{and} \quad \vec{F}_i = -\frac{\partial H}{\partial \vec{r}_i} = i\frac{\partial \mathcal{U}}{\partial \vec{r}_i} \tag{2.29}$$

that is, any conservative force can be expressed as the negative gradient of potential function $\mathcal{U}$.

The classical equations of motion are deterministic and time-reversible and, consequently, a mechanical system is completely described by the positions and momenta of its N atoms. This means that the position and momentum can be conceived as the coordinates of a single point in a phase space which represents the microstate of the system. The point moves through phase-space tracing out trajectories according to the equations of motion. Within the MD simulation, the phase-space trajectory is obtained by numerically solving Newton's second law, or, equivalently, two Hamilton's equations. The first step is to set up a proper initial state of the system by setting the initial spatial configuration of the nuclei, their initial velocities, and the initial forces imposed on them. From these starting values, the trajectory of the nuclei is integrated. Total entity of interacting nuclei can be considered as a classical many-body system, with interactions between the nuclei and subsequent changes in time described on a classical level. For such many-body system, it is impossible to solve differential equations of motion analytically, and it is necessary to resort to numerical integrations.

Seemingly simple, the integration of equations of motion is highly non-trivial due to the fact that a finite-timestep must be used. Under the assumption that the interaction

force is constant in small time intervals, discretisation scheme can be applied so that the equations of motion are solved in small steps (timesteps) while their derivatives are evaluated numerically. Timestep is system- and potential-dependent, while the state point of interest also needs to be taken into the account.

2.3.2 Calculating Forces

MD simulation consists of the numerical, step-by-step solution of the classical equations of motion starting from an initial state of the system. For this purpose, the forces $\vec{F}_i$ acting on the atoms have to be determined by derivation from a description of the interatomic interactions. Depending on how the interatomic interactions are calculated, the MD simulations can be separated into two categories: the traditional classical MD simulations, where the interactions between different nuclei are described by empirical potentials through a potential energy function $\mathcal{U}(\vec{r}^N)$, and the more recent *ab initio* MD simulations, where the interactions between the nuclei are calculated on-the-fly after the electronic structures of the system at each specific spatial configuration of the nuclei were obtained quantum mechanically in an *ab initio* manner.

2.3.2.1 Potential energy functions - classical MD

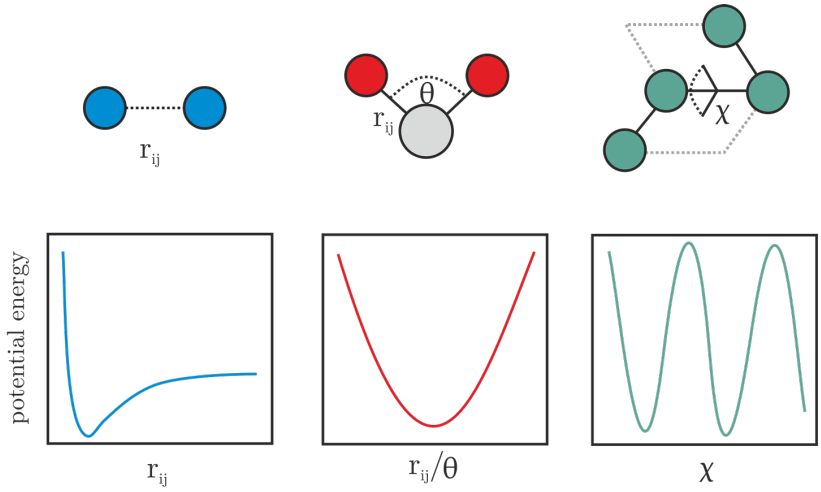

Figure 2.5: Schematic representation of the potential functions used in a force field: (left) potential between two interacting particles at a r_{ij} distance; (middle) harmonic potential for modelling an angle θ between three interacting particles; (right) potential for modelling a dihedral angle χ between quadruples of interacting atoms.

A potential energy function $\mathcal{U}(\vec{r}^N)$, known as a force field, is a mathematical equation that allows calculation of the potential energy of a system through terms describing various physical interactions which dictate its structure and properties. The interaction terms can be separated based on their contribution to internal or external potential energy as:

$$\mathcal{U}(\vec{r}^N)_{\text{tot}} = \mathcal{U}(\vec{r}^N)_{\text{internal}} + \mathcal{U}(\vec{r}^N)_{\text{external}} \tag{2.30}$$

$$\mathcal{U}(\vec{r}^N)_{\text{internal}} = \sum_{\text{bonds}} K_b(b-b_0)^2 + \sum_{\text{angles}} K_\theta(\theta-\theta_0)^2 + \sum_{\text{dihedrals}} K_\chi[1+cos(n\chi-\sigma)] \quad (2.31)$$

$$\mathcal{U}(\vec{r}^N)_{\text{external}} = \sum_{\text{nonbonded}} \left(\epsilon_{ij} \left[\left(\frac{r_{ij,\min}}{r_{i,j}} \right)^{12} - \left(\frac{r_{ij,\min}}{r_{i,j}} \right)^{6} \right] + \frac{q_i q_j}{\epsilon_D r_{i,j}} \right) \quad (2.32)$$

where, beyond the form of equations, it is important to differentiate between the terms associated with the structure subjected to the energy calculations (bond lengths b, valence angles θ, torsion angles χ, and distances between atoms, r_{ij}) and the parameters that allow for different types of atoms and molecular connectivities to be treated using the same equation shape. It is the quality of these parameters, as assessed by their ability to reproduce experimental or quantum-mechanical values of targeted data, that ultimately determines the accuracy of the results obtained from molecular simulations. A schematic representation of potentials is shown in Figure 2.5. Once the structure of the system is set up and all parameters required for the potential energy function are chosen, the determination of forces acting on the atoms is conducted as:

$$\vec{F}_i = -\frac{\partial}{\partial \vec{r}_i} \mathcal{U}(\vec{r}^N). \quad (2.33)$$

2.3.2.2 Ab initio MD

Despite the success of classical MD, the need of predefining a fixed interaction potential in form of a force field remains a resounding challenge. This is the most obvious for systems with many atomic types for which a substantial amount of interaction combinations has to be parametrised, or when there is a change in the electronic structure during a course of the simulation. Additionally, even after the sufficient potentials have been elaborated, changing a single species provokes enormous efforts to suitably re-parameterise the potential energy function. As a result, systematic studies are *a tour de force* if consistent potentials are not already available.

With the advent of *ab initio* molecular dynamics (AIMD), which unifies Newton's equations of motion and electronic Schrödinger equation, the scope of both MD and DFT has been greatly extended. The fundamental idea behind AIMD is to compute the forces on-the-fly as first-order derivatives of the ground-state energy by accurate electronic structure calculations as the MD trajectory is generated, allowing for complex simulations without relying on adjustable parameters which constitute its predictive power. This way, the electronic variables are active degrees of freedom in the course of a simulation rather than beforehand integrated parameters that are kept fixed in the form of interaction potentials. The approximation level is therefore shifted form the chosen definition of the force field to the exchange-correlation functional form of the Schrödinger equation. From the complementary derivations of AIMD methods, Born-Oppenheimer (BOMD), Ehrenfest, and Car-Parrinello (CPMD), the former will be described since it was employed

within this thesis, while details of the latter two can be found in further readings.[183, 184, 185]

2.3.3 Born-Oppenheimer MD

The BOMD is based on the aforementioned Born-Oppenheimer approximation, which rests on the fact that nuclei are much more massive than electrons, so the latter can be considered as particles that follow the nuclear motion adiabatically. This means the electrons respond instantaneously to the nuclear motion and nuclei can be seen as immobile with respect to the electronic motion. Hence, the nuclear configuration $\{\vec{r}_I\}$ can be fixed, and the electronic wavefunction solved through implicit dependence on that specific configuration. The total wavefunction in BOMD is, therefore, formulated as:

$$\Psi_{\text{tot}}(\{\vec{r}_i\},\{\vec{r}_I\};t) \approx \psi_{\text{BO}}(\{\vec{r}_i\},\{\vec{r}_I\})\chi_{\text{BO}}(\{\vec{r}_I\},t) \tag{2.34}$$

with a time-dependent nuclear term, χ_{BO}, and an electronic term, ψ_{BO}, which depends parametrically on $\vec{r}_I$. The electronic wavefunction, ψ_{BO}, has to satisfy the time-independent Schrödinger equation for the electrons with fixed nuclei:

$$\left(-\frac{1}{2}\sum_{i=1}^{N}\frac{\hbar^2}{m_e}\nabla_i^2 + \hat{V}_{I-i}(\vec{r}_i,\vec{r}_I)\right)\psi_{\text{BO}} = E_{I-i}(\vec{r}_I)\psi_{\text{BO}} \tag{2.35}$$

where $\hat{V}_{I-i}$ contains the Coulomb interaction energies and its definition depends on the choice of the exchange-correlation functional as defined earlier. This equation yields a set of eigenfunctions, $\psi_{\text{BO},i}$, with corresponding eigenvalues, $E_{I-i,i}$. The total time-independent Schrödinger equation for both electrons and nuclei, is given by:

$$\left(\frac{1}{2}\sum_{I=1}^{M}\frac{\hbar^2}{M_I}\nabla_I^2 - \frac{1}{2}\sum_{i=1}^{N}\frac{\hbar^2}{m_e}\nabla_i^2 + \hat{V}_{I-i}(\vec{r}_i,\vec{r}_I)\right)\chi_{\text{BO}}\psi_{\text{BO}} = E\chi_{\text{BO}}\psi_{\text{BO}}. \tag{2.36}$$

Multiplying both sides from left with ψ^*_{BO}, integrating over $\{\vec{r}_i\}$, and disregarding the terms with negligible contribution due to the mass difference between electrons and nuclei gives:

$$\left(-\frac{1}{2}\sum_{I=1}^{M}\frac{\hbar^2}{M_I}\nabla_I^2 + E_{I-i}(\{\vec{r}_I\})\right)\chi_{\text{BO}} = E\chi_{\text{BO}} \tag{2.37}$$

where the electronic energy $E_{I-i}(\{\vec{r}_I\})$ enters the nuclear equation as the internuclear potential. However, the electron equation results in a set of eigenvalues $E_{I-i,i}$, meaning each eigenvalue will give rise to a different internuclear potential. Owing to the fast movement of light-weighted electrons in contrast to the bulky nuclei, it can be assumed that the electrons will be able to adjust themselves to the electronic ground-state for the current nuclear position. The ground-state eigenvalue $E_{I-i,0}$ can therefore be used to set up the time-dependent Schrödinger equation for the system:

$$i\hbar\frac{\partial}{\partial t}\chi_{\mathrm{BO}} = \left(-\frac{1}{2}\sum_{I=1}^{M}\frac{\hbar^2}{M_I}\nabla_I^2 + E_{I-i,0}(\{\vec{r}_I\})\right)\chi_{\mathrm{BO}} \tag{2.38}$$

and final equations of motion for BOMD can be expressed as:

$$m_I\frac{d^2\vec{r}_I}{dt^2} = -\nabla_I \min_{\psi_{\mathrm{BO},0}}\{\langle\psi_{\mathrm{BO},0}|\hat{H}_{I-i}|\psi_{\mathrm{BO},0}\rangle\} \tag{2.39}$$

$$\hat{H}_{I-i}\psi_{\mathrm{BO},0} = E_{I-i}(\{\vec{r}_I\})\psi_{\mathrm{BO},0}. \tag{2.40}$$

Thus, the computation of the electronic structure is reduced to the solution of the time-independent electronic Schrödinger equation for specified nuclear configuration, which is then used for computations of forces acting on the nuclei at each time step. The only time-dependency of the electrons is due to the classical motion of the nuclei. The disadvantage of BOMD is, however, that a minimisation is required at each time step. Hence, it suffers severely from the dimensionality bottleneck as the number of active nuclear degrees of freedom increases.

2.3.4 MD Algorithm

The MD algorithm does not represent the cutting edge of research as it consists of numerically solving Newton's/Hamilton's equations of motion, a system of coupled ordinary differential equations. Once the force on and acceleration of each particle in the system are obtained from the initial nuclear positions, velocities, and interaction functions, they are used in conjunction with a standard finite difference numerical integration method to advance each atomic position over a duration of the timestep. Many methods exist to perform such numerical integrations, however, algorithm applied to MD problems must cope with expensive calculations of forces, typically involving a sum over all pairs of atoms, while accurately calculating dynamical properties and staying on the constant-energy hypersurface for long running times, in order to sample the correct ensemble. Thus, criteria governing the choice of an integration scheme are the conservation of energy and computational efficiency. In addition, to ensure rapid sampling over the phase-space, chosen timestep should be as large as possible without impairing accuracy or hypersurface evolution. Consequently, through years, MD algorithms have not included high derivatives of positions and velocities, which allowed for the timestep to be significantly increased without risking energy conservation. These observations collectively tend to favour the use of Verlet algorithm in one form or another, and the Verlet class of integrators is most commonly employed in MD simulations. While other approaches, such as Leap-Frog algorithm, are available, they will not be discussed.

2.3.4.1 The Verlet Algorithm

The discretised version of Newton's second law can be obtained using the central difference approximation for the second derivative with time increment Δt:

$$\frac{\vec{r}_i(t+\Delta t) - 2\vec{r}_i(t) + \vec{r}_i(t-\Delta t)}{\Delta t^2} = \frac{\vec{F}_i(t)}{m_i}. \tag{2.41}$$

In order to obtain energy conservation in an MD algorithm, invariance under the time inversion applies and the position of the particle after the time increment is given as:

$$\vec{r}_i(t+\Delta t) = 2\vec{r}_i(t) - \vec{r}_i(t-\Delta t) + \Delta t^2 \frac{\vec{F}_i(t)}{m_i}. \tag{2.42}$$

The new position therefore requires the knowledge of the current position, $\vec{r}_i(t)$, the position at previous timestep $\vec{r}_i(t-\Delta t)$, and the force acting on the particle, $\vec{F}_i(t)$. The Verlet class of integrators assumes that the positions $\vec{r}_i(t+\Delta t)$ and velocities $\vec{v}_i(t+\Delta t)$ of nuclei within the timestep can be reasonably approximated by Taylor expansions:

$$\vec{r}_i(t+\Delta t) = \vec{r}_i(t) + \vec{v}_i(t)\Delta t + \frac{\vec{F}_i(t)}{2m_i}\Delta t^2 + ... \tag{2.43}$$

$$\vec{v}_i(t+\Delta t) = \vec{r}_i(t) + \frac{\vec{F}_i(t)}{2m_i}\Delta t + ... \tag{2.44}$$

or, equivalently, for $\vec{r}_i(t-\Delta t)$:

$$\vec{r}_i(t-\Delta t) = \vec{r}_i(t) - \vec{v}_i(t)\Delta t + \frac{\vec{F}_i(t)}{2m_i}\Delta t^2 - \frac{d\vec{F}_i}{2m_i dt}\Delta t^3 + ... \tag{2.45}$$

Adding or subtracting the two equations then yields the expressions for $\vec{r}_i(t+\Delta t)$ and $\vec{v}_i(t)$:

$$\vec{r}_i(t+\Delta t) = 2\vec{r}_i(t) - \vec{r}_i(t-\Delta t) + m^{-1}\vec{F}_i(t)\Delta t^2 \tag{2.46}$$

$$\vec{v}_i(t+\Delta t) = \frac{\vec{r}_i(t+\Delta t) - \vec{r}_i(t-\Delta t)}{2\Delta t}. \tag{2.47}$$

This is the Verlet algorithm. It has many attractive properties as it is simple, time reversible, and conserves energy. However, velocities are calculated at each timestep from the central difference in the position of the particle rather than being taken into the account as dynamical variables. Additionally, the expressions for position and velocities involve differences between large, similar numbers, which leads to numerical inaccuracies. A variant of the method known as the velocity Verlet algorithm removes these shortcomings by explicitly taking velocities into account and replacing the subtractions of quantities by sums, and it is numerically preferable when using computers of finite precision. Velocity of the particle is used to obtain the difference between the positions at different times:

$$2\vec{r}_i(t+\Delta t) = \vec{r}_i(t+\Delta t) + 2\vec{r}_i(t) - \vec{r}_i(t-\Delta t) + \Delta t^2 m^{-1}\vec{F}_i(t) \tag{2.48}$$

$$2\vec{r}_i(t+\Delta t) = 2\vec{r}_i(t) + 2\Delta t\vec{v}_i(t) + \Delta t^2 m^{-1}\vec{F}_i(t) \tag{2.49}$$

$$\vec{r}_i(t+\Delta t) = \vec{r}_i(t) + \Delta t\vec{v}_i(t) + \frac{\Delta t^2}{2} m^{-1}\vec{F}_i(t). \tag{2.50}$$

The expressions for the velocities using this algorithm are:

$$\vec{v}_i(t+\frac{\Delta t}{2}) = \vec{v}_i(t) + \frac{\Delta t}{2} m^{-1}\vec{F}_i(t) \tag{2.51}$$

$$\vec{v}_i(t+\Delta t) = \vec{v}_i(t+\frac{\Delta t}{2}) + \frac{\Delta t}{2} m^{-1}\vec{F}_i(t+\Delta t). \tag{2.52}$$

From a computational point of view, velocity Verlet algorithm has the intrinsic advantage of explicitly calculating the velocities at every timestep resulting in higher precision.

2.3.5 Determination of properties

Ultimately, the macroscopic properties are calculated from the obtained phase-space trajectory. According to the molecular theory of matter, macroscopic properties result from the behaviour of collections of individual atoms; in particular, any measurable property A can be interpreted in terms of some function $A(\vec{r}^N, \vec{p}^N)$ that depends on the position of the phase point in the phase-space $\{\vec{r}^N, \vec{p}^N\}$, which is in turn a function of the positions and momenta of the constituting particles. A measured value of A, A_m, is not obtained from an experiment performed at an instant; rather, the experiment requires a finite duration. During that measuring period, individual atoms evolve through many positions and momenta; that is, the phase point moves along its trajectory in the phase-space. Therefore the measured value A_m is the phase function $A(\vec{r}^N, \vec{p}^N)$ averaged over a time interval t:

$$A_m = \frac{1}{t}\int_{t_0}^{t_0+t} A(\vec{r}^N(t), \vec{p}^N(t))dt. \tag{2.53}$$

For systems at thermodynamic equilibrium, this average must be independent of the location at the starting time t_0. Moreover, at equilibrium, it is assumed that this interval average reliably approximates the time average $\langle A \rangle$, which would be obtained from a measurement performed over an essentially infinite duration:

$$A_m \cong \langle A \rangle = \lim_{t\to\infty} \int_{t_0}^{t_0+t} A(\vec{r}^N(t), \vec{p}^N(t))dt. \tag{2.54}$$

2.3.6 Thermodynamics ensembles

Within the MD framework, obtained trajectory provides descriptions of the statistical properties of the system for it is positioned on a certain constant-energy surface in the phase-space. There is no exchange in the particles and/or energy between the system and

the surroundings, nor is there any change in the volume of the system (NVE ensemble). After a proper initial state is set up and MD discretisation scheme applied, if the time step is sufficiently small the total energy will be conserved (within a certain tolerance). If the ergodic hypothesis (given an infinite amount of time the trajectory will go through the entire constant-energy hypersurface in the phase-space) is further imposed, a proper micro-canonical ensemble will be simulated.

Most experiments, however, do not conserve these quantities and non-Hamiltonian extensions had to be proposed. The simplest example is an experiment carried out at a constant temperature T. In this case, the statistical behaviour of the system at a finite temperature must be accurately taken into the account, and the states associated with the system in the phase-space visited during the experiment are not within a certain constant-energy level anymore. To achieve this in simulations, the constant-volume and constant-temperature canonical (NVT) ensemble needs to be implemented by introducing a temperature coupling algorithm (thermostat) through which the energy exchange between the system and environment can be properly described. This modifies the Newton's equations of motion, rescaling the velocities of the particles such that the distribution of the momenta corresponds to the Maxwell distribution. In this case, the energy is not conserved but fluctuates around a constant value, thus, the configurations explored in the MD simulation do not have the same probability like in the NVE ensemble. One of the first successful attempts of incorporating deterministic trajectories in MD simulations at finite temperature included an additional artificial degree of freedom to control the temperature developed by Nosé and Hoover; the corresponding thermostat is therefore known as the Nosé-Hoover thermostat.[186]

Incorporation of the Nosé-Hoover thermostat assures simulation of a system which is (asymptotically, i.e. at large times) in the NVT ensemble by introducing a fictitious dynamical variable that accelerates or decelerates particles until the desired temperature is reached through the kinetic energy and the equipartition function. The physical meaning of such variable is that of friction, ζ, and it is included in the equation of motions to keep the kinetic energy constant as:

$$m_i \frac{d^2\vec{r}_i}{dt^2} = \vec{F}_i - \zeta m_i \vec{v}_i \tag{2.55}$$

$$m_i \frac{d\zeta}{dt} = \frac{1}{Q}\left[\sum_{i=1}^{N} m_i \frac{\vec{v}_i^2}{2} - \frac{3N-1}{2} k_B T\right] \tag{2.56}$$

where Q determines the relaxation of the dynamics of the friction, $\zeta(t)$, and can be considered as a fictional 'heat bath mass'. In a steady state, where $d\zeta/dt = 0$, this gives the kinetic energy of $[3(N+1)/2]k_B T$, satisfying the equipartition. The additional degree of freedom is that of ζ, and the temperature is therefore not fixed, but tends to reach and maintain the targeted value. The equations of motion of the Nosé-Hoover thermostat can be implemented by a small modification of the velocity Verlet algorithm:

$$\vec{r}_i(t+\Delta t) = \vec{r}_i(t) + \vec{v}_i(t)\Delta t + \left[\frac{\vec{F}_i(t)}{m_i} - \zeta(t)\vec{v}_i(t)\right]\frac{\Delta t^2}{2} \tag{2.57}$$

$$\vec{v}_i(t+\frac{\Delta t}{2}) = \vec{v}_i(t) + \frac{\Delta t}{2}[m^{-1}\vec{F}_i(t) - \zeta(t)\vec{v}_i(t)] \tag{2.58}$$

$$\zeta(t+\Delta t) = \zeta(t) + \frac{\Delta t}{2Q}\left[\sum_{i=1}^{N} m_i\frac{\vec{v}_i(t)^2}{2} - \frac{3N-1}{2}k_bT\right]. \tag{2.59}$$

Other ensembles such as constant-temperature and constant-pressure (NPT) ensemble can be achieved through similar principles, i.e. by introducing a barostat that rescales the positions of the particles leading to volume fluctuations.

2.4 Rare events

The key feature that has made molecular dynamics so appealing is its ability to inexpensively follow the dynamical evolution of the system, giving insight into the microscopic behaviour of the system on an extended timescale. In the same time, this is also the major limitation of MD: most of the interesting dynamics occurs as the system moves from one energy basin to another through infrequent rare events. Challenges that these short-living intermediate structures impose on experimental analysis methods make them even more attractive candidates for computational simulations. Another important task of theoretical chemistry and physics is the calculation of transition states (TS), but the transitions of interest are typically many orders of magnitude slower than the vibrations of atoms in motion. When coupled with the small timesteps (on the order of femtoseconds) needed for the total energy to remain conserved, this severely restricts the timescales accessible in MD simulations, leading to limited phase-space exploration. For example, for a process with a low energy barrier of 0.5 eV, required simulation time to obtain sufficient classical mechanics trajectory to capture this transition event is in order of 10^4 years, which is simply inaccessible. The 'rare event' problem is therefore devastating for MD simulations, and, for a minimum energy path connecting initial and finals states to be sampled, where such metastable intermediates (local minima) and saddle points (local maxima) are to be found, a different approach is required, such as nudged elastic band method (NEB) or metadynamics.

2.4.1 Metadynamics

Metadynamics is a computational technique aimed at enhancing the sampling of the phase-space of complex systems. It is based on the identification of a few selected degrees of freedom called collective variables (CVs), whose fluctuations are critical for crossing high free-energy barriers so that the rare event of interest can be captured during the simulation time. Consequently, instead of monitoring the full trajectory $r(t)$ of the system, a reduced trajectory $s(t) = s(r(t))$ is analysed. In this method, the sampling is accelerated

by a history-dependent bias potential constructed as a sum of Gaussian distributions cantered along the trajectory of the chosen CVs:

$$V_G(s(r),t) = \omega \sum_{t'=\tau_G,2\tau_G} e^{-\frac{(s(r)-s(r(t')))}{2\sigma_s^2}} \tag{2.60}$$

where the sum is for $t < t$, and $s(r)$ are collective variables generally expressed as non-linear functions of the atomic coordinates of the system. Three parameters enter into the definition of V_G: (1) the height ω of the Gaussian distributions, (2) the width σ_s of the Gaussian distributions, and (3) the frequency τ_G^{-1} at which the Gaussian distributions are deposited. These parameters determine the accuracy and efficiency of the free energy reconstruction. If the Gaussians are large, the free energy surface is explored at a fast pace, but the reconstructed profile will be affected by large errors. If the Gaussian are instead small or deposited infrequently, the reconstruction is more accurate, but takes a longer time. Typically, the width is chosen to be of the order of the standard deviation of the CV in a preliminary unbiased simulation in which the system explores a local minimum of the free energy surface. The height can be estimated from the expected energy barriers. The bias potential of chosen σ_s and ω fills the minima in the free energy surface, allowing the system to efficiently explore the space defined by the CVs where the energy wells in this collective coordinate space are identified, and the addition of positive Gaussian potentials discourages the system to revert back to the wells.

For any choice of the parameter ω, the bias potential $V_G(s(r),t)$ also represents an unbiased estimator of the free energy as a function of the reaction coordinate $s(r)$. It has been demonstrated that, after a transient time t_{eq}, which corresponds to the time needed to fill all the relevant free energy minima of the system, $V_G(s(r),t)$ reaches a stationary state in which it grows evenly fluctuating around an average. If $V_G(s(r),t)$ after t_{eq} is an unbiased estimator of -$F(s)$, at finite t the time average of $V_G(s(r),t)$ defined as:

$$\overline{V}_G(s(r)) = \frac{1}{t - t_{\text{eq}}} \int_{t_{\text{eq}}}^{t_{\text{sim}}} dt' V_G(s(r),t') \tag{2.61}$$

$$\lim_{t\to\infty} \overline{V}_G(s(r)) \sim -F(s) \tag{2.62}$$

shows deviations from $-F(s)$, which becomes smaller as t increases. This time average represents the best estimate of the free energy that can be obtained with metadynamics. Figure 2.6 shows the time evolution of the bias potential V_G as a function of the CV and the corresponding free-energy $F(x)$, for a model system with two wells.

The widest implementation of metadynamics is through PLUMED, an external plugin that can be interfaced with some of the most popular MD codes through a simple patching procedure.[187] However, a native implementation of classical and *ab initio* metadynamics is also available in ORAC, CPMD, and NAMD, as well as in CP2K.[188, 189, 190] Various versions of metadynamics are available in CP2K, such as extended Lagrangian metadynamics, well-tempered metadynamics, and the multi-walker scheme. The code offers a

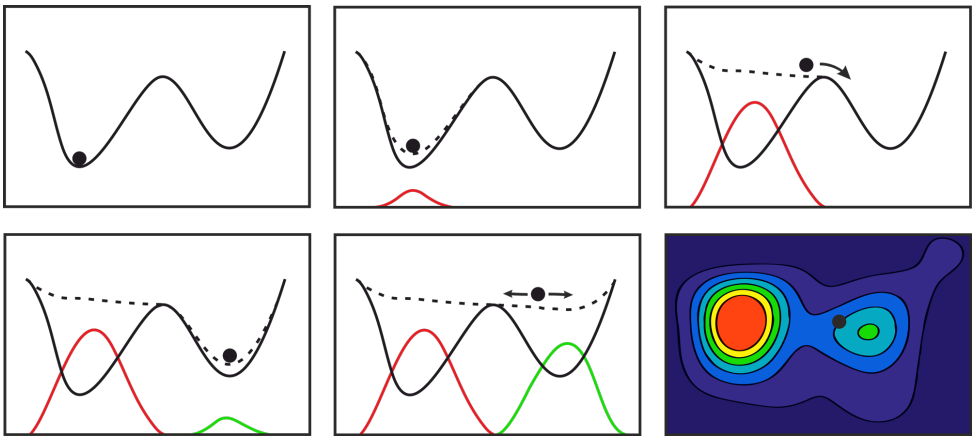

Figure 2.6: Time evolution of the metadynamics sampling of a system with two wells over one collective variable, CV, and corresponding energy landscape for sampling over two collective variables (bottom right). For sampling with one CV, CV is on the x-axis and free energy is on the y-axis; for sampling with two CVs, CVs are on x- and y- axes, and free energy is on the z-axis depicted by a colour map.

large choice of collective variables and a possibility of their combination to easily define new variables. A regular, non-tempered metadynamics formulation was used within this thesis as implemented in the CP2K software.

2.4.1.1 Collective variables

To minimise the complexity of the problem, a $3N$ dimensionality of the phase-space is reduced to the space with $M \ll 3N$ dimensions enclosed by CVs which can properly describe a transition of interest and are functions of the atomic coordinates. For rare event to be successfully simulated within this new CV-space, $s(r)$, the number of CVs should be kept at minimum, but still sufficient to clearly separate various metastable states and determine the position of the TS. These variables are usually derived from simple functions of the atomic positions such as bond lengths, angles, torsions, coordination numbers, but a single CV can also be a combination of multiple one-dimensional collective variables. The goal of these parameters is to provide dynamically meaningful measure of the progress of a rare transition state of a system when going from one local minimum to another. A good combination of CVs is able to easily distinguish among the minima, different metastable states, and transition states of the free-energy landscape. Although the choice of CVs is not unique and depends rather strongly on the system and the process of interest, the requirement of such variables to unambiguously identify and separate the different stable and metastable states guides this decision. The choice is not trivial; if selected poorly, an incomplete exploration can lead to an incorrect reconstruction of the free-energy landscape. Increased dimensionality of the CV space reduces the likelihood of such underperformance, but in the same decreases the efficiency of metadynamics given that the method scales exponentially with the number of variables involved. Time required to escape from a local minimum depends on the number of Gaussians needed to fill the

minimum well which is, in turn, proportional to $(1/\sigma)*N(\mathrm{CV})$. To maintain the efficiency, with each added CV the width of the Gaussians also has to increase; soon, the Gaussians reach a size comparable to that of the minima wells, leading to significant errors in the reconstruction of the free-energy landscape.

Hence, identification of appropriate CVs is crucial for a successful metadynamics simulation. One way of doing this is to perform an analysis of reactive trajectories between stable states and the free-energy landscapes. For a simple system with two wells, the ensemble of transition paths is defined as all the trajectories that exit from region of the first well and reach region of the second well or vice versa, with the ensemble of transition states defined as a collection of intermediate configurations that have an equal probability of reaching either region and are situated on the transition path. All of such configurations are lying on the iso-surface with probability $p = 0.5$. From this, obtained probability functions are used to parametrise good reaction coordinates. Another route is by trial and error, through intensive sampling of the system. Thus, although metadynamics does not require knowledge of the free-energy paths *a-priori*, comprehension of the system and its behaviour is indispensable. However, even though complex and novel systems require extensive testing in order to identify the adequate CVs, for simpler cases this is often not necessary, and the choice can be made based on the system specifications, experience, and taste.

2.4.2 NEB

Accurate estimates of TS can also be obtained by using a purely statistical approach - transition state theory. It is based on two assumptions: the transition rate is slow enough for reactant state to maintain a Boltzmann distribution, and a surface dividing reactants and products can be identified such that a trajectory from the initial (IS) to the final state (FS) only crosses it once, therefore representing a bottleneck of the transition. Due to the tight packing of atoms and most of the temperatures of interest not reaching the melting points, a harmonic approximation of the theory is typically sufficient in studies of reactions in crystallites and crystal surfaces. This greatly simplifies the search for the TS, which is now a saddle point at the edge of the potential energy basin corresponding to the initial state.

A first order saddle point of a surface is a maximum in one direction and a minimum in all the other directions, hence, a method for its identification has to involve maximisation of one degree of freedom and minimisation of the remaining degrees. A critical factor is in choosing a degree of freedom which will be maximised. Minimum energy path is a path connecting the IS and the FS with the greatest statistical weight and whose highest saddle point is a true TS of reaction. At any point of this path, the force acting on the atoms is pointing along the path only, and the energy of perpendicular degrees of freedom is stationary. A natural choice of a reaction coordinate is thus the relative distance of the states positioned on the path where at the maximum (the saddle point) the direction of the reaction coordinate is given by the normal mode eigenvector corresponding to the negative curvature. The minimum energy path can have one or more minima in addition to the IS

and FS, and these minima represent stable intermediate configurations. Correspondingly, more than one maximum can occur, each representing a saddle point.

Various approaches for the saddle-point sampling have been developed, with the two of the most popular and efficient strategies being nudged elastic band (NEB) and dimer method.[191, 192] NEB is an efficient technique for determination of the minimum energy paths between IS and FS of the system within the harmonic approximation. It can be used in combination with both *ab initio* and MD methods. The minimum energy path is found by constructing a set of images which represent initial guesses of the system states situated between the IS and the FS. A spring interaction is added between the images to ensure the continuity of the path. As created path mimics an elastic band and its optimisation involves minimisation of the forces acting on all images, with a force projection which prevents the added spring forces of interfering with the convergence of an elastic band to the minimum energy path.

An elastic band can be represented by $\{R_0, R_1, R_2, ..., R_N\}$, with R_0 and R_N being fixed points corresponding to the IS and FS, respectively. In order to decompose the true and the spring force into the components that are parallel and perpendicular to the minimum energy path, it is necessary to estimate the tangent on the path at every iteration step for each of the images. This process of force projection is known as nudging, and it allows the use of the spring forces without them competing with the true forces in the optimisation of the elastic band to the true curve of the minimum energy path. Then, the sum of the parallel component of the spring force, $F_i^S|_{\parallel}$, and the perpendicular component of the true force, $F_i^R|_{\perp}$, equals the total force acting on an individual image, F_i:

$$F_i = F_i^S|_{\parallel} - F_i^R|_{\perp} \tag{2.63}$$

$$F_i^R|_{\perp} = \nabla E(R_i)|_{\perp} = \nabla E(R_i) - \nabla E(R_i)\hat{\tau}_i \tag{2.64}$$

$$F_i^S|_{\parallel} = k(|R_{i+1} - R_i| - |R_i - R_{i-1}|)\hat{\tau}_i \tag{2.65}$$

where $\hat{\tau}_i$ is a normalised local tangent at image i, and k is a spring constant. To move the images to their respective forces, the elastic band has to be subjected to an optimisation algorithm with a final result of each image finding the lowest energy state while maintaining equal spacing to the neighbouring images. Saddle point is typically not found amongst the optimised images and TS energy has to be estimated by interpolation. This poor resolution of the optimised minimum energy path around the saddle point leads to a high level of uncertainty in the subsequent estimation of the activation energy which can be avoided through a modified version of the NEB method.

The climbing method, CI-NEB, is a modification of NEB in which the highest energy image is driven up to the saddle point.[193] A chosen image does not feel the spring forces along the elastic bands and its true force is inverted to sit along the local tangent. Consequently, its optimisation leads to the maximisation of the energy along the elastic

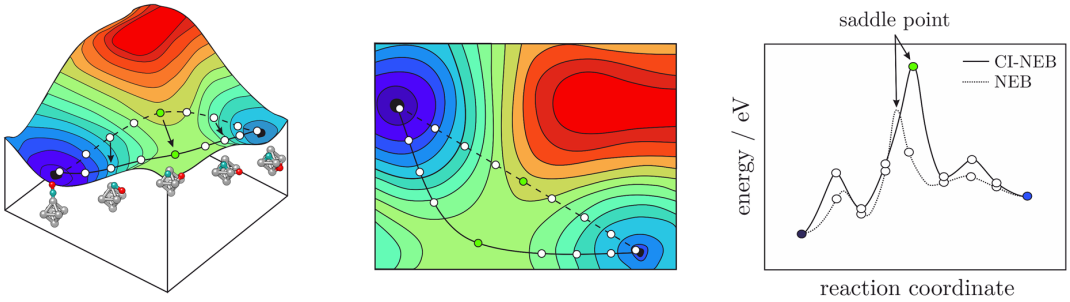

Figure 2.7: Principle of the NEB method: **left** three-dimensional representation of the potential energy surface with a dashed line representing the path corresponding to the initial guess for the intermediate states between the initial and final state, and a full line representing the minimal energy path after the NEB optimisation; **middle** two-dimensional representation of the same potential energy surface - initial guess is a linear extrapolation of the positions of atoms; **right** energy plot of the edge of the potential energy basin corresponding to the initial state as optimised by regular NEB and climbing-image CI-NEB.

band and minimisation of energy in all other directions, converging exactly to the saddle point of the minimum energy path. Because it does not feel the spring forces, the spacing from adjacent images will not be conserved. CI-NEB enforces a rigorous convergence of the saddle point whilst retaining the information on the shape of the minimal energy path and thus does not add significant computational effort compared to the regular NEB calculations. The image with the highest energy, $i_{\max}$, is identified in a few initial regular NEB iterations, after which its force is re-expressed as the full force due to the potential with the component along the elastic band inverted:

$$F_{i_{\max}} = F^R_{i_{\max}}|_{\parallel} = -\nabla E(R_{i_{\max}}) + 2\nabla E(R_{i_{\max}})|_{\parallel}. \tag{2.66}$$

This inversion of the true potential force parallel to the elastic band, $\nabla E(R_{i_{\max}})|_{\parallel}$, moves the chosen climbing image up the potential energy surface along the given elastic band and down the potential energy surface perpendicular to the given elastic band. The rest of the images define the degree of freedom for which a maximisation of the energy of the climbing image is performed. Since the images within the elastic band converge towards the minimum energy path, they provide a reliable approximation of the reaction coordinate around the saddle point and, as long as the CI-NEB calculation converges, the climbing image will reach a true maximum. Optimisation of all images is carried out simultaneously and there is no cost in turning one of them into a climbing image. A critical point is to generate enough images in the close proximity of the climbing image to obtain a good estimate of the reaction coordinate which determines the climbing direction. Principles of NEB and CI-NEB approaches are depicted in Figure 2.7.

CI-NEB transition state calculations within this thesis have been performed using the VTST transition state tool developed for finding saddle points and evaluating the transition state theory rate constants with VASP.

2.5 DFPT

DFT is to date the most widely used approach in computation of the ground-state electronic structure and total energy of systems of interest in chemistry, physics, and material science. The ground-state electron density also provides a way of obtaining first derivatives of the total energy, including the forces acting upon nuclei and the stress acting on the lattice degrees of freedom, which, in return, allow determination of equilibrium geometries, or further extension of DFT towards AIMD or TS calculations. These electronic and structural properties are collectively a basis for the prediction of chemical reactions, electronic transport, vibrational properties, thermal capacity, superconductivity, as well as that of dielectric, optic, and spectroscopic response of the system, all of which arise from the lattice-dynamical behaviour represented by second and higher order energy derivatives. Energy derivatives other than the first, however, cannot be directly calculated from the ground-state electron density alone, but additionally require knowledge of its response to the corresponding perturbation. This relationship between the electronic and the lattice-dynamical properties is established through the combination of DFT with linear response theory of lattice vibrations [194, 195], and it is known as the linear response or density functional perturbation theory, DFPT.

The DFPT formalism is very similar to that of DFT, which states that the total energy is a functional of the electron density, and it is thus possible to obtain ground-state electron density by minimising the total energy. Correspondingly, in DFPT, first order changes in density, wavefunction, and interaction potential are obtained by minimising the second order perturbation in the total energy.[196] This is proved by the $2n+1$ theorem, where the n^{th} order derivative of the density/wavefunction is required for determination of the $2n+1^{\text{th}}$ derivative of the total energy such that, for example, to obtain vibrational frequencies (second order derivative) one needs to compute the response of the electronic structure to a nuclear displacement (first order derivative). Nevertheless, applicability of this approach extends way beyond the study of vibrational properties, as linear response provides an analytical way of computing the second derivative of total energy with respect to a given perturbation:

$$\text{property} \propto \left(\frac{d}{dF}\right)^f \left(\frac{d}{dB}\right)^b \left(\frac{d}{dI}\right)^i \left(\frac{d}{dR}\right)^r E|_0. \tag{2.67}$$

A perturbation in ionic position gives the dynamical matrix and phonons, a perturbation in magnetic field gives NMR response, a perturbation in unit cell vectors gives elastic constants, a perturbation in an electric field gives dielectric response, and so on. DFPT equations for the electron density linear response of the perturbed system form a set of self-consistent equations completely analogous to the KS equations for the unperturbed case. Detailed equations behind the DFPT approach are beyond the scope of this thesis and can be found in [197, 198, 199].

In the following chapters, results of the DFT and MD studies on cobalt nanoparticles and their magnetic properties, size and shape dependence, oxidation behaviour, and organic functionalisation will be presented.

CHAPTER 3

HAPE OF Co NANOPARTICLES

The best way to explain it is to do it.
-Chapter 3, A Caucus-Race and a Long Tale

3.1 Introduction

3.1.1 Cobalt

Cobalt is a sturdy, grey d block transitional metal with seven electrons in $3d$ orbitals. Along nickel and iron, cobalt is the third naturally occurring magnetic metal, present mostly in minerals cobaltite (CoAsS), smaltite ((Co,Fe,Ni)As_2), glaucodot ((Co,Fe)AsS), erythrite ((Co,Ni)$_3$(AsO_4)$_2$×8H_2O), skutterudite ((Co,Ni)As_3), and ores of nickel, silver, copper, lead, and iron, from which it is most frequently obtained as a by-product. Co chemicals have been used as pigments in glass and ceramics for thousands of years. From the early twentieth century, major uses have been in the production of 'super-alloys' and permanent magnets, as well as high-strength steel and hard-metal cemented carbides. At the end of 1980s, about one-third of cobalt was employed in the production of Co-based compounds, which are today used primarily as catalysts and pigments.

To say that cobalt is highly reactive would be an overestimation - it reacts with oxygen but does not catch on fire unless it is in a powder form. It reacts with most acids to produce gaseous hydrogen; however, it does not react with water at room temperature. It has a high melting point (1495 °C) and it is valued for the resistance and ability to retain strength at high temperatures. From the structural point of view, cobalt can exist in three crystal phases: hcp, fcc, and ε-phase, which have similar energetic stabilities but distinct properties. Hcp structure is stable at room temperature and transforms to fcc just below 700 K.[200] ε-phase is found to be metastable under normal conditions and turns to the stable hcp phase by heating to 573 K in vacuum, whereas subsequent cooling does not reverse the phase transition. Connection between the crystal structure and magnetic properties - magnetic anisotropy at room temperature is 4.2×10^6, 2.7×10^6, and 1.5×10^6 erg cm^{-3}, for hcp, fcc, and ε-phase, respectively, is the key for their employment in different areas.[201, 202, 203] Both hcp and fcc Co showed a great performance for Fisher-Tropsch synthesis.[204, 205] Anisotropic high-coercivity hcp phase is preferred for the production of permanent magnets while the more symmetric low coercivity fcc phase

is useful for soft magnetic applications. ε-phase favours the formation of ordered films with applications in magnetic recording.[206] With an hcp→fcc phase transition occurring at high temperatures and with the highest anisotropy of the three, hexagonal crystal structure is of interest from biomedical standpoint.[207]

Cobalt is a naturally occurring element in the human body (0.0015 g or 0.000002 % of total body mass) and in that manner it has some beneficial effects as the essential component of vitamin B12. Additional exposure is most likely to occur by inhalation of dusts, fumes, and mists. Once accumulated to toxic levels, cobalt (mostly in the form of Co^{2+} ions) has been found to cause health issues including asthma, pneumonia, and allergies, and, based on the experimental animal studies, it is listed as a potential human carcinogen. However, International Agency for Research on Cancer (IARC) evaluated the evidences for the carcinogenicity of cobalt and cobalt compounds in humans as inadequate.[208] On the other hand, Co NPs gained medical value through antimicrobial activity [209, 210]; they were found to be biosafe and to have minimal hemolytic activity.[211] Conclusively, different cobalt compounds show distinctive behaviours and it is therefore important to avoid any generalisation and individually assess mentioned hazards, whereas the genotoxicity of cobalt alone is still a controversial issue.

3.1.2 Cobalt nanoparticles

Among the mNPs, Co NPs have attracted a considerable interest in a wide range of research fields owing to their magnetic, electronic, and catalytic properties, which are of scientific and technological importance in recording media, magnetic sensors, magnetic memories, magnetic fluids, magnetic composites, and catalysis. Through the years, it became evident that Co NPs can display a wealth of size- and phase-dependent structural, magnetic, and electronic properties.[212, 213, 214, 206] In particular, intensive studies were spurred by the exponential dependence of the magnetisation relaxation time on the NP volume.[215, 216, 217, 218]

This size and shape specificity naturally served as a building block for development of numerous preparation techniques to maximally utilise induced fluctuations in physical and chemical properties. Metallic Co NPs have been produced by wet-phase synthesis methods for more than 50 years [219], and subsequent modernisation and technological development today offer a wide range of synthetic preparation methods giving access to a good control of the NP size and shape. Correspondingly, experimentalists are now able to obtain primary Co particle sizes starting from only several nanometres up to the submicron sized materials, and test their chemical responses and application specific behaviour accordingly.[220, 221, 222, 223, 224, 225, 226, 227, 228]

Probably the greatest example of how diverse the properties of NPs with the same composition but different geometries and/or diameters can be is the nanoparticular catalysis. In the Fischer-Tropsch (FT) synthesis literature, the influence of Co NP size has been a long-lasting debate. Through the extensive research of both supported and unsupported particles, various examples are now known where the catalytic performance was

indeed found to be dependent on particle size.[229, 230] It was shown that the reaction rate of Co NPs with sizes in the range between 10 and 200 nm, where highly reducible catalysts can be obtained by conventional preparations, does not change significantly with the alternation in diameter.[231, 232] For smaller Co NPs, however, a decrease in FT performance has been reported through a decrease in the turnover frequency compared to the larger NPs, which is a result of a significant increase in the residence time of reactant molecules combined with a lower overall coverage.[233, 234] Crystallographic dependence of the catalysis rates was also observed, with the crystal phase and corresponding NP morphology affecting the formation of active sites with different intrinsic activity and density.[235] Sensitivity of FT synthesis on size and shape of Co NPs is now largely accepted and prevails as the main argument for changes in the activity of the catalyst.[236]

Contrary to catalysis, where chemical reactivity and physically accessible NP surface areas are key factors influenced by the change in diameter and atomic ordering, applications that rely on the magnetism of these nano-entities depend on the alternations in the electronic structure with the size and geometry instead. Due to a variety of applications that exploit naturally high magnetic moment of cobalt - from bio-imaging and magnetic hyperthermia to magnetic energy storage, the magnetic properties of Co NPs of different shapes and sizes have also been investigated.[237, 238, 239, 240] Generally, ferromagnetic Co NPs are larger than superparamagnetic Co NPs, and there is also a strong correlation between the crystal structure and magnetic properties as it is the case for the bulk phases. Hcp Co NPs are especially interesting, as the use of mNPs for high density information storage requires small diameters with high magneto-crystalline anisotropy at usable temperatures.[241, 242] Requirements and conditions of biomedical applications are different: body temperature, good stability and longevity in reactive environment, small diameters, and high magnetisation for a strong response within safe magnitudes of the external magnetic fields. In addition to easier movement through blood vessels and being less prone to phagocytosis, NPs of smaller size are also superparamagnetic without residual magnetisation, which is much safer for medical treatments. Size and shape were also pinpointed as determining factors for the NP uptake into cells.[241] Performance of Co NPs of varying sizes in MRI showed differences in their relaxivity times, with the magnitudes similar to those reported for iron oxide NPs with larger cores, suggesting potential development and future use as negative contrast agents.[64] Experimentally obtained heating rates for mNPs of different materials showed the occurrence of maximum power dissipation peaks at different sizes and accentuated Co NPs with diameters of ∼8 nm as one of the most promising candidates for the mNPH.[15] A detailed systematic study on the shape preference specifically of Co NPs with sizes relevant to biomedical treatments, however, has not as yet been conducted.

3.1.3 Motivation

Experimental studies have shown that transition metal NPs can either have regular phase ordering and exist as face-cantered cubic (fcc), body-centred cubic (bcc), or

hexagonal-close-packed (hcp) crystals or they can comprise several twinned fcc crystallites. [243] The term structural motif is often used to refer to the groups of NP shapes with similar internal structure and/or symmetry. Regular NP shapes are therefore called crystalline motifs, and include octahedral, tetrahedral, cubic shapes and their truncated variations for fcc and bcc phase, while hcp crystals are in the shape of hexagonal (usually truncated) bipyramids. Irregular icosahedral and decahedral twinned shapes are known as non-crystalline motifs, and they are characterised by a five-fold symmetry. Each of the shapes has a unique combination of exposed low Miller-index surfaces and the edge and vertex surface interconnections ,which are expected to govern distinctive trends in reactivity, magnetic behaviour, and functionalisation mechanisms.

Current experimental techniques are capable of producing size-selected clusters and NPs with a narrow size distribution. However, the task of identifying the atomic structure is much more demanding and requires exceptional precision, hence remaining an intriguing topic for both experimental and theoretical research. Computational simulations have so far found three-dimensional isomers to always be more stable than their planar counterparts for various monometallic and bimetallic clusters comprising of less than 10 atoms.[244, 245, 246, 247] There is little experimental data relevant to the geometric structure of so small metallic clusters as structural information is mostly obtained from low-temperature matrix studies (e.g., absorption, Raman, Mossbauer, and electron spin resonance), which are not particle-specific and often suffer from ill-defined guest-host interaction effects. Nevertheless, for those metallic clusters of a few atoms whose structures have been experimentally tackled, they were tentatively assigned as three-dimensional.[248, 249, 250] Moreover, the preference of non-crystalline over crystalline motifs was found for clusters with up to 50-100 atoms by both experiment and theory, with the crossover point between the competing structures depending on the transition metal specie. In the case of palladium, platinum, and gold, the icosahedron-to-decahedron and non-crystalline-to-crystalline fcc transitions were observed for $N < 100$.[251, 252, 253] On the other hand, same crossovers were assigned to sizes of $N > 300$ [254] and $N > 400$ [254] for rhodium and silver, respectively. For an hcp ruthenium, the intersection of icosahedral and hcp structures was found to be at $N = 103$.[255]

Despite the fact that for the most of transition and noble metals non-crystalline-to-crystalline intersections were observed far below large cluster sizes, for three ferromagnetic metals this is not the case. Experimentalists have been able to determine the most favourable shape for Fe, Ni, and Co clusters/NPs with up to 800 atoms.[256, 257] The geometry of Fe clusters is in favour of icosahedral structure, however, there is a clear competition with different crystalline motifs similar to the behaviour in the bulk phase. Therefore, a precise interpretation is accounted for as questionable. For nickel and cobalt clusters with up to 70 atoms, the exact structure is not well identified, icosahedral features are less evident, leading to suggested coexistence of isomer species. The two also experience differences in the preferential structures in this low-sized region. For larger sizes, however, a regular structure consistent with the filling of successive shells of atoms corresponding to an icosahedral geometry was experimentally observed in the case of both

Co and Ni even for the clusters/NPs with 800 atoms. Moreover, icosahedron was theoretically predicted to be the most stable structure up to 2300 atoms for Ni.[258, 259] This is amongst the highest size domains in which icosahedral geometry was shown to be more stable than the bulk phase crystalline motif for transition and noble metals.

To date, theoretical studies on Co clusters and NPs are deficient, and available results are not in a good agreement. Early DFT works were limited in terms of the system size and therefore considered clusters with up to 10 or 15 atoms, mostly excluding geometric optimisation.[260, 261, 262] Later study performed on systems up to 177 atoms, again without structural relaxation, took into account only fcc and bcc configurations.[263] The tight-biding MD studies relied only on the experimental data of the Co dimer.[264, 265] More recent works were carried out as spin-polarised relaxations, but only for a few chosen sizes ($2 \leq N \leq 20$ [266], $N < 6$ [267], and $N = 13$, 55, 147 [268]). The biggest study so far has been conducted for clusters/NPs with up to 365 atoms in various structural motifs by performing first-principles calculations, but without considering decahedron or variations in fcc motifs.[269] Altogether, many sizes have been disregarded, while for those discussed there is no consensus on the most stable geometry. Existing discrepancies among DFT calculations may be attributed to the choices of the basis sets and exchange-correlation functionals, omission of system optimisation, and incompleteness through discarding some of the non-crystalline or crystalline motifs. Semi-empirical potentials and parametrised tight-binding methods drastically reduce the computational cost compared to DFT, however, with the loss of accuracy and reliability. One of the latest MD studies on the isolated Co clusters has provided an insight in their growth in the gas phase.[270] Although MD allows for a much more complete exploration of the configurational space, the structures obtained for $N \leq 55$ are in a complete agreement with those predicted by DFT. Through the further increase in the cluster size, the study has demonstrated an occurrence of kinetic trapping effects which could have caused growth structures that significantly differ from the thermodynamic equilibrium geometries. Nevertheless, the growth mechanism coincides with the formation of mainly icosahedron-like structures, which is in agreement with experimental findings. The final size of the growing Co cluster/NP considered was 600 atoms.

The overall picture of the shape as a function of size is thus incomplete and the motif preference for larger Co NPs remains an open question. Factors that are governing the stability order of different structural motifs of NPs and which trigger the shape transitions within the specific size ranges are mainly of stacking character. Atomic stacking of each geometry is responsible for the prolongation of bonds, increase in the share of atoms with reduced coordination numbers, and appearance of other surface and volumetric contributions to the motif energy divergence. Such information can be extracted from the molecular and electronic structure of each motif, whereas a systematic study of the dependence and evolution of structural properties with the size and shape can be used to assign the border transition sizes between different structural forms and to elucidate the gradual transformation from the molecular finite systems to condensed matter regimes.

Magnetic properties and their progression with the changes in the NP size and shape

can also be obtained from the DFT predicted electronic structures. The total magnetisation is a prevalent factor in the response of biomedically employed NPs to the applied magnetic field, but its dependence on the NP morphology is a scarcely visited and very challenging topic in the experimental works. Within the recent studies on mNPs used in the MRI and magnetic hyperthermia treatments, MAE was also shown to greatly influence the contrast and heating efficacies, and this dependency is now established through the expressions for the Néel and Brownian relaxation as presented in the first chapter. Values of both total magnetisation and anisotropy energies of NPs with varying morphologies and sizes are accessible through accurate DFT calculations and are becoming a great tool in strategic design of nanoagents in biomedicine.

A Co NP with 8 nm in diameter which yields the best heating power according to the experimental studies would constitute of more than 10^4 atoms. To consider the importance of shape in the design of NPs for biomedical applications, preferential structural motifs and divergence of their magnetic properties with the NP size can provide valuable information. The main goal is, therefore, to identify the stability order of different crystalline and non-crystalline Co NPs within medium and large (10^2-10^4) size range by accounting for energetic gains and losses caused by the on-surface and in-core atomic arrangements. Even the most advanced equipment struggles with clusters/NPs involving a few hundred atoms since they are too big to analyse by spectroscopic methods, and yet too small to analyse by diffraction.[271] On the other hand, a systematic theoretical study of large Co NPs by accurate DFT calculations is still lacking, likely due to the hcp structure of the bulk material and costliness of computational calculations. NPs are expected to, beyond a certain size, exhibit bulk-wise structures, despite the experimentally reported preference for icosahedral geometries even up to 800 atoms. Advances in the efficiency of DFT codes allow for high-level relaxation of systems with complex interatomic interactions and systematic improvements are continuously seen in the system sizes that are successfully described by quantum level calculations. DFT calculations have been carried out for Co NPs of different structures containing up to 1500 atoms with the aim of predicting the transitions between stability regions of different motifs and to determine the most likely geometry of Co NPs at biomedically relevant sizes. To the best of author's knowledge, no such efforts have been undertaken to determine the crossover point of icosahedral and hcp structural motif for Co NPs until now. Size and strain effects on the evolution of structural, bonding, and magnetic properties of structural motifs have been explained, and trends of relevant magnetic features (total magnetisation, magnetic anisotropy) as a function of NP size and morphology were predicted.

3.2 Computational details

For both atomic clusters and NPs, the most favoured structure is defined by the global minimum of the potential energy surface. The thermodynamic limits of shape stabilities are uniquely defined for each cluster/NP size and composition, and great efforts have been devoted in finding methods for calculating potential energy surfaces and reliably obtaining

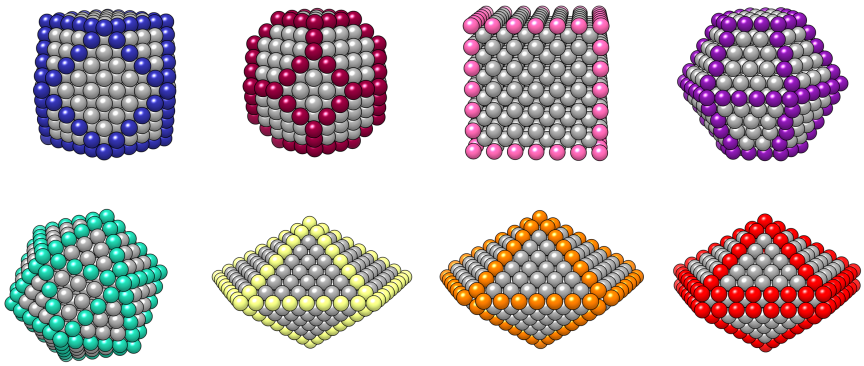

Figure 3.1: Models of crystalline (**top** panel left to right: fcc - cuboctahedron and truncated octahedron, bcc, and hcp), and non-crystalline (**bottom** panel left to right: icosahedron, regular, Marks, and Ino decahedron) NP motifs.

local and global minima of different systems. The search for a global minimum is a two-step task: first is a construction of an appropriate model for the interactions between atoms either by employing *ab initio* methods or by constructing semi-empirical potentials; the second step is to sample the isomers by a global optimisation algorithm. Regardless of the composition and size of the system, both of these steps impose challenging and extensive simulations as the number of possible isomeric structures grows non-linearly with the number of atoms, making such studies rather prohibitive. Additional risks of metastable wells and kinetic trapping effects further complicate the research efforts. A preliminary tracking of the general trends is therefore important to help and single out sequences of favourable structures in different size regions. This can be done on the basis of the construction of structures whose selection is motivated by energetic and morphological considerations.[272, 273, 274, 275] Structural motifs are geometrical families with highly symmetric structures and are therefore expected to have a good stability. Each crystalline shape is formed by introducing cuts into the bulk material in the directions of Miller-index surfaces. From fcc bulk one can therefore obtain a simple cube with (100) facets, an octahedron by using solely (111) facets, truncated octahedron by introducing six (100) facets along the six vertices of octahedron, or cuboctahedron by introducing (111) cuts along the eight vertices of a simple cube. Cutting an hcp bulk in the direction of the $(10\bar{1}1)$ surface, obtained shape is a hexagonal bipyramid which can be truncated by two (0001) facets, one at the tip of each pyramid. A non-crystalline icosahedral structure is, on the other hand, built by packing together twenty fcc tetrahedra sharing a common vertex, while a decahedron is obtained by packing five tetrahedra so that they have a common edge. Former can be truncated by five (100) facets, yielding an Ino decahedron, while further truncation at vertical edges by ten re-entrant (111) facets generates a Marks decahedron. All shapes are depicted in Figure 3.1.

The choice of sizes is, on the other hand, usually driven by the well-known oft-recurrence of clusters and NPs which have a complete, regular outer geometry designated

as full-shell clusters/NPs. These sizes are known as magic numbers, and they are given by the equations derived for each structural motif [276, 277]:

$$\text{FCC CUBOCTAHEDRON } N = \frac{10}{3}n^3 + 5n^2 + \frac{11}{3}n + 1 \tag{3.1}$$

$$\text{FCC TRUNCATED OCTAHEDRON } N = 16n^3 + 15n^2 + 6n + 1 \tag{3.2}$$

$$\text{BCC CUBE } N = 2n^3 + 3n^2 + 3n + 1 \tag{3.3}$$

$$\text{HCP TRUNCATED HEXAGONAL BIPYRAMID } N = \frac{7}{2}n^3 + \frac{21}{4}n^2 + \frac{7}{2}n + \frac{3}{4} \tag{3.4}$$

$$\text{ICOSAHEDRON } N = \frac{10}{3}n^3 + 5n^2 + \frac{11}{3}n + 1 \tag{3.5}$$

$$\text{DECAHEDRON } N = \frac{5}{6}n^3 + \frac{5}{2}n^2 + \frac{8}{3}n + 1 \tag{3.6}$$

where n represents the number of complete atomic shells within the cluster/NP, and N is the final number of atoms a full-shell cluster/NP contains.

The generic theoretical models proposed by Mackay, Ino, and Marks have predicted icosahedral shape as a global minimum for the smallest NPs, followed by decahedral structural motif at medium sizes, while larger NPs up to the bulk limit are the most stable when in the shape of a cuboctahedron with an fcc structure. In the later research, it was shown that structures of different symmetries are separated by fairly low-energy barriers, meaning the probabilities of their coexistence are strongly determined by their potential energies. Because the energy differences between the motifs are so small, the presence of high-index facets and relaxation of atoms at edges, exposed facets, and twin boundaries, which are not included in the generic models, as well as consideration of different phases and atomic centrings could significantly shift the crossover thresholds. *Ab initio* calculations, in contrast, are able to consider different shapes inclusive of fcc, bcc, and hcp phases, bond and interlayer centres, as well as all the geometrical degrees of freedom, thus providing much more reliable predictions.

To study progressive transitions of differently shaped Co NPs from smallest clusters to the bulk-like particles, multiple isomers (excluding bilayer structures) for the Co clusters ranging from 2 to 30 atoms (non-scalable regime) have been considered, while for the clusters/NPs with more than 30 but less than 1500 atoms (scalable regime) only the magic number system sizes have been taken into the account. As the main focus is on the medium and large size range, a detailed search for low lying isomers of clusters under 30 atoms via global optimisation with semi-empirical potentials [278, 279, 280] was omitted, whereas up to ten different isomers were considered in DFT optimisations.

Linear-scaling DFT methods are nowadays reaching a level of maturity when it comes to simulating insulating and semiconducting systems with hundreds of atoms. However, the continuum of states through the chemical potential and the partial occupancies make these DFT approaches unsuitable for metals. Another aspect which is particularly relevant when using DFT calculations for modelling metals is Brillouin zone sampling; due to the extremely complicated Fermi surface, a dense k-point mesh is necessary to sample the Brillouin zone adequately. For these reasons, careful choices of the basis set and simulation code have to be made prior to the calculations.

Basis set

Plane waves (PW) basis set is characterised by a universality of both atomic species and local environment - the same basis set can be used for any system. Additionally, PW do not suffer from the superposition error often occurred in localised basis sets (LB). Both of these features are advantageous when studying interactions in heterogeneous systems. However, PW must be expanded over the whole simulation box, which can come costly for modelling systems in vacuum.

When metallic systems are of interest, due to the sharp drop in the electronic occupation at the Fermi level at 0 K, it is imperative to use a finite temperature smearing of the Fermi surface to avoid unphysical oscillations in the electron density which leads to non-convergence.[281] Therefore, a finite non-zero temperature distribution is used to get better convergence rates for the SCF calculations. A comparative study of the performance of PW and LB basis sets on metallic surfaces has shown the computational cost of the LB method at the convergence threshold to be higher than the PW method, with the difference increasing with the k-point grid density.[282] Both methods consume similar computational time per SCF cycle with increase in the surface area. The overall results of both LB and PW basis sets are of desirable accuracy, and while PW converge faster, LB could offer better computational efficiency for systems with vacuum areas. However, for metallic systems, the choice of smearing function is also a major contributor. Mostly used smearing functions are Fermi-Dirac, Gaussian, and Methfessel-Paxton. The major benefit of Fermi-Dirac occupation is that the electronic smearing corresponds to a physical thermal distribution at temperature T. On the downside, it tails off very slowly, so a large number of slightly occupied conduction bands must be used to fully capture all of the occupied states. In the case of Methfessel-Paxton smearing, temperature is just a mathematical artefact to obtain a more accurate integration of the physical quantities at a lower cost. The advantage of this scheme is that the obtained energy is very close to the physical energy at $T = 0$ K, even for quite large smearing temperatures. It also allows much faster convergence with respect to k-points, especially for metals. Finally, convergence to self-consistency is significantly improved.

The Vienna Ab-initio Simulation Package (VASP) code [283] has been chosen to carry out spin-polarised calculations within the usual Kohn-Sham implementation of the density functional theory. In VASP, central quantities, like one-electron orbitals, electron density, and local potential are expressed in PW basis set. Interactions between the electrons

and ions are described using pseudopotentials. VASP allows for the choice of smearing method between any of the three aforementioned approaches, and has implementations of both Monkhorst-Pack grid and the tetrahedron method. Finally, VASP showed reliable performance in predicting magnetic properties of various systems.

Exchange-correlation functional

Most of the recent first-principles calculations for solid-state materials have been based on density functional theory within LDA or GGA exchange-correlation functionals. By now, it is well established that LDA methods fail when determining the ground-state of most bulk metals, while GGA predicts the correct structure. One example is bulk iron, which is predicted to have a ferromagnetic (FM) bcc ground-state by GGA, in agreement with experiments, rather than a paramagnetic fcc as found by LDA.[284, 285]

Deficiency of DFT-LDA/GGA when modelling small transition metal clusters is attributed to the incomplete cancellation of the Coulomb self-interaction and the tendency of most approximate exchange correlation functionals to over-delocalise valence electrons and to over-stabilise metallic ground-states, whereas many of the smallest transition and noble metal clusters show relatively large band gaps. Different pragmatic strategies to overcome those limitations have been implemented within VASP code, amongst them frequently used Hubbard LDA/GGA+U method proposed by Dudarev *et al*[286], in which only the difference between the Coulomb U and exchange J parameter is taken into account, namely $U_{\text{eff}} = U - J$. As predictive power of atom-coordination, metal-metal bond-formation, and effect of open and compact structures on energetics and electronic properties of small clusters is strongly dependent on the proper description of valence d-orbital electrons, it is important to estimate the shortcomings of GGA in this manner.

Nevertheless, while LDA+U method is well established for strongly correlated materials with well-localised orbitals, its application to weakly correlated transition metals is questionable. The localised formulation of the LDA+U is constructed to impose a finite discontinuity to the exchange-correlation potential. As this discontinuity is an important term of the fundamental gap of a system, it is particularly effective in improving the description of semiconductors and insulators, but in general not well suited to treat metals and other weakly correlated materials. Arguably the most important correlation effects in metals, namely fluctuation-induced mass renormalisation and itinerant exchange interactions, are hence missing from LDA+U. In fact, the excessive stabilisation of occupied states due to the $+U$ corrective potential can lead to a description of the ground state inconsistent with available experimental data that question its applicability in these cases.[287, 288] There are thus many problems concerning the electronic structure and itinerant magnetism of $3d$ metals when using the Hubbard model to improve the prediction of properties related to electronic localisation (such as magnetisation) without compromising the description of delocalised electrons. Applicability to moderately correlate systems is significantly better.[289, 290]

Various levels of theory have been used when predicting the structures of transition metal clusters.[245, 291, 292, 293, 294, 295, 296] Reliability of empirical potentials

suffers from the neglection of the directional nature of d-d interactions and quantum effects arising from spin magnetism and orbital symmetry. For *ab initio* methods, structural predictions are challenging because of the significant contribution from localised d electrons and strong electron correlation. However, if the determination of both geometry and electronic structure is to be achieved at the same level, which is desirable due to their strong interdependence, DFT proved to be a very efficient and reliable approach.[268, 297, 298, 299, 300, 301, 302] Specifically for Co, it was shown that the lowest energy structures and properties of small clusters are not as sensitive to the level of the exchange-correlation functional (including varying values of Hubbard and hybrid parameters), and results indicate that the differences between GGA, GGA+U, and hybrid methods are purely an electronic effect.[303] To verify energetic and structural invariance to the functional choice, GGA+U optimisations with proposed value of $U = 1.0$ eV have been performed for Co clusters under 30 atoms and the results compared to GGA.

While for small transition metal clusters with localised d orbitals GGA suffers from unphysical electron self-interaction, this deficiency diminishes as the clusters grow into NPs, and as NP sizes approach bulk-like hybridisation, and GGA is then expected to reliably predict structural parameters and relative energetics. Therefore, while a comparative study of hybrid functionals versus GGA for absolute values of electronic properties for the small size region remains a future work, searches for the most stable structures of medium and large Co NPs using these high-level quantum chemistry methods would be very expensive. Because DFT-GGA is widely used, reported, and relied upon, it is worthwhile to find the structural and energetic trends at this affordable level, especially for relative intra-motif comparison. Hence, only GGA functional was used to describe trends for Co clusters/NPs in the medium and large size range.

The spin-polarised DFT calculations were conducted for the mentioned systems using the VASP code within the PBE/GGA functional. The core electrons up to and including the $3p$ levels of Co were kept frozen, and their interaction with the valence electrons was described by the PAW pseudopotentials. The kinetic energy cutoff for wavefunctions was set to 500 eV, and the Monkhorst-Pack k-point grid included only Γ-point. Structural optimisations were carried out without any constraints, with the convergence criteria for the change in the total energy and interatomic forces between two steps of 1.0×10^{-6} and 1.0×10^{-2} eV/Å, respectively. The vacuum space in the unit cell was set to be more than 12 Å in each direction to avoid interactions with the neighbouring clusters.

Structural motifs and general trends in energetics

In general, cohesive energy of a cluster/NP with N atoms, E_N, can be expressed as:

$$E_N = aN + bN^{2/3} + cN^{1/3} + d \tag{3.7}$$

with a through d being material and shape-dependent coefficients. A volume contribution enters along with the bulk-like cohesive energy in a, surface contributions through the surface and twin boundary energies in b, edge and corner contributions in c and d, respectively. As a result of the competition between those contributions, different motifs

are the most stable in different size regions. For example, NPs characterised by a low surface energy adopt quasi-spherical shapes to optimise the surface/volume ratio, which comes at a cost of internal strain giving a volume contribution. In terms of calculations, the cohesive energy per atom, E_{coh}, is obtained as:

$$E_{\mathrm{coh}} = \frac{E_N^{\mathrm{DFT}} - N \times E_1^{\mathrm{DFT}}}{N} \tag{3.8}$$

where E_N^{DFT} and E_1^{DFT} are calculated energies of N-atom Co cluster/NP and the ground-state energy of a single Co atom, respectively. Cohesive energy per atom is roughly proportional to $N^{-1/3}$ through the expression for the NP surface energy:

$$\gamma S = E_N - N(E_{\mathrm{coh}}^{\mathrm{bulk}} + E_1) \tag{3.9}$$

where γ is the surface energy per unit area, S is the surface area, and $E_{\mathrm{coh}}^{\mathrm{bulk}}$ is DFT calculated cohesive energy of bulk Co. When combined with the expression for E_{coh}, a new relation is established:

$$E_{\mathrm{coh}} = E_{\mathrm{coh}}^{\mathrm{bulk}} + \frac{\gamma S}{N}. \tag{3.10}$$

Assuming that the NP is spherical, an assigned number of atoms N can be represented by $N = R^3/r^3$, where R and r are particle and atomic radius, respectively. The surface area S then equals $4\pi r^2 N^{2/3}$, and gives a final dependence of E_{coh} on γ:

$$E_{\mathrm{coh}} = E_{\mathrm{coh}}^{\mathrm{bulk}} + 4\pi r^2 \gamma N^{-1/3} \tag{3.11}$$

where E_{coh} is proportional to $N^{-1/3}$, and the surface energy per unit area is the proportionality constant. It is this linear relation that allows the evaluation of the intersection sizes between the motifs. Although the higher-order terms for edge and vertex contributions also affect cohesive energy, these are known to be minor compared to the surface energies, and it was shown they do not alter the overall characteristics of the stability plots.[304]

In many cases, to evaluate the stability order of different motifs, the second quantity, $\Delta(N)$, is plotted instead. $\Delta(N)$ is defined as:

$$\Delta(N) = \frac{E_N^{\mathrm{DFT}} - N \times E_{\mathrm{coh}}^{\mathrm{bulk}}}{N^{2/3}} \tag{3.12}$$

and represents the excess energy of cluster/NP with respect to a bulk solid roughly divided by the number of surface atoms. Since the cohesive energy of clusters/NP is less negative than in the bulk, $\Delta(N)$ is positive, and, in the limit of $N \to \infty$, it tends to a constant value for crystalline NPs, whereas it diverges for non-crystalline motifs presenting the volume strain. Other indicators of the structural stability are given by the first, $\Delta_1(N)$, and second, $\Delta_2(N)$, difference in the cohesive energy, which are a measures of the relative stability of a cluster/NP compared to that of nearby-sized clusters/NPs:

$$\Delta_1(N) = E_{\text{coh}}(N-1) - E_{\text{coh}}(N) \tag{3.13}$$

$$\Delta_2(N) = E_{\text{coh}}(N+1) + E_{\text{coh}}(N-1) - 2E_{\text{coh}}(N). \tag{3.14}$$

$\Delta_2(N)$ is the relative cohesive energy of a cluster/NP with N atoms with respect to those with $N-1$ and $N+1$ atoms, peaking at size with higher relative stability. The peaks correspond to the intensity anomalies or magic numbers of the mass spectrum.[305]

For small clusters and NPs, it is not possible to breakdown the vacuum-exposed surface into well-defined areas which could then be classified as specific Miller-index crystal facets due to the limited number of atoms which are almost exclusively parts of edges and vertices. NPs of sufficiently large sizes, on the other hand, have distinct facet areas with Miller-index stackings and their areas are dynamically dependent on the surface energies. All surfaces have energy associated with them because work is needed for their creation. Therefore, the term surface energy coincides with the work per unit area performed by the force that created the surface. Finally, surface energy can also be defined as the excess energy at the surface of a material compared to the bulk, quantifying the disruption of intermolecular bonds that occurs when a surface is formed. To characterise the surfaces, surface energies, γ, as a measure of the thermodynamic stability can be calculated as:

$$\gamma_u = \frac{E^{\text{DFT}}_{\text{unrelaxed slab}} - n \times E^{\text{DFT}}_{\text{bulk}}}{2A_{\text{slab}}} \tag{3.15}$$

$$\gamma_r = \frac{E^{\text{DFT}}_{\text{relaxed slab}} - n \times E^{\text{DFT}}_{\text{bulk}}}{A_{\text{slab}}} - \gamma_u \tag{3.16}$$

where γ_u and γ_r are the surface energies before and after relaxation, $E^{\text{DFT}}_{\text{unrelaxed slab}}$, $E^{\text{DFT}}_{\text{relaxed slab}}$, and $E^{\text{DFT}}_{\text{bulk}}$ are the calculated energies of the unrelaxed, relaxed slab, and bulk, respectively, A_{slab} is the surface area, and n is the ratio between the number of atoms in the slab and the number of atoms in the bulk. Surface for which the least amount of work is required, and which therefore has the lowest surface energy, is the most stable. Surfaces with close packings are known to have favourable surface energies due to the high number of bonds between the neighbouring atoms within the surface layer.

When constructing structural motifs, a key is to optimise surface-to-volume energy contribution. If a NP is cut from a bulk fcc crystal by only close-packed facets, one obtains a tetrahedron or an octahedron. Even though the whole surface area of those shapes is close-packed, the surface energy cannot be furtherly optimised because high surface-to-volume ratio would generate large volumetric strain. More spherical shapes with lower surface-to-volume ratios are obtained by introducing higher-energy facets as cuts at the vertices. An optimal depth of the cut gives the volumetrically most compact shape without compromising the surface energy contribution by large areas of high-in-energy facets. If the size of a NP is sufficiently large, the optimal cut is given by the

Gibbs-Wulff theorem [306], a theoretical method that allows prediction of the shape of macroscopic crystals under thermodynamic equilibrium by minimising the surface energy at a fixed volume.

For a particle with facets of areas A_{hkl} and corresponding surface energies per unit area, γ_{hkl}, the Gibbs surface free energy G can be written as $G = \sum \gamma_{hkl} A_{hkl}$. In 1901, Wulff suggested that the length of a vector drawn normal to a crystal face from the centre of the particle is proportional to the surface energy of the facet, $h_{hkl} = \lambda \gamma_{hkl}$. The polyhedron that corresponds to the lowest surface energy of a crystalline substance can thus be constructed by choosing a constant, λ, and a centre. Starting from the centre, one draws a plane that is normal to the hkl vector and has a distance $h_{hkl} = \lambda \gamma_{hkl}$ from the centre. This process is repeated for all sets of hkl Miller indices. The space enclosed by the set of planes defines the equilibrium shape of the particle, Figure 3.2. From this, it is possible to construct progressive paths of morphological changes according to the stabilisation of different surfaces, Figure 3.3. The proofs of the Wulff theorem can be found in [307, 308, 309]. As the contributions from the particle edges are neglected in the Wulff construction, the shape of small particles might deviate from the predictions, but experimental analysis indicates that particles in the range of couple of nanometres are generally consistent with this construction principle.[310, 311]

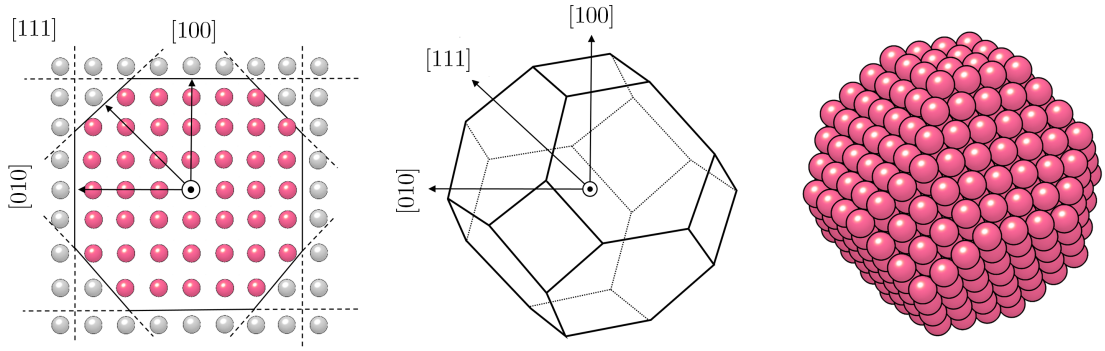

Figure 3.2: Illustration of the Wulff construction of an fcc particle (**left** panel). Crystal facet planes are represented by black lines, vectors normal to the planes by black arrows, and the centre of the particle by a black dot. Atoms enclosed in the equilibrium shape of nanoparticle are coloured red, while the rest of the bulk atoms are in grey. 3D morphology is shown in wire-frame (**middle** panel) and atomic representation (**right** panel).

From the Wulff construction, the truncation of octahedron at vertices would give an equilibrium structure for $\gamma_{100} h_{111} = \gamma_{111} h_{100}$. At larger sizes, higher-order facets can improve the sphericity of the particle. A more compact, quasi-spherical non-crystalline icosahedron can be constructed as proposed by Mackay, where a shape is composed of exclusively close-packed facets with a fivefold rotational axis.[312] Decahedron, which is also formed only by close-packed facets, is on the other hand far from being spherical. Vertex and edge truncations, suggested by Marks and Ino, can be implemented to achieve

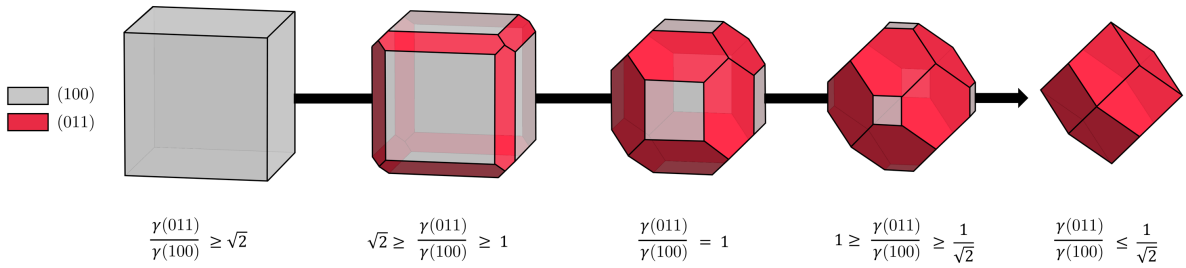

Figure 3.3: Morphology diagram according to surface energy modulations.

better surface-to-volume ratio as in the case of octahedron.[313, 314] However, such non-crystalline motifs are obtained at the expense of volume contribution for facets to be able to close the inter-surface gaps. Therefore, additional factors have to be accounted to the overall stability. One of them is the elastic strain energy that arises from the abnormal growth of the 10 (decahedron) or 20 (icosahedron) exposed (111) facets. Furtherly, for multiply-twinned shapes, which can be recognised by the intergrowth of surfaces of same Miller-index ((111) surface intergrowth for icosahedron and decahedron; $(10\bar{1}1)$ intergrowth for hcp hexagonal bipyramids), energetic cost or gain is accounted for through the twin boundary energy.[315, 316]

For example, a total energy of icosahedron, E_i, can be approximated by:

$$E_\mathrm{i} = E_\mathrm{coh} + E_\mathrm{surf} + E_\mathrm{els} + E_\mathrm{twin} \tag{3.17}$$

where E_coh, E_surf, E_els, and E_twin are the cohesive, surface, elastic strain, and twin boundary energies, respectively. By further inspection, these energy components can be grouped as volume-based (E_coh and E_els), or surface-based (E_surf and E_twin):

$$E_\mathrm{i} = -V_\mathrm{i}E_\mathrm{coh} + S_\mathrm{i}\gamma_{(111)} + V_\mathrm{i}W_\mathrm{i} + S_{\mathrm{t,i}}\gamma_\mathrm{t} \tag{3.18}$$

$$E_\mathrm{i} = -\frac{5\sqrt{2}}{3}r^8E_\mathrm{coh} + 5\sqrt{3}r^2\gamma_{(111)} + \frac{5\sqrt{2}}{3}r^8W_\mathrm{i} + \frac{15\sqrt{3}}{2}r^3\gamma_\mathrm{t} \tag{3.19}$$

where V_i and $S_{\mathrm{i/t,i}}$ are the NP volume and the total surface/twin boundary surface area, and W_i and γ_t are the elastic strain energy density and the twin boundary energy per unit area, respectively. Equivalent expression for decahedron is:

$$E_\mathrm{d} = -\frac{5\sqrt{2}}{12}r^8E_\mathrm{coh} + \frac{15\sqrt{3}}{2}r^2\gamma_{(111)} + \frac{5\sqrt{2}}{12}r^8W_\mathrm{i} + \frac{15\sqrt{3}}{4}r^3\gamma_\mathrm{t}. \tag{3.20}$$

r is the length of the edge of the icosahedron or decahedron. As previously stated, both of these non-crystalline shapes can be constructed by simple geometrical stacking of fcc tetrahedra, which introduces either gaps or defects in the close proximity of edge intergrowths. However, in the absence of any abnormalities as observed by high resolution

electron microscopy [317], it is assumed that the dislocations are uniformly distributed over the particle core as elastic strain. Since component tetrahedra have an fcc lattice, the elastic strain densities of icosahedron and decahedron can be determined based on the elastic constants of fcc Co:

$$W_{\mathrm{i}} = \frac{1}{6}\Big[(c_{11}+2c_{12})(2+\nu)^2 + 4c_{44}(1-\nu)^2\Big] \times \left(\frac{0.080362}{1-1.080362\nu^2}\right), \tag{3.21}$$

$$\nu = -\frac{2c_{11}+4c_{12}-c_{44}}{c_{11}+2c_{12}+c_{44}} \tag{3.22}$$

$$W_{\mathrm{d}} = \frac{1}{4}\Big[3(c_{11}-c_{12})\nu^2 + 2c_{44}(1-\nu')^2\Big] \times \left(\frac{0.024785}{1-1.024785\nu^2}\right), \tag{3.23}$$

$$\nu = \frac{c_{12}(c'+c_{12}) - c'(c'+c_{12})}{c'(c_{11}+c_{12}) - c_{12}(c'+c_{12})},\ \nu' = \frac{c''(c''+c_{12}) - c''(c_{11}+c_{12})}{c'(c_{11}+c_{12}) - c_{12}(c'+c_{12})} \tag{3.24}$$

$$c' = \frac{1}{2}(c_{11}+c_{12}+2c_{44}),\ c'' = \frac{1}{2}(c_{11}+c_{12}-2c_{44}). \tag{3.25}$$

A detailed derivation of these expressions can be found in [314]. Calculations of the elastic constants have been performed within the strain-stress formalism embedded in VASP. The elastic tensor was determined by performing six finite distortions of the lattice and deriving the elastic constants from the strain-stress relationship. Elastic constants, including both the contribution from distortions with rigid ions and from ionic relaxations, have been calculated. The plane wave cutoff was increased systematically until convergence up to 2 GPa was achieved.

Contributions of twinning fcc (111) and hcp ($10\bar{1}1$) surfaces present in icosahedral and decahedral, and hcp motifs, respectively, have been accounted for by considering the twin orientation of surface slabs, where the atomic positions of atoms above and below the fault plane are related to each other via a 180° rotation or a mirror plane reflection. The twin boundary energy per unit area, $_{\mathrm{t}}$, is calculated as:

$$\gamma_{\mathrm{t}} = \frac{E^{\mathrm{DFT}}_{\mathrm{original}} - E^{\mathrm{DFT}}_{\mathrm{twin}}}{2A_{\mathrm{slab}}} \tag{3.26}$$

where A_{slab} is the area of the twin boundary, and $E^{\mathrm{DFT}}_{\mathrm{original}}$ and $E^{\mathrm{DFT}}_{\mathrm{twin}}$ are the total energies of the original surface model and the twin boundary model, respectively.

Trends in magnetic properties

NP relaxations were carried out without any magnetic constraints and magnetic moments were determined iteratively through simultaneous optimisation during the SCF procedure. Computation of atomic spin moments was performed using Bader population analysis.[177] Bader analysis partitions space into non-overlapping atomic volumes and assigns all of the spin density within an atomic volume to that atom. It also does not directly depend on the basis set and can be readily applied to periodic and non-periodic

systems with collinear or non-collinear magnetism.[318] Various spin states were considered by specifying the fixed difference of the number of electrons in the up and down spin component within the VASP code.

To predict spin-orbit-related properties, namely orbital magnetic moments and magnetic anisotropy energies, fully relativistic calculations including spin-orbit coupling (SOC) were performed [319, 320] using the non-collinear version of the VASP code developed by Hobbs *et al* and Marsman and Hafner.[321, 322] These properties require extremely well converged wave functions and charge densities, and the criteria for termination of the SCF cycles was hence tightened to 10^{-7} eV/cell, and enforcing energy changes to less than a hundredth of a meV. The magnetic ground-state from the collinear scalar-relativistic calculations was used to initialise the non-collinear calculations. Two sets of self-consistent SOC non-collinear calculations were performed, one for each easy and hard magnetisation axis, and the MAE was determined in terms of the difference in their total energies:

$$\mathrm{MAE} = E(\uparrow) - E(\rightarrow). \tag{3.27}$$

The fact that a very accurate convergence of energy is required in the self-consistent cycle makes the calculations rather expensive. In principle, such approach, although time-consuming, is exact and straightforward.

3.3 Results

3.3.1 Bulk

Accurate structure of a bulk material is crucial for a proper description of derived nanomaterials. To obtain bulk cohesive energies, bulk calculations were conducted on fcc and hcp cells (Fm3m and P63/mmc space groups [323]) containing four and two cobalt atoms, respectively, Figure 3.4. All atoms were fully relaxed until appointed accuracy was reached. A test of convergence, which relies on successive increase of the cutoff energy in the plane wave expansion of the pseudo-wavefunctions until the total energy no longer changes, was performed in steps of 40 eV from 400 to 600 eV (including 500 eV), showed in Figure 3.5 left for hcp Co, and a kinetic cutoff energy of 500 eV was chosen as sufficient. Similarly, k-point grid convergence has been tested from 2×2×2 (fcc)/7×7×5 (hcp) to 20×20×20 (fcc)/21×21×19 (hcp), showed for hcp Co in Figure 3.5 right. Additional calculation has been carried out for the hexagonal unit cell by setting the smallest allowed spacing between k-points to 0.18 $\mathrm{Å}^{-1}$ to capture the difference in the length of a, b, and c vectors, and a 17×17×9 k-point mesh centred at Γ-point was generated, in satisfactory agreement with the convergence test. For all following bulk calculations, grids of 8×8×8 and 17×17×9 were employed for fcc and hcp Co, respectively.

Final lattice parameters after GGA (GGA+U, U_{eff} = 1.0 eV) relaxation are for fcc Co a = 3.517 Å (3.522 Å), and for hcp Co c/a = 1.616 (1.622). The calculated ratios deviate by less than 3 % from experiment (3.545 Å, 1.62 [324]). Computing the lattice constant with a denser k-point set (10×10×10 fcc / 21×21×19 hcp), and using more accurate linear

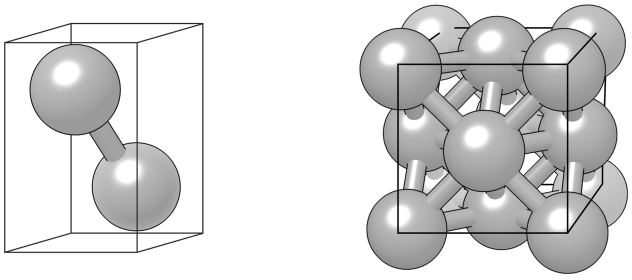

Figure 3.4: Unit cells of **left** hcp Co, and **right** fcc Co.

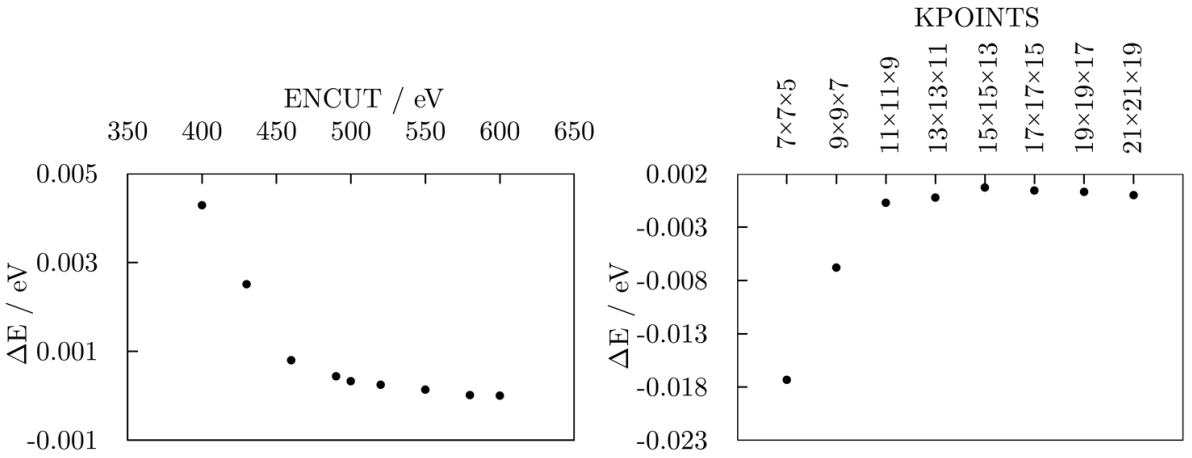

Figure 3.5: **left** Cutoff energy and **right** k-point mesh convergence for bulk hcp Co.

tetrahedron method in place of Methfessel-Paxton smearing results in lattice constants of a = 3.519 Å (3.523 Å) and c/a = 1.617 (1.624). Densities of state, DOS, are shown for hcp and fcc Co in Figure 3.6. The majority spin DOS are below the Fermi level and the d-states are completely occupied, whereas the minority spin DOS cut through the Fermi level capturing the asymmetry that gives a rise to the magnetic behaviour. These features of the DOS as calculated by GGA and GGA+U are not functional-dependent and they are consistent with previous studies.[325, 326, 327] Calculated magnetic moments are 1.581 μ_B GGA (1.679 μ_B GGA+U) for the hexagonal phase, and 1.615 μ_B (1.788 μ_B GGA+U) for the cubic phase, in good agreement with experimental data (1.72 μ_B hcp and 1.75 μ_B fcc [324]).

3.3.2 Small clusters - accessing the accuracy

Structural magic numbers affect the formation and abundances of larger NPs, whereas in the case of small clusters the combined electronic structure of all the atoms is of greater importance. The smallest clusters with $2 \leq N \leq 30$ atoms hence provide an excellent test for the method for two reasons, as they have so few atoms that the number of (meta-)stable structures is still low enough for the global-minimum to be easily accessible within

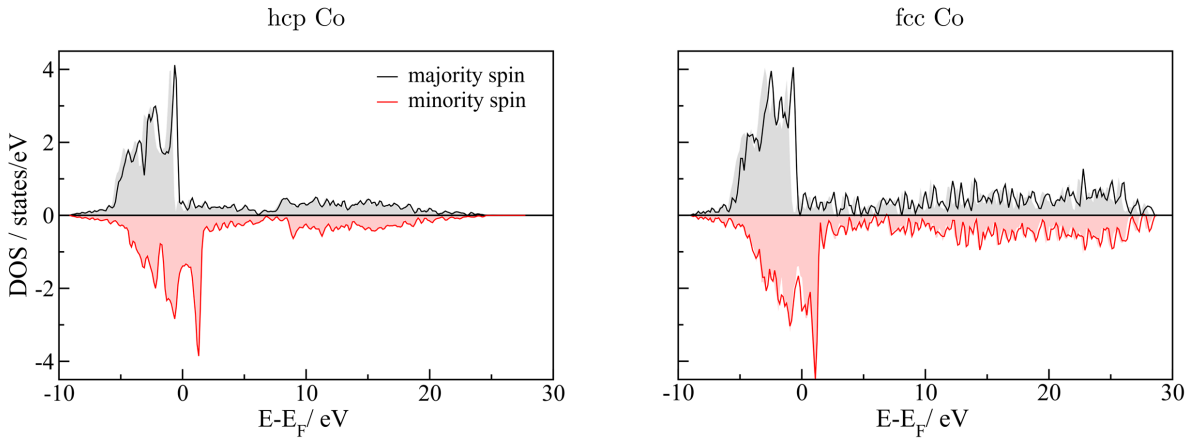

Figure 3.6: Densities of state, DOS, of **left** bulk hcp Co and **right** fcc Co as calculated by GGA (full lines) and GGA+U, $U_{\text{eff}} = 1.0$ eV (transparent blocks).

a 'sampling-by-hand' approach, and, since the plane wave method has its foundations in considerations for infinite, extended systems, modelling of small clusters is computationally the most challenging. Moreover, the biggest amount of data available on Co clusters covers systems with up to 30 atoms.

Figure 3.7 shows structures, cohesive energies, and average magnetic moments per atom for the most stable isomers of Co clusters with $2 \leq N \leq 30$ atoms as optimised by GGA and GGA+U ($U_{\text{eff}} = 1.0$ eV). Expanded results for second isomers are provided in Figure 3.8. General patterns of small transition metal clusters can be easily observed: for $N \geq 5$, the lowest lying isomers are three-dimensional with well-known high-symmetry geometries prevailing over non-symmetric structures. Amongst the two most stable isomers of Co clusters under ten atoms, most are square and pentagonal (bi)-pyramids with additional atoms incorporated to cap pyramid facets. For clusters with number of atoms close to the main and intermediate closed-shell sizes (N = 13, 19, 23), the most stable structures are derived from the respective crystalline and non-crystalline shapes, while the closed-shell clusters themselves have the lowest energy when shaped as one of the structural motifs (N = 13 - icosahedron, N = 19 - hcp, N = 23 - icosahedron). The structures predicted to be low-lying in energy are in a good agreement with those suggested in experimental works [328, 329, 248], with 19-atom hcp and octahedral structures being determined as more stable than double icosahedron.

Structural relaxation performed with the GGA+U method introduced no significant changes in geometries. Structures which were affected the most through the expansion of nearest neighbour distances of up to 10 % are planar isomers with under six Co atoms, and this is reflected in the energy difference between the first and second isomer when compared to GGA. In addition, compact icosahedron structures experienced less pronounced structural changes with approximate increase in the bond length of 0.1-0.3 %, while clusters with hexagonal symmetry had 1.0-2.5 % extension in average. Nevertheless,

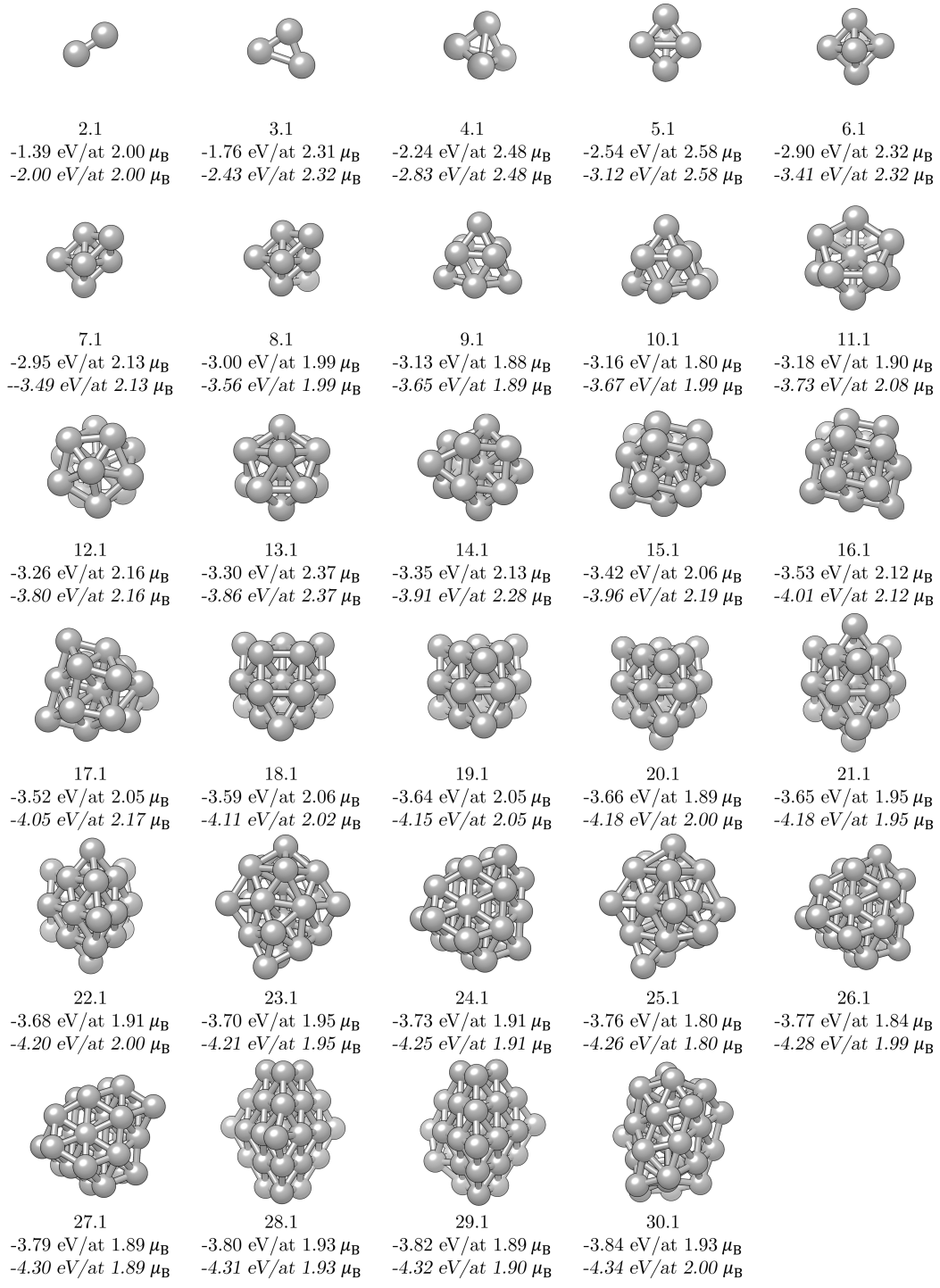

Figure 3.7: Optimised structures, cohesive energies, and average magnetic moments (per atom) as calculated by GGA and GGA+U ($U_{\text{eff}} = 1.0$ eV) for the most stable structures (N.1) of Co clusters with $2 \leq N \leq 30$ atoms.

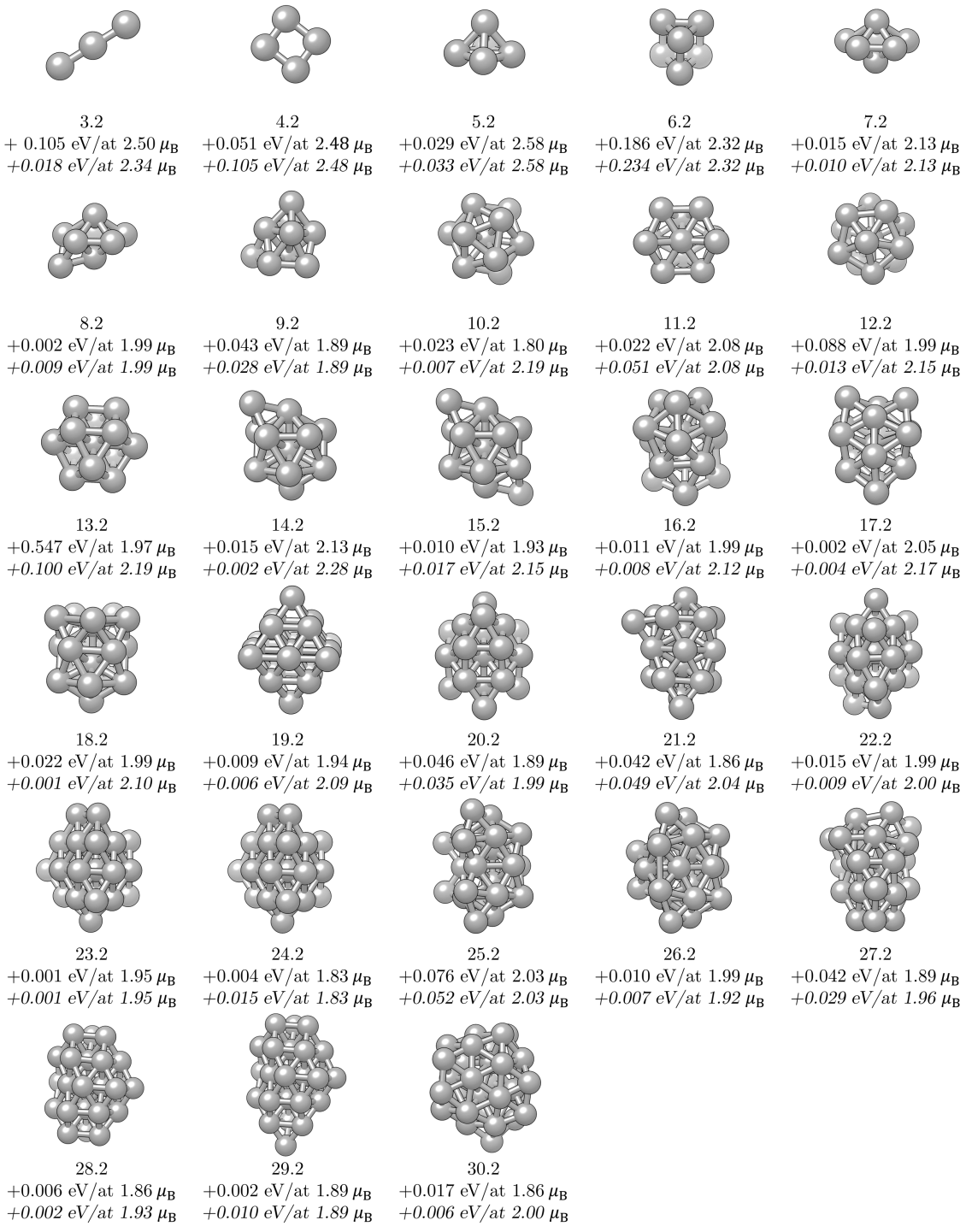

Figure 3.8: Optimised structures, cohesive energies, and average magnetic moments (per atom) as calculated by GGA and GGA+U ($U_{\text{eff}} = 1.0$ eV) for the second most stable isomers ($N.2$) of Co clusters with $2 \leq N \leq 30$ atoms.

energetic order of structural isomers does not change with the addition of the Hubbard parameter. Differences in the cohesive energies between first and second isomers are minimal, and mostly range between 0.01 and 0.10 eV. This coincides with experimental results which have found Co clusters in the range of 19 to 34 atoms as primarily polyicosahedral structures when saturated with ammonia. However, because atomic subshell closings in clusters of different symmetries occur in close sequences, it is expected that bare clusters adopt a variety of structures.[328] The obtained parameters are most often given within a couple of % of the results of other parameter-free electronic-structure calculations (LDA [260], GGA [263, 262], DV-LSD [330], BLYP [267]), with differences arising only when considering the relative order of different isomers. Moreover, none of the parameterised methods, i.e., the tight-binding approach [265] nor model potentials of Gupta [331], gives results that are systematically more accurate than parameter-free approaches.

With the aim of identifying general properties of the Co clusters, their evolution with the size, and accuracy of the results obtained, further detailed description of each isomer will not be carried out (as for most of them this has already been done elsewhere [265, 266]). Instead of discussing the individual clusters, different quantities shall be introduced to reduce the collected information to a few key numbers and allow for efficient comparison between GGA and GGA+U functionals.

Figure 3.9a shows comparison between calculated and experimental cohesive energies. Although GGA predicts a more uniform trend with the increase in the number of atoms, energy values are within the experimental range. GGA+U trend is completely consistent with the one obtained by GGA, with energies lower in general by 0.40-0.70 eV. To confirm the reliability of the energetic trends, the second derivation of energy as the stability function has been plotted in Figure 3.9b against the number of atoms in the cluster. This function has maxima for particularly stable clusters. The most pronounced peaks occur at N = 6, 9, 13, and 19 for both GGA and GGA+U, which is in agreement with previously determined closed-shell and intermediate closed-shell sizes for transition metal clusters. Previous study [266] failed in characterisation of the 13 atom cluster stability, which represents the first filled shell. Based on the occurrence of those four peaks, it can be concluded that cohesive energy values are reasonably predicted.

The magnetisation trends are shown in Figure 3.9c as magnetic moment per Co atom for high-spin states. Energies of low-spin state clusters were calculated to be less favourable by, on average, 0.35 eV per atom. Experimental values provided are taken from the work of Knickelbein which investigated Co clusters in a similar size range, (N = 7-32).[333] Magnetic moments obtained by GGA and GGA+U are mutually congruent, especially for the clusters with less than ten atoms. Underestimation of the magnetic moment compared to the experiment could partially be caused by the omittance of the orbital moment, which can be rather large in clusters in contrast to solids where it is usually strongly suppressed.[334] It was recently found that the orbital magnetic contributions that emerge in small Co clusters can even reach values that are an order of magnitude higher than those in the bulk.[335] Observed inconsistencies in the experimental and computed trends, however, can be improved for intermediate sizes ($10 \leq N \leq$

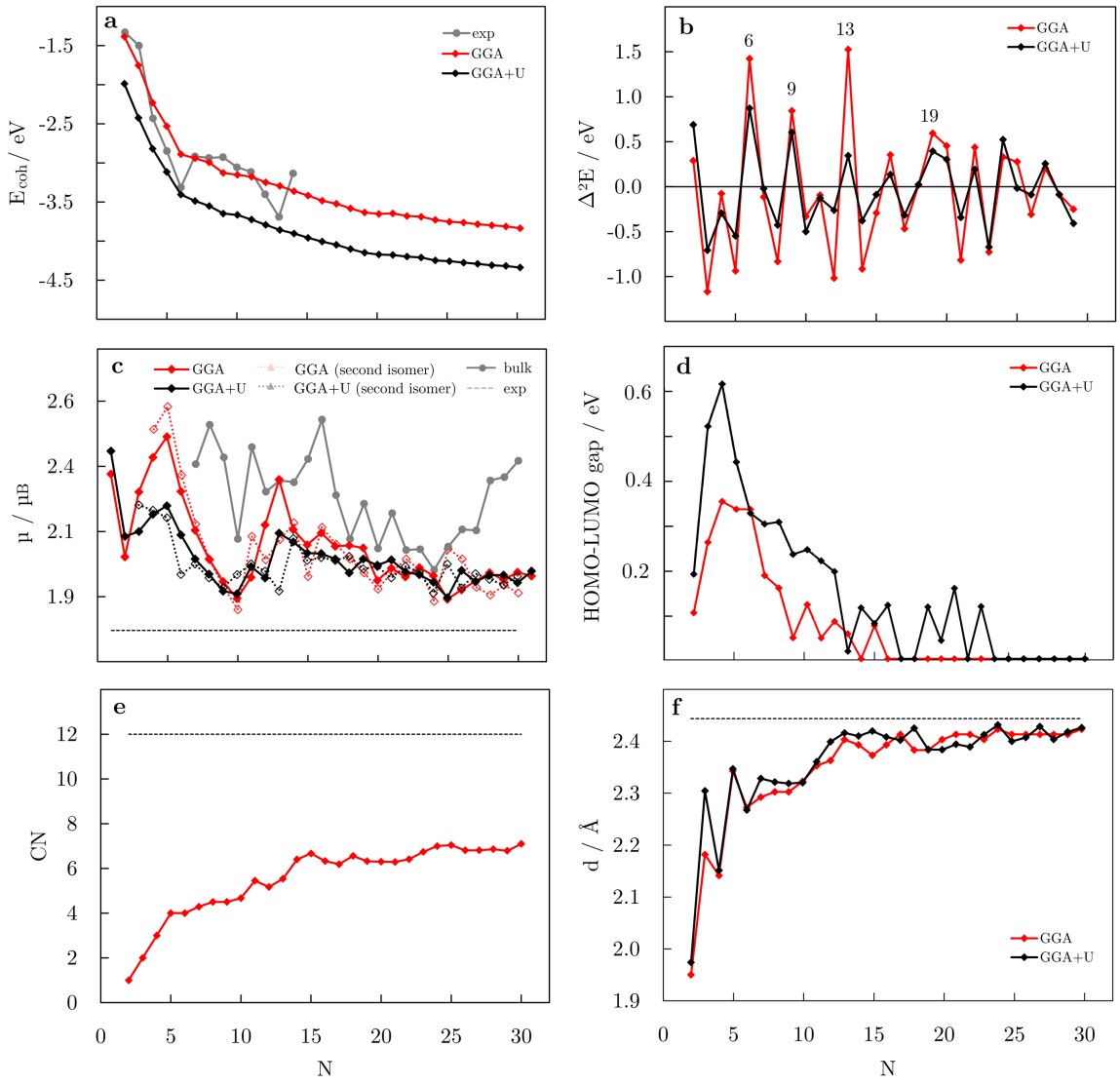

Figure 3.9: **a** cohesive energies per atom, E_{coh},; **b** second energy differences, $\Delta^2 E$,; **c** average magnetic moments per atom , μ,; **d** HOMO-LUMO gaps; **e** average coordination numbers, CN,; and **f** average bond lengths, d, for Co clusters with $2 \leq N \leq 30$ atoms as calculated by GGA and GGA+U ($U_{\mathrm{eff}} = 1.0$ eV). In **e** results are unchanged when going from GGA to GGA+U functional. Bulk values are represented with a dashed line; x-axis is the same for all graphs. Experimental values of cohesive energies are taken from [332], and of magnetic moments from [333].

25) by introducing magnetic moments of the second most stable isomers, which confirms the possible coexistence of different isomers in the cluster beam that has been proposed experimentally.[336] Additionally, experimental measurements of magnetic moments are challenging at the smallest sizes; the cluster beam intensities decrease rapidly, thermalisation can be very difficult to achieve, and the net magnetisation can change direction spontaneously due to thermal fluctuations. There are also temperature effects to be taken into the account - a severe problem is still the determination of the cluster temperature and the distribution of the rotation frequencies, which are dependent on the experimental conditions.[337, 338] As a result, variations in magnetisation values and trends can be found in the literature [339, 340, 341], making comparison rather difficult. Finally, magnetic moments of Co clusters approach the bulk value remarkably fast, even when compared to two of the metal's closest neighbours, iron and nickel.[342]

Certain properties, such as the HOMO-LUMO gaps, are not experimentally available. Nonetheless, Ni clusters showed clear similarities to Co clusters in both shape and reactivity [328, 343], making the energy gap comparison suitable. Obtained trend in changes in the energy gap with the increase in the number of atoms shown in Figure 3.9d quite resembles the trend of Ni clusters.[344] It is worth noting how, for both metals, gap values are significantly lower and clusters progress to metallic behaviour much faster than those of other transition metals.[345, 346] Calculated HOMO-LUMO gaps of Co clusters are calculated up to 0.36 eV (GGA) and 0.66 eV (GGA+U), with sizes of N = 3-6 having the largest interspace in the orbital occupancy. Clusters with more than fourteen atoms are already very close to the metallic state, with GGA predicting no band gap above N = 16, while GGA+U predicts small band gaps for clusters with intermediate sizes of N between 15 and 25. Differences between electronic configurations predicted by GGA and GGA+U are, considering magnetic moments and HOMO-LUMO gaps, minimal, which confirms that small modifications in structural parameters remain as the only distinction between the two methods.

Figures 3.9e and 3.9f summarise the quantities related to the structural properties, namely average coordination numbers, CN, and bond lengths. Two atoms are considered bonded if their interatomic distance is less than the average value of the first and second nearest-neighbour distances in the bulk (2.44 and 3.50 Å, respectively), which is in this case 3.00 Å. Atoms are classified as inner if CN $\geq$ 12, or surface atoms if CN<12. From the figures, it is clear that both properties oscillate mostly for the smallest clusters while increasing as a function of the size. Convergence towards the bulk values is obvious (2.44 Å nearest-neighbour distance and 12 coordination number), with average CN saturating at a slower pace. This is due to the large number of atoms still being characterised as surface atoms at such small sizes. Small differences in the average bond lengths between cluster structures relaxed by GGA and GGA+U were captured.

Everything considered, the properties of the smallest Co clusters, as the absolutely most critical cases, are in satisfactory qualitative agreement with the available experimental results when modelled by GGA and GGA+U. Both functionals show the same

trends of energetic, electronic, and structural properties, and predict equal geometries as the most stable isomers. The smallest Co clusters therefore have minimal sensitivity to the level of the exchange-correlation functional used. It is expected that, as the cluster sizes approach scalable regime where properties start more closely resembling characteristics of the bulk, the effect of the exchange-correlation functional would almost completely diminish, hence the less expensive GGA functional will be employed for optimisations of large Co NPs.

3.3.3 Large clusters - towards the behaviour of nanoparticles

Five kinds of motifs with variations in the centring have been considered for clusters/NPs with up to 1500 atoms, 2 non-crystalline (icosahedral and decahedral), and 3 crystalline (hcp, fcc, and bcc). By construction, icosahedron and decahedron have centres occupied by a single atom. Marks and Ino decahedra have been derived from the regular decahedron by truncation with ten re-entrant (111) facets or with five (100) facets at five twin boundaries, respectively. Crystalline clusters/NPs are cut off from a crystal lattice of the same phase and therefore conserve the lattice symmetry - this can be achieved by placing the cluster/NP origin either in the centre of an elemental cell or as an atom of the lattice. Thus, fcc cluster/NP structures include the atom-centred cuboctahedral and atom- and octahedron-centred truncated octahedral systems. Hcp clusters are truncated hexagonal bipyramids with centres located at a single atom, a triangle (two possible combinations, with and without the central atom in the second layer), or interstitially between the two (0001) layers. Bcc clusters can be an atom and interstitial-centred. Construction of differently centred motifs is represented in Figure 3.10, while structures of irregular decahedral geometries are shown in Figure 3.11.

3.3.3.1 Energetics

The stabilities of structural motifs were compared based on their cohesive energies, with the lowest cohesive energy appertaining to the most stable shape within the given size. Calculated cohesive energies are given in Table 3.1, and they are plotted as a function of $N^{-1/3}$ in Figure 3.12a. Dependencies are well represented by linear regression and extrapolated to larger NP sizes. For sizes below 100 atoms, stability of motifs based on the successive increase in the cohesive energy decreases going from the most stable icosahedron, over fcc truncated octahedron, hcp, fcc cuboctahedron, and decahedron to bcc as the least stable Co NP shape. Differences in energies for the NPs with the same number of atoms between any two shapes are close to or less than 0.10 eV per atom, except for crystalline bcc motif whose stability is lower by 0.30 eV per atom compared to decahedron which is the second least stable morphology in the smallest size region. Decahedron and cuboctahedron are separated by minimal differences in energy; however, there is no intersection in their stabilities even with the extrapolation of linear regression to larger diameters. Just under $N = 500$, hcp motif surpasses fcc truncated octahedron in stability. After that crossover, the order remains unchanged with icosahedron being the most stable throughout the whole range of small and medium sizes ($N \leq 5000$), which

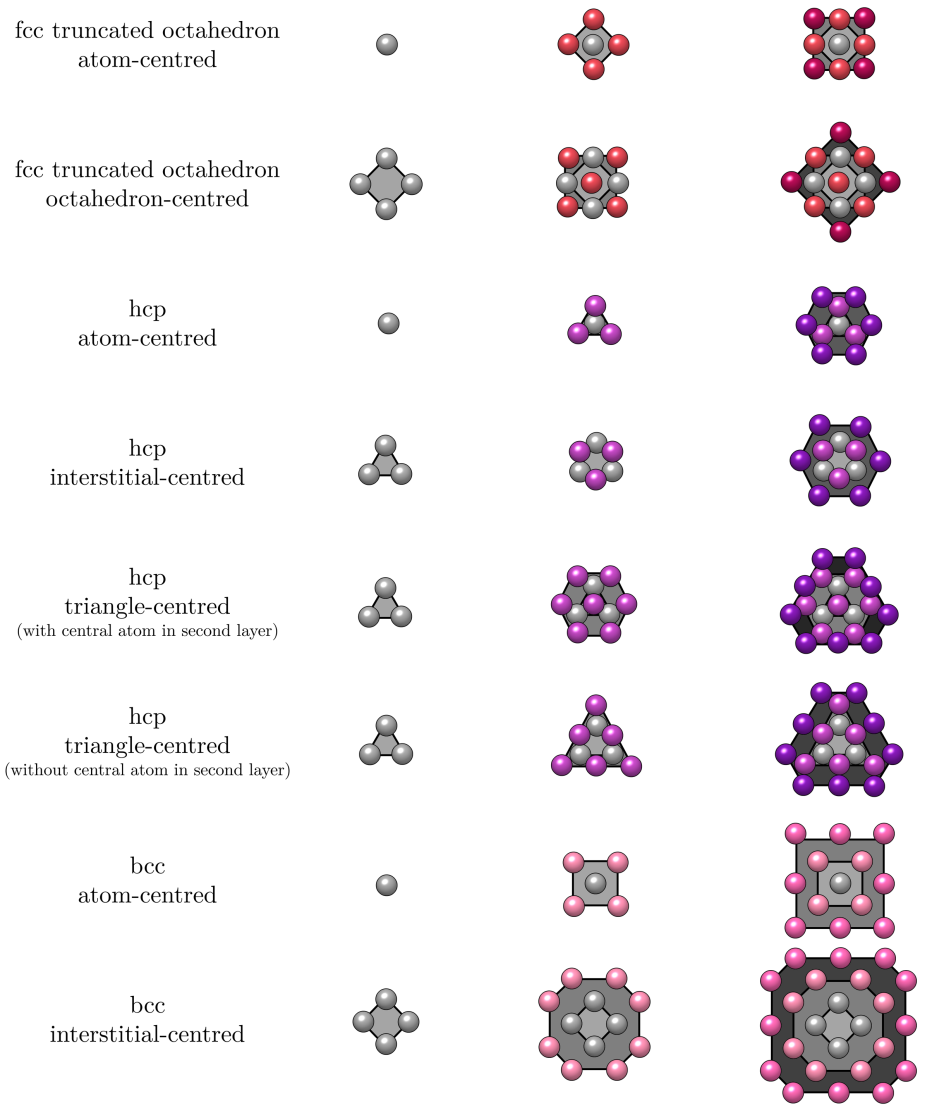

Figure 3.10: Construction of differently centred bcc, hcp, and fcc-type NPs.

is consistent with the experimental findings of its predominance within clusters with up to 800 atoms. The icosahedron-to-hcp transition is predicted to happen at around $N \approx 5500$. An enlarged view of the intersection is represented in Figure 3.12b. Equations of linear regressions were used to get a crude approximation of the crossover point, which is suggested to be at $N = 5341$.

Figure 3.12c captures the same stability trends of Co NPs of varying motifs with the limit of $N \to \infty$ forced to reach the calculated E_{coh} values of bulk fcc and hcp Co (-5.44 and -5.54 eV, respectively). As cohesive energy of hcp Co is known to be lower than that of the fcc counterpart [347, 348], the crossovers between fcc cuboctahedral,

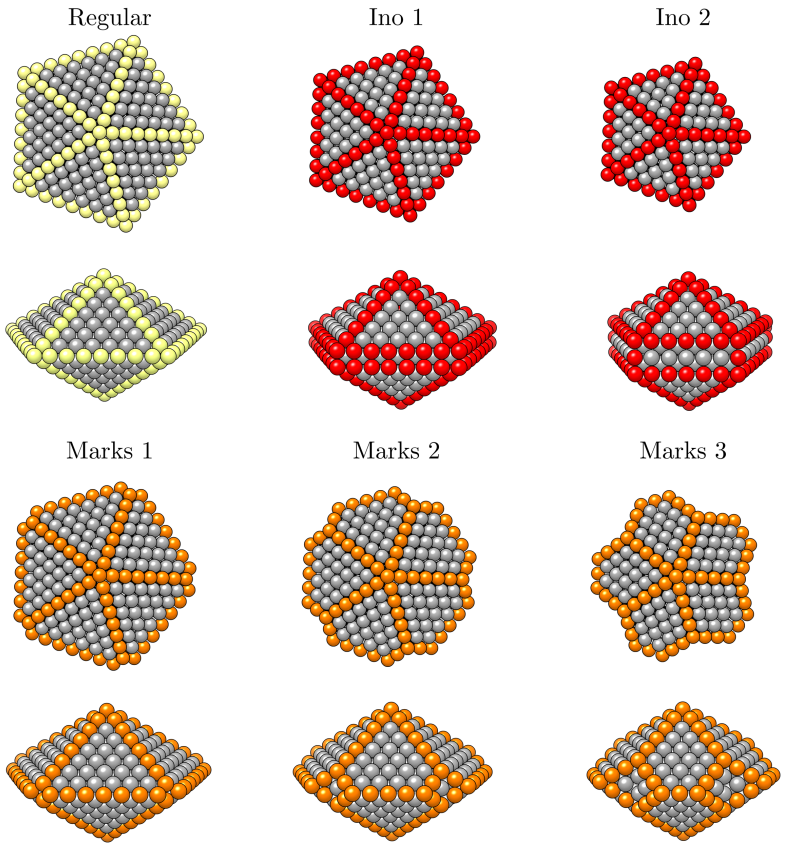

Figure 3.11: Top and side views of five types of Marks and Ino decahedra derived from the regular decahedral structure, which is given for comparison in top left.

icosahedral, and hcp Co NPs are preserved with a slight shift towards smaller NP sizes, Figure 3.12d. However, it should be kept in mind that the rearrangement of motifs with non-crystalline stacking towards either fcc or hcp bulk arrangements would be unlikely even at very large NP limits due to the kinetic trapping which was observed at large NP sizes and certain differences in the cohesive energies as N reaches ∞ might still persist. Nevertheless, both linear fitting with and without $E_{\mathrm{coh}}(N \rightarrow \infty) \simeq E_{\mathrm{coh}}(\mathrm{bulk})$ limit predict the icosahedron→hcp transition to occur at large NP diameters.

Intra-motif competition for differently centred crystalline shapes, namely four different hcp and two of each fcc-truncated octahedron and bcc shapes, is represented in Figure 3.13. Amongst considered hcp motifs, interstitial-centred NPs are predominant at smaller sizes, triangle-centred with the central atom in the second layer at intermediate sizes, and atom-centred at large sizes, with shape intersections calculated at $N = 120$ and $N = 340$. However, relative differences in the stabilities of four motifs are below 0.025 eV per atom regardless of the NP size. Fcc truncated octahedron showed better stability when centred as octahedron for up to $N = 205$, while atom-centred NPs dominate medium and large regions. Atom-centred bcc NPs become more stable over interstitially-centred specimens

Table 3.1: Cohesive energies of magic numbered Co NPs for icosahedron, decahedron, cuboctahedron, truncated octahedron, and hcp morphologies.

decahedron							
regular		Marks (1)		Marks (2)		Marks (3)	
N	E_{coh} / eV	N	E_{coh} / eV	N	E_{coh} / eV	N	E_{coh} / eV
105	-4.37	100	-4.38	80	-4.32	217	-4.64
287	-4.66	282	-4.67	262	-4.68	539	-4.84
609	-4.83	604	-4.84	584	-4.85		
1111	-4.94						

decahedron						fcc	
Ino (1)		Ino (2)		icosahedron		cuboctahedron	
N	E_{coh} / eV	N	E_{coh} / eV	N	E_{coh} / eV	N	E_{coh} / eV
85	-4.33	55	-4.19	55	-4.22	55	-4.12
257	-4.67	207	-4.62	147	-4.56	147	-4.48
569	-4.84	499	-4.82	309	-4.76	309	-4.69
				561	-4.88	561	-4.83
				923	-4.97	923	-4.90
				1415	-5.03		

fcc truncated octahedron				bcc			
atom-centred		octahedron-centred		atom-centred		interstitial-centred	
N	E_{coh} / eV	N	E_{coh} / eV	N	E_{coh} / eV	N	E_{coh} / eV
38	-4.33	140	-4.52	91	-4.01	84	-4.22
201	-4.63	260	-4.68	189	-4.42	180	-4.48
586	-4.87	490	-4.82	341	-4.59	330	-4.66
1289	-4.99	711	-4.98				

hcp							
atom-centred		triangle-centred (without atom in 2nd layer)		triangle-centred (with atom in 2nd layer)		interstitial-centred	
N	E_{coh} / eV	N	E_{coh} / eV	N	E_{coh} / eV	N	E_{coh} / eV
57	-4.17	140	-4.48	89	-4.36	114	-4.44
153	-4.53	310	-4.72	214	-4.64	258	-4.68
323	-4.74	570	-4.76	421	-4.80	492	-4.82
587	-4.87			732	-4.91		
967	-4.96						
1483	-5.04						

at $N = 584$, while energetic differences substantially grow as the NP size advances from the intersection. Although crossovers between distinct centrings occur at various size-ranges for each phase, atom-centred structures are always the most stable for largest sizes.

Figure 3.14 shows competition in stability between regular, Marks, and Ino decahedra. Any type of truncation of regular decahedra increases stability of this non-crystalline motif, especially for smaller clusters/NPs where Ino (2) decahedron shows the highest stability with cohesive energies lower by ∼0.10 eV per Co atom compared to the regular counterpart. Additional re-entrant (111) surfaces make Marks (3) decahedron dominant for medium-sized NPs with more than 230 atoms. Regular decahedron is the most stable only at sizes well above $N = 10^4$.

It should be noted that this type of linear fitting and a subsequent search for stability trends is constrained by assuming that the differences in stabilities of non-magic NPs of different structural motifs are close to the differences defined by the cohesive energies of

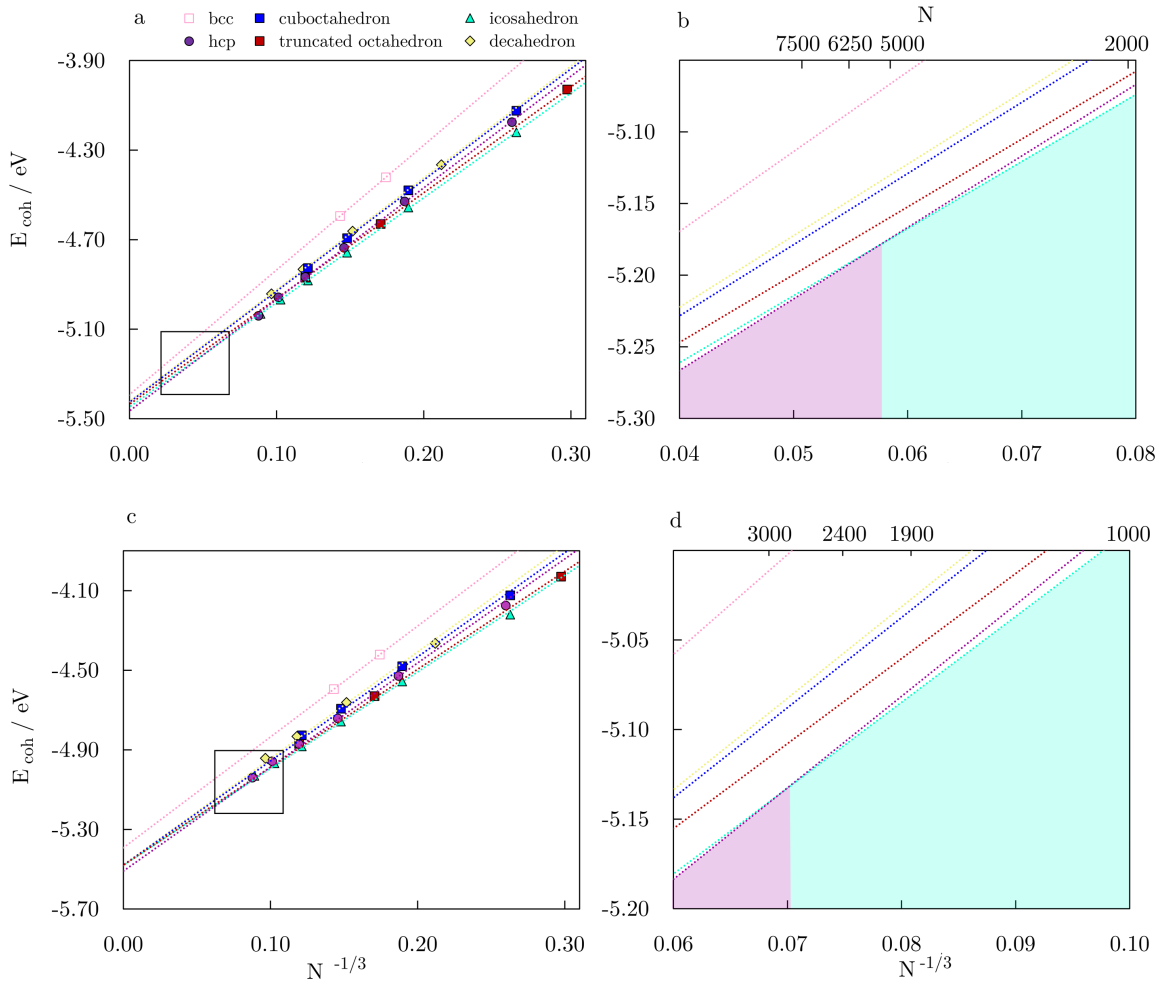

Figure 3.12: **a** Cohesive energies of Co NPs with 55-1500 atoms as a function of $N^{-1/3}$; **b** intersection between hcp and icosahedron (enlarged area from **a**); **c** cohesive energies of Co NPs with the $E_{\mathrm{coh}}(N \to \infty) \simeq E_{\mathrm{coh}}(\mathrm{bulk})$ limit and **d** the corresponding enlarged intersection; dotted lines represent linear regression.

magic NPs. By keeping in mind the experimental indications of the expected occurrence of more than one geometrical shape at practically any size, sharp motif transitions as predicted by linearly interpolated energetics of magic numbered NPs should be taken only as a guideline to the predominating geometry. However, recent works that have sampled the energy landscape beyond the magic numbers found a qualitative agreement, where the most dominant NP shape coincides with the one predicted by a simple 'magic number' fit.[349, 350, 351] The non-crystalline/crystalline distributions thus obtained for magic number Co NPs represent a good reference point for defining crossover sizes between the structural motifs. Note that shape alternations could occur in reported stability windows, but they should nevertheless be expected to contain the highest proportion of the energetically most favourable structure.

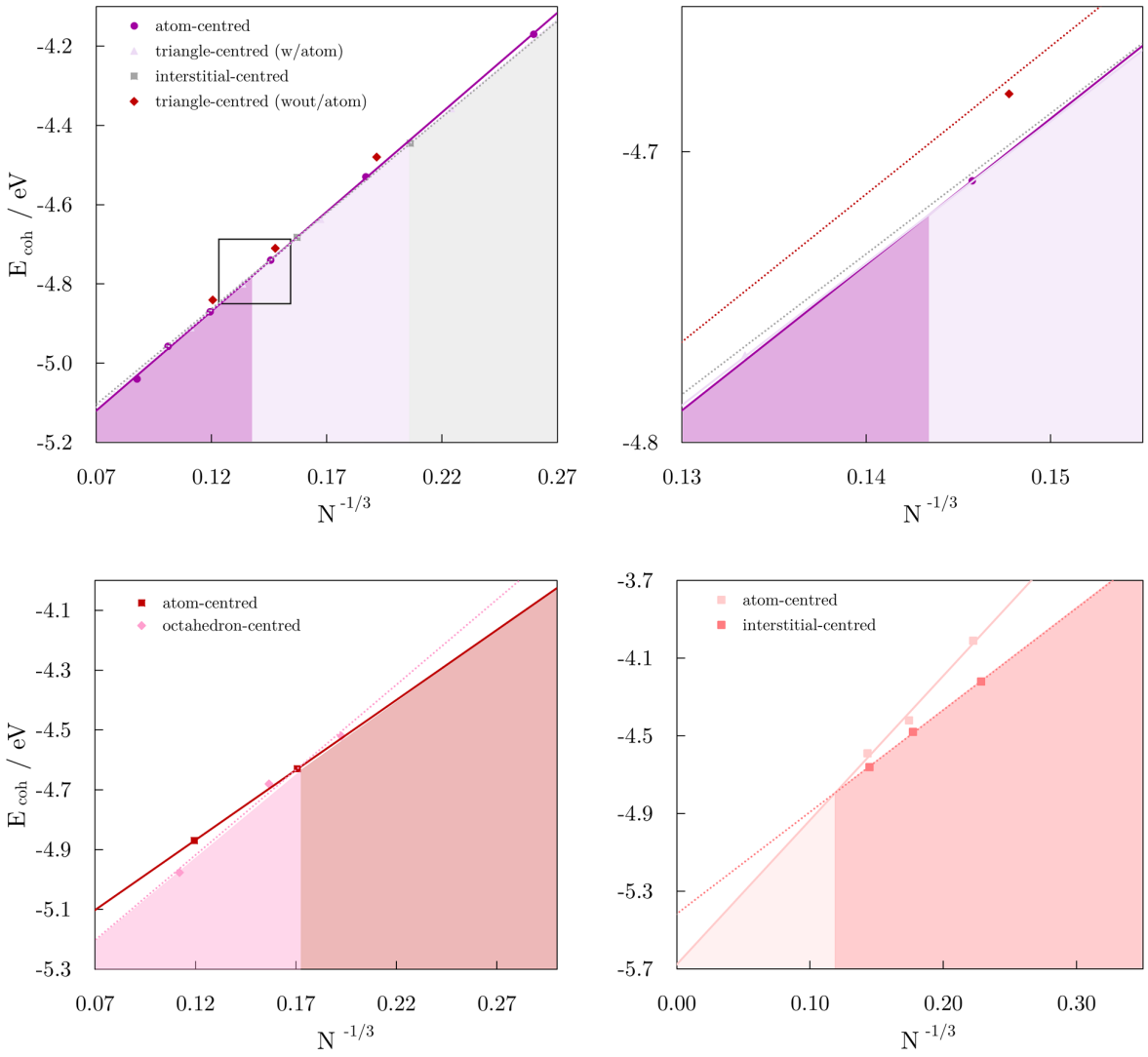

Figure 3.13: Cohesive energies of differently centred Co NPs **top left** hcp, **bottom left** fcc - truncated octahedron, and **bottom right** bcc. **Top right** is enlarged crossover area as framed in the **top left**.

A combined experimental and theoretical study of Wells *et al* [352] has explored the morphology changes of size-selected gold nanoclusters with 561±13, 742±17, and 923±23 atoms in order to reveal the hierarchy of atomic structures. Slow growth conditions have revealed decahedron as most commonly observed structure (∼45 %), followed by fcc (30-35 %), with only less than 5 % of structures identified as icosahedron; the remaining NPs were classified as amorphous. A key finding of the study was that the proportion of different isomers is, to within experimental accuracy, exactly the same for all three NP sizes, suggesting that the structure of the nanoclusters is already locked by the size of $N = 561$ for gold nanoclusters as they follow a template growth on smaller seeds. Atomistic simulations of the NP growth confirmed competition between decahedron and

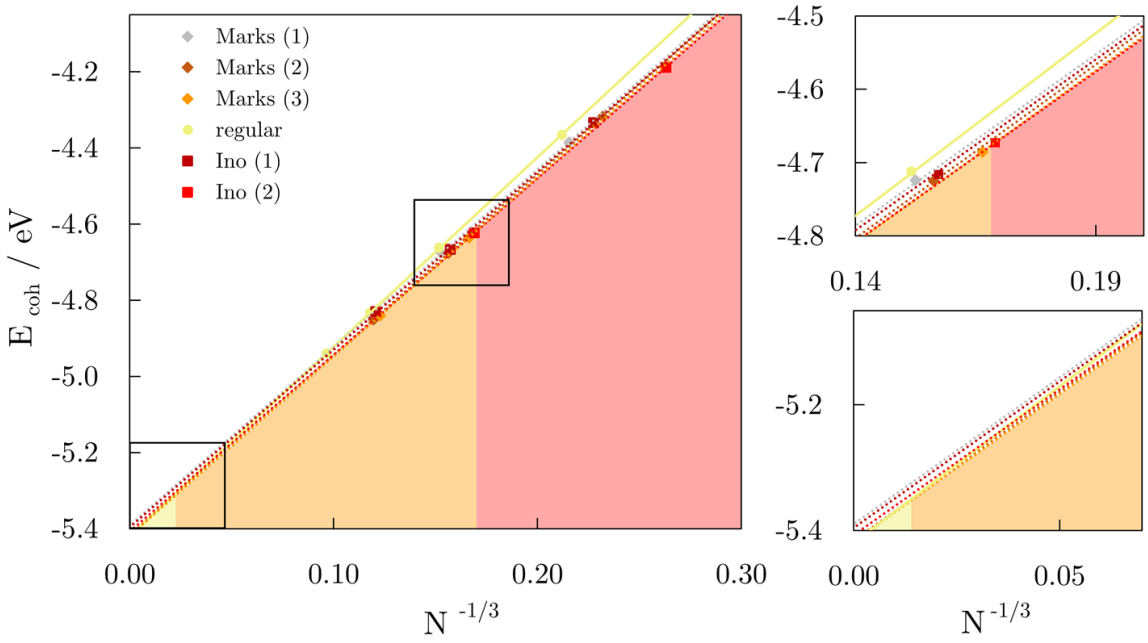

Figure 3.14: **left** Cohesive energies of different decahedron motifs: Marks, Ino, and regular decahedra; **right** enlarged crossover areas as framed on the left.

fcc geometries with similar isomer ratios to those observed experimentally. The most common structure produced in the simulations is decahedron, but the number of fcc structures is not far behind. Very few icosahedra were produced, together with a few alternations that were indicated as unclassified/amorphous structures. The predominance of fcc and decahedra isomers reflects the energetics obtained through a linear fitting approach. In addition, there were no solid-solid transitions observed during the growth process. Further, STEM irradiation showed a systematic tendency for decahedral NPs, whose preferential growth originated from smaller seeds, to convert into fcc structures, which are the most stable isomers if one can create them. This is attributed to the large energy associated with displacing atoms from the bulk crystalline structure of gold to create decahedron or icosahedron. MD simulations are therefore a confirmation that the structures of individual gold NPs within the population are already frozen in by the size of 561, such that subsequent growth by addition of atoms is templated onto smaller seed structures, preserving the structural motif as seen in the experiment. A certain possibility of kinetic trapping in the MD simulations should also be taken into the account. Nevertheless, beyond a certain size, the activation energy required to rearrange many or all of the atoms in the NP to achieve a final, lower energy configuration may be prohibitive at the growth temperatures employed.

Considering the natural hcp phase of cobalt and large internal strain of icosahedron when compared to decahedron and fcc structures due to the significant displacement of the atoms from their bulk crystal locations even for materials with natural fcc stacking

(as seen in the case of gold), growth of Co NPs in non-slow conditions is, according to the linear fitting approach, most likely to result in hcp-shaped NPs. However, confirmation through the continuous sampling of all NP sizes remains a topic for future work.

3.3.3.2 Structural and electronic properties

To understand the shifts in the most stable structures with the increase in the NP size, the effects of surface formation, twin boundaries, and elastic strain energy losses created at the expense of high surface-to-volume ratios have been estimated along with the evolution of structural (CN, Co-Co distances), electronic, and magnetic properties.

Table 3.2: Surface areas, S (in %), and surface energies, γ (in eV Å^{-2}) for magic numbered icosahedron, decahedron, cuboctahedron, truncated octahedron, and hcp Co NPs.

icosahedron			decahedron			cuboctahedron			truncated octahedron			hcp		
N	S	γ	N	S	γ	N	S	γ	N	S	γ	N	S	γ
55	76.36	0.169	105	78.10	0.300	55	76.36	0.255	38	84.21	0.443	57	77.19	0.374
147	62.59	0.148	287	63.41	0.134	147	62.59	0.223	201	60.70	0.282	153	62.75	0.363
309	52.43	0.137	609	52.87	0.127	309	52.43	0.208	586	53.92	0.256	323	52.63	0.362
561	44.92	0.133	1111	45.18	0.124	561	44.92	0.203	1289	44.84	0.232	587	44.97	0.357
923	39.22	0.131				923	39.22	0.201				967	39.30	0.352
1415	34.77	0.128										1483	34.79	0.337

Each of the crystalline and non-crystalline motifs is characterised by specific Miller-index surfaces. Fcc cuboctahedron is confined by six rectangular (100) surfaces and eight triangular (111) surfaces, while truncated octahedron has eight hexagonal (111) surfaces and six truncating rectangular (100) surfaces. Hcp bipyramids are tiled by two (0001) and twelve $(10\bar{1}1)$ hexagonal surfaces. Icosahedron and decahedron are built from twenty and ten (111) facets, respectively. The fcc (111) surface is well-known to be the lowest-energy surface amongst low Miller-index fcc and hcp Co surfaces.[353] The stability order of four surfaces building NP motifs based on their surface energies (as calculated by GGA) is: fcc (111) 2.30 J m^{-2} < hcp (0001) 2.33 J m^{-2} < hcp $(10\bar{1}1)$ 2.90 J m^{-2} < fcc (100) 3.02 J m^{-2}, where the surface energies of the two close packed surfaces (111) and (0001) differ by only 0.03 J m^{-2}. There is a connection to the coordination numbers, with the first two surfaces having CN=9, and the last two CN=8. Dependence of average CN on the shape and size of Co NPs is shown in Figure 3.15. Icosahedral NPs have the highest average CN for the whole size range as they contain 20 highly coordinated (111) facets. Decahedral CNs are lower as decahedron is built from 10 fcc (111) facets. Introduction of the lower-coordinated (100) surface within cuboctahedron and truncated octahedron lowers their average CNs. Since cuboctahedron has a higher share of (100) facets, the average CN is also lower when compared to the truncated octahedron. Hcp motif has the lowest CNs as majority of surface areas coincide with the $(10\bar{1}1)$ surface. Formation of icosahedron is therefore favoured, as fewer bonds need to be broken to achieve higher CN values, which lowers the energetic cost. When approximated linearly with respect to the $N^{-1/3}$, the difference between the average CN of all the motifs decreases with the growth of the NPs, eventually reaching the maximum of 12 bonds as in the bulk phases.

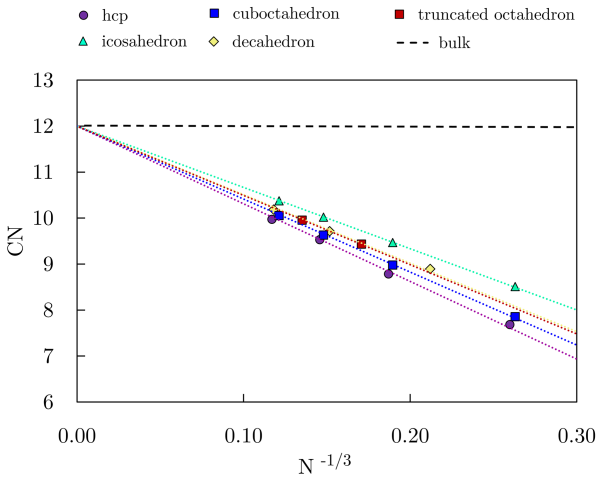

Figure 3.15: Average coordination number, CN, of Co NPs with 55-1500 atoms as a function of $N^{-1/3}$; the dotted lines represent the linear regression.

Table 3.2 summarises the total surface areas and corresponding surface energies of magic numbered Co NPs. The excess energy due to a free surface has two opposite effects: the energy loss related to the broken bonds and lower CNs, and the energy gain through the surface stress state. Of the motifs considered, hcp has the highest surface energy, owing to higher cohesive energy of hcp Co (5.54 eV as calculated by GGA) compared to the fcc bulk phase (5.44 eV as calculated by GGA), causing increased energy losses for hcp surface formation. This is also interconnected to variations in the energies of hcp and fcc surfaces. Of fcc-based motifs, icosahedron has the lowest surface energy, while decahedron, also built solely from the fcc (111) surface, has surface energies that are almost two times higher. This is a proof that motif shapes, despite the equivalent surface termination, cannot allow for the same intensity of surface relaxation due to the volumetric constraints. As the NP size decreases, surface formations have a significant influence on the overall stability as surface area dominates over volume; as a result, fcc motifs with mainly (111) surfaces, i.e. truncated octahedron and icosahedron, become favoured. However, decahedral NPs retain high surface areas even at larger sizes, with 609-atom NP still having more than 50 % of atoms on the surface. Although this wide surface expanse has a comparatively lower surface energy, it issues a high number of broken bonds, which is more and more unfavourable as the size increases, and prevents better stability compared to cuboctahedron characterised by high-energy (100) surface.

In addition to differences in the energetics of appearing surfaces, there are additional factors induced by specific geometries and surface intersections that may alter crossover sizes. The (111) fcc surface may be characterised by the lowest energy and the highest CN, but tetrahedral arrangements in the icosahedron and decahedron, while minimising the surface-to-volume ratio, also introduce an elastic strain contribution. The elastic strain energy density, W, is expressed in terms of elastic constants c_{11}, c_{12}, and c_{44} of fcc Co (Table 3.4), and it is calculated to be 1.95×10^{-4} eV Å^{-3} for decahedron and

Table 3.3: Surface energies (unrelaxed, γ_u, and relaxed, γ_r) and magnetic moments (μ per Co atom of first surface layer) for four surfaces that construct different Co NP motifs.

surface	γ_u / J m^{-2}	γ_r / J m^{-2}	μ/μ_B
hcp (0001)	2.37	2.33	1.72
hcp (10$\bar{1}$1)	2.96	2.90	1.81
fcc (111)	2.45	2.30	1.72
fcc (100)	3.25	3.02	1.82

Table 3.4: Calculated elastic constants of fcc Co and comparison with available data in GPa.

	c_{11}	c_{22}	c_{44}
this work	316.7	168.2	157.2
exp [314]	303.7	154.3	74.7
exp [354]	225	160	92
exp [355]	223	186	110
LDA [356]	325	189	156

2.92×10^{-3} eV Å^{-3} for icosahedron. Despite the known deficiencies of DFT for computing elastic properties and variations in existing experimental data, the obtained elastic strain energy densities have the same order of magnitude and similar values as those published previously (3.00×10^{-4} eV Å^{-3} for decahedron and 1.75×10^{-3} eV Å^{-3} for icosahedron [314]). The overall contributions to the cohesive energies of the decahedral and icosahedral Co NPs are expressed in terms of elastic strain energy in Table 3.5, and have the order of 10^{-3} and 10^{-2} eV per atom, respectively, with the values increasing with the growth in the NP size. For both icosahedron and decahedron, and for all the sizes, elastic strain energies are positive, meaning they destabilise the non-crystalline motifs.

Table 3.5: Elastic strain energy, E_{els}, for decahedral and icosahedral magic number Co NPs.

icosahedron			decahedron		
N	E_{els} / eV/atom	E_{els} / eV	N	E_{els} / eV/atom	E_{els} / eV
55	1.49×10^{-2}	0.82	105	9.64×10^{-4}	0.10
147	1.89×10^{-2}	2.78	287	1.21×10^{-3}	0.35
309	2.14×10^{-2}	6.61	609	1.35×10^{-3}	0.82
561	2.32×10^{-2}	13.02	1111	1.44×10^{-3}	1.60
923	2.42×10^{-2}	22.34			
1415	2.58×10^{-2}	36.45			

Table 3.6: Twin boundary energy per unit area, γ_t, for fcc (111) and hcp (10$\bar{1}$1) Co surfaces.

surface	number of layers	γ_t / eVÅ^{-2}
fcc (111)	6L	-2.09×10^{-3}
	9L	-2.00×10^{-3}
	12L	-2.24×10^{-3}
hcp (10$\bar{1}$1)	10L	1.63×10^{-2}
	12L	1.66×10^{-2}
	16L	1.65×10^{-2}

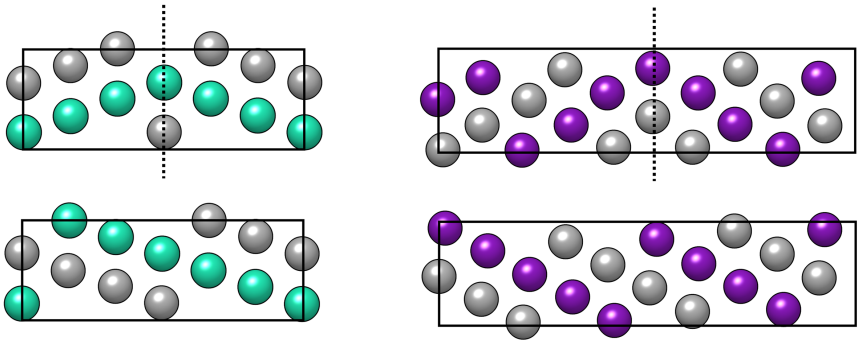

Figure 3.16: Twin boundary models (**top** panel) compared to the normal surface slabs (**bottom** panels) of **left** fcc (111) and **right** hcp $(10\bar{1}1)$ Co surfaces.

Another consequence of small volume packing that can either stabilise or destabilise different NP motifs is the presence of twin boundaries. To estimate the twin boundary energy per unit area for different motifs, twin boundary models of fcc (111) and hcp $(10\bar{1}1)$ surfaces, Figure 3.16, have been used, with the calculated twin boundary surface energies collected in Table 3.6. The obtained energies for the $(10\bar{1}1)$ twin boundary have positive values, indicating that this behaviour is undesirable and slightly destabilises hcp shapes. A similar phenomenon has been earlier observed for gold.[316] Contrary, for the (111) surface, twin boundary energy is negative and stabilises icosahedral and decahedral motifs. This is opposite to what has been seen for transition metals which are naturally present in the fcc bulk phase [315] due to the similarity of the local structure near the fcc (111) twin boundary to the hcp (0001) stacking which is the native bulk arrangement of Co. The twin boundary energy remains relatively unchanged with increasing periodic units, suggesting that its influence will eventually diminish as the NP size increases.

Finally, volumetric contributions as a consequence of dense atom packing within NP volume and exposure of wide surface areas to vacuum also play a significant role in shape stability. Figure 3.17 shows the average interatomic distances between the nearest-neighbour, surface-surface, surface-inner, and inner-inner Co atoms as a function of $N^{-1/3}$ for the motifs considered. Generally, the overall average interatomic distance is less than the bulk 2.44 Å and it increases as the NPs grow, relatively quickly approaching the bulk value for all motifs. Distances between the inner Co atoms are the only ones to increase compared to ideal 2.44 Å for all crystalline shapes, but also for decahedron, while distances that include one and two surface atoms are up to 3.8 and 1.5 % shorter than the bulk value, respectively. Icosahedra of all sizes, on the other hand, have surface-surface distances which are elongated more than the inner-inner distances, with the elongation of the latter appearing only after the NP size has reached 500 atoms. On the contrary, the only 'inconsistency' from crystalline geometries in the trend of decahedron is for the smallest 105-atom NP, where the distances between surface and inner Co atoms exceed that of the two surface Co atoms. Overall, for all shapes, the variation in the distances between the inner Co atoms is minor compared to the distances which include at least one surface Co

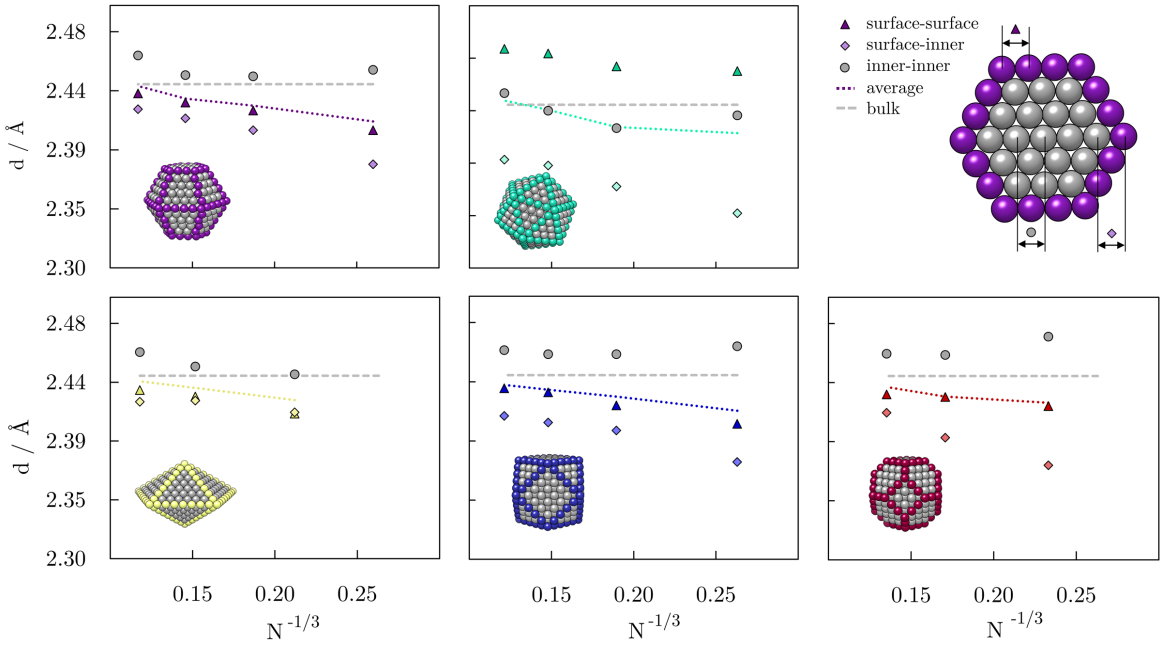

Figure 3.17: Average interatomic (dotted lines), surface-surface (**triangle**), surface-inner (**diamond**), and inner-inner (**circle**) atom distances in Co NPs (motifs represented with the structure) with 55-1500 atoms as a function of $N^{-1/3}$; the dashed lines represent the interatomic distance of bulk Co. In the top right, an explanation of distances on the hcp NP is given. x-axis is the same for all the graphs.

atom. Thus, the interatomic distances in the surface layer affect the average interatomic distance, and hence the stability of the motifs, the most. This is the most obvious for icosahedron which is limited by (111)-like close-packed facets only, and the surface energy gain is optimised at the expense of the volume contribution. Consequently, inter-shell bonds are substantially compressed, and intra-shell bonds are expanded, imposing high strain, which confirms indications that it can only be favoured at sizes where the number of atoms cannot generate significant volume stress. Absence of any further crossovers between motifs at large sizes is thus explained through both crystalline and decahedral geometries obeying distance constraints to minimise the volumetric losses.

Taking everything into consideration, the highest CN and the lowest surface energy together with the negative twin boundary energy make icosahedron the most stable motif for a wide range of Co NP sizes. However, these contributions are becoming less and less effective with increase in the size since inner-inner atom distances tend to become longer than average bulk Co-Co bonds with surface-surface distances prolonging even faster than for small sizes. Moreover, the surface area is naturally decreasing with the NP growth, which leads to a drop in the surface energy for all motifs, as shown in Figure 3.18. While the extent of the decrease in the surface energy of both crystalline and non-crystalline fcc shapes also reduces as the size increases, the hcp surface energy drops quicker as the NPs

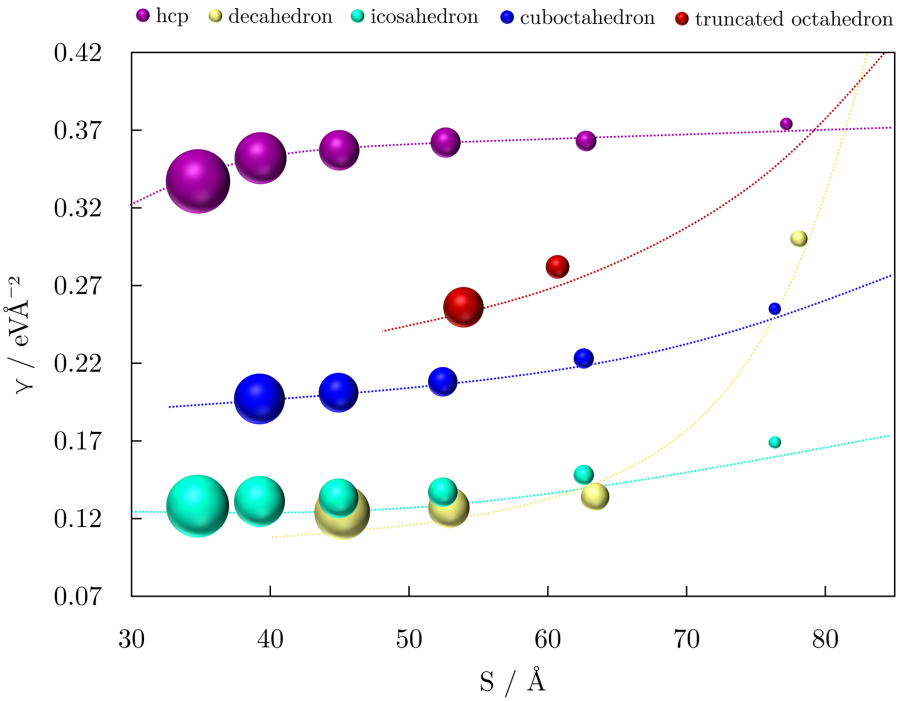

Figure 3.18: Effect of size on surface energy, γ, and surface area, S, for different motifs of Co NPs; the size of the bubble represents the size of the NP according to considered magic numbers.

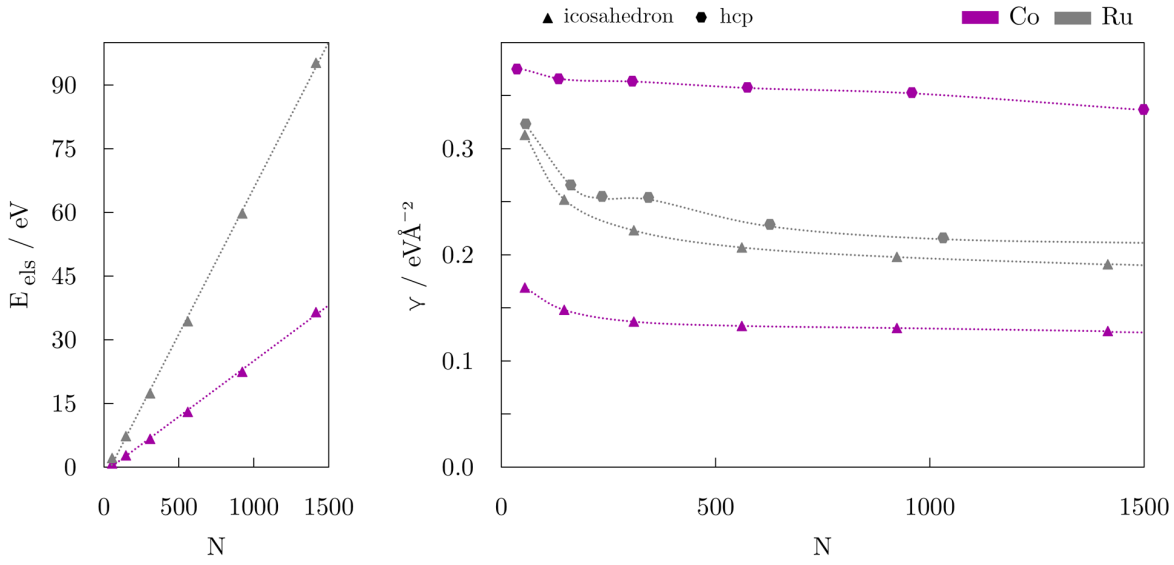

Figure 3.19: Comparison of the contributions of **left** elastic strain energies, and **right** surface energies to stability of ruthenium[304] and cobalt icosahedral (triangle symbol) and hcp (hexagon symbol) NPs.

approach medium and large size-range. Additionally, icosahedron and decahedron start reaching a plateau already at $N \sim 1000$, contrary to crystalline shapes. Nevertheless, even for NPs with more than 1000 atoms, there is still a noticeable difference in the surface energies of hcp and icosahedron motifs, which leads to a conclusion that volume and elastic strain become dominant factors in the (in)stability of the icosahedron only at very large sizes, where the surface energies of the two shapes become less distinct.

Compared to another hcp metal, ruthenium, for which the stability of hcp clusters/NPs overcomes icosahedron already at $N = 103$, cobalt requires significantly larger sizes in order to experience the same change. Figure 3.19 shows relation between size and strain effects of the two hcp metals. In the case of Ru, surface energies of icosahedron and hcp NPs lie close to each other even for sizes under 100 atoms. Surface energies of icosahedral Co NPs are lower than those of icosahedral Ru NPs, whereas they are higher for the hcp morphology. Combined with the higher values of elastic strain for Ru icosahedron, the surface contribution is, contrary to Co, expected to become negligible at much lower sizes, as it has been shown with a significant difference in the crossover point.

3.3.3.3 Wulff morphology

Based on the Wulff theorem, the equilibrium shape for large nanoclusters can be obtained from the values of the respective surface energies of a material. The standard structure used to calculate surface properties from first-principles is the surface slab - a supercell representing an infinite two-dimensional thin film oriented to expose the facet of interest and separated from periodic images by a vacuum.[357] The METADISE code [358] was employed to construct the structures of the seven low Miller-index Co surfaces: (0001), $(01\bar{1}0)$, $(01\bar{1}1)$, $(10\bar{1}0)$, $(10\bar{1}1)$, $(11\bar{2}0)$, $(11\bar{2}1)$ from the optimised hcp bulk geometry. METADISE code does not only consider periodicity in the plane direction, but also provides different atomic layer stacking resulting in a zero-dipole moment perpendicular to the surface plane, as is required for reliable and realistic surface energy calculations.[359] Two pairs of surfaces were identified to be mirror-images of each other, namely $(01\bar{1}0)$ and $(10\bar{1}0)$, and $(01\bar{1}1)$ and $(10\bar{1}1)$. Only one surface from each pair ($(01\bar{1}0)$ and $(10\bar{1}1)$) was therefore used for further modelling.

The convergence of slab and vacuum thickness was calculated such that there is no interaction between opposite surfaces through the bulk or between adjacent slabs. The vacuum thickness has been tested from 8 to 18 Å in steps of 2 Å, as shown for the $(01\bar{1}0)$ surface in Figure 3.20 (left). Already 12 Å of vacuum was found to be sufficient to hinder the interaction of periodic images for all surfaces. However, as the future calculations will consider adsorption of small molecules, thickness of 16 Å was chosen to account for the space occupied by adsorbates. An example of the slab thickness convergence for the $(01\bar{1}0)$ surface is depicted in Figure 3.20 (right), with four layers showing no interaction between opposite surfaces. To confirm the adequateness of the chosen slab thickness, the surface energies have been tested for both four- and six-layer slab models. For surfaces that contain atoms with a difference in z-coordinate smaller than 0.8 Å, such atoms have

been treated to be in the same layer since geometric relaxation showed the preference of their alignment.

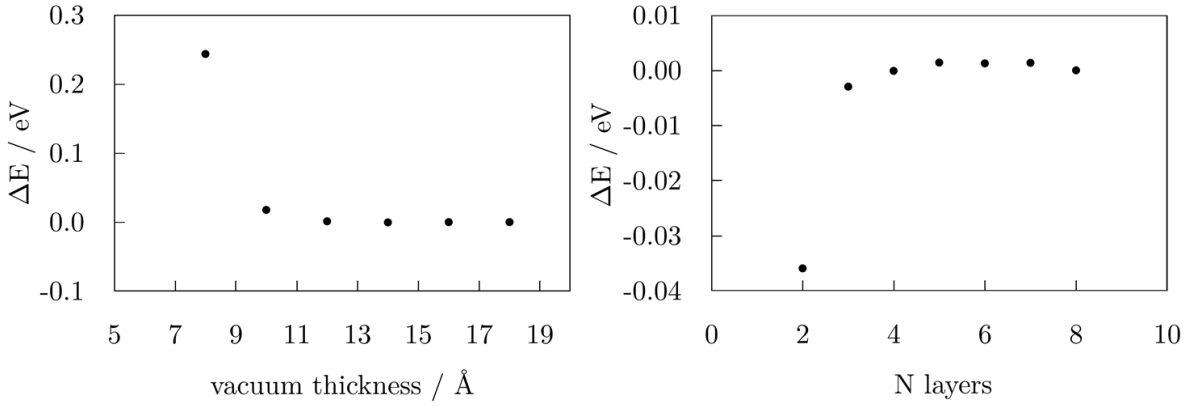

Figure 3.20: Vacuum thickness (**left**) and slab thickness (**right**) convergence for the $(01\bar{1}0)$ surface of hcp Co.

To alleviate the excess energy of broken bonds, surface atoms tend to relax to more energetically favourable positions. For many solids, this process is a simple compression or expansion of the layers near the surface, known as surface relaxation. It is important to allow for these atomistic relaxations as surface energy calculations in the literature show that they can reduce the unrelaxed surface energy by up to 30 %. The optimised slab model consists of four layers with the bottom two layers fixed at their bulk equilibrium positions and representing the bulk material, whereas the top two layers were allowed to fully relax. 16 Å vacuum was added in the direction perpendicular to the surface. Due to the unusual geometry of surface slabs under the constraints of periodic boundary conditions, special attention must be paid to the k-space integration of the surface Brillouin zone. Supercells were constructed of 3×3 for (0001), 3×2 for $(01\bar{1}0)$, 2×2 for $(11\bar{2}0)$ and $(11\bar{2}1)$ surfaces with 5×5×1 k-point mesh, and 3×2 with 5×4×1 mesh for the $(10\bar{1}1)$ surface due to the symmetry breaking.

A detailed electronic and structural description of each low Miller-index hcp Co surface is included in the next chapter, which investigates changes in the surface properties caused by oxidation processes. GGA calculated surface energies are: 2.33 J m^{-2} (0001), 2.90 J m^{-2} $(01\bar{1}0)$, 2.96 J m^{-2} $(10\bar{1}1)$, 3.21 J m^{-2} $(11\bar{2}0)$, and 2.95 J m^{-2} $(11\bar{2}1)$, and the resulting Wulff morphology of large hcp Co nanocrystals is depicted in Figure 3.21, together with structures of 1, 2, 4, and 8 nm diameter NPs as cut by METADISE. NPs progressively show more distinct features of low Miller-index surfaces as the diameter increases. On the smallest NPs, only (0001) and $(10\bar{1}1)$ surfaces are distinguishable. Appearance of other facets occurs for the 4 nm NP, which counts over 2200 atoms, whereas the 8 nm NP mirrors the Wulff morphology in much more detail. It is important to note that these theoretical results consider the crystals to be in vacuum at thermodynamics equilibrium at 0 K. Solvent, capping agents, and temperature can all affect the final morphology as

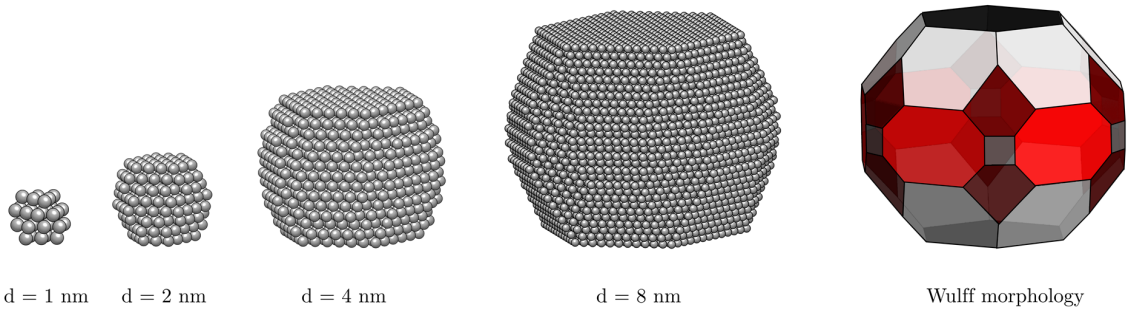

Figure 3.21: Structures of hcp Co NPs with increasing diameter cut with METADISE code based on the DFT surface energies. As a reference, predicted Wulff morphology is given on the right.

it depends on the surface energy of each crystal termination within the thermodynamic conditions.

3.3.3.4 Magnetic Properties

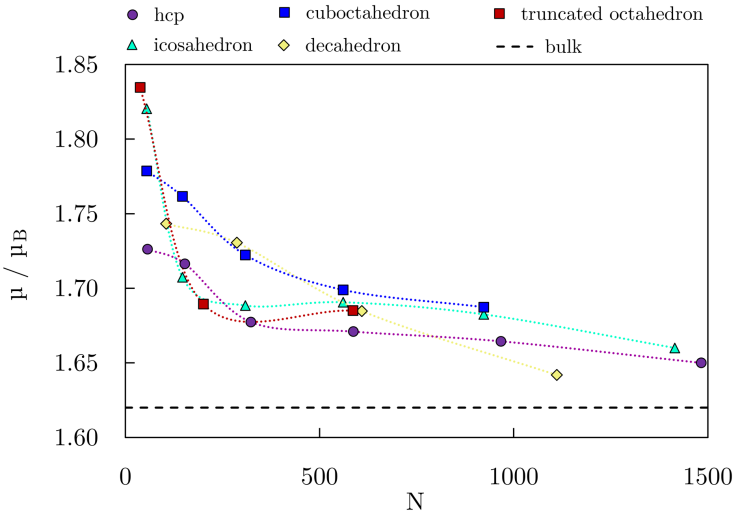

Figure 3.22: Average magnetic moments per atom of Co NPs with 55-1500 atoms as a function of N; the dotted lines are to guide an eye only.

Average magnetic moments per atom for each shape are shown in Figure 3.22 for high spin states (ferromagnetic ordering). Because of the system sizes, low spin states (random and ordered antiferromagnetic, as well as a mixture of ferromagnetic and antiferromagnetic coupling within the NP, Figure 3.23) were tested only for NPs with ~100-150 atoms. Ferromagnetic ordering was preferred by all motifs, with rather large differences in energies of distinct couplings, e.g. for a 147-atom icosahedron, the ordered antiferromagnetic

structure has an energy higher by 0.36 eV per atom when compared to the ferromagnetic ordering, while the mixed antiferromagnetic-ferromagnetic phase is less favourable by 0.30 eV per atom. For the 153-atom hcp NP, ordered antiferromagnetic structure is less stable by 0.46 eV, and the mixed phase by 0.30 eV per atom than the ferromagnetic phase. Random antiferromagnetic coupling was found to relax to ferromagnetic ordering. Magnetisation behaviour with change in the size and shape reflects the relation between morphologies, CNs, and surface shares. For sizes under 100 atoms, hcp crystalline motif has the lowest average magnetic moment despite its low average CN owing to the natural bulk packing. In medium size region, decahedron owes its high magnetic moment to the wide surface areas, while magnetisation of cuboctahedron arises due to the open geometry of fcc (100) surface, which, alongside low CNs, measures moments of 1.82 μ_B for the first layer atoms (Table 3.3). A detailed insight into the electronic structure differences that govern the magnetic behaviour of icosahedral and truncated octahedral Co NPs can be found in a recent study.[360]

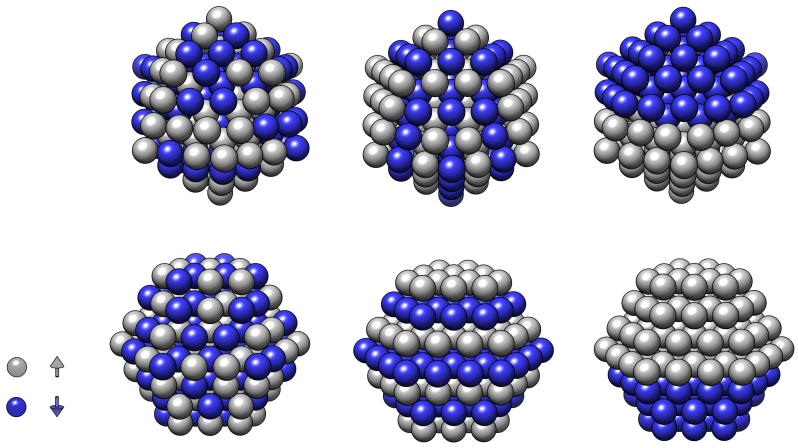

Figure 3.23: Different antiferromagnetic couplings of icosahedron (**top** panel) and hcp (**bottom** panel) Co NPs: random (**left**), layer-ordered (**middle**), and bulk-ordered (**right**).

Table 3.7: Calculated magnetic anisotropy energy of hcp and fcc bulk Co and available data in the literature. Directions of magnetisation are also given.

μeV/atom	hcp Co $[10\bar{1}0]$-[0001]	fcc Co [111]-[001]
this work	27.195	-1.536
other DFT	15-26	-2.4
[361, 320]	29	
exp [362, 363]	65	-1.3 - -1.6

Considering the monometallic nature, morphology of NPs only slightly influences the average magnetic moment per atom at large sizes. There are, however, other magnetic properties that are much more affected by the size and shape of nanostructures and they

play a significant role in different applications, such as magnetic anisotropy energy. Addition of spin-orbit coupling improves the calculated magnetic moments of bulk hcp and fcc Co, where spin components, S, are 1.596 μ_B and 1.664 μ_B, with orbital magnetic moments, L, of 0.071 μ_B and 0.074 μ_B, respectively. Total magnetic moments of 1.670 (hcp) and 1.738 (fcc) μ_B per atom correspond well to the experimentally determined magnetic moments of 1.72 and 1.75 μ_B. Considering that the MAE of bulk Co is of the order of several μeV, determination of anisotropy of Co systems has to be performed with high accuracy. A systematic study on the comparison of the MAE as obtained by various exchange-correlation functionals and initial parameters showed no prominent difference between different combinations of GGA functionals and pseudopotentials (namely PBE, PBE-pv, PBE-sv, and PW91), with all four correctly predicting the easy axis of magnetisation.[361] Additionally, the results of the study indicate that the magnitude of the MAE underestimation is similar regardless of the choice of exchange-correlation functional. Herein predicted MAE of bulk hcp and fcc Co are 27.20 μeV per atom (4.16×10^5 J m^{-3}) and -1.54 μeV per atom (-1.68×10^4 J m^{-3}), Table 3.7. Energies were obtained with dense k-point mesh set ups, 21×21×15 for hcp and 20×20×20 for fcc Co. Calculated value for the hcp phase is considerably lower compared to the experimental data (hcp 7-8$\times10^5$ J m^{-3} or 65 μeV/atom and fcc -2.36×10^4 J m^{-3} or -1.6 μeV/atom [364] at 0 K), which is well-known in the DFT community and agrees with other theoretical works.[361, 320] Despite this underestimation, calculations based on the unrestricted GGA relaxation of surface slabs predicted anisotropy energies for the (0001), (10$\bar{1}$1), and (111) Co surfaces of 6.57 μeV per atom (81.4 μJ m^{-2}), -0.70 μeV per atom (-7.98 μJ m^{-2}), and 16.63 μeV per atom (199.01 μJ m^{-2}), respectively, in good agreement with thin-film experimental measurements (53-70 μJ m^{-2} for the Co (0001) film deposited on Au [365], 17 μeV per atom for the Co/Au(111) system [366]). The qualitative trend for the variation of the MAE values as a function of the NP size and morphology is thus expected to be properly described.

Table 3.8: Magnetic anisotropy energies, MAE, of Co NPs of different morphologies and sizes as calculated by non-collinear DFT. Directions of magnetisation are also given, as represented in Figure 3.24.

	hcp	cuboctahedron	truncated octahedron	icosahedron	regular decahedron	Ino decahedron	Marks decahedron
MAE / kJ m^{-3}	[100]-[001]	[110]-[001]	[110]-[001]	[100]-[001]	[100]-[001]	[100]-[001]	[100]-[001]
0.70-1.00 nm	-1412.5	254.9	439.9	30.2			-37.0
1.50-2.00 nm	-397.9	211.8	194.5	65.6	-398.2	-520.8	-266.1

Expensiveness of non-collinear DFT calculations limited the determination of MAE to particles with 1-2 nm diameters (50-200 atoms). Considered NP morphologies and their accompanying axes of magnetisation are depicted in Figure 3.24, while the obtained MAE are summarised in Table 3.8. For hcp NPs, the two chosen orientations of the magnetisation were the one along the z-axis perpendicular to the (0001) facets and the other along the x-axis in the direction of an edge joining two (10$\bar{1}$1) facets. The later was determined as an easy magnetisation axis, with MAE values of -1412.5 and -397.9 kJ m^{-3} for NPs containing 57 and 153 atoms. For morphologies originating from the cubic phase,

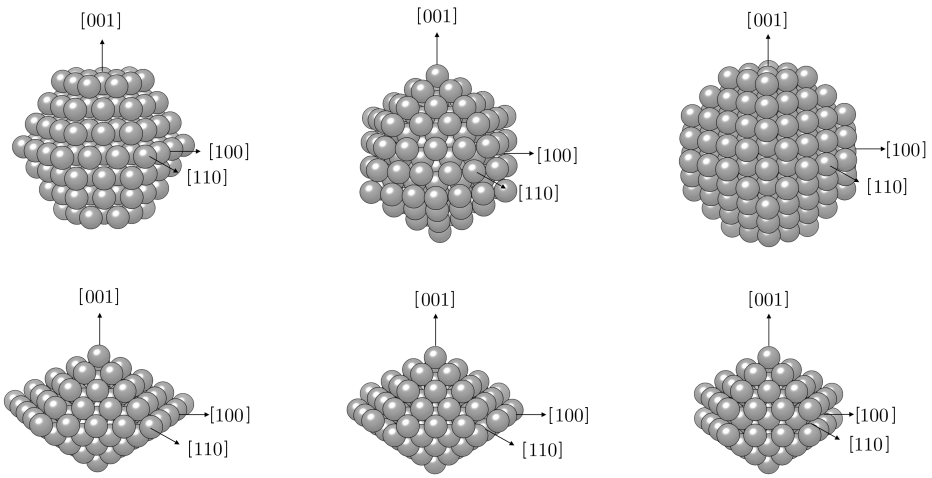

Figure 3.24: Schematic representation of magnetisation axes considered in calculations of magnetic anisotropy of Co NPs with varying morphologies (**top**: hcp, icosahedron, truncated octahedron; **bottom**: regular, Marks, and Ino decahedron).

namely cuboctahedron and truncated octahedron, considered magnetisation orientations were consistent with the growth directions of exposed facets or their conjoining edges, as in the case of hcp NPs. Axis coinciding with the directional growth of the (001) surface was detected as an easy magnetisation axis for both morphologies, and MAE calculated at 439.9 kJ m^{-3} for a 38-atom truncated octahedron and 254.9 kJ m^{-3} for a 55-atom cuboctahedron, considerably lower compared to the 57-atom hcp NP. MAE of 201-atom truncated octahedron and 147-atom cuboctahedron NPs were calculated at 194.5 and 211.8 kJ m^{-3}, respectively. Icosahedron was found to have the lowest MAE value, which was calculated at 65.6 kJ m^{-3} for the 55-atom NP, and 30.2 kJ m^{-3} for the NP with 147 atoms. Finally, anisotropy energies of the least curvaceous NP shapes, regular and irregular decahedra, were found at respectable values for 1.50-2.00 nm diameters: -266.1 kJ m^{-3} for the 100-atom Marks decahedron, -398.2 kJ m^{-3} for the 105-atom regular decahedron, and -52.08 kJ m^{-3} for Ino decahedron with 147 atoms.

The reversed MAE directions of crystalline NPs compared to the hcp and fcc Co bulk are a consequence of the various types of anisotropy present within the NPs, such as surface anisotropy, shape anisotropy, and magneto-crystalline anisotropy, which arise from the abrupt ending of the crystallite and reduced number of closest neighbours, symmetry breaking, surface relaxation, and varying facet population and orientation.[367, 368] The NP shape and surface anisotropies can become comparable to or even higher than the bulk magneto-crystalline anisotropy, becoming significant in preferential orientation of NP magnetisation. For a Co truncated octahedron, the shape anisotropy has been evaluated at the order of 10^6 erg cm^{-3} - the same order as fcc bulk anisotropy (2.7×10^6 erg cm^{-3}).[369] Similar was found for magnetite NPs, with obtained shape and magneto-crystalline anisotropies of the same order (55.53×10^3 J m^{-3} and 512.43×10^3 J m^{-3}, respectively [370]), or even dominating shape anisotropy with a prefactor of an order of

magnitude higher.[371] There are also contributions from the (111) and (100) facets with in-plane anisotropy, and from the edges with an easy direction along their axes. Apices usually give no contribution to the anisotropy of fcc NPs since locally the cubic symmetry is not broken. Additionally, various crystalline faces present on a single NP are characterised by different atomic coordination and consequently surface anisotropies. Dominant contribution of the intrinsic surface anisotropy to the total MAE has been confirmed in multiple studies for magnetite and maghemite NPs.[372, 373, 374] For Co nanoclusters, experimentally determined surface, shape, and magneto-crystalline anisotropy constants were -0.22 MJ m^{-3}, 0.09 MJ m^{-3} and -0.01 MJ m^{-3}, respectively. Similar was measured for Fe nanoclusters, -0.32 MJ m^{-3}, 0.00 MJ m^{-3}, and 0.05 MJ m^{-3}. By changing facet appearances of Co NPs, different values were obtained: shape anisotropy -0.06 MJ m^{-3} (the opposite sign compared to previous results), surface anisotropy -0.24 MJ m^{-3}, and magneto-crystalline anisotropy 0.05 MJ m^{-3}.[375] Opposite easy axis directions were also captured for the fcc polycrystalline Co NPs when the appearance of certain facets was changed.[376] In addition, NPs may undergo an external stress which relaxes in the particle volume leading to the magneto-elastic anisotropy. A cumulative contribution of each anisotropy type ultimately determines the preferential orientation of NP magnetisation, contrary to the uniaxial anisotropy of bulk. Magnetic axes for shape and surface anisotropy may not be the same since the former is related to the particle morphology, whereas the latter depends on the faceting. In conclusion, in the case of NPs, the contribution of the spins at the surface layer to the magnetic anisotropy becomes important, sometimes even dominant and, most often, the direction in which the NP is the longest results in the easy magnetisation axis.

Experimentally measured magnetic anisotropy energies of Co NPs are reported in the range of 6.0-30.0 kJ m^{-3}, consistently above the Co bulk values.[377, 378, 369] MAE obtained in this study range from 30.2 kJ m^{-3} to 1412.5 kJ m^{-3}. Geometrical shapes of the particles are not always provided in experimental studies, but it is suspected that they are mostly fcc crystalline or icosahedral Co NPs. Moreover, several studies of various NPs and for different sizes have observed the coexistence of crystallographic structures in both gas and the deposited phase [379, 380, 381, 382], especially without further annealing. Calculated MAE of fcc motifs as a function of NP diameter in this work (MAE ($\sim$0.7, 1.0, 1.4, 1.5 nm) = 439.9, 254.5, 211.7, 194.5 kJ m^{-3}) correspond well to the experimentally measured fcc NP trend (MAE (1.9, 2.7, 3.2, 3.5, 3.8, 4.7, 5.5 nm) $\approx$ 218, 135, 114, 110, 154, 182, 180 kJ m^{-3})[218], Figure 3.25. Experimental data has been complemented by the Néel pair modelling to correlate the observed MAE features to the increased importance of the exposed fcc facets, namely those of the (100) and (111) fcc surfaces. Addition of a single facet does not significantly contribute to the NP geometry, but it is sufficient to break the symmetry and induce a change in the MAE. Such increase of the surface area successfully reproduced experimentally observed effects of the increased MAE values with respect to the bulk for small sizes and varying MAE trend with decreasing size. Calculated MAE for 0.7-2.0 nm icosahedra (30.2 and 65.6 kJ m^{-3}) correspond well to the derived values of 10-400 kJ m^{-3} for icosahedral Co NPs in the 3.1-4.3 nm size range.[383] For a specific case of 3.0 nm truncated octahedral particles, experimental anisotropy constants

are in the range of 10-200 kJ m^{-3}, also in a good agreement with the herein obtained value of 194.5 kJ m^{-3} for a 2.0 nm NP.[384]

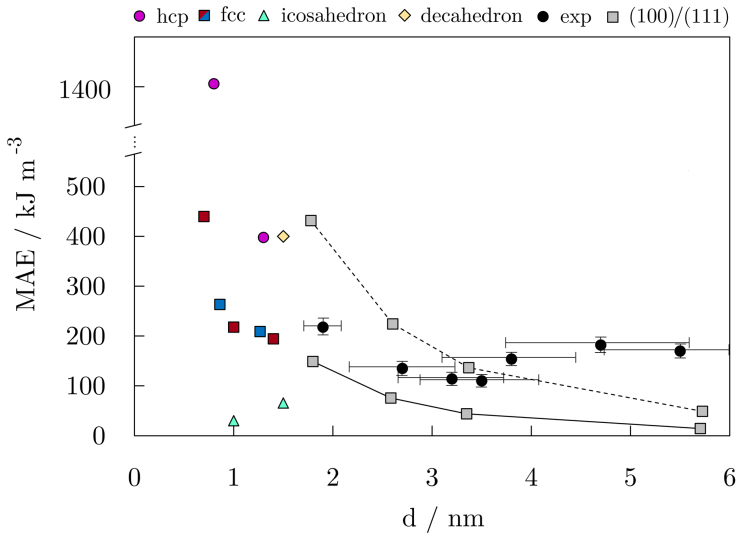

Figure 3.25: DFT predicted magnetic anisotropy energies, MAE, for Co NPs of varying diameters and morphologies in comparison with experimental and Néel pair (100) and (111) surface correlated values. Experimental and Néel pair modelling results are taken from [218].

In general, the spin moments, S_i, of Co atoms within the considered NP morphologies depend insignificantly on the direction of magnetisation. Conversely, local orbital moments, L_i, were shown to be very sensitive to the chosen magnetisation axis and, by including the SOC, geometrically equivalent sites within the NP may become magnetically and electronically inequivalent, giving different local contributions to the average orbital moment of the system. This inverse behaviour of spin and orbital moments is characteristic for magnetic nanostructures defined by a large exchange regime as found in various transition metal NPs with alternating symmetries as well as in the magnetic thin films of distinct packings.[385, 386]

Table 3.9: Average orbital moments per Co atom, L_i, as a function of magnetisation axis, NP morphology, and size.

	hcp		cuboctahedron		truncated octahedron		icosahedron		regular decahedron		Ino/Marks decahedron	
L/μeV	$\bar{L}_{[001]}$	$\bar{L}_{[100]}$	$\bar{L}_{[001]}$	$\bar{L}_{[110]}$	$\bar{L}_{[001]}$	$\bar{L}_{[110]}$	$\bar{L}_{[001]}$	$\bar{L}_{[100]}$	$\bar{L}_{[001]}$	$\bar{L}_{[100]}$	$\bar{L}_{[001]}$	$\bar{L}_{[100]}$
0.75-1.00 nm	0.083	0.085	0.091	0.088	0.084	0.084	0.090	0.087			0.083	0.085
1.50-2.00 nm	0.088	0.085			0.083	0.082	0.090	0.089	0.085	0.093	0.091	0.093

For the NP sizes considered, distribution of inequivalent sites as a function of the direction of magnetisation can be very complex. Average orbital moments per atom, L_i, are presented in Table 3.9 as a function of magnetisation axis, NP morphology, and

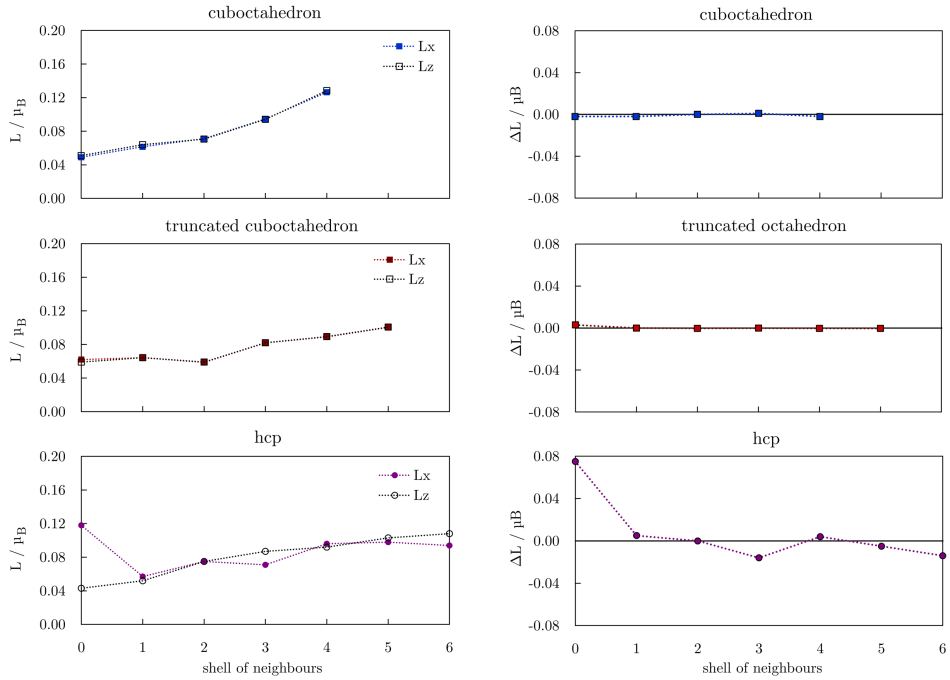

Figure 3.26: Average local-orbital moments (**left**), L_x and L_z, and difference in local moments (right), $\Delta L = L_z - L_x$, for Co NPs of crystalline morphologies as a function of the shell of neighbours. In all cases, L_x and L_z correspond to the hard and easy magnetisation axes.

size. Cumulatively, any dependence of L_i in this averaged form is hardly noticeable. The biggest deviation between the average orbital moments of two magnetisation directions of 0.008 μ_B is captured for regular decahedron, whereas the remaining morphologies have minimal differences in the 0.000-0.003 μ_B range. Differences are in the same range when comparing NPs of the same shape that differ in the size.

A more comprehensive characterisation can be obtained from the average local orbital moment contribution as a function of neighbour shells, as shown in Figure 3.26 for crystalline and Figure 3.27 for non-crystalline morphologies for the smallest diameters considered. Shells of neighbours were distributed regarding the radial distance from the central atom. In general, and in agreement with the previous studies [387, 376], values of L are in most cases enhanced with respect to those of the hcp and fcc Co bulk, which are 0.070 and 0.073 μ_B per atom, respectively. Crystalline morphologies tend to have inclining trend of increase in the L with the distancing from the NP centre, the largest enhancement being obtained at the less coordinated surface sites; for example, orbital moments of central and vertex atoms of cuboctahedron differ for more than 0.10 μ_B. However, a large part of this increase is already lost in the inner NP regions. Non-crystalline NPs show a more pronounced variance of local orbital moments from shell to shell. A linear type of an orbital moment increase with the distance from the centre observed for crystalline morphologies is replaced by an oscillating trend between the inner neighbouring shells. For morphologies whose geometry differs considerably for the investigated directions, namely

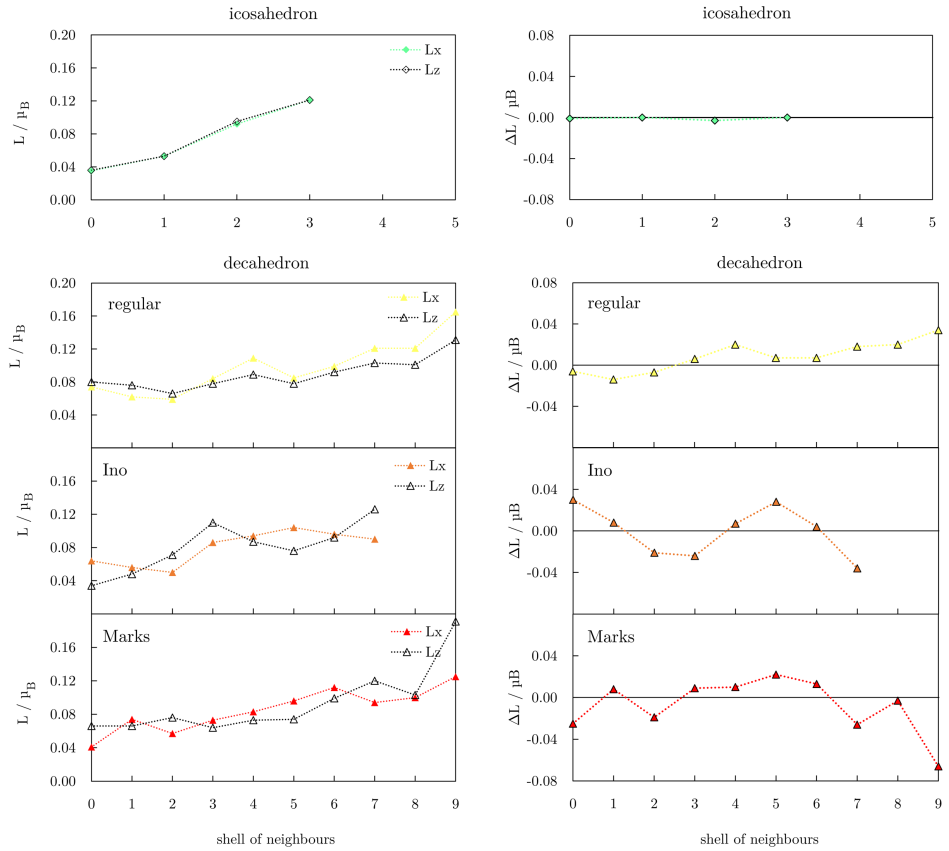

Figure 3.27: Average local-orbital moments (**left**), L_x and L_z, and difference in local moments (**right**), $\Delta L = L_z - L_x$, for Co NPs of non-crystalline morphologies as a function of the shell of neighbours. In all cases, L_x and L_z correspond to the hard and easy magnetisation axes.

Ino and Marks decahedra, the trend of average L with the increasing distance of the neighbour shells is very distinguishable between the directions of magnetisation, while for the others change in the magnetisation axes influences the value of the orbital moments with minimal effects on the overall curve. Considering the difference of the average orbital moments in each shell between the two orientations of magnetisation, $\Delta L_{xz} = L_z - L_x$, hcp geometry shows the largest deviation of crystalline shapes, while almost no distinction in L_z and L_x is observed for all shells in fcc motifs. This invariance was also observed for icosahedron. Regular and truncated decahedra, on the other hand, presented both negative and positive differences as moving from the inner atoms to those located at the NP surface.

Nevertheless, individual contributions to the average of the certain shell are arising from all possible distortions within the morphology and are hence significantly different for the two magnetisation axes. In order to analyse this local environment dependence, atom-resolved local magnetic anisotropies and orbital magnetic moments are given in Figure 3.28 for crystalline and in Figure 3.29 for non-crystalline morphologies. It is obvious that, despite the close proximity of shell-decomposed orbital moments of the two

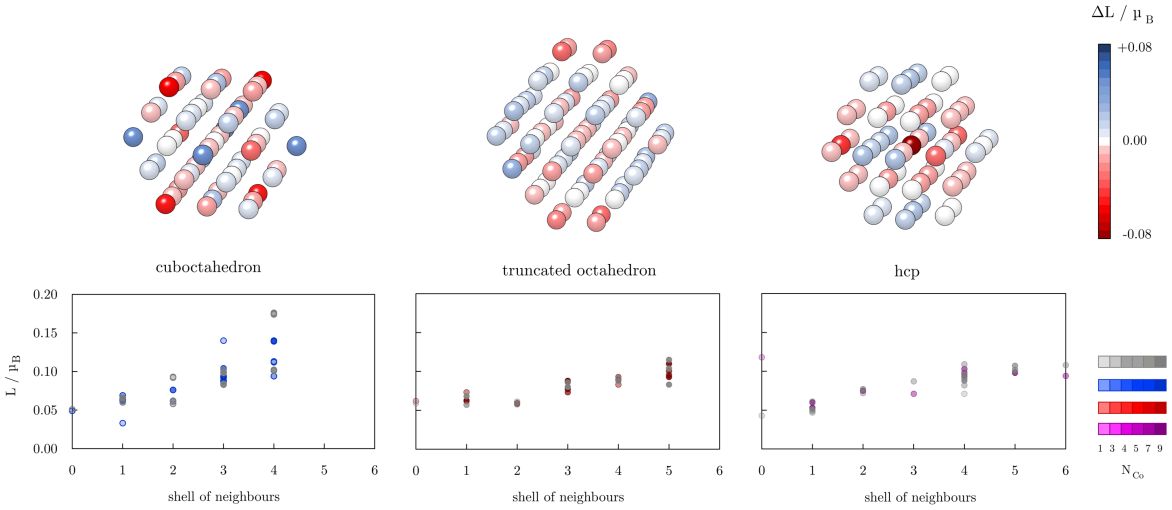

Figure 3.28: Atom-resolved local anisotropies, ΔL, (**top** panel) and orbital moments, L_{i}, as a function of the distance from the NP centre (**bottom** panel) of crystalline Co NPs. The colour coding of the spheres characterises the variation in ΔL and legend is given on the top right. L_{x} moments are given by coloured circles, L_{z} moments by grey circles. Depending on the symmetry, a considerable number of atoms may possess an identical distance to the NP centre. The number of over-lapping symbols is thus represented by the saturation of the colours as indicated by the scale bars on the bottom right.

magnetisation directions within the crystalline morphologies, orbital magnetic moments of individual atoms deviate more significantly with the change of the axis of magnetisation. Certain atoms placed in the inner regions of the NP are seen to have up to three times enhanced orbital moments compared to the bulk. For fcc morphologies, atoms of the outer shell, especially vertex atoms, have the most pronounced local MAE, ΔL, which are in general higher for cuboctahedron than for truncated octahedron. Hcp Co NPs, on the other hand, showed increased ΔL values for the inner atoms, with the highest ΔL on the central atom. Both positive and negative local MAE are captured for varying sites or crystalline NPs.

Observed atom-resolved orbital moments in general span a larger range of values for non-crystalline morphologies with less symmetry (decahedra) compared to their crystalline counterparts. Moderate ΔL values are observed for the outer atoms of icosahedron, while zero anisotropy characterises the core atoms. Similarly, the outer shells of regular, Ino, and Marks decahedra showed higher ΔL compared to the inner counterparts. Within the regular decahedron, there is additionally a pattern of positive ΔL in local magnetic moments in the core sites and negative ΔL for the outer atoms. After Marks truncation, seven marginal vertex Co atoms experience a substantial change in the orbital moment maintain negative ΔL. Local MAE of both inner and outer atoms of Ino decahedron range from highly negative to highly positive values. Central atom, in contrast to regular and Marks decahedra, contributes with a negative local magnetic anisotropy.

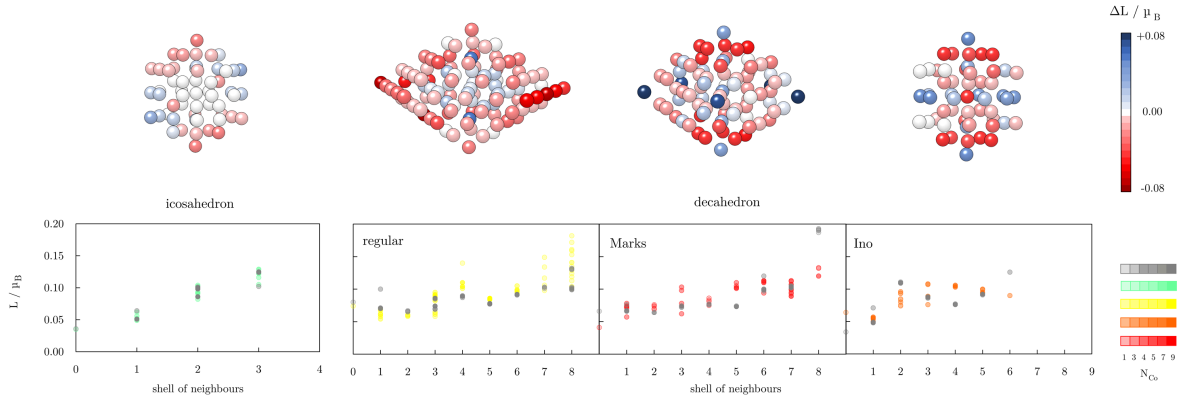

Figure 3.29: Atom-resolved local anisotropies, ΔL, (**top** panel) and orbital moments, L_i, as a function of the distance from the NP centre (**bottom** panel) of non-crystalline Co NPs. For the colour codes, see Figure 3.28.

These alternations within the atomically localised orbital moments of varying morphologies are indicators of a complex behaviour of the local magnetic anisotropies due to the second-order perturbation theory relation of the anisotropy in orbital moments and anisotropy in electronic energy, L_z-$L_x \propto E_z$-E_x [388], but they also give an anticipation on expected differences in total MAE. The results clearly indicate the fundamental role the precise geometrical details play in determination of the magnetic behaviour of Co NPs.

3.4 Conclusion

The dependence of stability and properties of NPs on their shape and size paves the way to the understanding of the intrinsic features these tiny yet powerful structures are bearing. Various motifs of Co NPs, including crystalline and non-crystalline, atom-, triangle-, and interstitial-centred configurations have been modelled to reveal the transition sizes between different geometric forms and structural and energetic contributions to their (in)stability.

DFT calculations have shown to be sufficiently accurate in predicting the stability of small Co clusters and they were employed to define size and strain effects that govern the formation of different shapes as the NP size increases. Icosahedron was determined as the most stable motif for NPs up to ~5500 atoms by virtue of the low surface energy and negative twin boundary energies. The high CN also has a significant contribution, with volumetric and elastic strain effects becoming dominant only at large sizes. Minimisation of the internal strain energy becomes important only when the surface energies of icosahedron and hcp NPs reach comparable values, which is true only for very large NPs. Considering decahedral motif, the energetic cost of having larger surfaces is too great unless exceptional electronic configurations exist, which is not the case for Co NPs.

Finally, while deviation of the magnetic moments with the NP morphology was found

to be insignificant for large size ranges, hcp and decahedral Co NPs showed substantially higher anisotropy values compared to the fcc-crystalline and icosahedral NPs. High MAE values give hcp Co NPs an intrinsic advantage for use in biomedical applications, providing wider tuning possibilities and less impactful functionalisation-induced quenching.

Highlights of the chapter

- **Identified the crossover point between icosahedron and hcp motif.**
- **Traced the crossover size to the size and strain effects.**
- **Quantified dependence of atom-resolved orbital moment anisotropy on NP morphology.**
- **Predicted magnetic anisotropy dependence on NP size and shape.**

CHAPTER 4

OXIDATION OF COBALT NPs

"The time has come," the walrus said, "to talk of many things:
Of shoes and ships - and sealing wax - of cabbages and kings."
-Chapter 4, The Rabbit Sends in a Little Bill

4.1 Introduction

4.1.1 Reactivity of cobalt NPs

A lot of effort in nanosynthetic chemistry has been devoted to obtaining better control of the size, shape, and composition of NPs which can make use of the tuning of unique nanoscale properties. However, chemical transformations through the reaction processes and diffusion mechanisms often lead to changes in the NP compositions and morphologies.

Most transition metals are known to rapidly oxidise in air from their bulk phases, and this process makes it easy to naturally synthesize corresponding oxide compounds. Extensive studies of such conversions were triggered by severe property alternations as metal transforms from a conductor to a ceramic material. Nevertheless, oxidation is not as well investigated for the metallic nanomaterials which, unlike bulk metals, generally show size- and shape-dependent kinetics and thermodynamics of topochemical processes. This alternation in the reactivity is governed by the high surface area and contribution of the surface energy, which is lower for bulk metal oxides than for the corresponding bulk metals. In addition, because of the standard atomic diffusion values, chemical reactions in the solid state are believed to be slow and difficult to control, while enhanced atomic diffusion at the nanoscale caused by the large surface areas and crystal defects can be used to design or at least restrain the fate of the NPs. Hence, nanocrystals are in general less resistant to oxidation than bulk crystalline materials.[389, 390, 391]

Bulk phase transitions and multiple oxide forms make the kinetics of cobalt oxidation rather complex. The mechanism of cobalt oxide formation at high temperatures above the hcp→fcc transition at 700 K, where the theory of thermally activated ionic diffusion satisfactorily describes the kinetics of oxidation, is well understood and supported by experimental studies. More complex low-temperature Co oxidation, which usually occurs in multiple stages, is less investigated, but studies have shown the formation of cobalt

oxide films at room temperature, followed by a further oxidation to higher order oxides at increased oxygen pressures.[392, 393] Oxidation of bulk metallic cobalt by water, such as in the process of Fischer-Tropsch synthesis, was found not to be thermodynamically feasible at low or typical FT operation temperatures of 493-523 K - for it to occur, the water partial pressure relative to that of hydrogen must be in excess of 128, which cannot be reached in industrial production.[394]

Data available on the oxidation reactivity of Co NPs mainly consists of the oxidation and reduction of small Co crystallites under standard FT conditions, where water generated as a by-product leads to the deactivation of active Co catalytic sites. In the study of the oxidation of small Co NPs as a function of the particle diameter, it was shown that sizes below 4.4 nm experience significant oxidation by water to Co(II) even under standard FT conditions, contrary to the bulk system. Interestingly, pre-adsorbed molecules of hydrogen or carbon monoxide had no influence on the rate of oxidation.[230, 395] Study of the oxidation kinetics of colloidal Co nanocrystals in organic solvent by dissolved O_2 at room temperature has shown that the overall degree of oxidation is largely determined by the concentration of oxygen during the initial exposure to the oxidising environment. Subsequent varying of the O_2 concentration has only had a weak effect on the overall rate of oxidation. This is expected to impose a great challenge in the preparation of colloidal Co nanocrystals, making the high-level control of the environment a key requirement. On the other hand, initially formed oxide might be sufficiently passivating upon prolonged exposure, and controlled peroxidation can be performed to limit the long-term oxidation.[396] Therefore, oxidation of small Co crystallites or formation of an oxide shell could be thermodynamically feasible under conditions that do not allow the oxidation of bulk metallic Co, which might prove significant for many applications.

4.1.2 Cobalt oxides

Five oxides of cobalt have been reported [CoO_2, Co_2O_3, CoO(OH), Co_3O_4, and CoO]. The sequential desorption of oxygen from CoO_x produces oxides with different oxidation states by appropriate thermal decomposition:

$$CoO_x \xrightarrow{260°C} CoO(OH) \xrightarrow{310°C} Co_3O_4 \xrightarrow{870°C} CoO \tag{4.1}$$

Generally, the lowest energy magnetic structures contain Co^{2+} and Co^{4+} ions with average magnetic moments of 2.75±0.05 μ_B and 1.23 μ_B, respectively. Co^{3+} ions are always found to be in the non-magnetic state. However, cobalt oxides with a valence of more than three are unstable in the natural environment.

CoO, cobalt(II) oxide or cobalt monoxide is the lowest oxidation state Co oxide found in the nature. It can be in form of olive-green or red crystals, or as a greyish/black powder. CoO crystals adopt the periclase (rock salt) structure with a lattice constant of 4.260 Å, and they can be characterised as a wide band gap semiconductor with the indirect energy gap of ∼2.6-3.0 eV.[397, 398] CoO is known to have antiferromagnetic ordering of type II (AF-II), where the Co atoms located on the (111) plane present a ferromagnetic

ordering, while the metal atoms on two adjacent (111) planes have an antiferromagnetic arrangement.[399, 400] However, CoO loses magnetisation at Nèel temperature of 291 K. CoO NPs, on the other hand, exhibit superparamagnetism or low-temperature ferromagnetism, depending on the size and shape.[401] These shape-selective properties of CoO NPs could be used for applications like sensors, catalysis, information storage, and electrode materials.[402]

Co_3O_4, cobalt (II,III) oxide, is a mixed valence compound denoted as $Co(II)Co(III)_2O_4$ or $CoO{\cdot}Co_2O_3$ and it is a solid in black colouration. Co_3O_4 adopts the normal spinel structure with tetrahedrally coordinated Co^{2+} ions and octahedrally coordinated Co^{3+} ions enclosed in a cubic close-packed lattice with a constant of 8.080 Å.[403, 404] The ratio of Co^{2+} and Co^{3+} ions is $1:2$, and Co^{2+} ions form an antiferromagnetic structure below the Nèel temperature of 40 K, above which Co_3O_4 is not magnetic. This antiparallel magnetic ordering within the tetrahedral sub-lattice is due to the lack of magnetic carriers in the octahedral positions similar to the antiferromagnetism ordering found within the octahedral positions of the normal $LiMn_2O_4$ spinel[405, 406], and contrary to the ferrimagnetic Fe_3O_4, which has magnetic carriers in both sub-lattices.[407] Upon heating, it converts to CoO. When reduced to the nanometre scale, Co_3O_4 NPs were found to have interesting magnetic, optical, and electrochemical properties which make it an attractive contributor in device applications.[408] Efforts have thus been directed to the synthesis and investigation of properties of Co_3O_4 nanostructures, which have so far shown many size- and shape-dependent properties with potential applications in electrocatalysis, batteries, supercapacitors, energy storage, and gas sensors.[409, 410, 411, 412]

Besides the two cobalt oxides that form under readily attainable oxygen partial pressures, the metastable form Co_2O_3 has also been reported in the literature as an hcp structure with lattice parameters $a = 4.640$ Å and $c = 5.750$ Å. However, whether the Co_2O_3 oxide really exists as a stable solid crystal is still uncertain since the study of the interaction of oxygen and air with clean Co surfaces through x-ray photoelectron spectroscopy could not prove its existence.[413]

4.1.3 Motivation

Oxidation of metallic magnetic nanocrystals is an important issue in many applications since it results not only in changes of electronic and lattice structures, but also alternates magnetic properties. For example, partial oxidation of Co nanocrystals to CoO can result in exchange bias at the interface between ferromagnetic Co and antiferromagnetic CoO at low temperatures, modifying magnetisation and magnetic anisotropy of nanocrystals.

When employed in biomedical applications, NPs inevitably come in contact with oxidising species such as water or oxygen, which is why less reactive metal oxide NPs were prioritised over metallic NPs. However, limited magnetic response arising from the lower magnetic moments of metal oxides showed to be insufficient, triggering a new objective for the overall research: to which extent would spontaneous oxidation influence metallic NPs,

and is that the biggest challenge of the field? Pure metals introduced a lot of contradictions in biomedical applications in terms of safety issues. When it comes to prioritising between the potential consequences and up to a few orders of magnitude increased efficiency, a balance should be found considering the risks taken, the perks gained, and possibility of modifications that could rule the former or the latter out.

Most metals are highly reactive towards oxygen; sometimes such response to the oxidising environment is desirable, as in the case of catalysis or fuel cells, and sometimes it would much rather be avoided, as is the case with corrosion. Since adsorption of oxygen is decisive in many material processes, it has been extensively studied both experimentally [414, 415, 416] and theoretically.[417, 418, 419, 420] Oxidation has been associated with oxygen atoms adsorbed on the surface, the formation of surface oxide films, and even with the formation of bulk metal oxides of transition metals, nominally ranging from Sc [421, 422] to Zn [423, 424], and rare earth metals such as La [425, 426] and U [427, 428]. Even on the noblest of metals (Pd, Ag, Pt, Au) oxidised surfaces or islands have been implicated in the observed oxidation activity.[429, 430, 431, 432, 433, 434] Accordingly, oxidation of Co has been of interest due to its importance in electrocatalysis, control of hydrocarbon emissions, and as an elementary step in FT synthesis where the active form of Co-catalyst was found to be metallic cobalt. The amount of experimental work where Co single crystals were used is considerably lower than for, e.g., noble metals. This is due to the difficulty of working with Co crystals: the hcp→fcc phase transition in combination with high chemical sensitivity makes preparation of a clean, well-ordered surface difficult. In experimental studies which described the interaction of oxygen with Co single crystal surfaces, structural analysis revealed the mixture of the two phases which, for low oxygen coverage, chemisorbed a layer of atomic oxygen, whereas a higher coverage led to the formation of a Co_xO_y-type oxide, starting with CoO and ultimately producing Co_3O_4. The rate of oxide formation was found to be strongly dependent on the surface temperature. The theory of adsorption has reached a level where it is possible to calculate free energies, as well as the electronic and atomic structure, of medium-sized systems with predictive accuracy. The number of theoretical studies that address similar processes to give atomic-level insights in oxidation of Co have, however, mainly been devoted to explore its oxidation behaviour in a much simpler cubic phase.[435, 436, 437] Apart from the Co (0001) surface [438, 439], no theoretical work on the interaction of oxidising species with hexagonal phase of Co has been presented.

If oxidation of the hcp Co NPs was to occur in the presence of oxygen *in vivo*, the formation of oxides could cause the loss of the highly desirable magnetic properties and NPs could therefore not be used in biomedical treatments without additional modifications. In that case, any possible toxicity would be inhibited, and the aim would be in preventing oxidation and maintaining high levels of magnetisation (suppressing at the same time possible harmful effects) rather than considering the toxicity problem first. Hence, an oxygen adsorption on hcp Co low Miller-index surfaces has been systematically analysed through DFT calculations. The main question of interest is if the oxidation is spontaneous and should it be prioritised over the possible toxicity of Co NPs.

4.2 Computational details

Comparison between GGA and GGA+U approaches in the modelling of small Co clusters showed only minor structural and energetic deviations between the two methods. However, when it comes to the more complex systems with metal/non-metal interactions, a series of studies indicated serious deficiencies of LDA/GGA in predicting certain properties, such as large deviations of binding energies compared to experiment [440], smaller band gaps for semiconductor systems [441, 442], incorrect localisation of the f-states in cerium oxides [443, 444], and wrong predictions of the most favourable adsorption sites for CO on Pt (111) surface [445], to name a few. These problems can be attributed to the incomplete cancellation of the Coulomb self-interaction and the tendency of most exchange correlation functionals to over-delocalise valence electrons, limitations that can be improved through the addition of the Hubbard U term. As predictive power for simulating bond-formation between oxidising species and metal surfaces is highly dependent on the proper description of valence d electrons, GGA and GGA+U approaches were compared for the case of Co oxidation. Additionally, GGA+U has already been found to improve the accuracy in predicting the energetics of redox processes from first principles.[446, 447]

Exchange-correlation functional

The GGA/PBE functional was used, and the long-range dispersion interactions were added through the DFT-D3 method with Becke-Johnson damping.[448] The core electrons up to and including the $3p$ levels for Co and $2s$ levels for O were kept frozen and their interaction with the valence electrons was described by the PAW method. The conjugate gradient technique, with energy and force convergence criteria of 10^{-6} eV and 0.01 eV/Å, was used to perform geometry optimisations. For comparison, GGA+U calculations were carried out through Dudarev approach where targeted U_{eff} was altered from 0.0 to 6.0 eV to determine the appropriate value for the best compromise between redox behaviour and electronic structures of all materials involved.

It has to be noted, however, that there exists a rather large error in the GGA binding energy of most covalent molecules, including O_2, known in the literature as the overbinding [417, 449], whereas bond length and vibrational frequency are sufficiently accurate. The O_2 overbinding error represents essentially a constant shift in the GGA predicted oxidation energies and it can be corrected by fitting the calculated formation energy to the empirically measured formation energy from the thermochemistry tables to minimise the error. Herein, the O_2 formation energy was first calculated using the GGA/PBE functional. To improve the accuracy, the zero-point energy (ZPE) was also considered. Finally, the ground-state energy could then be corrected for the overbinding values calculated by subtracting the empirically measured energy from the GGA calculated energy: $E_{\text{OB}} = \Delta H_{\text{f}} + E_{\text{ZPE}} - \Delta H_{\text{f}}^{\text{exp}}$, where E_{OB} is the overbinding energy, ΔH_{f} is the calculated formation enthalpy, E_{ZPE} is the calculated zero-point energy, and $\Delta H_{\text{f}}^{\text{exp}}$ is the experimental formation enthalpy. DFT values obtained are -5.92 eV and 0.11 eV for ΔH_{f} and E_{ZPE}, respectively. Combined with $\Delta H_{\text{f}}^{\text{exp}}$ of -5.16 eV[324], the overbinding energy of -0.86 eV was detected, giving a correction of -0.43 eV per O atom. By doing so, the

binding energy per oxygen atom obtained is -2.58 eV (-3.01 eV without correction, corresponding well to other DFT works: 3.12 eV [173], 3.04 eV [419]), with the bond length of 2.33 bohr and vibrational frequency of 1567 cm^{-1}. Agreement with experimental results (-2.56 eV, 2.28 bohrs, 1580 cm^{-1}) is satisfactory after the correction. This approach was adapted throughout this thesis, and subsequent removal of the O_2 binding error makes it possible to address the correlation effects in $3d$ transition metal oxides by implementing the GGA+U method.

The performance of alternating U values was tested through a systematic study of oxidation reactions of hcp Co to CoO and Co_3O_4, and CoO to Co_3O_4 to capture three main oxidation transitions:

$$2Co + O_2 \rightarrow 2CoO \tag{4.2}$$

$$\frac{3}{2}Co + O_2 \rightarrow \frac{1}{2}Co_3O_4 \tag{4.3}$$

$$6CoO + O_2 \rightarrow 2Co_3O_4. \tag{4.4}$$

To compare modelled behaviour with experimental oxidation, reaction energies have been calculated on a per O_2 molecule basis (utilising the corrected energy for the O_2 molecule) as such experimental data is widely available and similar procedures have shown to be satisfactory for a series of transition metals, oxides, and mixed oxides:

$$\Delta H_0 = \frac{E_{MO_x} - E_M - \frac{x}{2}E_{O_2}}{\frac{x}{2}} \tag{4.5}$$

for oxidation of metals or:

$$\Delta H_0 = \frac{E_{MO_y} - E_{MO_x} - \frac{y\text{-}x}{2}E_{O_2}}{\frac{y\text{-}x}{2}} \tag{4.6}$$

for further oxidation of metal oxides. Accurate formation enthalpies of hcp Co (E_M), CoO, and Co_3O_4 ($E_{MO_{x/y}}$), have been calculated from respective bulk unit cells after the full relaxation was performed (all atoms, cell shape, and cell volume). Experimental formation enthalpies at T = 298.15 K were taken from the JANAF thermochemical tables.[450]

Hcp Co formation energy was calculated by using 1×1×1 unit cell with two atoms in their respective ferromagnetic ordering. Employed cut-off was 500 eV with the 11×11×9 k-point mesh. To correctly describe the antiferromagnetic nature of CoO, it was modelled as a 2×2×2 supercell with the atoms in the adjacent (111) planes positioned such that the lowest magnetic ordering is achieved. The cut-off energy and k-point mesh used were 500 eV and 9×9×9. Co_3O_4 was modelled within its normal spinel structure as a 1×1×1 unit cell with antiferromagnetic ordering, 500 eV cut-off, and 8×8×8 grid. Formation enthalpies of described oxidation reactions as calculated within GGA+U approach, together with electronic properties of all three materials, were compared with experimental values and results are summarised in Figure 4.1. The best possible description of three reactions of

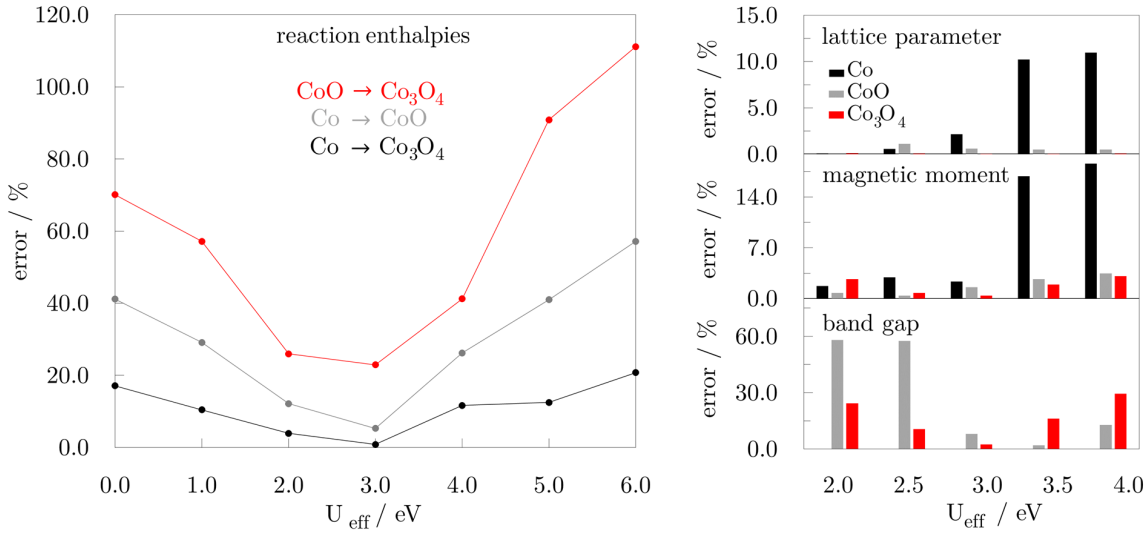

Figure 4.1: **left**: Errors in calculated reaction enthalpies for oxidation of hcp Co and CoO as a function of Hubbard U_{eff} and **right**: errors in structural and electronic properties of hcp Co, CoO, and Co_3O_4. Experimental values are taken from [451, 452, 453] (lattice parameters), [324, 454, 403] (magnetic moments - spin component only), [455, 456] (band gaps).

interest falls within a U_{eff} = 2.0 - 4.0 eV range. To assure the validity of obtained values within the electronic and structural properties, lattice parameter, magnetic moment, and band gap values of the three materials have been tested for U_{eff} = 2.0, 2.5, 3.0, 3.5, and 4.0 eV. Lattice parameters and magnetic moments are well maintained (percent error lower than 2.5 and 5.0 %, respectively) for U_{eff} below 3.5 eV. However, only U_{eff} = 3.0 eV comes close to capturing correct band gaps of Co oxides. The herein fitted U_{eff} coincides with those previously reported and used in the literature: the group of Ceder *et al* has investigated a large number of oxidation reactions of 3*d* metals and obtained the optimal U value of 3.3 eV for cobalt oxides after taking into the consideration a relatively large enthalpy difference of 28 kJ per mole of O_2 between room temperature and 0 K DFT modelling temperature.[446, 447] García-Mota studied the construction of Pourbaix diagrams for oxygen evolution reaction on Co_3O_4 and CoOOH surfaces with the inclusion of Hubbard U and found that U_{eff} = 3.52 eV reproduces experimentally observed trends in the activity of these oxides.[457, 458] Finally, different studies on interplay between geometry distortion (e.g., doping), redox activities, and magnetic ordering of cobalt oxides consistently show effective U values in the 3.0-4.0 eV range to reliably capture complex electronic and magnetic structures.[459, 460, 461] Therefore, U_{eff} = 3.0 eV was employed for comparison of GGA and GGA+U approaches in the oxidation behaviour of hcp Co.

Energetic parameters

Description of Co oxidation energetics was initialised by the characterisation of bare low Miller-index hcp Co surfaces through the calculation of their surface energies and work functions. Surface energies were calculated as described in the previous chapter.

Work function, as an energy required to completely withdraw an electron from the solid, was obtained as the difference between the vacuum electrostatic potential energy, E_{vac}, and the energy of the Fermi level, E_{F}.

Oxidation was probed as on- and sub-surface oxygen adsorption. Initial position of the oxygen atom was 2.2 Å above surface, in correspondence with cobalt-oxygen distances [413] in cobalt oxides, for all on-surface sites, with adsorption allowed only on the relaxed side of the slab. For each site on-surface, oxygen atom and the top two layers of the slab were relaxed, whereas for the sub-surface adsorption, slab models of six layers were used with the relaxation of top four layers. To study the relative stabilities of different adsorption sites, the most favourable adsorption position has been determined for each surface by calculating the adsorption energy, E_{ads}:

$$E_{\mathrm{ads}} = E_{\mathrm{slab+O}} - (E_{\mathrm{slab}} + E_{\mathrm{O}}) \tag{4.7}$$

where $E_{\mathrm{slab+O}}$, E_{slab}, and E_{O} are the DFT energies of the system with adsorbed oxygen, the clean surface, and the oxygen atom, respectively. As oxygen adsorbs or desorbs on the surface from or to gas-phase O_2, it is essential to reference all DFT energies to the ground-state energy of the O_2 molecule in the gas phase. To account for this, E_{O} derived to correct for the well-known GGA O_2 overbinding discussed previously has been employed in all adsorption and thermodynamic processes which included oxygen adsorbates.[462] Negative adsorption energy represents spontaneous oxidation, with the most negative E_{ads} indicating the most favourable adsorption site. Work functions of the oxidised surfaces were calculated as for the clean surfaces.

Subsequently, the coverage of adsorbed oxygen has been gradually increased. The coverage, θ, is expressed (in monolayers, ML) as a number of O atoms adsorbed over a number of surface Co atoms, $\theta = n_{\mathrm{O\ adsorbed}}/n_{\mathrm{Co\ per\ layer}}$, with a full monolayer (1.00 ML) reached for $n_{\mathrm{O\ adsorbed}} = n_{\mathrm{Co\ per\ layer}}$. Adsorption energies were computed as adsorption energies per oxygen atom:

$$E_{\mathrm{ads}} = \frac{1}{n}[E_{\mathrm{slab}+n\mathrm{O}} - (E_{\mathrm{slab}} + nE_{\mathrm{O}})] \tag{4.8}$$

where $E_{\mathrm{surface}+n\mathrm{O}}$, E_{surface}, and E_{O} are the DFT energies of the system with n adsorbed oxygen atoms, clean surface, and corrected energy of the oxygen atom, respectively. Surface energies after the adsorption have been calculated as:

$$\gamma_{\mathrm{slab}+n\mathrm{O}} = \frac{E_{\mathrm{relaxed\ slab}+n\mathrm{O}} - [m \times E_{\mathrm{bulk}} + n \times E_{\mathrm{O}}]}{A_{\mathrm{slab}}} - \frac{E_{\mathrm{unrelaxed\ slab}} - m \times E_{\mathrm{bulk}}}{2A_{\mathrm{slab}}} \tag{4.9}$$

where $\gamma_{\mathrm{slab}+n\mathrm{O}}$ is the surface energy with n adsorbed oxygen atoms, and m is the ratio of number of Co atoms in the surface slab and bulk, $m = n_{\mathrm{Co\ slab}}/n_{\mathrm{Co\ bulk}}$. Wulff morphologies of single Co crystal after the adsorption of oxygen were constructed with obtained surface energies.

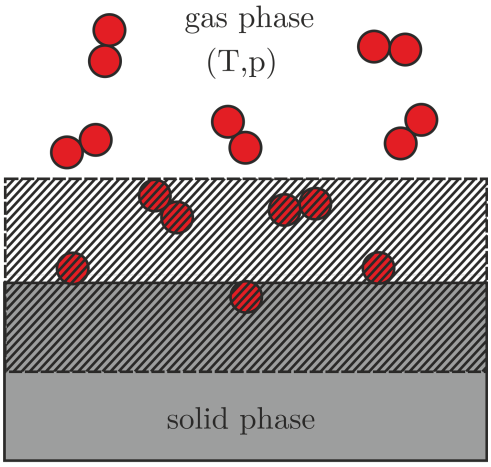

Figure 4.2: Schematic representation of the system containing a single-crystal metal surface in contact with a surrounding gas phase of an adsorbate characterised by defined temperature T and pressure p. The shaded area represents the finite part of the system that is affected by the presence of the surface.

However, the extent of oxidation as well as the structure of formed Co-O entities (or cobalt oxides) also depend on the environmental conditions, amongst which the temperature and partial pressure of O_2 are the most important. A large family of problems involves the relative stability of possible surface structures at different environmental conditions, and their solution can be reached by using the *ab initio* thermodynamics. In this method, the stability of a surface structure (prior or after the oxidation) is evaluated by its surface free energy, σ, which can be considered as the Gibbs free energy needed to create the specific surface structure per surface area. The bulk structure is usually taken as a reference point for the adsorbing material, and the most environmentally abundant gas phase component for the adsorbate, Figure 4.2. Therefore, chemical potential of Co is taken to be the same as in the bulk, and chemical potential of atomic oxygen is taken as half of the Gibbs free energy of gaseous O_2:

$$\sigma = \frac{1}{A_{\text{slab}}}(G_{\text{slab+O}} - N_{\text{Co}}\mu_{\text{Co}} - N_{\text{O}}\mu_{\text{O}}) \tag{4.10}$$

where $G_{\text{slab+O}}$ is the free energy of the system containing surface slab and adsorbed oxygen, N_{Co} and N_{O} are numbers of Co and O atoms that are constructing the system, and μ_{Co} and μ_{O} are chemical potentials of Co and O, respectively. In this sense, the more negative the σ, the more stable the surface structure created from the Co bulk and available O_2(g) in the surroundings. Dependence of surface free energies on external conditions is directly related to the effect of external conditions on chemical potentials of constituting elements. As the surface slab is a solid, μ_{Co} can be considered constant regardless the temperature/pressure changes, leaving μ_{O} as the main variable. Additionally, different surfaces are expected to show distinct trends due to the varying oxidation reactivity. Ul-

timately, a graph showing the stability of surface structures in the presence of gaseous oxygen under alternating conditions can be constructed for each surface, known as a surface phase diagram. Similar to the phase diagram, the surface phase diagram contains information about transition borders between bare surfaces and their oxidised counterparts, terminating with the oxide formation. This principle was successfully applied to various systems, including RuO_2, FeO, TiO_2, CeO_2, Co_3O_4.[463, 464, 465, 466, 467]

Thermodynamics of different oxygen coverages in equilibrium with an oxygen reservoir was introduced by comparison of surface free energies at constant temperature, T, with pressure changes expressed within oxygen chemical potential, $\mu_O(T,p)$: $\sigma(\mu_O) = \gamma_r + \Delta\sigma(\mu_O)$. General expression for the change in the surface free energy upon adsorption, $\Delta\sigma(\mu_O)$, in equilibrium with O in the gas phase at given conditions of temperature, T, and pressure, p, can be written as:

$$\Delta\sigma(\mu_O) = \frac{1}{A_{slab}}(G_{slab+O}(T,p) - G_{slab}(T,p) - \Delta N_O \mu_O(T,p) - \Delta N_{Co}\mu_{Co}) \tag{4.11}$$

where G_{slab+O} and G_{slab} are Gibbs free energies of the clean and oxidised surfaces, respectively, A is the surface area, and $\Delta N_{Co/O}$ are variations in numbers of Co/O atoms in the system with respect to the reference state which is taken to be an initial slab structure. Since slab models were not changed throughout the adsorption process, last term equals zero. Term for Gibbs free energy for clean and oxidised surfaces is given as:

$$G(T,p) = F(T,V) + pV \tag{4.12}$$

$$F(T,V) = E_{total}(V, N_O, N_{Co}) + F_{vib}(T,V) \tag{4.13}$$

$$F_{vib}(T,V) = E_{vib}(T,V) - TS_{vib}(T,V) = \frac{1}{2}\sum_i h\nu_i + k_B T \sum_i \ln(1 - e^{-\frac{h\nu_i}{k_B T}}) \tag{4.14}$$

where F is the Helmholtz energy, E_{vib} and S_{vib} are vibrational contributions to energy and entropy, ν_i are the normal mode frequencies, and V is the cell volume. Whereas for computing bare surface energies no additional contributions to the total energy have been taken into the account, oxygen vibrational modes are not negligible and vibrational energies should be accounted for in oxidised surface Gibbs free energy. pV term was not included due to the pressures considered being lower than 100 atm. However, Reuter *et al* [468] proposed an approach which completely neglects vibrational contributions, leaving total energy as a predominant term. In this case, overall expression can be rewritten as:

$$\Delta\sigma(\mu_O) \approx \frac{1}{A_{slab}}(E_{slab+O} - E_{slab} - \Delta N_O \mu_O(T,p)) \tag{4.15}$$

and it now represents a direct connection between the surface structure and external conditions. Another possibility is to account for oxygen vibrations and assume that surface vibrational contribution is the same with and without adsorbate:

$$\Delta\sigma(\mu_O) \approx \frac{1}{A_{slab}}[(E_{slab+O} + F_{vib,O}) - E_{slab} - \Delta N_O \mu_O(T,p)] \quad (4.16)$$

where $F_{vib,O}$ is the vibrational energy of adsorbed oxygen. T and p dependence is included through the μ_O:

$$\mu_O(T,p) = \frac{1}{2}\left[E_{O_2} + \Delta g_{O_2}(T,p_0) + k_B T \ln\left(\frac{p_{O_2}}{p_0}\right)\right] \quad (4.17)$$

where p_0 is the atmospheric pressure of 1 bar, and $\Delta g_{O_2}(T,p_0)$ is the change in the Gibbs free energy of oxygen between 0 K and T including vibrational, rotational, and entropy contributions to free energy at p_0 pressure. Changes in the Gibbs free energy have been extracted from thermodynamic tables.[450] Last term represents the change in the energy of oxygen between p_0 and p_{O_2} at temperature T. Using these expressions, Gibbs free energies of systems going from no oxygen to a full monolayer coverage are reported as a function of μ_O with and without inclusion of vibrational contributions in form of surface phase diagrams.

4.3 Results

4.3.1 Bulk

When it comes to NPs, surface area is dominating the overall volume. Therefore, characterisation of surfaces is the main route for testing the theoretical model. The first step of any surface calculation is self-consistent determination of the bulk lattice constant in order to perform an accurate calculation of layer relaxations. Otherwise, inaccurate lattice constant could lead to artificial horizontal forces pushing the slab layers apart or pulling them together. Bulk calculations were conducted on the same principle as in the previous chapter and hcp cell was fully relaxed by employing GGA and GGA+U, where the value of the Hubbard parameter was set to 3.0 eV corresponding to the results of a systematic study on bulk oxidation reactions.

Table 4.1: GGA and GGA+U (U_{eff} = 3.0 eV) calculated cell parameters, magnetic moment, and bulk modulus for the hcp Co bulk phase and comparison with previous studies.

		this work			theory		
		GGA	GGA+U	experiment [324]	GGA [469]	GGA+U [470]	HSE06 [469]
cell parameter	a,b /Å	2.464	2.444	2.51	2.496	-	2.508
	c /Å	3.983	4.051	4.07	4.030	-	4.070
	c/a	1.617	1.657	1.62	1.615	1.60	1.782
magnetic moment	/μ_B	1.581	1.760	1.72	1.59	1.725	2.09
bulk modulus	/GPa	226.8	182.5	191	207	166.3	107

Lattice parameters obtained through GGA (GGA+U) relaxation are a = 2.463 (2.444) and c = 3.984 (4.051) Å, resulting in a c/a ratio of 1.616 (1.657). c/a ratios deviate less than 3 % from experiment (1.62[324]), and while both methods similarly underestimate

an a vector, GGA+U gives a length of c vector closer to the experimental value, Table 4.1. Using a 21×21×9 k-point mesh and increasing the accuracy of the smearing method results in a lattice constant of c/a = 1.617 (1.660). The numerical errors in the lattice constant are thus very small, and, most importantly, negligible in comparison to the expected absolute layer relaxations, meaning the more expensive set up can be avoided.

Accuracy of the electronic structure has been verified through DOS, Figure 4.3. Key features were described in the previous chapter. Localisation of d-orbitals by implementation of Hubbard U (U_{eff} = 3.0 eV) was achieved, and majority spin electrons were pushed towards more negative energies by approximately 2.5 eV. A magnetic moment of 1.581 μ_{B} GGA (1.660 μ_{B} GGA+U) has been calculated and it corresponds well to the experimental value of 1.72 μ_{B}.[324] Mechanical stability has been determined through the bulk modulus as a measure of compression resistance of the substance. Murnaghan's equation of state[471] was used to fit the data comprising of volume and energy changes induced by volume compression and a value of 226.8 GPa GGA (182.5 GPa GGA+U) was obtained in agreement with existing data, Table 4.1.

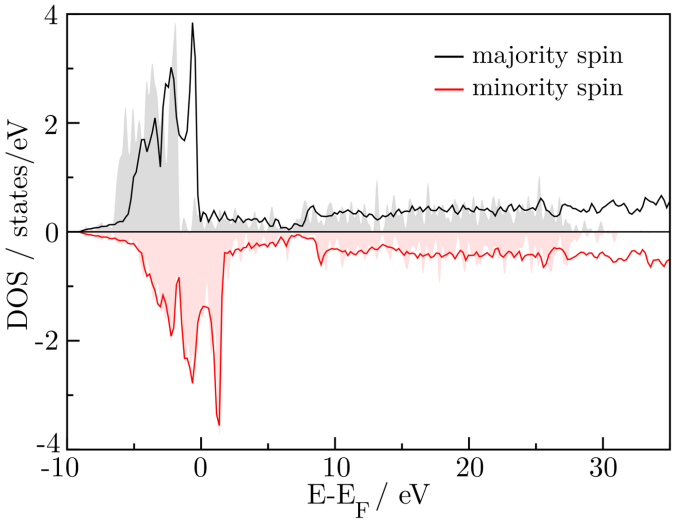

Figure 4.3: Densities of state of bulk hcp Co as calculated by GGA (full lines) and GGA+U, U_{eff} = 3.0 eV (transparent blocks).

4.3.2 Surfaces

Relationship between different surfaces based on the ratio of their surface energies allows a prediction of the NP geometry through the Wulff theorem. This is true not only for the bare surfaces, but also after the adsorbates have been introduced if the surface energies can be adequately addressed. The simplest form of surface or NP oxidation is through the adsorption of oxygen. Considering the atomic nature of the oxygen adsorbate, a minimal difference is expected in behaviour of monoatomic surfaces and corresponding clusters/NPs. Nevertheless, to perform such adsorption on a slab model is computationally much more cost effective. Oxidation behaviour of hcp Co was therefore carried out

on the five inequivalent low Miller-index surfaces: (0001), (01$\bar{1}$0), (10$\bar{1}$1), (11$\bar{2}$0), (11$\bar{2}$1), whose supercells were constructed such that the geometry of the surface is as close to a square (a similar to b) as possible to allow for the investigation of different adsorption arrangements.

Post-relaxation, the (0001) surface has a hexagonal lattice with lattice vectors $a = b =$ 7.39 Å GGA (7.33 Å GGA+U, α = 120°) and the nearest neighbours aligned with a distance of 2.46 (2.44) Å. The (01$\bar{1}$0) and (11$\bar{2}$0) surfaces are rectangular; the former has the lattice vectors a =7.39 Å (7.33 Å GGA+U), b = 7.96 Å (8.10 Å GGA+U, α = 90°), and the latter a = 7.96 Å (8.10 Å GGA+U) and b = 8.52 Å (8.47 Å GGA+U, α = 90°). Single atomic layer is constructed of two pairs of rows, each row having 3 atoms for the (01$\bar{1}$0) and 2 atoms for the (11$\bar{2}$0) surface. Pairs of rows are elevated for 0.63 (0.77) and 0.56 (0.11) Å GGA (GGA+U), respectively. Distances between nearest neighbours of the same row are 2.46 (2.44) Å and 3.98 (4.05) Å, and between atoms in elevated rows 2.43 (2.49) Å and 2.40 (2.51) Å. Similar arrangement has been captured experimentally for the (10$\bar{1}$0) surface.[472] The (10$\bar{1}$1) and (11$\bar{2}$1) are oblique surfaces with a = 7.33 Å (7.33 Å GGA+U) and b = 9.46 Å (9.46 Å GGA+U, α = 104.97°), and a = 8.53 Å (8.47 Å GGA+U) and b = 9.36 Å (9.46 Å GGA+U, α = 63.42°). Similar to the (01$\bar{1}$0) and (11$\bar{2}$0) surfaces, they have two pairs of rows with difference in the z-coordinate of 0.28 Å(0.30 Å GGA+U) and 0.53 Å (0.13 Å GGA+U), respectively. Nearest neighbours are separated by 2.44 Å and 4.26 Å (4.23 Å GGA+U), while the atoms in elevated rows are separated by 2.47 Å (2.40 Å GGA+U) and 2.44 Å (2.58 Å GGA+U). Top views of the five low Miller-index hcp Co surfaces are shown in Figure 4.4.

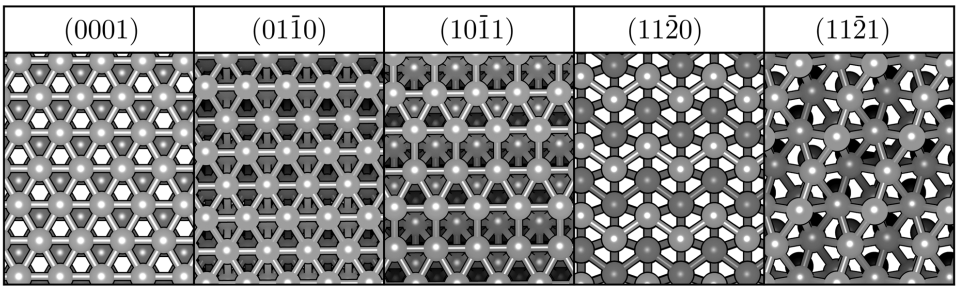

Figure 4.4: Top views of five low Miller-index hcp Co surfaces; darkness in colouration corresponds to the positioning of atoms - the darker the colour, the lower the atomic layer.

Structural information that can be extracted from experiments is mostly limited to the extent of the interlayer contraction or expansion. Quantitative structure determination with a low energy electron diffraction method[473] predicts interlayer contraction of ∼3% for the first pair of (0001) surface layers. For the same surface, GGA (GGA+U) gives a 3.58 % (2.56 %) contraction in the spacing between the first and second layer of atoms, meaning that either method can capture correctly both the intensity of the interchange and its nature. The disparity in the relaxation of remaining layers can be ascribed to the choice of the slab model, but also to the diffraction method being exceptionally sensitive

to the examination of high order layers.[474] Experimental studies did not investigate other surfaces from the structural aspect.

Electronic properties of the surfaces have been analysed through DOS, Figure 4.5. The plots show that the bulk-like metallic nature is retained at all low-index surfaces together with the magnetic properties which are assigned to the asymmetry of the majority and minority spins. The results also indicate that the used slab thickness is sufficient in retaining the bulk-like electronic properties for all five surfaces. Energetic comparison was obtained based on the surface energies, Table 4.2. The second parameter calculated to characterise each surface was the electronic work function, ϕ.

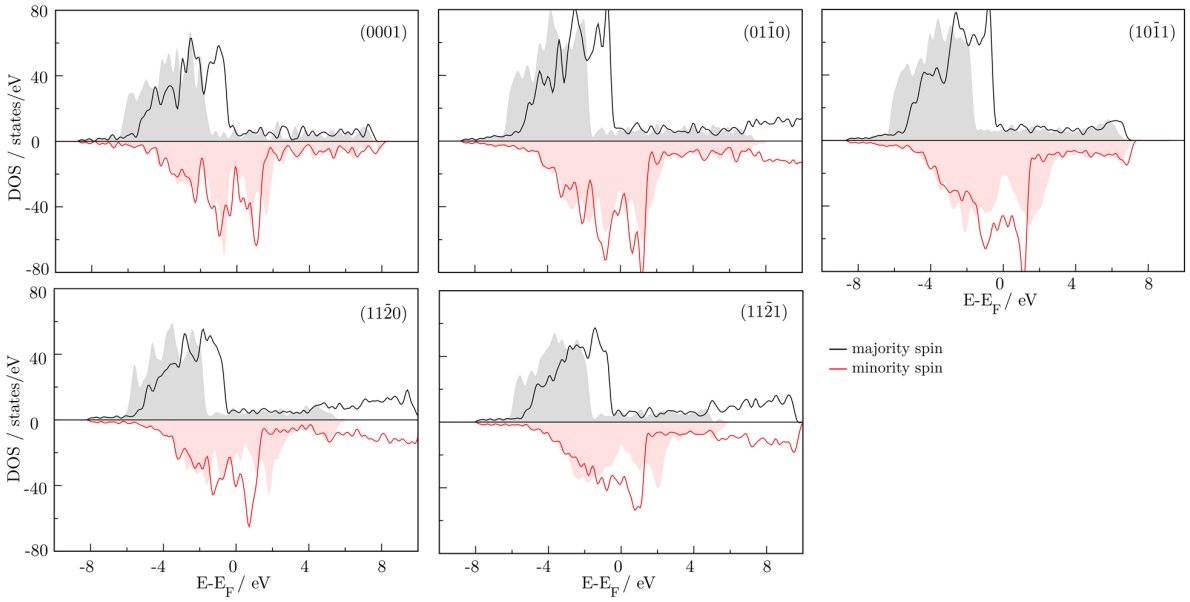

Figure 4.5: DOS for the (0001), (01$\bar{1}$0), (10$\bar{1}$1), (11$\bar{2}$0), and (11$\bar{2}$1) hcp Co surfaces as calculated by GGA (full lines) and GGA+U, U_{eff} = 3.0 eV (transparent blocks). Axes are the same for all graphs.

GGA surface relaxations assigned the lowest surface energy of 2.37 J m^{-2} to the (0001) surface, followed by the (01$\bar{1}$0) surface (2.87 J m^{-2}), (11$\bar{2}$1) surface (2.90 J m^{-2}), (10$\bar{1}$1) surface (2.92 J m^{-2}), and, finally, the (11$\bar{2}$0) surface (3.17 J m^{-2}). The surface energy order upon GGA+U (U_{eff} = 3.0 eV) relaxation is quite different. By introducing the Hubbard parameter, the lowest surface energy is that of the (10$\bar{1}$1) surface (2.11 J m^{-2}), while the work per area unit for the formation of the (0001) surface is 2.43 J m^{-2}. The final sequence in surface stability is accordingly: (10$\bar{1}$1)>(11$\bar{2}$0)>(11$\bar{2}$1)>(01$\bar{1}$0)=(0001). The difference in the surface energies calculated for four- and six-layer slabs showed to be insignificant, and the remaining calculations were carried out with four-layer slab models. This energetic analysis established what is so far the biggest difference in the results from the two methods. However, surface energy values obtained with GGA and GGA+U (U_{eff} = 3.0 eV) for the close-packed (0001) surface differ only by 0.10 eV.

Table 4.2: Calculated unrelaxed (γ_u) and relaxed (γ_r) surface energies for four (six in brackets) layer slabs, relaxation rates (R), and work functions (ϕ) of five low Miller-index hcp Co surfaces together with experimental, semi-empirical, and theoretical relaxed surface energies.

	γ_u/J m^{-2} this study		γ_r/J m^{-2} this study		γ_r/J m^{-2} experiment /	γ_r/J m^{-2} theory	this study GGA/GGA+U	
surface	GGA	GGA+U	GGA	GGA+U	empirical	GGA	R/%	ϕ/eV
(0001)	2.37 (2.33)	2.52 (2.42)	2.33 (2.29)	2.43 (2.39)	2.55 [475] (exp) 2.99 [476] (MEAM) 2.86 [477] (EET)	2.78 [478] 2.11 [479]	-1.69 / -3.57	5.49 / 5.64
(01$\bar{1}$0)	2.90 (2.84)	2.47 (2.49)	2.87 (2.82)	2.43 (2.40)	2.96 [477] (EET) 3.42 [476] (MEAM)	3.04 [478] 2.24 [479]	-1.03 / -1.62	5.02 / 5.27
(10$\bar{1}$1)	2.96 (2.88)	2.19 (2.16)	2.92 (2.85)	2.11 (2.06)	2.61 [477] (EET) 4.52 [476] (MEAM)	2.39 [479]	-1.35 / -3.65	5.08 / 5.01
(11$\bar{2}$0)	3.21 (3.18)	2.33 (2.29)	3.17 (3.12)	2.28 (2.25)	4.81 [476] (MEAM) 3.41 [477] (EET)		-1.25 / -2.15	3.93 / 3.80
(11$\bar{2}$1)	2.95 (2.95)	2.33 (2.32)	2.90 (2.88)	2.22 (2.11)	4.94 [476] (MEAM)		-1.69 / -4.72	3.55 / 3.57

Note: MEAM - Modified Embedded Atom Method
EET - Empirical Electron Theory

Work function can give an insight in the differences of the electronic properties of surfaces which consequentially govern their reactivity. It generally tends to be greater for dense crystal facets than for those with more open lattices, which agrees well with the hexagonally-packed (0001) surface having the highest work function value of 5.49 eV (5.64 eV GGA+U). Correspondingly, low work functions of only 3.55 (3.57) and 3.93 (3.80) eV, respectively, accurately describe loosely packed (11$\bar{2}$0) and (11$\bar{2}$1) surfaces. Literature results are available only for the (0001) surface, with an experimental value of 5.55 eV[480] and an LDA value of 5.62 eV [481], giving the percent error of only 1.08 % (1.62 %), which can be mainly ascribed to the temperature difference (experiment carried out at 180 K).

Inconsistencies in surface energies and stability orders published previously make comparison with other works difficult. Nevertheless, agreement with experimental results on the (0001) surface [475] is very good, thus providing confidence in the suitability of the parameters used. Discrepancies with available semi-empirical and computational results, Table 4.2, can be attributed to the choice of the slab model, exchange-correlation functional, and, most importantly, inclusion of the long-range dispersion interactions in the present work which have been disregarded in earlier studies.[478, 479] Considering scarcity of experimental results for any but the (0001) surface, whose high symmetry reduces the differences in the two methods, it is difficult to suggest to which extent the addition of Hubbard parameter influences the description of d-electrons on a surface level.

The Wulff morphologies of NPs constructed using the calculated relaxed surface energies from GGA and GGA+U calculations are shown in Figure 4.6. All five low Miller-index surfaces appear in the final structure in both cases, with the (10$\bar{1}$1) surface covering the biggest area of the NP. The most noticeable differences between the two morphologies are areas of the (0001) and (01$\bar{1}$0) surfaces that are more prominent in the GGA mor-

phology, whereas the $(11\bar{2}0)$ and $(11\bar{2}1)$ are more dominant in the GGA+U predicted morphology.

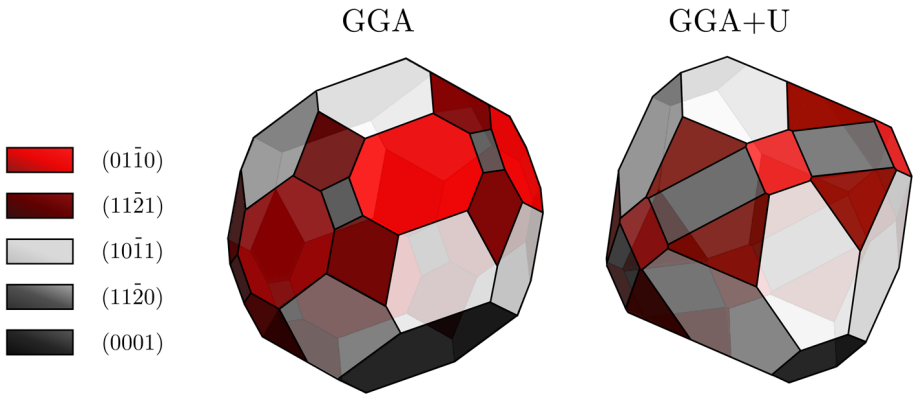

Figure 4.6: Wulff morphology of hcp Co NPs as obtained from the surface energies calculated by GGA and GGA+U, U_{eff} = 3.0 eV.

4.3.3 Oxidation

As shown, a single hcp Co crystal can display various facets whose stabilities and exposed areas substantially differ, and Wulff construction can be used to determine the equilibrium crystal shape. In a more complex scenario, for example by placing metallic NPs in an oxidative environment, metal oxide can form on the exposed surfaces. In first-principles studies, it is often a routine task to determine the stability of a certain oxidising species after the adsorption by examining the structural properties and adsorption energies. Extension of this technique leads to the determination of the surface stability in the presence of the adsorbate, similar to the determination of surface energies in vacuum, which can then be used to determine the equilibrium shape of a crystal in oxidative conditions. Such procedure accurately captures morphological changes and gives an insight into the influence of the alteration in the exposed surfaces upon oxidation on other properties of interest, e.g. magnetisation.

Apart from the Co (0001) surface [438, 439], no theoretical work on the interaction of oxygen with the hexagonal phase of cobalt has been published. Conducted work showed that the (0001) facet oxidation is very exothermic even in mild conditions and at low oxygen concentrations. Based on these results for the (0001) low-index plane, it is natural to expand the scope of investigation to account for the changes of a single crystal morphology upon oxidation, and this was done herein by including five inequivalent low Miller-index hcp Co surfaces. The oxygen adsorption has been systematically analysed on-surface and sub-surface to confirm the aforementioned hypothesis of *in vivo* oxidation and to provide accompanying morphology change of the NP.

Differences in the structural appearance of distinctive surfaces affect their reactivity. In the case of the (0001) surface, surface geometry generates all atop (T) and bridge (B) positions to be exactly the same, with two possible hollow positions: hollow fcc (F), with adsorbing atom atop the second layer Co atom, and hollow hcp (H), with no Co atoms beneath the adsorbate. All four other surfaces have pairs of differently elevated rows of Co atoms. Due to the differences in the elevation, there are also pairs of atop (T_1, T_2), bridge (B_1, B_2), and hollow (H_1, H_2) positions such that, for example, there exists one atop position above higher elevated row of atoms, and one above lower row of atoms. Possible adsorption sites are shown for the (0001) and (10$\bar{1}$1) surfaces in Figure 4.7.

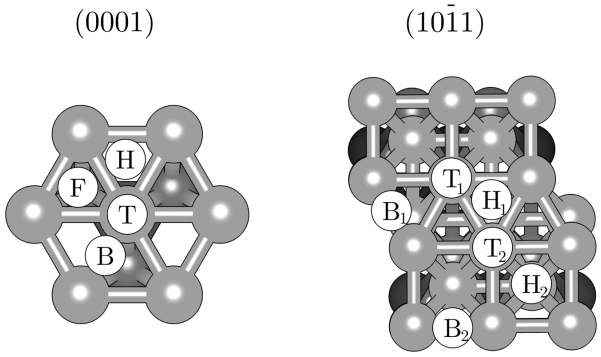

Figure 4.7: Available adsorption sites on the (0001) and (10$\bar{1}$1) hcp Co surfaces: atop (T, T_1, T_2), bridge (B, B_1, B_2), and hollow (fcc-F, hcp-H, H_1, H_2).

4.3.3.1 Energetic and structural parameters

Oxygen adsorption has been performed to identify the most favourable amongst available surface sites based on the computed energetic properties. Calculated adsorption energies are listed, along with structural parameters, in Table 4.3. The most stable adsorption site for each surface is represented in top and side view in Figure 4.8 (as obtained by the GGA relaxation). Results from both GGA and GGA+U indicate that the three-fold hollow sites are by far more stable than the atop position in the case of the (0001) surface. GGA relaxation gives hollow F as the most stable adsorption position with an adsorption energy of -3.12 eV, while the adsorption energy of -3.69 eV makes hollow H more stable when relaxed within GGA+U. The absolute difference in the adsorption energies between the two hollow positions ($|\Delta$F-H$|$ = 0.10/0.24 eV (GGA/GGA+U)) is relatively maintained across the two approaches, and it is in total considerably lesser than the difference between the hollow and atop positions (H-T 1.41/1.46 and F-T 1.51/1.21 eV), which is expected since the hollows differ from each other only starting from the third atomic layer. When the oxygen atom is initially positioned in the bridge site, it either relaxes to the H site (GGA) or completely rearranges the top two atomic layers before repositioning into the hollow (GGA+U). Due to the rearrangement, computing the adsorption energy through employment of the E_{surface} as calculated for the un-rearranged

Table 4.3: Calculated adsorption energies using GGA and GGA+U (U_{eff} = 3.0 eV) approaches, adsorbate-surface (d_z) and adsorbate-nearest Co atom ($d_{\text{Co-O}}$) distances, together with observed changes in the stacking of atoms (in brackets) for single oxygen atom adsorption on five inequivalent low Miller-index surfaces of hcp Co. CN denotes coordination number of oxygen for initially ascribed positions.

			E_{ads} / eV		$\bar{d}_z$ / Å		$\bar{d}_{\text{Co-O}}$ / Å	
surface	site	CN	GGA	GGA+U	GGA	GGA+U	GGA	GGA+U
(0001)	T	1	-1.61	-2.23	1.634	1.638	1.634	1.638
	B	2	-3.02 (H)	-5.49 (rearranged)	1.166	1.168	1.856	1.876
	F	3	-3.02	-3.69	1.166	1.249	1.856	1.872
	H	3	-3.12	-3.45	1.138	1.503	1.849	1.879
	t	4	-3.09	-2.40	-0.993	-0.655	1.844	2.037
	o	6	-0.29	-1.38	-0.688	-0.958	1.837	1.915
(01$\bar{1}$0)	T_1	1	-1.94	-2.92	1.619	1.643	1.619	1.643
	T_2	5	-3.21 (H_1)	-4.18	0.936	0.588	1.860	1.880
	B_1	2	-2.88	-3.84	1.230	1.009	1.771	1.796
	B_2	4	-2.99	-4.16	0.685	0.301	1.889	1.931
	H_1	3	-3.21	-4.57	0.935	0.839	1.860	1.870
	H_2	4	-2.99 (B_2)	-4.16 (B_2)	0.685	0.276	1.889	1.952
	s_1	7	0.30	-2.90	-0.827	-1.178	1.844	1.942
	s_2	7	0.31	-2.78	-0.780	-1.951	1.837	1.875
(10$\bar{1}$1)	T_1	1	-3.60 (H_1)	-3.27 (H_1)	0.742	0.983	1.945	1.877
	T_2	1	-3.60 (H_1)	-3.24 (H_2)	0.743	1.084	1.945	1.870
	B_1	2	-3.42 (H_2)	-3.30 (H_2)	1.012	1.024	1.853	1.869
	B_2	4	-3.30 (H_2)	-3.27 (H_2)	0.973	1.092	1.850	1.879
	H_1	4	-3.60	-3.29	0.743	0.972	1.944	1.889
	H_2	3	-3.30	-3.27	0.978	1.069	1.860	1.891
	s	5		-1.39		-1.156		1.933
(11$\bar{2}$0)	T_1	1	-3.16 (B_1)	-4.76 (B_1)	0.740	0.690	1.880	1.898
	T_2	1	-3.16 (B_1)	-4.81 (B_1)	0.697	0.559	1.879	1.918
	B_1	4	-3.16	-4.78	0.698	0.644	1.880	2.047
	B_2	5	-3.16	-5.03	0.738	0.591	1.880	2.036
	H_1	4	-2.95	-4.49	0.435	0.525	1.887	1.836
	H_2	2	-2.89	-4.41	1.285	1.191	1.778	1.801
(11$\bar{2}$1)	T_1	1	-2.11	-2.65	1.618	1.613	1.620	1.634
	T_2	1	-3.28 (H_2)	-4.11 (H_1)	0.664	0.511	1.837	1.841
	B_1	2	-3.25 (H_1)	-4.15 (H_1)	0.479	0.420	1.843	1.970
	B_2	3	-3.25 (H_1)	-4.24 (H_1)	0.479	0.395	1.843	1.885
	H_1	3	-3.31	-4.09	0.660	0.519	1.843	1.860
	H_2	4	-3.28	-3.85	0.663	0.395	1.838	1.844

surface has no physical meaning, and adsorption energy obtained (-5.49 eV) is omitted from any further discussion. Three adsorption sites on the (0001) surface have been identified for subsurface adsorption, two tetrahedral and one octahedral position. However, after geometry optimisation, O atom placed in the second tetrahedral position repositioned on-surface. More stable position between octahedral and remaining tetrahedral site is, for both GGA and GGA+U calculations, tetrahedral site with the adsorption energy of -3.09 eV (GGA)/-2.40 eV (GGA+U). GGA therefore predicts similar preference for oxygen subsurface incorporation as for the on-surface adsorption. On contrary, on-surface adsorption is ∼1.00 eV more preferred than the tetrahedral subsurface site in the case of GGA+U relaxation.

From a structural point of view, the oxygen-surface distances are in accord with the energetic parameters - the more negative the adsorption energy, the closer the adsorbate is to the surface. When considering the Co-O distances, among the positions with the same oxygen CN, the oxygen atom will be closest to the Co atoms in the site with the most negative energy. Since in the atop site O atom binds only to a single Co atom, CN=1, the bond is naturally shorter. A complete list of the CNs for all sites is also given in Table 4.3. The interlayer changes induced by the O adsorption depend on the relative position of each layer in respect to the adsorbate atom. Interlayer spacing between the first and second layer decreases as a consequence of attractive forces between oxygen and Co atoms of both layers, while the spacing between the second and third layer, whose atoms are hardly affected by adsorption, increases.

Among six possible adsorption sites on the $(01\bar{1}0)$ surface, the only threefold site (H_1) is the most favourable after relaxation by both GGA (E_{ads} = -3.21 eV) and GGA+U (E_{ads} = -4.57 eV). Although there are three positions which have higher CNs compared to the H_1 site (T_2, B_2, and H_2), the oxygen atom is unable to settle in the centre therefore forming bonds of different lengths with four or five closest Co atoms. The T_2 position, where oxygen is adsorbed atop one Co atom from the lower levelled row of the first atomic layer, showed appreciably reduced adsorption energy (by 1.25 eV) compared to the T_1 position within GGA+U optimisation, as on the basis of the oxygen CN. When relaxed by GGA, oxygen spontaneously moves from T_2 to the H_1 position, whereas both GGA and GGA+U captured movement of oxygen from initial H_2 position to the equally four-coordinated B_2 adsorption site, which is the second most stable after H_1, with relative differences between the two being 0.22 eV (GGA) and 0.41 eV (GGA+U). The oxygen CN has the same effect on the Co-O distances as on the (0001) surface. There are two inequivalent subsurface adsorption sites, both significantly less stable than on-surface positions. When optimised within GGA+U, their stability is comparable to the least favourable on-surface adsorption site, however, adsorption energies computed by GGA are positive, implying that subsurface adsorption is unfavourable.

On the $(10\bar{1}1)$ surface, the oxygen atom also prefers to adsorb in the hollow site. Moreover, all atop (T_1 and T_2) and bridge (B_1 and B_2) sites experienced movement of the oxygen atom towards one of the available H sites during relaxation by either GGA

or GGA+U. None of the changes in the positions resulted in a shift of the first and/or second layer atoms. The adsorption energies of the two H sites differ for 0.30 eV (GGA) and 0.05 eV (GGA+U). Fourfold H_1 position is more stable since oxygen positioned in the threefold H_2 binds to two Co atoms of the higher row and one of the lower row of the first layer, while in H_1 it centres in between two pairs of Co atoms, one of the higher and one of the lower row. The $(10\bar{1}1)$ surface atop sites are so unfavourable that repositioning of the adsorbate is energetically more acceptable than binding to a single Co atom. One sub-surface oxidation site was found but, with an adsorption energy of -1.23 eV (GGA)/-1.39 eV (GGA+U), it is not even half as exothermic as the on-surface adsorption. Possible subsurface adsorption sites are shown in Figure 4.9.

In the case of the more open $(11\bar{2}0)$ surface, bridge sites predominate for the atomic adsorption. The reason behind this is the nearest neighbour distance between Co atoms of 4.05 Å (∼1.50 Å further away than for the (0001), $(01\bar{1}0)$, or $(10\bar{1}1)$ surface), which makes hollow sites less coordinated compared to the previous three surfaces. The adsorption energies of B_1 as the most favourable adsorption site are -3.16 eV for GGA, and -4.78 eV for GGA+U approach, while hollow site H_1 has E_{ads} higher for 0.21 and 0.29 eV, respectively. Accordingly, the oxygen atom moves from the atop sites, which initially have low CNs, to the most stable B_1 position.

Similar to the $(11\bar{2}0)$ surface, the $(11\bar{2}1)$ surface is also open, with the nearest neighbour distance of surface atoms increased even further to 4.23 Å. Positioning of the O atom in between the closest two Co atoms, even if oxygen is completely aligned with the surface, would still imply the Co-O distance longer than what is anticipated for the bond formation. Accordingly, hollow adsorption is more acceptable solution, or one should expect a significant rearrangement of Co atoms closer to the centred oxygen. H_1 was computed to be the most favourable site with the adsorption energy of -3.31 eV for GGA and -4.09 eV for GGA+U. Due to the remoteness of Co atoms, T_1 atop position does not experience repositioning of the adsorbed oxygen and it is less stable with E_{ads} = -2.11 eV (GGA) and E_{ads} = -2.65 eV (GGA+U). Adsorption of oxygen in the second atop position (T_2) and both of the bridge adsorption sites showed preference for movement towards H_1 hollow without surface atomic rearrangements. The $(11\bar{2}0)$ and $(11\bar{2}1)$ surfaces were found to be too open to accommodate an oxygen atom in-between the layers.

In general, the most favourable positions are threefold sites since they offer the highest oxygen CN where O atom can still remain perfectly centred with respect to the closest equivalent Co atoms. Sites presenting less local symmetry (atop and bridge sites for the (0001), $(01\bar{1}0)$, $(10\bar{1}1)$, and $(11\bar{2}1)$ surfaces, and atop and hollow sites for the $(11\bar{2}0)$ surface) are either substantially higher in energy (by ∼1.50 eV) or so unfavourable that the oxygen atom prefers to reposition into a more stable site. As such, adsorbed O atom tends to occupy the exact positions which would be taken by Co atoms in the next surface layer, thus continuing the substrate stacking sequence whenever possible. This tendency helps to explain the minor structural changes observed in the positions of slab atoms with respect to their starting geometry. In addition, despite the differences in the adsorption energies of up to 1.00 eV, GGA and GGA+U approaches showed more similarities than

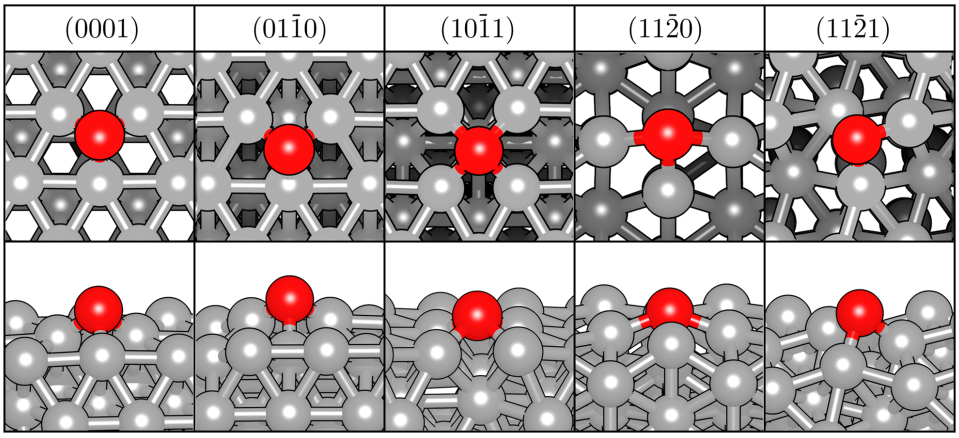

Figure 4.8: Top and side views of the adsorption of a single oxygen atom in the most favourable adsorption site (as computed by GGA) for five low Miller-index hcp Co surfaces.

deviations in predicted adsorption behaviour on all five surfaces. Both compute analogous magnitudes of E_{ads} and capture the relations in adsorption energies of different sites, as well as predict the adsorbate repositioning (with an exception of the $T_2 \rightarrow H_1$ transition occurrence on the (01$\bar{1}$0) surface which was not captured within the GGA+U relaxation).

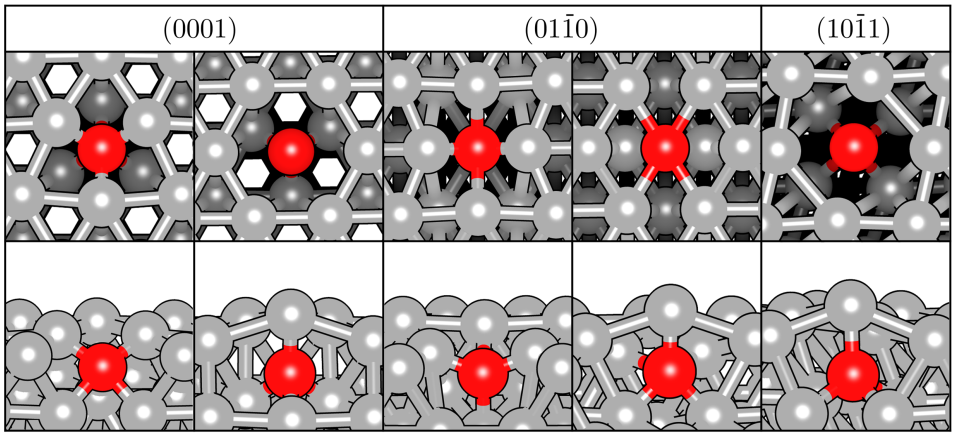

Figure 4.9: Top and side views of the subsurface adsorption of a single oxygen atom (as computed by GGA) for three low Miller-index hcp Co surfaces. Co atoms positioned directly above adsorbed oxygen are removed from top views for clarity. There are no possible adsorption sites for subsurface adsorption on the (11$\bar{2}$0) and (11$\bar{2}$1) surfaces.

Comparison with previous theoretical studies is limited owing to the absence of data in the literature on all except the (0001) surface. Previous GGA works provided adsorption energies and Co-O distances only in hollows F and H as positions with the highest oxygen coordination. Luo *et al* found that oxygen adsorbs in the H hollow releasing E_{ads} of -5.92 eV [482], while Gong *et al* provided the adsorption energy and Co-O distance of -5.34 eV and 1.885 Å, respectively, for the same site.[483] Hollow H was also reported by Ma *et*

al to be preferred energetically by 0.1 eV over hollow F, with the adsorption energy of -5.12 eV and Co-O distance of 1.86 Å.[438] In a unison with these results, Ge and Neurock calculated the adsorption energies of single O atom to be -5.53 eV in hollow H and -5.43 eV in hollow F.[484] Contrary to the E_{ads} reported here, all adsorption energies available in the literature were calculated with respect to the atomic oxygen, while molecular oxygen (as predominant oxidising specie) was chosen as a reference within this study. For the sake of comparison, results of this study are (within this paragraph only) re-expressed with respect to atomic oxygen, as E_{ads}(H) = -4.93 eV (GGA), -5.59 eV (GGA+U), and E_{ads}(F) = -5.02 eV (GGA), -5.35 eV (GGA+U). The energetic and structural parameters obtained for the (0001) surface are, overall, in a good agreement with the existing data, and present differences are most likely a result of the inclusion of dispersion corrections within this study.

4.3.4 Effect of increased coverage

After determination of the most stable adsorption sites for single O atom adsorption, the coverage has been gradually increased in order to understand the influence the oxygen concentration has on the properties of Co surfaces, especially magnetisation. With the growing coverage, the number of possible combinations of O atom arrangements increases drastically; to subdue the number of calculations, but also to evade the risk of omitting the low energy structures, the adsorption energies from the single O atom adsorption were taken as criteria for choosing a reasonable configuration set. Additionally, both sub-surface and a combination of on- and sub-surface adsorption were modelled alongside the on-surface adsorption.

4.3.4.1 Energetic and structural parameters

Included sites and final energetic parameters are listed in Table 4.4. The adsorption energy per O atom is getting more positive with the increase in the oxygen coverage, a trend which has already been reported for other transition metals [449, 485] and the Co (0001) surface.[438] This is an expected phenomenon arising due to the charge redistribution and saturation in the oxidation of the top-most surface Co atoms through the formation of ionic bonds with O adsorbates which also leads to the electron depletion on the nearby adsorption sites as well as because of the oxygen-oxygen interactions which are uniformly repulsive for all surfaces. However, some unusual features have been observed, indicating a complex interaction between metallic cobalt and atomic oxygen.

On the (0001) surface, multiple O atom adsorption was considered for both threefold hollow sites, along with their combinations (H+F). The differences in the adsorption energies per O atom between hollows F and H decrease with the increase in the coverage, showing that the site preference of oxygen becomes negligible. Similar to the adsorption of a single O atom, GGA predicts multiple adsorption in F position to be more favourable than with oxygen atoms adsorbed in H hollows, while GGA+U stabilities are reversed. Relative differences are conserved regardless of the approached used. The biggest divergence of the two methods is in the behaviour of Co atoms that are at the interception

Table 4.4: Adsorption energies (per O atom), E_{ads}, for adsorption of up to a full monolayer of oxygen on the low Miller-index surfaces of hcp Co as calculated by GGA and GGA+U, U_{eff} = 3.0 eV.

			$E_{\text{ads(per O atom)}}$ / eV				$E_{\text{ads(per O atom)}}$ / eV	
surface	θ / ML	site	GGA	GGA+U	θ / ML	site	GGA	GGA+U
(0001)	0.22	F	-2.99	-3.51	0.56	H	-2.62	-3.12
		H	-2.91	-3.58	0.67	F	-2.52	-2.78
		F+H	-2.97	-3.57		H	-2.51	-2.74
	0.33	F	-2.94	-3.23	0.78	F	-2.34	-2.35
		H	-2.88	-3.39		H	-2.32	-2.35
		F+H	-2.92	-3.59	0.89	F	-2.19	-2.24
	0.44	F	-2.82	-3.20		H	-2.17	-2.23
		H	-2.79	-3.27	1.00	F	-2.05	-2.13
	0.56	F	-2.65	-3.13		H	-2.05	-2.15
$(01\bar{1}0)$	0.17	H_1	-3.17	-4.58	0.50	H_1	-3.04	-3.08
		B_2	-2.86	-3.04	0.58	H_1	-2.65	-2.93
	0.25	H_1	-3.18	-4.55	0.67	H_1	-2.54	-3.16
		B_2	-2.90	-3.68	0.75	H_1	-2.33	-3.14
	0.33	H_1	-3.03	-3.82	0.83	H_1	-2.29	-3.13
	0.38	H_1	-3.06	-3.70	0.88	H_1	-2.12	-3.04
	0.42	H_1	-2.99	-3.28	1.00	H_1	-1.97	-2.84
$(10\bar{1}1)$	0.17	H_1	-3.42	-4.07	0.58	H_1	-2.89	-2.97
	0.25	H_1	-3.58	-3.72	0.67	H_1	-2.81	-2.88
	0.33	H_1	-3.40	-3.54	0.75	H_1	-2.55	-2.94
	0.38	H_1	-3.25	-3.46	0.83	H_1	-2.48	-2.94
	0.42	H_1	-3.11	-3.28	0.88	H_1	-2.37	-2.87
	0.50	H_1	-3.07	-3.21	1.00	H_1	-2.06	-2.63
$(11\bar{2}0)$	0.25	H_1	-2.90	-3.49	0.50	B_1	-3.05	-3.54
		B_1	-3.11	-3.96	0.63	B_1	-3.07	-3.55
	0.38	H_1	-2.91	-3.26	0.75	B_1	-3.01	-3.57
		B_1	-3.09	-3.57	0.88	B_1	-2.91	-3.54
	0.50	H_1	-2.88	-3.08	1.00	B_1	-2.84	-3.54
$(11\bar{2}1)$	0.25	H_1	-3.28	-3.88	0.63	H_1	-3.19	-3.37
	0.38	H_1	-3.30	-3.75	0.75	H_1	-3.07	-3.16
	0.50	H_1	-3.29	-3.49	0.88	H_1	-2.89	-3.24
					1.00	H_1	-2.69	-3.14

of two or more adsorbate atoms, ∼0.20-0.30 ML, and when the coverage is lower than ∼0.70 ML. After the GGA relaxation, adsorption of three (0.33 ML) to six (0.67 ML) O atoms moderately elevates middle-most Co atom or a pair of Co atoms without extensive structural change to the surface. However, when relaxed by GGA+U, such elevation can become a complete withdrawal of Co atom from the surface, resulting in the formation of entities known as cobalt-oxygen islands. Such creations bear partial CoO character, compound whose properties GGA fails to model correctly, as seen through the test of varying U_{eff} values, which is probably the main reason for the differences in obtained structural and energetic parameters. Distinction minimises for higher coverages, when formation of Co_3O_4 is expected. This is, for the sake of comparison, shown for multiple adsorption in hollow H in Figure 4.10.

Structural aspects are, in general, following patterns of the single oxygen adsorption, that is, adsorbed O atoms situated closer to the surface have more negative adsorption

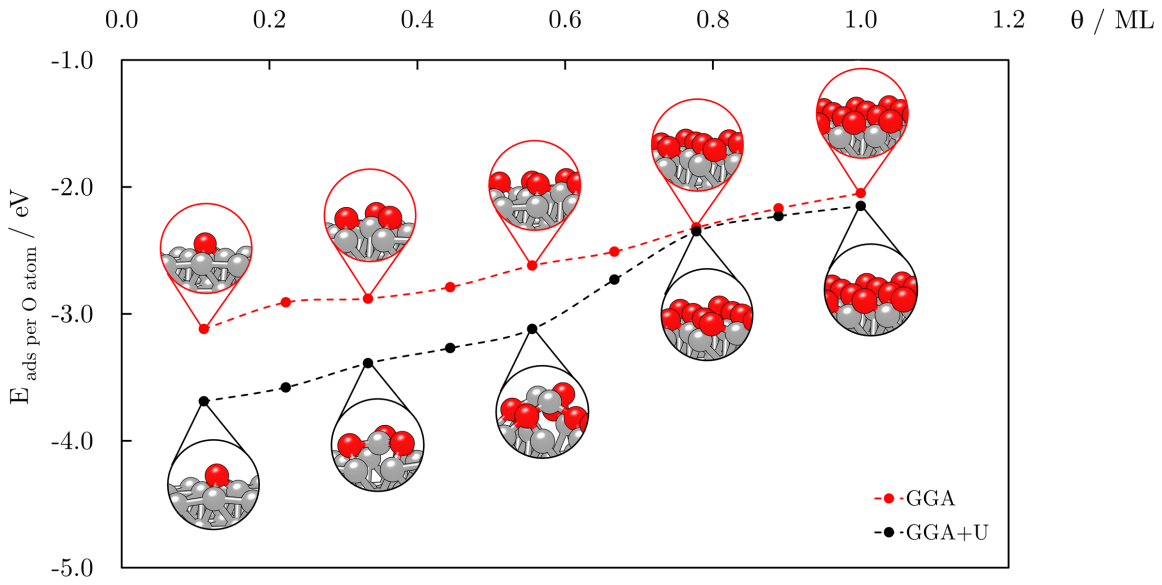

Figure 4.10: Adsorption energies (per O atom) as a function of the oxygen coverage on the (0001) surface as computed by GGA and GGA+U, U_{eff} = 3.0 eV.

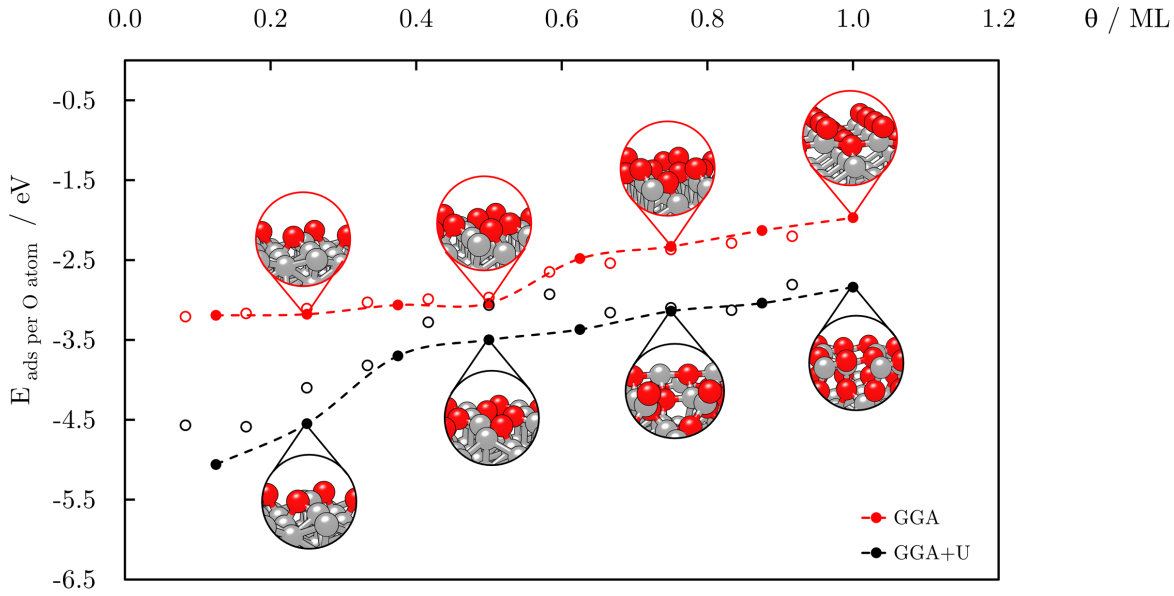

Figure 4.11: Adsorption energies (per O atom) as a function of the oxygen coverage on the $(01\bar{1}0)$ surface as computed by GGA and GGA+U (U_{eff} = 3.0 eV). Empty and filled circles correspond to the 3×2 and 4×1 supercells, respectively.

energies. Additionally, the distance between the O atoms increases after relaxation, and displacement towards one edge of the triangular hollow facet for coverages under 0.60 ML

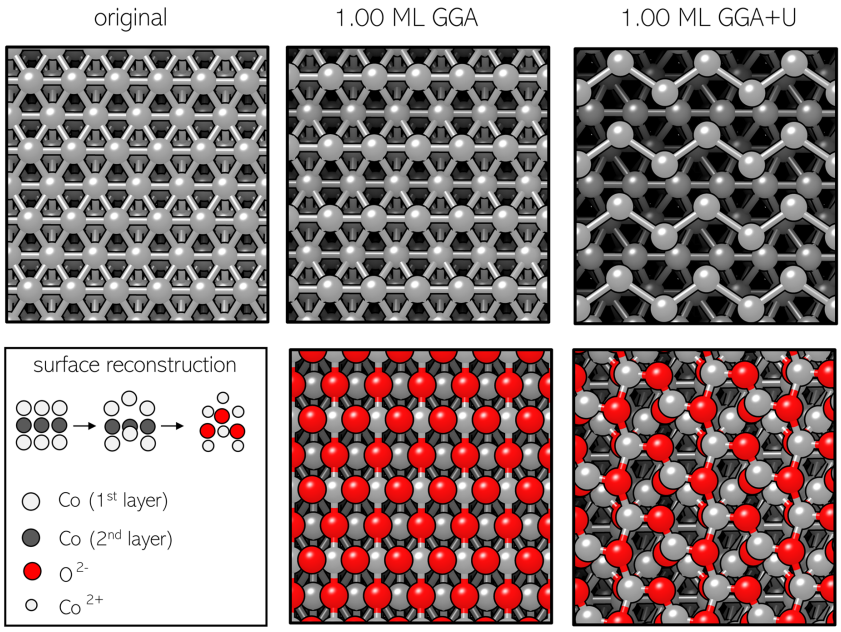

Figure 4.12: Reconstruction of the $(01\bar{1}0)$ surface upon the full monolayer oxygen adsorption as computed by GGA and GGA+U (U_{eff} = 3.0 eV). **top** panel: Top views of the bare surface and post-adsorption surface with O atoms hidden for clarity; **bottom** panel: suggested surface reconstruction for GGA+U adsorption and top views of systems after the adsorption of a full oxygen monolayer.

can be observed owing to the lateral interactions between O atoms which are uniformly repulsive for all surfaces. The repulsive interaction is emphasised particularly between the oxygen atoms that bind the same Co atom. As the repulsion gets stronger with the increase in the number of O atoms, the adsorbates are moving further away from the surface as the number of available adsorption sites towards which adsorbed O atoms could be displaced reduces. Generally, oxygen co-adsorption induces similar relaxation of the lattice and layer displacements as the single oxygen adsorption, but modified by the mutual effect of multiple O atoms on interposed Co atoms. With full coverage reached, a small expansion in the interlayer distance between the second and third atomic layer is observed, emphasizing the stronger impact of multiple O atoms on the second layer compared to the single oxygen adsorption.

Effect of the adsorption site on the increased oxygen coverage on the $(01\bar{1}0)$ surface was probed for 0.17 and 0.25 ML in B_2 and H_1 sites, Table 4.4. In both cases, H_1 adsorption was noticeably more favoured, with adsorption energies per O atom more negative by 0.30 and 1.54 eV for 0.17 ML coverage and by 0.28 and 0.87 eV for 0.25 ML, respectively, when optimised by GGA and GGA+U. Further adsorption was, therefore, carried out only in the energetically most preferred adsorption site, H_1. To be able to capture the zigzag oxygen adsorption patterns suggested by the work of Koch *et al* [472],

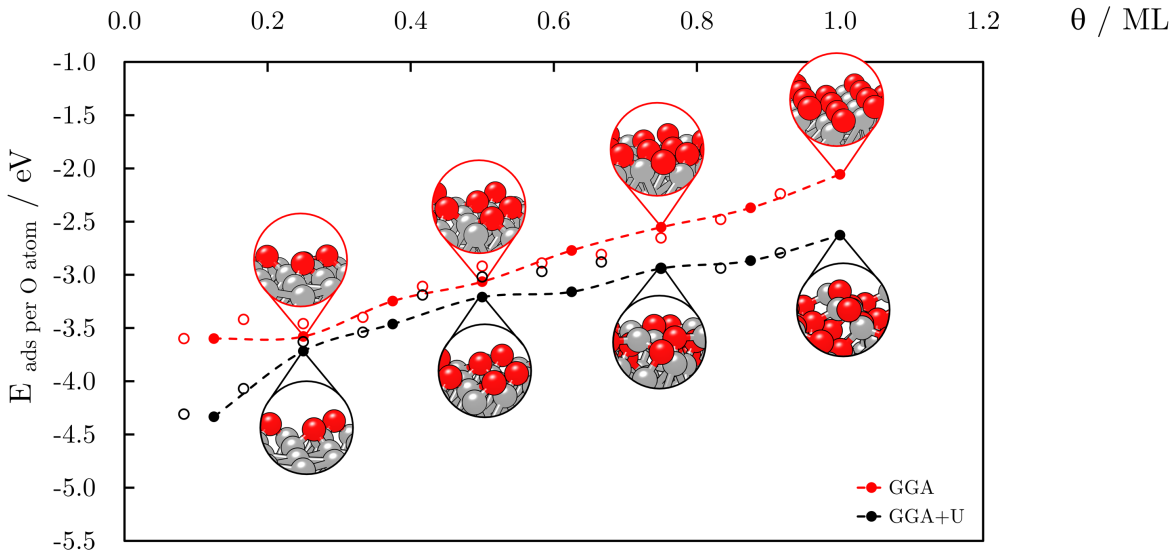

Figure 4.13: Adsorption energies (per O atom) as a function of the oxygen coverage on the $(10\bar{1}1)$ surface as computed by GGA and GGA+U (U_{eff} = 3.0 eV). Empty and filled circles correspond to the 3×2 and 4×1 supercells, respectively.

adsorption has been performed on the elongated 4×1 supercell alongside the square-like 3×2 supercell. Adsorption energies as a function of the coverage are depicted in Figure 4.11. GGA results indicate minimal increase in the adsorption energy per O atom for coverages under 0.50 ML affected by the row structure of the $(01\bar{1}0)$ surface, which allows for incorporation of O atoms in between the rows to minimise the repulsion compared to the energy-consuming elevation of Co atoms on the flat (0001) surface. GGA+U, on the other hand, tends to maximise the number of formed Co-O bonds as well as to minimise oxygen-oxygen repulsion, where an increased distance between the surface Co atoms still requires energetically significant rearrangements and the adsorption energies are hence considerably less negative with the increase in the coverage. It is also evident, especially on the GGA+U level, how much zigzag adsorption achieved by elongated 4×1 supercell improves the local displacement of surface atoms for Co-O bond formation and reduces the repulsion between the adsorbate atoms. For a 0.50 ML coverage, the difference in the E_{ads} between the adsorbate arrangement on the 3×2 and 4×1 supercell as optimised by GGA+U is 0.43 eV per O atom. Further increase in the coverage induces full incorporation of certain oxygen atoms within the first layer Co atoms for the GGA optimisation, and sub-surface O adsorption for the GGA+U optimisation, which leads to a less steep increase of the adsorption energies. This difference in the adsorption behaviour reflects well previously predicted unfavourable GGA sub-surface oxygen incorporation. Additionally, the sub-surface adsorption at high coverages compensates the energetic cost of the reconstruction of the row-like $(01\bar{1}0)$ surface arrangement at the GGA+U level. Final structures for a full monolayer coverage significantly differ in both layout and adsorption energy when comparing the two functionals. GGA predicts adsorption of oxygen atoms

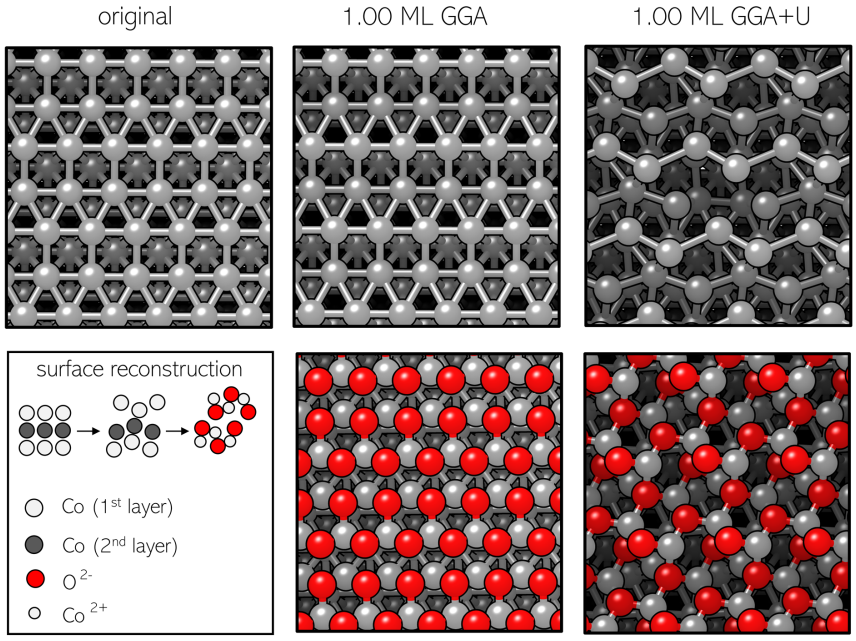

Figure 4.14: Reconstruction of the $(10\bar{1}1)$ surface after the adsorption of a full oxygen monolayer as computed by GGA and GGA+U (U_{eff} = 3.0 eV). **top** panel: Top views of the bare surface and post-adsorption surface with O atoms hidden for clarity; **bottom** panel: suggested surface reconstruction for GGA+U adsorption and top views of systems after the adsorption of a full monolayer of oxygen.

in channels of the row-like surface configuration, while GGA+U initiated rearrangement of surface atoms to accommodate O atoms in a zigzag fashion. The latter reconstruction coincides with the suggestions made by Koch *et al* [472] and it is schematically represented in Figure 4.12.

Adsorption of a single oxygen atom on the $(10\bar{1}1)$ surface was shown to be possible only in the H_1 adsorption site, and increase in the oxygen coverage was therefore conducted in the same position, Table 4.3. Since this surface bears a high level of structural resemblance to the $(01\bar{1}0)$ surface, which contributed to the similarity in the single O adsorption energies, motivated by the results of the former, different configurations for higher coverages were also tested for the 4×1 and 3×2 supercells. Adsorption energy trends for GGA and GGA+U are represented in Figure 4.13. Compared to the $(01\bar{1}0)$ surface, there is a more noticeable change in the adsorption energy per O atom for coverages under 0.50 ML when optimised by GGA. This can be attributed to the difference in the height of the rows within the same layer (0.27 Å for the $(10\bar{1}1)$ surface as compared to 0.70 Å for the $(01\bar{1}0)$ surface), which contributes less to the shielding of the oxygen-oxygen repulsion and consequently increases the E_{ads}. This closer-packed surface geometry also influences the local movement of surface Co atoms triggered by GGA+U for Co-O bond formation, and the relative difference between the GGA and GGA+U adsorption energies is less prominent than on the $(01\bar{1}0)$ surface. However, zigzag arrangement of the adsorbate

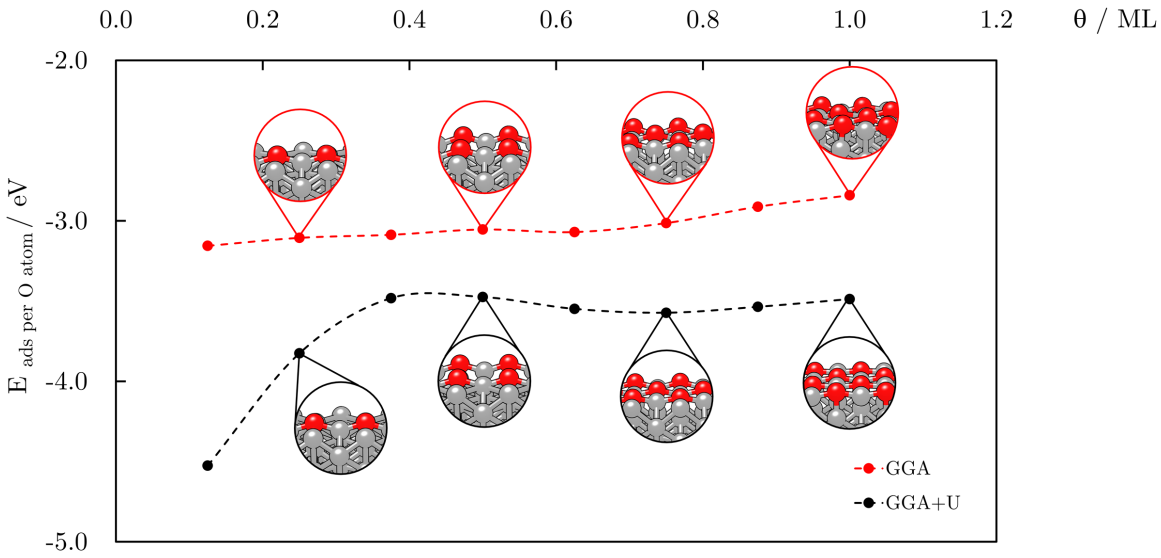

Figure 4.15: Adsorption energies (per O atom) as a function of the oxygen coverage on the $(11\bar{2}0)$ surface as computed by GGA and GGA+U (U_{eff} = 3.0 eV).

atoms on the 4×1 supercell is still favoured, for example by 0.19 eV per O atom for a 0.50 ML coverage within the GGA+U functional. Much alike the $(01\bar{1}0)$ surface, coverages higher than 0.50 ML initiate the sub-surface adsorption at the GGA+U level. However, due to the very close stacking of the slab layers, the extent of the surface reconstruction is considerably lower, and repulsion between the on-surface and sub-surface adsorbed O atoms prevents formation of the exact pattern observed on the $(01\bar{1}0)$ surface, although the similarity of the configuration is evident, as shown in Figure 4.14.

On the $(11\bar{2}0)$ surface, higher coverages of oxygen were tested in both the preferred B_1 and the second most stable H_1 adsorption site, Table 4.3. The initial energy difference of 0.20 eV between the two positions remained unchanged for low coverages. Coverages above 0.50 ML were therefore studied only in the B_1 site. Compared to the previous three surfaces, open geometry of the $(11\bar{2}0)$ surface imposes different conditions on oxygen adsorption. Due to large distances between the closest surface Co atoms, in order for adsorbed oxygen atoms to directly interact with more than one Co atom, they need to adsorb close to or exactly within the first layer of the surface. Upon such adsorption, O atoms are levelled with the surface Co atoms and their repulsion is shielded regardless of the coverage, meaning there is energetically no need for local displacement of surface Co atoms or for their extraction above the surface level. This is also the reason that the adsorption energy per O atom is a monotone function of the coverage for both GGA and GGA+U, Figure 4.15. The main difference between the approaches is in the positioning of O atoms: GGA incorporates them slightly above the atomic plane of the first layer, while optimisation with GGA+U results in O atoms adsorbed at approximately the same height of first layer Co atoms. The energetic deviation for the lowest coverages (0.125

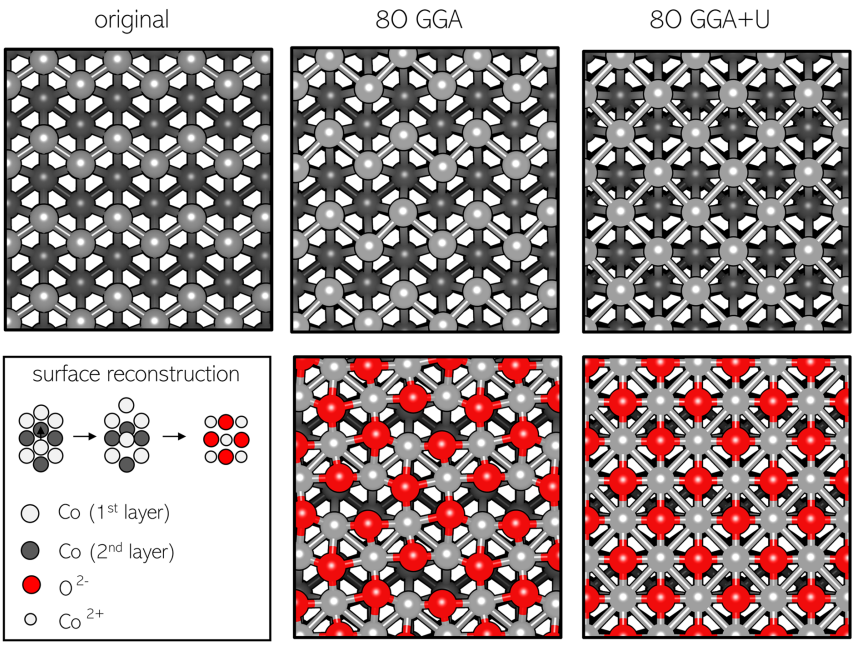

Figure 4.16: Reconstruction of the $(11\bar{2}0)$ surface after the adsorption of a full oxygen monolayer as computed by GGA and GGA+U (U_{eff} = 3.0 eV). **top** panel: Top views of the bare surface and post-adsorption surface with O atoms hidden for clarity; **bottom** panel: suggested surface reconstruction for GGA+U adsorption and top views of systems after the adsorption of a full monolayer of oxygen.

and 0.25 ML) arises from an additional bond that O atoms adsorbed through GGA+U form by longitudinal repositioning of the closest Co surface atom. Experimental study suggests rearrangement of the original $(11\bar{2}0)$ surface towards a centred lattice through the movement of Co atoms and centring of each adsorbed oxygen between four Co atoms.[486] As CoO crystallizes in the rock salt structure, this arrangement is identical with the CoO (100) plane. Although both GGA and GGA+U predict lengthening of the Co-Co bond in the first layer upon the 1.00 ML oxygen adsorption, GGA structural changes are not as prominent and final geometry has only half of the adsorbed O atoms binding to four Co atoms, while the rest form bonds with only three surface atoms. GGA+U geometry, on the other hand, corresponds well to the experimental predictions, and the first layer is completely rearranged to form a perfectly centred lattice, Figure 4.16. This is a direct consequence of the open geometry of the $(11\bar{2}0)$ surface and a zigzag row-like arrangement of Co atoms which ensures enough channel space for complete incorporation of O atoms. The three previous surfaces, on contrary, have close-packed slabs, but remaining $(11\bar{2}1)$ surface could experience similar behaviour.

The $(11\bar{2}1)$ surface showed clear preference of hollow site adsorption, and the effect of increased coverage was therefore continued in this position, Table 4.3. Although the open nature of this surface resembles the stacking of the $(11\bar{2}0)$ surface, Co atoms within a layer are distanced even more, allowing them to line up in a less staggered, almost

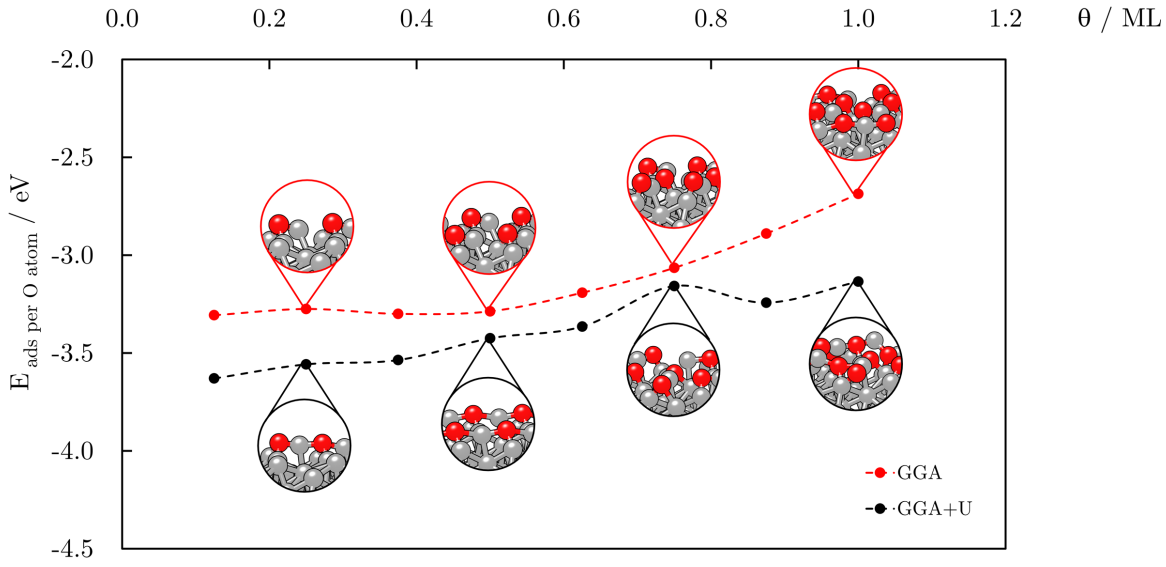

Figure 4.17: Adsorption energies (per O atom) as a function of the oxygen coverage on the $(11\bar{2}1)$ surface as computed by GGA and GGA+U (U_{eff} = 3.0 eV).

flat fashion. Additionally, long distances between the closest Co atoms avert oxygen atoms to form more Co-O bonds by geometrical shifts even when lowered to the level of surface Co atoms. When relaxed by GGA+U, the 0.50 ML coverage led to the adsorbate atoms filling in the gaps in between chains of Co atoms of the second slab layer, and the trend continued for all higher coverages. This is reflected in the dependence of the E_{ads} versus coverage, Figure 4.17, which is not as monotone as for the $(11\bar{2}0)$ surface, but the change in the E_{ads} is still less steep than for the three close-packed surfaces. Induced reconstructions for a full oxygen monolayer are shown in Figure 4.18. 1.00 ML GGA relaxation indicates a minimal surface reconstruction with incorporation of O atoms diagonally in a channel-like fashion. Full oxygen monolayer as optimised by GGA+U, on the other hand, pulls out the top-most Co atoms from the surface, creating atoms isolated enough for the formation of cobalt-oxygen entities containing three oxygen atoms per single Co atom. Co-O formations are stacked such that each pair of closest neighbours shares one oxygen atom.

4.3.4.2 Electronic and magnetic properties

Hybridisation of the electronic bands of oxygen with the bands of the substrate Co atoms leads to significant changes in the electronic properties of the top-most layers. Table 4.5 summarises pre- and post-adsorption work function, Bader charges, and magnetic moments for investigated oxygen coverages on the five inequivalent low Miller-index surfaces of hcp Co.

Relative to the bare surfaces, the work function increases with the oxygen coverage.

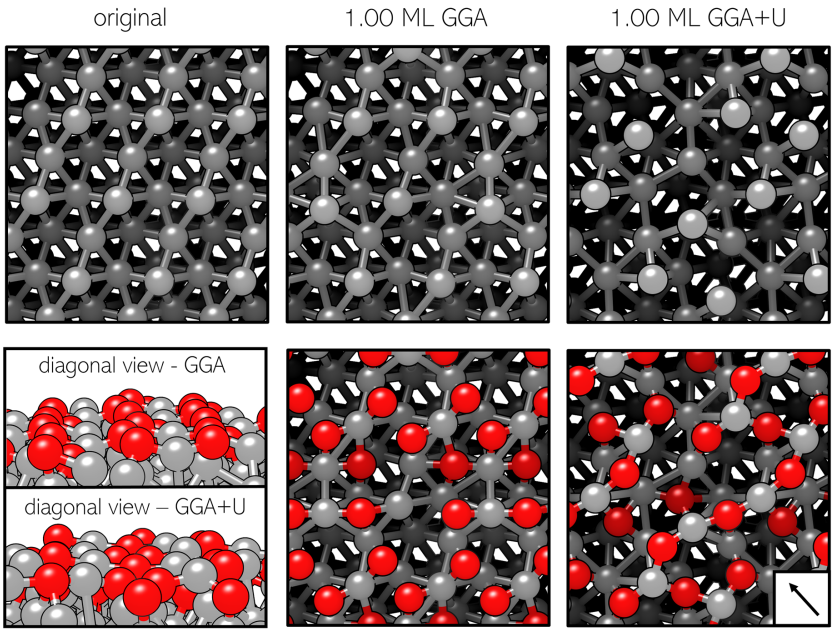

Figure 4.18: Reconstruction of the $(11\bar{2}1)$ surface after the adsorption of a full oxygen monolayer as computed by GGA and GGA+U (U_{eff} = 3.0 eV). **top** panel: top views of the bare surface prior to the adsorption of oxygen, and surfaces after the adsorption of a full oxygen monolayer (O atoms hidden for clarity); **bottom** panel: top views after the adsorption of a full oxygen monolayer with O atoms. In the bottom left, a diagonal side view in the direction of the arrow.

This behaviour is characteristic for the adsorption of oxygen on any metal due to a significant transfer of electrons from surface atoms to the oxygen resulting from differences in the electronegativity: χ_{O} = 3.44 eV and χ_{Co} = 1.88 eV [487], generating large inward pointing surface dipole moment. Exceptions are coverages with induced sub-surface oxygen adsorption at the GGA+U level (coverages above 0.50 ML for all except the (0001) surface), where the work function values oscillate. The differences in the work function of bare surfaces and surfaces with high oxygen coverages are between 1.15 and 2.35 eV, depending on the surface and functional used. This corresponds well to previous experimental results [488] and similar measurements carried out on other transition metals, where metals with higher electronegativity do not experience changes as prominent as cobalt (Rh ∼1.50 eV [489] (χ_{Rh} = 2.28), Pd ∼1.60 eV [490] (χ_{Pd} = 2.20), Ru ∼1.61 eV [485] (χ_{Ru} = 2.20), Pb ∼0.84 eV [491] (χ_{Pb} = 2.33)).

Confirmation of the increase in the work function comes from the Bader analysis. Bader charges of adsorbed O atoms are negative, which implies a charge transfer from the surface to the adsorbate. At low coverages (θ <0.50 ML), the Bader charge of oxygen on the (0001) surface is close to 1.00 e^- per O atom, which is reduced to 0.70/0.69 e^- (GGA/GGA+U) at a full monolayer, indicating the repulsion between oxygen atoms and partial return of the negative charge to the surface. Similar trend is observed for other surfaces when modelled by the GGA functional. GGA+U results show an increase in the

charge transfer to the adsorbates once they are incorporated within the first layer of Co atoms or in the sub-surface levels. The highest jump in the charge of O atoms from 0.99 to 1.28 e^- is recorded for the full monolayer on the $(11\bar{2}0)$ surface as a direct consequence of the rearrangement of surface Co atoms which doubled the number of Co-O bonds.

The magnetisation trends for all surfaces as calculated by GGA and GGA+U are shown in Figure 4.19. The surface Co atoms have larger magnetic moments than the bulk atoms (magnetic moment higher from 0.08 μ_B for the (0001), to 0.37 μ_B for the $(11\bar{2}1)$ surface), which is influenced by the narrowing of the $3d$ electron bands. When oxygen adsorption takes place, an initial enhancement of the magnetic moments of atoms not directly involved in the adsorption process is a result of the oxygen-induced surface expansion. An increase or reduction in the values of magnetic moments of Co atoms that bind oxygen adsorbates is connected to the formation of entities or layers with cobalt oxide characteristics, as illustrated below.

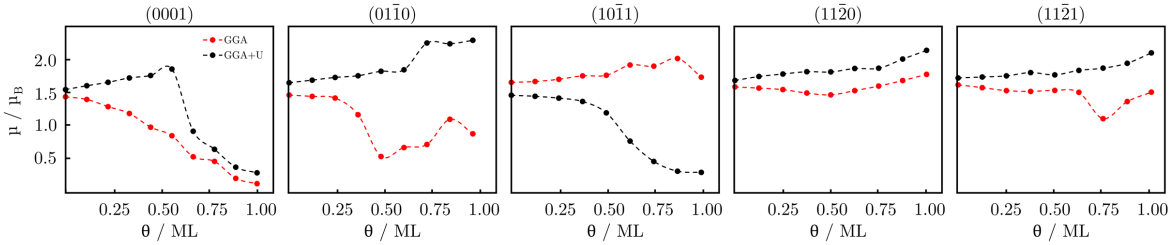

Figure 4.19: Magnetisation (magnetic moment per Co atom of the first surface layer) as a function of the oxygen coverage for five inequivalent low Miller-index hcp Co surfaces.

Previous experimental studies of cobalt oxidation captured the growth of cobalt oxides in the (111) direction on the (0001) surface.[492] Due to the specific arrangement of magnetically active sites, the (111) surface of CoO contains alternating rows of spin-up and spin-down Co atoms, while the (111) surface of Co_3O_4, in addition to alternating rows, also contains full layers of non-magnetic Co (III) ions. Figure 4.20 shows optimised magnetic ordering of the (0001) surface with different oxygen coverages (O atoms adsorbed in hollow H, but results are similar for hollow F) and CoO/Co_3O_4 (111) surfaces as modelled by GGA and GGA+U (U_{eff} = 3.0 eV) with accompanying pDOS. Both GGA and GGA+U relaxed the structures to prolong Co-Co bonds for Co atoms that are interacting with adsorbates and form Co-O entities which have interacting Co atoms pulled above the surface level, as shown in the previous subsection, however, differences in the elongation intensity substantially influence the electronic and magnetic properties of final structures. For coverages under 0.60 ML of oxygen, cobalt atoms within the Co-O formations as optimised by GGA have their bond distances with first- and second-layer Co atoms increased by 4-5 % and 14-16 %, respectively, whereas they couple antiferromagnetically with each other. Co-O bond lengths are, in average, 1.84 Å. The magnetic moment of spin-up surface Co atoms is between 1.27 and 1.38 μ_B, while that of spin-down Co atom reaches 0.80 to 0.95 μ_B. GGA+U optimisation of the same coverages forms Co-O entities

Table 4.5: Changes in the electronic properties for oxidised hcp Co surfaces.

surface/position	θ / ML	work function / eV		Bader charge of O / e^- (per atom)		magnetisation (first layer average) / μ_B		magnetisation of O / μ_B/atom	
		GGA	GGA+U	GGA	GGA+U	GGA	GGA+U	GGA	GGA+U
	0.00	5.49	5.64	-	-	1.71	1.84	-	-
	0.11	5.66	5.96	-0.99	-1.00	1.67	1.91	0.14	0.22
	0.22	5.94	6.08	-0.92	-1.05	1.54	1.97	0.10	0.26
(0001)	0.33	6.01	6.11	-0.91	-1.07	1.41	2.05	0.02	0.28
F (GGA)	0.44	6.33	6.10	-0.87	-1.04	1.17	2.10	0.02	0.28
H (GGA+U)	0.56	6.70	6.21	-0.81	-1.03	1.01	2.21	0.01	0.26
	0.67	6.75	6.69	-0.79	-0.78	0.64	1.09	0.02	0.04
	0.78	7.06	6.88	-0.75	-0.73	0.55	0.77	0.01	0.02
	0.89	7.06	7.26	-0.73	-0.70	0.25	0.45	0.01	0.02
	1.00	7.21	7.05	-0.71	-0.69	0.15	0.35	0.01	0.00
	0.00	5.02	5.27	-	-	1.73	1.99	-	-
	0.08	5.27	5.49	-1.00	-1.00	1.77	2.01	0.17	0.18
	0.13	5.83	5.94	-0.95	-0.93	1.73	2.02	0.11	0.16
	0.25	5.65	5.84	-0.88	-0.92	1.72	2.05	0.03	0.16
	0.38	6.10	6.20	-0.93	-0.89	1.53	2.08	0.08	0.21
$(01\bar{1}0)$	0.42	6.05	6.53	-0.89	-0.88	1.40	1.93	0.14	0.17
H_1	0.50	6.21	6.95	-0.86	-0.79	1.08	2.12	0.10	0.17
	0.58	6.30	6.22	-0.82	-1.09	1.19	2.02	0.09	0.17
	0.63	6.55	5.98	-0.79	-1.17	1.15	2.13	0.09	0.23
	0.75	6.69	6.62	-0.76	-0.90	1.18	2.43	0.11	0.14
	0.83	6.76	6.89	-0.95	-1.19	1.33	2.42	0.19	0.24
	0.88	7.21	6.50	-0.90	-1.17	1.53	2.49	0.11	0.19
	1.00	7.35	6.84	-0.65	-1.17	0.87	2.51	0.20	0.24
	0.00	5.08	5.02	-	-	1.76	1.97	-	-
	0.08	5.11	5.22	-1.10	-1.12	1.73	1.96	0.15	0.13
	0.13	5.62	5.18	-1.06	-1.11	1.73	1.99	0.19	0.20
	0.25	5.42	5.66	-1.06	-1.03	1.69	2.05	0.16	0.21
	0.38	5.72	5.69	-1.06	-1.03	1.61	2.08	0.14	0.20
$(10\bar{1}1)$	0.42	5.78	6.02	-0.99	-1.02	1.67	2.02	0.17	0.17
H_1	0.50	5.83	6.43	-0.99	-1.02	1.34	2.15	0.09	0.27
	0.58	5.90	5.47	-0.93	-1.03	1.19	2.11	0.07	0.20
	0.63	6.46	5.88	-0.88	-1.18	1.05	2.34	0.04	0.20
	0.75	6.69	6.16	-0.84	-1.07	0.59	2.26	0.02	0.15
	0.83	6.89	5.92	-0.79	-1.18	0.60	2.35	0.04	0.21
	0.88	6.97	5.83	-0.82	-1.18	0.47	2.47	0.04	0.23
	1.00	7.23	6.23	-0.91	-1.12	0.53	2.11	0.11	0.04
	0.00	3.93	3.80	-	-	1.88	2.00	-	-
	0.13	3.84	4.25	-1.09	-0.99	1.86	2.07	0.16	0.24
	0.25	3.97	4.51	-1.08	-0.97	1.84	2.12	0.16	0.21
$(11\bar{2}0)$	0.38	4.00	4.91	-1.07	-0.97	1.77	2.16	0.14	0.19
B_1	0.50	4.09	5.18	-1.07	-0.96	1.74	2.19	0.15	0.19
	0.63	4.26	5.32	-1.10	-1.19	1.82	2.26	0.20	0.19
	0.75	4.41	5.22	-1.09	-1.21	1.90	2.30	0.21	0.18
	0.88	4.20	5.51	-1.09	-1.24	2.00	2.39	0.25	0.19
	1.00	4.74	5.00	-1.08	-1.28	2.11	2.56	0.30	0.21
	0.00	3.55	3.57	-	-	1.96	2.09	-	-
	0.13	3.88	3.68	-1.03	-1.10	1.91	2.10	0.17	0.22
	0.25	3.90	3.93	-1.02	-1.10	1.86	2.17	0.16	0.19
$(11\bar{2}1)$	0.38	4.09	4.07	-1.02	-1.09	1.84	2.19	0.17	0.18
H_1	0.50	4.34	4.04	-1.01	-1.10	1.86	2.14	0.19	0.16
	0.63	4.60	4.27	-0.98	-1.14	1.83	2.22	0.20	0.21
	0.75	4.83	4.75	-0.89	-1.11	1.35	2.26	0.08	0.25
	0.88	4.76	4.42	-0.94	-1.14	1.66	2.35	0.18	0.26
	1.00	4.69	4.21	-0.96	-1.17	1.83	2.52	0.19	0.24

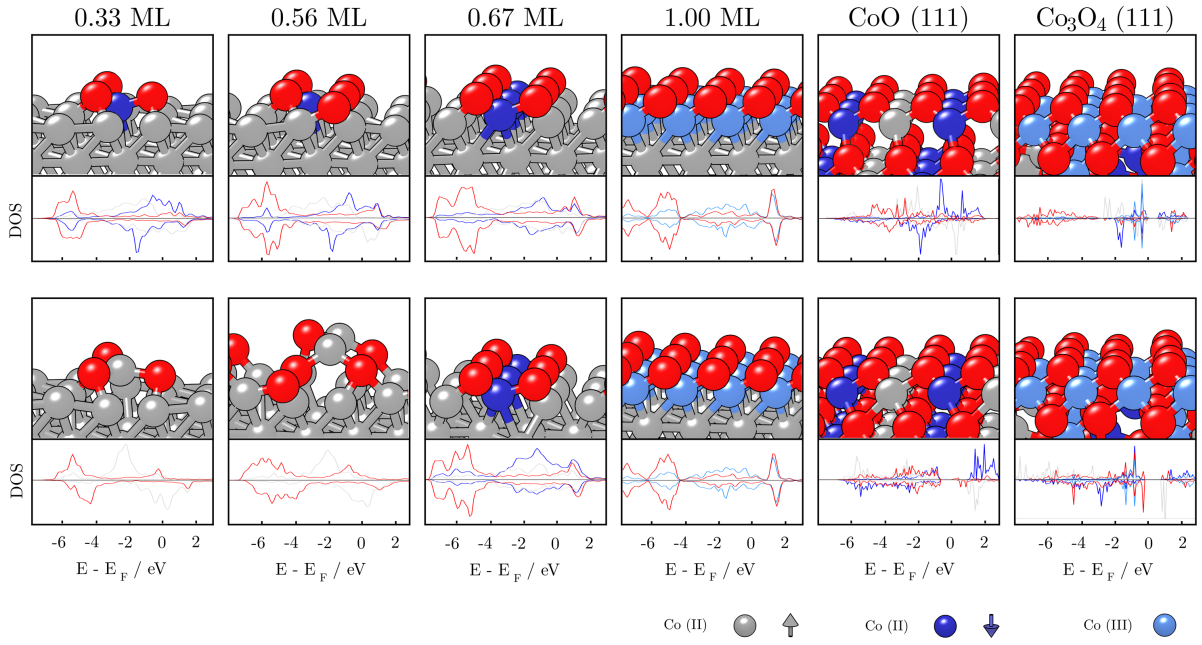

Figure 4.20: Optimised magnetic orderings for the 0.33, 0.56, 0.67, and 1.00 ML oxygen coverages in hollow H position on the (0001) surface as computed by GGA (**top** panel) and GGA+U (**bottom** panel, U_{eff} = 3.0 eV); orderings of cobalt oxide (111) surfaces* are provided on the right. Below structures, pDOS in a.u. (range -2.5 to 2.5 states/eV) for $3d$ orbitals of one Co atom form the Co-O island and surface layers (if distinguishable), and each of the Co (II) and Co (III) distinct atoms from cobalt oxides are provided, together with $2p$ orbitals of O atoms (scaled as $1/N(\text{O})$). Grey, dark blue, and light blue spheres represent Co (II)-up spin, Co(II)-down spin, and Co (III) atoms, respectively, with oxygen shown as red spheres. All axes are the same for all the graphs. *CoO and Co_3O_4 surfaces are shown in oxygen terminations for convenience of representation.

with Co-Co bonds of extracted Co atom and first/second layer Co atoms prolonged by 4-12 % and 48-59 %, respectively, without changing the ferromagnetic nature of surface atoms. The average length of Co-O bond is 1.97 Å. Unlike GGA, GGA+U predicts a slight increase of the magnetic moment of Co atoms that bind to oxygen, with magnetic moments in the range of 1.98 to 2.37 μ_{B}. This corresponds better to the experimental suggestions of Co-O formations having CoO character with an expanded intralayer lattice parameter [493], where Co-O distance in the CoO (111) surface is approximately 1.85 Å and magnetic moment of Co atoms ranges from 2.30 to 2.60 μ_{B}. For medium coverages (0.68 - 0.78 ML), both GGA and GGA+U give similar geometries with oxygen atoms adsorbed such that three aligned surface Co atoms each form bonds with three O atoms. Induced elongations in Co-Co bonds of interacting cobalt atoms and cobalt atoms from the first and second layer are 2.0-3.5 % and 10.0-11.5 %, respectively, for both functionals. Predicted magnetic coupling is also in accord - Co atoms bonded to three O atoms have spin-down orientation, whilst the rest are oriented with a spin-up. The major difference is in the final magnetic moments; while GGA predicts spin-down moments to drop to

0.02-0.03 μ_B and spin-up moments between 0.69 and 1.18 μ_B, GGA+U calculates considerably higher values of 0.50-0.68 μ_B and 1.20-1.85 μ_B, respectively. Co-O distances correspond well between the two methods, with values in the range of 1.79 and 1.85 Å. Despite the spin-down orientation of the three double-interacting Co atoms, their low magnetic moments and d-electron pDOS resemble octahedral Co (III) ions of Co_3O_4 the most. Finally, for coverages above 0.80 ML, obtained values, including bond lengths, pDOSe, magnetic moments, and magnetic orderings correspond rather well for GGA and GGA+U. Oxygen atoms adsorb symmetrically and, for the full monolayer, each Co atom of the first layer experiences the same structural change; no elongation of Co-Co bonds is observed within the layer, while the bonds between the Co atoms of the first two layers increase by 5.12-5.60 %. Full first layer is predicted to have minimal magnetisation of 0.15/0.35 μ_B (GGA/GGA+U) with the ferromagnetic coupling. The main $2p$ O and $3d$ Co hybridisation peaks are situated between -0.5 and -2.0, and -4.0 and -5.0 eV, which is consistent with the non-magnetic Co (III) ions of Co_3O_4. Two steeper drops in the trends of magnetisation per Co atom of the first layer (seen between 0.55 and 0.67 ML, and between 0.76 and 0.88 ML, Figure 4.19) can now be assigned to the formation of extended area of Co-O aggregates with cobalt oxide properties. Changes in the magnetic moments of second layer Co atoms are within ±0.20 μ_B for any oxygen coverage. Magnetic orderings opposite of the ones optimised by GGA/GGA+U have been forced onto the Co atoms and computed to be significantly higher in energy.

Figure 4.21 depicts optimised magnetic orderings and pDOS of the moderate and high oxygen coverages on the $(01\bar{1}0)$ surface as modelled by GGA and GGA+U. Both functionals predict no changes in the ferromagnetic ordering with the increase in the coverage of up to and including 0.50 ML. For the 0.50 ML coverage, magnetic moments of surface Co atoms in the higher row of the first layer are reduced to 0.73 μ_B and those of Co atoms in the lower row to 1.38-1.43 μ_B when optimised by GGA, while relaxation with GGA+U maintains magnetic moments in the range of 2.02-2.25 μ_B. There is also a minimal increase in the Co-Co nearest neighbour distances by 0.8 to 1.6 %, and average bond length of a Co-O bond is 1.80 Å for both functionals. Higher coverage sub-surface adsorption as modelled by the implementation of the Hubbard U parameter induces significant changes in the magnetic moments and magnetic coupling of the top-most Co atoms. While GGA optimised a ferromagnetic ordering with magnetic moments similar to those at lower coverages, namely 0.94 and 1.43 μ_B, antiferromagnetic coupling was achieved through the GGA+U relaxation with increased magnetic moments of 2.33-2.89 μ_B and Co-O bond lengths of 1.81 to 1.89 Å for the on-surface and 2.11-2.16 Å for the sub-surface adsorbed O atoms. At a full monolayer, GGA and GGA+U final structures show substantially different arrangements. The former assigned antiferromagnetic coupling with magnetic moments of 1.22 μ_B to top-most Co atoms and ferromagnetic coupling with magnetic moments of 0.62 μ_B for the next highest row of Co atoms. Co-O distances are 2.00-2.01 Å within the layer of O atoms incorporated between the Co rows, and 1.73-1.78 Å for the bonds formed between the on-surface adsorbed O atoms and underlying Co atoms. GGA+U, on the other hand, predicts structural reconstruction through the sub-surface adsorption, which leads to a combination of ferromagnetic and antiferromagnetic

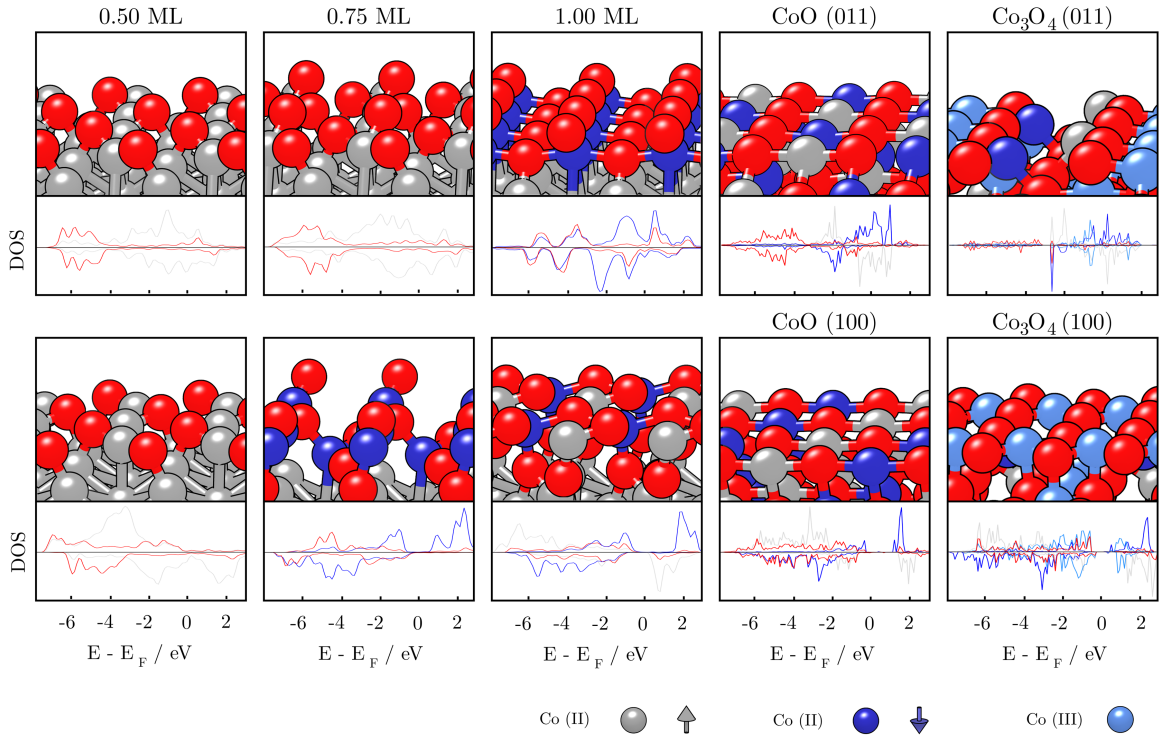

Figure 4.21: Optimised magnetic orderings for the 0.50 ML, 0.75 ML, and 1.00 ML oxygen coverages in hollow position on the $(01\bar{1}0)$ surface as computed by GGA (**top** panel) and GGA+U (**bottom** panel, $U_{\text{eff}} = 3.0$ eV); orderings of cobalt oxide (011) and (100) surfaces* are provided on the right. Below structures, pDOS in a.u. (range -2.5 to 2.5 states/eV) for $3d$ orbitals of magnetically distinguishable surface Co atoms, together with $2p$ orbitals of O atoms (scaled as $1/N(\text{O})$). Grey, dark blue, and light blue spheres represent Co (II) up spin, Co(II) down spin, and Co (III) atoms, respectively, with oxygen shown as red spheres. All axes are the same for all the graphs. *CoO and Co_3O_4 surfaces are shown in oxygen terminations for convenience of representation.

surface Co states. Magnetic moments are between 2.28 and 2.90 μ_{B}, while Co-O bonds vary between short bonds of ∼1.90 Å and long Co-O distances of 2.11-2.14 Å. While the row-like stacking of oxygen atoms at a 1.00 ML coverage relaxed by GGA reminds of the (011) surface of cobalt oxides, surface rearrangement triggered by the addition of Hubbard parameter is much more similar to the CoO (100) surface. Although neither magnetic ordering exactly coincides with that of the CoO surfaces, the difference in the optimised and oxide antiferromagnetic orderings is less than 0.08 eV per Co atom. There are no experimental evidences of the orientational growth of cobalt oxides on the $(01\bar{1}0)$ hcp Co surface.

Oxidation of the $(10\bar{1}1)$ surface was also not as yet probed experimentally. Geometry of this surface is, as previously shown, the most similar to the geometry of the $(01\bar{1}0)$ surface, which could implicate resemblance in the effect of oxygen adsorbates on the

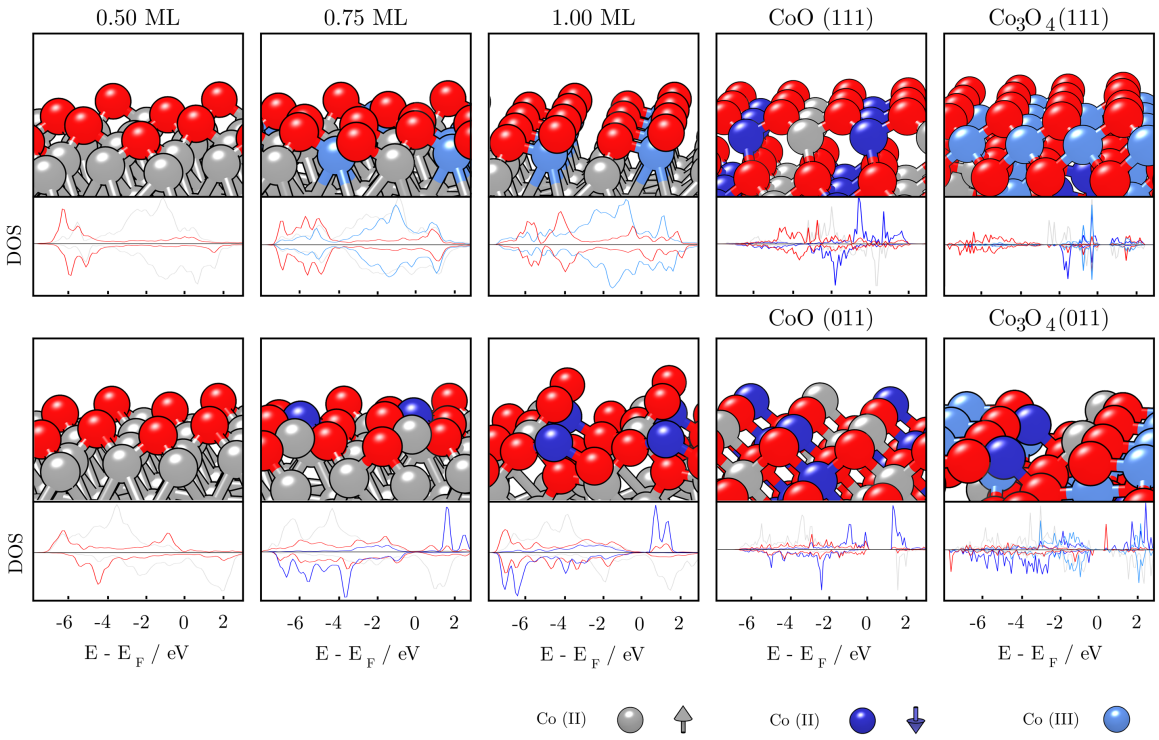

Figure 4.22: Optimised magnetic orderings for the 0.50 ML, 0.75 ML, and 1.00 ML oxygen coverages in hollow position on the $(10\bar{1}1)$ surface as computed by GGA (**top** panel) and GGA+U (**bottom** panel, U_{eff} = 3.0 eV); orderings of cobalt oxide (111) and (011) surfaces* are provided on the right. Below structures, pDOS in a.u. (range -2.5 to 2.5 states/eV) for $3d$ orbitals of magnetically distinguishable surface Co atoms, together with $2p$ orbitals of O atoms (scaled as $1/N(\text{O})$). Grey, dark blue, and light blue spheres represent Co (II) up spin, Co(II) down spin, and Co (III) atoms, respectively, with oxygen shown as red spheres. All axes are the same for all the graphs. *CoO and Co_3O_4 surfaces are shown in oxygen terminations for convenience of representation.

electronic structure. Figure 4.22 shows optimised magnetic ordering of the $(10\bar{1}1)$ surface with different oxygen coverages as modelled by GGA and GGA+U (U_{eff} = 3.0 eV) with accompanying pDOS. For coverages under and including half a monolayer, there are no changes in the ferromagnetic coupling of surface Co atoms and difference in the functionals can be traced solely to the increased values of magnetic moments caused by the addition of the Hubbard U parameter. Calculated magnetic moments are in the 1.20-1.79 μ_{B} range for GGA, and in the 1.91-2.23 μ_{B} range for GGA+U. For coverages above 0.50 ML, magnetic moments of the top-most Co atoms start to drop significantly, but maintain the ferromagnetic ordering when relaxed by GGA. At 0.75 ML, half of the surface atoms have magnetic moments between 0.78 and 1.42 μ_{B}, whereas the other half is almost non-magnetic with an average value of 0.17 μ_{B}. Once a full monolayer is reached, magnetic moments of all surface atoms reduce below 0.68 μ_{B}. GGA+U results, on the other hand, captured changes in the magnetic coupling of certain Co surface atoms for coverages

above 0.50 ML, with a slight increase in the magnetic moments to values of 2.25-2.66 μ_B. At a full monolayer coverage, half of the surface atoms have antiferromagnetic coupling and magnetic moments of ~2.38 μ_B, while the rest experience ferromagnetic coupling with reduced magnetic moments, 0.83-1.55 μ_B. This drop in magnetisation could be a first indication of the Co_3O_4 formation. Low magnetic moments achieved through the 1.00 ML GGA relaxation indicate oxidation of surface Co atoms to a non-magnetic Co(III) state; this non-magnetic layer of Co atoms is characteristic for the (111) Co_3O_4 surface. Arrangement of Co and O atoms also coincides with the (111) oxide growth. Reconstruction of the initial row-like geometry of the $(10\bar{1}1)$ surface through the GGA+U full monolayer adsorption points out that the orientation of the cobalt oxide growth would more likely be CoO (011) or CoO (100) surface. When compared to the $(01\bar{1}0)$ surface, because of the prolonged Co-Co distances, further reconstruction towards the CoO (100) surface is not expected since already at 1.00 ML some oxygen atoms are unable to form bonds with more than two surface Co atoms. Therefore, (011) is suggested as the orientation of growth of cobalt oxides on the $(10\bar{1}1)$ hcp Co surface.

Experiments suggest (100) CoO directional growth on the $(11\bar{2}0)$ surface of hcp Co.[486] This CoO surface is characterised by diagonally alternating rows of spin-up and spin-down Co atoms intersected by rows of oxygen atoms. Co_3O_4 (100) surface additionally has layers of intersecting Co(III) and O atoms. Figure 4.23 shows optimised magnetic ordering of the $(11\bar{2}0)$ surface with different oxygen coverages (O atoms adsorbed in the B_1 position) and CoO/Co_3O_4 (100) surfaces as modelled by GGA and GGA+U (U_{eff} = 3.0 eV) with accompanying pDOS. As showed previously, addition of the Hubbard U parameter induces changes in structural relaxations, and this is significantly more prominent during the adsorption of oxygen on the open $(11\bar{2}0)$ surface and it is reflected in the final magnetic and electronic properties. Coverages under 0.50 ML are characterised by a full ferromagnetic ordering, with the magnetic moments of Co atoms directly interacting with the adsorbed oxygen increased by 0.05-0.20 μ_B compared to the bare surface for both GGA and GGA+U functionals. At a coverage of 0.50 ML, two surface Co atoms showed antiferromagnetic coupling with magnetic moments of 1.90 μ_B when optimised by GGA+U. This behaviour was not observed within GGA, even if the antiferromagnetic ordering was initiated before the relaxation. Further increase in the oxygen coverage showed preference of ferromagnetic coupling, with magnetic moments reaching values between 1.90 and 2.15 μ_B for GGA, and between 2.10 and 2.45 μ_B for GGA+U. However, structures where Co atoms have alternating ferro- and antiferromagnetic coupling were successfully optimised with GGA+U, and obtained energies were higher by less than 0.50 eV (~0.015 eV per Co atom) when compared to fully ferromagnetic geometries. Once the full coverage is reached, reconstruction occurs and antiferromagnetic ordering identical to the one of the (100) CoO surface is achieved through the GGA+U relaxation, and calculated magnetic moments of both spin-up and spin-down Co atoms are 2.20-2.60 μ_B. GGA, on the other hand, triggers atomic rearrangement of lower intensity, resulting in the ferromagnetic coupling and magnetic moments between 2.07 and 2.15 μ_B. Co-O bonds are, owing to the GGA+U rearrangements, formed between each O atom and four surrounding Co atoms with bond lengths of 2.05-2.11 Å, well within the average 2.08 Å

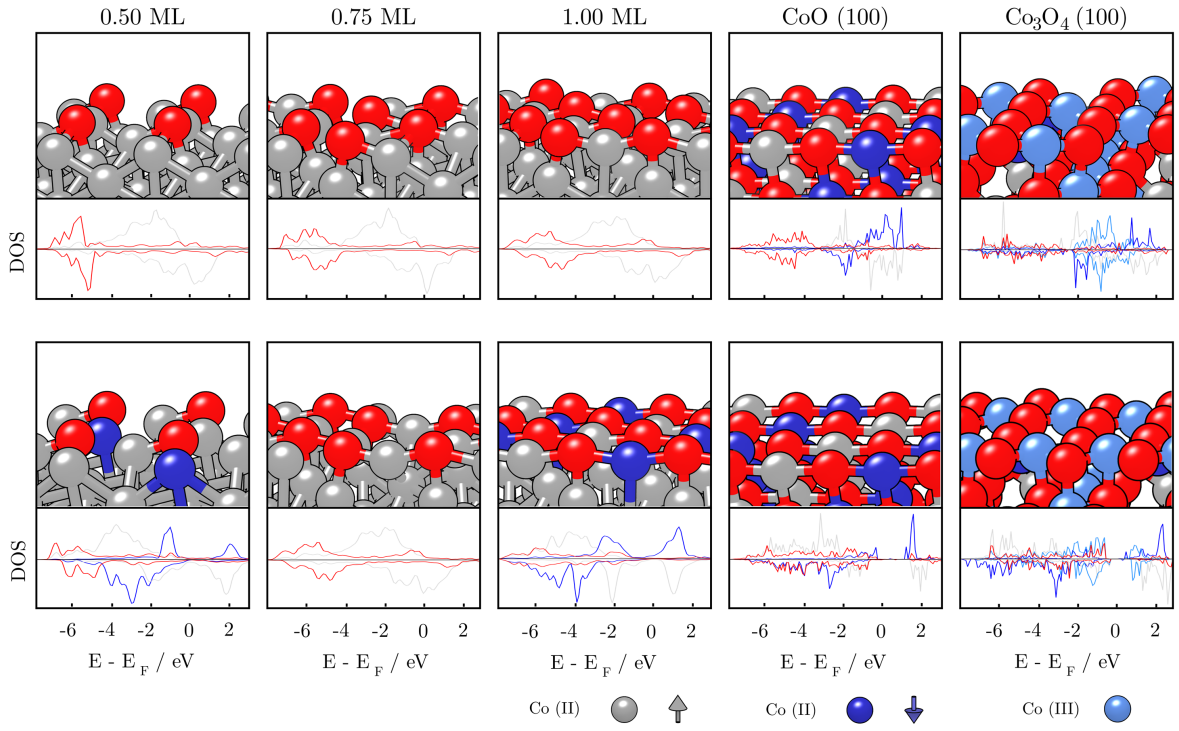

Figure 4.23: Optimised magnetic orderings for the 0.50 ML, 0.75 ML, and 1.00 ML oxygen coverages in bridge B_1 position on the $(11\bar{2}0)$ surface as computed by GGA (**top** panel) and GGA+U (**bottom** panel, U_{eff} = 3.0 eV); orderings of cobalt oxide (100) surfaces* are provided on the right. Below structures, pDOS in a.u. (range -2.5 to 2.5 states/eV) for $3d$ orbitals of magnetically distinguishable surface Co atoms, together with $2p$ orbitals of O atoms (scaled as $1/N(\text{O})$). Grey, dark blue, and light blue spheres represent Co(II) up spin, Co(II) down spin, and Co(III) atoms, respectively, with oxygen shown as red spheres. All axes are the same for all the graphs. *CoO and Co_3O_4 surfaces are shown in oxygen terminations for convenience of representation.

Co-O bond of the CoO (100) surface. When relaxed by GGA, O atoms bonded with four Co atoms form two shorter (1.93-1.97 Å) and two longer bonds (2.25-2.37 Å). Growth of Co_3O_4 was not observed and adsorption within the full monolayer of oxygen on the $(11\bar{2}0)$ surface.

The oxidation of the $(11\bar{2}1)$ surface of hcp Co was not a topic of any scientific publication, either experimental or computational. Figure 4.24 shows optimised magnetic ordering of the $(11\bar{2}1)$ surface with different oxygen coverages (O atoms adsorbed in the H_1 position) as modelled by GGA and GGA+U (U_{eff} = 3.0 eV) with accompanying pDOS. The $(11\bar{2}1)$ surface is structurally the most open low Miller-index hcp Co surface, resulting in a minimal change of magnetic moments for oxygen coverages below 0.50 ML and a ~2.5-4.0 % enhancement of Co-Co bonds within a chain-like composition for those Co atoms that directly interacted with the adsorbates. Magnetic moments of surface Co atoms were lowered by less than 0.05 μ_B and they maintained ferromagnetic ordering for

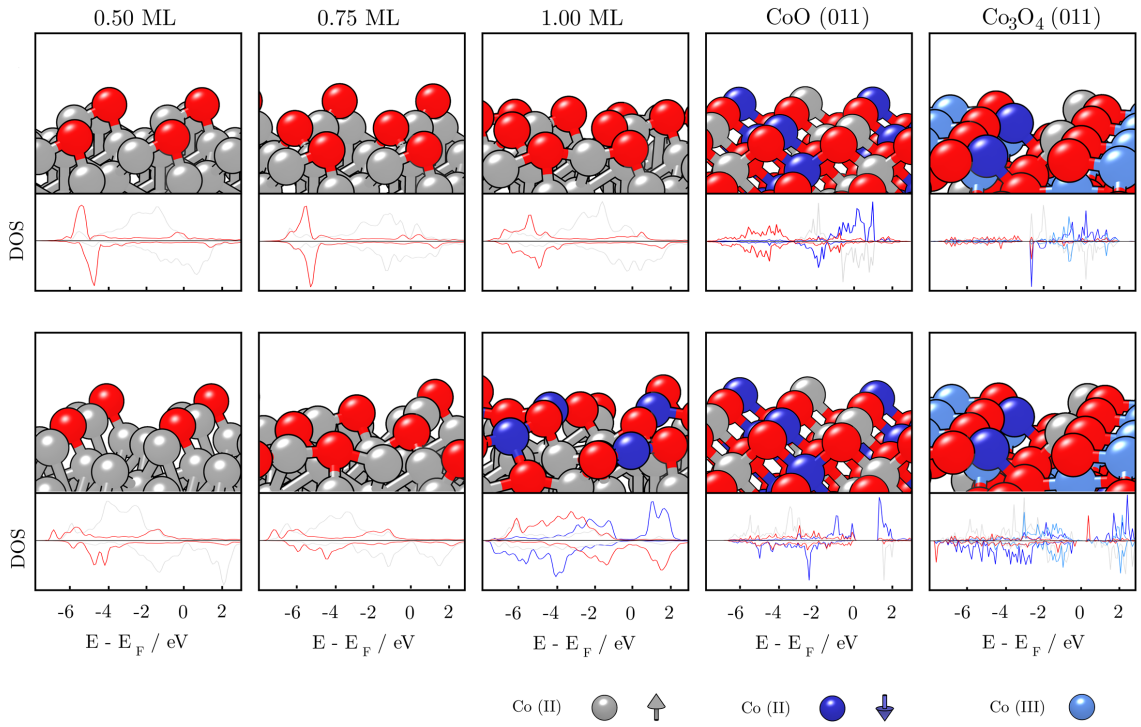

Figure 4.24: Optimised magnetic orderings for the 0.50, 0.75, and 1.00 ML oxygen coverages in hollow H_1 position on the $(11\bar{2}1)$ surface as computed by GGA (**top** panel) and GGA+U (**bottom** panel, U_{eff} = 3.0 eV); orderings of cobalt oxide (011) surfaces* are provided on the right. Below structures, pDOS in a.u. (range -2.5 to 2.5 states/eV) for $3d$ orbitals of magnetically distinguishable surface Co atoms, together with $2p$ orbitals of O atoms (scaled as $1/N(\text{O})$). Grey, dark blue, and light blue spheres represent Co(II) up spin, Co(II) down spin, and Co(III) atoms, respectively, with oxygen shown as red spheres. All axes are the same for all the graphs. *CoO and Co_3O_4 surfaces are shown in oxygen terminations for convenience of representation.

both GGA and GGA+U. From 0.50 ML to 0.75 ML, magnetic moments started gradually decreasing when systems were relaxed with GGA, and, at 0.75 ML, four out of eight surface Co atoms reached values between 0.67 and 0.89 μ_{B}, with the magnetic moments of the remaining atoms in the 1.37-1.81 μ_{B} range, all still ferromagnetic. At higher coverages of 0.88 and 1.00 ML, the ferromagnetic coupling gave moments of 1.62-2.07 μ_{B} for the top-most Co atoms. GGA+U, on the other hand, predicted a steady increase in the magnetic moments of all surface Co atoms as the adsorption proceeded from 0.50 ML to higher coverages. At 0.50 ML and 0.75 ML, all surface atoms were ferromagnetic, with the lowest moments in the 2.04-2.16 μ_{B} range, and the highest in the 2.21-2.32 μ_{B} range. When a full monolayer was adsorbed, half of the surface atoms experienced antiferromagnetic coupling with magnetic moments of 2.49-2.58 μ_{B} and lengths of Co-O bonds of 1.85-1.95 Å with the O atoms adsorbed at the level of the first layer, and 2.01-2.05 Å with the O atoms adsorbed in the openings between the slab layers. As the construction of the $(11\bar{2}1)$ surface is even more open than that of the $(11\bar{2}0)$ surface, despite the structural similarity, rearrangement to the CoO (100) like geometry is energetically not feasible.

CoO (011) surface has features that correspond to those of the (100) surface, with each Co atom binding only two closest O atoms within the same layer and similar diagonal alternations of antiferromagnetic and ferromagnetic orderings. Magnetic moments of Co atoms are in the 2.50-2.61 μ_B range, with Co-O bonds of 2.07-2.11 Å within a layer and 2.02-2.05 Å between the two layers. Both structural and electronic properties of the full oxygen monolayer on the $(11\bar{2}1)$ surface as relaxed by GGA+U resemble the (011) CoO surface to a reasonable extent. It is also unlikely that an increased number of O atoms would eventually lead to the CoO (100)-like surface reconstruction as its layers are built up from the same share of Co and O atoms, while the rearrangement was not achieved with a full oxygen monolayer adsorbed on the $(11\bar{2}1)$ surface. Therefore, (011) surface is suggested through this work as a direction of growth of cobalt (II) oxide on the hcp Co $(11\bar{2}1)$ surface. Co_3O_4 was, as in the case of the $(11\bar{2}0)$ surface, not initiated at tested coverages.

Altogether, inclusion of the Hubbard U parameter showed moderate changes to the structural and electronic properties of hcp Co surfaces with low oxygen coverages when compared to GGA functional, while in the case of high coverages that could potentially initiate oxide formation significant differences between the two methods were observed. For the two surfaces that have been experimentally probed, namely the (0001) and $(11\bar{2}0)$ surface, results obtained with GGA+U are more consistent with the proposed directions of oxide growth and it is therefore likely that the directional growth for the rest of the surfaces predicted on the GGA+U level is also more reliable. Nevertheless, further experimental studies are necessary to confirm the accuracy of the obtained results.

4.3.4.3 NP morphology

Figure 4.25 displays the progression of Wulff morphology from bare crystallites over low (∼0.11 ML) and moderate (∼0.50 ML) to full (1.00 ML) oxygen coverages as predicted by GGA and GGA+U. Structures of nanocrystals for 0.11 and 0.50 ML coverages show a high level of resemblance between the two methods, in agreement with minimal differences in calculated structural and electronic properties. At 0.11 ML, the area of the $(10\bar{1}1)$ surface, which has the highest affinity for oxygen adsorption as shown through the most negative adsorption energies, increases at the expense of the $(11\bar{2}1)$ surface, while the area of the $(01\bar{1}0)$ surface increases at the expense of the $(11\bar{2}0)$ surface. This is in accord with the trend of single oxygen adsorption energies. Further adsorption favours continued expenditure of the $(01\bar{1}0)$ surface and reoccurrence of the $(11\bar{2}1)$ surface. By reaching the full monolayer, GGA and GGA+U predict substantially different surface geometries, with the GGA+U sub-surface incorporation of oxygen within the $(01\bar{1}0)$ and $(10\bar{1}1)$ surfaces being the most prominent distinction. Final GGA and GGA+U morphologies at 1.00 ML accordingly demonstrate apparent dissimilarities; the former consists of high shares of the $(10\bar{1}1)$ and $(11\bar{2}0)$ surfaces with a moderate appearance of the (0001) and $(01\bar{1}0)$ surface. GGA+U, on the other hand, shows dominant growth of the $(01\bar{1}0)$ and $(10\bar{1}1)$ surfaces with decreased (0001) truncations.

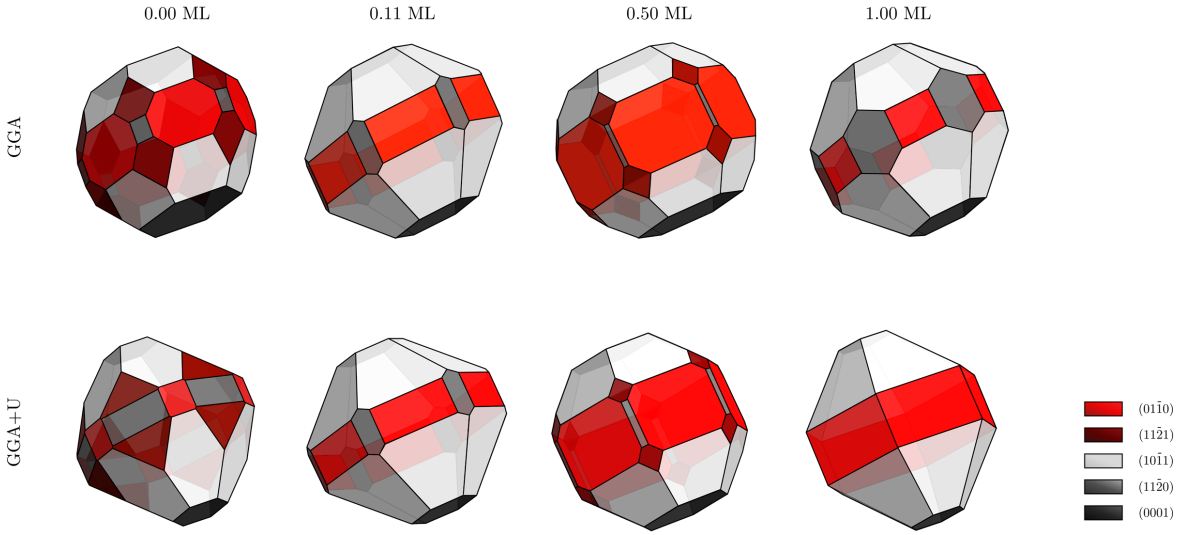

Figure 4.25: Wulff crystal morphologies for hcp Co NPs with ∼0.11, ∼0.50, and 1.00 ML of oxygen as predicted by **top** panel: GGA and **bottom** panel GGA+U (U_{eff} = 3.0 eV).

4.3.4.4 Surface oxidation phase diagrams

Trustworthy description of a more realistic situation can be obtained by placing surfaces in contact with the environment in which oxygen is represented by its gaseous thermodynamic properties. To acquire that, it is necessary to combine adsorption energy calculations with a distinctive feature which includes, for example, pressure and temperature of the gas - chemical potential of oxygen, μ_{O}. Once the chemical potential is implemented, gaseous conditions are well represented and comparison of systems oxidised at different stages can be provided through the surface phase diagrams. This is the general idea behind the *ab initio* atomistic thermodynamics: to use DFT results in calculation of appropriate thermodynamic functions like the Gibbs free energy and employ it in the prediction of the system behaviour.

Gibbs free energy plots have been constructed for five inequivalent low Miller-index hcp Co surfaces for a wide range of μ_{O}, from -6.0 to 0.0 eV, and shown for the (0001) surface (GGA+U) in Figure 4.26. Scale of pressure ratio (with p_0 = 1 bar) for ∼36-37 °C has been provided, as well as the conditions of the μ_{O} for the formation of the two cobalt oxides, namely CoO at -2.22 eV and Co_3O_4 at -0.45 eV. Under these conditions the following reactions occur:

$$\text{Co} + 1/2\text{O}_2 \rightleftarrows \text{CoO} \tag{4.18}$$

$$3\text{CoO} + 1/2\text{O}_2 \rightleftarrows \text{Co}_3\text{O}_4. \tag{4.19}$$

From a thermodynamics point of view, the most stable surface composition in equilibrium with the oxygen environment under particular conditions of T and p is determined by

the minimum energy over possible system states. Hence, an adsorbate phase will become more stable than the reference metal surface when its Gibbs free energy at a specific μ_O becomes lower than that of the bare surface. If there are multiple possible phases, the one with the lowest Gibbs free energy occurs. Finally, for $\mu_O > \Delta H_f$ (MO_x, T = 0 K)/x, the bulk oxide will always be the most stable phase.

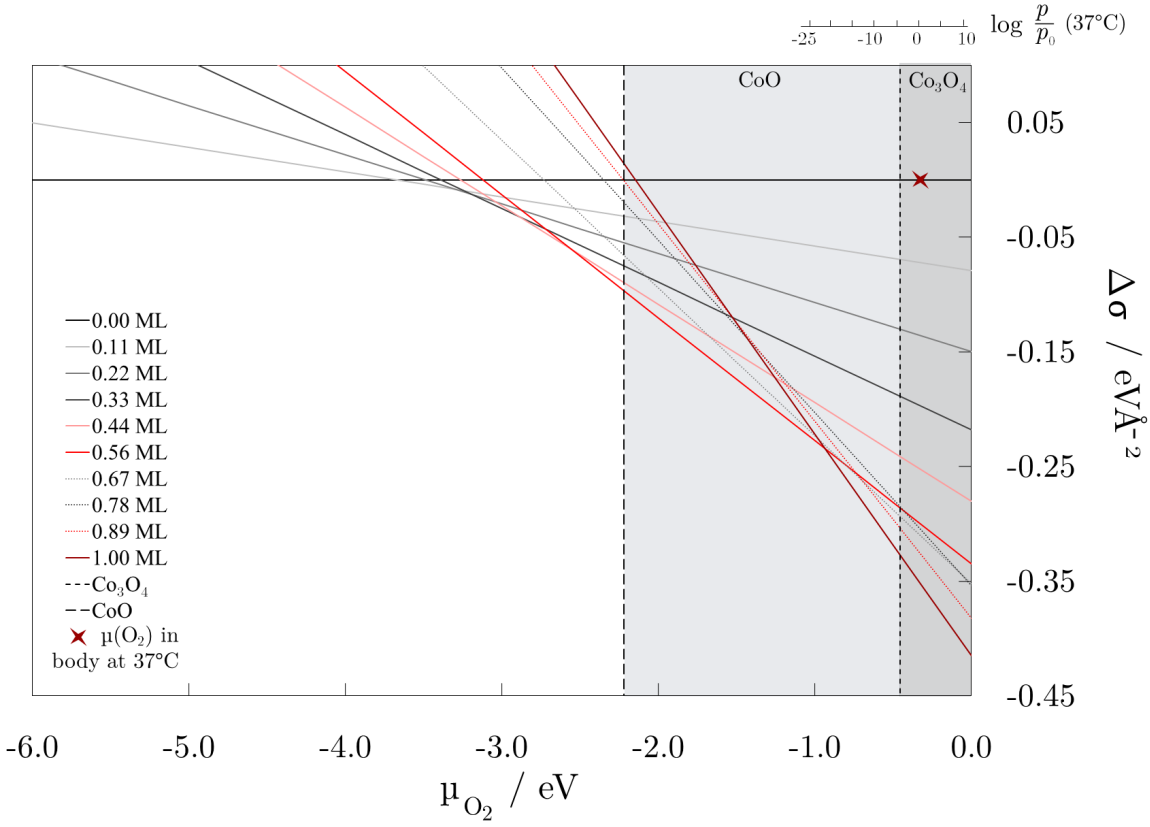

Figure 4.26: Gibbs free energy plot for the (0001) surface with various oxygen coverages as calculated by GGA+U (U_{eff} = 3.0 eV). Corresponding pressure scale at body temperature of ~37 °C is indicated. Long and short dashed lines denote potentials of formation of bulk cobalt oxides CoO and Co_3O_4, respectively.

Considering the Gibbs free energy plot of the (0001) surface, the bare surface will appear at negative potentials up to ~-3.70 eV. Upon further increase of μ_O, oxygen overlayers become progressively more favourable, with coverage of 0.11 ML dominating up to -3.45 eV, coverage of 0.22 ML between -3.45 and -3.35 eV, and coverage of 0.33 ML between -3.35 and -3.00 eV, after which the most stable coverage is that of 0.44 ML. From ~-2.70 eV to the boundary where cobalt oxides are formed, a coverage of 0.56 ML dominates. Around the upper limit of μ_O = -2.22 eV, oxygen overlayers may exist as metastable structures, whereas CoO is the thermodynamically most stable phase. Other surfaces follow the same pattern, with the bare surfaces persisting at low chemical potentials (up to -4.00/-3.50 eV), through low oxygen coverages dominating at moderately

negative μ_O (from -3.50 to -2.50 eV) and high coverages spanning to the narrowest potential range (from -2.50 to -2.22 eV), leading to the formation oxides at potentials above -2.22 eV.

Surface phase diagrams are represented as a function of T and $\log_p$ for all surfaces in Figure 4.27 as obtained by GGA and GGA+U simulations. GGA and GGA+U phase diagrams of the (0001) surface are fairly similar, corresponding to the resemblance in the structural and electronic properties. Formation of the CoO is expected for the 0.62-0.77 ML coverages for both functionals, which agrees well with the analysis of magnetic moments where antiferromagnetic state of Co atoms interacting with adsorbates at 0.66 ML coverage was coupled to the formation of the (111) surface of CoO. Potential of the Co_3O_4 formation lies within the full oxygen coverage area, in agreement with predicted magnetic structure. For the $(01\bar{1}0)$ surface, GGA results imply formation of CoO at moderate ∼0.50 ML coverage, while GGA+U predicts it for a full monolayer. Magnetic and structural analysis of GGA/GGA+U results also confirms this through the difference in the expected directional growth of cobalt oxides for the $(01\bar{1}0)$ surface. This also applies to the difference in the GGA and GGA+U geometries of the $(10\bar{1}1)$ surface. Appearance of the antiferromagnetism for a share of surface Co atoms interacting with adsorbed oxygen at coverages above 0.85 ML when modelled by GGA+U can now be ascribed to the formation of cobalt (II) oxide. The $(11\bar{2}0)$ and $(11\bar{2}1)$ surfaces showed a substantial level of structural sensibility on the choice of the exchange functional, however, as high coverages are needed for oxide formation on those surfaces, corresponding areas on the phase diagrams are similar and CoO is expected to form deeply in the full monolayer stability zone. This is also the case for the further oxidation of CoO to Co_3O_4 on all five hcp Co surfaces. Since a full monolayer of oxygen was the highest coverage included, the exact coverage necessary for such transition remains a topic for future studies.

Figure 4.27 also depicts surface phase diagrams for the five surfaces after the inclusion of oxygen vibrational energy as calculated by GGA+U. Inclusion of vibrational corrections shows noticeable effects in the conditions at which specific coverages would appear as the most stable phases, whereas minor alternations can be seen in the ratios of their stability zones. Transitions between different phases are shifted to lower temperatures by ∼100 K.

These results correspond well to the experimentally tested formation of cobalt oxides [492, 494] and temperatures obtained for the Co_3O_4 →CoO conversion. For the (0001) surface, spectroscopic methods revealed that high oxygen exposure (p_{O_2} = 0.5 Torr) at 295 K tends to form the spinel oxide, but the situation changes in favour of CoO when annealed to 700 K; at low exposures CoO is formed even at 295 K.[494] Meanwhile, for the $(11\bar{2}0)$ surface oxidation occurs at 170-230 K, with CoO intensities growing until 450 K.[488] Further studies provide similar temperature ranges.[492, 495] If the partial pressure of oxygen in blood is considered (p = 0.133 bar) at the body temperature (∼36-37 °C), the corresponding chemical potential of oxygen (-0.31 eV) and the predominant surface structures are far into the cobalt oxides area, making it difficult to retain bare Co surfaces under these conditions.

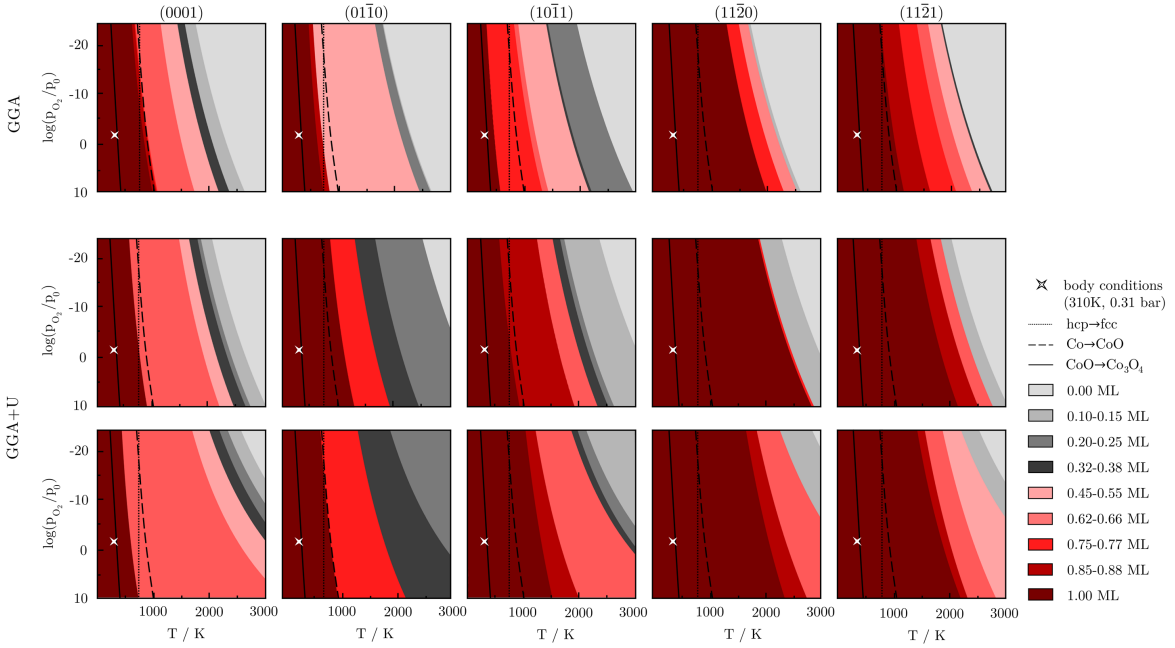

Figure 4.27: Pressure-temperature surface phase diagrams for five inequivalent low Miller-index hcp Co surfaces as calculated by GGA (**top** panel) and GGA+U (**middle** panel without vibrational contributions and **bottom** panel with vibrational contributions, $U_{\text{eff}} = 3.0$ eV). T and $\log_p$ scales are the same for all figures. Conditions of cobalt oxides formation and hcp→fcc phase transition have also been provided.

4.4 Conclusion

A knock-out criterion for implementation of Co NPs in biomedical applications is their poor stability against oxidation and hydrolysis into non-magnetic oxide components. The study on the oxidation of low Miller-index hcp Co surfaces indicates energetically spontaneous oxygen adsorption with the preference to place the adsorbent in the sites with the highest CN or to incorporate it sub-surfaciously where possible, such that it remains centred in between structurally equivalent surface Co atoms on all examined surfaces. Electronic changes in the work function and Bader charges consistently show electron transfer from surface Co atoms to the adsorbed oxygen atoms. Oscillations in the magnetic behaviour upon oxygen adsorption differ for each surface, and increase/decrease in the magnetic moments and appearance of antiferromagnetic states were traced to the corresponding surfaces of CoO and/or Co_3O_4. Considering structural rearrangements, bond distances, and magnetic coupling for the adsorption of a full monolayer of oxygen on each surface, proposed directional growths of cobalt oxides for the (0001) and (11$\bar{2}$0) surfaces, namely (111) and (100), completely agree with previous experimental findings. Correspondingly, predictions were made for the remaining three surfaces. Growth of cobalt oxides is expected in the (100) direction on the (01$\bar{1}$0) surface, while (011) direction was found as most likely for the (10$\bar{1}$1) and (11$\bar{2}$1) surfaces. Morphological changes induced by the oxygen adsorption show increase in the areas of the (01$\bar{1}$0) and (10$\bar{1}$1) surfaces for

which the sub-surface incorporation of oxygen was found to occur most effectively.

Considering the thermodynamics, bare surfaces are stable only under the conditions of extremely low oxygen chemical potentials, μ_O <-3.5 eV. For temperatures below the hcp→fcc transition, surfaces with a full oxygen monolayer are thermodynamically preferred over a whole range of relevant pressures. CoO is expected to form upon the monolayer adsorption on all five surfaces in a wide range of temperature/pressure conditions. Moreover, formation of cobalt oxide with the highest oxidation state of cobalt (Co_3O_4) is likely to happen at low temperatures. If body conditions are considered (∼36-37 °C and p_O = 0.133 bar), Co_3O_4 represents the thermodynamically most stable phase even at low oxygen partial pressures. Thus, if bare Co NPs were used in the biomedical environment, non-magnetic oxides would form, making the preservation of the favourable magnetisation as important issue as NP toxicity. In order to prevent direct contact between Co NP surfaces and oxygen or other oxidising agents, a protective coating should be introduced. What has to be kept in mind are the requirements coating has to meet in order to grant the NP bio-incorporation. First, it has to be biocompatible with human organism and second, if at all possible, it should not affect the magnetic properties of cobalt. Additional functionalisation possibilities such as drug delivery, although not crucial, are also advantageous.

"It would be so nice if something made sense for a change."
-Chapter 4, The Rabbit Sends in a Little Bill

Highlights of the chapter

- **Identified structural rearrangements of the hcp Co surfaces upon oxygen adsorption and predicted directional growth of cobalt oxides.**
- **Proposed morphological changes of Co NPs induced by oxidation.**
- **Complete oxidation of all surfaces within conditions of body temperature and blood partial pressure of oxygen confirmed by temperature-pressure phase diagrams.**

CHAPTER 5

FUNCTIONALISATION OF Co NPs

Alice had begun to think that very few things indeed were really impossible.
"How puzzling all these changes are! I'm never sure what I'm
going to be, from one minute to another."
-Chapter 5, Advice from a Caterpillar

5.1 Introduction

5.1.1 Chemistry of functionalisation

Utilisation of magnetic nanomaterials in biomedicine requires controlled surface reactivity, consistently high levels of magnetisation, and often interactions with biomacromolecules. For example, NPs with specifically designed surface interaction sites can impart enhanced binding capacity necessary for effective intracellular delivery.[496, 497] On the contrary, non-interaction can be just as important whilst preventing NPs to be captured by the immune system.[498, 499, 500] A process that refers to such modifications is surface functionalisation, and it includes conjugation of surfactants or inorganic coatings on the NP surface to tune the reactivity, enhance the magnetisation, and increase the precision of hitting chosen targets by alternating selectivity. In addition, modified physical properties, reduced tendency of agglomeration, and non-invasive characteristics of functionalised NPs are all significant when such foreign entities are introduced into the organism. Considerable efforts have been applied to study the NP functionalisation, and while tailoring biocompatible NP interfaces is a challenging task, chemists have developed a well-equipped toolbox to achieve functionality through synthesis. There are now numbers of verified strategies and NPs have been functionalised with a variety of ligands, from small molecules [501, 502], over dendrimers [503, 504], to polymers [505, 506] and biomolecules [507, 508] as per applicability, efficiency, and application-specific requirements.

The methods for functionalisation of noble metal NPs are already very well looked into in the literature, with gold NPs being the main focus due to their respectable oxidation resistance and well-investigated synthesis methods. They have been successfully modified by thiols [509, 510], disulphides [511, 512], amines [513, 514], phosphines [515, 516], carboxylic acids [517, 518]. Thiol-protected gold NPs gathered the most interest, where the

anchoring of thiols on gold surfaces occurs through the formation of exceptionally strong gold-sulphur bond.[519] Despite the enviable technological interest of these systems, the sulphur-metal inter-facial chemistry and the exact nature of the ligand binding, which is a potential driving force for a strategic design of these nanocomposites and their subsequent applications, remains an active, yet challenging topic in nanoscience.[520, 521]

The chemistry of functionalisation determines the NP interaction with the biological environment, but also with the application specific modality technique, and it is responsible for the NP fate through the application timeline. It is therefore important to investigate functionalisation mechanisms and chemical nature of NP-ligand coordination as this information allows for the improvements in the design, surfactant suitability, and feasibility of various functionalisation approaches. Over the last years, great progress has been made in understanding the structural arrangement of thiol ligands within both thiol monolayers on extended gold surfaces and monolayer-protected gold NPs. Elemental analysis and computational simulations uniformly suggest that approximately two gold surface atoms are needed per adsorbed thiol molecule regardless of the form of gold substrate, and the most attention has been given to the identification of sulphur-adatom motifs and their effect on the system properties.[522, 523, 126] Alternative structures without gold adatoms were also found, and coexistence of the two was observed to allow denser packing and higher surface coverages.[524] A delicate balance between the forces that direct the formation of different binding structures, yielding a fundamental insight in the synthetic strategies, can only be inspected through the electronic structure of these interfaces. There is also an essential difference between gold surfaces and nanostructures to be taken into the consideration; the former are noble, while the latter are reactive due to the involvement of Au-s orbitals in the bonding process.[525] The noble character of the surface arises from fully occupied $5d$ orbitals which are relatively unreactive, with only a minority of $6s$ band density in the close proximity to the Fermi level.

Coordination of thiol compounds to gold atoms can take a form of either weak interaction through physisorption or strong Au-S bonds of chemisorption process. In chemical compounds and molecular materials, formation of Au-S bond is well established, and a broad range of chemical and electrochemical experiments has now been applied to various surfactant-substrate systems to yield a reasonable consensus. The available results are reliable enough to associate observed deviations with variations in the thiol chains and to assign a significant portion of charge donation to the alkyl and aryl groups rather than to surface gold atoms.[526, 527] Given this information, Au-S species can be considered as Au(I)-thiolates if Au-s orbitals dominate the interaction. On the contrary, if the hybridisation is mainly established through Au-d orbitals, they should be labelled as Au(0)-thiyl structures. Theoretically predicted sulphur-gold adatom model corresponds well to the NP features observed experimentally. Its occurrence has been attributed to the formation of closed electron shells that result from covalent bonding of the metallic NP core with adatom-bound surfactants, which is directly parallel to Pauling valence theory for molecules. This stabilisation effect is conventionally ascribed to a certain degree of ionic bonding, where core atoms are in the zero oxidation state, Au(0), while the adatoms are

oxidised by sulphur to a Au(I) state.[528] Interaction between sulphur and the rest of the atoms is thus based on the aurophilic forces. However, recent DFT studies have provided contrasting results, showing that the Au-S bond is essentially covalent with minor bond polarisation arising from minimal electronegativity differences (Au 2.54, S 2.58). Computations indicate that gold atoms remain as Au(0) and sulphur atoms remain in thiyl form with no evidence of thiolate or Au(I) formation.[529, 530, 531] However, Au-S bond is indeed quite strong, and the formation of adatoms is affected by the binding topology of the surfactants such that the number of Au-S bonds formed as well as that between the adatom and nearest neighbour Au atoms is maximised. This understanding unifies gold-sulphur surface chemistry with that of other ligands and chemically similar gold compounds, forming the basis for future methodological developments.

5.1.2 Biocompatible cobalt NPs

The oxidation of Co NPs upon the exposure to oxygen even in mild conditions, as shown in the previous chapter, is an intrinsic problem in many potential applications as it leads to the formation of cobalt oxides, thus significantly reducing beneficial magnetic properties. This problem is more pronounced when the size of the NPs is reduced within a couple of nanometres in diameter as the electronic properties of surface atoms change with the increase in the surface-to-volume ratio. To address this problem, various protection strategies have been developed to stabilise Co NPs against oxidation, including carbon, silica, and alumina coatings, and different surfactants and polymers.[532, 533, 534, 535, 536] However, the post-modification methods for inorganic coatings are laborious, and the formation of multicore is often observed, hence granting more attention to the functionalisation by adsorption of organic surfactants. The overall efforts are, nevertheless, still far behind those devoted to gold NPs.

To this end, Co NPs have mainly been functionalised with acidic organic surfactants. Since cobalt is a relatively reactive transition metal, a dense surfactant coverage is crucial to prevent oxidation. Sun and Murray have demonstrated systematic synthesis of nearly monodisperse Co nanocrystals ranging from 2 to 11 nm protected by oleic acid, lauric acid, trioctylphosphonic acid, and pyridine, while concentrating on the dispersion characteristics and self-organisation into magnetic superlattices.[537] A combination of oleic acid and triphenylphosphine remained a popular method for obtaining monodisperse Co NPs since the phenyl group in triphenylphosphine can provide greater steric hindrance than the straight-chained alkyl groups, which was shown to be beneficial in controlling the size of the non-magnetic metal NPs [538, 539, 516], and it was speculated that this could be transferred to the stabilisation of magnetic NPs. The combination of oleic acid and triphenylphosphine was observed to promote relatively narrow size distribution [540] and as-synthesized Co NPs were found to be fairly stable against oxidation when kept in heptane.[541] The differences between long-chain acids were also tested; olefinic acids are advantageous in forming effective dense-packed coatings for better control of NP growth, stability, and reactivity over corresponding aliphatic counterparts because of their bent shape. Comparative study of oleic, elaidic, and stearic acid and their mixtures indi-

cated roughly the same performance for all acids, yielding spherical NPs with narrow size distribution.[542] In addition, transformation from cis-oleic acid to its trans-configuration (corresponding to elaidic acid) was observed, leading to the formation of a densely-packed acid monolayer on the NP surface. The study was extended to investigate magnetic properties: synthesised nanocomposites were below the critical size and each particle contained only one magnetic domain corresponding to the superparamagnetic state. The oleic acid-protected Co NPs were also prepared through an alcohol treatment by re-dispersion in methanol, ethanol, and 2-propanol, testing the impact of different stabilisation techniques on the isothermal oxidation. A significant long term oxidation deceleration was observed for alcohol-based preparations regardless of the alcohol used.[391]

Positive outcomes of these acid-functionalisation strategies boosted attempts of incorporation of other surfactants in the protection of Co NPs. Novel ligands were obtained from oleic acid through the conjugation with 2-mecaptoimidazole via thiolene reaction, and, when coupled with Co cores, resulting NPs were of cubical or octahedral shape, as opposed to spheres formed in the presence of oleic acid only.[543] Further improvement in the functionalisation was sought-after in more complex surfactants, such as polymer molecules. Oxidation resistance tests of polycaprolactone- and polystyrene-protected Co NPs indicated that the polymer shell has a certain impact on the diffusion process of oxygen towards the metal core, with polystyrene counterparts showing higher deceleration of oxygen penetration. Both nanocomposites were superparamagnetic.[391] Highly crystalline, well-dispersed Co 3.5-3.7 nm nanocrystals have also been developed through conjugation with a surfactant/polymer complex layer, maintaining the superparamagnetism and improved air-stability.[544]

5.1.3 Motivation

The unprecedented bio-incorporation of metallic NPs can cause irreversible damage on the molecular and cellular level. In the absence of surface modification, these NPs generally show non-selective distribution and inability to overcome certain biological hindrances such as blood brain barrier, and thus fail to satisfy necessary preconditions for biomedical implementation. Addition of molecular moieties through surface functionalisation enhances the advantageous properties of metallic core while reducing negative immunity response, enabling NPs to play a major role in the field of medicine. Biocompatibility is thus the key for the integration of magnetic metallic NPs into biomedicine, and while titanium implants owe their biocompatibility to thin oxide layers formed on the surface in the presence of air and water [545, 546], the same phenomenon is a substantial drawback when magnetic Co NPs transform into the non-magnetic oxide compounds.[547]

Functionalisation of Co NPs has received considerably less attention compared to gold and other noble metal NPs. Structural information of such nanocomposites is scarce, and details on the surfactant-metal interactions are deficient. As seen through the gold-thiol example, understanding of the interaction between the surfactant and metallic core is of great importance in adjustment of functionalisation techniques for achieving optimal,

application-relevant chemical and physical properties. In order to obtain biocompatibility and prevent oxidation, a surfactant which is effective in adjusting the reactivity of the NPs without affecting their magnetic properties is usually employed.[548, 549, 550] Understanding the surface chemistry of functionalisation therefore plays a major role in tuning the properties and the performance of the final nanocomposite.[551, 152] A variety of ligands have so far been tested to enhance biocompatibility, improve growth control, stabilise the particle dispersions, prevent agglomeration, provide functionality, and limit the surface reactions. By now it is known that metallic NPs experience strong Van der Waals and magnetic dipole interactions, hence only surfactants which covalently bond to the metal can considerably promote NP stability. Covalent bonding of carboxylic acids to the surface metal atoms through carboxyl group makes them an excellent choice as capping agents. The interaction between the carboxylate head and the metal atoms can adopt four different modes [552, 553, 554]: if one metal atom binds with one oxygen atom, the mode is called monodentate; if both carboxyl oxygen atoms are involved, they can form complexes with either one or two different metal atoms, referred to as chelate and bidentate, respectively; the final possible interaction is of ionic nature. Which motif dominates for a specific ligand-metal pair depends on the properties of the metal surface and the structure of the adsorbed carboxylic acid. Experimentally, the actual binding interaction may be distinguished by infrared (IR) spectroscopy due to the characteristically shifted carbonyl band signals.

Experimentally observed dense protective monolayer of oleic acid, whose centre positioned cis-double-bond allows formation of the kink necessary for the effective stabilisation, showed to produce metallic nanocomposites in a highly uniform size range.[215, 548, 555] It was additionally found that the bonding nature of oleic acid can have a critical effect on magnetisation.[556] A detailed knowledge of the type of interaction between carboxylic acids and Co NPs could hence allow fine-tuning of the size, morphology, and magnetic properties. However, experimental results are inconclusive on the binding mode between carboxylic acids and Co NPs. Older investigations gave a uniform conclusion on oleic [540, 215, 537] and elaidic [542] acid chemisorption onto Co surfaces, yielding NPs in a narrow distribution, but they did not provide the exact binding mode. In literature, there exist (to the best of author's knowledge) only two such works that suggest an interaction type between the Co atoms and carboxylate head of oleic acid. According to Wu *et al* [557], oleic acid is chemisorbed as a carboxylate onto the Co NPs, and the two carboxyl oxygen atoms are coordinated symmetrically to the two Co atoms with a shift of the carbonyl IR band corresponding to bridging bidentate, where the interaction between the COO- group and the Co atom is covalent. On the other hand, Ansari *et al* [211] presented an IR spectrum which demonstrates the chemisorption of the acid as a carboxylate onto the Co NP through the absence of ($-$COOH) characteristic peak, suggesting the non-existence of physically absorbed molecules and the formation of a monolayer on the surface. The shift of carbonyl band in their case corresponds to the monodentate interaction, where the single carboxyl oxygen atom forms covalent bond with one surface Co atom. In the case of cobalt ferrites, oleic acid was found to always chemisorb covalently in a form of a bridging bidentate.[556, 558, 559]

To resolve a disagreement between existing literature, metadynamics simulations were performed to efficiently explore the interaction between Co NPs and carboxylic group from the viewpoint of the relative free energy differences of various free energy minima and connecting free energy barriers prior to the complete functionalisation of the NPs. This was extended towards surfactants characterised by different functional groups, namely thiols and amines.

5.2 Computational details

Choice of a system

Extended surface slab models are often useful for modelling the interaction with simple atomic adsorbates or small linear molecules since the effects of irregular, curved, stepped, porous, and otherwise deformed NP surfaces can be largely excluded. However, changes in the reactivity become notable for large surfactants, i.e., when the NP diameter is less than 20 times the length of the surfactants in their extended conformation. For example, the length of a straight C18 alkyl ion corresponding to the carbon chain of oleic acid is about 3 nm, and NP needs to be reaching 60 nm in diameter for curvature effects to become marginal. The maximum size of NPs employed in biomedicine should not exceed 20 nm, including the protective coating, which significantly magnifies the effects of surface curvature, edges, and vertices in their functionalisation. Size of the system which can be modelled within *ab initio* approaches is, however, a major challenge of current computational efforts and has to be chosen critically to reduce the cost without jeopardising efficiency of the results. To confirm the binding mode of carboxylic acid and also to predict binding modes of other types of ligands and characteristics of functionalised Co NPs, a combination of *ab initio* methods, including DFT, *ab initio* MD, and metadynamics was employed. For this level of theory, it is necessary to find the optimal size of system components (NP size and length of the carbon chain of a ligand) in terms of realistic reactivity and acceptable computational cost.

To determine the optimal NP size, the adsorption characteristics of atomic and molecular adsorbates have been investigated and compared for different sizes of hcp-shaped Co clusters/NPs, going from 6 to 323 atoms, as well as for the extended slab models. Oxygen was chosen as an atomic adsorbate, whereas molecular adsorption was tested on acetic acid. Calculations were carried out using the VASP code, with a spin-polarised formalism and the GGA/PBE functional. The core electrons up to and including the $3p$ levels of Co, $2p$ levels of C, and $2s$ levels of O were kept frozen and their interaction with the valence electrons was described by the PAW method. The DFT-D3 method with Becke-Johnson damping was used to include the long-range dispersion interactions. The kinetic energy cutoff of the wave functions was set to 500 eV. The Monkhorst-Pack k-point grid included Γ-point for cluster/NP systems. For the (0001) and (10$\bar{1}$1) surfaces, 3×3 and 3×2 supercells with 4 atomic layers (top two relaxed, bottom two constrained in the bulk-relaxed positions) were used, with 5×5×1 and 5×4×1 k-point meshes, respectively. Structural optimisations were carried out without any constraints, with convergence criteria of 1.0×10^{-6}

eV/atom for the electronic energy and 1.0×10^{-2} eV/Å for the atomic forces. The vacuum space in the unit cell was set to 12 Å in the z-direction to avoid interactions between the periodic images, while clusters/NPs were positioned in the centre of the cell with sizes adjusted such that there is at least 12 Å of vacuum in each direction. Energy analysis included calculation of adsorption energies for each of the two appearing facets within the cluster/NP models, namely the (0001) and $(10\bar{1}1)$ surfaces, but also computation of the dissociation barriers for the carboxy functional group as separation of hydrogen from the molecule is a key event in the functionalisation process. Barriers were evaluated through CI-NEB calculations.

The size of the carboxylic acid alkyl chain also needed to be critically evaluated. Earlier studies on the interaction of primary carboxylic and mercapto-carboxylic acids [560, 561] with zeolites and ZnO surfaces have shown that the adsorption modes and dielectric properties of hybrid systems are rather insensitive to the chain length since the interaction state is localised on the specific atom (either carboxyl oxygen or mercapto-sulphur). In comparison, experimental investigation of configurational isomers, oleic and elaidic acid found that cis to trans transformation occurs spontaneously, meaning that oleic acid can be replaced with elaidic acid without compromising the NP-surfactant interface or the quality of the final product. Oleic acid, as the experimental compound of interest, and valeric acid, as a segment of oleic acid cut at the fourth carbon atom of the alkyl chain where the distance from the carboxyl group is larger than three bonds thus diminishing the inductive effect, have been compared based on the energetic and electronic properties upon the adsorption. It is anticipated that the carbon chain size will not significantly affect the properties of interest and the computational cost can therefore be substantially reduced by using the shorter valeric acid.

Binding mode sampling

In the light of Co NP functionalisation, a detailed examination of the interface in the synthesis conditions at the molecular level is paramount in order to address the effect of surfactants on the nanocomposite properties. To sample binding modes and inter-mode transitions that could occur in the functionalisation process, interaction of a single molecule of carboxylic acid and a Co NP was modelled using AIMD simulations, in conjunction with the metadynamics algorithm. First principles spin-polarised molecular dynamics simulations implementing the Born-Oppenheimer scheme were performed using CP2K code [562, 190] with the PBE exchange-correlation functional and the Goedecker, Teter, and Hutter (GTH) Gaussian basis set.[563] The system comprising of an interacting valeric acid molecule on a Co NP was placed in a cubic box 25 Å a side and equilibrated in the constant temperature NVT ensemble in duration of 3.0 ps. The Nosé-Hoover thermostat was set to 500 K, in accordance with the experimental synthesis temperatures (160-250 °C [215, 557, 211]), and a time step of 1.0 fs was used for the integration of the equations of motion.

The metadynamics algorithm enables the efficient exploration of the free energy landscape of a system by reducing its degrees of freedom as a function of suitable collective

variables. Considering the complex nature of the system, combination of AIMD and metadynamics is an ideal strategy to investigate binding changes of carboxylic acids. To capture these changes, the CV has to be chosen such that each binding mode has a corresponding CV value which is distinct from the CV values of all other binding modes. While in some systems the proper selection of the relevant CVs is not obvious and requires a significant research effort regarding the oscillations of different descriptors which are potential CV candidates with the change in the states of the system and during the transitions that exist in a given mechanism, there are also cases where this can be an intuitive decision. As previously described, a lot of information is already known about the carboxylic acid-metal NP interaction through the experimentally defined modes (monodentate, bidentate, chelate) [552, 553, 554] which differ in the number of metallic atoms involved in the binding and the final number of established acid-NP bonds. The most prominent differences between these modes of interaction of carboxylic acids with metallic NPs are hence the coordination numbers (CNs) of the two carboxyl oxygen atoms, O_a and O_b, with respect to surface metal atoms. By going from a bidentate mode, for which both CN (O_a-Co) and CN (O_b-Co) equal one (1,1), to a monodentate, the CN of one oxygen decreases to zero, while other oxygen can bind to one, two, or three Co atoms, yielding combinations of (0,1), (0,2), and (0,3), respectively. Transition to a chelate interaction induces binding of both O atoms to the same Co atom, which would at the first sight give exactly the same combination of CNs of the bidentate binding, namely (1,1). However, the oxygen-oxygen repulsion results in an increased distance between the oxygen atoms in the chelate configuration, causing the prolongation of the Co-O bonds, giving an approximate CN combination of (0.5,0.5) for the same Co-O reference value. Thus, being able to distinguish between the most relevant structures, CN (O_a-Co) and CN (O_b-Co) were chosen for the projection of the metadynamics free energy landscape:

$$s_{\mathrm{AB}}(r) = \mathrm{CN(Co\text{-}O)} = \frac{1}{N_{\mathrm{O}}} \sum_{1}^{N_{\mathrm{O}}} \left\{ \sum_{1}^{N_{\mathrm{Co}}} \frac{1 - (\frac{r_{\mathrm{Co\text{-}O}}}{r_{\mathrm{Co\text{-}O,0}}})^n}{1 - (\frac{r_{\mathrm{Co\text{-}O}}}{r_{\mathrm{Co\text{-}O,0}}})^m} \right\} \tag{5.1}$$

where n and m determine the curvature of the function used to compute the CN and $r_{\mathrm{Co\text{-}O,0}}$ is the reference Co-O distance. For each pair of atoms, this function is approaching unity when the bond distance $r_{\mathrm{Co\text{-}O}}$ is close to the reference Co-O value $r_{\mathrm{Co\text{-}O,0}}$, and it is ∼zero when it is much larger than the reference Co-O distance, $r_{\mathrm{Co\text{-}O}} \gg r_{\mathrm{Co\text{-}O,0}}$. The reference Co-O distance $r_{\mathrm{Co\text{-}O,0}}$ was determined as an average distance captured during the AIMD relaxation after the system equilibration. After the selection of $r_{\mathrm{Co\text{-}O,0}}$, preliminary runs were performed in order to monitor the dynamics of chosen variables by setting up unbiased AIMD simulations and monitoring the CV values while the system explores the configurations around the initial geometry, i.e. belonging to the same (initial) basin of attraction on the free energy surface. The evaluation of the CV fluctuation amplitudes helps in justifying the choice of the collective variables as well as to set the width of the Gaussian beads that are going to build up the penalty potential along the biased metadynamics run.

Metadynamics simulations were performed with two CNs as CVs, with exponents $n = 8$

and $m = 14$ [564], requiring a bidimensional exploration of the free energy. Convergence was tested based on the choice of the height of Gaussian hills, which was set to $3k_BT$, $1.5k_BT$, and k_BT with a width of 0.05 Å^{-1}. Final parameters were $\omega = 3k_BT$ and σ_s =0.05 Å^{-1}, and hills were deposited every 50 fs. The metadynamics simulations were carried out for 15.0 ps, after which one of the carboxyl oxygen atoms bound to a new Co atom that was not included in the binding states observed thus far, hence reproducing previously formed interaction modes on a different site of the NP. This was considered a terminating event, as it indicates that the molecule has exhausted all the binding possibilities with the initially assigned pair of Co atoms. Visual Molecular Dynamics (VMD) package was used for post-processing.[565]

In addition, IR spectra of the observed binding modes were calculated within the perturbation theory at the PBE level. Density-functional perturbation theory (DFPT) or linear response theory has become applicable for interpreting macroscopic parameters such as linear optical properties - the static dielectric tensor, the piezoelectric tensor, the vibrational frequencies, and the matrix of the Born effective charges.[566, 567, 568] To obtain vibrational spectra, vibrational modes (normal modes for molecules or phonons for crystals) are first determined by a direct diagonalization of the dynamical matrix. The dynamical matrix expresses the force acting on individual atoms due to the displacements from the equilibrium geometry. In the harmonic approximation, this force is essentially given by the integral of the charge density response to the displacement of one atom, times the variation of the ionic potential due to the displacement of another. Displacements are performed for each atom and each coordinate followed by calculating the forces for the corresponding geometry. One further linear system, corresponding to the perturbation due to the application of a homogeneous electric field, must be solved in order to calculate the molecular polarizability. The Born effective charge of a crystalline system, defined as the induced polarisation due to a unit sublattice displacement, is a fundamental quantity connecting the longitudinal- and transverse-optical phonon modes of the lattice to the external infrared radiation. The ionic effective charges are essentially the second derivatives of the energy of the molecule with respect to an applied electric field and to the amplitude of a vibrational distortion and as such, they are directly accessible to second order DFPT. The electric polarisation induced by the applied field further yields the dielectric constant of the crystal. Thus, after finding the equilibrium geometry of the system, the dipole moment and the polarizability and their derivatives with respect to the atomic coordinates can be determined by a finite differencing of energies and forces with respect to the electric field vector. In a dipole approximation, the intensities of infrared-active modes are given by the corresponding oscillator strengths which are proportional to the square of the dipole induced by the phonon that is excited by the IR radiation. This is a trivial by-product of a phonon calculation determined by the Born effective charges and the displacement vectors:

$$I(\omega) = \sum_{\alpha=1}^{3} \left| \sum_{i=1}^{M} \sum_{\beta=1}^{3} Z^*_{\alpha\beta}(i) e_\beta(i) \right|^2 \tag{5.2}$$

where $e_\beta(i)$ are the normalised vibrational eigenvectors, α and β indicate the Cartesian polarisations, i labels the different atoms of the system, and $Z^*_{\alpha\beta}(i)$ is the Born effective charge tensor of the i-th atom. The $Z^*_{\alpha\beta}(i)$ is to be understood as a coefficient of proportionality between a change of macroscopic polarisation in direction α caused by an atomic displacement in direction β under conditions of zero external field. As the accessibility of DFPT is growing, it became a powerful and accurate method to compute the vibrational spectra of extended systems.

Alternative method is to extract the vibrational spectra from AIMD runs since they allow conformational sampling in the phase space. The traditional calculation of normal mode-dependent dipole and polarizability derivatives in the static DFPT approach is replaced by Fourier transforms of the dipole and polarizability correlation functions in the time domain dynamics simulations.[569, 570] Since neither dipole moment nor polarizability belong to the directly obtainable AIMD properties, the first step towards the calculation of vibrational spectra is to obtain the power spectrum via the Fourier transform, f, of the autocorrelation of the particle velocities:

$$f(\omega) \propto \int_0^\infty dt e^{-i\omega t} \langle \vec{v}(0) \cdot \vec{v}(t) \rangle. \tag{5.3}$$

where $\vec{v}(0)$ and $\vec{v}(t)$ represent initial particle velocity and velocity the particle develops at time t. The power spectrum features peaks at all vibrational frequencies of the system, and it can also be understood as a vibrational density of states. In a similar manner, IR spectra can be calculated from the autocorrelation of the molecular dipole moment μ:

$$f(\omega) \propto \frac{\omega}{2\pi} \int_0^\infty dt e^{-i\omega t} \langle \vec{\mu}(0) \cdot \vec{\mu}(t) \rangle. \tag{5.4}$$

The intensity of this spectrum corresponds to the amplitude of the oscillation in the correlation function so that large changes in the dipole moment or the polarizability lead to a large peak in the spectrum and vice versa. By coupling the AIMD code such as CP2K with TRAVIS [571], the free analyser of molecular dynamics trajectories, one can compute IR spectra from the AIMD trajectory.

For the purpose of confirming the organic ligand-Co NP binding modes observed in the metadynamics simulations, DFPT linear response calculations, which are directly available in VASP, were used to obtain the matrix of Born effective charges. Phonopy code [572] was employed to prepare vibrational frequencies/eigenvectors from a calculation of lattice dynamics and the IR post-processing tools were implemented to calculate the vibrational intensities using the formula by Ginozzi and Baroni.[573] It is well-known that vibrational frequencies obtained by quantum-chemical calculations are typically larger than those evaluated experimentally, and thus, empirical scaling factors are often used for obtaining a better match. However, since the current work focuses on the changes in the ligand spectra induced by different binding modes to the NP rather than on the absolute values of the frequencies, the scaling was not carried out.

5.3 Results

5.3.1 Size-dependent adsorption on Co NPs

The Co_N model clusters/NPs studied for the size-dependent adsorption consisted of 6, 13, 19, 30, 57, 76, 153, and 323 atoms arranged in an hcp-like atomic packing to capture the progression towards the behaviour or large hcp NPs. All except the smallest 6 and 13-atom clusters exhibit facets of (0001) and (10$\bar{1}$1) orientations to minimise the overall surface energy. Size-dependent adsorption of molecules of interest (O and CH_3COOH) was, therefore, examined by depositing molecules on both NP surfaces, as well as on the surface slab models for completeness.

5.3.1.1 Oxygen adsorption

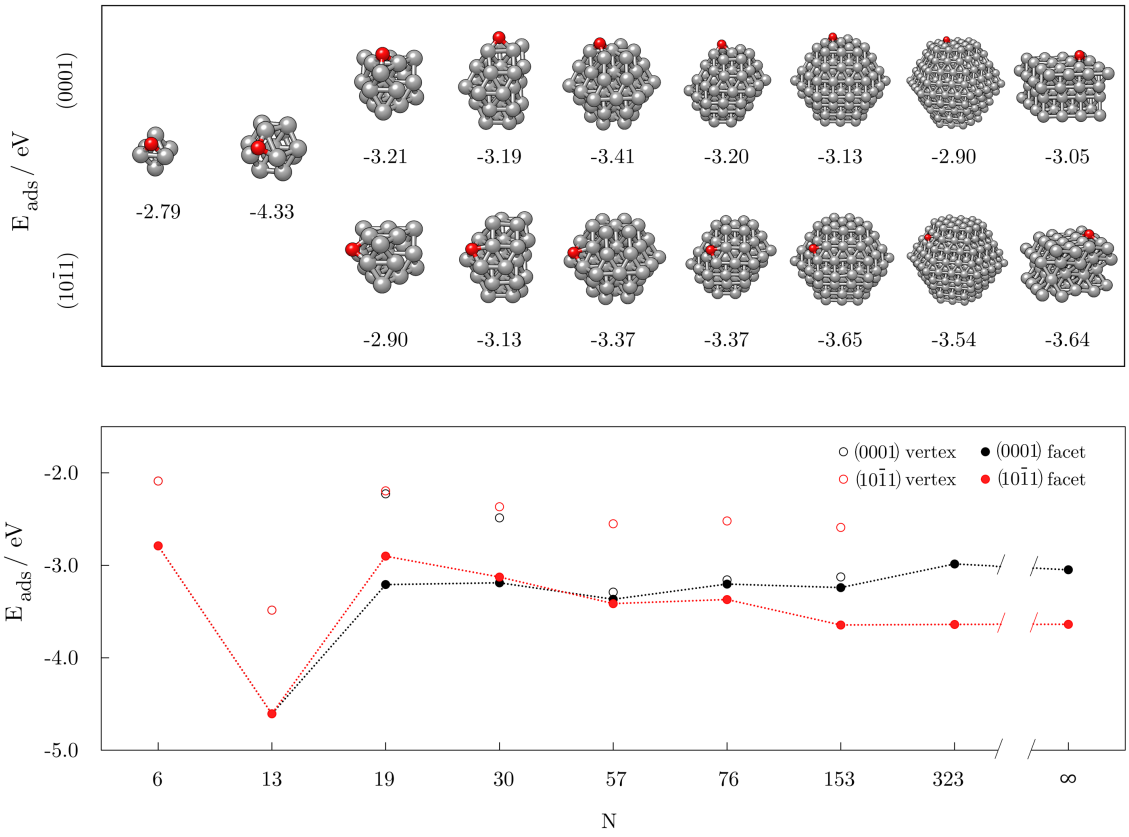

Figure 5.1: **top**: Optimised geometries of oxygen atom adsorbed on the (0001) and (10$\bar{1}$1) surfaces of Co_N clusters/NPs and the extended surfaces (∞) in the most stable adsorption sites with accompanying adsorption energies, E_{ads} (in eV). Grey and red spheres represent cobalt and oxygen atoms, respectively. **bottom**: Adsorption energies as a function of cluster/NP size for the oxygen adsorption in vertex and facet sites of the (0001) and (10$\bar{1}$1) surfaces; lines are to guide an eye only.

Figure 5.1 shows final structures after the adsorption of a single oxygen atom with the accompanying adsorption energies for the most stable adsorption site together with the adsorption energies of different sites as a function of the cluster/NP size. Oxygen atom, regardless of the cluster/NP size or the surface stacking, binds in the hollow position which allows interaction with three Co atoms of the (0001) surface. On the $(10\bar{1}1)$ surface, clusters with more than 19 atoms can accommodate oxygen in the centre of four Co atoms, while the smaller surface area of the 19-atom cluster limits the interaction to three Co atoms. With the exception of the smallest sizes (N = 6,13), adsorption energies for facet interaction fall within a limited range of -3.25±0.40 eV. The E_{ads} of the largest NPs considered, N = 153 and N = 323, differ only slightly from those of the periodic slab models, namely $E_{\mathrm{ads},N=153}$ = -3.13/-3.65 eV and $E_{\mathrm{ads},N=323}$ = -2.90/-3.54 eV for the $(0001)/(10\bar{1}1)$ surface ($E_{\mathrm{ads},(0001)}$ = -3.05 eV; $E_{\mathrm{ads},(10\bar{1}1)}$ = -3.64 eV). The deviations in the E_{ads} for the two smallest clusters ($E_{\mathrm{ads},N=6}$ = -2.79 eV; $E_{\mathrm{ads},N=13}$ = -4.33 eV) are caused by the limited surface areas available for the adsorption. In general, vertex adsorption is weaker by ∼0.70-1.15 eV. This distinction between facet and vertex interaction strength drastically changes from N = 57 onwards for the (0001) surface due to the spontaneous shift of the oxygen adsorbate to form bonds with two edge Co atoms, reducing the difference to less than 0.15 eV.

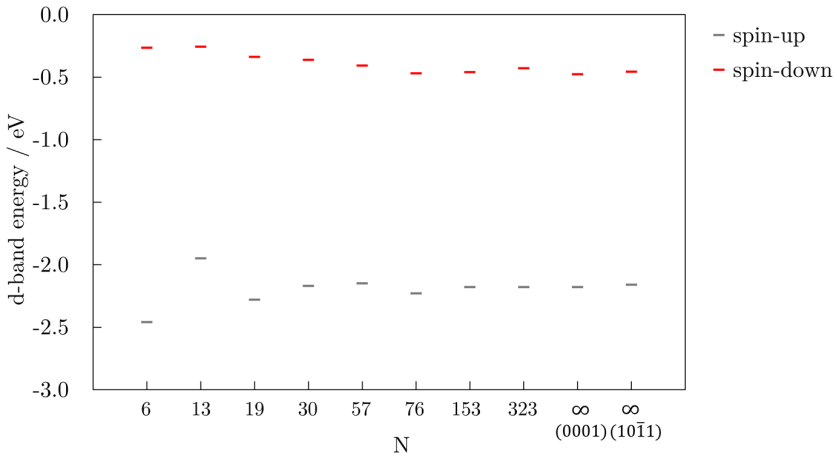

Figure 5.2: d-band energies for $3d$ spin-up (grey) and spin-down (red) electrons of Co as a function of cluster/NP size, N. Results for surface slabs are shown as $N = \infty$.

d-band energies, ε_{d}, are shown in Figure 5.2 for both the $3d$ spin-up and spin-down electrons of Co in differently sized clusters/NPs and the infinite surfaces. They were calculated using the definition of Hammer *et al* [574]

$$\varepsilon_{\mathrm{d}} = \frac{\int_{-\infty}^{\infty} n_{\mathrm{d}}(\varepsilon)\varepsilon d\varepsilon}{\int_{-\infty}^{\infty} n_{\mathrm{d}}(\varepsilon) d\epsilon} \tag{5.5}$$

by integrating the density of state (n_{d}) multiplied by the corresponding state energy ε,

as implemented in the VASP postprocessing tool Vaspkit. The energy window was set up to the Fermi level. Small clusters experience the influence of quantum effects, resulting in a non-scalable regime, which often makes it hard to identify a quantitative dependence of the adsorption energy on the cluster size. Nevertheless, *d*-band energy sequence of spin-up electrons, which are responsible for the Co-O interaction, mirrors the trend of oxygen adsorption fairly accurately, with the 13-atom cluster having the most positive *d*-band energy and, hence, the strongest interaction with oxygen.

It is evident that even with a simple monoatomic adsorbate the two surfaces that characterise hcp Co NPs behave differently. The correspondence between the facet and vertex adsorption energies for varying cluster/NP sizes is captured only after surpassing 50 atoms per particle, owing it mostly to the pronounced electronic effects in smaller clusters. This effect might be furtherly intensified when it comes to the adsorption of larger molecular entities.

5.3.1.2 Acetic acid adsorption

Optimised structures and corresponding adsorption energies for the undissociated adsorption of acetic acid on Co clusters/NPs, as well as the energy trends for facet and vertex adsorption are shown in Figure 5.3. Compared to the single oxygen atom adsorption, where electronic effects make for the biggest change in the adsorption behaviour of differently sized clusters/NPs, the adsorption of CH_3COOH molecules depends on both the geometry of the particles as well as on their electronic properties. Vertex adsorption is characterised by a single bond between a self-standing -COOH oxygen and a Co vertex atom with carboxyl hydrogen in the bridging position over the two surface Co atoms closest to the oxygen binding site without established physical bonds. Adsorption on the facet results in a similar arrangement, with a self-standing carboxyl oxygen atop one facet Co atom. When the carboxyl oxygen was placed in the hollow as the most favourable adsorption site for a single oxygen atom, the established interaction was weaker, probably due to the inconvenience of accommodating carboxyl hydrogen atom so close to the NP surface. Of the sizes investigated, $N = 57$ is the smallest particle size whose (0001) and $(10\bar{1}1)$ surface areas are sufficiently large to allow for the facet adsorption mode to take place. Hence, in the case of the acetic acid adsorption, clusters with 19 and 30 atoms still belong to the non-scalable regime, where the adsorption strength, specifically on the $(10\bar{1}1)$ surface (-1.59 eV for $N = 13$, -0.47 eV for $N = 19$, and -1.16 eV for $N = 30$), notably oscillates amongst sizes. For larger NPs, adsorption of acetic acid molecule in the vertex site is stronger compared to the facet interaction by 0.55/0.62 eV on the (0001)/$(10\bar{1}1)$ surface on 57-atom Co NP, and by 0.15-0.30 eV on $N > 57$ NPs. After reaching the values of $E_{\mathrm{ads,N=57}}$ = -0.53/-0.57 eV for the (0001)/$(10\bar{1}1)$ facet adsorption, adsorption energies for this mode of interaction reach a plateau at -0.78±0.05 eV for the (0001), and at -1.00±0.05 eV for the $(10\bar{1}1)$ surface. This trend, initiating at $N = 57$, progresses towards the asymptotic value computed for the infinite surface slabs, $E_{\mathrm{ads,(0001)}}$ = -0.78 and $E_{\mathrm{ads,(0001)}}$ = -1.02 eV.

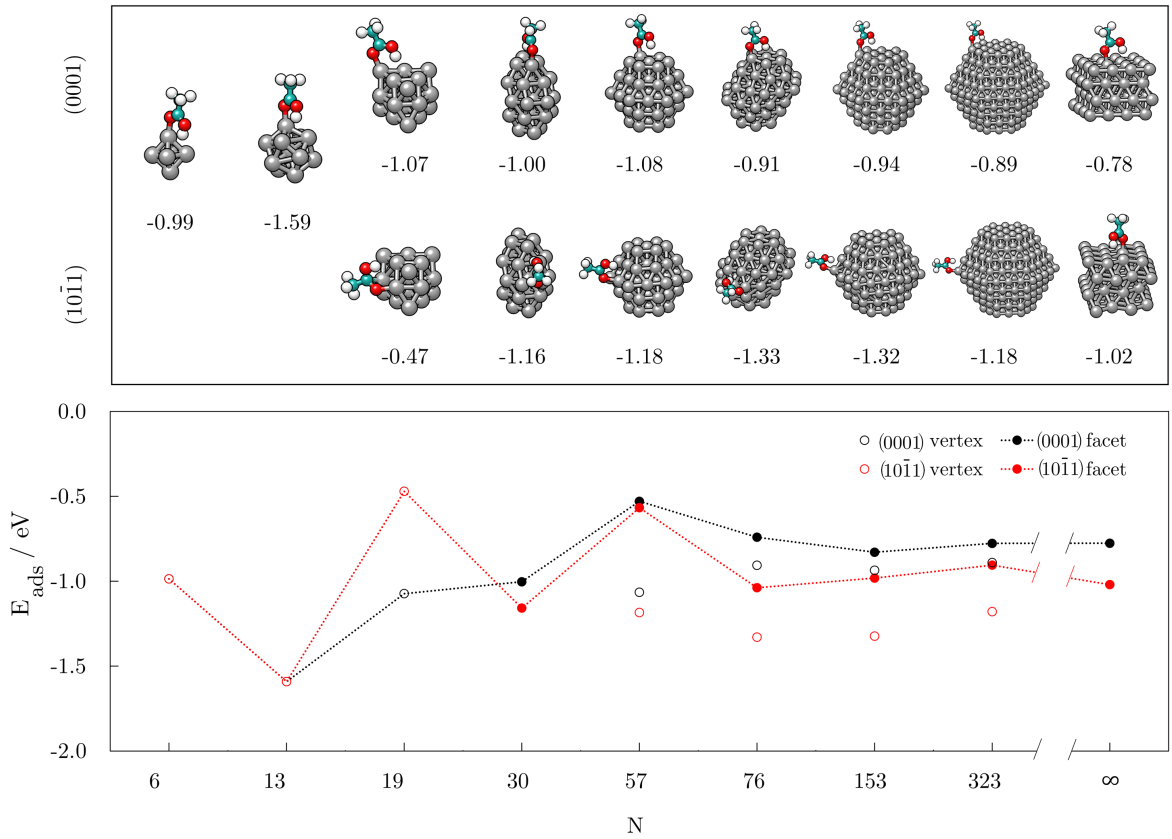

Figure 5.3: **top**: Optimised geometries of acetic acid adsorbed in an undissociated state on the (0001) and (10$\bar{1}$1) surfaces of Co_N clusters/NPs and the extended surfaces (∞) in the most stable adsorption site with accompanying adsorption energies, E_{ads} (in eV). Grey, red, teal, and white spheres represent cobalt, oxygen, carbon, and hydrogen atoms, respectively. **bottom**: Adsorption energies as a function of cluster/NP size for acetic acid adsorption in vertex and facet sites of the (0001) and (10$\bar{1}$1) surfaces; lines are to guide an eye only.

Geometries of the systems upon dissociation of acetic acid and their adsorption energies as a function of the cluster/NP size are presented in Figure 5.4. Preferred interaction mode in dissociated state consists of two single bonds between each of the carboxyl oxygen atoms and one Co atom of the neighbouring pair, while the dissociated carboxyl hydrogen adsorbs in the available hollow position over the three ((0001) surface) or four ((10$\bar{1}$1) surface) Co atoms close to the oxygen binding site, but without sharing any of the oxygen-interacting Co atoms. An exception is a 6-atom Co cluster, whose small facet areas have insufficient number of Co atoms for described arrangement, instead forming a single Co-O bond with hydrogen bridging over two Co atoms. Dissociation was probed for both vertex and facet adsorption sites for the larger NP sizes, and established interaction was found to be, in general, about two times stronger with respect to the undissociated acid adsorption. Nonetheless, the difference in the E_{ads} of the two sites is maintained at similar values as the undissociated states; vertex interaction is more favourable by

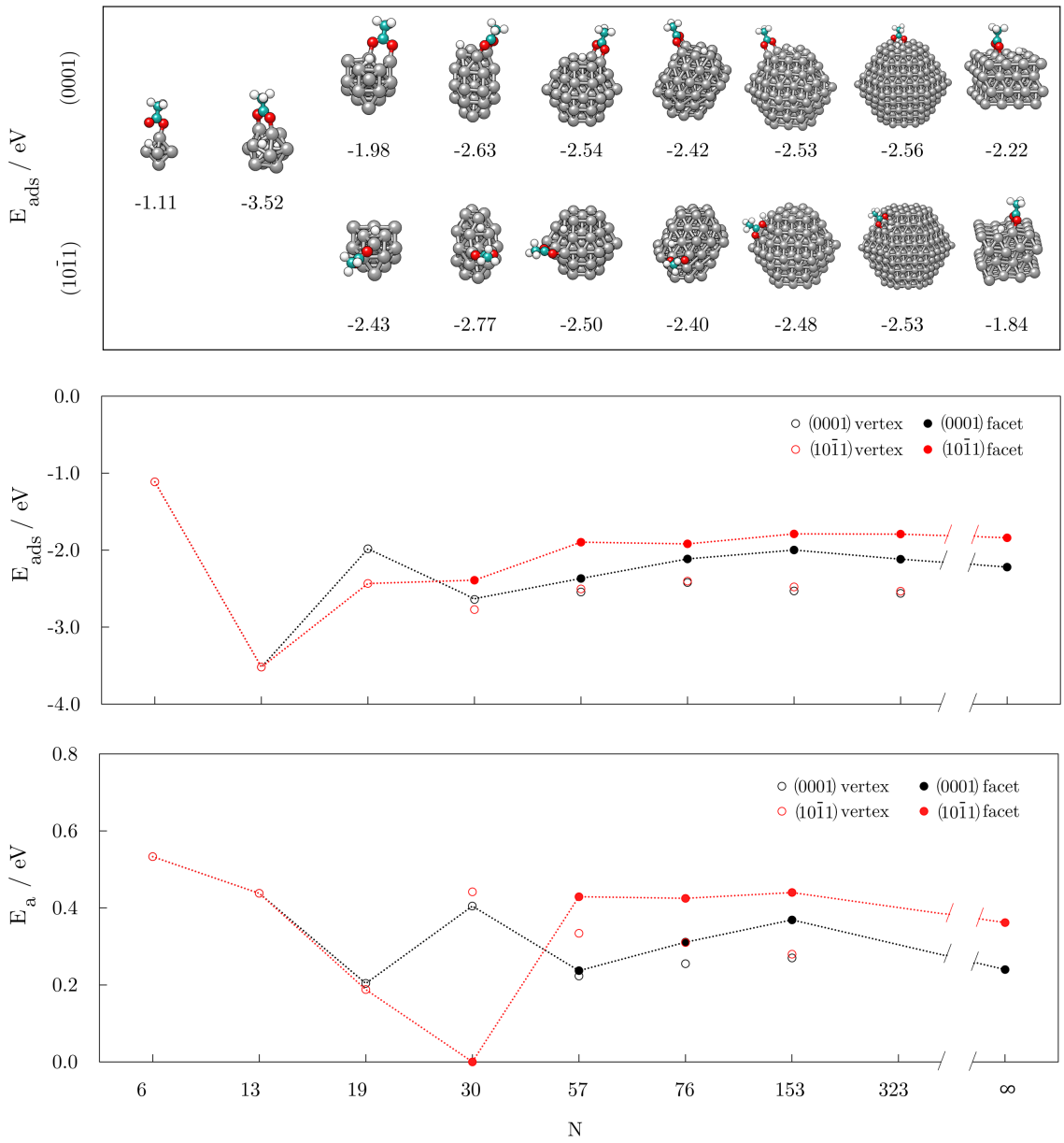

Figure 5.4: **top**: Optimised geometries of acetic acid adsorbed in a dissociated state on the (0001) and (10$\bar{1}$1) surfaces of Co_N clusters/NPs and the extended surfaces (∞) in the most stable adsorption site with accompanying adsorption energies, E_{ads} (in eV). Grey, red, teal, and white spheres represent cobalt, oxygen, carbon, and hydrogen atoms, respectively. **middle**: Adsorption energies as a function of cluster/NP size for dissociative acetic acid adsorption in vertex and facet sites of the (0001) and (10$\bar{1}$1) surfaces; lines are to guide an eye only. **bottom**: Activation energies, E_a, for the dissociation of acetic acid as a function of cluster/NP size.

0.18-0.70 eV. Relation between the varying cluster/NP sizes has, however, experienced notable changes. E_{ads} for the vertex adsorption on the (10$\bar{1}$1) facets are within a narrow

-2.60±0.20 eV energy window for all but the smallest two cluster sizes. On the (0001) surface, the vertex interaction range is slightly larger, spanning values of -2.30±0.35 eV. The oscillations in adsorption behaviour have hence reduced to cluster sizes with under 15 Co atoms, where adsorption energies significantly deviate from listed averages ($E_{\mathrm{ads,N=6}}$ = -1.11 eV and $E_{\mathrm{ads,N=13}}$ = -3.52 eV). However, the dissociation process is highly dependent on the energy barrier imposed by the geometric and electronic properties of the cluster/NP, and it is the activation energy of differently sized systems which determines the continuity of the adsorption behaviour in the scalable regime.

Energy barrier for the dissociation of acetic acid on the 6-atom Co cluster has a respectable value of 0.53 eV, which is also the highest E_{a} amongst the studied system sizes. Dissociation on the cluster with 13 atoms gives the second highest energy barrier of 0.44 eV. Activation energies for dissociation on the two distinctive surfaces of 19-atom Co cluster are less than half of the $E_{\mathrm{a,N=13}}$, with almost identical values of 0.20 eV on the (0001) and 0.19 eV on the $(10\bar{1}1)$ surface. Despite enlarged surface areas, particle with N = 30 atoms showed an increase in the E_{a} compared to the lower size clusters, and energy barriers were calculated at 0.41 eV and 0.44 eV on the (0001) and $(10\bar{1}1)$ surfaces, respectively. However, an enhanced number of atoms per facet allowed for an additional arrangement of dissociated components of acetic acid with hydrogen atom situated within the same area of the $(10\bar{1}1)$ surface as the remaining skeleton of the acid molecule, resembling adsorption states formed on larger NPs. In this specific case, no energy barrier was captured and dissociation occurred spontaneously. For NPs with $N > 50$, calculated energy barriers for vertex-based dissociation were consistently lower compared to their facet counterparts. E_{a} for the dissociation on the facet of the $(10\bar{1}1)$ surface, which accounts for more than 80 % NP surface area, was found to remain unchanged at 0.43±0.10 eV regardless of the size progression, fairly close to the 0.36 eV barrier calculated for the infinite slab model. On the (0001) surface, there is a moderate incline in the activation energies, which were calculated to be $E_{\mathrm{a,N=57}}$ = 0.24 eV, $E_{\mathrm{a,N=76}}$ = 0.31 eV, and $E_{\mathrm{a,N=153}}$ = 0.37 eV. All NPs show lower barriers on the (0001) surface compared to the $(10\bar{1}1)$ surface, likely due to the stronger tendency of hydrogen to form bonds within the hexagonal stacking of the former. Systems with the 323-atom Co NPs counted too many atoms for an efficient NEB run.

Accordingly, the nature of the interaction between the Co NP and acetic acid is governed by both electronic and structural characteristics of the clusters/NPs in question. Although the adsorption energies of both undissociated and dissociated interaction modes on the 30-atom particle complement nicely the trend of larger NPs, disparity in the activation energies suggests a potential inconsistency in the overall interaction behaviour. It can therefore be concluded that NPs with ∼50 atoms are precisely at the border where the domination of the electronic effects of large Co NPs vanishes and the ascendency of geometric effects of small Co clusters onsets.

5.3.2 Interaction modes of organic molecules on Co NPs

5.3.2.1 Carboxylic acids

After the 57-atom Co NP was shown to accurately represent the carboxylic acid-Co NP interaction at affordable computational cost, the stability and the likelihood of the possible binding modes can be explored. To provide insight in the mechanisms and barriers while taking into the account temperature effects, metadynamics was employed to enforce the transition between the interaction modes based on the CNs of the two carboxyl oxygen atoms, O_a and O_b, with respect to surface metal atoms. The system comprising of a Co NP with 57 atoms and a single molecule of valeric acid was initially equilibrated to the temperature of experimental synthesis (T = 500 K) in duration of 3.0 ps. The starting point of equilibration was interaction of valeric acid with single Co atom through the free-standing oxygen of carboxy functional group. Fluctuations in T, potential energy, and Co-O bonds during the equilibration are shown in Figure 5.5. The carboxylic hydrogen dissociated within less than 0.25 ps, followed by the attachment of the second carboxyl oxygen to the NP surface, yielding a bidentate interaction with both carboxyl oxygen atoms atop two neighbouring Co surface atoms. No further changes in the mode of interaction were observed throughout the equilibration period. Both Co-O distances in a monodentate and bidentate modes observed during the 3.0 ps AIMD run oscillated around 2.0 Å, as shown in Figure 5.5, top. This corresponds well with the bond lengths between acetic acid and differently sized Co clusters and surfaces optimised within the DFT approach, where the measured Co-O bonds are in the 2.00-2.07 Å and 1.92-1.97 Å ranges for the undissociative and dissociative adsorption on largest clusters, respectively. Bonds formed between the 57-atom Co cluster and acetic acid were optimised at 2.09 and 1.91 Å for undissociated and dissociated case. On clusters under 50 atoms, the bonds are slightly shorter and have an average value of ∼1.97 Å when acid molecule is undissociated, and ∼1.91 Å after dissociation. On the (0001) and (10$\bar{1}$1) surfaces, undissociated adsorption yielded 2.00 and 2.05 Å bonds, whereas a shortening occurred upon the dissociation and formation of the bridging bidentate with bonds of ∼1.97 Å. Accordingly, this value was used as the reference Co-O distance in the definition of CVs for metadynamics simulation.

Metadynamics was conducted in duration of 15.00 ps. Co-O distances and CNs of O_a and O_b have been presented for the whole metadynamics trajectory in Figure 5.6, alongside the representative structures. The starting structure was bridging bidentate, with each carboxyl oxygen bonded to one Co atom, as continued from the AIMD equilibration. After 2.50 ps, O_a formed a bridge in between the neighbouring Co atoms of the bridging bidentate interaction mode, resulting in a bridging chelate form which was stable for a short period before returning to the bridging bidentate. Around 0.50 ps later, O_b created a mirroring structure which persisted for a similar amount of time. The first monodentate interaction with a single O-Co bond formed between the NP and O_b atom of valeric acid occurred after approximately 4.75 ps, but the additional bond between O_a and Co was formed again in less than 0.25 ps. Before the next monodentate appearance, bridging chelate structure was captured three more times. The next appearance of monodentate

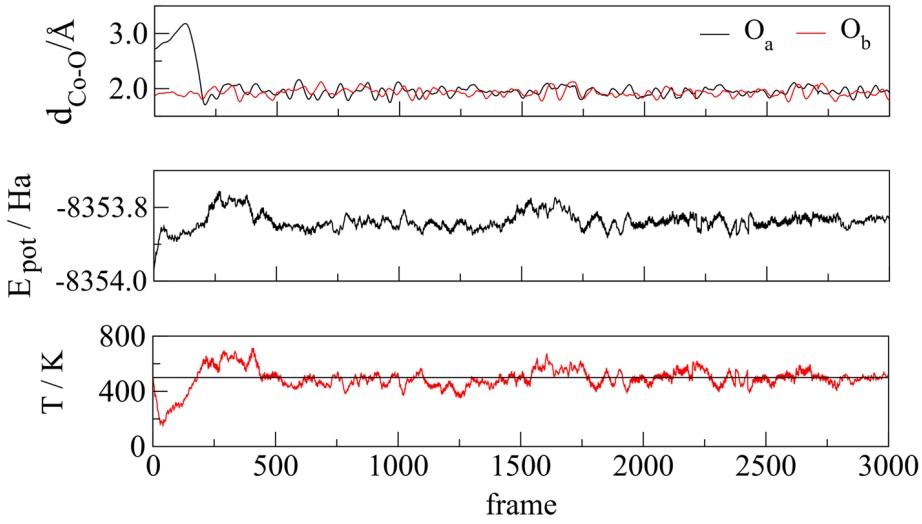

Figure 5.5: Co-O distances (**top** panel), potential energy (**middle** panel), and temperature (**bottom** panel, with horizontal line representing the temperature of the thermostat, $T = 500$ K) during the 3.0 ps *ab initio* molecular dynamics equilibration of valeric acid on the 57-atom Co NP.

was formed between the O_a oxygen of valeric acid and two neighbouring Co atoms rather than one Co surface atom as in the previous monodentate interaction, and it was stable for about 0.50 ps. The same type of bridging monodentate binding, with O_a and O_b alternating in the bond formation during the run, could have been seen twice before the original atop monodentate mode with single Co-O bond was again established. In most of the transitions between bridging bidentate and both atop or bridging monodentate (or vice versa), a bridging chelate interaction behaved as an intermediate state. Towards the end of the simulation run, a normal chelate mode with both carboxyl oxygen atoms forming bonds with the same Co atom appeared. No desorption of valeric acid was observed on the time scale of the entire simulation. After 15.00 ps, instead of the desorption of the molecule, O_b bonded to the surface Co atom that was so far not involved in any of the binding modes. This event was taken as termination point of the metadynamics simulation as valeric acid has exhausted possible modes of interaction within the neighbouring Co atoms it was initially bonded to. Ultimately, five distinct interaction modes were captured: atop monodentate, where one of carboxyl oxygen atoms binds one Co atom; bridging monodentate, where one O atom has two bonds with a pair of neighbouring Co atoms; bridging bidentate, where each carboxyl oxygen binds a single Co atom from a neighbouring pair; normal chelate, where both O atoms bind to the same Co atom; and, finally, bridging chelate, where one O atom forms two bonds, one with each atom from Co pair, while the other O atom forms a single bond with one of the Co atoms from the same pair. The bridging bidentate mode was formed for about half of the simulation time, ~48 %, with the bridging monodentate, atop monodentate, and bridging chelate modes

having a similar share of ∼18, ∼15 and ∼13 %, respectively. A normal chelate was the least occurring binding mode, only ∼6 % of the 15.00 ps simulation time.

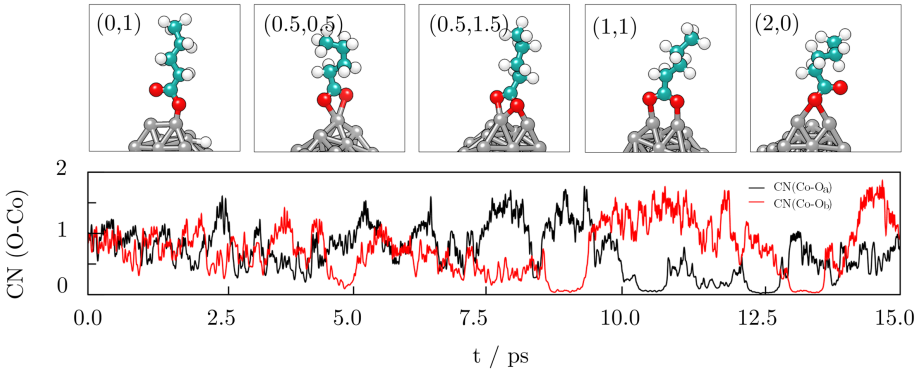

Figure 5.6: Representative structures (**top** panel) and changes in the coordination numbers, CN, (**bottom** panel) for valeric acid-Co NP interaction.

The type of interaction between the carboxylate head and metal atoms can be experimentally determined by the wavenumber separation (Δ) between the asymmetric ($\nu_{as}(COO^-)$) and symmetric ($\nu_s(COO^-)$) stretches of COO^- [557, 575, 576]: the largest Δ (∼200-320 cm^{-1}) corresponds to the monodentate interaction, medium Δ (∼140-190 cm^{-1}) to the bridging bidentate interaction, and the smallest Δ (<110 cm^{-1}) to the chelate interaction. To confirm the metadynamically observed forms of interaction, geometries corresponding to the main binding modes from the metadynamics trajectory were selected and their IR spectra, together with that of valeric acid in vacuum, simulated, Figure 5.7. The IR spectrum of the pure acid shows good agreement with the positions of the fundamental frequencies of carboxylic acids. The intense peak at 1749.0 cm^{-1} is characteristic for the C=O stretch and the one at 1120.5 cm^{-1} for the C-O stretch, while series of peaks at ∼3000 cm^{-1} belong to the -CH_2 and -CH_3 symmetric and asymmetric stretches. The broad O-H stretch feature observed between 3500 and 2500 cm^{-1} in experimentally measured spectra is missing since the acid molecule was modelled in vacuum. After adsorption, the intense C=O peak disappears, and two new peaks as features of carboxylate are formed instead. Positions of the two peaks are distinctive for each binding mode and can be found at 1292.5 and 1612.2 cm^{-1} for atop monodentate, 1176.6 and 1485.5 cm^{-1} for bridging monodentate, 1358.3 and 1490.8 cm^{-1} for bridging bidentate, 1487.4 and 1577.0 cm^{-1} for normal chelate, and 1234.0 and 1273.2 cm^{-1} for bridging chelate. The obtained wavenumber Δ separations between the asymmetric and symmetric stretches are 319.7, 308.9, 132.5, 89.6, and 42.2 cm^{-1} for atop monodentate, bridging monodentate, bridging bidentate, normal chelate, and bridging chelate, respectively, which, following the experimental trends discussed above, confirm the assigned interaction modes.

The next question that arises is to what extent does the binding mode interchange occur; i.e., what are the pathways and barriers taking place, considering finite-temperature

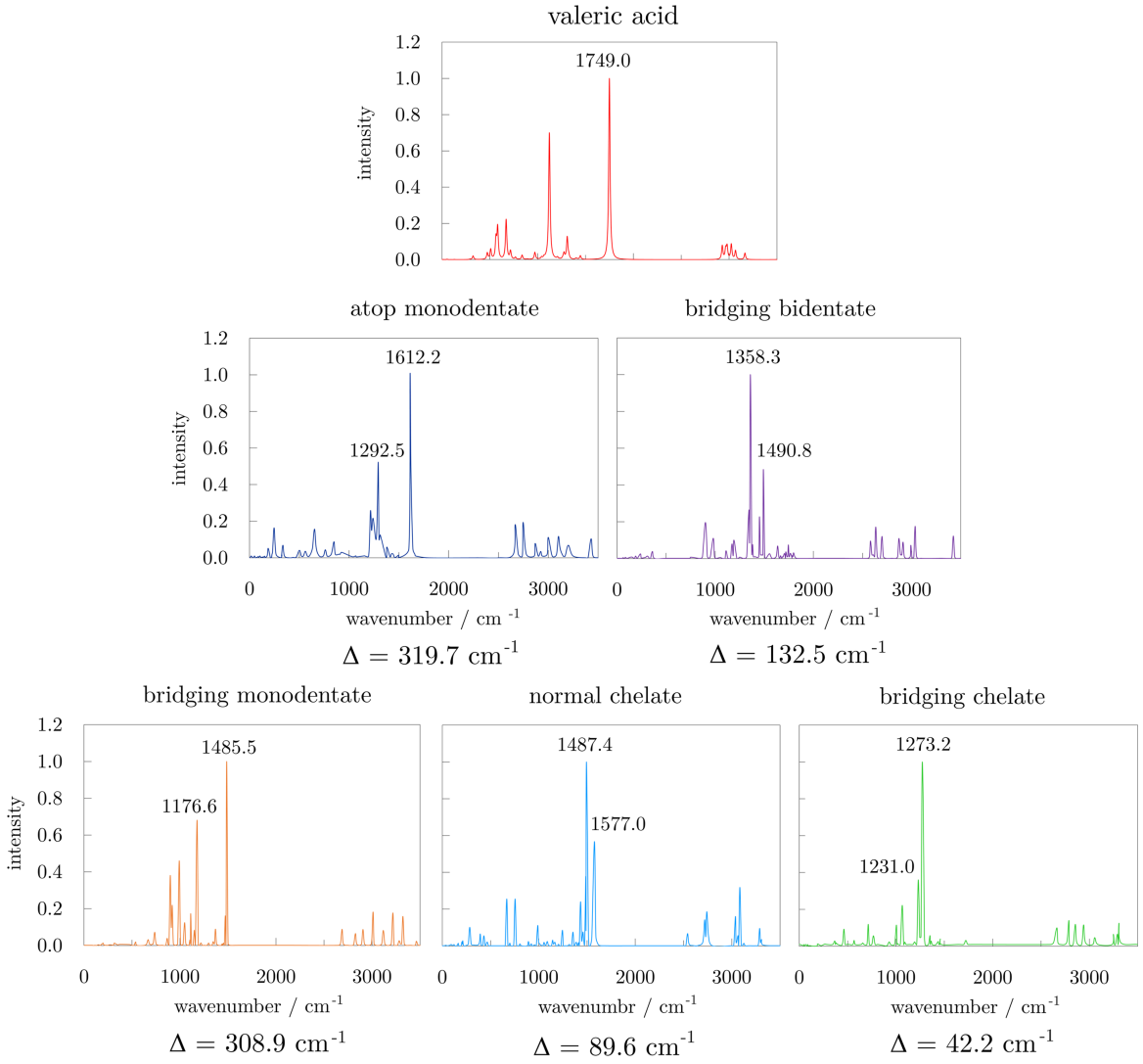

Figure 5.7: Simulated IR spectra of valeric acid in vacuum (**top** panel) and adsorbed on the 57-atom Co NP (**middle** and **bottom** panels) as atop and bridging monodentate, bridging bidentate, normal chelate, and bridging chelate, with accompanying wavenumber separations (Δ) between the asymmetric and symmetric stretches of COO^-. Both axes are the same for all spectra.

effects at the appropriate thermodynamic conditions. To investigate the underlying mechanisms in pertinent detail, the reconstructed free energy surface projected onto the plane spanning the two CVs, CN (O_a-Co) and CN (O_b-Co), has been plotted in Figure 5.8. Several minima beyond the one defining the starting structure are readily identified and denoted using Roman numerals. Minimum I represents the bridging bidentate and it is by far the most stable structure with an energy of -139 kJ mol^{-1}. Minima denoted as IIa and IIb are atop monodentate structures with O_a and O_b attached to one surface Co atom, respectively. They are higher in energy with respect to bridging bidentate, and sit at around -115 kJ mol^{-1}. Bridging chelates are represented by IVa and IVb and they

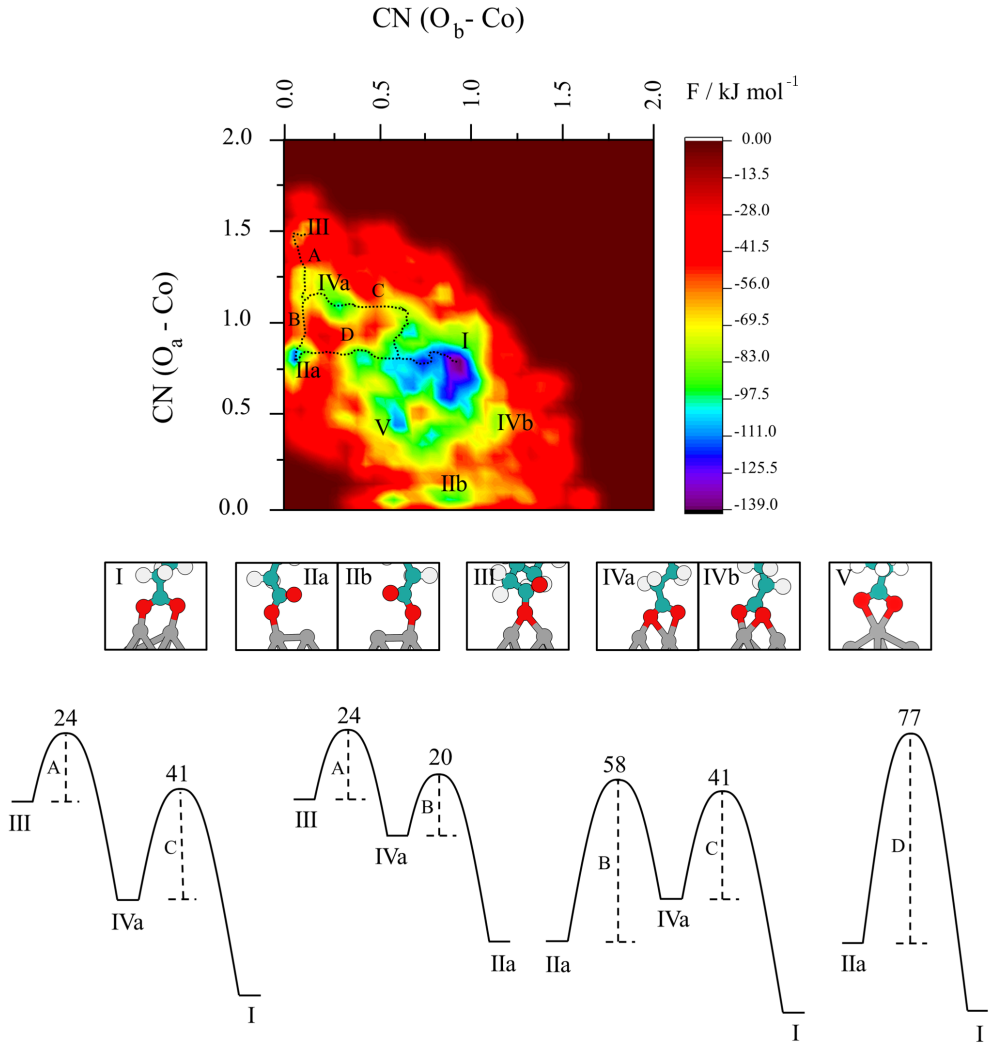

Figure 5.8: Free energy surface for the interaction of valeric acid and the 57-atom Co NP in the **top** panel; Roman numbers denote different minima, with accompanying letters a and b standing for the configurations differing only by the carboxyl oxygen atom, O_a or O_b, which binds to the NP surface. All structures are visually represented in the **middle** panel. Upper case letters illustrate the lowest energy paths whose mechanisms are proposed together with the free energy barriers (in kJ/mol) for individual processes in the **bottom** panel.

are energetically less favourable at -90 kJ mol^{-1}, while standard chelating mode, labelled as minimum V, lies at -104 kJ mol^{-1}. Bridging monodentate, III, is least likely to be formed with an energy of -60 kJ mol^{-1}. A wide area in energy up to -70 kJ mol^{-1} around the global minimum can be assigned to exhaustive efforts of the system to stay in the bridging bidentate mode even when one or both Co-O bonds do not reach the ideal value of 2.0 Å. What clearly emerges from Figure 5.8 is that the bridging bidentate is the most

favourable mode of interaction between carboxylic acids and Co NPs.

Figure 5.8 also illustrates possible transitions between the minima. From the minima IIa/b to the global minimum I there are two possible pathways, one with a bridging chelate as an intermediate (B, C) and another direct pathway (D). The formation of the intermediate chelating state IV allows the molecule to access a lower energy pathway. In particular, shift from the atop monodentate directly to the bridging bidentate global minimum following route D requires the system to overcome an energy barrier of 77 kJ mol^{-1}. However, transition through the chelate interaction separates the process into two steps (B, C), for which the barriers of 58 and 41 kJ mol^{-1} are both lower than in the direct D route. Other pathways include bridging monodentate as a starting point, with two possible final destinations: the atop monodentate (A, B), or the global minimum, bridging bidentate (A, C). Going from a bridging monodentate to the atop analogue requires overcoming an energy barrier of 24 kJ mol^{-1}, which increases to 41 kJ mol^{-1} if bridging bidentate is the final structure. In general, all transitions between minima are moderately energetically costly, with the rate-determining steps depending on the pathway. Normal chelate interaction is not directly placed on the monodentate-bidentate transition pathways.

Two lowest energy modes in the free energy landscape of valeric acid-cobalt NP system as sampled with metadynamics coincide with the binding forms proposed through the experimental works of Wu *et al* and Ansari *et al*. Additionally, through simulations it was possible to identify the stability and occurrence of the two modes and their transition mechanisms, which appointed bridging bidentate as a global minimum of the system. Thus, the correspondence to the experiments and accuracy of the approach used can be considered satisfactory for revealing the interaction modes and their relations for the case of organic molecules bonded to metallic NPs.

5.3.2.2 Thiols

Thiols have been widely used for functionalisation of gold NPs, and experimental and theoretical studies have found that the thiolates resulting from S-H bond cleavage bind to two gold atoms in average and can either coexist with the undissociated intact molecules or completely dominate if accompanied by the formation of molecular hydrogen.[577] On the other hand, doping of gold NPs with other metals resulted in a significantly different arrangement of thiol ligands compared to the pure thiol-capped Au particles.[578] A DFT study on the adsorption of methanethiol on the Co (0001) surface found dissociative adsorption in the threefold hollow sites, fcc and hcp, to be most energetically favourable and suggested that CH_3SH does not adsorb molecularly onto the surface.[579]

A 57-atom Co NP and a single molecule of 1-pentanethiol were equilibrated for 3.00 ps at the temperature of T = 450 K.[580, 581, 582] Progression of the T, potential energy, and S-Co/S-H interatomic distances is shown in Figure 5.9. Hydrogen of the thiol group dissociated from the 1-pentanethiol within first 0.25 ps of the equilibration and continued to move freely around the NP. Subsequently, S-Co was the only remaining form of

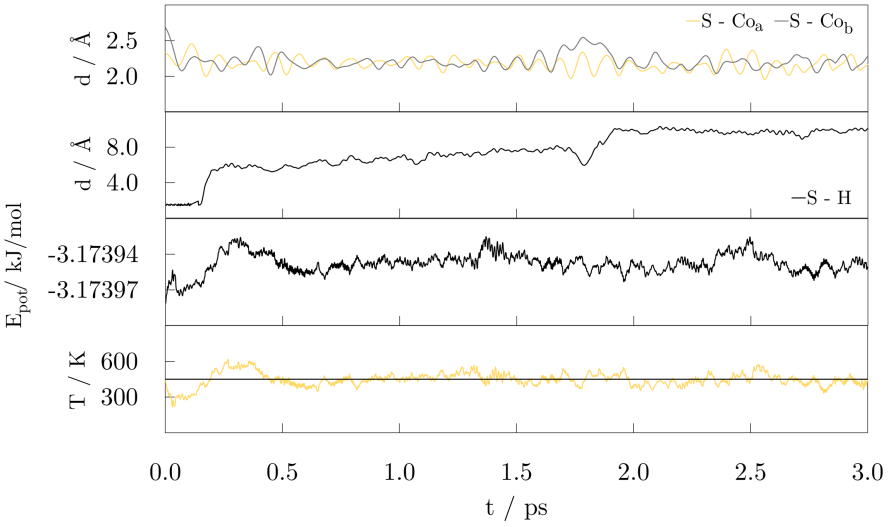

Figure 5.9: S-H and S-Co distances (**top** two panels), potential energy (**middle** panel), and temperature (**bottom** panel, with horizontal line representing the temperature of the thermostat, T = 450 K) during the *ab initio* molecular dynamics equilibration of 1-pentanethiol on the 57-atom Co NP.

interaction between the ligand and Co NP to be included in the definition of possible binding modes, leading to a single CV, CN(S-Co). From the fluctuations of bonds formed between sulphur and two of the Co atoms during the equilibration, a distance of 2.15 Å was defined as a reference bond distance.

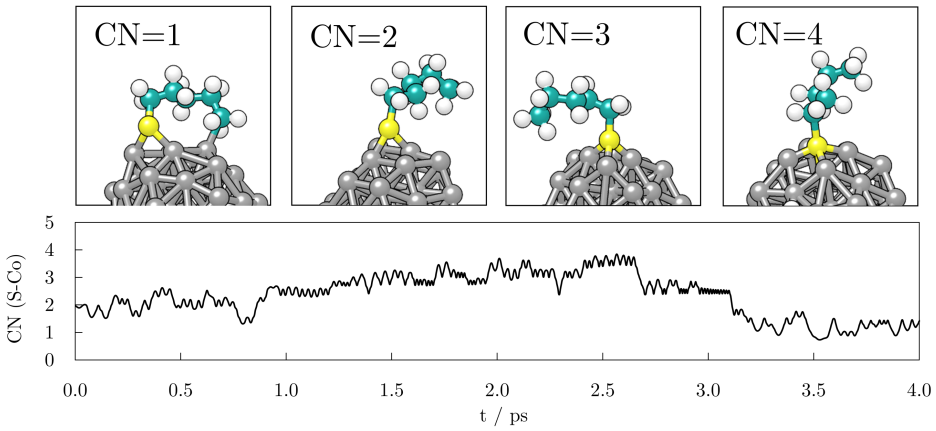

Figure 5.10: Representative structures (**top** panel) and changes in the coordination number, CN(S-Co) (**bottom** panel) for the 1-pentanethiol-Co NP system. Grey, teal, yellow, and white spheres represent cobalt, carbon, sulhpur, and hydrogen atoms, respectively.

Sampling of possible binding modes was carried out as a single CV metadynamics simulation. Progression of the CN(S-Co) and structures of captured interaction modes

are shown in Figure 5.10. Initial structure taken from the AIMD equilibration of the system with sulphur atom binding two neighbouring Co atoms, herein named bridging monodentate, remained stable for the first 0.80 ps of the metadynamics run. In the next 0.20 ps, sulphur moved towards a three-fold hollow position forming a third S-Co bond. This interaction mode, labelled as three-fold monodentate, was observed for the majority of simulation time. Only at about 2.50 ps structural rearrangement of surface Co atoms initiated by the penetration of the sulphur atom allowed for a four-fold monodentate binding to occur. The four-fold monodentate is characterised by bonds of four neighbouring Co atoms with the sulphur atom of the 1-pentanethiol, where S atom is levelled with the NP surface. This interaction was stable for ∼0.50 ps before returning to the three-fold binding composition. After 3.25 ps, bridging monodentate was again observed for a short time, followed by the elongation of both S-Co bonds. After about 0.50 ps, ending C atom of the 1-pentanethiol carbon chain started interacting with Co atoms of the remote edge of the NP. Formed binding mode between the thiol ligand and the NP is hence named S-C-bidentate, and it was observed for the remaining time of the simulation. Metadynamics sampling was stopped once the C-Co interaction made S-Co bonds significantly stretched, leading towards zero CN for S-Co interaction. Altogether, four distinct binding modes were defined for the interaction of the 57-atom Co NP and 1-pentanethiol: bridging, three-fold, and four-fold monodentates with sulphur atom binding one, two, and three Co atoms, respectively, and a S-C-bidentate, where sulphur of the -SH functional group and carbon on the opposite end of the molecule interact with remote parts of the NP. The three-fold monodentate was the mode of interaction through the 44 % of the simulation time, bridging and four-fold monodentate interactions were observed for the 23 and 20 % of the time, while the S-C-bidentate mode persisted for 12.5 %.

IR spectra of primary alkyl-thiols do not have as distinctive features as the IR spectra of carboxylic acids, Figure 5.11. A weak S-H stretch is captured at 2635.4 cm^{-1}, with an intensive C-S stretch peak at 527.4 cm^{-1}, corresponding well to experimental wavenumbers. As dissociation of thiol hydrogen occurred during the equilibration run, S-H peak is absent from the IR spectra of all interaction modes captured in the metadynamics simulation. Peaks corresponding to the C-S stretches of different binding modes experienced a significant decrease in the intensity and were slightly shifted to higher wavenumbers, namely to 580.1 cm^{-1} in the case of S-C-bidentate, to 547.9 cm^{-1} for the bridging monodentate, to 549.6 cm^{-1} for the three-fold monodentate, and to 602.1 cm^{-1} for the four-fold monodentate. In the lack of additional wavenumber descriptors, it would be very difficult to define the form of interaction of thiol molecule with Co NP solely from their IR spectra. Only evident difference can be seen between the S-C bidentate with the highest intensity peak situated at around 1500 cm^{-1} and the three monodentate interaction modes, where the most intense band is found in the 2500-3500 cm^{-1} region.

The stability, transitions, and barriers between different binding modes were analysed through the reconstructed energy profile as a function of the CV, Figure 5.12. Minima I and II, representing S-C bidentate and bridging monodentate, have similar stability with energies of -1.22 and -1.32 eV, respectively. Minimum III is a global minimum of the

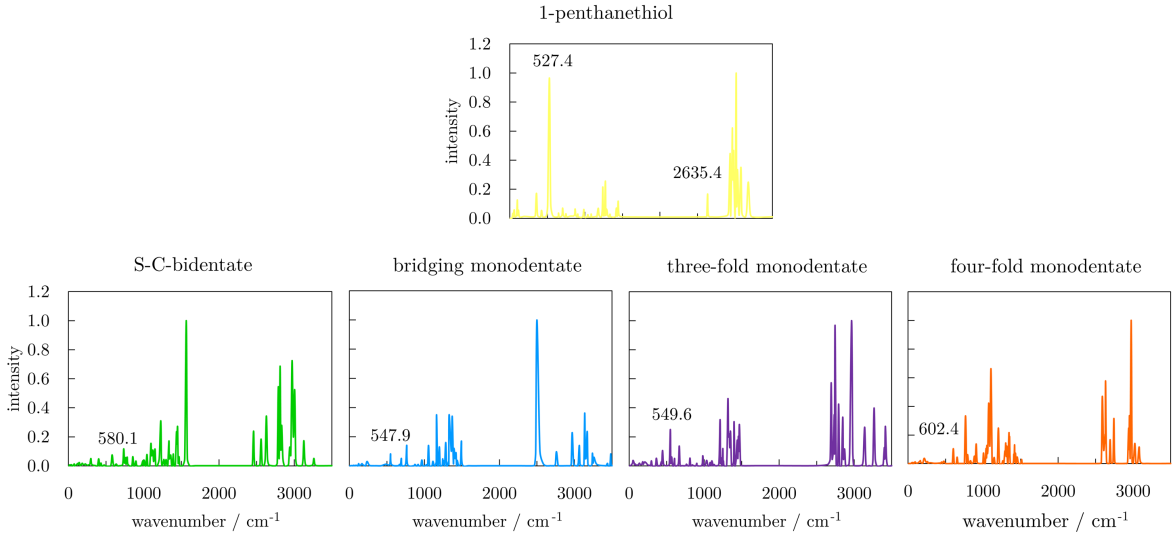

Figure 5.11: Simulated IR spectra of 1-pentanethiol in vacuum (**top** panel) and adsorbed on the 57-atom Co NP (**bottom** panel) as S-C bidentate, bridging monodentate, three-fold monodentate, and four-fold monodentate. Both axes are the same for all spectra.

system and corresponds to the three-fold monodentate interaction. It is favoured over other binding modes with the energy of -3.27 eV. Similar to the case of carboxylic acid energy landscape, the well of this structure is fairly large and extends to higher CNs, maintaining energies that are considerably lower than other minima. Final interaction mode, four-fold monodentate, is positioned in minimum IV with least favourable energy of -0.65 eV.

Energy barriers for the binding mode transitions can also be determined from the energy profile. S-C-bidentate and bridging monodentate modes, which have similar stabilities, are separated by a relatively low 0.25 eV barrier. Barrier for reaching the global minimum III from either minimum II or minimum IV is even more modest at only 0.03 and 0.02 eV. However, for system to leave the global minimum, it needs to overcome a significant energy cost. In particular, the shift to the bridging monodentate minimum imposes a barrier of 1.98 eV, followed by a 0.15 eV barrier for the transition to minimum I. Rearrangement of Co atoms to accommodate sulphur atom within four-fold monodentate interaction mode comes even more costly, with a transition barrier of 2.63 eV.

Three-fold monodentate is thus the most favoured structure sampled within the 1-pentanethiol-57-atom Co NP system, with high energy barriers for transitions towards other forms of interaction.

5.3.2.3 Amines

For the amine-protection of metallic NPs, the interaction options are less explored. In general, there are two binding modes mentioned in the literature: in the case of charged

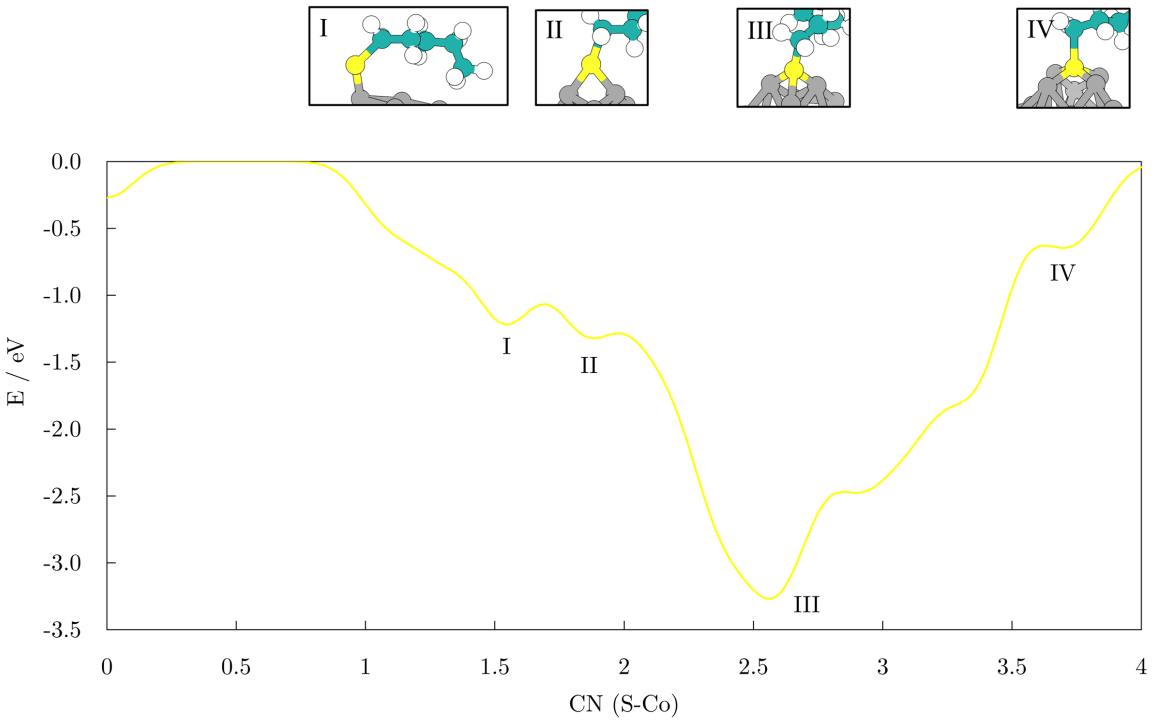

Figure 5.12: Free energy landscape for the 1-pentanethiol on the 57-atom Co NP spanned over the collective variable, CN(S-Co), with captured binding mode structures denoted by Roman numbers.

particles, the ligand with amino functional group mainly binds via electrostatic interactions, and the accepted binding mode is established as bonding of amine through the lone-pair of nitrogen to the particle; for tertiary amines, the binding through the H atom with the Pt NPs is suggested.[583] There are, to the best of author's knowledge, no reported binding modes of amines on Co NPs. The system comprising of a Co NP with 57 atoms and a single molecule of 1-pentanamine was initially equilibrated in duration of 3.00 ps at the temperature of T = 450 K.[580, 581, 582] No desorption of -NH_2 hydrogen atoms was observed throughout the equilibration. Figure 5.13 shows fluctuations in T, potential energy, and N-H/N-Co bonds. According to the thus far suggested binding modes of amines on metallic NPs, major contributors to the established interactions are formation of bond(s) between nitrogen and Co atoms, as well as breakage of the bond(s) between nitrogen and hydrogen. Therefore, CN(N-Co) and CN(N-H) were used as CVs. Reference distances employed in the definition of these CVs were taken as values averaged over the equilibration run, namely 2.0 Å for the N-Co, and 1.1 Å for the N-H.

Metadynamics was conducted in duration of 5.00 ps. CN(N-Co) and CN(N-H) are plotted in the bottom panel of Figure 5.14 for the whole trajectory, with the captured binding modes represented in the top panel. Initial structure with -NH_2 group bonded through the nitrogen atom to a single Co atom was taken from the ending of the AIMD

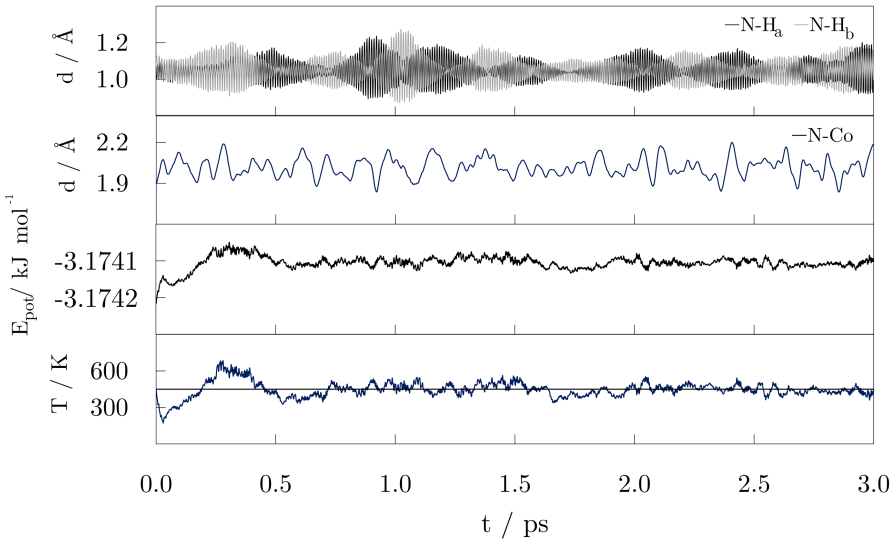

Figure 5.13: N-H and N-Co distances (**top** two panels), potential energy (**middle** panel), and temperature (**bottom** panel, with horizontal line representing the temperature of the thermostat, T = 450 K) during the ab initio molecular dynamics equilibration of 1-pentanamine on the 57-atom Co NP.

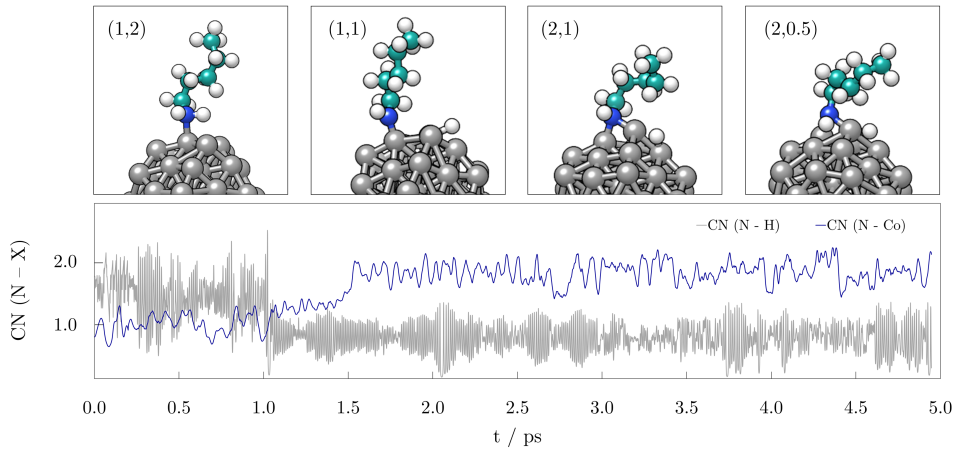

Figure 5.14: Representative structures (**top** panel) and changes in the collective variables, CN, (**bottom** panel) of 1-pentanamine on the 57-atom Co NP.

equilibration. This form of interaction, herein named NH_2-atop monodentate, remained unchanged for the first picosecond of the metadynamics run, when one hydrogen atom dissociated from the amine group. After dissociation, an average length of the N-Co bond shortened to 1.80 Å, which gave a CN(N-Co) of approximately 1.5 with the initially set up reference value of 2.00 Å. For the next half a picosecond, nitrogen remained bonded to one Co atom as an NH-atop monodentate, before forming an NH-bridging monodentate between the two neighbouring Co atoms. This bridging interaction prevailed for the rest of

the metadynamics run. The bond between nitrogen and the non-cleaved hydrogen of the amine group significantly stretched only in a few short periods as to indicate possibility of second dissociation; however, such event never occurred. This unfavourable state was labelled as NH-bidentate. There was no indication of nitrogen forming bonds with more than two Co atoms. After the simulation has reached 5.00 ps, nitrogen atom shifted towards a new pair of Co atoms, and this was taken as an indication of no remaining possibilities of distinct binding modes. Desorption of 1-pentanamine was not observed on the time scale of the entire simulation. Four interaction modes of 1-pentanamine were captured on the 57-atom Co NP: NH_2-atop monodentate, where -NH_2 functional group remains intact and connects to the NP through a single N-Co bond; NH-atop monodentate, where N atom maintains a bond with one Co atom and one H atom of the -NH_2 group, while the second hydrogen dissociates onto the NP surface; NH-bridging monodentate, where dissociated form of 1-pentanamine interacts through the nitrogen with two neighbouring Co atoms; and, ultimately, NH-bidentate, where both N and H atoms of dissociated 1-pentamine interact with the NP. During the metadynamics run, NH_2-atop monodentate was an active binding more for ∼20 % of metadynamics run, NH-atop monodentate and NH-bidentate for ∼10 and ∼8 %, respectively, while the NH-bridging monodentate was the dominating binding form persisting for more than 62 % of the simulation time.

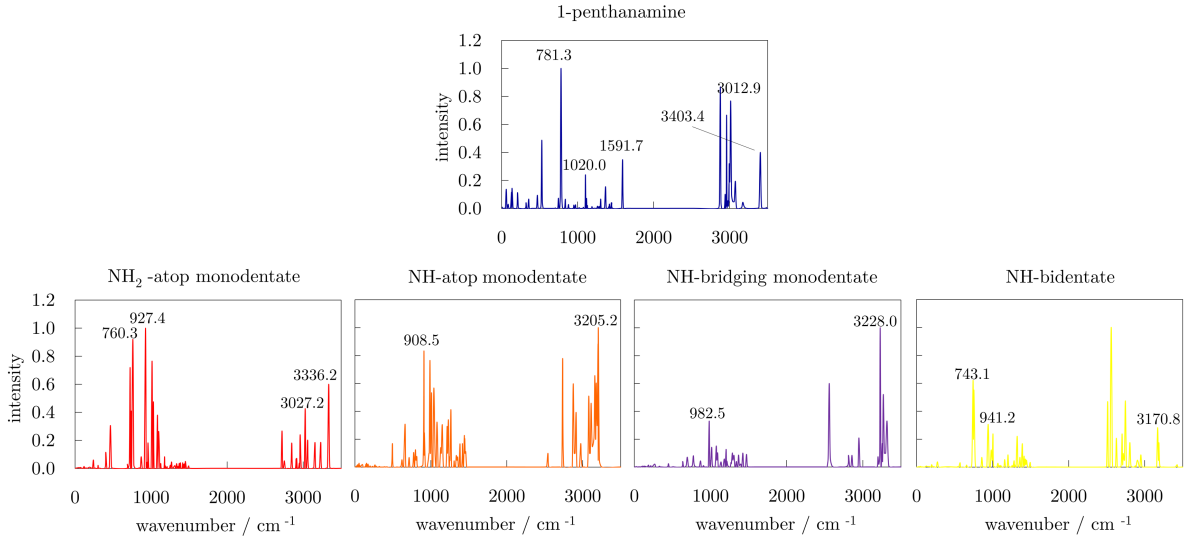

Figure 5.15: Simulated IR spectra of 1-petanamine in vacuum (**top** panel) and its four distinct binding modes (**bottom** panel) over 57-atom Co NP as sampled through metadynamics. Wavenumbers of stretching and bending modes relevant to the amino functional group (N-H and C-N interactions) are provided. Both axes are the same for all the graphs.

The IR spectra of the four distinct interaction modes of 1-pentanamine identified during the metadynamics run were simulated and are shown, together with the IR spectrum of the free adsorbate in vacuum, in Figure 5.15. The IR spectrum of 1-pentanamine has

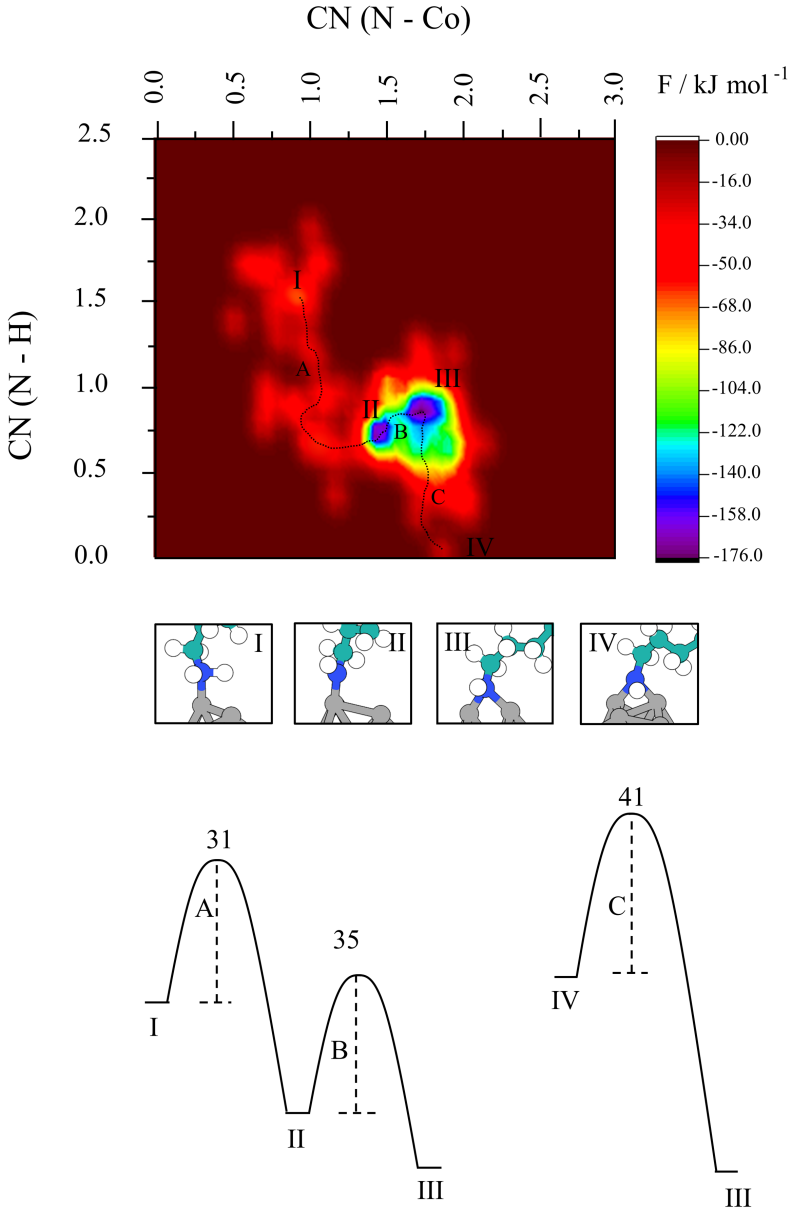

Figure 5.16: Free energy surface for the adsorption process of 1-pentanamine on the 57-atom Co NP (**top** panel); Roman numbers denote different minima and correspond to the represented structures (**middle** panel). Upper case letters illustrate the lowest energy paths whose mechanisms are proposed together with the free energy barriers (in kJ/mol) for individual processes (**bottom** panel)

all features of the primary amines: two bands for two N-H stretches can be found at 3403.3 and 3012.9 cm^{-1}, and that of N-H bend and N-H wag at 1591.7 cm^{-1} and 781.3 cm^{-1}, respectively; C-N stretch band is positioned at 1020.0 cm^{-1}. Prior to dissociation, 1-pentanamine adsorbs in an undissociated form as a NH_2-atop monodentate. Binding of

amino nitrogen to the NP causes a shift of the N-H stretch bands to 3336.2 and 3027.2 cm^{-1} and a shift of the N-H wag to 760.3 cm^{-1}, both of which decrease in intensity. The C-N stretch band is shifted more prominently to 927.4 cm^{-1} and its intensity is significantly increased, while the band of the N-H bend is not anymore observed. Upon dissociation, there remains only one N-H stretch band for the NH-atop monodentate at 3205.2 cm^{-1}. The 908.5 cm^{-1} band of the C-N stretch remains of a high intensity similar to the NH_2-atop monodentate, with bands around 750.0 cm^{-1} denoting single N-H wag experienced considerable reduction in intensity. Additional N-Co bond in NH-bridging monodentate contributed to a decrease in the intensity of the C-N stretch which can be found at 982.5 cm^{-1}. The band of the single N-H stretch in this interaction mode is positioned at 3228.0 cm^{-1}. Final interaction mode, NH-bidentate, where both nitrogen and hydrogen interact with the NP, shows the least prominent band of the N-H stretch which is shifted to a lower wavenumber value of 3170.8 cm^{-1}. As nitrogen is still bridging two Co atoms, a medium intensity band of the C-N stretch is observed at 941.2 cm^{-1}.

Although the alternations in the bands relevant to the amino group upon the binding mode changes are not as straightforward as in the case of carboxylic acids, it is still possible to distinguish between different interaction modes based on their IR spectra. Captured changes coincide with the experimental observations on amine-functionalised Pt NPs, which showed that the typical amine bands are usually shifted to lower wavenumbers, broadened, and less intense than in the free ligand.[583]

To investigate the stability of detected binding modes and the interchanging pathways, the free energy surface as a function of the two CVs, CN(N-Co) and CN(N-H), was plotted in Figure 5.16. Four minima were identified and labelled with Roman numbers. Minimum I is that of the NH_2-atop monodentate, arising from the (1,2) pair of CN(N-Co) and CN(N-H), with an energy of -57 kJ mol^{-1}. Minima II and III correspond to the forms of interactions after the dissociation of one hydrogen atom. The former, with the (1.5,1) CN combination corresponds to the NH-atop monodentate, whilst the latter CN combination of (2,1) stands for the NH-bridging monodentate. Both minima are significantly lower in energy when compared to the NH_2-atop monodentate, and sit at -151 and -158 kJ mol^{-1}, respectively. Flickering of the hydrogen atom attached to the nitrogen has led to the constant alternations in the length of the N-H bond and the value of the CN(N-H) collective variable, resulting in the increased area of the NH-atop and NH-bridging monodentate wells. NH-bidentate is found at minimum IV, with the (2,0) CNs pair and, with an energy of -43 kJ mol^{-1}, it is least likely to form. Possible transitions between the distinct binding modes and their energy barriers are also captured in Figure 5.16. For system to reach low energy structures II and/or III starting from minimum I, it has to cross a couple of moderate energy barriers, all in the 25-32 kJ mol^{-1} range. The minimum II to minimum III transition is characterised by a 35 kJ mol^{-1} barrier. If minimum IV is a starting point, barrier for reaching more favourable structures (minima II and III) is $\sim$41 kJ mol^{-1}. However, transitions from the minima II and III towards either minimum I or minimum IV are much more energetically costly.

Altogether, energetically most favourable binding mode of 1-pentanamine on the 57-

Co NP is found to be the NH-bridging monodentate, where one hydrogen atom from the -NH_2 functional group dissociates to interact with the surface Co atoms on its own, and the remaining form of 1-pentanamine binds the two neighbouring Co atoms through two N-Co bonds. This binding mode is characterised by a significantly reduced intensity of the C-N stretch IR band and a pronounced N-H stretch peak.

5.4 Conclusion

The role of ligands in the alternations of the behaviour and properties of metallic NPs derives from the varying forms of ligand-NP interactions, as shown by many experimental studies. It is hence important to distinguish between the binding modes and possibility of their occurrence in the functionalisation processes. Combination of *ab initio* molecular dynamics and metadynamics calculations clarified the interaction modes of Co NPs with three families of biomedically relevant organic ligands, namely carboxylic acids, thiols, and primary amines.

On the basis of the size-dependent adsorption of molecular entities, a 57-atom Co NP was suggested as an entry particle size for the scalable NP-ligand behaviour. Following metadynamics simulations have provided important insights into the free energy landscape around the two experimentally observed binding modes of carboxylic acids on Co NPs, identifying bridging bidentate as the global minimum. For the thiol-Co NP system, three-fold monodentate was detected as the most favourable structure, whereas NH-bridging monodentate was predicted to be the dominating amine-Co NP binding form. Observed interaction strengths (-1.44 eV for carboxylic acids, -3.45 eV for thiols, -1.82 eV for amines) coincide with the adsorption energies of similar molecules adsorbed on the (0001) surface of hcp Co. Interaction of the (0001) surface and formic acid was found to have an adsorption energy of -0.68 eV in molecular state and -0.75 eV after dissociation.[133] Calculated adsorption energies of nitrogen-based species, from amines to imines and nitriles on Co (0001) were in a -1.16 to -2.82 eV range.[584] Finally, adsorption of methanethiol on the (0001) surface shown adsorption energies of about -3.00 eV for low coverages.[585] Specific IR features were also successfully captured.

It is thus fair to say that the accuracy of *ab initio* simulations of interaction forms and lattice dynamics on smaller ligand-NP systems is satisfactory, and the real value is their ability to provide predictions for those ligand-metal pairs which are not easily accessible to experimental techniques. Determination of the binding modes between the two modalities is a first step towards simulating the organic coatings on Co NPs and ligand-induced behaviour of the magnetic Co core. These data will also stimulate a deeper investigation on the role of the capping agents in metal NP synthesis and their *in vivo* behaviour.

Highlights of the chapter

- **Identified a 57-atom Co NP as an entry particle size for the scalable NP-ligand behaviour.**
- **Resolved experimental literature discrepancy of the carboxylic acid-Co NP binding mode by defining bridging bidentate as the global minimum.**
- **Proposed interaction modes for thiol- and amine-Co NP systems.**
- **Simulated IR spectra for distinct binding modes of carboxylic acid, thiol, and amine ligands on Co NP.**

CHAPTER 6

MECHANISM OF FUNCTIONALISATION

"Would you tell me, please, which way I ought to go from here?"
"That depends a good deal on where you want to get to," said the Cat.
"I don't much care where -" said Alice.
"Then it doesn't matter which way you go," said the Cat.
"-so long as I get somewhere," Alice added as an explanation.
"Oh, you're sure to do that," said the Cat, "if you only walk long enough."
-Chapter 6, Pig and Pepper

6.1 Introduction

6.1.1 Functionalisation strategies

With the growing potential of mNPs in biomedicine and the increasing concerns of their nanotoxicity, the interaction between surfactants and magnetic cores is proving to be of fundamental interest for effective bio-functionalisation. Due to the complicated interplay between the interactions involved at the bio-nanointerface, the structure-activity relationship, and mechanism behind the nanocomposite formation, it is important to get an insight in the mutually inclusive dependence of mNP functionalisation on the density and composition of the surface coating beyond a single molecule contact. In these multiligand-NP structures, prediction of the interactions is a non-trivial task; covalent bonding [586], non-covalent bonding [587], coupling reaction assisted immobilisation [588], simple coating/deposition [589], and Stöber technique [590, 591] have all been described as possible governing forces of nanoscale biomolecular functionalisation.

The preferable conjugation of polyphenol, which possesses highly active medicinal properties, with gold NPs was studied to gain an in-depth understanding of the nature of the participating functional groups involved in the NP reduction and capping.[592] Using the experimental data alone, validation of the role of various moieties, molecular conformations, and surface passivation of Au NPs could not be clearly achieved. Conceptual comprehension was gained from the quantum chemical calculations, establishing connection of the molecular and electronic structure of surfactant molecules and their binding affinity to metal ions in various conditions. Steric repulsions due to the methoxy-methoxy interactions were found to be an important factor in determining the lowest

energy conformer, whereas the breakage of intramolecular H-bonding was proposed to lead to the increased availability of ligands. Similarly, the hydrogen bonding was found to play an important role in the drug loading processes of drug molecules-nanographene surface systems.[593]

Moreover, very little is known about the reaction pathways of hydrogen atoms dissociated during the conjugation of organic surfactants with metal NPs. Even in the case of well-investigated thiol-gold systems, there are only a few very recent theoretical studies of the hydrogen transfer mechanism supporting an experimentally suggested release of H_2 in the functionalisation process.[594, 595] Previous AIMD work showed that interaction of two thiols with a four-atom gold cluster results in the production of H_2 and formation of substructures containing adatom-like gold atoms pulled away from the cluster surface with almost linear RS-Au-SR bonding patterns. Such gold adatom-mediated substructures with alternating gold and sulphur atoms were first detected within the self-assembly of alkanethiolates on the Au(111) surface [596] and are now known as staple motifs.[597, 598] Later, the interaction of small gold clusters with one to 38 atoms was examined by DFT, which confirmed the thermodynamics of the H_2 generation and subsequent staple motif formation.[599] To the best of author's knowledge, no information is available on cobalt-organic surfactant systems.

Comprehension of the role of hydrogen bonds, dissociated atoms, and steric, intermolecular dependence adds to the understanding of the interaction of multiple surfactant molecules with nanosystems, and it can be very useful for tailoring optimised surfaces to control the drug loading or effective NP protection. Thus, to obtain information above the sole nature of the ligand bonding, an atomic perspective for the functionalisation mechanism of fully protected NPs is needed.

6.1.2 Motivation

In the light of previous chapters, the most important practical question regarding the design of metallic NPs for use in biomedicine is how to ensure a sufficiently long lifetime of the NPs in the organism. This requires both that the NPs do not disintegrate, aggregate, or lose their integrity otherwise, and that they are not removed by the immune system. Additionally, for mNPH, NPs should maintain the high levels of magnetisation throughout the duration of the therapy.

Virtually nothing is known regarding the functionalisation mechanism or reactivity of ligand-protected Co NPs beyond the basic information on the binding modes of a few potential ligands. The ability of the chosen ligand to function according to the biological requirements depends largely on the structure of the coating, which is a complicated function of the coating density and type of the molecule in combination with material, size, and shape of the NP core, whereas the functionalisation mechanism is a prevailing factor.

To explore the mechanism behind the functionalisation of Co NPs with carboxylic acids, *ab initio* molecular dynamics was employed to investigate the coating process with

valeric acid, $CH_3(CH_2)_3COOH$. The structure and stability of the formed nanocomposite were traced throughout the simulation with a particular focus on the changes in the adsorption rate and binding modes of the adsorbed molecules. After the three stages of the functionalisation process were identified, the detected reactivity changes caused by the increased acid coverage and carboxyl hydrogen dissociation paved the way towards simulations of energy barriers accompanying H_2 generation and desorption.

6.2 Computational details

As a baseline for simulating the functionalisation mechanism, the reference case of a single particle in the presence of acid molecules was established. The previously optimised 57-atom hcp Co NP was placed in the simulation box together with 14 optimised molecules of valeric acid (corresponding to a coverage of one molecule per facet if all molecules were to be adsorbed). The real density of the liquid was inaccessible to model by AIMD. AIMD simulations were performed using CP2K with the GGA/PBE functional and the GTH basis set. The chosen system was simulated in the NVT ensemble during 10.00 ps of Born-Oppenheimer MD. A Nosé-Hoover thermostat was set at the synthesis temperature of T = 500 K [211, 600, 215], and a time step of 1.0 fs was used for the integration of the equations of motion.

Hydrogen dissociation and formation of H_2 were studied by the NEB method and *ab initio* metadynamics. NEB simulations were performed using the VASP package within the GGA/PBE exchange-correlation functional. The DFT-D3 method with Becke-Johnson damping was used to include the long-range dispersion interactions and the k-point grid contained only the Γ point. All intermediate and transition states were fully optimised and Hessian calculations were performed to verify the existence of one imaginary frequency for the transition states. CP2K was instead used for the metadynamics trajectories, during which Gaussian hills with a height of 0.01 Hartree and a width of 0.05 were deposited every 50 fs.

6.3 Results

6.3.1 Functionalisation mechanism

The functionalisation mechanism for carboxylic acid-protected Co NPs was investigated by surrounding a single 57-atom Co NP with 14 valeric acid molecules and performing an AIMD relaxation of the system in duration of 10.00 ps. Initial and final arrangements are shown in the top panel of Figure 6.1. The bottom panel of Figure 6.1 contains the simulation timescale with a few intermediate configurations capturing key events.

Initially, the NP and the randomly oriented acid molecules were separated by a distance of about 8 Å. Acid molecules immediately started to move and were progressively captured on the NP surface in the form of a monodentate. Adsorption of the first molecule

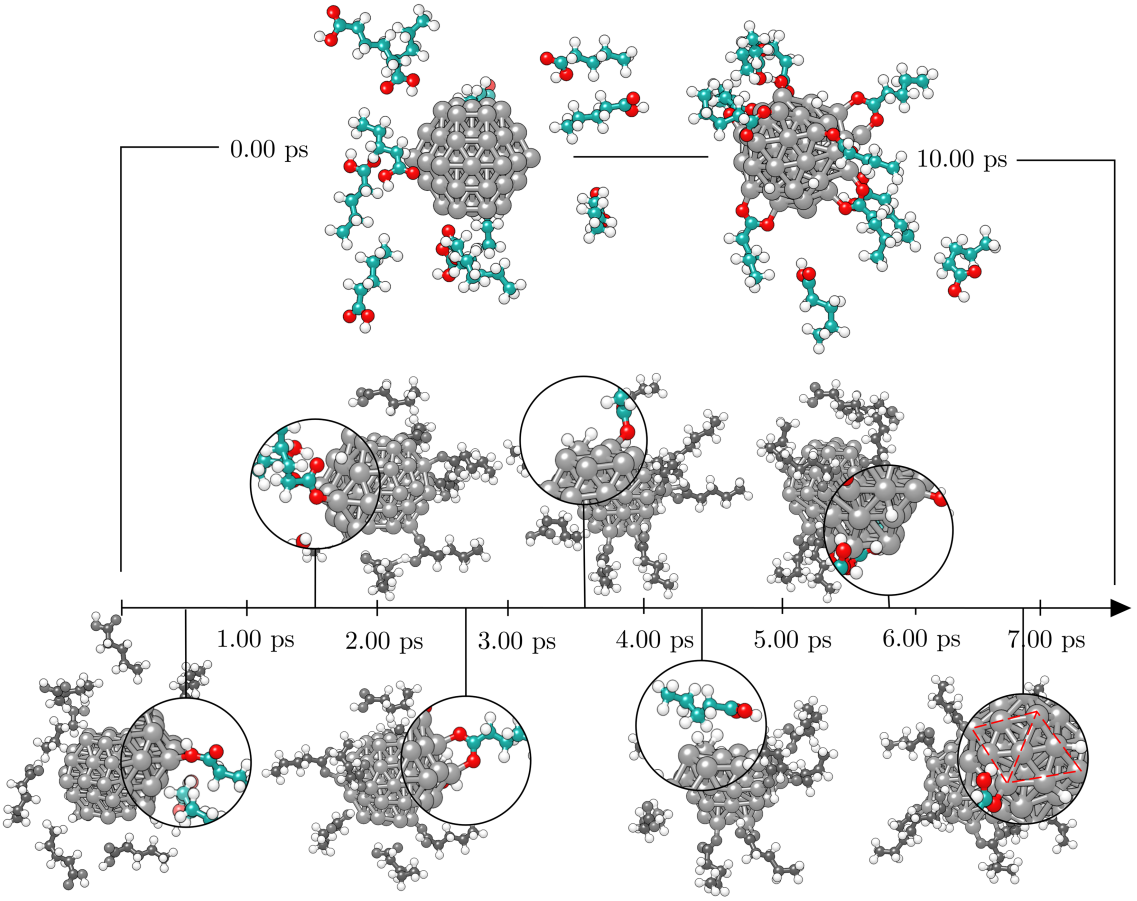

Figure 6.1: Timeline of the 10.00 ps *ab initio* molecular dynamics run on the 57-atom Co NP-14 valeric acid molecules system with initial and final geometries given on the **top** left and right, respectively, and seven key events featured on the **bottom** in the order of their occurrence during the simulation: adsorption of the first acid (0.60 ps), first dissociation (1.60 ps), formation of a bridging bidentate (2.50 ps), grouping of dissociated H atoms (3.20 ps), desorption of an acid molecule (4.40 ps), further grouping of dissociated H atoms (5.75 ps), hcp→icosahedron transformation (6.80 ps). Grey, teal, red, and white spheres represent cobalt, carbon, oxygen, and hydrogen atoms, respectively.

occurred just after half a picosecond. The molecule adsorbed onto the vertex Co atom of the $(10\bar{1}1)$ surface through the -COOH oxygen atom which was bound to the carboxyl hydrogen. Shortly after, the second adsorbate molecule bound to another $(10\bar{1}1)$ surface vertex, but this time the bond was established between Co atom and the freestanding oxygen of carboxyl functional group. At 1.00 ps, a total of five molecules have already interacted with the NP, one of them forming a bond with the (0001) surface vertex atom. Interestingly, regardless of the initial orientation, acid molecules showed no preference on through which oxygen atom of the carboxyl group they adsorb; even if the -OH was initially further away than the corresponding freestanding O atom of the -COOH group, some molecules interacted through the former. Within the next picosecond, half of the

molecules attached to the NP mostly to vertex Co atoms, and still no pattern was observed regarding the oxygen atom through which the monodentate adsorption took place. There were also instances where an interchange in the interacting oxygen atom would occur within single acid molecule. The coating at this point could have been characterised as isotropic - adsorbed molecules were positioned at distant parts of the NP and no aggregation took place. Just before the simulation time reached 2.00 ps, one carboxyl hydrogen dissociated from its parent acid. Less than 0.15 ps after, a second dissociation happened. Each of the dissociated molecules formed two Co-O bonds, adsorbing in a bridging bidentate mode. The dissociated hydrogen atoms moved effortlessly across the NP surface through available bridge and hollow sites. As the simulation proceeded, within the next two picoseconds two more acids lost their carboxyl hydrogen atoms, while two previously unbound molecules adsorbed as monodentates. Even though a portion of adsorbed acid molecules still interacted through the -OH oxygen atom, dissociation occurred in all four occasions on acids that were binding with a freestanding oxygen of the -COOH group. Dissociated acids were noticed to quickly form bridging bidentate interactions, typically within 0.25 ps after dissociation. In one instance, an intermediate chelate state was observed. Movement of the dissociated hydrogen atoms started to be more localised, with a pair from the two earliest dissociations pulsing around the same vertex Co atom, simply interchanging amongst each other's positions. This caused the nearby acid molecule, which was actively interacting with the NP for over two picoseconds, to desorb at ∼4.00 ps, followed by the adsorption of a new acid molecule at the site available farther away. Grouping of the other pair of dissociated hydrogen atoms was also captured just after 4.50 ps on the vertex on the opposite side of the NP. At the end of the 5.00 ps, nine acid molecules were attached to the NP surface and four had their carboxyl hydrogen atoms dissociated and were interacting in the bridging bidentate mode. The remaining five molecules were adsorbed undissociated in the monodentate binding mode. No significant disruption in the NP shape was observed thus far, as indicated by minimal changes in the radius of gyration, r_g, Figure 6.2.

Except for the constant flickering of dissociated hydrogen atoms, no further events were observed within the next half picosecond when an additional valeric acid molecule was adsorbed. With almost 40 % of Co atoms on the NP surface now directly interacting with carboxyl oxygen atoms, the shape of the NP started to distort. Throughout the change, captured average values of the radius of gyration were around 3.96 Å, Figure 6.2. Just after 6.00 ps, another dissociation occurred. It took almost a full picosecond for the latest carboxylic acid that dissociated to establish a bridging bidentate interaction because of pulsating hydrogen atoms that were limiting the availability of surface Co atoms. This was followed by a dissociation of yet another valeric acid at 7.00 ps, at which point the newly released H atom grouped quickly with the one dissociated previously. By the time this acid formed a bridging bidentate mode with two Co atoms, the shape of the NP became icosahedral, and initial r_g values were retrieved in correspondence with equivalent Co-Co distances of hcp and icosahedral Co NPs. The next dissociation was observed at 7.70 ps. Subsequent grouping of hydrogen atoms was followed by a desorption of yet another valeric acid molecule, whose adsorption was observed in the early stages of

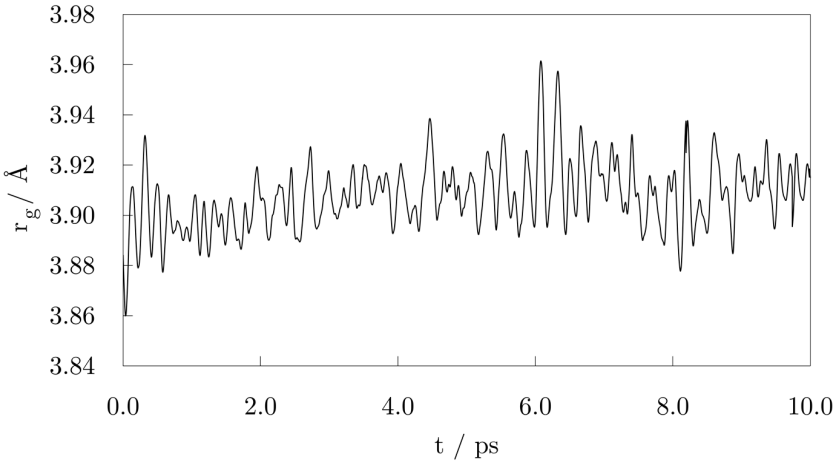

Figure 6.2: Radius of gyration, r_g, after the 10.00 ps of the *ab initio* molecular dynamics run of the functionalisation of 57-atom Co NP with 14 valeric acid molecules.

simulation (at 0.45 ps), just before the time has reached 8.25 ps. The final dissociation happened just after 8.75 ps of the simulation time. The last picosecond was marked as the longest time without any events, and the simulation was terminated at 10.00 ps.

At the end of the 10.00 ps run, ten acid molecules were attached to the NP surface and eight had their carboxyl hydrogen atoms dissociated, interacting through the bridging bidentate mode. The remaining two molecules were adsorbed undissociated as monodentates, one bonding to the vertex Co atom and the other to the edge Co atom. One of the O-Co bonds was established through the -OH oxygen atom. That specific valeric acid molecule underwent multiple attempts to form a permanent bond with the cluster (average O–Co bond of interacting acid molecules being 1.9 Å), however, for the majority of the simulation time it was at a 2.2-2.4 Å distance from the NP surface, giving place to dissociated hydrogen atoms. Adsorbed acid molecules were distributed evenly across the (0001) and $(10\bar{1}1)$ surface areas, with the exception of vertex sites where dissociated hydrogen atoms resided.

To evaluate the stability of the adsorption system, the potential energy during the 10.00 ps run was plotted in Figure 6.3. The figure illustrates a significant decrease in the potential energy during the early stage of the simulation up to 1.00 ps, followed by a relatively stable period of about 0.50 ps. Another noticeable drop in energy occurred at ∼2.00 ps also followed by a stagnant trend of a more subtle decline that extends to 4.25 ps, when a first occurrence of a stability loss can be seen. After about 0.25 ps, the potential energy curve restores the negative slope. These stability alternations occurred throughout the remaining simulation time, whereas the on-going potential energy decrease faded away after 7.00 ps, seemingly reaching equilibrium state in the number of adsorbed carboxylic acid molecules. Two additional striking drops at 7.10 ps and 8.75 ps correspond to the stability gained through the shape modification, and a further adsorption event as a response to the hydrogen-triggered desorption destabilisation.

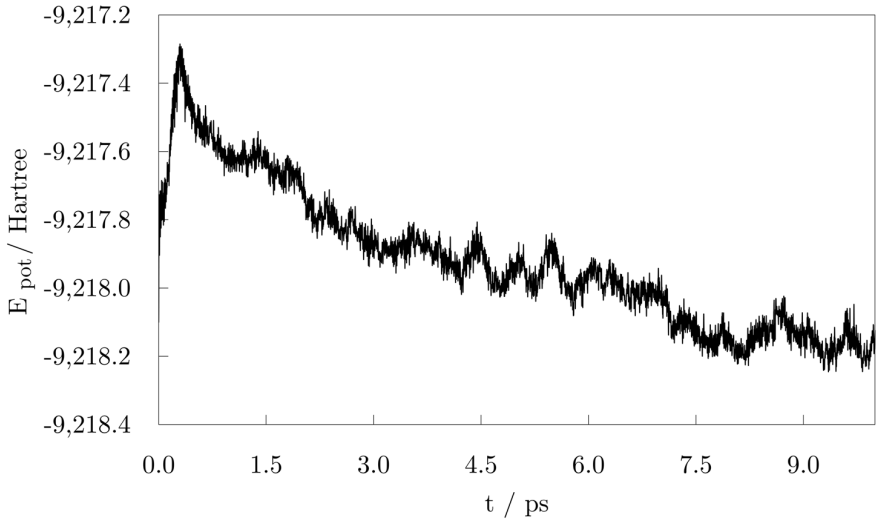

Figure 6.3: Potential energy, E_{pot}, as a function of time during the 10.00 ps *ab initio* molecular dynamics run on the 57-atom Co NP - 14 valeric acid molecules system.

As the potential energy trend displays, the functionalisation process can be divided into three distinct stages. Stage 1, in which a decrease in the potential energy is solely due to the effective adsorption of valeric acid molecules across the NP surface at a relatively constant adsorption rate (first two picoseconds). In stage 2, the rate of adsorption is slowed down, and fluctuations in the potential energy are caused by hydrogen dissociations and established bridging bidentate binding (between 2.00 ps and 4.50 ps). Finally, stage 3 comprises of alternating destabilisation and re-stabilisation periods characterised by desorption of valeric acid molecules near the locations of dissociated hydrogen atoms and adsorption/dissociation of previously non-adsorbed/non-dissociated acid molecules on distinct sites of the NP. In this final stage, the adsorption rate has reached the plateau, and adsorption is only induced in the instances of hydrogen-caused acid detachment to regain the equilibrium state of the system.

A schematic representation of the AIMD-predicted reaction mechanism is shown in Figure 6.4. Considering that the available literature on the binding of carboxylic ligands to monometallic and bimetallic NPs and surfaces reports the bridging bidentate as the preferred mode of interaction in most cases with the occasional dominance of the chelate biding [601, 602, 603, 594, 604], it is likely that the proposed functionalisation mechanism, or certain aspects of it, are also applicable to those systems. The true mechanisms for the acid functionalisation of other metallic NPs are, however, subject to future research efforts.

The observed behaviour, together with the known layout of organic coatings to be synthesised with the respective loss of hydrogen, indicates that the fate of hydrogen should also be investigated. Throughout the simulation time, as more acid molecules lost their carboxyl hydrogen atoms, desorption started to occur, destabilising the system.

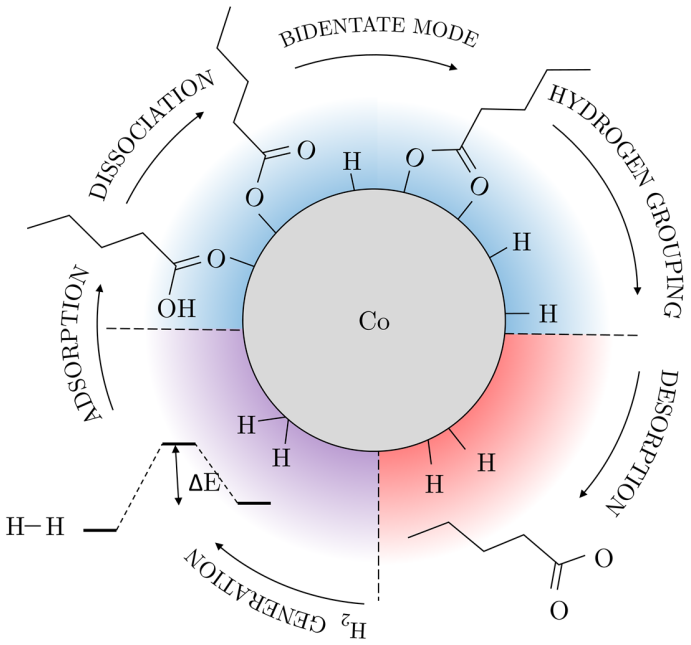

Figure 6.4: Schematic representation of the AIMD-predicted mechanism for the acid-functionalisation of Co NPs. Colour scheme is as follows: steps shaded in blue are spontaneous and stabilising, steps shaded in red are destabilising, and steps shaded in purple are hindered by an energy barrier, but, once overcome, they lead to further stabilisation of the system.

Since it is very unlikely that hydrogen atoms would detach from the NP on the timescale of the AIMD simulations, a combination of NEB and *ab initio* metadynamics was chosen to model the occurrence and energetics of this rare event.

6.3.2 Fate of dissociated hydrogen

To provide a greater understanding of the functionalisation mechanism of Co NPs by carboxylic acids, NEB calculations were carried out for dissociation, transfer, and recombination of hydrogen atoms associated with the carboxyl group, and the study was further extended to thiol and amine ligands for comparison. To reduce the computational cost of expensive NEB calculations, 2C-atom chain ligands were used, i.e. acetic acid CH_3COOH, ethanethiol CH_3CH_2SH, and ethanamine $CH_3CH_2NH_2$, instead of the initially adopted 5-C atom counterparts. The effects of coverage and finite temperature were tested through the metadynamics simulations.

6.3.2.1 Single ligand adsorption

Adsorption energies of a single molecule of acetic acid, ethanethiol, and ethanamine at various available sites of the 13-atom cluster and 57-atom Co NP can be found in Table 6.1. Adsorption is spontaneous for all investigated positions, with the strongest

interaction on the 13-atom cluster accompanied by the adsorption energies of -1.59 eV for acetic acid, -1.81 eV for ethanethiol, and -1.87 eV for ethanamine. The adsorption process is followed by the structural hcp→icosahedron rearrangement of the 13-atom cluster, in accord with predicted isomer energies.[265, 605] Adsorption on the facet site of the 57-atom NP showed to be only half as strong as adsorption on the vertices, with adsorption energies of -0.57/-0.53 and -1.08/-1.07 eV for facet and vertex adsorption of acetic acid on the (0001)/(10$\bar{1}$1) surfaces, respectively. Adsorption energies of ethanethiol were found to be -1.13/-0.90 eV on the (0001)/(10$\bar{1}$1) facet sites, and -1.19 eV on NP vertex. Adsorption of ethanamine on either of the facets gives an adsorption energy of -0.80 eV, while the (10$\bar{1}$1) vertex interaction with E_{ads} = -1.32 eV is found to be stronger than the (0001) vertex interaction, E_{ads} = -1.20 eV.

Table 6.1: Adsorption energies, E_{ads}, and Co-O distances, $d_{Co\text{-}O}$, after the adsorption of acetic acid, ethanethiol, and ethanamine on 13-atom cluster and 57-atom Co NP as calculated by DFT.

		acetic acid		ethanethiol		ethanamine	
N	position	E_{ads} / eV	$d_{Co\text{-}O}$ / Å	E_{ads} / eV	$d_{Co\text{-}O}$ / Å	E_{ads} / eV	$d_{Co\text{-}O}$
13	vertex	-1.59	1.944	-1.81	2.167	-1.87	2.016
57	0001 facet	-0.57	2.104	-1.13	2.216	-0.80	2.106
	0001 vertex	-1.08	1.956	-1.19	2.187	-1.20	2.047
	10$\bar{1}$1 facet	-0.53	2.039	-0.90	2.222	-0.80	2.103
	10$\bar{1}$1 vertex	-1.07	2.026	-1.19	2.197	-1.32	2.022

Next, the reaction pathway to the formation of H-Co-OOCCH$_3$, H-Co-SCH$_2$CH$_3$, and H-Co-NHCH$_2$CH$_3$ complexes was modelled to determine the rate-limiting step. The reaction pathways together with the optimised structures are shown in Figure 6.5 for acetic acid, Figure 6.6 for ethanethiol, and Figure 6.7 for ethanamine, for both 13-atom cluster and 57-atom NP.

For the acetic acid, the first TS involves transfer of the carboxyl hydrogen over a Co-Co bridge towards the nearest available three-fold adsorption site. The formed interaction mode has no Co atoms shared between the dissociated hydrogen and the bonding carboxyl oxygen atoms. Considering the limited size of the 13-atom cluster, the only possible transition is over the cluster edge, with an energy barrier of 0.70 eV. Extended surface areas of the 57-atom NP allow transfer of hydrogen within the same facet during dissociation, which considerably reduces the energy barrier to 0.15 eV in the case of the (0001) surface, and to 0.13 eV in the case of the (10$\bar{1}$1) surface. Once the hydrogen dissociates, it is relatively free to move around over sites which are not saturated by Co-O interactions. This is shown by low hydrogen movement barriers calculated at 0.09 eV on the 13-atom cluster, and 0.20, and 0.18 eV on the (0001) and (10$\bar{1}$1) surfaces of the 57-atom NP.

TS of ethanethiol dissociation is characterised by a similar transfer of thiol hydrogen over a Co-Co bridge, with the rest of the molecule tilting in the opposite direction to form a second S-Co bond, Figure 6.6. The difference from the acetic acid case is that the hydrogen adsorbs in the closest three-fold hollow adsorption site by sharing one of the Co atoms which interacts with the sulphur. This TS lies 0.26 eV above the undissociated

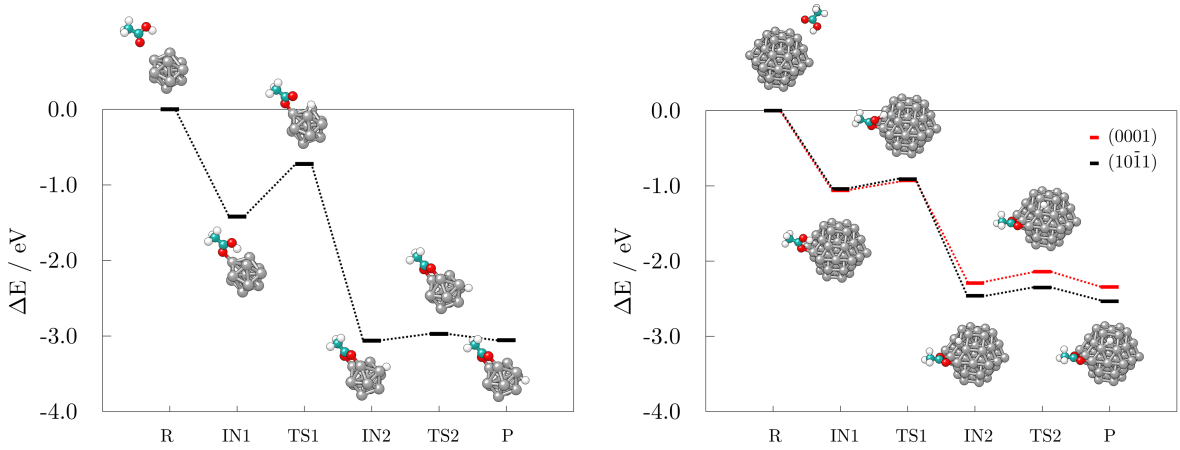

Figure 6.5: Reaction pathway and accompanying optimised structures of single acetic acid adsorption, dissociation, and subsequent hydrogen movement on the 13-atom cluster (**left**) and 57-atom Co NP (**right**). Two mechanisms on the 57-atom NP are for the adsorption on the (0001) and (10$\bar{1}$1) facets, with depicted structures corresponding to the (10$\bar{1}$1) surface. R, IN(1,2), TS(1,2), and P stand for reactants, intermediate and transition states, and products, respectively. Grey, teal, red, and white spheres represent cobalt, carbon, oxygen, and hydrogen atoms, respectively.

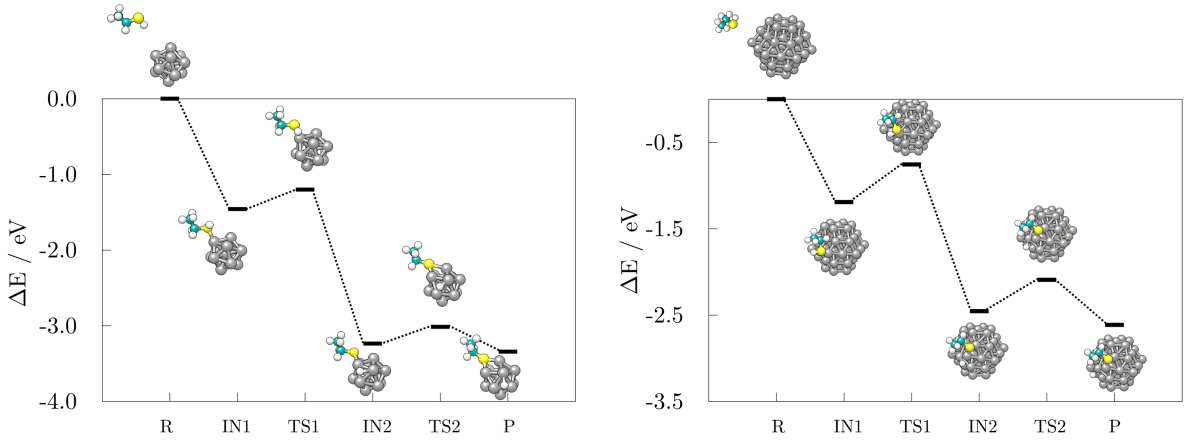

Figure 6.6: Reaction pathway and accompanying optimised structures of single ethanethiol adsorption, dissociation, and subsequent hydrogen movement on the 13-atom cluster (**left**) and 57-atom Co NP (**right**). R, IN(1,2), TS(1,2), and P stand for reactants, intermediate and transition states, and products, respectively. Grey, teal, yellow, and white spheres represent cobalt, carbon, sulphur, and hydrogen atoms, respectively.

ethanethiol-13-atom cluster complex, and 0.44 eV above the undissociated ethanethiol-57-atom NP complex. Energy barriers for the hydrogen movement are still relatively low, i.e. 0.22 and 0.33 eV for the 13-atom cluster and 57-atom NP, respectively.

Captured energy barriers for the dissociation of ethanamine are significantly higher than those of acetic acid and ethanethiol dissociations. On the 13-atom cluster, a barrier of 1.24 eV was calculated, and on the 57-atom NP, obtained activation energy was 1.42 eV. Both TS are characterised by a detachment of one amino hydrogen and its retention on the Co atom interacting with the ethanamine molecule. Upon successful dissociation, the detached H atom adsorbs in the closest available bridge site, while sharing one of the N-interacting Co atoms. Movement of dissociated hydrogen has similar energetic restrictions as in the previous cases, 0.23 and 0.46 eV for $N = 13$ and $N = 57$, respectively.

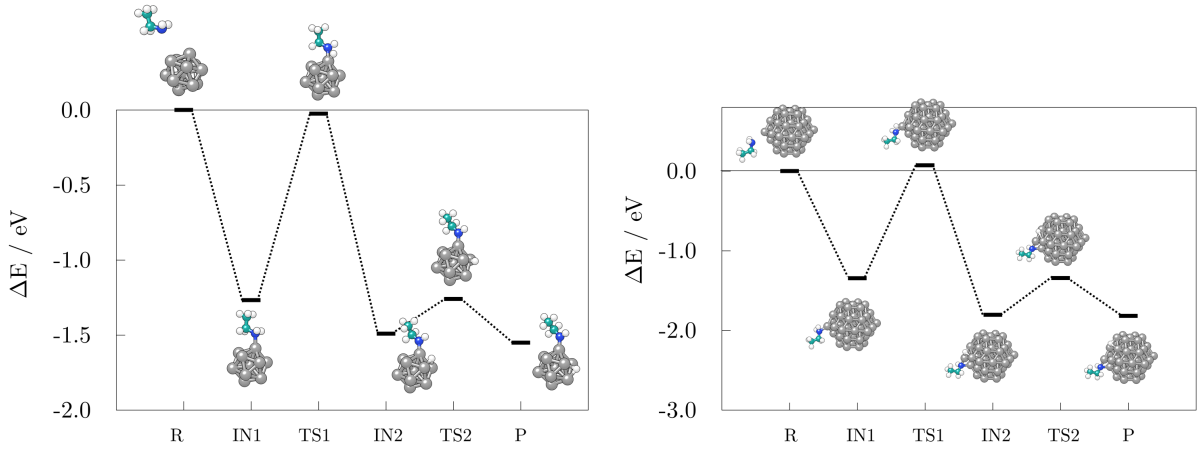

Figure 6.7: Reaction pathway and accompanying optimised structures of single ethanamine adsorption, dissociation, and subsequent hydrogen movement on the 13-atom cluster (**left**) and 57-atom Co NP (**right**). R, IN(1,2), TS(1,2), and P stand for reactants, intermediate and transition states, and products, respectively. Grey, teal, blue, and white spheres represent cobalt, carbon, nitrogen, and hydrogen atoms, respectively.

The dissociation TS are positioned significantly below the energy of separated reactants and thus, dissociation reactions should proceed easily, as seen in the AIMD run where spontaneous dissociation of valeric acid was observed on the 57-atom Co NP.

6.3.2.2 Ligand-ligand interaction and H_2 formation

To develop an understanding of the formation of H_2 from dissociated hydrogen atoms, a second ligand molecule is required. Adsorption of the second ligand onto the site which is already coordinated, such that the two molecules both bind to the same cluster/NP atom, was shown to be preferred in the case of thiol adsorption on the gold cluster, and it was accompanied by the rearrangement into a so called staple motif.[599] The formation of such motifs as well as the influence of the adsorption sites of the second molecule on the generation of H_2 were probed on the 13-atom cluster and 57-atom Co NP.

The reaction mechanism for the adsorption and dissociation of the second acetic acid molecule in both uncoordinated and coordinated sites, and recombination of the pair of

dissociated hydrogen atoms on the 13-atom Co cluster is shown in the left panel of Figure 6.8. The dissociation of the second acid molecule is spontaneous and the movement barrier for the dissociated hydrogen atom is, similar to the single molecule case, fairly low: 0.18 eV when the second acid is adsorbed at the uncoordinated site, and 0.03 eV when it is adsorbed at the coordination site of the first acid. H_2 desorption, however, requires for two hydrogen atoms to interact within a single vertex Co atom, which is followed by a slight pull-out of the interacting Co atom. This TS has a rather large energy barrier of 1.76 eV when two acids are adsorbed on remote sites, and 1.13 eV if they share the adsorption site. Adsorption of the second acetic acid to the uncoordinated Co atom (E_{ads} = -1.25 eV) is favoured over sharing the interaction site (E_{ads} = -0.65 eV) by 0.60 eV in the undissociated state, and by 0.35 eV after dissociation. Once the hydrogen molecule is formed, the cluster-acid complexes have similar stabilities. However, the reaction energy for the production of hydrogen gas starting from the adsorption of the second acid in the uncoordinated site is -0.33 eV, and it almost triples to -0.89 eV in the case when one Co atom is shared between the two adsorbed acids.

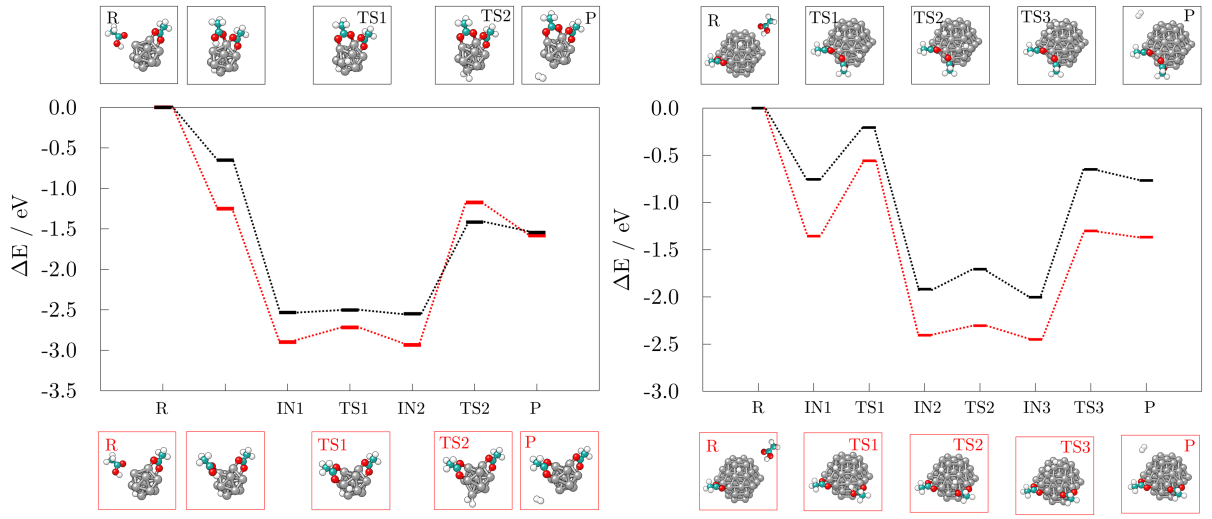

Figure 6.8: Reaction pathway and accompanying optimised structures of the adsorption and dissociation of second acetic acid and subsequent recombination of hydrogen atoms into hydrogen gas on the 13-atom cluster (**left**) and on the $(10\bar{1}1)$ surface of the 57-atom (**right**) Co NP. Red pathway corresponds to the adsorption of second acid molecule on the uncoordinated site on the cluster, while black pathway corresponds to the adsorption on the coordination site of the initially adsorbed acid. R, IN(1,2,3), TS(1,2,3), and P stand for reactants, intermediate and transition states, and products, respectively. Grey, teal, red, and white spheres represent cobalt, carbon, oxygen, and hydrogen atoms, respectively.

The 57-atom NP offers many distinct uncoordinated adsorption sites, but since the vertices showed significantly favoured adsorption, only vertex positions will be considered for the adsorption of the second acid. There is no obvious preference between the (0001) and $(10\bar{1}1)$ surfaces for the adsorption in a position that is remote from the site that

already interacts with previously adsorbed acid - the difference in the E_{ads} is only 0.06 eV ($E_{ads}(0001)$ = -1.20 eV and $E_{ads}(10\bar{1}1)$ = -1.26 eV). Optimisation of the two acids adsorbed as to share a (0001) vertex atom has led to the repositioning of one of the acids, resulting in their remote adsorption. Adsorption on the uncoordinated portion of the NP remains favoured by 0.60 eV over the shared Co atom site on the $(10\bar{1}1)$ surface (E_{ads} = -0.67 eV), as in the case of the 13-atom cluster.

The subsequent reaction mechanism for the dissociation of the second acetic acid and H_2 generation at the $(101\bar{1}1)$ surface of the 57-atom NP is shown in the right panel of Figure 6.8. In contrast to the 13-atom cluster, the dissociation barrier for the second acetic acid is 0.80 eV when adsorbed in the uncoordinated site and 0.55 eV when sharing the adsorption site with another acid. This is considerably higher than the 0.15 eV barrier of the initially adsorbed molecule, however, dissociation of multiple acids was captured during the AIMD functionalisation run. The subsequent movement of dissociated hydrogen remained relatively unconstrained with energy costs between 0.10 and 0.25 eV. The desorption and formation of H_2 upon the adsorption of two acetic acid molecules at different parts of the 57-atom NP is accompanied by an energy barrier of 1.15 eV. The barrier is thus reduced by 0.61 eV compared to the same adsorption arrangement on the 13-atom cluster. Structural distortion of the desorption Co site is also significantly less pronounced. Where two acids are coordinated to share the interacting Co atom, desorption of H_2 is energetically more restricted with a barrier of 1.35 eV, 0.22 eV higher than on the cluster with 13 Co atoms. Another pronounced difference between the two particle sizes is the stability of the formed acid-particle complexes, with shared coordination site complex on the 57-atom NP being 0.60 eV less stable compared to its counterpart with two acids in distinct adsorption sites. The reaction energy of H_2 generation in reference to the acid-particle complex with one dissociated and one undissociated acetic acid is -0.010 eV, and it remains unchanged at -0.012 eV with the interaction within the shared adsorption site. Results for the adsorption at the uncoordinated site of the (0001) surface are fairly similar to the $(10\bar{1}1)$ surface, and detailed description has thus been omitted. Calculated energy barrier for the dissociation of the second acid is calculated at 0.63 eV and that of the hydrogen movement at 0.18 eV. TS of H_2 desorption lies 1.17 eV higher in energy compared to the preceding intermediate state.

Finally, a third acid molecule was adsorbed onto the 57-atom Co NP. Only the interaction within a distinct $(10\bar{1}1)$ facet was considered, with the first two acids not sharing their adsorption sites. The sole adsorption of another acid in an undissociated form did not alter the barrier of H_2 generation and desorption, which was found to be 1.21 eV. However, upon dissociation, the energy barrier was reduced to 0.65 eV, with a reaction energy for hydrogen recombination of -0.18 eV, Figure 6.9.

H_2 generation was probed in both uncoordinated and coordinated adsorption sites also for ethanethiol, and the reaction mechanisms are presented in Figure 6.10. The TS barrier for the dissociation of the second ethanethiol on the 13-atom cluster is 0.20 eV when adsorbed on the uncoordinated site, and 0.36 eV in the case of shared interaction, which

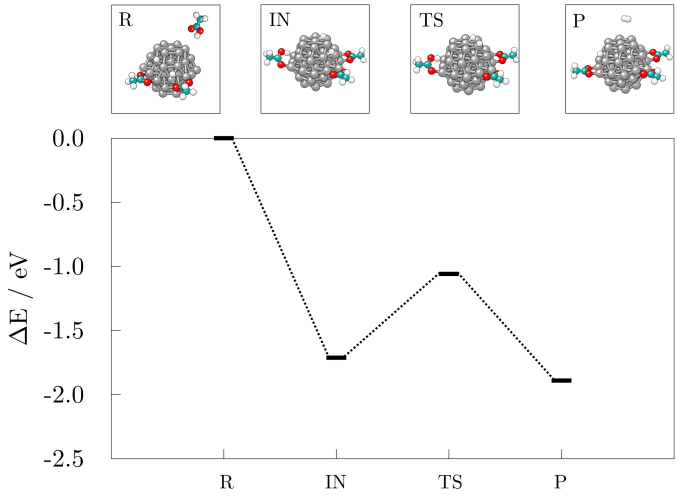

Figure 6.9: Reaction pathway and accompanying optimised structures of the adsorption and dissociation of third acetic acid and subsequent recombination of hydrogen atoms into hydrogen gas on the $(10\bar{1}1)$ surface of the 57-atom Co NP. R, IN, TS, and P stand for reactants, intermediate and transition states, and products, respectively. Grey, teal, red, and white spheres represent cobalt, carbon, oxygen, and hydrogen atoms, respectively.

is similar to the dissociation of the first ethanethiol molecule. Likewise, the dissociated hydrogen atom can move around the cluster with minimal effort, the movement barrier being ~0.20 eV regardless of the adsorption site. Energy barrier and reaction energy for the production and desorption of H_2 are, however, much more sensitive to the ligand arrangement. For hydrogen gas to form, a barrier of 1.49 eV needs to be overcome if the second ligand molecule adsorbs on a remote site. The energetic cost increases to 1.65 eV when the two adsorbate molecules share an interacting Co atom. A difference in the reaction energy of products in reference to the initially adsorbed state of the two molecules is of a greater importance - adsorption within the same site of the cluster lowers the reaction energy from the endothermic value of 0.32 eV to the slightly exothermic value of -0.03 eV. Thus, compared to the acetic acid, the formation of H_2 is more favourable when the two ethanethiol molecules share the adsrotpion site on the 13-atom Co cluster. Formation of a staple motif is not as pronounced as on gold clusters, but the Co atom positioned between the two sulphur atoms is slightly dislocated from the cluster, and the distance to the centre Co atom is prolonged by 5.8 %.

Adsorption energies for the adsorption of the second thiol molecule on the 57-atom Co NP in the uncoordinated and in the site of the first ethanethiol are -1.97 and -2.04 eV, respectively. However, the favourability of the interaction within the same Co atom is lost upon the dissociation of the second ligand molecule, which is characterised by a 0.42 eV barrier when two molecules are adsorbed separately and a 0.58 eV barrier if they are adsorbed in the same adsorption site. The hydrogen movement is energetically less consuming with 0.12-0.17 eV barriers. The TS for the H_2 desorption is accompanied by

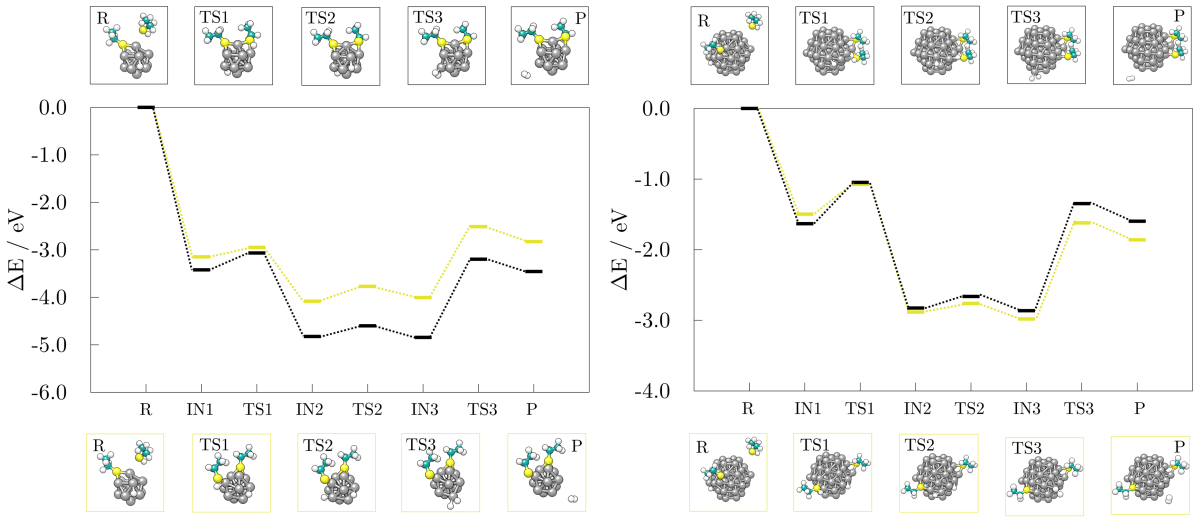

Figure 6.10: Reaction pathway and accompanying optimised structures of the adsorption and dissociation of second ethanethiol and subsequent recombination of hydrogen atoms into hydrogen gas on the 13-atom cluster (**left**) and on the $(10\bar{1}1)$ surface of the 57-atom (**right**) Co NP. Yellow pathway corresponds to the adsorption of second ethanethiol molecule on the uncoordinated site, while black pathway corresponds to the adsorption on the coordination site of the initially adsorbed ethanethiol. R, IN(1,2,3), TS(1,2,3), and P stand for reactants, intermediate and transition states, and products, respectively. Grey, teal, yellow, and white spheres represent cobalt, carbon, sulphur, and hydrogen atoms, respectively.

energy barriers of 1.36 eV for the two ethanethiol molecules in separate adsorption sites, and 1.52 eV for the staple-like arrangement. These are reduced by 0.10 eV on average in comparison to the 13-atom cluster. Nevertheless, the reaction energy for the hydrogen recombination process is much more favourable when two adsorbates are not directly interacting within the same site (-0.36 eV) than when they share the interaction atom (0.03 eV).

Reaction pathways of the second ethanamine dissociation and H_2 formation are shown in Figure 6.11. It was not possible to optimise the staple-like geometry, probably due to the bulkiness of the amino functional group. Dissociation TS lies 1.26 and 1.28 eV above the undissociated 13- and 57-atom complexes, respectively, and it structurally coincides with the TS of the single ethanamine dissociation. Energy requirements for the hydrogen movement are still in the 0.05-0.25 eV range. Nevertheless, energy barrier for the H_2 generation and detachment on the 13-atom cluster was not identified. A geometry which was observed as a TS for the formation of gaseous hydrogen from acid and thiol 13-atom cluster complexes was found to be 0.43 eV more stable than the expected system structure after the H_2 desorption. On the 57-atom NP, the TS was successfully relaxed with the activation energy of 1.29 eV. Contrary to the geometries observed in the acid and thiol cases, structure of the transition point of the H_2 generation on the 57-atom NP with two ethanamine molecules adsorbed is that of an H_2 interacting with the vertex Co atom

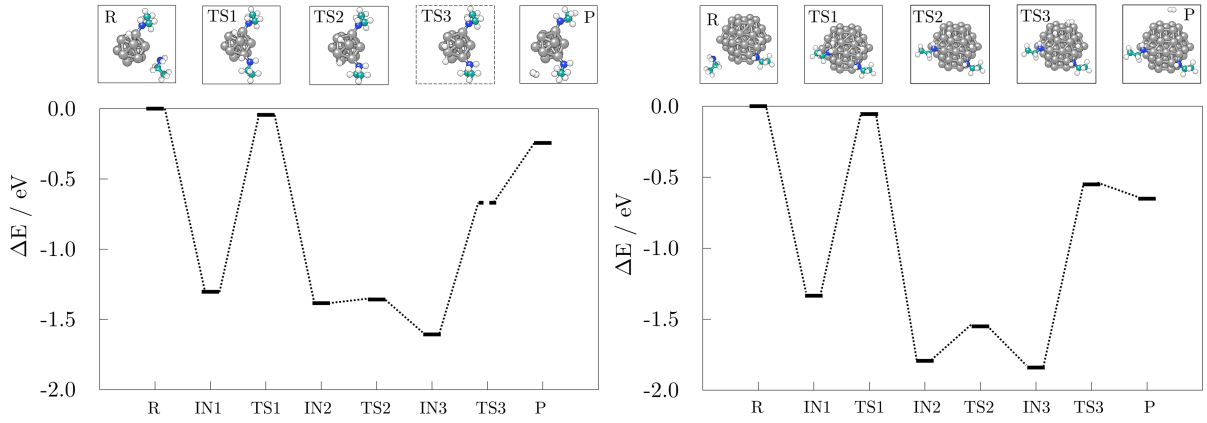

Figure 6.11: Reaction pathway and accompanying optimised structures of the adsorption and dissociation of second ethanamine and subsequent recombination of hydrogen atoms into hydrogen gas on the 13-atom cluster (**left**) and on the $(10\bar{1}1)$ surface of the 57-atom (**right**) Co NP. R, IN(1,2,3), TS(1,2,3), and P stand for reactants, intermediate and transition states, and products, respectively. Grey, teal, blue, and white spheres represent cobalt, carbon, nitrogen, and hydrogen atoms, respectively.

through a single H atom. Post-H_2 desorption structure was found to be unfavourable compared to the double-dissociated state, with an energy difference of 1.14 eV.

6.3.2.3 H_2 generation metadynamics

A 5.00 ps metadynamics run was used to completely explore the free energy landscape, with the distance between the two dissociated -COOH hydrogen atoms implemented as a CV to capture the H_2 generation transition barriers more realistically. The starting geometry was taken from the AIMD functionalisation run prior to the first acid desorption event. The observed H-H distances and the resulting free energy landscape as a function of the H-H distance are shown in Figure 6.12.

Initially, the two hydrogen atoms were bridging the same vertex Co atom at a mutual distance of 2.76 Å, where they were observed to interchange positions for a significant period of time throughout the AIMD run, as depicted in the top left of Figure 6.13. The same interchanging trend was continued for the majority of the first picosecond of the metadynamics simulation, with H atoms 'orbiting' around the vertex Co atom through hollow and bridge sites. Just before the simulation time reached 1.00 ps, the H-H distance approached that of the H_2 bond, and the newly formed hydrogen molecule detached from the NP, also shown in Figure 6.13. The system was in this state for about 0.30 ps, followed by a dissociation of the H_2 entity and a re-adsorption of the H atoms on a site of the NP which did not coincide with the detachment point. The hydrogen atoms shortly maintained a shared type of interaction within the same Co atom before exploring distant parts of the NP away from each other. In the period between 3.50 and 4.00 ps, additional dissociations of two carboxylic acids were observed, inducing independent movement of

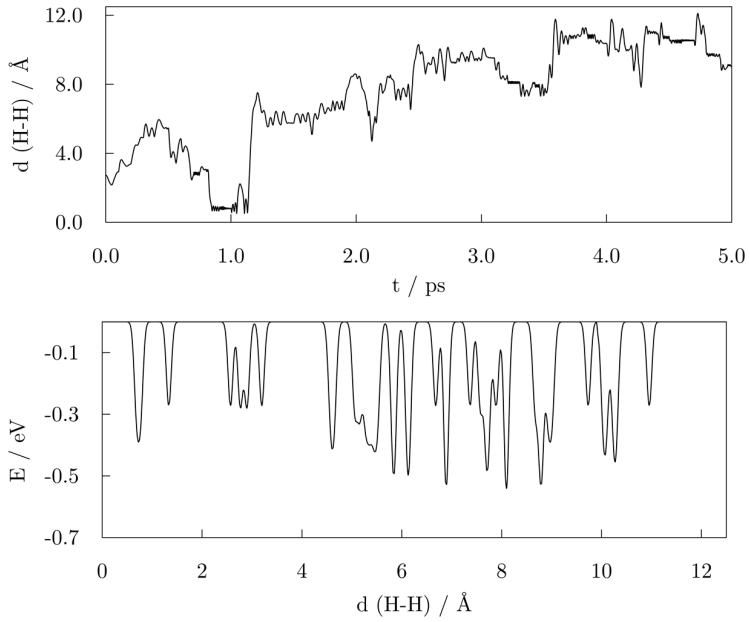

Figure 6.12: **top**: H-H distance progression during the 5.0 ps metadynamics run for the system comprising of 57-atom Co NP and 14 valeric acid molecules; **bottom**: resulting free energy landscape as a function of the H-H distance.

the two H atoms of interest towards remote, newly dissociated H atoms to form new grouping sites. At about 4.50 ps, the H atoms of one of the new H-H pairs formed the transition state previously observed for the two hydrogen atoms of interest and desorbed from the NP in form of H_2 shortly after. This event was taken as a termination point of the simulation, and it is depicted in the top right of Figure 6.13.

The bottom panel of Figure 6.12 depicts the free energy landscape as spanned over the H-H distance CV. The numerous minima captured for distances above 2.00 Å correspond to the positioning of two dissociated hydrogen atoms in various hollow and bridge positions available around the NP. With energies between -0.28 and -0.53 eV, different combinations of hydrogen atoms situated in hollow and/or bridge positions presented similar energetic favourability. The alternating environment of available sites (proximity of edges, vertices, and adsorbed acid molecules) also affects the energetics of the obtained minima. The energy barriers for the transitions between these states range from as low as 0.03 eV up to 0.50 eV, and they are a confirmation of the low energy cost of hydrogen movement, as predicted by DFT. A minimum with energy of -0.27 eV at 1.32 Å H-H distance corresponds to the structure where the two H atoms abandoned favourable multifold positions each forming a single bond with the same vertex Co atom, which resembles the DFT-predicted TS structures. In contrast to the DFT geometry, the interacting Co

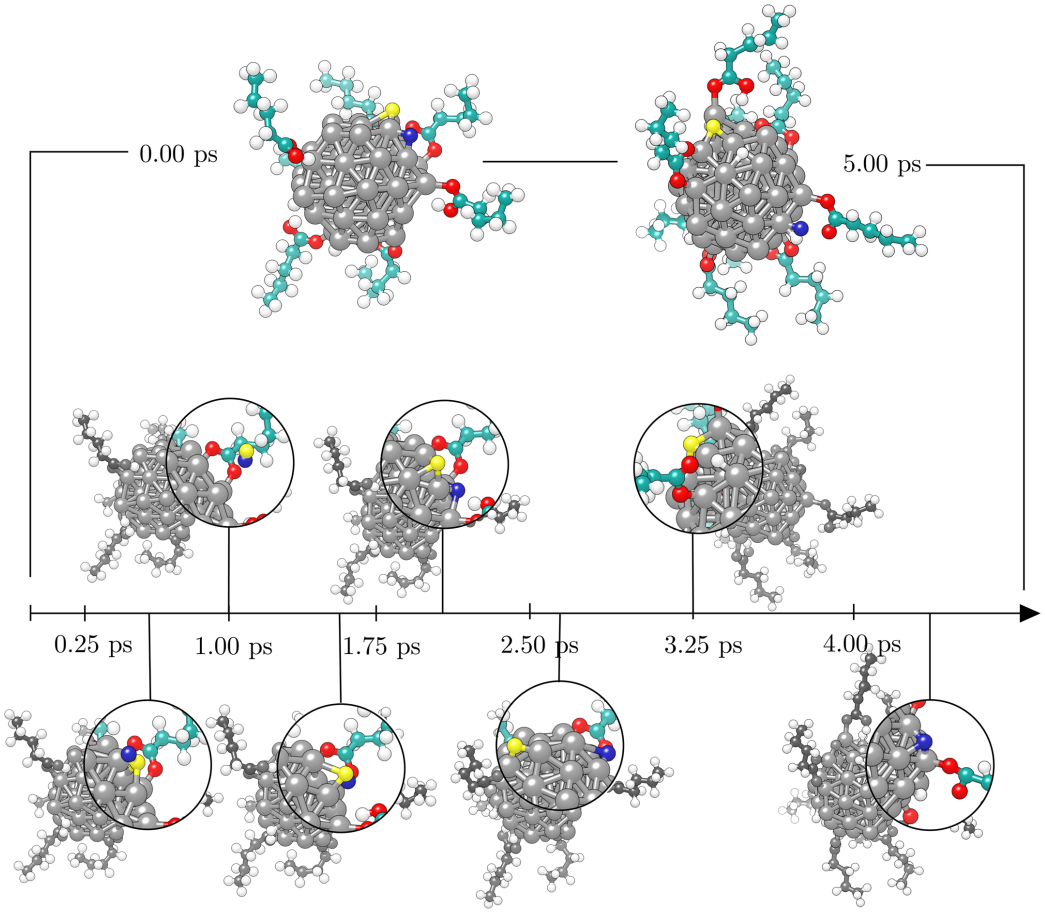

Figure 6.13: Timeline of the 5.00 ps metadynamics run on the 57-atom Co NP-14 valeric acids system with initial and final geometries given on the **top** right and left, respectively, and seven key events featured on the **bottom** in the order of their occurrence. Acid molecules adsorbed on the front of the NP were hidden for clarity. The two hydrogen atoms of interest, whose H-H distance was taken as a collective variable, are distinguished as yellow and blue spheres. Grey, teal, red, and white spheres represent cobalt, carbon, oxygen, and hydrogen atoms, respectively.

atom was not pulled out from the NP during the metadynamics simulation. Finally, another minimum is observed for the H-H distance of 0.75 Å, which corresponds to the bond length of diatomic H_2 molecule, its energy being -0.39 eV. Hence, the transition from the simultaneous interaction of both H atoms within the same vertex to the generation and detachment of the H_2 molecule is predicted to have an energy cost of ~0.27 eV. This is a notably lower energy barrier than calculated by DFT, which gives an indication of the influence of adsorbed valeric acid molecules and the experimental temperature conditions on the strain and electronic properties of the NP.

Metadynamics investigation of the H_2 formation within the thiol protected four-atom gold cluster captured a rearrangement of Au atoms followed by an energy barrier of 1.21 eV for the hydrogen molecule desorption.[606] A model of this size presents only a limited potential of predicting the behaviour of NPs. DFT calculations at 0 K have already

shown significant differences in the energetics as the cluster size grows and a transition barrier of H_2 generation on a 12-atom Au cluster was predicted at 0.67 eV, around half that of the four-atom one.[599] This trend correlates with the reduction in the transition barrier obtained when going from 13-atom cluster to 57-atom Co NP predicted here. The lower energy barrier of Au clusters compared to Co clusters emanates from the formation of thiolate staple motifs, which were not found to be as favourable in the case of cobalt. Additionally, it is well-known that hydrogen binds weaker to cobalt than to gold clusters[607, 608], offering a compromise in the energy costs despite the failure to form highly stable staple motifs. Overall, the 57-atom Co NP used in this study is believed to offer a fairly good representation of the NP behaviour. The energy barrier for the detachment of H_2 obtained in metadynamics simulations is found to be lower than that has been reported for Au clusters, which can be explained by the differences in the binding energy of hydrogen and the increased number of adsorbate molecules present.

When considering adsorption strengths of hydrogen on the NPs and surfaces of different metals, calculated binding energies can vary by up to ±1.50 eV, which could significantly alter the energy costs of H_2 formation and desorption.[609, 610, 611] In addition, most favourable adsorption sites are also case-dependent, and hence the fate of dissociated hydrogen atoms captured here for the acid-functionalised Co NPs is not expected to be maintained across the transition metal row. Moreover, bimetallic alloying at the nanoscale is an increasingly popular strategy to tune material properties, and it could possibly provide a transparent solution for the reduction of hydrogen desorption barriers in cases where the established interaction is too strong on monometallic NPs, with examples of modified hydrogen binding available in the literature.

6.4 Conclusion

The mechanism of carboxylic acid functionalisation of Co NPs was probed with AIMD and it can be resolved in three stages: stage of sole adsorption, stage of concurrent dissociation of interacting molecules and adsorption of non-interacting molecules, and stage of alternating adsorption, dissociation, and desorption processes with the extensive aggregation of dissociated hydrogen atoms. The latter has shown to prevent any further adsorption of acid molecules and hinder the formation of the protective coating of a higher density despite 40 % of surface atoms being available.

The investigation of H_2 formation and detachment from the NP revealed energetically feasible barriers for the H_2 generation within the functionalisation process, and reduction of the barrier is observed for larger NPs. Furthermore, the H_2 desorption energy has similar trends as the well-studied thiol-gold systems when predicted by DFT, while metadynamics simulations, which incorporated synthesis temperature and multiple ligand molecules, showed a significant reduction in the energy barriers. These insights into carboxylic acid functionalisation will help design Co NPs suitable for a range of biomedical applications.

Highlights of the chapter

- **Identified three stages of the carboxylic acid Co NP functionalisation process.**
- **Identified presence of multiple molecules as a crucial factor for favourable generation and desorption of gaseous hydrogen.**
- **Energy barrier of H_2 generation within the functionalisation process was calculated to be 0.27 eV.**

CHAPTER 7

LIGAND MEDIATED MAGNETISM

"Come, we shall have some fun now!" thought Alice. "I'm glad they've begun asking riddles - I believe I can guess that," she added aloud. "Do you mean that you think you can find out the answer to it?" said the March Hare. "Exactly so," said Alice.
-Chapter 7, A Mad Tea-Party

7.1 Introduction

7.1.1 Magnetism at nanoscale

Nanosized metallic counterparts are known to exhibit enhanced electronic and magnetic properties compared to their respective bulk phases. Average magnetic moments of Co atoms in nanoclusters were measured by gas phase experiments to be as high as 2.6 μ_B, which is more than 50 % higher than the magnetic moment of bulk hcp Co (1.72 μ_B) as a result of the atom under-coordination.[612] This was confirmed on small and medium Co clusters and NPs, as presented in Chapter 3, together with the dependence on the morphology. Addition of new species, either to the metal core by creating nanoalloys or to the surface in form of an inorganic or organic coating, can also have a significant impact on the final electronic structure of the NP. The extent of ligand-induced changes depends on the type of both metal and ligand in question. Experiments indicate that gold NPs functionalised with organic molecules show complex magnetic behaviours despite the fact that the starting structures are non-magnetic. Overall magnetisation ranges from 0.0036-1.00 μ_B measured on thiolate-capped gold NPs, to over 10 Bohr magnetons per adsorbed molecule of polypeptides on gold substrates.[613, 614, 615] Similarly, two types of Co NPs of substantially dissimilar structural and magnetic features were synthesised in the presence of precursors containing different ligands.[221] The divergence in the properties was directly linked to the difference in the chemical environments. Phosphide-based ligands caused a 38 % loss of NP magnetisation, corresponding to a partial quenching of the magnetic contribution of surface atoms due to the electron-withdrawing power and volume bulkiness of the molecules. In comparison, Co NPs synthesised via amino-route displayed unaltered magnetic properties. Stabilising amino functional group has an opposite chemical nature: it is a strong electron-donor and it is hence not detrimental to the magnetic properties of Co NPs.

7.1.2 Motivation

Understanding contributions of ligand nature and structure to the electronic, and consequently physical and chemical properties of nanosystems is crucial for effective utilisation of ligand-mediated magnetisation alternations. DFT calculations have proven to be a reliable tool in describing magnetism of metallic and semiconducting materials as well as explaining the mechanisms behind the occurrence of such magnetic behaviours. Using DFT calculations, the origin of unexpected magnetisation within protected Au NPs has been traced to the charge transfer between organic molecules and metallic core that can lead to the rearrangement in the occupied energy states which is associated with the magnetic properties of these complex systems.[616, 617] Unusual magnetic behaviour was connected only to thiol ligands, while nitrogen-based molecules did not bring similar changes. Ligand effects on magnetic moments of Co NPs were not as much investigated. Recent computational studies showed magnetic quenching of different cobalt systems, where the intensity of quenching depends on the ligand type, indicating that the magnetisation of a nanocluster can be tuned by careful coating design.[618] Eleven unique ligand shell compositions were considered, mainly combinations of phosphine and halogen functional groups, displaying different strengths of decrease in the magnetisation compared to bare cobalt clusters. Since the type of ligand used was detected to control the exchange of electrons, electronegativity of the binding group could provide some insight in the final magnetisation of the composite system. Finally, it was found that, with increase in the size of the cluster, dependence of magnetic properties on the presence of ligand molecules, although dampened, still persists. The extended study has additionally detected/determined how does the arrangement or the coverage of the ligands on the nanoparticle surface control the distribution of local magnetic moments in Co NPs.[619] Some of the ligands that established weak interactions with the surface atoms have still had long-range effects on central atoms despite the absence of a chemical bond. Additionally, it was shown within the studies on magnetic hyperthermia that the heating efficiency is proportional not only to the saturation magnetisation, but it also depends on the value of MAE.[71, 620] It was recently demonstrated that the deposition of a self-assembled monolayer of alkanethiolates on a ultrathin Co film grown on Au(111) induces a spin reorientation transition from in-plane to out-of-plane magnetization, changing the anisotropy values.[366]

However, a broad understanding of the fundamental principles that describe the changes in the magnetism of Co NPs functionalised by biomedically acceptable ligands does not currently exist. Thiols have been widely utilised for the protection of gold NPs that were implemented in chemical and biological sensing. On the other hand, carboxylic acids can strongly bind to metallic nanoparticles through the formation of covalent bonds and such systems were synthesised with respectable stability. This work hence focuses on the evolution of the electronic and magnetic properties of carboxylic acid and thiol protected cobalt NPs as a function of the ligand coverage. Evaluation of this dependence was conducted through the analysis of atomic Bader charges, magnetic and orbital moments, densities of state, and magnetic anisotropy energies, and correlation of these values to

general trends present in the systems considered.

7.2 Computational details

The structural and magnetic properties of ligand-protected Co NPs were determined in the spin-polarised DFT framework using VASP within the GGA/PBE exchange functional. The spatially confined core electrons were treated through the PAW approach, while the intrinsically non-periodic nature of the system restricted the Brillouin zone sampling to the Γ-point. The wavefunctions of the valence electrons were expanded to 400 eV energy cutoff, which was sufficiently large to satisfy requirements of the accuracy in small energy differences needed to determine the MAE. The DFT-D3 method with Becke-Johnson damping was used to include the long-range dispersion interactions with ligand molecules.[448]

The geometry choice was narrowed to two morphologies of interest: icosahedron, which is well-known as the most stable shape for small and medium Co NPs [270, 256, 257, 621], and hcp, as the expected geometry for large NPs because of the natural hcp stacking of the bulk material. Moreover, several publications relate the use of hcp Co NPs for magnetisation-based applications due to the requirement of small NPs with high anisotropy at usable temperatures, and hcp Co NPs of varying diameters were already successfully synthesised.[242, 326, 227, 213, 207] Additional motivation is in the hcp→icosahedron rearrangement observed in the AIMD simulation of the carboxylic acid functionalisation mechanism in Chapter 6.

For the comparison of varying functional groups, molecules of acetic acid, ethanethiol, and ethanamine were employed. As it has been shown that size-dependent effects are not prevalent in changes of the magnetic properties of Co clusters induced by ligand coatings[619], only the influence of the coating density on the magnetisation of the 55-atom icosahedron and 57-atom hcp Co NPs was considered. Ten different coverages of three ligand functional groups commonly used for biocompatibility (-SH, -COOH, and -NH_2) were modelled on the icosahedral NP, increasing from 10 % to a full 100 % coverage in steps of 10 %. Acetic acid, ethanamine, and ethanethiol were chosen as ligand molecules. Motivated by previous results from AIMD simulations which captured spontaneous dissociation of the 5C counterpart ligands and the accompanying generation of gaseous hydrogen, ligand molecules were herein introduced to the surface in their dissociated forms. In accord with the identified most favourable binding modes (Chapter 5), the initial forms of interaction of acetic acid, ethanamine, and ethanethiol molecules were bridging bidentate, bridging monodentate, and three-fold monodentate, respectively. No changes in the interaction modes were observed upon the structural optimisation. Density of the passivating coating was determined as the number of Co atoms interacting with adsorbed molecules over the total number of surface Co atoms, where full coverage is reached once every surface Co atom interacts with one ligand molecule through a single bond. On the hcp NP, the role of progressive passivation of two different facets exposed on the surface of the NP, (0001) and $(10\bar{1}1)$, by carboxylic acid ligands was examined.

Optimised structures of representative systems are shown in Figure 7.1. Together, these systems sample a range of possible biocompatible shells used to form ligand-protected Co NPs, with carboxyl and thiol molecules commonly seen as coatings of respectable stabilities in literature.

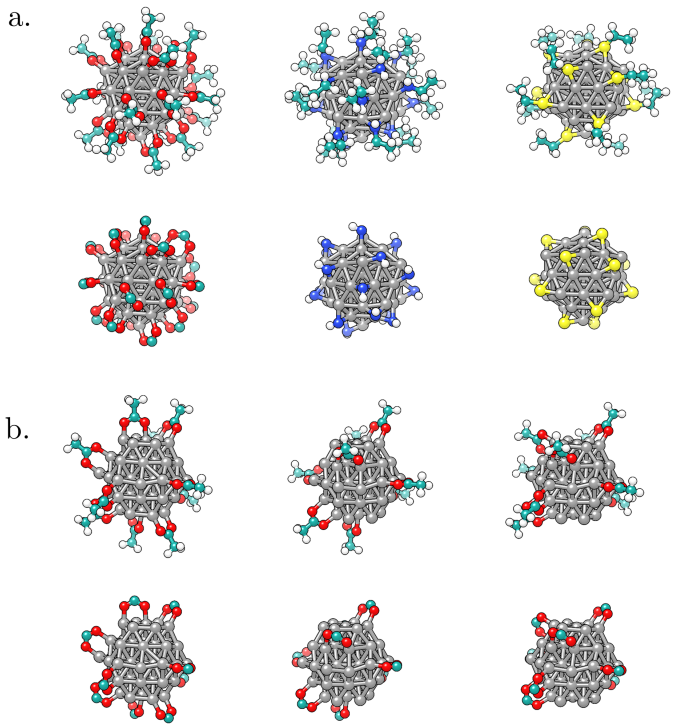

Figure 7.1: Optimised geometries of representative Co NP-ligand systems considered: **a.** 100 % coverage of carboxylic acid, amine, and thiol coating on 55-atom icosahedral Co NP; **b.** 50 % coverage of carboxylic acid coating on 57-atom hcp Co NP with primary distribution on the (0001) surface, mixed over both types of surfaces, and concentrated on the $(10\bar{1}1)$ surface. Each case is shown as a full molecule representation (**top** panel) and by only including ligand functional groups (**bottom** panel).

Relaxations were carried out with a convergence criterion of 10^{-6} eV between consecutive steps without any structural, symmetry, or magnetic constraints. Interaction strength of adsorbed molecules was captured through the binding energy per ligand molecule, E_{b}, which was calculated as:

$$E_{\mathrm{b}} = \frac{[(E_{\mathrm{Co}_N\mathrm{L}_M} + \frac{M}{2}E_{\mathrm{H}_2}) - (E_{Co_N} + ME_{\mathrm{H\text{-}L}})]}{M} \tag{7.1}$$

where the energies of the bare NP and a hydrogenated version of the ligand are deducted from the combined energies of ligand-passivated NP and a hydrogen molecule. M is a number of ligand molecules adsorbed on the NP. Negative energy indicates spontaneous

interaction. Charge distribution was calculated using the Bader charge analysis, as implemented by Henkelman *et al.*[177] The difference in electron density was calculated as:

$$\Delta\rho = \rho_{\mathrm{Co}_N\mathrm{L}_M} - (\rho_{\mathrm{Co}_N} + \rho_{M\times\mathrm{L}}). \tag{7.2}$$

where $\rho_{\mathrm{Co}_N\mathrm{L}_M}$, ρ_{Co_N}, and $\rho_{M\times\mathrm{L}}$ are electron densities of ligand-protected Co NP, bare Co NP, and ligand molecules, respectively. Magnetic moments were determined iteratively through simultaneous optimisation during the self-consistent field procedure.

To predict spin-orbit-related properties, namely orbital magnetic moments and magnetic anisotropy energies, fully relativistic calculations including spin-orbit coupling were performed[319, 320] within the non-collinear version of the VASP code. These properties require extremely well converged wave functions and charge densities, hence the criteria for termination of the SCF cycles was tightened to 10^{-7} eV/cell and energy changes to less than a hundredth of a meV. Two sets of self-consistent SOC non-collinear calculations were performed, one for each easy and hard magnetic axis, and the MAE was determined as a difference in the total energies, MAE= $E(\uparrow) - E(\downarrow)$, as defined in Chapter 3.

7.3 Results

7.3.1 Multiple-ligand binding over Co NPs

Binding sites and the preferential adsorption energetics over 55-atom icosahedron and 57-atom hcp Co NPs are shown in Figure 7.2 for different ligands. To achieve the most favourable binding on one of twenty (111) facets of icosahedron, molecules which interact with two surface Co atoms (-COOH and -NH_2 ligands) bind vertex-edge Co-Co pair (shown in blue). After vertex-edge pairs have been saturated at high ligand coverages, further ligand molecules are limited to bind in the only other option which remains available - two Co atoms positioned on different edges of the (111) facet (shown in red). Thiol molecules require three Co atoms per ligand, and stronger binding is established for edge-vertex-edge combination (shown in blue) compared to the three edge Co atoms interaction which positions the molecule in the centre of the (111) facet (shown in red). Facets exposed on the surface of hcp NP in addition to edge and vertex atoms also contain central atoms with higher CNs. When those atoms interact with the ligand molecule, released adsorption energy significantly reduces (shown in red).

Calculated binding energies (per molecules) for varying coverages and distinctly functionalised ligands are listed in Table 7.1. On the icosahedron, average interaction per molecule first strengthens with the growing number of molecules before a slight binding energy decrease caused by the bulkiness of carbon chains at high coverages for all three types of ligands. Thiol has shown the strongest binding with an average E_b of -2.05 eV, while the E_b of ethanamine was only half of that. The interaction strength of acetic acid molecules experiences the most pronounced change as the density of the coating increases, going from -0.942 eV at 10 % coverage to -1.665 eV at 60 %, accounting for a 75 %

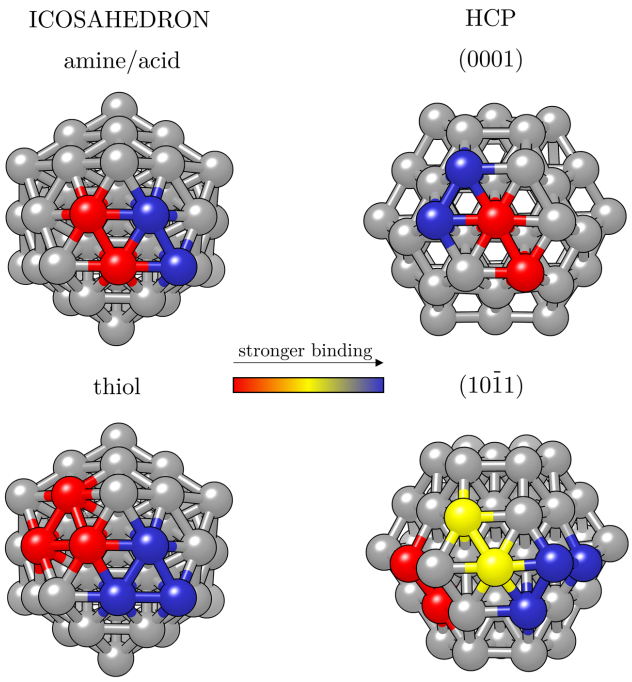

Figure 7.2: Different binding positions and their respective interaction strength for various ligands and facets on 55-atom icosahedral (**left** panel) and 57-atom hcp (**right** panel) Co NP.

stronger binding. On the hcp NP, calculated E_b of carboxylic acid ligands at low densities were more favourable when majority of the molecules were situated on the (0001) facets. By reaching coverages of 40-50 %, interaction on the (10$\bar{1}$1) surface starts to prevail in strength. When comparing the two morphologies, it was found that the binding energies of acidic ligands interacting with the icosahedron are notably lower than those captured on the hcp NP for the similar coating densities. For the 10 % coverage this difference is of the order of 1.00 eV. Icosahedron interaction strengths become competitive around 50-60 % coating density when the difference in E_b falls below 0.20 eV, which agrees well with the AIMD simulation of carboxylic acid functionalisation where the transformation from hcp to icosahedral shape of the Co NP was captured shortly after the coverage of 40 % was reached. Additional energy difference is also compensated by the favourable energetic stability of the icosahedral morphology at this size.

7.3.2 Magnetic properties of ligand-protected Co NPs

Figure 7.3 depicts relationship between the total magnetic moment, TMM, of the icosahedral and hcp Co NPs with different ligand coverages and the Bader charge of the Co core, q, of the same systems. In general, these TMM/q trends are controlled by the ligand binding group, electronegativity of the binding atoms, and their tendency to pair the surface atom spins in formed bonds. Hence, the nature of the ligand-metal bond can provide an insight in expected magnetic moments of the systems within each ligand family.

Table 7.1: Binding energy per ligand, E_b, for different coverage densities (in %) of carboxylic acid, amine, and thiol ligands on 55-atom icosahedron and carboxylic acid ligands in varying arrangements on 57-atom hcp Co NP.

E_b / eV	icosahedron			
%	acid	amine	%	thiol
10	-0.942	-1.062		
20	-1.162	-1.085	14	-1.950
30	-1.327	-1.067	21	-2.038
40	-1.378	-1.060	29	-2.053
50	-1.508	-1.027	43	-2.069
60	-1.665	-1.017	50	-2.084
70	-1.634	-1.003	64	-2.062
80	-1.624	-0.997	78	-2.053
90	-1.537	-0.919	93	-2.046
100	-1.516	-0.909	100	-2.045

E_b / eV	hcp		
%	(0001)	mixed	$(10\bar{1}1)$
10	-1.893		-1.688
20	-1.876	-1.723	-1.668
30	-1.828	-1.680	-1.665
40	-1.703	-1.699	-1.689
50	-1.670	-1.711	-1.707
60	-1.651	-1.773	-1.829
70	-1.604	-1.796	-1.838
80		-1.706	
90		-1.663	
100		-1.608	

It is therefore not surprising that there exists a linear-like relation between the systems with similar coverage densities of different ligands. At a 100 % coverage on icosahedron, oxygen-containing functional group of carboxylic acid ligands brings the charge of the Co core to 13.94 $|e^-|$ with a corresponding TMM of 103.318 μ_B, which is 3.3 μ_B higher than the TMM of the bare NP. On the other hand, NPs with 100 % coatings of amine and thiol ligands, which contain less electronegative nitrogen and sulphur atoms, maintain higher core electron density, reaching the charges of 10.55 and 7.09 $|e^-|$, respectively. This is also reflected in the TMMs, which were calculated to be 95.057 and 93.180 μ_B. Found relationship between the core charge and TMM coincides with earlier studies on a 13-atom Co cluster passivated by halogen ligands.[618] Step-like trends were captured for increasing coverage within each ligand family and can also be seen in Figure 7.3. Similarly, as the number of adsorbed carboxylic acid ligands increases on the hcp NP, the core loses more electrons and the TMM of the system gets enhanced in the step-like fashion. The non-linear trends arise from two different factors, first being saturation of the most favourable binding sites which for coverages above 40 % requires further adsorption to proceed in the remaining positions around the NP, Figure 7.2. Second factor is the symmetry, where only at fairly high coverages of $> 70\%$ all of the exposed facets interact with a similar share of the total number of interacting ligands, causing a symmetric multifold effect on the magnetic moments of all inner Co atoms.

The relationship between the atomic decomposed local magnetic moments, LMM, of 100 % passivated NPs is captured in Figure 7.4 as a function of the CNs of Co atoms. In unpassivated NPs, there is little dependence in the local magnetic moment on the position of the atom within the specific NP segment (core, inner, and surface segment), as showed in Chapter 3. The distribution of LMM across segments is governed by the CNs of Co atoms, and consequently, the average spacing between *d*-band energy levels. Discernible deviation from these grouped LMMs is captured for each passivation case. Specifically, both hcp and icosahedron Nps passivated by carboxylic acid ligands see an enhancement in the LMMs of surface-based Co atoms. The change is less prominent for the atoms exempted from the direct interaction with the ligands whose magnetic moments slightly

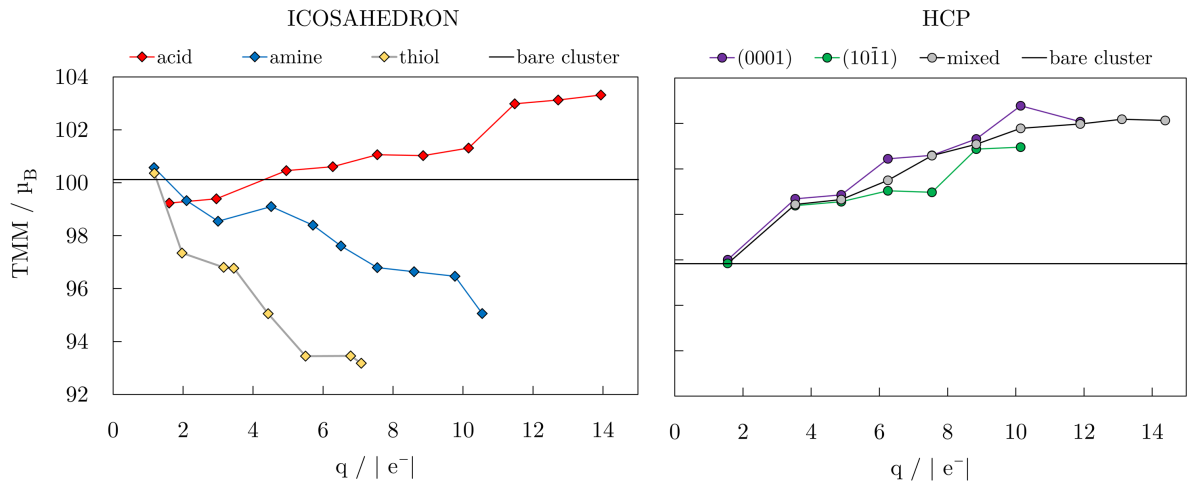

Figure 7.3: Total magnetic moment, TMM, as a function of Bader charge of Co core, q, for ligand-protected 55-atom icosahedron and 57-atom hcp Co NPs; connecting lines are to guide an eye only. TMMs of bare 55- and 57-atom icosahedral and hcp Co NPs are also indicated.

decreased, except for the central atom of the hcp NP which experienced an increase of 0.40 μ_B. Amine and thiol ligands show opposite behaviour. Passivation by amine is followed by a substantial drop in the LMMs of many Co atoms of all NP segments, although about one third of surface atoms showed an increase in the magnetic moments. The decline is even more pronounced for thiol-protected icosahedral NP, where only a handful of the 55 atoms did not lose from their unpassivated LMM values.

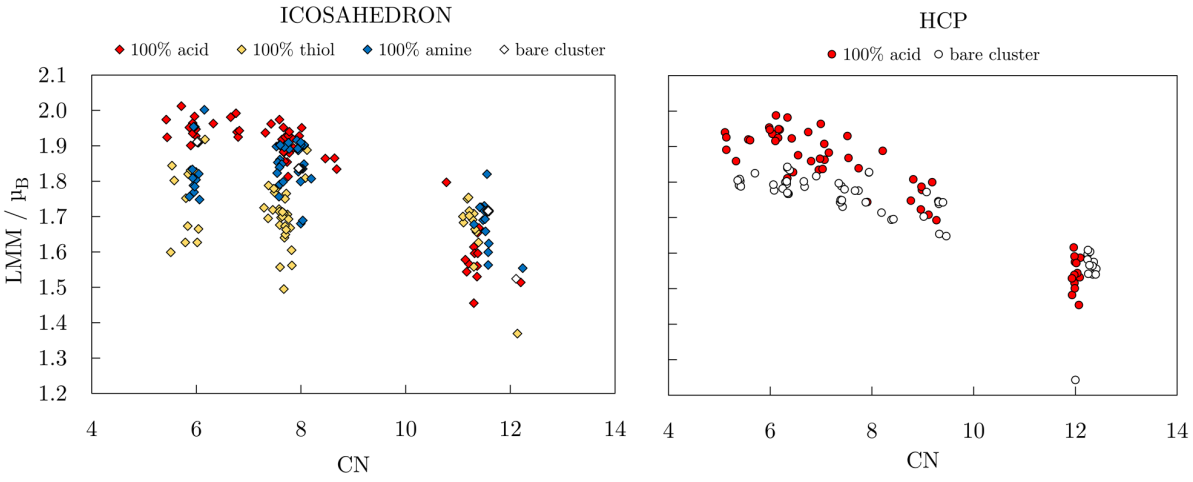

Figure 7.4: Total magnetic moment, TMM, as a function of Bader charge of Co core, q, for ligand-protected 55-atom icosahedron and 57-atom hcp Co NPs; connecting lines are to guide an eye only. TMMs of bare 55- and 57-atom icosahedral and hcp Co NPs are also indicated.

To get an insight into the functionalisation-induced changes in the magnetic anisotropy, ligand-protected NPs were simulated under two different directions of magnetisation corresponding to those depicted for the bare NPs in Figure 3.24, and obtained MAE are shown as a function of coverage in Figure 7.5. Starting from a very low value of 0.081 meV for unprotected icosahedron, all three families of ligands cause an increase in the MAE. The rates of this increase are, however, significantly different. Amine coating results in the lowest enhancement of MAE, which is calculated for a 100 % coverage at -1.424 meV. There is also a change in the direction of the easy axis of magnetisation for amine-protected NPs between the 60 and 70 % coverage densities. For acid and thiol coatings, the absolute value of MAE is steadily increasing as the density grows, with a slightly faster pace in the case of the acidic ligand. However, for the maximum coverages of 90 and 100 %, MAE of both acid- and thiol-protected NPs reach similar energies around the absolute values between 2.650 and 2.910 meV.

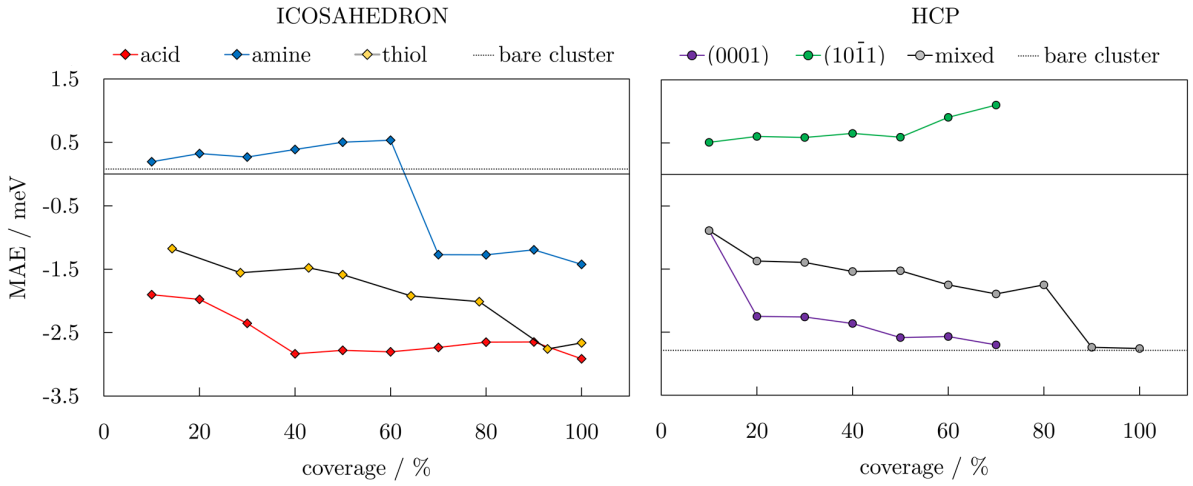

Figure 7.5: Magnetic anisotropy energy, MAE, as a function of coverage for varying ligand families and arrangements; dotted lines indicate values of bare 55- and 57-atom icosahedral and hcp Co NPs. Directions of magnetisation are consistent with those of bare NPs shown in Figure 3.24.

Arrangement of ligand molecules around the two types of surfaces of the hcp NP also showed significant effect on the anisotropy energies. By placing all of the ligand molecules on the (10$\bar{1}$1) facets, anisotropy energy is substantially decreased (0.91 meV for a 60 % coverage) and the easy axis of magnetisation reversed compared to the bare NP. If the ligands predominantly interact with the (0001) surface, reduction of the MAE of the bare NP is not as formidable (-2.57 meV for a 60 % coverage). Obtained MAE values for a mixed arrangement of the ligands are somewhere in between. Anisotropy energy of the bare NP is regained only at very high acid coverages, 90 and/or 100 %, where it reaches values of -2.74 and -2.76 meV. The overall trends resemble the step-like ones of the TMMs shown in Figure 7.3. However, an additional factor influencing trends of the MAE values

comes from the orientation of the molecules bonded in the less favourable adsorption sites. The directional variation of adsorption sites affects also the direction of the easy axis of magnetisation, similar to the effect of axial ligands and their interaction angles on the anisotropy of transition metal complexes.[622, 623, 624] For amine-protected icosahedral Co NPs, this is reflected through the continuous decrease in the binding energy and ligand-surface angles, Table 7.7, indicating reduced influence of higher coverage molecules on surface Co atoms. In the case of hcp Co NPs with acid ligands, opposite binding energy trends on two exposed facet types and shares of adsorbed ligands on each of them dictate the preferential magnetisation axis.

Table 7.2: Magnetic properties and Bader charge analysis of systems with a Co_{55} icosahedral core and different carboxylic acid coverages in % as a function of position in the NP. Magnetic moments are in μ_B and charges in $|e^-|$.

coverage	total magnetic moment	centre atom LMM	average inner LMM	average surface LMM	total core charge	centre atom charge	average inner charge	average surface charge
0	100.118	1.715	1.701	1.857	0.27	-0.137	0.034	-0.004
10	99.235	1.542	1.679	1.796	1.60	-0.178	0.046	0.028
20	99.393	1.483	1.666	1.800	2.95	-0.183	0.040	0.062
30	100.457	1.449	1.663	1.818	4.95	-0.191	0.033	0.112
40	100.608	1.443	1.657	1.819	6.28	-0.186	0.032	0.144
50	101.058	1.310	1.653	1.831	7.55	-0.194	0.028	0.176
60	101.025	1.306	1.622	1.832	8.86	-0.195	0.024	0.208
70	101.313	1.316	1.607	1.836	10.16	-0.201	0.018	0.241
80	102.983	1.454	1.635	1.864	11.48	-0.205	0.013	0.274
90	103.126	1.540	1.616	1.870	12.72	-0.198	0.001	0.307
100	103.318	1.590	1.590	1.879	13.94	-0.207	-0.006	0.339

Table 7.3: Magnetic properties and Bader charge analysis of systems with a Co_{55} icosahedral core and different amine coverages in % as a function of position in the NP. Magnetic moments are in μ_B and charges in $|e^-|$.

coverage	total magnetic moment	centre atom LMM	average inner LMM	average surface LMM	total core charge	centre atom charge	average inner charge	average surface charge
0	100.118	1.715	1.701	1.857	0.27	-0.137	0.034	-0.004
10	100.571	1.649	1.707	1.821	1.17	-0.145	0.056	0.010
20	99.325	1.514	1.675	1.794	2.10	-0.195	0.029	0.041
30	98.776	1.489	1.637	1.767	3.20	-0.166	0.026	0.064
40	99.098	1.515	1.671	1.809	4.52	-0.174	0.017	0.102
50	98.606	1.554	1.675	1.804	5.54	-0.184	0.020	0.126
60	98.312	1.540	1.645	1.774	6.51	-0.181	0.018	0.150
70	96.792	1.570	1.630	1.738	7.55	-0.164	0.028	0.175
80	96.639	1.577	1.644	1.732	8.60	-0.190	0.023	0.202
90	96.670	1.459	1.592	1.741	9.77	-0.184	0.018	0.231
100	95.057	1.543	1.565	1.707	10.55	-0.175	0.010	0.252

To understand these trends better, atomic charges and spin magnetic moments were decomposed as a function of the NP segments for each ligand coverage density, Tables

Table 7.4: Magnetic properties and Bader charge analysis of systems with a Co_{55} icosahedral core and different thiol coverages in % as a function of position in the NP. Magnetic moments are in μ_B and charges in $|e^-|$.

coverage	total magnetic moment	centre atom LMM	average inner LMM	average surface LMM	total core charge	centre atom charge	average inner charge	average surface charge
0	100.118	1.715	1.701	1.857	0.27	-0.137	0.034	-0.004
14	100.536	1.603	1.712	1.817	1.18	-0.159	0.040	0.016
21	97.664	1.415	1.668	1.747	1.50	-0.171	0.038	0.020
29	97.344	1.391	1.665	1.741	1.97	-0.190	0.035	0.036
43	96.804	1.399	1.679	1.753	3.16	-0.185	0.032	0.070
50	96.772	1.469	1.659	1.740	3.45	-0.183	0.025	0.074
64	95.052	1.469	1.652	1.700	4.43	-0.181	0.030	0.096
78	93.446	1.340	1.633	1.670	5.50	-0.191	0.025	0.123
93	93.454	1.327	1.635	1.662	6.79	-0.198	0.043	0.157
100	94.180	1.369	1.654	1.676	7.09	-0.187	0.040	0.161

Table 7.5: Magnetic properties and Bader charge analysis of systems with a Co_{57} hcp core and different carboxylic acid coverages in % as a function of position in the NP. Magnetic moments are in μ_B and charges in $|e^-|$.

coverage	total magnetic moment	centre atom LMM	average inner LMM	average surface LMM	total core charge	centre atom charge	average inner charge	average surface charge
0	96.179	1.215	1.538	1.732	0.29	-0.020	0.033	-0.003
10	98.008	1.243	1.543	1.726	1.55	-0.045	0.029	0.027
20	100.391	1.428	1.572	1.764	3.53	-0.026	0.025	0.073
30	100.666	1.397	1.565	1.768	4.88	-0.033	0.021	0.105
40	102.451	1.442	1.594	1.795	6.25	-0.045	0.016	0.137
50	102.598	1.489	1.583	1.797	7.54	-0.040	0.011	0.168
60	102.912	1.493	1.577	1.803	8.84	-0.038	0.008	0.199
70	103.784	1.544	1.605	1.830	10.14	-0.044	0.004	0.229
80	104.093	1.567	1.558	1.822	11.89	-0.026	-0.005	0.267
90	104.189	1.573	1.553	1.824	13.11	-0.040	-0.011	0.299
100	104.137	1.532	1.541	1.826	14.38	-0.032	-0.011	0.330

7.2-7.5. The most pronounced changes in the average charge values are, in all cases, present on the surface atoms, which is to be expected from the direct interactions with the functional groups of ligands. The areas with the most significantly affected magnetic properties, however, differentiate for distinct ligand families. In carboxylic acid-protected NPs, average magnetic moments of centre and inner segments of Co core are affected more than those of surface Co atoms. For NPs functionalised by amine molecules, quenching of magnetic moments of similar intensity is experienced in all three segments of the Co core. Thiol-mediated changes in the magnetic moments are, on the other hand, the most pronounced for surface atoms and the central atom, while a reduced effect is observed on the atoms of the inner segment. In each case, magnetic moments obtained through the non-collinear calculations show insignificant difference between the absolute (spin-orbit coupling included) and total magnetisation (spin-orbit coupling not included) of the NPs (Δ = 0.05-0.20 μ_B per NP/0.001-0.005 μ_B per atom). This indicates that there exists almost no antiferromagnetic coupling between the metal atoms and ligand molecules.

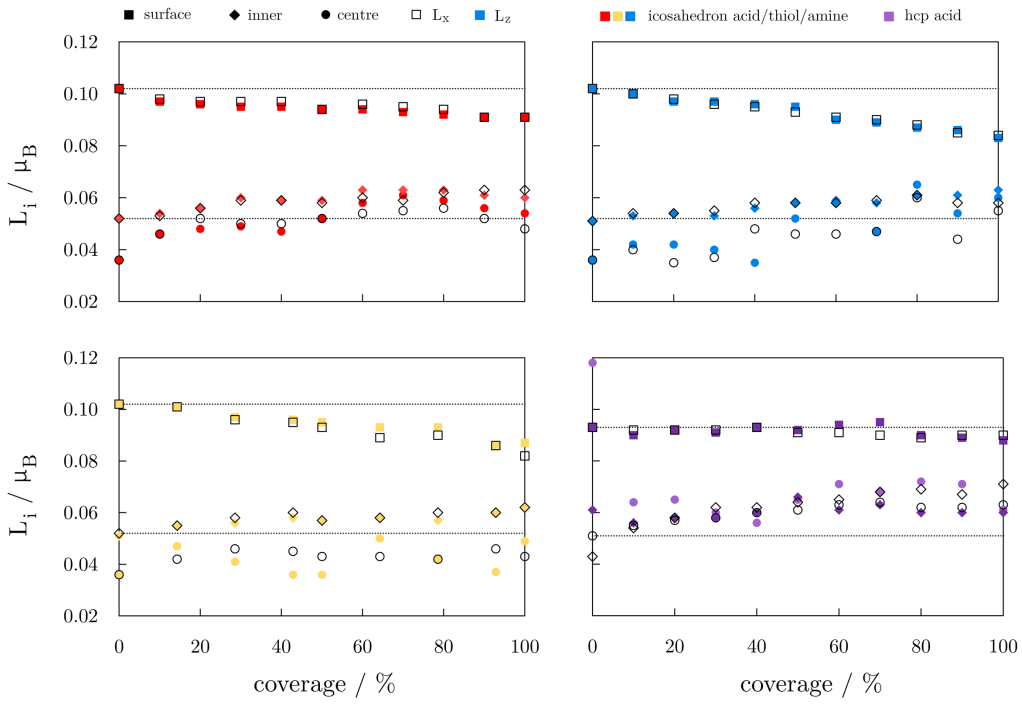

Figure 7.6: Average orbital moments for three segments (centre ∘, inner ⋄, surface □) of ligand-protected Co NPs as a function of the ligand coverage. Two directions of magnetisation are shown as empty and filled symbols, with colours representing varying ligands on icoahedral and hcp Co cores (red, yellow, and blue: acid, thiol, and amine-protected icosahedron, purple: acid-protected hcp Co NP). Dotted lines are average surface and inner orbital moments of bare NPs.

Figure 7.6 represents average orbital magnetic moments per core segment as a function of the coverage of different ligands. In general, there is a steady decrease of orbital moments on the surface, and a moderate increase of orbital moments of the inner atoms, but the overall change does not exceed 0.02 μ_B. Orbital moment of the central atom oscillates the most from one coverage to another. Nevertheless, there is no clear connection between the local anisotropies ($\Delta L = L_z - L_x$) as a function of the coverage and the observed MAE trends.

7.3.3 Structural and electronic properties of ligand-protected Co NPs

Absence of the change in the absolute magnetisation and the $L_z - L_x \propto Ez - E_x$ correlation with the anisotropy energies which was observed for bare NPs indicates that the spin-orbit coupling has minimal contribution in the MAE changes of the protected NPs. These changes also do not relate to any structural rearrangement of Co atoms caused by the ligand binding, which is shown by the consistent Co-Co distances over the coverages considered, Tables 7.6-7.9. In average, Co-Co bonds are shortened or prolonged for ±2.0 % and mostly between the inner and surface Co atoms. Modifications in the binding

geometry of ligands are also minimal and arise due to the aforementioned difference in the adsorption sites. Hence, considering the invariance in the orbital moments and structural descriptors, the major contribution to the changes in the MAE of functionalised NPs comes from the re-distribution of the electron density. Here the nature of the bond between the ligand and metal atoms plays the critical role.

Table 7.6: Average Co-Co distance, bond lengths, and angles formed between surface Co atoms of 55-atom icosahedral cluster and carboxyl head group. All distances are in Å and angles in °.

coverage	centre-inner	inner-inner	inner-surface	surface-surface	surface-ligand	Co-Co-O angle
0	2.357	2.480	2.350	2.468	-	-
10	2.366	2.490	2.354	2.471	1.949	86.209
20	2.367	2.500	2.362	2.463	1.960	86.312
30	2.366	2.489	2.379	2.468	1.956	86.124
40	2.368	2.485	2.389	2.471	1.954	86.855
50	2.363	2.474	2.381	2.467	1.946	85.806
60	2.368	2.485	2.389	2.471	1.954	86.855
70	2.370	2.510	2.384	2.465	1.945	86.421
80	2.368	2.499	2.382	2.474	1.953	86.593
90	2.368	2.480	2.391	2.490	1.964	86.544
100	2.366	2.480	2.406	2.472	1.953	86.342

Table 7.7: Average Co-Co distance, bond lengths, and angles formed between surface Co atoms of 55-atom icosahedral cluster and amine head group. All distances are in Å and angles in °.

coverage	centre-inner	inner-inner	inner-surface	surface-surface	surface-ligand	Co-N-Co angle
0	2.357	2.480	2.350	2.468	-	-
10	2.358	2.481	2.362	2.469	1.969	75.397
20	2.353	2.475	2.369	2.479	1.968	75.173
30	2.348	2.468	2.358	2.474	1.968	74.755
40	2.354	2.475	2.373	2.479	1.977	75.045
50	2.352	2.474	2.373	2.473	1.976	74.505
60	2.354	2.475	2.370	2.456	1.972	74.518
70	2.351	2.473	2.378	2.467	1.974	74.683
80	2.355	2.476	2.390	2.473	1.976	74.082
90	2.353	2.476	2.398	2.473	1.984	73.832
100	2.353	2.476	2.396	2.474	1.979	73.600

Electronic properties for a single Co-molecule pair for all three ligand types considered are shown in Figure 7.7 in the form of pDOS and the change in electron density induced from molecule's binding, $\Delta\rho$.In the case of the -COOH functional group, which contains highly electronegative oxygen and polarises the bond more strongly than the other two ligand families, the interaction with the surface is more localised. This smaller bond volume induces the electronic repulsion energy within the bond, which contributes towards the drive of electrons to remain unpaired and also leads to a small magnetic moment of the ligand itself, Table 7.10. Another distinct behaviour is the effect experienced by inner parts of the NP, where different ligands can cause similar charge accumulation but have

Table 7.8: Average Co-Co distance, bond lengths, and angles formed between surface Co atoms of 55-atom icosahedral cluster and thiol head group. All distances are in Å and angles in °.

coverage	centre-inner	inner-inner	inner-surface	surface-surface	surface-ligand	Co-N-Co angle
0	2.357	2.480	2.350	2.468	-	-
14	2.358	2.479	2.357	2.478	2.228	72.068
21	2.351	2.472	2.364	2.475	2.207	72.265
29	2.355	2.475	2.358	2.477	2.211	71.854
43	2.358	2.479	2.370	2.473	2.215	71.959
50	2.351	2.468	2.367	2.476	2.226	71.658
64	2.359	2.481	2.370	2.472	2.208	72.311
78	2.355	2.472	2.378	2.470	2.215	71.707
93	2.357	2.476	2.387	2.478	2.219	72.234
100	2.359	2.479	2.382	2.477	2.221	72.038

Table 7.9: Average Co-Co distance, bond lengths, and angles formed between surface Co atoms of 57-atom hcp cluster and carboxyl head group. All distances are in Å and angles in °.

coverage	centre-inner	inner-inner	inner-surface	surface-surface	surface-ligand	Co-N-Co angle
0	2.449	2.453	2.392	2.402	-	-
10	2.440	2.441	2.411	2.408	1.914	86.392
20	2.442	2.450	2.389	2.414	1.933	85.115
30	2.442	2.444	2.403	2.415	1.932	85.060
40	2.440	2.438	2.409	2.425	1.935	85.499
50	2.441	2.451	2..412	2.418	1.957	85.896
60	2.441	2.442	2.404	2.428	1.946	86.830
70	2.443	2.439	2.420	2.432	1.950	86.792
80	2.446	2.448	2.419	2.436	1.952	86.052
90	2.438	2.438	2.423	2.442	1.945	86.893
100	2.434	2.432	2.422	2.433	1.959	86.407

Table 7.10: Average magnetic moments in μ_B and charge in $|e^-|$ per ligand molecule for different ligand-NP pairs.

ligand-NP pair	magnetic moment per ligand	charge per ligand
carboxylic acid-icosahedron	0.089	-0.643
amine-icosahedron	0.050	-0.482
thiol-icosahedron	0.055	-0.478
carboxylic acid-hcp	0.081	-0.633

a completely opposite impact on the spin magnetic moments. The electron localising ability hence also controls the distribution of the spin density, with -SH group quenching the magnetic moment of the central atom the most. When analysing the aspects of binding within the DOS, all of the ligands hybridise with the $2p$ and $3d$ states of interacting Co atom across the entire band in majority spin channels, but hybridisation in minority spin channels is lacking around the Fermi level. And while the majority $3d$ spin states remain completely occupied with negligible energy changes, shifts in the minority states did occur. Compared to the d-band centre energies of bare icosahedral NP, which are found at -2.28 eV for majority and at -0.49 eV for minority spins (referenced to the Fermi level), amine

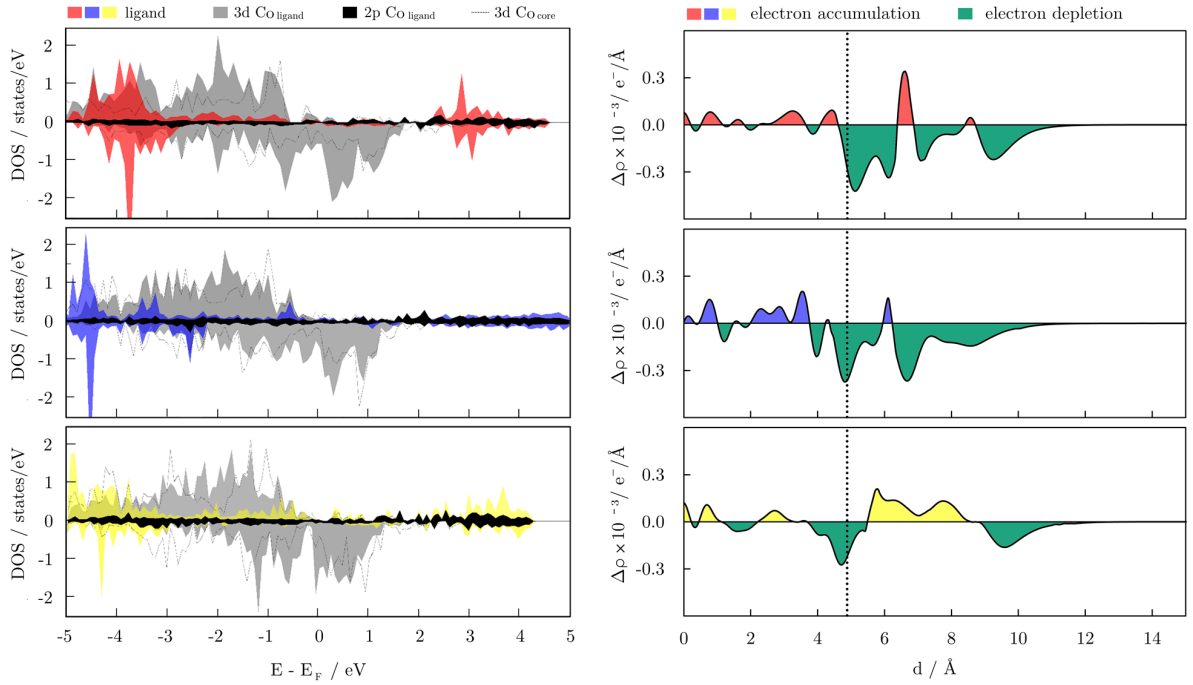

Figure 7.7: **left**: projected densities of state, DOS, for a single molecule of acetic acid (red), ethanamine (blue), and ethanethiol (yellow) interacting with a 55-atom icosahedral Co NP. Both majority and minority spins are shown. DOS of the surface Co atoms interacting with the molecule are shown as filled blocks, while DOS of the inner Co atom directly beneath the interaction site are shown as dotted lines. **right**: Radial probability density function of the difference in the electron density, $\Delta\rho$, induced from the binding of the ligand molecules as a function of the distance from the centre, d. Vertical dashed line corresponds to the position of the surface Co atoms relative to the central atom, and colours correspond to those of ligands' DOS.

functionalisation has an insignificant impact on both, calculated to be at -2.28 and -0.47 eV, respectively. However, shifts occurred in –COOH and –SH protected NPs are much more pronounced, with energies of -2.27 and -0.32 eV for majority and minority spins in the case of carboxylic acid binding, and -2.20 and -0.60 eV for majority and minority spins in the case of thiol functionalisation. Since both acid- and thiol-mediated anisotropy changes resulted in similar values for maximal coverages, either positive or negative shift of minority spins can be employed to increase the final MAE. It should be taken into the account that the electronic effects shown here are captured for a single molecule and would certainly be multiplied within the denser coatings.

For the carboxylic acids interacting with the hcp CO NP, changes in the d-band centre energy are similar in the nature to the change induced on the icosahedron regardless of the arrangement over NP surfaces. The DOS for the two surface cases are shown in Figure 7.8. Majority spin d-band energy centre of the bare hcp NP is at -2.16 eV, and that of minority spins is found at -0.38 eV. For the (0001) surface atoms bonded to the ligand

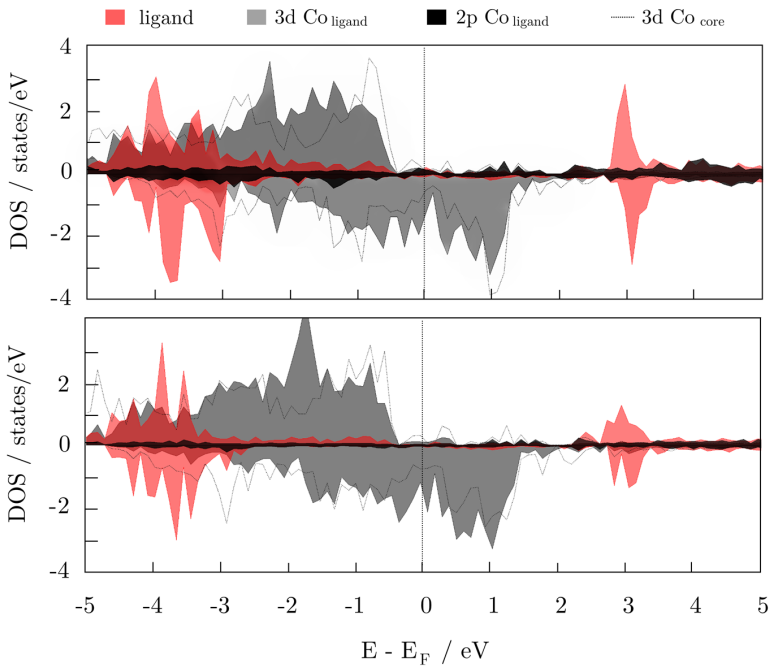

Figure 7.8: Densities of state, DOS, for a single molecule of acetic acid interacting with a (0001) surface (**top** panel) and a (10$\bar{1}$1) surface (**bottom** panel) of the 57-atom hcp Co NP. Both majority and minority spins are shown. DOS of the surface Co atoms interacting with the molecule are shown as filled blocks, while DOS of the inner Co atom directly beneath the interaction site are shown as dotted lines.

molecule, those energies are altered to -2.18 and -0.33 eV, respectively, whereas calculated d-band centre energies for the interacting Co atoms of the (10$\bar{1}$1) surface are found at -2.11 and -0.25 eV. The overall effect of the ligand is, hence, unchanged with the position of the adsorption, and, cumulatively, all the ligand molecules contribute to the shift of the minority spin d-band centre towards the Fermi level. An opposite effect of the carboxylic acid protective coating on the MAE values of icosahedral and hcp Co NPs then clearly has to come from the directional adsorption of the ligand molecules. Favoured adsorption positions on the hcp NPs are either parallel or perpendicular to the x- and/or z-axis, while compact folding of (111) facets in the icosahedral morphology does not allow for such directional arrangement of ligands, which facilitates reversed MAE performance.

7.4 Conclusion

Chemistry of the established interactions between the functionalising ligands and mNPs which stands behind their effects on the NP properties can be a robust way to tune the desired magnetic behaviour of final nanocomposites. Amine and thiol functionalisation resulted in a significant reduction of total magnetisation of Co NPs, whereas the increasing magnetic anisotropy energy trend progressed at a notably slower pace for

amine than for thiol functional group. On the other hand, carboxylic acid-protected Co NPs showed an increase in magnetic moments and high magnetic anisotropy energies for both icosahedral and hcp morphologies.

Descriptors of ligand binding have captured shifts of the minority spin d-band centre energy as the most prominent difference between the three ligand families. While amine-mediated shift was minimal, those induced through thiol and acid binding were of similar intensity, but of opposite sign, indicating that change in either direction is beneficial to enhance the MAE of icosahedral Co NPs. However, to achieve high MAE values and maintain the favourable magnetisation of bare Co NPs, positive shift mediated through carboxylic acid interaction is the best of considered options.

Taken together, given the important role of biocompatibility-inducing ligands in the magnetic behaviour of protected Co NPs, theoretical insights of such phenomena can boost targeted design of nanomaterials with favourable magnetic moments and anisotropy energies.

Highlights of the chapter

- **Identified varying effects of three ligand families on magnetic properties of Co NPs.**
- **Identified carboxylic acid as the ligand family which increases both magnetic moments and absolute values of MAE of either Co NP morphology.**
- **Established relation between MAE and directional adsorption of ligands.**

CHAPTER 8

SUMMARY AND PERSPECTIVES

"Either it brings tears to their eyes, or else -" "Or else what?"
said Alice, for the Knight had made a sudden pause.
"Or else it doesn't, you know."
-Chapter 8, The Queen's Croquet-Ground

8.1 Summary

This thesis aimed to use first principles based methods to study the possible implementation of metallic magnetic nanomaterials, Co NPs specifically, in addressing the issues of side effects and insufficient magnetisation of nanomaterials currently employed in cancer theranostics through optimisation of their magnetic properties. The work has taken advantage of the enhanced supercomputing technologies by simulating more realistic particle models to obtain a comprehensive and detailed picture of the progression of relevant magnetic characteristics of Co NPs with the changes in the NP morphology, increase in the NP size, oxidation in environmental conditions, and biocompatible functionalisation.

Initial objective was in probing the size- and shape-dependence on the varying energetics of Co NPs, which identified large NPs ($N \approx 5500$ or d ~3-4 nm) as the crossover size between the icosahedral and hexagonal motifs. Employing NP models with up to several nanometres in diameter provided great analytical means on structural, electronic, and magnetic basis, for detecting parameters which affect morphology stability trends, allowing for an in-depth explanation of experimentally observed icosahedral structure for medium-sized Co NPs. This rationalisation of the non-crystalline-to-crystalline transition size ranges for metallic Co is expected to aid the synthetic efforts for Co NP morphologies of favourable electronic and/or magnetic properties, as it now completes the series of studies directed towards NP geometries of mainly fcc-bulk metals (but also an hcp Ru) which stimulated efficient experimental production of various morphologies with desired properties.

Another issue frequently revisited in the literature is oxidation of metal NPs, owing its relevance to the annihilation of the original NP properties and conditions directed towards specific effectiveness of surface reactions and application-desired performance. The

considerably lower number of experiments conducted on Co single crystals compared to other metal NPs (caused by the hcp→fcc phase transition and high chemical sensitivity), required for a better characterisation of their oxidation activity. Equilibrium models for the oxidation of NP-appearing surfaces were used to clarify surface-oxygen compositions and possible oxide formation relevant to observed magnetic behaviour. Direction of CoO and Co_3O_4 growth has been successfully captured for the two surfaces examined experimentally ((111) directional growth on the Co(0001) surface, and (100) directional growth on the Co $(11\bar{2}0)$ surface), and for the first time proposed for the remaining surfaces ((100) directional growth on the Co$(01\bar{1}0)$ surface, (011) directional growth on the Co$(10\bar{1}1)$ and Co$(11\bar{2}1)$ surfaces), one of which (Co$(10\bar{1}1)$) is a major contributor to the hcp NP geometry. The results were extended to predict the metal behaviour in equilibrium with an oxygen environment through the use of *ab initio* thermodynamics, attempting to take maximum advantage of experimental thermodynamic data. Suggested temperature-pressure phase diagrams identified oxide phases as main oxidation products on all surfaces. The results help illuminate the coupling between reaction conditions, surface reactivity, and surface composition necessary to develop complete theories of environmentally-induced oxidation of Co NPs.

In the light of detected oxide formation at biologically fundamental temperature and oxygen partial pressure conditions, the remaining portion of this work has been dedicated to the investigation of the Co NP functionalisation strategies. Starting with the discrepancy in the experimentally provided binding modes of carboxylic acids on Co NPs, metadynamics simulations were successfully applied to sample the configurational and free energy space of carboxylic acid-Co NP system via the implementation of collective variables related to the coordination number distribution function between the NP surface and the ligand of interest. After confirming bridging bidentate as a global minimum for acid interaction, the most favourable thiol- and amine-binding modes were predicted to be a three-fold monodentate and an NH-bidentate, respectively. Simulated IR spectra of defined interactions of carboxylic acid with the Co NP show good agreement with experiments, giving the corroboration value to obtained thiol- and amine-interacting IR spectra for evaluation of the (so-far not measured) experimental counterparts.

Combining the atomic-level information on distinct ligand-Co NP systems with the enhanced sampling methods (NEB and metadynamics), this work also provided structural and energetic characterisation of the carboxylic acid, thiol, and amine Co NP functionalisation mechanism. Spontaneous dissociation of hydrogen atoms, which are an active part of the functional groups of organic ligands, was determined as the most important factor governing the density of the formed functionalised coating. Through the NEB calculations, multiple cases leading to the H_2 formation were probed, including the formation of staple motifs with the two ligand molecules sharing an interacting site, motivated by the studies on thiol-gold systems. Transition states with reasonable activation energies were determined as transition points towards the desorption of the gaseous H_2, although staple motif stability was not detected. Exploiting the ability of the metadynamics approach to estimate the free energy of visited states in combination with temperature and

multiple-ligand effects, the landscape of dissociated hydrogen atoms was reconstructed to a thermodynamically more realistic picture, indicating low barriers for the formation of the hydrogen gas.

The possibility to characterise the changes in the magnetic moments and magnetic anisotropies induced by the ligand functionalisation through the NP models for Co NPs with distinct morphologies is probably the most important achievement of this thesis. In the correlation with the spin-orbit coupling, electronic states hybridisation, and directional adsorption, this method can investigate details behind magnetic changes otherwise invisible to experiments. Significant increase in both total magnetic moment and MAE was calculated for the acid-protected Co NPs. Amine ligands were detected to moderately reduce the NP magnetic moments and moderately increase the anisotropy. Substantial quenching of NP magnetisation was captured for thiol-protected NPs, but the found MAE trend was corresponding to the one of carboxylic acids. Increased total magnetic moments and anisotropy energies are hence expected to facilitate improved response of acid-protected Co nanoagents in various diagnostic and therapeutic treatments based on the magnetic relaxations of employed mNPs (such as MRI and mNPH). Characterisation of the nature of the Co NP magnetisation and anisotropy de/increase in correlation with the ligand of interest created an opportunity to hypothesize a role of the Co atoms electronic state shifts and the symmetry-directed ligand incorporation on the NP surface in the phenomenon of ligand-mediated magnetic behaviour of different nanocomposites. The approach can be used in particular to characterise systems which have not been so far probed experimentally, proving the great prediction power of computationally driven efforts.

8.2 Perspectives

In this thesis, the concentration was on defining the sound model for predicting biomedically relevant magnetic properties of bare, oxidised, and ligand-protected Co NPs. For the future, one can envisage extending this work in a number of directions. First, it would be interesting to examine the changes in the magnetic properties if Co NPs are replaced by alternative Co-based nanoalloys, such as CoAu NPs. This is particularly beneficial for the technological development, because gold is inert and provides strong thiol functionalisation. Work along these lines is in progress. Secondly, performance in the realistic environment is not reachable within the proposed *ab initio* models, giving place to the extensions in form of molecular dynamics simulations, for which further studies on the quantitative prediction of the magnetic temperature gradient around the protected Co NPs incorporated in the lipid membranes would be of specific interest. Finally, there is a gap between the theoretically and experimentally studied Co systems, where the NP sizes accessible by accurate first principles calculations are within the small and medium clusters/NP limit, while experimental methods have fewer challenges and are less influenced by the external conditions in the large diameter regions. Many of the morphology- and ligand-mediated properties are also difficult to obtain upon synthesis due to the size, shape, and coating thickness distributions within the sample. Ultimately, shortage of

studies on protected magnetic NPs, NP anisotropies, and NP morphology-magnetic ordering connections makes verification of theoretically predicted values difficult. Direct bridging of this gap is desired through new experimental measurements, with the purpose of confirming or improving herein described trends. Overall, the strong dependence of key magnetic properties of Co NPs towards the structural and ligand-coupled parameters investigated in this work should stimulate experimental efforts to develop methods with sound control over the size, morphology, and functionalisation of Co nanocrystals, and in particular explore their magnetic behaviour for potential applications in cancer theranostics.

By taking a general view about the problem of medical implementation of metallic NPs, nature has been able to finely tune the magnetic properties through the selection of size, shape, and composition of the material. By changing the relative proportion or surrounding conditions, it is able to alternate the balance between round and squared, magnetic and non-magnetic, formation and decomposition, entropy and enthalpy, shaping the final scenario as it sees fit. Emerging abilities of property fine-tuning and inherent details behind it as accessed by experimental and complementary computational methods allow for the new generation of nanosystems, adding to the immense repertoire of application-specific functions and biomedical agents necessary to improve the quality of life.

"But", said Alice, "if the world has absolutely no sense,
who's stopping us from inventing one?"

BIBLIOGRAPHY

[1] B W Stewart and C P Wild. *World cancer report 2014*. World Health Organization, 2014.

[2] Y. Chen, P. Jungsuwadee, M. Vore, D. A. Butterfield, and D. K. St. Clair. *Molecular Interventions*, 7:147–156, 2007.

[3] Samir Mitragotri, Daniel G. Anderson, Xiaoyuan Chen, Edward K. Chow, Dean Ho, Alexander V. Kabanov, Jeffrey M. Karp, Kazunori Kataoka, Chad A. Mirkin, Sarah Hurst Petrosko, Jinjun Shi, Molly M. Stevens, Shouheng Sun, Sweehin Teoh, Subbu S. Venkatraman, Younan Xia, Shutao Wang, Zhen Gu, and Chenjie Xu. *ACS Nano*, 9:6644–6654, 2015.

[4] Adam J. Cole, Allan E. David, Jianxin Wang, Craig J. Galbán, Hannah L. Hill, and Victor C. Yang. *Biomaterials*, 32:2183–2193, 2011.

[5] Jaber Beik, Ziaeddin Abed, Fatemeh S. Ghoreishi, Samira Hosseini-Nami, Saeed Mehrzadi, Ali Shakeri-Zadeh, and S. Kamran Kamrava. *Journal of Controlled Release*, 235:205–221, 2016.

[6] Klaus Maier-Hauff, Frank Ulrich, Dirk Nestler, Hendrik Niehoff, Peter Wust, Burghard Thiesen, Helmut Orawa, Volker Budach, and Andreas Jordan. *Journal of Neuro-Oncology*, 103:317–324, 2011.

[7] Poornima Budime Santhosh and Nataša Poklar Ulrih. *Cancer Letters*, 336:8–17, 2013.

[8] Pablo Guardia, Riccardo Di Corato, Lenaic Lartigue, Claire Wilhelm, Ana Espinosa, Mar Garcia-Hernandez, Florence Gazeau, Liberato Manna, and Teresa Pellegrino. *ACS Nano*, 6:3080–3091, 2012.

[9] Jelena Kolosnjaj-Tabi, Riccardo Di Corato, Lénaic Lartigue, Iris Marangon, Pablo Guardia, Amanda K.A. Silva, Nathalie Luciani, Olivier Clément, Patrice Flaud, Jaykrishna V. Singh, Paolo Decuzzi, Teresa Pellegrino, Claire Wilhelm, and Florence Gazeau. *ACS Nano*, 8:4268–4283, 2014.

[10] Carlos Martinez-Boubeta, Konstantinos Simeonidis, Antonios Makridis, Makis Angelakeris, Oscar Iglesias, Pablo Guardia, Andreu Cabot, Lluis Yedra, Sonia Estradé, Francesca Peiró, Zineb Saghi, Paul A. Midgley, Iván Conde-Leborán, David Serantes, and Daniel Baldomir. *Scientific Reports*, 3:1–8, 2013.

[11] Jae-Hyun Lee, Jung-tak Jang, Jin-sil Choi, Seung Ho Moon, Seung-hyun Noh, Ji-wook Kim, Jin-Gyu Kim, Il-Sun Kim, Kook In Park, and Jinwoo Cheon. *Nature Nanotechnology*, 6:418–422, 2011.

[12] Lénaic Lartigue, Pierre Hugounenq, Damien Alloyeau, Sarah P. Clarke, Michael Lévy, Jean Claude Bacri, Rana Bazzi, Dermot F. Brougham, Claire Wilhelm, and Florence Gazeau. *ACS Nano*, 6:10935–10949, 2012.

[13] Jung Tak Jang, Hyunsoo Nah, Jae Hyun Lee, Seung Ho Moon, Min Gyu Kim, and Jinwoo Cheon. *Angewandte Chemie - International Edition*, 48:1234–1238, 2009.

[14] Sandhya Moise, Eva Céspedes, Dalibor Soukup, James M. Byrne, Alicia J. El Haj, and Neil D. Telling. *Scientific Reports*, 7:39922, 2017.

[15] A H Habib, C L Ondeck, P Chaudhary, M R Bockstaller, and M. E. McHenry. *Journal of Applied Physics*, 103:07A307, 2008.

[16] L. V. Lutsev, A. I. Stognij, and N. N. Novitskii. *Physical Review B - Condensed Matter and Materials Physics*, 80:40–42, 2009.

[17] Mariane Trépanier, Ajay K. Dalai, and Nicolas Abatzoglou. *Applied Catalysis A: General*, 374:79–86, 2010.

[18] Lars Ole Simonsen, Henrik Harbak, and Poul Bennekou. *Science of the Total Environment*, 432:210–215, 2012.

[19] X. M. Lin, C. M. Sorensen, K. J. Klabunde, and G. C. Hadjipanayis. *Langmuir*, 14:7140–7146, 1998.

[20] T. Ibusuki, S. Kojima, O. Kitakami, and Y. Shimada. *IEEE Transactions Magnetics*, 37:2223–2225, 2001.

[21] H. T. Zhang, J. Ding, and G. M. Chow. *Langmuir*, 24:375–378, 2008.

[22] R. Sinclair, H. Li, S. Madsen, and H. Dai. *Ultramicroscopy*, 134:167–174, 2013.

[23] R. Skomski, B. Balamurugan, P. Manchanda, M. Chipara, and D. J. Sellmyer. *IEEE Transactions Magnetics*, 53:2300307, 2017.

[24] Chao Wang, Xijiang Han, Xiaolin Zhang, Surong Hu, Tao Zhang, Jinyu Wang, Yunchen Du, Xiaohong Wang, and Ping Xu. *Journal of Physical Chemistry C*, 114:14826–14830, 2010.

[25] H. Shao, Y. Huang, H. S. Lee, Y. J. Suh, and C. O. Kim. *Current Applied Physics*, 6:195–197, 2006.

[26] Shigeyoshi Saito, Mana Tsugeno, Daichi Koto, Yuki Mori, Yoshichika Yoshioka, Satoshi Nohara, and Kenya Murase. *International Journal of Nanomedicine*, 7:5415–5421, 2012.

[27] Branka Babić-Stojić, Vukoman Jokanović, Dušan Milivojević, Miroslav Požek, Zvonko Jagličić, Darko Makovec, Nataša Jović Orsini, Mirjana Marković, Katarina Arsikin, and Verica Paunović. *Current Apllied Physics*, 18:141–149, 2018.

[28] Gábor Kovács, Sergey M. Kozlov, and Konstantin M. Neyman. *Journal of Physical Chemistry C*, 121:10803–10808, 2017.

[29] J. Magnus Rahm and Paul Erhart. *Journal of Physical Chemistry C*, 122:28439–28445, 2018.

[30] Lin Yanhong, Wang Dejun, Zhao Qidong, Yang Min, and Zhang Qinglin. *Journal of Physical Chemistry B*, 108:3202–3206, 2004.

[31] Jeremy A. Scher, Jennifer M. Elward, and Arindam Chakraborty. *Journal of Physical Chemistry C*, 120:24999–25009, 2016.

[32] Prashant K. Jain, Xiaohua Huang, Ivan H. El-Sayed, and Mostafa A. El-Sayed. *Plasmonics*, 2:107–118, 2007.

[33] Vincenzo Amendola, Roberto Pilot, Marco Frasconi, Onofrio M. Maragò, and Maria Antonia Iatì. *Journal of Physics: Condensed Matter*, 29:203008, 2017.

[34] Tobias Neuberger, Bernhard Schöpf, Heinrich Hofmann, Margarete Hofmann, and Brigitte Von Rechenberg. *Journal of Magnetism and Magnetic Materials*, 293:483–496, 2005.

[35] Maria Mikhaylova, Do Kyung Kim, Natalia P. Bobrysheva, Mikhail Osmolowsky, Valentin Semenov, Thomas Tsakalakos, and Mamoun Muhammed. *Langmuir*, 20:2472–2477, 2004.

[36] Gareth L. Nealon, Bertrand Donnio, Romain Greget, Jean Paul Kappler, Emmanuel Terazzi, and Jean Louis Gallani. *Nanoscale*, 4:5244–5258, 2012.

[37] X. M. Lin, C. M. Sorensen, K. J. Klabunde, and G. C. Hadjipanayis. *Langmuir*, 14:7140–7146, 2002.

[38] Marin Tadic, Dobrica Nikolic, Matjaz Panjan, and Graeme R. Blake. *Journal of Alloys and Compounds*, 647:1061–1068, 2015.

[39] V.N. Nikiforov, B.L. Oksengendler, Mityagin A.Yu., Andrey N. Ignatenko, and V.Yu. Irkhin. *Laser Phys. Lett.*, 13:025601, 2012.

[40] Hongxiao Zhao, Zhi Zheng, Ka Wai Wong, Shumin Wang, Baojun Huang, and Dapeng Li. *Electrochemistry Communications*, 9:2606–2610, 2007.

[41] Guangmin Zhou, Da Wei Wang, Feng Li, Lili Zhang, Na Li, Zhong Shuai Wu, Lei Wen, Gao Qing Lu, and Hui Ming Cheng. *Chemistry of Materials*, 22:5306–5313, 2010.

[42] Andreas Moser, Kentaro Takano, David T Margulies, Manfred Albrecht, Yoshiaki Sonobe, Yoshihiro Ikeda, Shouheng Sun, and Eric E Fullerton. *Journal of Physics D: Applied Physics*, 35:R157–R167, 2002.

[43] Jian Ping Wang. *Proceedings of the IEEE*, 96:1847–1863, 2008.

[44] Pedro Tartaj, Maria P. Morales, Teresita Gonzalez-Carreño, Sabino Veintemillas-Verdaguer, and Carlos J. Serna. *Advanced Materials*, 23:5243–5249, 2011.

[45] P. A. Chernavskii, J.-A. Dalmon, N. S. Perov, and A. Y. Khodakov. *Oil & Gas Science and Technology - Revue de l'IFP*, 64:25–48, 2009.

[46] Samuel C N Tang and Irene M C Lo. *Water Research*, 47:2613–2632, 2013.

[47] Aleeza Farrukh, Attia Akram, Abdul Ghaffar, Sara Hanif, Almas Hamid, Hatice Duran, and Basit Yameen. *ACS applied materials & interfaces*, 5:3784–93, 2013.

[48] Alexandre Konate, Xiao He, Zhiyong Zhang, Yuhui Ma, Peng Zhang, Gibson Maswayi Alugongo, and Yukui Rui. *Sustainability (Switzerland)*, 9:790, 2017.

[49] Yong-Mei Hao, Chen Man, and Zhong-Bo Hu. *Journal of Hazardous Materials*, 184:392–399, 2010.

[50] Jing Hu, Guohua Chen, and Irene M C Lo. *Water Research*, 39:4528–4536, 2005.

[51] Ayush Verma, Oktay Uzun, Yuhua Hu, Ying Hu, Hee Sun Han, Nicki Watson, Suelin Chen, Darrell J. Irvine, and Francesco Stellacci. *Nature Materials*, 7:588–595, 2008.

[52] Teresa A.P. Rocha-Santos. *TrAC - Trends in Analytical Chemistry*, 62:28–36, 2014.

[53] A.A. Al-rashdi. *Analytical Chemistry Research*, 10:9–17, 2016.

[54] Yeonjeong Ha, Chun Huh, Kishore Mohanty, Ijung Kim, Saebom Ko, Jennifer A. Maynard, and Yimin Huang. *ACS Applied Nano Materials*, 1:512–521, 2018.

[55] M. Babincová, P. Sourivong, D. Leszczynska, and P. Babinec. *Medical Hypotheses*, 55:459–460, 2000.

[56] Ronald E. Rosensweig. *Ferrohydrodynamics*. Courier Corporation, 1997.

[57] Laura L Vatta, Ron D Sanderson, and Klaus R Koch. *Pure Appl. Chem*, 78:1793–1801, 2006.

[58] Fabian Kiessling, Marianne E. Mertens, Jan Grim, and Twan Lammers. *Radiology*, 273:10–28, 2014.

[59] Yi-Xiang J. Wang. *Quantitative Imaging in Medicine and Surgery*, 1:35–40, 2011.

[60] Yi-Xiang J. Wang. *World J Gastroenterol*, 21:13400–13402, 2015.

[61] Robert M. Taylor, Dale L. Huber, Todd C. Monson, Victor Esch, and Laurel O. Sillerud. *Journal of Vacuum Science Technology B, Nanotechnology and Microelectronics: Materials, Processing, Measurement, and Phenomena*, 30:02C101, 2012.

[62] Everett E. Carpenter. *Journal of Magnetism and Magnetic Materials*, 225:17–20, 2001.

[63] Costas G. Hadjipanayis, Michael J. Bonder, Srinivasan Balakrishnan, Xiaoxia Wang, Hui Mao, and George C. Hadjipanayis. *Small*, 4:1925–1929, 2008.

[64] Laura M. Parkes, Richard Hodgson, Le T. Lu, Le D. Tung, Ian Robinson, David G. Fernig, and Nguyen T. K. Thanh. *Contrast Media & Molecular Imaging*, 3:150–156, 2008.

[65] Louis-s Bouchard, M Sabieh Anwar, Gang L Liu, Byron Hann, Z Harry Xie, Joe W Gray, Xueding Wang, Alexander Pines, and Fanqing Frank Chen. *Proceedings of the National Academy of Sciences of the United States of America*, 106:4085–4089, 2009.

[66] J. W.J. Bergs, N. A.P. Franken, J. Haveman, E. D. Geijsen, J. Crezee, and C. van Bree. *International Journal of Hyperthermia*, 23:329–341, 2007.

[67] Adam Chicheł, Janusz Skowronek, Magda Kubaszewska, and Marek Kanikowski. *Reports of Practical Oncology and Radiotherapy*, 12:267–275, 2007.

[68] Nader Saniei. *Heat Transfer Engineering*, 30:915–917, 2009.

[69] Susanne Kossatz, Julia Grandke, Pierre Couleaud, Alfonso Latorre, Antonio Aires, Kieran Crosbie-Staunton, Robert Ludwig, Heidi Dähring, Volker Ettelt, Ana Lazaro-Carrillo, Macarena Calero, Maha Sader, José Courty, Yuri Volkov, Adriele Prina-Mello, Angeles Villanueva, Álvaro Somoza, Aitziber L Cortajarena, Rodolfo Miranda, and Ingrid Hilger. *Breast Cancer Research*, 17:66, 2015.

[70] Rhythm R. Shah, Todd P. Davis, Amanda L. Glover, David E. Nikles, and Christopher S. Brazel. *Journal of Magnetism and Magnetic Materials*, 387:96–106, 2015.

[71] Lisa M. Bauer, Shu F. Situ, Mark A. Griswold, and Anna Cristina Samia. *Nanoscale*, 8:12162–12169, 2016.

[72] Eric C. Abenojar, Sameera Wickramasinghe, Jesbaniris Bas-Concepcion, and Anna Cristina S. Samia. *Progress in Natural Science: Materials International*, 26:440–448, 2016.

[73] Luanne A. Thomas, Linda Dekker, Mathew Kallumadil, Paul Southern, Michael Wilson, Sean P. Nair, Quentin A. Pankhurst, and Ivan P. Parkin. *J. Mater. Chem.*, 19:6529–6535, 2009.

[74] Klaus Maier-Hauff, Ronny Rothe, Regina Scholz, Uwe Gneveckow, Peter Wust, Burghard Thiesen, Annelie Feussner, Andreas Deimling, Norbert Waldoefner, Roland Felix, and Andreas Jordan. *Journal of Neuro-Oncology*, 81:53–60, 2007.

[75] Silvio Dutz and Rudolf Hergt. *International Journal of Hyperthermia*, 29:790–800, 2013.

[76] Manfred Johannsen, Uwe Gneveckow, Burghard Thiesen, Kasra Taymoorian, Chie Hee Cho, Norbert Waldöfner, Regina Scholz, Andreas Jordan, Stefan A. Loening, and Peter Wust. *European Urology*, 52:1653–1662, 2007.

[77] E.K. Ruuge and A.N. Rusetski. *Journal of Magnetism and Magnetic Materials*, 122:335–339, 1993.

[78] P.A. Voltairas, D.I. Fotiadis, and L.K. Michalis. *Journal of Biomechanics*, 35:813–821, 2002.

[79] Andrew D. Grief and Giles Richardson. *Journal of Magnetism and Magnetic Materials*, 293:455–463, 2005.

[80] Benjamin B. Yellen, Zachary G. Forbes, Derek S. Halverson, Gregory Fridman, Kenneth A. Barbee, Michael Chorny, Robert Levy, and Gary Friedman. *Journal of Magnetism and Magnetic Materials*, 293:647–654, 2005.

[81] Axel J. Rosengart, Michael D. Kaminski, Haitao Chen, Patricia L. Caviness, Armin D. Ebner, and James A. Ritter. *Journal of Magnetism and Magnetic Materials*, 293:633–638, 2005.

[82] L. Asin, M.R. Ibarra, A. Tres, and G.F. Goya. *Pharmaceutical Research*, 29:1319–1327, 2012.

[83] Bipul Kumar, Kanika Jalodia, Pradeep Kumar, and Hemant K. Gautam. *Journal of Drug Delivery Science and Technology*, 41:260–268, 2017.

[84] Rudolf Hergt, Silvio Dutz, Robert Müller, and Matthias Zeisberger. *Journal of Physics Condensed Matter*, 18:S2919, 2006.

[85] G. Vallejo-Fernandez, O. Whear, A. G. Roca, S. Hussain, J. Timmis, V. Patel, and K. O'Grady. *Journal of Physics D: Applied Physics*, 46:312001, 2013.

[86] Alison E. Deatsch and Benjamin A. Evans. *Journal of Magnetism and Magnetic Materials*, 354:163–172, 2014.

[87] Florian Winau, Otto Westphal, and Rolf Winau. *Microbes and Infection*, 6:786–789, 2004.

[88] Kenneth Widder, George Flouret, and Andrew Senyei. *Journal of Pharmaceutical Sciences*, 68:79–82, 1979.

[89] Klaus Mosbach and Ulf Schröder. *FEBS Letters*, 102:112–116, 1979.

[90] Andrew Senyei, Kenneth Widder, and George Czerlinski. *Journal of Applied Physics*, 49:3578–3583, 1978.

[91] Brigitte Städler, Andrew D. Price, and Alexander N. Zelikin. *Advanced Functional Materials*, 21:14–28, 2001.

[92] Christien Oussoren and Gert Storm. *Advanced Drug Delivery Reviews*, 50:143–156, 2001.

[93] C. Barbé, J. Bartlett, L. Kong, K. Finnie, H. Q. Lin, M. Larkin, S. Calleja, A. Bush, and G. Calleja. *Advanced Materials*, 16:1959–1966, 2004.

[94] Kazunori Kataoka, Atsushi Harada, and Yukio Nagasaki. *Advanced Drug Delivery Reviews*, 47:113–131, 2001.

[95] Claudia Corbo, Roberto Molinaro, Alessandro Parodi, Naama E Toledano Furman, Francesco Salvatore, and Ennio Tasciotti. *Nanomedicine*, 11:81–100, 2016.

[96] Daniel F. Moyano, Meir Goldsmith, David J. Solfiell, Dalit Landesman-Milo, Oscar R. Miranda, Dan Peer, and Vincent M. Rotello. *Journal of the American Chemical Society*, 134:3965–3967, 2012.

[97] Tapan K Jain, Marco a. Morales, Sanjeeb K Sahoo, Diandra L Leslie-Pelecky, and Vinod Labhasetwar. *Molecular Pharmaceutics*, 2:194–205, 2005.

[98] Joan Estelrich, María Jesús Sánchez-Martín, and Maria Antònia Busquets. *International Journal of Nanomedicine*, 10:1727–1741, 2015.

[99] Khalisanni Khalid, Xuefei Tan, Hayyiratul Fatimah Mohd Zaid, Yang Tao, Chien Lye Chew, Dinh-Toi Chu, Man Kee Lam, Yeek-Chia Ho, Jun Wei Lim, and Lai Chin Wei. *Bioengineered*, 11:328–355, 2020.

[100] P. R. Lockman, R. J. Mumper, M. A. Khan, and D. D. Allen. *Drug Development and Industrial Pharmacy*, 28:1–13, 2002.

[101] Cláudia Saraiva, Catarina Praça, Raquel Ferreira, Tiago Santos, Lino Ferreira, and Liliana Bernardino. *Journal of Controlled Release*, 235:34–47, 2016.

[102] Yuping Bao, Hector Calderon, and Kannan M. Krishnan. *Journal of Physical Chemistry C*, 111:1941–1944, 2007.

[103] C. Petrarca, A.M. Poma, G. Vecchiotti, G. Bernardini, Q. Niu, A.G. Cattaneo, M. Di Gioacchino, and E. Sabbioni. *Nanotechnology Reviews*, 9:1522–1538, 2020.

[104] P.H. Linh, P.V. Thach, Thuan N.A., N.C. Thuan, D.H. Manh, N.X. Phuc, and L.V. Hong. *Journal of Physics: Conference Series*, 187:012069, 2009.

[105] W.M. Daoush. *Journal of Nanomedicine Research*, 5:00118, 2017.

[106] Seymour H. Koenig and Kenneth E. Kellar. *Magnetic Resonance in Medicine*, 34:227–233, 1995.

[107] Alain Roch, Robert N. Muller, and Pierre Gillis. *The Journal of Chemical Physics*, 110:5403–5411, 1999.

[108] Zijian Zhou, Lijiao Yang, Jinhao Gao, and Xiaoyuan Chen. *Advanced Materials*, 31:1804567, 2019.

[109] Marie Devreux, Céline Henoumont, Fabienne Dioury, Dimitri Stanicki, Sébastien Boutry, Lionel Larbanoix, Clotilde Ferroud, Robert N. Muller, and Sophie Laurent. *European Journal of Inorganic Chemistry*, 2019:3354–3365, 2019.

[110] Luis M. De León-Rodríguez, André F. Martins, Marco C. Pinho, Neil M. Rofsky, and A. Dean Sherry. *Journal of Magnetic Resonance Imaging*, 42:545–565, 2015.

[111] Hendrick W. de Haan. *Magnetic Resonance in Medicine*, 66:1748–1758, 2011.

[112] Tae-Hyun Shin, Youngseon Choi, Soojin Kim, and Jinwoo Cheon. *Chem. Soc. Rev.*, 44:4501–4516, 2015.

[113] Nina Kostevšek. *Magnetochemistry*, 6, 2020.

[114] John Pearce, Andrew Giustini, Robert Stigliano, and P. Jack Hoopes. *Journal of Nanotechnology in Engineering and Medicine*, 4:0110071–01100714, 2013.

[115] Dalibor Soukup, Sandhya Moise, Eva Céspedes, Jon Dobson, and Neil D. Telling. *ACS Nano*, 9:231–240, 2015.

[116] John Pearce, Andrew Giustini, Robert Stigliano, and P. Jack Hoopes. *Journal of Nanotechnology in Engineering and Medicine*, 4:011005, 2013.

[117] J. Carrey, B. Mehdaoui, and M. Respaud. *Journal of Applied Physics*, 109:083921, 2011.

[118] William J. Atkinson, Ivan A. Brezovich, and Dev P. Chakraborty. *IEEE Transactions on Biomedical Engineering*, BME-31:70–75, 1984.

[119] Z. Nemati, J. Alonso, L.M. Martinez, H. Khurshid, E. Garaio, J.A. Garcia, and H. Srikanth. *The Journal of Physical Chemistry C*, 120:8370–8379, 2016.

[120] H. Khurshid, J. Alonso, Z. Nemati, M. H. Phan, P. Mukherjee, M. L. Fdez-Gubieda, J. M. Barandiarán, and H. Srikanth. *Journal of Applied Physics*, 117:17A337, 2015.

[121] Li Ying Zhang, Hong Chen Gu, and Xu Man Wang. *Journal of Magnetism and Magnetic Materials*, 311:228–233, 2007.

[122] K. Kekalo, I. Baker, R. Meyers, and J. Shyong. *Nano LIFE*, 5:1550002, 2015.

[123] Mohamed S.A. Darwish. *Journal of Molecular Liquids*, 231:80–85, 2017.

[124] Marie-Alexandra Neouze and Ulrich Schubert. *Monatshefte für Chemie - Chemical issnly*, 139:183–195, 2008.

[125] A. Badia, L. Demers, L. Dickinson, F. G. Morin, R. B. Lennox, and L. Reven. *Journal of the American Chemical Society*, 119:11104–11105, 1997.

[126] Pablo D. Jadzinsky, Guillermo Calero, Christopher J. Ackerson, David A. Bushnell, and Roger D. Kornberg. *Science*, 318:430–433, 2007.

[127] Arnim Henglein and Dan Meisel. *The Journal of Physical Chemistry B*, 102:8364–8366, 1998.

[128] Kevin K. Meagher, Andrew B. Bocarsly, Steven L. Bernasek, and T. A. Ramanarayanan. *The Journal of Physical Chemistry B*, 104:3320–3326, 2000.

[129] Yu Luo, Jia Yang, Jingchao Li, Zhibo Yu, Guixiang Zhang, Xiangyang Shi, and Mingwu Shen. *Colloids and Surfaces B: Biointerfaces*, 136:506–513, 2015.

[130] Joanna N. James, Jeong Woo Han, and David S. Sholl. *Applied Surface Science*, 301:199–207, 2014.

[131] Yan-Xiong Ran, Zhen-Yi Du, Yun-Peng Guo, Jie Feng, and Wen-Ying Li. Density functional theory study of acetic acid steam reforming on ni(111). *Applied Surface Science*, 400:97–109, 2017.

[132] Chaoquan Hu, Siu-Wa Ting, Kwong-Yu Chan, and Wei Huang. *International Journal of Hydrogen Energy*, 37:15956–15965, 2012.

[133] Jeffrey J. Sims, Cherif Aghiles Ould Hamou, Romain Réocreux, Carine Michel, and Javier B. Giorgi. *The Journal of Physical Chemistry C*, 122:20279–20288, 2018.

[134] Xinbao Li, Yingying Zhu, Geng Chen, Guohua Yang, Zan Wu, and Bengt Sunden. *International Journal of Hydrogen Energy*, 42:24726–24736, 2017.

[135] V. B. Barbeta, R. F. Jardim, P. K. Kiyohara, F. B. Effenberger, and L. M. Rossi. *Journal of Applied Physics*, 107:073913, 2010.

[136] Ryouta Tatumi, Tomoki Akita, and Hisashi Fujihara. *Chemical Communications*, pages 3349–3351, 2006.

[137] Xing-Can Shen, Xiu-Zhong Fang, Ying-Hua Zhou, and Hong Liang. *Chemistry Letters*, 33:1468–1469, 2004.

[138] Chaozhang Huang and Bin Hu. *Spectrochimica Acta - Part B Atomic Spectroscopy*, 63:437–444, 2008.

[139] A. A. El-Gendy, E. M.M. Ibrahim, V. O. Khavrus, Y. Krupskaya, S. Hampel, A. Leonhardt, B. Büchner, and R. Klingeler. *Carbon*, 47:2821–2828, 2009.

[140] Quirin M. Kainz, Soraia Fernandes, Corina M. Eichenseer, Francesca Besostri, Helmut Körner, Rainer Müller, and Oliver Reiser. *Faraday Discuss.*, 175:27–40, 2014.

[141] Wuyou Fu, Haibin Yang, Hari-Bala, Shikai Liu, Minghui Li, and Guangtian Zou. *Materials Chemistry and Physics*, 100:246–250, 2006.

[142] Qinghong Zhang, Jincan Kang, and Ye Wang. *ChemCatChem*, 2:1030–1058, 2010.

[143] Wei-Jen Chen, Pei-Jane Tsai, and Yu-Chie Chen. *Small*, 4:485–491, 2008.

[144] Jun Lin, Weilie Zhou, A. Kumbhar, J. Wiemann, Jiye Fang, E.E. Carpenter, and C.J. O'Connor. *Journal of Solid State Chemistry*, 159:26–31, 2001.

[145] Saimon Moraes Silva, Roya Tavallaie, Lydia Sandiford, Richard D. Tilley, and J. Justin Gooding. *Chem. Commun.*, 52:7528–7540, 2016.

[146] Yuping Bao and Kannan M. Krishnan. *Journal of Magnetism and Magnetic Materials*, 293:15–19, 2005.

[147] Everett E. Carpenter, Claudio Sangregorio, and Charles J. Connor. *IEEE Transactions on Magnetics*, 35:3496–3498, 1999.

[148] Min Chen, Saeki Yamamuro, Dorothy Farrell, and Sara A. Majetich. *Journal of Applied Physics*, 93:7551–7553, 2003.

[149] Sung-Jin Cho, Juan-Carlos Idrobo, Justin Olamit, Kai Liu, Nigel D. Browning, and Susan M. Kauzlarich. *Chemistry of Materials*, 17:3181–3186, 2005.

[150] Cristina Ileana Covaliu, Daniela Berger, Cristian Matei, Lucian Diamandescu, Eugeniu Vasile, Camelia Cristea, Valentin Ionita, and Horia Iovu. *Journal of Nanoparticle Research*, 13:6169–6180, 2011.

[151] Quirin M. Kainz and Oliver Reiser. *Accounts of Chemical Research*, 47:667–677, 2014.

[152] Maria Patitsa, Konstantina Karathanou, Zoi Kanaki, Lamprini Tzioga, Natassa Pippa, Constantinos Demetzos, DImitris A. Verganelakis, Zoe Cournia, and Apostolos Klinakis. *Scientific Reports*, 7:775, 2017.

[153] J. C. Slater. *Physical Review*, 35:210–211, 1930.

[154] E. J. Baerends, D. E. Ellis, and P. Ros. *Chemical Physics*, 2:41–51, 1973.

[155] C F Fischer. *Hartree-Fock method for atoms. A numerical approach.* John Wiley Sons, 1977.

[156] Per Olov Löwdin. *Physical Review*, 97:1490–1508, 1955.

[157] J. C. Slater. *Physical Review*, 34:1293–1322, 1929.

[158] Frederick A. Matsen and Antonio A. Cantu. *The Journal of Physical Chemistry*, 73:2488–2494, 1969.

[159] I. Ekeland. *Journal of Mathematical Analysis and Applications*, 47:234–353, 1974.

[160] P. Hohenberg and W. Kohn. *Physical Review*, 136:864–871, 1964.

[161] S. T. Epstein and C. M. Rosenthal. *The Journal of Chemical Physics*, 64:247–249, 1976.

[162] J. C. Slater. *Physics TOday*, 35:36–43, 1982.

[163] Robert A Harris, Donald F Heller, and William M Gelbart. *The Journal of Chemical Physics*, 61:3854–3855, 1974.

[164] L. H. Thomas. *Mathematical Proceedings of the Cambridge Philosophical Society*, 23:542–548, 1927.

[165] R. K. Nesbet. *International Journal of Quantum Chemistry*, 90:262–265, 2002.

[166] P.A.M. Dirac and F.R.S. Fowler. *Proceedings of the Royal Society of London*, 126:360–365, 1930.

[167] Milton S. Plesset. *International Journal of Quantum Chemistry*, 41:278–290, 1932.

[168] W. Kohn and L. J. Sham. *Physical Review Letters*, 137:A1697, 1965.

[169] W. Kohn and L. J. Sham. *Physical Review*, 140:A1133–A1138, 1965.

[170] Manoj K. Harbola and Viraht Sahni. *Physical Review Letters*, 62:489–492, 1989.

[171] J. W. Negele. *Physical Review C*, 1:1260–1321, 1970.

[172] U von Barth and L. Hedin. *Journal of Physics C: Solid State Physics*, 5:1629–1642, 1972.

[173] John P. Perdew, Kieron Burke, and Matthias Ernzerhof. *Physical Review Letters*, 77:3865–3868, 1996.

[174] John P. Perdew and Yue Wang. *Physical Review B*, 45:13244–13249, 1992.

[175] W. Kohn, A. D. Becke, and R. G. Parr. *Journal of Physical Chemistry*, 100:12974–12980, 1996.

[176] H. J. Schulz. *Physical Review Letters*, 64:2831–2834, 1990.

[177] Graeme Henkelman, Andri Arnaldsson, and Hannes Jónsson. *Computational Materials Science*, 36:354–360, 2006.

[178] J. Kolaczkiewicz and E. Bauer. *Surface Science*, 144:495–511, 1984.

[179] A.W. Dweydari and C.H.B. Mee. *Physica Status Solidi*, 27:223–230, 1975.

[180] J.R. Macdonald and C.A. Jr. Carlow. *J. Chem. Phys.*, 39:412, 1963.

[181] C. Leung, L. Kao, S. Su, J. Feng, and T. Chan. *Physical Review B - Condensed Matter and Materials Physics*, 68:1–6, 2003.

[182] V. Wang, N. Xu, J.C. Liu, G. Tang, and W.T. Geng. *Computer Physics Communications*, 267:108033, 2021.

[183] Mark E. Tuckerman and Michele Parrinello. *Physical Review Letters*, 101:1302–1315, 1994.

[184] Xiaosong Li, John C. Tully, H. Bernhard Schlegel, and Michael J. Frisch. *The Journal of Chemical Physics*, 123:084106, 2005.

[185] Jürg Hutter. *Wiley Interdisciplinary Reviews: Computational Molecular Science*, 2:604–612, 2012.

[186] Shuichi Nosé. *The Journal of Chemical Physics*, 81:511–519, 1984.

[187] M. Bonomi, D. Branduardi, G. Bussi, C. Camilloni, D. Provasi, P. Raiteri, D. Donadio, F. Marinelli, F. Pietrucci, and R.A. Broglia. *Comp. Phys. Comm.*, 180:1961–1972, 2009.

[188] G.F. Marsili, S.and Signorini, R. Chelli, M. Marchi, and P. Procacci. *J. Comput. Chem.*, 2:1106–1116, 2010.

[189] J.C. Phillips, R. Braun, W. Wang, J. Gumbart, E. Tajkhorshid, E. Villa, C. Chipot, R.D. Skeel, L. Kale, and K. Schulten. *Phys. Rev. B*, 26:1781–1802, 2005.

[190] Jürg Hutter, Marcella Iannuzzi, Florian Schiffmann, and Joost Vandevondele. *Wiley Interdisciplinary Reviews: Computational Molecular Science*, 4:15–25, 2014.

[191] Graeme Henkelman, Gísli Jóhannesson, and Hannes Jónsson. *Theoretical Methods in Condensed Phase Chemistry*, pages 269–302, 2005.

[192] Graeme Henkelman and Hannes Jónsson. *The Journal of Chemical Physics*, 111:7010–7022, 1999.

[193] Graeme Henkelman and Hannes Jónsson. *Journal of Chemical Physics*, 113:9978–9985, 2000.

[194] P. D. DeCicco, F. A. Johnson, and Robert Allan Smith. *Proceedings of the Royal Society of London. A. Mathematical and Physical Sciences*, 310:111–119, 1969.

[195] Robert M. Pick, Morrel H. Cohen, and Richard M. Martin. *Phys. Rev. B*, 1:910–920, 1970.

[196] X. Gonze, J.-C. Charlier, D.C. Allan, and M.P. Teter. *Phys. Rev. B*, 50:13035–13038, 1994.

[197] N. E. Zein. *Fizika Tverdogo Tela*, 26:3028–3034, 1984.

[198] Stefano Baroni, Paolo Giannozzi, and Andrea Testa. *Phys. Rev. Lett.*, 58:1861–1864, 1987.

[199] Xavier Gonze. *Phys. Rev. A*, 52:1086–1095, 1995.

[200] T. Nishizawa and K. Ishida. *Bulletin of Alloy Phase Diagrams*, 4:387–390, 1983.

[201] Victor F Puntes and Kannan M Krishnan. *IEEE Transactions on Magnetics*, 37:2210–2212, 2001.

[202] H. T. Yang, C. M. Shen, Y. K. Su, T. Z. Yang, H. J. Gao, and Y. G. Wang. *Applied Physics Letters*, 82:4729–4731, 2003.

[203] P Gambardella, S Rusponi, M Veronese, S S Dhesi, C Grazioli, A Dallmeyer, I Cabria, R Zeller, P H Dederichs, K Kern, C Carbone, and H Brune. *Science*, 300:1130–1133, 2003.

[204] Hai Yan Su, Yonghui Zhao, Jin Xun Liu, Keju Sun, and Wei Xue Li. *Catalysis Science and Technology*, 7:2967–2977, 2017.

[205] Muthu Kumaran Gnanamani, Gary Jacobs, Wilson D. Shafer, and Burtron H. Davis. *Catalysis Today*, 215:13–17, 2013.

[206] William Hines, Joseph Budnick, David Perry, Sara Majetich, Ryan Booth, and Madhur Sachan. *Physica Status Solidi (B) Basic Research*, 248:741–747, 2011.

[207] K. Srinivasa Rao, T. Balaji, Y. Lingappaa, M. Ravi Prakash Reddy, and T. L. Prakash. *Journal of Experimental Nanoscience*, 8:162–170, 2013.

[208] IARC. *Cobalt in Hard Metals and Cobalt Sulfate, Gallium Arsenide, Indium Phosphide and Vanadium Pentoxide. IARC Monographs on the Evaluation of Carcinogenic Risks to Humans*. 2006.

[209] Sampath Marimuthu, Abdul Abdul Rahuman, Arivarasan Vishnu Kirthi, Thirunavukkarasu Santhoshkumar, Chidambaram Jayaseelan, and Govindasamy Rajakumar. *Parasitology Research*, 112:4105–4112, 2013.

[210] N. S. Alahmadi, J. W. Betts, F. Cheng, M. G. Francesconi, S. M. Kelly, A. Kornherr, T. J. Prior, and J. D. Wadhawan. *RSC Advances*, 7:20020–20026, 2017.

[211] S. M. Ansari, R. D. Bhor, K. R. Pai, D. Sen, S. Mazumder, Kartik Ghosh, Y. D. Kolekar, and C. V. Ramana. *Applied Surface Science*, 414:171–187, 2017.

[212] H. T. Yang, C. M. Shen, Y. K. Su, T. Z. Yang, H. J. Gao, and Y. G. Wang. *Applied Physics Letters*, 82:4729–4731, 2003.

[213] Vladimir V. Matveev, Dmitry A. Baranov, Gleb Yu Yurkov, Nikita G. Akatiev, Ivan P. Dotsenko, and Sergey P. Gubin. *Chemical Physics Letters*, 422:402–405, 2006.

[214] Yuping Bao, Wei An, C. Heath Turner, and Kannan M. Krishnan. *Langmuir*, 26:478–483, 2010.

[215] H. T. Yang, C. M. Shen, Y. G. Wang, Y. K. Su, T. Z. Yang, and H. J. Gao. *Nanotechnology*, 15:70–74, 2004.

[216] X. M. Lin, C. M. Sorensen, K. J. Klabunde, and G. C. Hajipanayis. *Journal of Materials Research*, 14:1542–1547, 1999.

[217] E. Romanus, N. Matoussevitch, S. Prass, J. Heinrich, R. Müller, D. V. Berkov, H. Bönnemann, and P. Weber. *Applied Organometallic Chemistry*, 18:548–552, 2004.

[218] Simón Oyarzún, Alexandre Tamion, Florent Tournus, Véronique Dupuis, and Matthias Hillenkamp. *Scientific Reports*, 5:16–21, 2015.

[219] J. R. Thomas. *Journal of Applied Physics*, 37:2914–2915, 1966.

[220] Hee Dong Jang, Dae Won Hwang, Dong Pyo Kim, Heon Chang Kim, Byung Yoon Lee, and In Bum Jeong. *Materials Research Bulletin*, 39:63–70, 2004.

[221] Olivier Margeat, Catherine Amiens, Bruno Chaudret, Pierre Lecante, and Robert E. Benfield. *Chemistry of Materials*, 17:107–111, 2005.

[222] Nisha Shukla, Erik B. Svedberg, John Ell, and A. J. Roy. *Materials Letters*, 60:1950–1955, 2006.

[223] Zhongjie Zhang, Xiangying Chen, Xingfa Zhang, and Chengwu Shi. *Solid State Communications*, 139:403–405, 2006.

[224] Huiping Shao, Yuqiang Huang, HyoSook Lee, Yong Jae Suh, and Chong Oh Kim. *Journal of Magnetism and Magnetic Materials*, 304:e28–e30, 2006.

[225] Hao Li and Shijun Liao. *Solid State Communications*, 145:118–121, 2008.

[226] Jin Zhang and Christopher Q. Lan. *Materials Letters*, 62:1521–1524, 2008.

[227] Jahangeer Ahmed, Shudhanshu Sharma, Kandalam V. Ramanujachary, Samuel E. Lofland, and Ashok K. Ganguli. *Journal of Colloid and Interface Science*, 336:814–819, 2009.

[228] B. Gojdka, V. Hrkac, T. Strunskus, V. Zaporojtchenko, L. Kienle, and F. Faupel. *Nanotechnology*, 22, 2011.

[229] Robert C. Reuel and Calvin H. Bartholomew. *Journal of Catalysis*, 85:78–88, 1984.

[230] Gonzalo Prieto, Agustín Martínez, Patricia Concepción, and Ramón Moreno-Tost. *Journal of Catalysis*, 266:129–144, 2009.

[231] Enrique Iglesia, Stuart L. Soled, and Rocco A. Fiato. *Journal of Catalysis*, 137:212–224, 1992.

[232] G. Leendert Bezemer, Johannes H. Bitter, Herman P.C.E. Kuipers, Heiko Oosterbeek, Johannes E. Holewijn, Xiaoding Xu, Freek Kapteijn, A. Jos Van Diilen, and Krijn P. De Jong. *Journal of the American Chemical Society*, 128:3956–3964, 2006.

[233] J. P. Den Breejen, P. B. Radstake, G. L. Bezemer, J. H. Bitter, V. Frøseth, A. Holmen, and K. P. De Jong. *Journal of the American Chemical Society*, 131:7197–7203, 2009.

[234] Gérôme Melaet, Avery E. Lindeman, and Gabor A. Somorjai. *Topics in Catalysis*, 57:500–507, 2014.

[235] Jin-Xun Liu, Hai-Yan Su, Da-Peng Sun, Bing-Yan Zhang, and Wei-Xue Li. *Journal of the American Chemical Society*, 135:16284–16287, 2013.

[236] Jin-Xun Liu, Peng Wang, Wayne Xu, and Emiel J.M. Hensen. *Engineering*, 3:467–476, 2017.

[237] Guangjun Cheng, Danilo Romero, Gerald T. Fraser, and A. R.Hight Walker. *Langmuir*, 21:12055–12059, 2005.

[238] Guangjun Cheng, Robert D. Shull, and A. R. Hight Walker. *Journal of Magnetism and Magnetic Materials*, 321:1351–1355, 2009.

[239] Li Tan, Bing Liu, Konrad Siemensmeyer, Ulrich Glebe, and Alexander Böker. *Polymers*, 10:11–14, 2018.

[240] A. Kumbhar, L. Spinu, F. Agnoli, K. . Wang, W. Zhou, and C. J. O'Connor. *IEEE Transactions on Magnetics*, 37:2216–2218, 2001.

[241] C. Petit, Z. L. Wang, and M. P. Pileni. *Journal of Physical Chemistry B*, 109:15309–15316, 2005.

[242] L. Meziane, C. Salzemann, C. Aubert, H. Gérard, C. Petit, and M. Petit. *Nanoscale*, 8:18640–18645, 2016.

[243] Stefanos Mourdikoudis, Roger M. Pallares, and Nguyen T.K. Thanh. *Nanoscale*, 10:12871–12934, 2018.

[244] Jérôme Cuny, Nathalie Tarrat, Fernand Spiegelman, Arthur Huguenot, and Mathias Rapacioli. *Journal of Physics Condensed Matter*, 30:303001, 2018.

[245] F. Aguilera-Granja, J. L. Rodríguez-López, K. Michaelian, E. O. Berlanga-Ramírez, and A. Vega. *Physical Review B - Condensed Matter and Materials Physics*, 66:224410, 2002.

[246] C. D. Dong and X. G. Gong. *Physical Review B - Condensed Matter and Materials Physics*, 78:020409, 2008.

[247] Mark B. Knickelbein. *Journal of Chemical Physics*, 116:9703–9711, 2002.

[248] Stephen J. Riley. *Journal of Non-Crystalline Solids*, 205-207:781–787, 1996.

[249] André Fielicke, Andrei Kirilyuk, Christian Ratsch, Jörg Behler, Matthias Scheffler, Gert Von Helden, and Gerard Meijer. *Physical Review Letters*, 93:023401–1, 2004.

[250] Lai Sheng Wang and Hongbin Wu. *Physical Review B - Condensed Matter and Materials Physics*, 55:12884–12887, 1997.

[251] Paola Nava, Marek Sierka, and Reinhart Ahlrichs. *Physical Chemistry Chemical Physics*, 5:3372–3381, 2003.

[252] F. Baletto, R. Ferrando, A. Fortunelli, F. Montalenti, and C. Mottet. *Journal of Chemical Physics*, 116:3856–3863, 2002.

[253] Walter Vogel, John Bradley, Oliver Vollmer, and Ingo Abraham. *The Journal of Physical Chemistry B*, 102:10853–10859, 1998.

[254] Chang Hong Chien, Estela Blaisten-Barojas, and Mark R. Pederson. *Journal of Chemical Physics*, 112:2301–2307, 2000.

[255] Y. Nanba, T. Ishimoto, and M. Koyama. *Journal of Physical Chemistry C*, 121:27445–27452, 2017.

[256] M. Pellarin, B. Baguenard, J. L. Vialle, J. Lermé, M. Broyer, J. Miller, and A. Perez. *Chemical Physics Letters*, 217:349–356, 1994.

[257] T. D. Klots, B. J. Winter, E. K. Parks, and S. J. Riley. *The Journal of Chemical Physics*, 95:8919–8930, 1991.

[258] Charles L. Cleveland and Uzi Landman. *The Journal of Chemical Physics*, 94:7376–7396, 1991.

[259] Francesca Baletto and Riccardo Ferrando. *Reviews of Modern Physics*, 77:371–423, 2005.

[260] Zhi-qiang Li and Bing-lin Gu. *Physical Review B*, 47:13611–13614, 1993.

[261] Christine Jamorski and Ana Martinez. *Physical Review B - Condensed Matter and Materials Physics*, 55:10905–10921, 1997.

[262] P. Młynarski, M. Iglesias, M. Pereiro, D. Baldomir, and L. Wojtczak. *Vacuum*, 54:143–149, 1999.

[263] Javier Guevara, Francisco Parisi, Ana Maria Llois, and Mariana Weissmann. *Physical Review B - Condensed Matter and Materials Physics*, 55:13283–13287, 1997.

[264] Antonis N. Andriotis and Madhu Menon. *Physical Review B*, 57:10069–10081, 1998.

[265] J. L. Rodríguez-López, F. Aguilera-Granja, K. Michaelian, and A. Vega. *Physical Review B - Condensed Matter and Materials Physics*, 67:174413, 2003.

[266] S. Datta, M. Kabir, S. Ganguly, B. Sanyal, T. Saha-Dasgupta, and A. Mookerjee. *Physical Review B - Condensed Matter and Materials Physics*, 76:014429, 2007.

[267] Ali Sebetci. *Chemical Physics*, 354:196–201, 2008.

[268] Ranber Singh and Peter Kroll. *Physical Review B - Condensed Matter and Materials Physics*, 78:245404, 2008.

[269] Jaime Souto-Casares, Masahiro Sakurai, and James R. Chelikowsky. *Physical Review B*, 93:174418, 2016.

[270] Sébastien Rives, Alain Catherinot, Frédéric Dumas-Bouchiat, Corinne Champeaux, Arnaud Videcoq, and Riccardo Ferrando. *Physical Review B - Condensed Matter and Materials Physics*, 77:085407, 2008.

[271] Keisuke Takahashi. PhD thesis, Chalmers University of Technology, 2011.

[272] Hui Li, Lei Li, Andreas Pedersen, Yi Gao, Navneet Khetrapal, Hannes Jónsson, and Xiao Cheng Zeng. *Nano Letters*, 15:682–688, 2015.

[273] Ilya V. Yudanov, Riadh Sahnoun, Konstantin M. Neyman, and Notker Rösch. *Journal of Chemical Physics*, 117:9887–9896, 2002.

[274] Davide Bochicchio and Riccardo Ferrando. *Nano Letters*, 10:4211–4216, 2010.

[275] K. Michaelian, M. R. Beltrán, and I. L. Garzón. *Physical Review B - Condensed Matter and Materials Physics*, 65:041403, 2002.

[276] Boon K Teo and N J A Sloane. *Inorg. Chem.*, 26:4545–4558, 1985.

[277] Forrest H. Kaatz and Adhemar Bultheel. *Nanoscale Research Letters*, 14:150, 2019.

[278] Jośe Rogan, Griselda García, Claudia Loyola, W. Orellana, Ricardo Ramírez, and Miguel Kiwi. *Journal of Chemical Physics*, 125:214708, 2006.

[279] A. Sebetci and Z. B. Güvenç. *European Physical Journal D*, 30:71–79, 2004.

[280] Madhu Menon, John Connolly, Nectarios Lathiotakis, and Antonis Andriotis. *Physical Review B*, 50:8903, 1994.

[281] Torbjörn Björkman and Oscar Gråsäs. *International Journal of Quantum Chemistry*, 111:1025–1030, 2011.

[282] Kapil Adhikari, Aurab Chakrabarty, Othmane Bouhali, Normand Mousseau, Charlotte S. Becquart, and Fedwa El-Mellouhi. *Journal of Computational Science*, 29:163–167, 2018.

[283] G. Kresse and J. Furthmüller. *Computational Materials Science*, 6:15–50, 1996.

[284] A. van de Walle and G. Ceder. *Physical Review B*, 59:14992–15001, 1999.

[285] C. S. Wang, B. M. Klein, and H. Krakauer. *Phys. Rev. Lett.*, 54:1852–1855, 1985.

[286] S. L. Dudarev, G. A. Botton, S. Y. Savrasov, C. J. Humphreys, and A. P. Sutton. *Phys. Rev. B*, 57:1505–1509, 1998.

[287] A.G. Petukhov, I.I. Mayin, L. Chioncel, and A.I. Liechtenstein. *Phys. Rev. B*, 67:153106, 2003.

[288] M. Cococcioni and S. de Gironcoli. *Phys. Rev. B*, 71:035105, 2005.

[289] I. Yang, S.Y. Savrasov, and Kotliar G. *Phys. Rev. Lett.*, 87:216405, 2001.

[290] A. Shick and W. Pickett. *Phys. Rev. Lett.*, 86:300, 2001.

[291] L. L. Wang and D. D. Johnson. *Physical Review B - Condensed Matter and Materials Physics*, 75:235405, 2007.

[292] C. M. Chang and M. Y. Chou. *Physical Review Letters*, 93:133401, 2004.

[293] F. Aguilera-Granja, A. García-Fuente, and A. Vega. *Physical Review B - Condensed Matter and Materials Physics*, 78:134425, 2008.

[294] Mukul Kabir, Abhijit Mookerjee, and A. K. Bhattacharya. *Physical Review A - Atomic, Molecular, and Optical Physics*, 69:043203, 2004.

[295] Xueguang Shao, Xiaomeng Liu, and Wensheng Cai. *Journal of Chemical Theory and Computation*, 1:762–768, 2005.

[296] M. Moseler, H. Häkkinen, R. N. Barnett, and U. Landman. *Physical Review Letters*, 86:2545–2548, 2001.

[297] David Holec, Franz Dieter Fischer, and Dieter Vollath. *Computational Materials Science*, 134:137–144, 2017.

[298] Thomas M. Soini, Xiufang Ma, Olcay Üzengi Aktürk, Suwit Suthirakun, Alexander Genest, and Notker Rösch. *Surface Science*, 643:156–163, 2016.

[299] G. L. Gutsev, C. W. Weatherford, K. G. Belay, B. R. Ramachandran, and P. Jena. *Journal of Chemical Physics*, 138:164303, 2013.

[300] Juarez L.F. Da Silva, Hyoung Gyu Kim, Maurício J. Piotrowski, Maurício J. Prieto, and Germano Tremiliosi-Filho. *Physical Review B - Condensed Matter and Materials Physics*, 82:205424, 2010.

[301] Maurício J. Piotrowski, Paulo Piquini, and Juarez L.F. Da Silva. *Journal of Physical Chemistry C*, 116:18432–18439, 2012.

[302] J. Oviedo and R. E. Palmer. *Journal of Chemical Physics*, 117:9548–9551, 2002.

[303] Maurício J. Piotrowski, Paulo Piquini, Ladir Cândido, and Juarez L.F. Da Silva. *Physical Chemistry Chemical Physics*, 13:17242–17248, 2011.

[304] Yusuke Nanba, Takayoshi Ishimoto, and Michihisa Koyama. *The Journal of Physical Chemistry C*, 121:27445–27452, 2017.

[305] W. D. Knight, Keith Clemenger, Walt A. de Heer, Winston A. Saunders, M. Y. Chou, and Marvin L. Cohen. *Phys. Rev. Lett.*, 52:2141–2143, 1984.

[306] G. Wulff. *Zeitschrift für Kristallographie - Crystalline Materials*, 34, 1901.

[307] Irene Fonseca. *Proceedings of the Royal Society A: Mathematical, Physical and Engineering Sciences*, 432:125–145, 1991.

[308] Alexander Dinghas. *Zeitschrift für Kristallographie - Crystalline Materials*, 105:304–314, 1943.

[309] Conyers Herring. *Phys. Rev.*, 82:87–93, 1951.

[310] L. D. Marks. *Reports on Progress in Physics*, 57:603–649, 1994.

[311] H. Graoui, S. Giorgio, and C. R. Enry. *Philosophical Magazine B: Physics of Condensed Matter; Statistical Mechanics, Electronic, Optical and Magnetic Properties*, 81:1649–1658, 2001.

[312] A. L. Mackay. *Acta Crystallographica*, 15:916–918, 1962.

[313] Shozo Ino. *Journal of the Physical Society of Japan*, 21:346–362, 1966.

[314] Shozo Ino. *Journal of the Physical Society of Japan*, 27:941–953, 1969.

[315] Jian-hua Xu, W. Lin, and A. J. Freeman. *Physical Review B*, 43:2018–2024, 1991.

[316] Cheng Wang, Huiyuan Wang, Tianlong Huang, Xuena Xue, Feng Qiu, and Qichuan Jiang. *Scientific Reports*, 5:10213, 2015.

[317] Tsutomu Komoda. *Japanese Journal of Applied Physics*, 7:27–30, 1968.

[318] R. F. W. Bader, P. J. MacDougall, and C. D. H. Lau. *Journal of the American Chemical Society*, 106:1594–1605, 1984.

[319] Ruqian Wu and A.J. Freeman. *Journal of Magnetism and Magnetic Materials*, 200:498–514, 1999.

[320] G. H. O. Daalderop, P J Kelly, and M. F. H. Schuurmans. *Physical Review B*, 41:11919–11937, 1990.

[321] D. Hobbs, G. Kresse, and J. Hafner. *Physical Review B - Condensed Matter and Materials Physics*, 62:11556–11570, 2000.

[322] M. Marsman and J. Hafner. *Physical Review B - Condensed Matter and Materials Physics*, 66:11556–11570, 2002.

[323] R. W. G. Wyckoff. *Crystal structures*, volume 2. Interscience Publishers, 1963.

[324] Charles Kittel. *Introduction to Solid State Physics*. Springer, 2010.

[325] S. Matar, a. Houari, and M. Belkhir. *Physical Review B*, 75:1–7, 2007.

[326] Víctor A. De La Peña O'Shea, Pilar Ramírez De la Piscina, Narcis Homs, Guillem Aromí, and José L.G. Fierro. *Chemistry of Materials*, 21:5637–5643, 2009.

[327] Saeedeh Arabzadeh and Mohamad Reza Benam. *International Journal Of Engineering Research*, 3:1604–1606, 2013.

[328] E. K. Parks, B. J. Winter, T. D. Klots, and S. J. Riley. *The Journal of Chemical Physics*, 96:8267–8274, 1992.

[329] E. K. Parks, T. D. Klots, B. J. Winter, and S. J. Riley. *The Journal of Chemical Physics*, 99:5831–5839, 1993.

[330] Yuannan Xie and John A. Blackman. *Physical Review B - Condensed Matter and Materials Physics*, 66:155417, 2002.

[331] Xia Wu, Zheng Wei, Yan Sun, Yi Lin Feng, and Qi Man Liu. *Chemical Physics Letters*, 660:11–17, 2016.

[332] David A. Hales, C. X. Su, Li Lian, and P. B. Armentrout. *The Journal of Chemical Physics*, 100:1049–1057, 1994.

[333] Mark B. Knickelbein. *The Journal of Chemical Physics*, 125:044308, 2006.

[334] Michael Martins and Wilfried Wurth. *Journal of Physics Condensed Matter*, 28:503002, 2016.

[335] V. Zamudio-Bayer, K. Hirsch, A. Langenberg, A. Ławicki, A. Terasaki, B. Von Issendorff, and J. T. Lau. *Journal of Physics Condensed Matter*, 30:464002, 2018.

[336] J. P. Bucher, D. C. Douglass, and L. A. Bloomfield. *Physical Review Letters*, 66:3052–3055, 1991.

[337] P. J. Jensen and K. H. Bennemann. *Computational Materials Science*, 2:488–490, 1994.

[338] Prajna Mukherjee, Bikash C Gupta, Puru Jena, Prajna Mukherjee, Bikash C Gupta, and Puru Jena. *J. Appl. Phys.*, 119, 2016.

[339] I M Billas, a Châtelain, and W a de Heer. *Science (New York, N.Y.)*, 265:1682–1684, 1994.

[340] Xiaoshan Xu, Shuangye Yin, Ramiro Moro, and Walt A. de Heer. *Physical Review Letters*, 95:237209, 2005.

[341] Xiaoshan Xu, Shuangye Yin, Ramiro Moro, Anthony Liang, John Bowlan, and Walt A. De Heer. *Physical Review Letters*, 107:057203, 2011.

[342] Isabelle M.L. Billas, A. Châtelain, and Walt A. de Heer. *Journal of Magnetism and Magnetic Materials*, 168:64–84, 1997.

[343] Gerasimos S Anagnostatos and D von Oertzen. *Atomic and nuclear clusters*. Springer, 1995.

[344] B. V. Reddy, S. K. Nayak, S. N. Khanna, B. K. Rao, and P. Jena. *Journal of Physical Chemistry A*, 102:1748–1759, 1998.

[345] Liang Hong, Haoliang Wang, Jingxin Cheng, Xiaoming Huang, Linwei Sai, and Jijun Zhao. *Computational and Theoretical Chemistry*, 993:36–44, 2012.

[346] Francisco E. Jorge and Alexsandro S. Santos. *Journal of the Brazilian Chemical Society*, 29:838–844, 2018.

[347] H. Lin, J.X. Liu, H. Fan, and W.X. Li. *J. Phys. Chem. C*, 124:11005–11014, 2020.

[348] Víctor Antonio de la Peña O'Shea, Iberio de P. R. Moreira, Alberto Roldán, and Francesc Illas. *The Journal of Chemical Physics*, 133:024701, 2010.

[349] Yu Ya Gafner, S. L. Gafner, Zh V. Golonenko, L. V. Redel, and V. I. Khrustalev. *IOP Conference Series: Materials Science and Engineering*, 110:012015, 2016.

[350] J. Magnus Rahm and Paul Erhart. *Nano Letters*, 17:5775–5781, 2017.

[351] Anna L. Garden, Andreas Pedersen, and Hannes Jónsson. *Nanoscale*, 10:5124–5132, 2018.

[352] Dawn M. Wells, Giulia Rossi, Riccardo Ferrando, and Richard E. Palmer. *Nanoscale*, 7:6498–6503, 2015.

[353] Meiying Liu, Linlin Chen, Chunming Lin, Liqing Zhang, and Hongfei Song. *Journal of Colloid and Interface Science*, 410:116–123, 2013.

[354] J Gump, Hua Xia, M Chirita, R Sooryakumar, M A Tomaz, G R Harp, J Gump, Hua Xia, M Chirita, and R Sooryakumar. *Journal of Applied Physics*, 86:6005, 2018.

[355] B. Strauss, F. Frey, W. Petry, J. Trampenau, and K. Nicolaus. *Physical Review B - Condensed Matter and Materials Physics*, 54:6035–6038, 1996.

[356] G. Y. Guo and H. H. Wang. *Chinese Journal of Physics*, 38:949–961, 2000.

[357] Wenhao Sun and Gerbrand Ceder. *Surface Science*, 617:53–59, 2013.

[358] Graeme W. Watson, E. Toby Kelsey, Nora H. de Leeuw, Duncan J. Harris, and Stephen C. Parker. *Journal of the Chemical Society, Faraday Transactions*, 92:433, 1996.

[359] P W Tasker. *Journal of Physics C: Solid State Physics*, 12:4977–4984, 1979.

[360] Jacques R. Eone, Olivier M. Bengone, and Christine Goyhenex. *Journal of Physical Chemistry C*, 123:4531–4539, 2019.

[361] Juan Wang, Jan-Michael Albina, Tomio Iwasaki, Hiroshi Moriya, and Yoshitaka Umeno. *Journal of Materials Research*, 28:1559–1566, 2013.

[362] T. Suzuki, D. Weller, C.-A. Chang, R. Savoy, T. Huang, B. A. Gurney, and V. Speriosu. *Applied Physics Letters*, 64:2736–2738, 1994.

[363] D. Weller, G. R. Harp, R. F. C. Farrow, A. Cebollada, and J. Sticht. *Phys. Rev. Lett.*, 72:2097–2100, 1994.

[364] *Journal of Magnetism and Magnetic Materials*, 44:239–248, 1984.

[365] P Bruno. 18:1291–1298, 1988.

[366] Paolo Campiglio, Romain Breitwieser, Vincent Repain, Solène Guitteny, Cyril Chacon, Amandine Bellec, Jérôme Lagoute, Yann Girard, Sylvie Rousset, Adele Sassella, Mighfar Imam, and Shobhana Narasimhan. *New Journal of Physics*, 17, 2015.

[367] T. O. Strandberg, C. M. Canali, and A. H. MacDonald. *Phys. Rev. B*, 73:144415, 2006.

[368] Per-Anker Lindgård and Peter V. Hendriksen. *Phys. Rev. B*, 49:12291–12294, 1994.

[369] M. Jamet, V. Dupuis, P. Mélinon, G. Guiraud, A. Pérez, W. Wernsdorfer, A. Traverse, and B. Baguenard. *Phys. Rev. B*, 62:493–499, 2000.

[370] I. Hrianca, C. Caizer, and Z. Schlett. *Journal of Applied Physics*, 92:2125–2132, 2002.

[371] R. Moreno, S. Poyser, and D. Meilak. *Sci Rep*, 10:2722, 2020.

[372] Chun-Rong Lin, Ray-Kuang Chiang, Jiun-Shen Wang, and Ti-Wen Sung. *Journal of Applied Physics*, 99:08N710, 2006.

[373] D. Fiorani, A.M. Testa, F. Lucari, F. D'Orazio, and H. Romero. *Physica B: Condensed Matter*, 320:122–126, 2002.

[374] G. Salazar-Alvarez, J. Qin, V. Šepelák, I. Bergmann, M. Vasilakaki, K. N. Trohidou, J. D. Ardisson, W. A. A. Macedo, M. Mikhaylova, M. Muhammed, M. D. Baró, and J. Nogués. *Journal of the American Chemical Society*, 130:13234–13239, 2008.

[375] Matthieu Jamet, Wolfgang Wernsdorfer, Christophe Thirion, Véronique Dupuis, Patrice Mélinon, Alain Pérez, and Dominique Mailly. *Phys. Rev. B*, 69:024401, 2004.

[376] R. A. Guirado-López and J. M. Montejano-Carrizales. *Phys. Rev. B*, 75:184435, 2007.

[377] J.P. Chen, C.M. Sorensen, and K.J. Klabunde. *Physical Review B*, 51:527–533, 1995.

[378] Lin He and Chinping Chen. *Phys. Rev. B*, 75:184424, 2007.

[379] Z. W. Wang and R. E. Palmer. *Phys. Rev. Lett.*, 108:245502, 2012.

[380] Ingo Barke, Hannes Hartmann, Daniela Rupp, Leonie Flückiger, Mario Sauppe, Marcus Adolph, Sebastian Schorb, Christoph Bostedt, Rolf Treusch, Christian Peltz, Stephan Bartling, Thomas Fennel, Karl-Heinz Meiwes-Broer, and Thomas Möller. *Nature Communications*, 6:6187, 2015.

[381] F. Tournus, K. Sato, T. Epicier, T. J. Konno, and V. Dupuis. *Phys. Rev. Lett.*, 110:055501, 2013.

[382] Federico Masini, Patricia Hernández-Fernández, Davide Deiana, Christian Ejersbo Strebel, David Norman McCarthy, Anders Bodin, Paolo Malacrida, Ifan Stephens, and Ib Chorkendorff. *Phys. Chem. Chem. Phys.*, 16:26506–26513, 2014.

[383] Robert Morel, Ariel Brenac, Céline Portemont, Thierry Deutsch, and Lucien Notin. *Journal of Magnetism and Magnetic Materials*, 308:296–304, 2007.

[384] M. Jamet, W. Wernsdorfer, C. Thirion, D. Mailly, V. Dupuis, P. Mélinon, and A. Pérez. *Journal of Physics: Condensed Matter*, 12:4676, 2000.

[385] J. Dorantes-Dávila, H. Dreyssé, and G. M. Pastor. *Phys. Rev. B*, 55:15033–15042, 1997.

[386] R. A. Guirado-López, J. Dorantes-Dávila, and G. M. Pastor. *Phys. Rev. Lett.*, 90:226402, 2003.

[387] J. Dorantes-Da´vila, H. Dreysse´, and G. M. Pastor. *Phys. Rev. B*, 46:10432–10436, 1992.

[388] Taichi Kosugi, Takashi Miyake, and Shoji Ishibashi. *Journal of the Physical Society of Japan*, 83:044707, 2014.

[389] A. V. Mugtasimov, P. A. Chernavskii, G. V. Pankina, and V. V. Lunin. *Russian Journal of Physical Chemistry A*, 82:495–498, 2008.

[390] Christine Lancelot, Vitaly V. Ordomsky, Odile Stéphan, Majid Sadeqzadeh, Héline Karaca, Maxime Lacroix, Daniel Curulla-Ferré, Francis Luck, Pascal Fongarland, Anne Griboval-Constant, and Andrei Y. Khodakov. *ACS Catalysis*, 4:4510–4515, 2014.

[391] Celin Dobbrow and Annette M. Schmidt. *Beilstein Journal of Nanotechnology*, 3:75–81, 2012.

[392] Earl A. Gulbransen and Kenneth F. Andrew. *Journal of The Electrochemical Society*, 98:241, 1951.

[393] Iva Saric, Robert Peter, and Mladen Petravic. *Journal of Physical Chemistry C*, 120:22421–22425, 2016.

[394] Eric Van Steen, Michael Claeys, Mark E. Dry, Jan Van De Loosdrecht, Elvera L. Viljoen, and Jacobus L. Visagie. *Journal of Physical Chemistry B*, 109:3575–3577, 2005.

[395] Don Hyung Ha, Liane M. Moreau, Shreyas Honrao, Richard G. Hennig, and Richard D. Robinson. *Journal of Physical Chemistry C*, 117:14303–14312, 2013.

[396] Shengguo Jia, Chih Hao Hsia, and Dong Hee Son. *Journal of Physical Chemistry C*, 115:92–96, 2011.

[397] R. J. Powell and W. E. Spicer. *Phys. Rev. B*, 2:2182–2193, 1970.

[398] V I Anisimov, M A Korotin, and E Z Kurmaev. *Journal of Physics: Condensed Matter*, 2:3973–3987, 1990.

[399] W. L. Roth. *Physical Review*, 110:1333–1341, 1958.

[400] U. D. Wdowik and K. Parlinski. *Physical Review B - Condensed Matter and Materials Physics*, 75:104306, 2007.

[401] N. J.O. Silva, A. Millán, F. Palacio, M. Martins, T. Trindade, I. Puente-Orench, and J. Campo. *Physical Review B - Condensed Matter and Materials Physics*, 82:094433, 2010.

[402] Subrata Kundu, A. J. Nelson, S. K. McCall, Tony Van Buuren, and Hong Liang. *Journal of Nanoparticle Research*, 15:1587, 2013.

[403] W. L. Roth. *Journal of Physics and Chemistry of Solids*, 25:1–10, 1964.

[404] D. Scheerlinck and S. Hautecler. *Physica Status Solidi (B)*, 73:223–228, 1976.

[405] A. S. Wills, N. P. Raju, and J. E. Greedan. *Chemistry of Materials*, 11:1510–1518, 1999.

[406] Izumi Tomeno, Yusuke Kasuya, and Yorihiko Tsunoda. *Physical Review B - Condensed Matter and Materials Physics*, 64:944221–944228, 2001.

[407] Ze Zhang and Sashi Satpathy. *Physical Review B*, 44:13319–13331, 1991.

[408] Xiaohe Liu, Guanzhou Qiu, and Xingguo Li. *Nanotechnology*, 16:3035–3040, 2005.

[409] Masoud Salavati-Niasari, Afsaneh Khansari, and Fatemeh Davar. *Inorganica Chimica Acta*, 362:4937–4942, 2009.

[410] Jianbo Xu, Ping Gao, and T. S. Zhao. *Energy and Environmental Science*, 5:5333–5339, 2012.

[411] Lei Fu, Zhimin Liu, Yunqi Liu, Buxing Han, Pingan Hu, Lingchao Cao, and Daoben Zhu. *Advanced Materials*, 17:217–221, 2005.

[412] Wei Yang Li, Li Na Xu, and Jun Chen. *Advanced Functional Materials*, 15:851–857, 2005.

[413] T.J. Chuang, C.R. Brundle, and D.W. Rice. *Surf. Sci.*, 59:413–429, 1976.

[414] H.a. Engelhardt and D. Menzel. *Surface Science*, 57:591–618, 1976.

[415] P. Michel and Ch Jardin. *Surface Science*, 36:478–487, 1973.

[416] Flemming Besenbacher and Jens K. Nørskov. *Progress in Surface Science*, 44:5–66, 1993.

[417] Hongqing Shi and Catherine Stampfl. *Physical Review B*, 76:075327, 2007.

[418] Rachel B. Getman, Ye Xu, and William F. Schneider. *The Journal of Physical Chemistry C*, 112:9559–9572, 2008.

[419] Hong Zhang, Aloysius Soon, Bernard Delley, and Catherine Stampfl. *Physical Review B*, 78:045436, 2008.

[420] S. López-Moreno and A. H. Romero. *The Journal of Chemical Physics*, 142:154702, 2015.

[421] J.K. Gimzewski, S. Affrossman, M.T. Gibson, L.M. Watson, and D.J. Fabian. *Surface Science*, 80:298–305, 1979.

[422] Jinlan Wang, Yanbiao Wang, Guangfen Wu, Xiuyun Zhang, Xiaojun Zhao, and Mingli Yang. *Physical Chemistry Chemical Physics*, 11:5980, 2009.

[423] Yongfa Zhu and Yangming Sun. *Surface Science*, 275:357–364, 1992.

[424] R. Nakamura, J. G. Lee, D. Tokozakura, H. Mori, and H. Nakajima. *Materials Letters*, 61:1060–1063, 2007.

[425] Michael S. Palmer, Matthew Neurock, and Michael M. Olken. *Journal of Physical Chemistry B*, 106:6543–6547, 2002.

[426] G. Strasser, G. Rosina, E. Bertel, and P.P. Netzer. *Surface Science*, 152-153:765–775, 1985.

[427] A. G. Ritchie. *Journal of Nuclear Materials*, 102:170–182, 1981.

[428] M N Huda and A K Ray. *International Journal of Quantum Chemistry*, 102:98–105, 2005.

[429] B. K. Min, X. Deng, D. Pinnaduwage, R. Schalek, and C. M. Friend. *Physical Review B - Condensed Matter and Materials Physics*, 72:121410, 2005.

[430] Angelos Michaelides, Karsten Reuter, and Matthias Scheffler. *Journal of Vacuum Science & Technology A: Vacuum, Surfaces, and Films*, 23:1487–1497, 2005.

[431] Hairong Tang, Anton Van Der Ven, and Bernhardt L. Trout. *Physical Review B - Condensed Matter and Materials Physics*, 70:045420, 2004.

[432] V. I. Bukhtiyarov, M. Hävecker, V. V. Kaichev, A. Knop-Gericke, R. W. Mayer, and R. Schlögl. *Physical Review B*, 67:235422, 2003.

[433] J.M Gottfried, K.J Schmidt, S.L.M Schroeder, and K Christmann. *Surface Science*, 525:184–196, 2003.

[434] Gary W. Simmons, Yarw Nan Wang, Juan Marcos, and Kamil Klier. *The Journal of Physical Chemistry*, 95:4522–4528, 1991.

[435] W Clemens, E Vescovo, T Kachel, C. Carbone, and W. Eberhardt. *Physical Review B*, 46:4198–4204, 1992.

[436] S. H. Ma, Z. Y. Jiao, T. X. Wang, and X. Q. Dai. *The European Physical Journal B*, 88:4, 2015.

[437] Wusong Liu, Naihua Miao, Linggang Zhu, Jian Zhou, and Zhimei Sun. *Physical Chemistry Chemical Physics*, 19:32404–32411, 2017.

[438] S.H. Ma, Z.Y. Jiao, T.X. Wang, and X.Q. Dai. *Surface Science*, 619:90–97, 2014.

[439] A. C. (Ali Can) Kizilkaya, J. W. (Hans) Niemantsverdriet, and C. J. (Kees-Jan) Weststrate. *The Journal of Physical Chemistry C*, 120:4833–4842, 2016.

[440] Juarez L.F. Da Silva, Catherine Stampfl, and Matthias Scheffler. *Surface Science*, 600:703–715, 2006.

[441] Aron Walsh, Juarez L F Da Silva, Su-Huai Wei, C. Körber, A. Klein, L. F J Piper, Alex DeMasi, Kevin E. Smith, G. Panaccione, P. Torelli, D. J. Payne, A. Bourlange, and R. G. Egdell. *Physical Review Letters*, 100:167402, 2008.

[442] Aron Walsh, Juarez L. F. Da Silva, and Su-Huai Wei. *Physical Review Letters*, 100:256401, 2008.

[443] P. Jeffrey Hay, Richard L. Martin, Jamal Uddin, and Gustavo E. Scuseria. *The Journal of Chemical Physics*, 125:034712, 2006.

[444] Juarez L. F. Da Silva. *Physical Review B*, 76:193108, 2007.

[445] Peter J Feibelman, B Hammer, F Wagner, M Scheffler, R Stumpf, R Watwe, and J Dumesic. *J. Phys. Chem. B*, 105:4018–4025, 2001.

[446] Lei Wang, Thomas Maxisch, and Gerbrand Ceder. *Physical Review B - Condensed Matter and Materials Physics*, 73:195107, 2006.

[447] Anubhav Jain, Geoffroy Hautier, Shyue Ping Ong, Charles J. Moore, Christopher C. Fischer, Kristin A. Persson, and Gerbrand Ceder. *Physical Review B - Condensed Matter and Materials Physics*, 84:045115, 2011.

[448] Stefan Grimme, Stephan Ehrlich, and Lars Goerigk. *Journal of Computational Chemistry*, 32:1456–1465, 2011.

[449] Wei-Xue Li, Catherine Stampfl, and Matthias Scheffler. *Physical Review B*, 65:075407, 2002.

[450] M Chase. NIST-JANAF Thermochemical Tables, 4th Edition. page 1952, 1998.

[451] A. Taylor and R. W. Floyd. *Acta Crystallographica*, 3:285–289, 1950.

[452] W. Jauch, M. Reehuis, H. J. Bleif, F. Kubanek, and P. Pattison. *Physical Review B - Condensed Matter and Materials Physics*, 64:052102, 2001.

[453] M. Lenglet and B. Lefez. *Solid State Communications*, 98:689–694, 1996.

[454] Shin Imada and Takeo Jo. *Journal of Magnetism and Magnetic Materials*, 104-107:2001–2002, 1992.

[455] J. van Elp, J. L. Wieland, H. Eskes, P. Kuiper, G. A. Sawatzky, F. M. F. de Groot, and T. S. Turner. *Physical Review B*, 44:6090–6103, 1991.

[456] Kwang Joo Kim and Young Ran Park. *Solid State Communications*, 127:25–28, 2003.

[457] M. Garcia-Mota, M. Bajdich, V. Viswanathan, A. Vojvodic, A.T. Bell, and J.K. Norskov. *J. Phys. Chem. C*, 116:21077–21082, 2012.

[458] M. Bajdich, M. Garcia-Mota, A. Vojvodic, J.K. Norskov, and A.T. Bell. *J. Am. hem. Soc.*, 135:13521–13530, 2013.

[459] A.L. Dalverny, Filhol J.S., F. Femoigno, and M.L. Doublet. *J. Phys. Chem. C*, 114:21750–21756, 2010.

[460] X. Shi, S.L. Bernasek, and A. Selloni. *J. Phys. Chem. C*, 120:14892–14898, 2016.

[461] K. Kwapien, S. Piccinin, and S. Fabris. *J. Phys. Chem. Lett.*, 4:4223–4230, 2013.

[462] G Herzberg and K. P. Huber. *Molecular Spectra and Molecular Structure*. Springer, 1979.

[463] Qiang Sun, Karsten Reuter, and Matthias Scheffler. *Phys. Rev. B*, 67:205424, 2003.

[464] Karsten Reuter and Matthias Scheffler. *Phys. Rev. Lett.*, 90:046103, 2003.

[465] Zbynek Novotny, Narasimham Mulakaluri, Zoltan Edes, Michael Schmid, Rossitza Pentcheva, Ulrike Diebold, and Gareth S. Parkinson. *Phys. Rev. B*, 87:195410, 2013.

[466] Venkatesh Botu, Rampi Ramprasad, and Ashish B. Mhadeshwar. *Surface Science*, 619:49–58, 2014.

[467] Christopher Penschke, Joachim Paier, and Joachim Sauer. *The Journal of Physical Chemistry C*, 117:5274–5285, 2013.

[468] Karsten Reuter and Matthias Scheffler. *Physical Review B*, 65:035406, 2001.

[469] Young-Rok Jang and Byung Deok Yu. *Journal of the Physical Society of Japan*, 81:114715, 2012.

[470] Yousif Shoaib Mohammed, Yu Yan, Hongxia Wang, Kai Li, and Xiaobo Du. *Journal of Magnetism and Magnetic Materials*, 322:653–657, 2010.

[471] F. D. Murnaghan. *Proceedings of the National Academy of Sciences*, 30:244–247, 1944.

[472] R. Koch, E. Schwarz, K. Schmidt, B. Burg, K. Christmann, and K. H. Rieder. *Physical Review Letters*, 71:1047–1050, 1993.

[473] J.E. Prieto, Ch Rath, S. Müller, R Miranda, and K Heinz. *Surface Science*, 401:248–260, 1998.

[474] B. W. Lee, R. Alsenz, A. Ignatiev, and M. A. Van Hove. *Phys. Rev. B*, 17:1510–1520, 1978.

[475] W.R. Tyson and W.A. Miller. *Surface Science*, 62:267–276, 1977.

[476] Jian-Min Zhang, Dou-Dou Wang, and Ke-Wei Xu. *Applied Surface Science*, 253:2018–2024, 2006.

[477] Bao Qin Fu, Wei Liu, and Zhi Lin Li. *Applied Surface Science*, 255:9348–9357, 2009.

[478] L. Vitos, A.V. Ruban, H.L. Skriver, and J. Kollár. *Surface Science*, 411:186–202, 1998.

[479] Van Bac Nguyen, Magali Benoit, Nicolas Combe, and Hao Tang. *Phys. Chem. Chem. Phys. Phys. Chem. Chem. Phys*, 4636:4636–4647, 2017.

[480] J Lahtinen, J Vaari, and K Kauraala. *Surface Science*, 418:502–510, 1998.

[481] Tuo Li, Benjamin L. Rickman, and W. Andreas Schroeder. *Phys. Rev. ST Accel. Beams*, 18:073401, 2015.

[482] Wenjia Luo and Aravind Asthagiri. *The Journal of Physical Chemistry C*, 118:15274–15285, 2014.

[483] Xue-Qing Gong, R. Raval, and P. Hu. *Surface Science*, 562:247–256, 2004.

[484] Qingfeng Ge and Matthew Neurock. *The Journal of Physical Chemistry B*, 110:15368–15380, 2006.

[485] S Schwegmann, A P Seitsonen, V. De Renzi, H Dietrich, H Bludau, M Gierer, H Over, K Jacobi, M Scheffler, and G Ertl. *Physical Review B*, 57:15487–15495, 1998.

[486] B Klingenberg, F Grellner, D Borgmann, and G Wedler. *Surface Science*, 296:374–382, 1993.

[487] A.L. Allred. *Journal of Inorganic and Nuclear Chemistry*, 17:215–221, 1961.

[488] F Grellner, B Klingenberg, D Borgmann, and G Wedler. *Journal of Electron Spectroscopy and Related Phenomena*, 71:107–115, 1995.

[489] M. V. Ganduglia-Pirovano and M. Scheffler. *Physical Review B*, 59:15533–15543, 1999.

[490] Mira Todorova, Karsten Reuter, and Matthias Scheffler. *Journal of Physical Chemistry B*, 108:14477–14483, 2004.

[491] Bo Sun, Ping Zhang, Zhigang Wang, Suqing Duan, Xian Geng Zhao, Xucun Ma, and Qi Kun Xue. *Physical Review B - Condensed Matter and Materials Physics*, 78:1–12, 2008.

[492] M. E. Bridge and R. M. Lambert. *Surface Science*, 82:413–424, 1979.

[493] B.W Lee, A. Ignatiev, J.A Taylor, and J.W Rabalais. *Solid State Communications*, 33:1205–1208, 1980.

[494] R. B. Moyes and M. W. Roberts. *Journal of Catalysis*, 49:216–224, 1977.

[495] S. Mrowec and K. Przybylski. *Oxidation of Metals*, 11:365–381, 1977.

[496] Soo Hyeon Lee, Ki Hyun Bae, Sun Hwa Kim, Kyu Ri Lee, and Tae Gwan Park. *International Journal of Pharmaceutics*, 364:94–101, 2008.

[497] Partha Ghosh, Xiaochao Yang, Rochelle Arvizo, Zheng Jiang Zhu, Sarit S. Agasti, Zhihong Mo, and Vincent M. Rotello. *Journal of the American Chemical Society*, 132:2642–2645, 2010.

[498] Yueh Hsia Luo, Louis W. Chang, and Pinpin Lin. *BioMed Research International*, 2015:143720, 2015.

[499] Simon Heidegger, Dorothée Gößl, Alexandra Schmidt, Stefan Niedermayer, Christian Argyo, Stefan Endres, Thomas Bein, and Carole Bourquin. *Nanoscale*, 8:938–948, 2016.

[500] Donald E. Owens and Nicholas A. Peppas. *International Journal of Pharmaceutics*, 307:93–102, 2006.

[501] Carlos Tassa, Jay L. Duffner, Timothy A. Lewis, Ralph Weissleder, Stuart L. Schreiber, Angela N. Koehler, and Stanley Y. Shaw. *Bioconjugate Chemistry*, 21:14–19, 2010.

[502] Yiping Chen, Yunlei Xianyu, and Xingyu Jiang. *Accounts of Chemical Research*, 50:310–319, 2017.

[503] Sang Keun Oh, Yanhui Niu, and Richard M. Crooks. *Langmuir*, 21:10209–10213, 2005.

[504] Xiangyang Shi, Suhe Wang, Haiping Sun, and James R. Baker. *Soft Matter*, 3:71–74, 2007.

[505] Liheng Feng, Chunlei Zhu, Huanxiang Yuan, Libing Liu, Fengting Lv, and Shu Wang. *Chemical Society Reviews*, 42:6620–6633, 2013.

[506] Jurate Virkutyte and Rajender S. Varma. *Chemical Science*, 2:837–846, 2011.

[507] Stephanie G. Grancharov, Hao Zeng, Shouheng Sun, Shan X. Wang, Stephen O'Brien, C. B. Murray, J. R. Kirtley, and G. A. Held. *Journal of Physical Chemistry B*, 109:13030–13035, 2005.

[508] Ronen Polsky, Ron Gill, Lubov Kaganovsky, and Itamar Willner. *Analytical Chemistry*, 78:2268–2271, 2006.

[509] Gerd H. Woehrle, Leif O. Brown, and James E. Hutchison. *Journal of the American Chemical Society*, 127:2172–2183, 2005.

[510] A. I. Frenkel, S. Nemzer, I. Pister, L. Soussan, T. Harris, Y. Sun, and M. H. Rafailovich. *Journal of Chemical Physics*, 123, 2005.

[511] Lon A. Porter, David Ji, Sarah L. Westcott, Michael Graupe, Roman S. Czernuszewicz, Naomi J. Halas, and T. Randall Lee. *Langmuir*, 14:7378–7386, 1998.

[512] Anna A. Volkert, Varuni Subramaniam, Michael R. Ivanov, Amanda M. Goodman, and Amanda J. Haes. *ACS Nano*, 5:4570–4580, 2011.

[513] Xueqing Gao, Guangrui Xu, Yan Zhao, Shuni Li, Feng Shi, and Yu Chen. *RSC Advances*, 5:88045–88051, 2015.

[514] Benjamin Marchetti, Yvonne Joseph, and Helmut Bertagnolli. *Journal of Nanoparticle Research*, 13:3353–3362, 2011.

[515] Patrick M. Shem, Rajesh Sardar, and Jennifer S. Shumaker-Parry. *Langmuir*, 25:13279–13283, 2009.

[516] W. W. Weare, S. M. Reed, M. G. Warner, and J. E. Hutchison. *Journal of the American Chemical Society*, 122:12890–12891, 2000.

[517] Md Abdul Aziz, Jong Pil Kim, and Munetaka Oyama. *Gold Bulletin*, 47:127–132, 2014.

[518] Ilona Papp, Christian Sieben, Kai Ludwig, Meike Roskamp, Christoph Böttcher, Sabine Schlecht, Andreas Herrmann, and Rainer Haag. *Small*, 6:2900–2906, 2010.

[519] Yurui Xue, Xun Li, Hongbin Li, and Wenke Zhang. *Nature Communications*, 5:4348, 2014.

[520] Rajesh Sardar, Alison M. Funston, Paul Mulvaney, and Royce W. Murray. *Langmuir*, 25:13840–13851, 2009.

[521] Evangelina Pensa, Emiliano Cortés, Gastón Corthey, Pilar Carro, Carolina Vericat, Mariano H. Fonticelli, Guillermo Benítez, Aldo A. Rubert, and Roberto C. Salvarezza. *Accounts of Chemical Research*, 45:1183–1192, 2012.

[522] M. Walter, J. Akola, O. Lopez-Acevedo, P. D. Jadzinsky, G. Calero, C. J. Ackerson, R. L. Whetten, H. Gronbeck, and H. Hakkinen. *Proceedings of the National Academy of Sciences*, 105:9157–9162, 2008.

[523] Hannu Häkkinen. *Nature Chemistry*, 4:443–455, 2012.

[524] Jiawei Yan, Runhai Ouyang, Palle S. Jensen, Erhad Ascic, David Tanner, Bingwei Mao, Jingdong Zhang, Chunguang Tang, Noel S. Hush, Jens Ulstrup, and Jeffrey R. Reimers. *Journal of the American Chemical Society*, 136:17087–17094, 2014.

[525] Thomas Bürgi. *Nanoscale*, 7:15553–15567, 2015.

[526] Henrik Grönbeck. *Journal of Physical Chemistry C*, 114:15973–15978, 2010.

[527] Ante Bilić, Jeffrey R. Reimers, and Noel S. Hush. *Journal of Chemical Physics*, 122:094708, 2005.

[528] Ezequiel De La Llave, Romain Clarenc, David J. Schiffrin, and Federico J. Williams. *Journal of Physical Chemistry C*, 118:468–475, 2014.

[529] Jeffrey R. Reimers, Yun Wang, Burak O. Cankurtaran, and Michael J. Ford. *Journal of the American Chemical Society*, 132:8378–8384, 2010.

[530] Young Kyu Han, Hyemi Kim, Jaehoon Jung, and Young Cheol Choi. *Journal of Physical Chemistry C*, 114:7548–7552, 2010.

[531] Yan Li, Giulia Galli, and François Gygi. *ACS Nano*, 2:1896–1902, 2008.

[532] L. Tan, B. Liu, K. Siemensmeyer, U. Glebe, and A. Böker. 10:1053, 2018.

[533] H T Yang, C M Shen, Y G Wang, Y K Su, T Z Yang, and H J Gao. *Nanotechnology*, 15:70–74, 2003.

[534] An-Hui Lu, Wen-Cui Li, Nina Matoussevitch, Bernd Spliethoff, Helmut Bönnemann, and Ferdi Schüth. *Chem. Commun.*, pages 98–100, 2005.

[535] Yoshio Kobayashi, Mitsuru Horie, Mikio Konno, Benito Rodríguez-González, and Luis M. Liz-Marzán. *The Journal of Physical Chemistry B*, 107:7420–7425, 2003.

[536] Robert N. Grass, Evagelos K. Athanassiou, and Wendelin J. Stark. *Angewandte Chemie - International Edition*, 46:4909–4912, 2007.

[537] Shouheng Sun and C. B. Murray. *Journal of Applied Physics*, 85:4325–4330, 1999.

[538] L. Clarke, M. N. Wybourne, L. O. Brown, J. E. Hutchison, M. Yan, S. X. Cai, and J. F.W. Keana. *Semiconductor Science and Technology*, 13:A111, 1998.

[539] Ronald P. Andres, Thomas Bein, Matt Dorogi, Sue Feng, Jason I. Henderson, Clifford P. Kubiak, William Mahoney, Richard G. Osifchin, and R. Reifenberger. *Science*, 272:1323–1325, 1996.

[540] Yikun Su, Xing OuYang, and Jiaoning Tang. *Applied Surface Science*, 256:2353–2356, 2010.

[541] Wenjuan Yang, Yanwei Wen, Dawen Zeng, Qingbo Wang, Rong Chen, Weichao Wang, and Bin Shan. *J. Mater. Chem. A*, 2:20770–20775, 2014.

[542] Yu Lu, Xianmao Lu, Brian T. Mayers, Thurston Herricks, and Younan Xia. *Journal of Solid State Chemistry*, 181:1530–1538, 2008.

[543] Lev Bromberg, Liang Chen, Emily P. Chang, Sa Wang, and T. Alan Hatton. *Chemistry of Materials*, 22:5383–5391, 2010.

[544] Xian Hua Zhang, Kin Man Ho, Ai Hua Wu, Kin Hung Wong, and Pei Li. *Langmuir*, 26:6009–6014, 2010.

[545] J. Pan, D. Thierry, and C. Leygraf. *Electrochimica Acta*, 41:1143–1153, 1996.

[546] C. Larsson, P. Thomsen, B. O. Aronsson, M. Rodahl, J. Lausmaa, B. Kasemo, and L. E. Ericson. *Biomaterials*, 17:605–616, 1996.

[547] Barbara Farkaš, David Santos-Carballal, Abdelaziz Cadi-Essadek, and Nora H. de Leeuw. *Materialia*, 7:100381, 2019.

[548] Wei Wu, Quanguo He, and Changzhong Jiang. *Nanoscale Research Letters*, 3:397–415, 2008.

[549] Vasilios Georgakilas, Michal Otyepka, Athanasios B. Bourlinos, Vimlesh Chandra, Namdong Kim, K. Christian Kemp, Pavel Hobza, Radek Zboril, and Kwang S. Kim. *Chemical Reviews*, 112:6156–6214, 2012.

[550] Taegyu Kang, Fangyuan Li, Seungmin Baik, Wei Shao, Daishun Ling, and Taeghwan Hyeon. *Biomaterials*, 136:98–114, 2017.

[551] J. Fouineau, K. Brymora, L. Ourry, F. Mammeri, N. Yaacoub, F. Calvayrac, S. Ammar-Merah, and J. M. Greneche. *Journal of Physical Chemistry C*, 117:14295–14302, 2013.

[552] Lawrence H. Dubois, Bernard R. Zegarski, and Ralph G. Nuzzo. *Langmuir*, 2:412–417, 1986.

[553] M. Wühn, J. Weckesser, and Ch Wöll. *Langmuir*, 17:7605–7612, 2001.

[554] Alexander Weddemann, Inga Ennen, Anna Regtmeier, Camelia Albon, Annalena Wolff, Katrin Eckstädt, Nadine Mill, Michael K.H. Peter, Jochen Mattay, Carolin Plattner, Norbert Sewald, and Andreas Hütten. *Beilstein Journal of Nanotechnology*, 1:75–93, 2010.

[555] Anh Tuan Le, Le Thi Tam, Phuong Dinh Tam, P. T. Huy, Tran Quang Huy, Nguyen Van Hieu, A. A. Kudrinskiy, and Yu A. Krutyakov. *Materials Science and Engineering C*, 30:910–916, 2010.

[556] V Raghavendra Reddy, Ajay Gupta, Vasant Sathe, Ram Jane Choudhary, Mukta V Limaye, Shashi B Singh, Sadgopal K Date, Deepti Kothari, V Raghavendra Reddy, Ajay Gupta, Vasant Sathe, Ram Jane Choudhary, and Sulabha K Kulkarni. *Journal of Physical Chemistry B*, 113:9070–6, 2009.

[557] Nianqiang Wu, Lei Fu, Ming Su, Mohammed Aslam, Ka Chun Wong, and Vinayak P. Dravid. *Nano Letters*, 4:383–386, 2004.

[558] Sonja Jovanović, Matjaž Spreitzer, Melita Tramšek, Zvonko Trontelj, and Danilo Suvorov. *Journal of Physical Chemistry C*, 118:13844–13856, 2014.

[559] A. Dey and M. K. Purkait. *Journal of Industrial and Engineering Chemistry*, 24:181–187, 2015.

[560] Xinbao Li, Yuan Zhao, Shurong Wang, Yingying Zhu, and Guohua Yang. *Catalysis Letters*, 146:2015–2024, 2016.

[561] Dennis Franke, Michael Lorke, Th Frauenheim, and A. L. Rosa. *Journal of Physical Chemistry C*, 122:24838–24842, 2018.

[562] Joost Vandevondele, Matthias Krack, Fawzi Mohamed, Michele Parrinello, Thomas Chassaing, and Jürg Hutter. *Computer Physics Communications*, 167:103–128, 2005.

[563] Joost VandeVondele and Jürg Hutter. *Journal of Chemical Physics*, 127:114105, 2007.

[564] Alessandro Laio and Francesco L. Gervasio. *Reports on Progress in Physics*, 71:126601, 2008.

[565] William Humphrey, Andrew Dalke, and Klaus Schulten. *Journal of Molecular Graphics*, 14:33–38, 1996.

[566] K. Refson, P.R. Tulip, and S.J. Clark. *Phys. Rev. B*, 73:155114, 2006.

[567] T. Lin, X.Y. Liu, and C. He. *J. Phys. Chem. B*, 116:1524–1535, 2012.

[568] E. Moreira, C.A. Barboza, E.L. Albuquerque, U.L. Fulco, J.M. Henriques, and A.I. Araujo. *Journal of Physics and Chemistry of Solids*, 77:85–91, 2015.

[569] P.H. Berens and K.R. Wilson. *J. Chem. Phys.*, 74:4872–4882, 1981.

[570] M. Thomas, M. Brehm, R. Fligg, P. Vohringer, and B. Kirchner. *Phys. Chem. Chem. Phys.*, 15:6608–6622, 2011.

[571] M. Brehm and B. Kirchner. *J. Chem. Inf. Model.*, 51:2007–2023, 2011.

[572] Atsushi Togo and Isao Tanaka. *Scripta Materialia*, 108:1–5, 2015.

[573] P. Giannozzi and S. Baroni. *J. Chem. Phys.*, 100:8537, 1994.

[574] B. Hammer and J.K. Norskov. *Advances in Catalysis*, 45:71–129, 2000.

[575] Ling Zhang, Rong He, and Hong Chen Gu. *Applied Surface Science*, 253:2611–2617, 2006.

[576] U. Terranova and D. R. Bowler. *Journal of Physical Chemistry C*, 116:4408–4415, 2012.

[577] Henrik Gronbeck, Alessandro Curioni, and Wanda Andreoni. *Journal of the American Chemical Society*, 122:3839–3842, 2000.

[578] Huayan Yang, Yu Wang, Huaqi Huang, Lars Gell, Lauri Lehtovaara, Sami Malola, Hannu Hakkinen, and Nanfeng Zheng. *Nature Communications*, 4:2422, 2013.

[579] Li-Gang Wang, Evgeny Yu Tsymbal, and Sheila S Jaswal. *Physical Review B*, 70:075410, 2004.

[580] Maria Mikhaylova, Do Kyung Kim, Catherine C. Berry, Andrei Zagorodni, Muhammet Toprak, Adam S. G. Curtis, and Mamoun Muhammed. *Chemistry of Materials*, 16:2344–2354, 2004.

[581] Leyu Wang, Jie Bao, Lu Wang, Fang Zhang, and Yadong Li. *Chemistry – A European Journal*, 12:6341–6347, 2006.

[582] Raghavendra A. Bohara, Nanasaheb D. Thorat, Hemraj M. Yadav, and Shivaji H. Pawar. *New Journal of Chemistry*, 38:2979, 2014.

[583] Patricia Wand, Johannes D. Bartl, Ueli Heiz, Martin Tschurl, and Mirza Cokoja. *Journal of Colloid and Interface Science*, 478:72–80, 2016.

[584] Gisela Lozano-Blanco and Andrew J. Adamczyk. *Surface Science*, 688:31–44, 2019.

[585] L. G. Wang, E. Y. Tsymbal, and S. S. Jaswal. *Phys. Rev. B*, 70:075410, 2004.

[586] Murugan Veerapandian and Kyusik Yun. *Synthesis and Reactivity in Inorganic, Metal-Organic, and Nano-Metal Chemistry*, 40:56–64, 2010.

[587] Dietmar Knopp, Dianping Tang, and Reinhard Niessner. *Analytica Chimica Acta*, 647:14–30, 2009.

[588] Hua Wang, David G. Castner, Buddy D. Ratner, and Shaoyi Jiang. *Langmuir*, 20:1877–1887, 2004.

[589] Christopher E. Bunker, Kyle C. Novak, Elena A. Guliants, Barbara A. Harruff, M. Jaouad Meziani, Yi Lin, and Ya-Ping Sun. *Langmuir*, 23:10342–10347, 2007.

[590] Brian G. Trewyn, Igor I. Slowing, Supratim Giri, Hung-Ting Chen, and Victor S.-Y. Lin. *Accounts of Chemical Research*, 40:846–853, 2007.

[591] Heather R. Luckarift, Shankar Balasubramanian, Sheetal Paliwal, Glenn R. Johnson, and Aleksandr L. Simonian. *Colloids and Surfaces B: Biointerfaces*, 58:28–33, 2007.

[592] Dheeraj K. Singh, Ramya Jagannathan, Puneet Khandelwal, Priya Mary Abraham, and Pankaj Poddar. *Nanoscale*, 5:1882–1893, 2013.

[593] M.M. Mirhosseini, R. Khordad, and B. Vaseghi. *Chinese Journal of Physics*, 62:99–105, 2019.

[594] Janet Petroski, Mei Chou, and Carol Creutz. *Journal of Organometallic Chemistry*, 694:1138–1143, 2009.

[595] John E. Matthiesen, Deepa Jose, Christopher M. Sorensen, and Kenneth J. Klabunde. *Journal of the American Chemical Society*, 134:9376–9379, 2012.

[596] Peter Maksymovych, Dan C. Sorescu, and John T. Yates. *Phys. Rev. Lett.*, 97:146103, 2006.

[597] P. D. Jadzinsky, G. Calero, C. J. Ackerson, D. A. Bushnell, and R. D. Kornberg. *Science*, 318:430–433, 2007.

[598] De-en Jiang, Murilo L. Tiago, Weidong Luo, and Sheng Dai. *Journal of the American Chemical Society*, 130:2777–2779, 2008.

[599] Brian M. Barngrover and Christine M. Aikens. *Journal of Physical Chemistry A*, 117:5377–5384, 2013.

[600] Teck L. Tan, Lin Lin Wang, Jia Zhang, Duane D. Johnson, and Kewu Bai. *ACS Catalysis*, 5:2376–2383, 2015.

[601] M. Moskovits and J. S. Suh. *Journal of the American Chemical Society*, 107:6826–6829, 1985.

[602] Hitesh G. Bagaria, Earl T. Ada, Mohammed Shamsuzzoha, David E. Nikles, and Duane T. Johnson. *Langmuir*, 22:7732–7737, 2006.

[603] Dmitri S. Kilin, Oleg V. Prezhdo, and Younan Xia. *Chemical Physics Letters*, 458:113–116, 2008.

[604] Takuma Hachisu, Takahiro Yotsumoto, Atsushi Sugiyama, and Tetsuya Osaka. *ECS Transactions*, 16:199–206, 2019.

[605] Barbara Farkaš and Nora H de Leeuw. *Nanotechnology*, 31:195711, 2020.

[606] Víctor Rojas-Cervellera, Ernest Giralt, and Carme Rovira. *Inorganic Chemistry*, 51:11422–11429, 2012.

[607] Amado García-Ruiz, Alan Santoveña-Uribe, Juan Palomares-Báez, Marco Chávez-Rojo, Carlos Rodríguez-Proenza, Rodrigo Esparza, José Rodríguez-López, Gabriel Luna-Bárcenas, and Cristy Azanza-Ricardo. *Materials*, 11:1882, 2018.

[608] H.W. Ghebriel and A. Kshirsagar. *Jorunal of Chemical Physics*, 126:244705, 2007.

[609] Peter Ferrin, Shampa Kandoi, Anand Udaykumar Nilekar, and Manos Mavrikakis. *Surface Science*, 606:679–689, 2012.

[610] Lilja Kristinsdóttir and Egill Skúlason. *Surface Science*, 606:1400–1404, 2012.

[611] P. Nordlander, S. Holloway, and J. K. Nørskov. *Surface Science*, 136:59–81, 1984.

[612] M. Respaud, J. M. Broto, H. Rakoto, A. R. Fert, L. Thomas, B. Barbara, M. Verelst, E. Snoeck, P. Lecante, A. Mosset, J. Osuna, T. Ould Ely, C. Amiens, and B. Chaudret. *Physical Review B*, 57:2925–2935, 1998.

[613] T. Ichii, T. Fukuma, K. Kobayashi, H. Yamada, and Matsushige K. *Applied Surface Science*, 210:99–104, 2003.

[614] P. Crespo, R. Litrán, T. C. Rojas, M. Multigner, J. M. De La Fuente, J. C. Sánchez-López, M. A. García, A. Hernando, S. Penadés, and A. Fernández. *Physical Review Letters*, 93:4–7, 2004.

[615] C. Vericat, M. E. Vela, G. Benitez, P. Carro, and R. C. Salvarezza. *Chemical Society Reviews*, 39:1805–1834, 2010.

[616] Luis Puerta, Héctor J. Franco, Juan Murgich, Carlos Gonzalez, Yamil Simón-Manso, and Vladimiro Mujica. *Journal of Physical Chemistry A*, 112:9771–9783, 2008.

[617] C. Gonzalez, Y. Simón-Manso, M. Marquez, and V. Mujica. *Journal of Physical Chemistry B*, 110:687–691, 2006.

[618] Michael J. Hartmann, Jill E. Millstone, and Hannu Häkkinen. *Journal of Physical Chemistry C*, 120:20822–20827, 2016.

[619] Michael J. Hartmann, Jill E. Millstone, and Hannu Häkkinen. *Physical Chemistry Chemical Physics*, 20:4563–4570, 2018.

[620] H. Khurshid, J. Alonso, Z. Nemati, M. H. Phan, P. Mukherjee, M. L. Fdez-Gubieda, J. M. Barandiarán, and H. Srikanth. *Journal of Applied Physics*, 117:17A337, 2015.

[621] Thomas Rapps, Reinhart Ahlrichs, Eugen Waldt, Manfred M. Kappes, and Detlef Schooss. *Angewandte Chemie International Edition*, 52:6102–6105, 2013.

[622] Arpan Mondal, Shu-Qi Wu, Osamu Sato, and Sanjit Konar. *Chemistry – A European Journal*, 26:4780–4789, 2020.

[623] Dong Shao, Shao-Liang Zhang, Le Shi, Yi-Quan Zhang, and Xin-Yi Wang. *Inorganic Chemistry*, 55:10859–10869, 2016.

[624] Wen-Bin Sun, Peng-Fei Yan, Shang-Da Jiang, Bing-Wu Wang, Yi-Quan Zhang, Hong-Feng Li, Peng Chen, Zhe-Ming Wang, and Song Gao. *Chem. Sci.*, 7:684–691, 2016.